Transactions of the ASME

Journal of Fluids Engineering

Published Quarterly by The American Society of Mechanical Engineers

VOLUME 113 • NUMBER 3 • SEPTEMBER 1991

(Contents continued on page 398)

Transactions of the ASME, Journal of Fluids Engineering (ISSN 0098-2202) is published quarterly (Mar., June, Sept., Dec.) for $110.00 per year by The American Society of Mechanical Engineers, 345 East 47th Street, New York, NY 10017. Second class postage paid at New York, NY and additional mailing offices. POSTMASTER: Send address changes to Transactions of the ASME, Journal of Fluids Engineering, c/o THE AMERICAN SOCIETY OF MECHANICAL ENGINEERS, 22 Law Drive, Box 2300, Fairfield, NJ 07007-2300.
CHANGES OF ADDRESS must be received at Society headquarters seven weeks before they are to be effective. Please send old label and new address.
PRICES: To members, $36.00, annually; to nonmembers, $110.00. Add $20.00 for postage to countries outside the United States and Canada.
STATEMENT from By-Laws. The Society shall not be responsible for statements or opinions advanced in papers or . . . printed in its publications (B7.1, Par. 3).

INDEXED by Applied Mechanics Reviews and Engineering Information, Inc.
Canadian Goods & Services Tax Registration #126148048

Contents (continued)

Journal of Fluids Engineering

Editorial

In 1987, the Coordinating Group for Fluid Measurements (CGFM) of the Fluids Engineering Division (FED) was asked by Dr. Frank White, the Technical Editor of the *Journal of Fluids Engineering* (JFE) at that time, to prepare a set of guidelines on estimating experimental uncertainty. The purpose was to alert the authors of the Journal to the fact that estimates of experimental uncertainty enhance the value of information reported. It was also felt that the publication of such guidelines would improve the uniformity of presenting experimental data in the pages of the Journal. Many members of the Committee felt at that time that other reasons justified the publication of such guidelines, as for example, the need for authors to differentiate between bias and precision error and the need to handle correctly single-sample experiments.

The CGFM reviewed existing standards, including PTC 19.1 and the material presented in a collection of papers from JFE in 1985. There is no question that the basic information on how to handle uncertainty is already published. However, it is not written in a practical format as evidenced by usage (or the lack thereof). Existing information is in articles that are too long, depend too much on multiple sample analysis, do not provide perception on how to handle bias error, and give the impression that uncertainty analysis requires disproportionate attention. The current statement in JFE refers authors to those articles but leaves the actual reporting format up to each author without stringent requirements.

Over the past two years the CGFM has struggled to reach a consensus agreement on this statement. A perception has evolved that there must necessarily be three steps to develop good practices in reporting uncertainty estimates. First, a broad outline of policy must be introduced to recognize bias and precision error and the limits for the uncertainty band. Second, terminology must be standardized. Much of the problem in communicating information about uncertainty is in the language. The particular problem is that a differentiation between single and multiple sample experiments *in the context of the notion that these are but endpoints on a continuum* must be made. This seems simple enough, but it is incredibly difficult to accomplish. Third, procedures for handling error, and especially bias error, need to be standardized. So far this seems only possible by using examples.

CGFM intends to continue the steps outlined above, and considers the first step as having been completed with the publication of the following guidelines. These guidelines were arrived at after long discussions and exchange of arguments between the CGFM, some technical associate editors of the Journal, some reviewers and the Technical Editor. Special appreciation is extended to H. W. Coleman and W. G. Steele, the principal authors of the adopted statement.

Edwin P. Rood
Chairman, Coordinating Group for Fluid Measurements

Demetri P. Telionis
Technical Editor, Journal of Fluids Engineering

Journal of Fluids Engineering Policy on Reporting Uncertainties in Experimental Measurements and Results

GUIDELINES

An uncertainty analysis of experimental measurements is necessary for the results to be used to their fullest value. Authors submitting papers for publication to this Journal are expected to describe the uncertainties in their experimental measurements and in the results calculated from those measurements.

The presentation of experimental data should include the following information:

(1) The precision limit, P. The $\pm P$ interval about a result (single or averaged) is the experimenter's 95 percent confidence estimate of the band within which the mean of many such results would fall, if the experiment were repeated many times under the same conditions and using the same equipment. The precision limit is thus an estimate of the scatter (or lack of repeatability) caused by random errors and unsteadiness.

(2) The bias limit, B. The bias limit is an estimate of the magnitude of the fixed, constant error. When the true bias error in a result is defined as β, the quantity B is the experimenter's 95 percent confidence estimate such that $|\beta| \leq B$.

(3) The uncertainty U. The $\pm U$ interval about the result is the band within which the experimenter is 95 percent confident the true value of the result lies. The 95 percent confidence uncertainty is calculated from

$$U = [B^2 + P^2]^{1/2} \quad (1)$$

(4) A brief description of, or reference to, the methods used for the uncertainty analysis. (If estimates are made at a confidence level other than 95 percent, adequate explanation of the techniques used must be provided.)

The estimates of precision limits and bias limits should be made corresponding to a time interval appropriate to the experiment.

It is preferred that the following additional information also be included:

(1) The precision limit and bias limits for the variables and parameters used in calculating each result.

(2) A statement comparing the observed scatter in results on repeated trials (if performed) with the expected scatter ($\pm P$) based on the uncertainty analysis.

Although it is natural in any experimental paper to discuss sources of experimental error in the body of the text, this alone does not satisfy our requirement. All reported data must show uncertainty estimates. All tables should carry estimates. All figures reporting new data should contain uncertainty estimates either on the figure itself or in the caption.

A list of references on the topic, many of which appeared in the pages of this Journal is provided here in alphabetical order.

EXAMPLE

Consider an experiment in which the pressure drop characteristics for fully developed flow conditions in a particular type of circular pipe are determined over a range of water flow rates. The outcome of this experiment might be presented by plotting one result—the Fanning friction factor, f, versus another result, the Reynolds number, Re. To obtain each "data point" that would be plotted on such a figure, the values of f and Re could be calculated from

$$f=\frac{\pi^2}{32}\frac{D^5}{\rho Q^2}\frac{(p_1-p_2)}{(x_2-x_1)} \tag{2}$$

and

$$\mathrm{Re}=\frac{4}{\pi}\frac{\rho Q}{\mu D} \tag{3}$$

where Q is the volumetric flow rate of the water with density ρ and dynamic viscosity μ, D is the pipe diameter, p is the static pressure, x is axial position along the pipe, and the subscripts 1 and 2 refer to the upstream and downstream pressure tap locations, respectively.

The measured variables (Q, D, p_1, p_2, x_1, x_2) and the parameters found from reference property data (ρ, μ) contain bias errors and precision errors. For example, calibrating pressure transducers under static conditions may later introduce bias errors if the measured field involves dynamic motions. Other bias errors arise from calibration of the measurement systems for p and Q against imperfect standards and from using property values originally determined in imperfect experiments. Precision errors could arise, for example, from sensitivity of the pressure transducer, flowmeter and data acquisition system to variations in ambient temperature and humidity. Inability to hold flow rate exactly constant during a period of data acquisition could also appear as a variation in the pressure measurements.

Errors in these quantities will propagate through Eqs. (2) and (3) to produce bias and precision errors in the results f and Re. The techniques of uncertainty analysis described in the references can be used to obtain estimates of the bias limits and precision limits for the variables and parameters and the bias limit, B, the precision limit, P, and the uncertainty, U, in the quantities f and Re.

If the two pressures, p_1 and p_2, are measured successively using the same absolute pressure transducer, the bias errors in the measurements of the two variables will not be independent of each other. This phenomenon of correlated bias errors occurs fairly often in the fluid and thermal sciences, usually when variables are measured using the same transducer or using different transducers that have been calibrated against the same standard. These effects must be taken into account in the uncertainty analysis. A method for doing this is shown in one example in ANSI/ASME PTC 19.1 and is derived and discussed in detail in Chapter 4 of Coleman and Steele (1989).

References

Abernethy, R. B., Benedict, R. P., and Dowdell, R. B., 1985, "ASME Measurement Uncertainty," ASME JOURNAL OF FLUIDS ENGINEERING, Vol. 107, pp. 161–164.

Coleman, H. W., and Steele, W. G., 1989, *Experimentation and Uncertainty Analysis for Engineers*, John Wiley & Sons, New York.

Kline, S. J., and McClintock, F. A., 1953, "Describing Uncertainties in Single-Sample Experiments," *Mechanical Engineering*, Vol. 75, pp. 3–8.

Kline, S. J., 1985, "1983 Symposium on Uncertainty Analysis Closure," ASME JOURNAL OF FLUIDS ENGINEERING, Vol. 107, pp. 181–182.

Kline, S. J., "The Purposes of Uncertainty Analysis," ASME JOURNAL OF FLUIDS ENGINEERING, Vol. 107, pp. 153–160.

Lassahn, G. D., 1985, "Uncertainty Definition," ASME JOURNAL OF FLUIDS ENGINEERING, Vol. 107, p. 179.

Measurement Uncertainty, ANSI/ASME PTC 19.1—1985 Part 1, 1986.

Moffat, R. J., 1982, "Contributions to the Theory of Single-Sample Uncertainty Analysis," ASME JOURNAL OF FLUIDS ENGINEERING, Vol. 104, pp. 250–260.

Moffat, R. J., 1985, "Using Uncertainty Analysis in the Planning of an Experiment," ASME JOURNAL OF FLUIDS ENGINEERING, Vol. 107, pp. 173–178.

Moffat, R. J., 1988, "Describing the Uncertainties in Experimental Results," *Experimental Thermal and Fluid Science*, Vol. 1, pp. 3–17.

Smith, R. E., Jr., and Wehofer, S., 1985, "From Measurement Uncertainty to Measurement Communications, Credibility, and Cost Control in Propulsion Ground Test Facilities," ASME JOURNAL OF FLUIDS ENGINEERING, Vol. 107, pp. 165–172.

An Assessment of Computational Fluid Dynamic Techniques in the Analysis and Design of Turbomachinery—The 1990 Freeman Scholar Lecture

B. Lakshminarayana
Evan Pugh Professor,
Department of Aerospace Engineering,
The Pennsylvania State University,
University Park, PA 16802
Fellow ASME

The objective of this paper is to review and assess various computational fluid dynamic techniques used for the analysis and design of turbomachinery. Assessments of accuracy, efficiency, range of applicability, effect of physical approximations, and turbulence models are carried out. Suggestions are made as to the most appropriate technique to be used in a given situation. The emphasis of the paper is on the Euler and Navier-Stokes solvers with a brief assessment of boundary layer solutions, quasi three-dimensional and quasi-viscous techniques. A brief review of the techniques and assessment of the following methods are carried out: pressure-based method, explicit and implicit time marching techniques, pseudo-compressibility technique for incompressible flow, and zonal techniques. Recommendations are made with regard to the most appropriate technique for various flow regimes and types of turbomachinery, incompressible and compressible flows, cascades, rotors, stators, liquid-handling and gas-handling turbomachinery. Computational fluid dynamics has reached a high level of maturity; Euler codes are routinely used in design and analysis, and the Navier-Stokes codes will also be commonplace before the end of this decade. But to capture the realism in turbomachinery rotors and multi-stage turbomachinery, it is necessary to integrate the physical models along with the computational techniques. Turbulence and transition modeling, grid generation, and numerical techniques play a key role. Finally, recommendations are made for future research, including the need for validation data, improved acceleration schemes, techniques for two-phase flow, improved turbulence and transition models, development of zonal techniques, and grid generation techniques to handle complex geometries.

1 Introduction and Scope of the Review

Turbomachinery flows are among the most complex flows encountered in fluid dynamic practice. In most instances, they are three-dimensional, with laminar, transitional and turbulent flow; separated flows are frequently encountered. The flow may be incompressible, subsonic, transonic, or supersonic; some turbomachinery flows include all of these flow regimes. The flow may be single-phase or two-phase (liquid-solid or liquid-gas). The viscous and turbulent regions encounter complex stress and strain due to three-dimensionality, appreciable pressure gradients in all directions, rotation, curvature, shock-boundary layer interaction, heat transfer and interacting boundary layers. The flow is dominated by vortical flows: secondary, leakage, trailing, horseshoe and scraping vortices. The absolute flow is always unsteady in a rotor, and both the relative and absolute flows are unsteady in a multi-stage environment. The equations are strongly coupled and complex boundary conditions are often encountered (transpiration, periodicity, etc.). The free stream turbulence is usually high.

A large number of flow and thermal parameters are encountered: Reynolds number, Mach number, rotation number, Richardson number, Prandtl number, Eckert's number, Thoma coefficient, flow incidence, etc. The geometrical parameters are also complex and many: camber, blade and blade-row spacing, varying thickness from hub-to-tip and from leading-to-trailing edge, stagger and skew, lean, twist, dihedral, flare, aspect ratio, hub/tip ratio, annulus and hub wall shapes, leading and trailing edge radii, tip clearance, blades with cooling holes, tandem blades, part-span dampers, etc. Not all these effects are present in any given blade row. The flow and geometrical variables dictate the nature of governing equations and flow solvers to be used.

Contributed by the Fluids Engineering Division for publication in the JOURNAL OF FLUIDS ENGINEERING. Manuscript received at ASME Headquarters July 19, 1991.

The discipline of Computational Fluid Dynamics (CFD) has fostered a unified approach to turbomachinery analysis and design. The practice of treating hydraulic machinery, steam turbines, pumps, and gas handling machinery separately is giving way to a more integrated approach. These developments are facilitated by a common denominator—the governing equations are the same for all turbomachinery, with additional constitutive equations employed to handle special cases (e.g., two-phase flows). The boundary conditions encountered in turbomachinery are among the most complex in the CFD field. The equations have to be solved as coupled systems because boundary layer approximations are not valid in many instances.

The emergence of CFD about 10 to 15 years ago provided a major impetus to solve the Euler and Navier-Stokes equations governing the flow field in external and internal flows. Major progress has been made during the last decade in the area of technique development, grid generation, turbulence modeling, application of proper boundary conditions, pre- and post-data processing, and computer architecture. The computational techniques provide an efficient method for the analysis and design of fluid machinery. The use of CFD by fluid machinery manufacturers has increased significantly over the past decade, resulting in a shorter hardware development cycle. Combined with measurements, CFD provides a complimentary tool for simulation, design, optimization and, most importantly, for analysis of complex three-dimensional flows hitherto inaccessible to the engineer. In many instances, it is the only simulation available, because the actual testing of fluid machinery, with detailed measurement in rotating passages, is cumbersome and, in many cases, impossible.

Lack of a coherent and critical review of various techniques and models and their applicability to fluid machinery is a handicap for the fluid dynamicists engaged in design and analysis. At the present time, the turbomachinery CFD field is confusing, with a wide variety of techniques and turbulence models, contradictory at times and often the claims are overstated. An improved understanding of recent advances in computational techniques for fluid machinery and application of this knowledge for the design of more efficient, compact, reliable and quieter fluid machinery should provide substantial improvement over existing design and analytical techniques. A review such as the one carried out here will provide an important link between the computational fluid dynamicists, fluid machinery researchers and the fluid machinery practitioners. What is needed is a critical evaluation of the various computational methods and their ability to capture flow physics accurately. The objective of this paper is to carry out such a review, assessing accuracy, limitations, efficiency, validity in design and analysis, range of applicability, effect of physical and numerical approximations, and to make recommendations and suggest the future course of research. An additional objective is to provide guidance for analytical and design engineers in incorporating these research results into the design and analysis of the next generation of fluid machinery.

The essential ingredients for an accurate solution of the flow field are the following:

(1) Governing equations, including turbulence transport equations; validity of approximations made.
(2) Enforcement of proper boundary conditions.
(3) Adequate grid resolution.
(4) Turbulence modeling.
(5) Numerical technique—effect of artificial dissipation, discretization, convergence history, and assessment.
(6) Efficient code/algorithm development, including vectorization.
(7) Computer architecture, including parallel processing.
(8) Assessment of computational techniques through calibration and validation.

It is impossible to cover all of these topics in a short review, hence the review will be mainly concerned with items (1), (4), (5), and (8).

The computational techniques widely used in turbomachinery practice can be broadly classified as follows:

(1) Inviscid solvers for two-dimensional flows (blade rows).
(2) Quasi-three-dimensional techniques.
(3) Boundary layer solutions, including momentum integral techniques.
(4) Parabolized Navier-Stokes/Space-marching techniques.
(5) Full Euler and Navier-Stokes equations for compressible and incompressible flows.

The emphasis of this review is the latter two topics. The major thrust is to assess various techniques applied to nu-

Nomenclature

A = aspect ratio
a = speed of sound
C = blade chord
C_s, C_1, C_2, C_{ϵ_1}, C_ϵ, C_{ϵ_2}, C_k, C_μ = constants in Reynolds stress and k-ϵ equations (Eqs. (2)–(7))
C_p = blade pressure coefficient/specific heat
dA = infinitesimal area
e = fluctuating specific total energy
E = specific total energy (Eq. (1))
E_0 = $E + V^2/2$
E, F, G = flux vector (Eq. (1))
h = semi-blade height
H = static enthalpy (Eq. (1))
H_0 = stagnation enthalpy (Eq. (1))
i = incidence
k = turbulence kinetic energy
M = Mach number
N = distance normal to the surface of blade normalized by chord length
n = iteration level, time step
p = static pressure
P = production of turbulence kinetic energy/stagnation pressure
Pr = Prandtl number
ps, ss = pressure and suction surface
q = heat transfer rate (Eq. (1))
Q = primary transport variable vector (Eq. (1))
r, θ, z = cylindrical coordinate system
R = radius (for rotor $R = 1$ at the tip)
R_T = turbulent Reynolds number ($k^2/\nu\epsilon$)
Re = Reynolds number (based on chord)
s, n = streamwise and normal distance
S = streamwise distance from leading edge, normalized by chord length/source term vector (Eq. (1))
S_{ik} = strain tensor
St = Stanton number
t = blade spacing/time
T = temperature
U = blade speed
V = absolute velocity
w = fluctuating relative velocity
W = relative velocity

merous geometries encountered in practice, and provide recommendations as to the most appropriate computational technique for the design and analysis of turbomachinery.

The cascade solution (e.g., panel method), quasi-three-dimensional solution, and boundary layer solutions have been widely used for more than two decades and are now well established as research and design tools in industry. These classical techniques, which have been in use since the early seventies, will not be covered in detail in this review, but a brief assessment will be made.

The selection of topics covered in this paper is based on recent developments. Adler (1980) and McNally and Sockol (1981) provided a comprehensive review of computational methods for turbomachinery flows and the techniques developed mainly in the 1970's. The major emphasis of this paper will be on techniques for numerical solution of two-dimensional and three-dimensional Euler and Navier-Stokes equations and design methodology for turbomachinery, developed in the 1980's. Lakshminarayana (1986) reviewed the turbulence models used in turbomachinery flow. Hence, the review of turbulence modeling applicable to turbomachinery flow will be brief. The topic of transition in general and application to turbomachinery in particular are reviewed by Narasimha (1985) and Mayle (1991), respectively. Even though transition modeling is of prime importance in turbomachinery flow prediction, the state-of-the-art knowledge is unsatisfactory for the prediction of flow through turbines, compressors and pumps. For brevity, transition modeling is not covered in this review. One other review relevant to this topic is by Shang (1985), who assessed the various computational techniques for the prediction of flow over an aircraft. There are many reviews on numerical techniques, the most comprehensive of which is Hirsch's (1990) book. In view of this, no attempt will be made in this paper to provide a detailed description and analysis of various numerical techniques.

The topics covered in this review include: finite-difference and finite-volume techniques, brief exposure to turbulence modeling, space-marching/parabolized Navier-Stokes solution, full Euler and Navier-Stokes solution, incompressible through supersonic flow regimes, applicability to analysis and design, assessment and validation of physical, numerical and geometrical approximations. The configurations covered include cascades, compressors, hydraulic and gas turbines, and pumps.

The following topics are not covered: grid generation, finite-element techniques, details of numerical techniques, transition, heat transfer, unsteady flows, hybrid analytical/numerical solutions, and quasi-three-dimensional and boundary layer solutions. A brief assessment of the latter two techniques is given for the sake of completeness.

Major advances have been made in the numerical solutions of the Navier-Stokes equations. It is neither possible nor necessary to cover all of the approaches in a short review such as this paper. Hence, only those techniques which are likely, in the opinion of the author, to be used widely will be covered. Most turbomachinery flows are turbulent in nature and hence the emphasis is placed on turbulent flows.

In the area of design, Navier-Stokes solutions are used in the final stages to check problem areas (e.g., laminar, and turbulent separation, adverse pressure gradient areas, shock location, etc.) and before the end of the decade, they will find widespread use in the early stages of design. Hence, an assessment of Navier-Stokes techniques is timely. It is hoped that this review article will provide a basis for the selection of technique and code for particular applications.

A final section on future research required to advance the state-of-the-art CFD techniques to capture real flow physics and to improve accuracy and efficiency is provided. Since the design phase involves a large number of repetitive calculations, a code has to be efficient. An improvement in computer time of at least one order of magnitude or major reduction in computational cost through improved computer architecture is necessary before Navier-Stokes solutions can become a day-to-day tool in industry.

2 Governing Equations and Boundary Conditions

The governing equations employed are in either control volume formulation (for finite volume discretization) or differential form (for finite difference discretization). The most appropriate coordinate system for turbomachinery application is the rotating cylindrical coordinate system. The equations in control volume formulation can be found in most text books. For example, White (1991, pp. 96–100) has provided the con-

Nomenclature (cont.)

$W_{i,j}$ = $\partial W_i/\partial x_j$
X = axial distance from leading edge
x, y, z = Cartesian coordinate system
Y = tangential distance (blade-to-blade)
Z = distance normal to endwall
α = absolute flow angle measured from the axial direction
β_1, β_2 = relative inlet and outlet flow angle measured from axial direction
ΔV = infinitesimal volume
$\Delta t, \Delta x, \Delta y$ = time and spatial steps
ϵ = turbulent energy dissipation rate
ϵ_{ipj} = alternating tensor
λ = stagger angle
μ = molecular viscosity
μ_t = turbulent eddy viscosity
ρ = density
$\rho\overline{w_i w_j}$, $\rho\overline{w_\theta^2}$, etc. = turbulent stresses (Eq. (1))
σ = net positive suction head/$0.5V^2$
τ = shear stress
ψ_{loss} = stagnation pressure loss coefficient (based on relative stagnation pressure for rotor flows)
Ω = angular velocity
δ_{ik} = Kronecker delta

Subscripts

e = edge condition
is = isentropic
m = meridional component
O = stagnation properties
OR = stagnation properties in relative system
r, θ, z = radial, tangential and axial components
s, n, r = streamwise, normal and radial components
w = wall
z = axial component
x, y, z = components in Cartesian system
∞ = free stream
1, 2 = inlet, exit

Superscript

$\overline{}$ = passage averaged

tinuity, momentum, and energy equations in control volume formulation.

The most appropriate system of equations in differential form are the Reynolds averaged Navier-Stokes equations in a rotating cylindrical coordinate system given by:

$$\frac{\partial Q}{\partial t}+\frac{1}{r}\frac{\partial (rE)}{\partial r}+\frac{1}{r}\frac{\partial F}{\partial \theta}+\frac{\partial G}{\partial z}=\frac{1}{r}S \tag{1}$$

Conservation Variables Q, flux vectors E, F, G, Source Term S are given by:

$$Q=\begin{bmatrix}\rho\\ \rho W_r\\ \rho W_\theta\\ \rho W_z\\ \rho E_0\end{bmatrix},\quad E=\begin{bmatrix}\rho W_r\\ \rho W_r^2+p-\tau_{rr}\\ \rho W_r W_\theta-\tau_{r\theta}\\ \rho W_r W_z-\tau_{rz}\\ \rho W_r H_0-W_r\tau_{rr}-W_\theta\tau_{r\theta}-W_z\tau_{zr}+q_r\end{bmatrix},$$

$$F=\begin{bmatrix}\rho W_\theta\\ \rho W_\theta W_r-\tau_{\theta r}\\ \rho W_\theta^2+p-\tau_{\theta\theta}\\ \rho W_\theta W_z-\tau_{\theta z}\\ \rho W_\theta H_0-W_r\tau_{\theta r}-W_\theta\tau_{\theta\theta}-W_z\tau_{\theta z}+q_\theta\end{bmatrix},$$

$$G=\begin{bmatrix}\rho W_z\\ \rho W_z W_r-\tau_{zr}\\ \rho W_z W_\theta-\tau_{z\theta}\\ \rho W_z^2+p-\tau_{zz}\\ W_z H_0-W_r\tau_{zr}-W_\theta\tau_{z\theta}-W_z\tau_{zz}+q_z\end{bmatrix},$$

$$S=\begin{bmatrix}0\\ p+\rho W_\theta^2+\rho\Omega^2 r^2+2\rho r\Omega W_\theta\\ -\rho W_r W_\theta-2\rho r\Omega W_r\\ 0\\ 0\end{bmatrix}$$

Components of shear stress tensor and heat flux vector are given by:

$$\tau_{\theta\theta}=\frac{2}{3}\mu\left[2\left(\frac{1}{r}\frac{\partial W_\theta}{\partial\theta}+\frac{W_r}{r}\right)-\frac{\partial W_z}{\partial z}-\frac{\partial W_r}{\partial r}\right]-\rho\overline{w_\theta^2}\qquad q_\theta=-\gamma\left(\frac{\mu}{\mathrm{Pr}}\right)\frac{1}{r}\frac{\partial E}{\partial\theta}+\rho\overline{w_\theta e}$$

$$\tau_{zz}=\frac{2}{3}\mu\left[2\frac{\partial W_z}{\partial z}-\frac{\partial W_r}{\partial r}-\frac{W_r}{r}-\frac{1}{r}\frac{\partial W_\theta}{\partial\theta}\right]-\rho w_z^2\qquad q_z=-\gamma\left(\frac{\mu}{\mathrm{Pr}}\right)\frac{\partial E}{\partial z}+\rho\overline{w_z e}$$

$$\tau_{rr}=\frac{2}{3}\mu\left[2\frac{\partial W_r}{\partial r}-\frac{W_r}{r}-\frac{1}{r}\frac{\partial W_\theta}{\partial\theta}-\frac{\partial W_z}{\partial z}\right]-\rho\overline{w_r^2}\qquad q_r=-\gamma\left(\frac{\mu}{\mathrm{Pr}}\right)\frac{\partial E}{\partial r}+\rho\overline{w_r e}$$

$$\tau_{z\theta}=\tau_{\theta z}=\mu\left[\frac{\partial W_\theta}{\partial z}+\frac{1}{r}\frac{\partial W_z}{\partial\theta}\right]-\rho\overline{w_z w_\theta}$$

$$\tau_{rz}=\tau_{zr}=\mu\left[\frac{\partial W_z}{\partial r}+\frac{\partial W_r}{\partial z}\right]-\rho\overline{w_r w_z}$$

$$\tau_{r\theta}=\tau_{\theta r}=\mu\left[\frac{1}{r}\frac{\partial W_r}{\partial\theta}+\frac{\partial W_\theta}{\partial r}-\frac{W_\theta}{r}\right]-\rho\overline{w_r w_\theta}$$

Various approximations to these equations will be dealt with later. The independent variables in these equations are W_r, W_θ, W_z, ρ, p, E, H_0, $\rho\overline{w_i w_j}$, $\rho\overline{w_i e}$. An equation of state ($P=\rho RT$), Sutherland's viscosity law, and constant Pr number assumptions will enable prediction of all the variables for laminar flow. The formulation assumes Stokes hypothesis that the second viscosity is $-2\mu/3$.

For turbulent flow, nine additional variables ($\rho\overline{w_i w_j}$, $\rho\overline{w_i e}$) have to be evaluated. The most general transport equations for turbulence are the Reynolds stress equations. Many of the terms in these equations have to be modeled. The modeled Reynolds stress equations are given by (Launder et al., 1976)

$$(\rho\overline{w_i w_k}W_j)_{,j}=C_s\frac{k}{\epsilon}\left[\overline{w_j w_l}\left(\overline{w_i w_k}\right)_{,l}\right]_{,j}-\left[\rho\overline{w_i w_j}W_{k,j}+\rho\overline{w_j w_k}W_{i,j}\right]$$

(1) (2) (3)

$$-C_1\rho\frac{\epsilon}{k}\left(\overline{w_i w_k}-\frac{2}{3}\delta_{ik}k\right)-C_2\left(P_{ik}-\frac{2}{3}\delta_{ik}P\right)$$

(4)

$$-\frac{2}{3}\rho\epsilon\delta_{ij}-2\rho\Omega_p(\epsilon_{ipj}\overline{w_k w_j}+\epsilon_{kpj}\overline{w_i w_j}) \tag{2}$$

(5) (6)

where $P_{ik}=-\rho(\overline{w_i w_j}\,W_{k,j}+\overline{w_k w_j}\,W_{i,j})$ and $C_s=0.23$, $C_1=1.5$, $C_2=0.6$.

The terms marked 1—6 represent convection, diffusion, production, pressure-strain, dissipation, and redistribution due to Coriolis force, respectively. Details of modeling for nonrotating flows can be found in Launder et al. (1976) and Lumley (1980). Raj and Lakshminarayana (1974) investigated the effect of rotation on various terms in the Reynolds stress equations and derived a dissipation equation for rotating flow. An additional transport equation for dissipation of a kinetic energy is necessary to solve Eq. (2).

The model presented above is one of the simplest and satisfies many of the physical constraints. Shih and Lumley (1986) provided one of the most accurate modeling of these equations, which satisfy the realizability condition (requiring that the diagonal terms of the turbulent stress tensor remain positive and the Schwartz inequality hold for all nondiagonal terms), thus ensuring physically realizable values, and the condition of material indifference, which requires that the modeled terms have the same tensor form as the original terms, ensuring that the turbulent products are independent of the frame of reference.

The modeled transport equations for turbulent kinetic energy (k) and dissipation (ϵ) are given by: (Jones and Launder, 1972)

$$(\rho k W_j)_{,j}=\left[\left(\mu+\frac{\mu_t}{C_k}\right)k_{,i}\right]_j+P-\rho\epsilon \tag{3}$$

(1) (2) (3) (4)

$$(\rho\epsilon W_j)_{,j}=\left[\left(\mu+\frac{\mu_t}{C_\epsilon}\right)\epsilon_{,i}\right]_j+C_{\epsilon_1}\rho\frac{\epsilon}{k}P-C_{\epsilon_2}\rho\frac{\epsilon^2}{k} \tag{4}$$

(1) (2) (3) (4)

The usual constants are:

$C_k=1.0$, $C_\epsilon=0.23$, $C_{\epsilon_1}=1.44$, $C_{\epsilon_2}=1.92$,

and $P=-\rho\overline{w_i w_j}\,W_{i,j}$, $\epsilon=2\nu\overline{S'_{ij}S'_{ij}}$, $S'_{ij}=$ fluctuating strain

In Eqs. (3) and (4), the terms 1–4 are convection, diffusion, production, and dissipation. There have been many modifications to these equations (some ad hoc) to account for curvature, rotation and near-wall effect. These are discussed in Lakshminarayana (1986), Patel et al. (1985) and Speziale et al. (1990).

Equations (2)–(4) are modeled equations, and most of the modeling is based on physical mechanisms in simple flows. For complex flows, the diffusion and dissipation terms have to be modified to include complex strain effects. The direct effect of rotation is included in Eq. (2); the indirect curvature effects can be incorporated by writing Eq. (2) in generalized tensor form. An assessment of turbulence models employed in CFD is given in a later section.

Boundary Conditions for Turbomachinery Blade Rows. Specification and enforcement of proper boundary conditions are essential to accurately capture the physics of the flow. Scott (1985) provided a detailed discussion on boundary conditions for turbomachinery. The important variables are $\underline{W}$, p, ρ, T, k, ϵ, T, $P_0(h_0)$. If there is no injection, a no-slip boundary condition is imposed on $\underline{W}$ for the Navier-Stokes equation on the solid surfaces. For inviscid equations (without injection), the velocity vectors are parallel to the surface. For temperature, either the wall temperature or the normal temperature gradient is specified. For the nonadiabatic wall condition, it is necessary to carry out a heat transfer analysis to derive the wall temperature. For inviscid and adiabatic flows, the pressure and velocities are related by energy equations; hence, the pressure can be derived at the boundary from the prescribed or derived velocity for the Navier-Stokes equation. Typically, either $\partial p/\partial n$ is assumed to be zero or $\partial p/\partial n$ is evaluated by solving the normal momentum equation at the surface.

The prescription of the inflow and the outflow boundary conditions is one of the most important tasks. Strictly speaking, these surfaces should be located far upstream and far downstream, where the influence of the blade row under consideration is negligible. Current computer capability and sometimes grid topology makes it prohibitive to employ the ideal conditions. Hence, most investigators locate them usually at about one to one half-chord upstream and downstream. The prescription of the conditions at inlet and exit boundaries depends on the flow regime (subsonic or supersonic) and the nature of equations. Most authors prescribe T_0 (or h_0), P_0 and either the flow angles or the relative velocity components at inflow boundaries where the axial velocity is subsonic. The static pressure is prescribed at the outlet for subsonic flow, and hence the inlet static pressure is part of the solution in time-iterative methods. If the equations are solved in the rotating coordinate system, inlet relative stagnation pressure (P_{OR}) and temperature (T_{OR}) and the blade speed are typically prescribed. The static pressure is usually prescribed at the hub at the exit, and the radial distribution is determined from a simple radial equilibrium equation $\partial p/\partial r = \rho V_\theta^2/r$ using the computed flow outlet angle. If the k-ϵ model is employed for turbulence closure, the upstream values are prescribed for k, and the ϵ value is derived from a solution of the ϵ equation (or approximated by a length scale). The downstream condition has to be iterated or a gradient boundary condition is prescribed ($\partial k/\partial s = \partial \epsilon/\partial s = 0$).

To simulate infinite blade row conditions, it is essential to enforce periodic boundary conditions upstream and downstream of the blade row. This is accomplished by setting the dependent variables equal at the two periodic boundaries, using the adjoining periodic surfaces. In implicit techniques (elliptic and hyperbolic), a tridiagonal matrix of length N results for the solution of the flow between boundaries. For the enforcement of periodic boundary conditions, an additional grid point is incorporated into the system, resulting in a cyclic $(N + 1)$ system of simultaneous equations; this results in a cyclic tridiagonal matrix system.

3 Assessment of Turbulence Models

The turbulence in turbomachinery flows is affected by rotation, curvature, three-dimensionality, separation, freestream turbulence, compressibility, large scale unsteadiness, heat transfer and other complex strain effects. Only the Reynolds stress Eq. (2) contains some of these effects explicitly. In the zero-equation or algebraic eddy-viscosity formulation, the Reynolds stress transport equations are not employed. The turbulent motion is assumed to be analogous to molecular motion, and the molecular viscosity is replaced by an eddy viscosity given by:

$$\overline{w_i w_j} = \mu_t [W_{i,j} + W_{j,i}] - \frac{2}{3}\delta_{ij} k \tag{5}$$

Turbulence is a property of the flow rather than of the fluid; hence, empirical correlations are employed to represent the variation of eddy viscosity inside a boundary layer. The model is not suitable for most turbomachinery applications (Lakshminarayana, 1986), even though it is still widely used in both external and internal flows.

The algebraic eddy-viscosity model is strictly valid only for two-dimensional "simple shear flows." Various data and comparisons available indicate the following conclusions:

(1) The model is adequate for two-dimensional compressible flows with a mild pressure gradient. The mean velocity field is predicted well.

(2) The model is suitable for three-dimensional boundary layers with small cross flows.

(3) The model is not valid for flows with curvature, rotation, or separation.

(4) The model is not valid for pressure or turbulence-driven secondary flows and when abrupt changes in strain or shear rate are present.

(5) The model cannot accurately predict shock-induced separated flow.

It should be noted that for an attached two-dimensional boundary layer with a mild pressure gradient, there is very little advantage in resorting to a higher-order model. The algebraic eddy viscosity model is adequate for the prediction of the mean velocity field.

An improvement over the empirically determined eddy viscosity distribution is the model proposed by Jones and Launder et al. (1972) which relates the eddy viscosity to local properties of turbulence:

$$\mu_t = C_\mu \rho \frac{k^2}{\epsilon} \tag{6}$$

Most authors use the constant value $C_\mu = 0.09$; hence, μ_t is assumed to be scalar, severely restricting its applications to complex flows.

In the "two-equation" model, the turbulent kinetic energy and dissipation equations (Eqs. (3) and (4)) are solved to calculate μ_t from Eq. (6) and μ in Eq. (1) is replaced by $\mu + \mu_t$. The k-ϵ model has been successfully used to predict two-dimensional attached flows with pressure gradient. The mean and gross properties of turbulence are predicted well. Due to the shortcomings associated with the assumption of isotropy, the model fails for flows with rotation, curvature, strong three-dimensionality and separation. The constants used in these models are based on well-documented two-dimensional boundary layer data. Numerous attempts to modify and refine the k-ϵ model to include curvature, rotation and other effects have not been successful; hence, the k-ϵ model should be replaced with higher order turbulence models. The effect of rotation is to redistribute the energy (term 6 in Eq. (2)); hence, the rotation effect does not appear explicitly in transport of kinetic energy. The kinetic energy is neither destroyed nor produced by rotation effects, but rotation has a major effect on redistribution of $\overline{w_i w_j}$.

Some of the conclusions concerning the k-ϵ models based on the results from various investigators (Lakshminarayana, 1986) are as follows:

(1) The k-ϵ equations have been widely used for two-dimensional flows with a pressure gradient. Mean velocities are predicted fairly accurately for these cases, and gross properties of the turbulence are predicted well. The model is good for attached two-dimensional boundary layers. For these cases, the Reynolds Stress Model (RSM) has little advantage over the k-ϵ model.

(2) The k-ϵ model is much superior to algebraic eddy viscosity models.

(3) The predictions from the k-ϵ model are not good for three-dimensional flows. Shortcomings are due to the modelling of the pressure-strain term, assumption of isotropy and low Reynolds number formulation near the wall. An isotropic eddy viscosity is adequate for three-dimensional boundary layers with very small cross flow, but fails for significant cross flows and swirl.

(4) The model fails for flow with rotation, curvature, strong swirl, three-dimensionality, and shock-induced separation.

When curvature, rotation, and other extra strain effects are present, the Reynolds stress closure equations can provide a more realistic and rigorous approach to account for these complex strain fields. These models require empirical modeling of C_μ or modification to constants in the k and ϵ transport equations. Some of these attempts will be described below.

Algebraic Reynolds Stress Model. The modeled Reynolds stress equations (Eq. (2)) are extremely complicated to solve for a three-dimensional flow. There are six Reynolds stress transport equations, resulting in a total of 10–12 transport equations for the mean flow and turbulence quantities. This is beyond the routine capability of today's supercomputers. Therefore, several attempts have been made to simplify the Reynolds stress transport equations. The simplification is aimed at reducing these partial differential equations to algebraic equations.

One of the successful models is due to Rodi (1976), who provided an algebraic equation for the Reynolds stresses. In this approach, the source term in the Reynolds stress equation is assumed to be proportional to the source terms in the kinetic energy equation. The net transport of stress ($\overline{w_i w_j}$) is assumed to be proportional to the net transport of k, the proportionality factor being $\overline{w_i w_j}/k$. Galmes and Lakshminarayana (1984) extended Rodi's analysis to flow with rotation. Their generalized equations are given below.

$$\frac{\overline{w_i w_k}}{k} = \frac{2}{3}\delta_{ik} + \frac{R_{ik}\left(1-\frac{C_2 F}{2}\right) + \left(P_{ik} - \frac{2}{3}\delta_{ik}P\right)(1-C_2F)}{P+\rho\epsilon(C_1F-1)} - \frac{\frac{2}{3}\rho k R_T^{-1/2}\overline{\delta_{ik}}}{P+\rho\epsilon(C_1F-1)}$$

$$R_{ik} = -2\rho\Omega^p(\epsilon_{ipj}\overline{w_k w_j} + \epsilon_{kpj}\overline{w_i w_j}) \tag{7}$$

where F is a wall damping function.

It should be remarked here that even though the diffusion and advection of $\overline{w_i w_k}$ do not appear explicitly, they appear implicitly through the transport equations for k and ϵ. Therefore, the ARSM cannot be used alone, but should be employed in conjunction with the k-ϵ equations. Thus, the $k\epsilon$-ARSM model would constitute Eqs. (3), (4), (6), and (7).

There have been many attempts to use the ARSM models in conjunction with the k-ϵ models for the computation of turbulent flows. These attempts may be classified as follows:

(1) Modified k-ϵ via C_μ from the ARSM

(2) Coupled k-ϵ/ARSM models.

In the former models, the value of C_μ is corrected locally through the ARSM (Warfield and Lakshminarayana, 1987). These models still employ the eddy viscosity concept. These models seem to predict most complex flows involving rotation and curvature. In the latter model, k-ϵ and ARSM models are solved as coupled equations.

The use of the k-ϵ/ARSM does not entail any significant additional resources because these are algebraic equations, and computational time is increased only moderately. The dramatic effect of curvature and rotation, and the inability of the k-ϵ model in capturing these effects can be seen in recent predictions by Hutchings and Iannuzzelli (1987) who utilize Rodi and Scheurer's (1983) ARSM. The predictions from standard k-ϵ models for the swirling flow in a duct is shown compared with experimental data in Fig. 1. The k-ϵ model misses the major features of the flow completely, while k-ϵ/ARSM provide excellent agreement with the data. The k-ϵ model fails to predict the basic features of the swirling flow, such as the recirculating zone along the center line.

Zhang and Lakshminarayana (1990), recently modified Eq. (7) to include the Reynolds stress model proposed by Shih and Lumley (1986) and successfully predicted the three-dimensional boundary layer profile on a compressor rotor blade (Popovski and Lakshminarayana, 1986). The comparison shown in Fig. 2 indicates that the prediction of mean velocity profiles, especially the radial component, is substantially improved with ARSM. The location and magnitude of the maximum radial velocity is not captured well at $S = 0.87$ and $R = 0.75$. The predictions at all other radial locations are predicted well through the use of the coupled k-ϵ/ARSM model.

In summary, k-ϵ/ARSM models simulate the turbulent stresses more realistically by relating the properties to local conditions. The k-ϵ/ARSM model is efficient and inexpensive, and predicts important features of the flow. The rotation and curvature effects are captured directly instead of through modeling. Hah (1984), Warfield and Lakshminarayana (1987, 1989), and Hah and Lakshminarayana (1980a, 1980b) have made extensive use of ARSM models to predict three-dimensional viscous flows inside turbomachinery including rotor wakes, turbine endwall flows, and tip clearance flows.

The full Reynolds stress model (RSM) provides a more realistic physical simulation of turbulent flow and is potentially the superior model. However, it is very complex, and the least tested model so far. Nevertheless, its use is likely to become widespread during the next decade for both simple and complex flows. Even this model does not constitute a complete closure for turbulence. Details of the model can be found in Launder et al. (1976) and Lumley (1980). Launder et al. (1987) used the RSM model to compute the flow in a rotating duct. Their predictions are about the same quality as the results from the ARSM (Warfield and Lakshminarayana, 1987a).

For three-dimensional flows with curvature, rotation, or shock separation, the k-ϵ equations should be coupled with either an ARSM or RSM to provide adequate prediction of the mean and the turbulence flow field. If the interest lies only in the mean quantities, the k-ϵ model modified to include a vectorial representation of C_μ (through the ARSM) may be adequate. For cases where shock-induced separation exists, none of the present models would predict the turbulence amplification through the shock. In terms of specific models for the coupled k-ϵ/ARSM, the curvature effects are captured well by Rodi and Sheuerer (1983) and Pourahamadi and Humphrey (1983). The rotation effects are captured well by the models by Warfield and Lakshminarayana (1987) and Zhang and Lakshminarayana (1990).

Many of the investigators employ slip conditions, both for turbulence and mean velocity, and this may mask many of the deficiencies in the turbulence modeling or the code. It is desirable to determine wall conditions from the ARSM. None of these models have been tested on very complex flows such as the shroud wall boundary layer development, where the viscous layer is subjected to sudden application and removal of strain through a series of rotating and stationary blade rows.

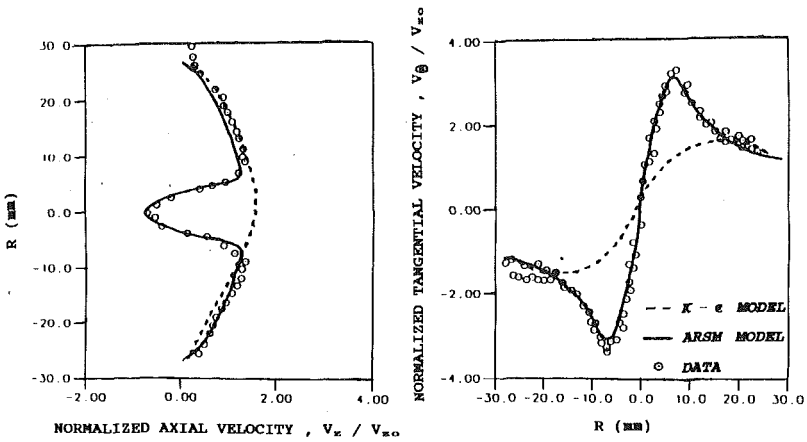

Fig. 1 Confined vortex flow
(data: Escudier et al., 1980; computation: Hutchings and Iannuzzelli, 1987)

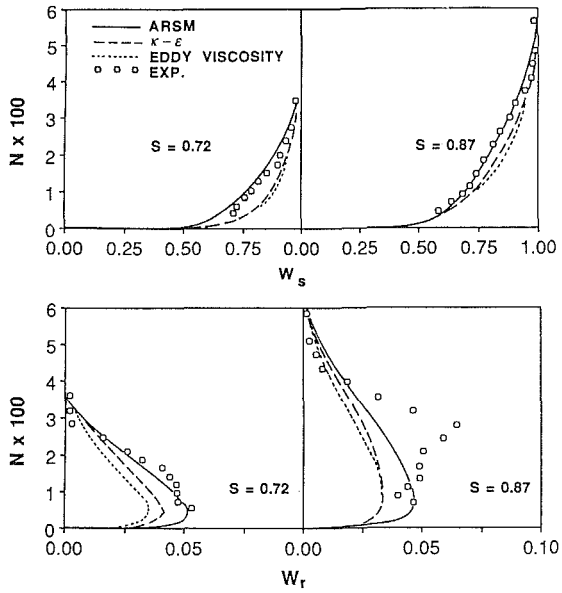

Fig. 2 Compressor rotor suction surface boundary layer at midspan (Zhang and Lakshminarayana, 1990)—Penn State Low Speed Compressor
(Outer dia = 0.936 m, speed 1080 rpm, Reynolds number 2.8 × 10^5, 21 rotor blades, tip chord = 15.41 cm)

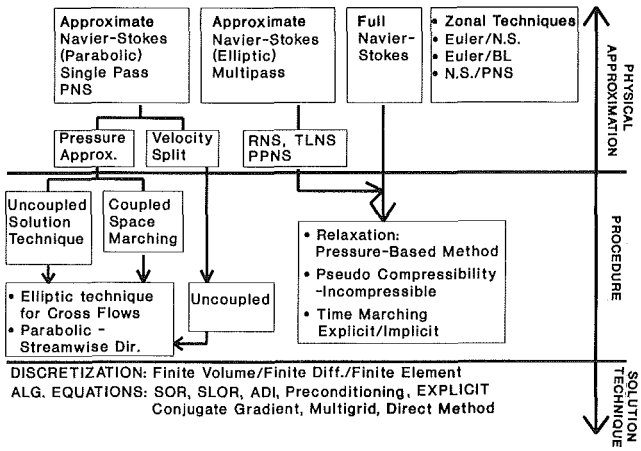

Fig. 3 Computational techniques for turbomachinery

The numerical computation of turbomachinery flows using large eddy simulation is prohibitively expensive, and its use is presently limited to very simple flows (flat plate boundary layer, channel flows, etc.)

4 Overview of Approximations

There are two types of approximations in the numerical solution of governing equations. The governing equations are approximated depending on the physics of the flow field. Further approximations are in numerical discretization and techniques in solving these equations. The local accuracy of solutions progressively diminishes as approximate equations are solved numerically. The classification for Navier-Stokes equations is illustrated in Fig. 3. The most general equations are the time-dependent Navier-Stokes equations. The range of validity covers the entire spectrum of turbomachinery.

The techniques, classified according to the physical approximations made, are as follows:

(1) Inviscid flow: The viscous terms are neglected and the resulting equations are solved by any of the following techniques: panel method (incompressible, irrotational, two-dimensional flow), potential equation (irrotational, 2D, 3D), stream function equation (2D), Euler equation (2D, 3D).

(2) Boundary layer approximations: In this technique, the viscous approximation involves the neglect of streamwise diffusion terms. The pressure field is assumed to be imposed by the inviscid layer and this is prescribed from an inviscid analysis. This assumption is valid when the viscous layers are thin compared to the blade spacing. It is not valid in the endwall region of the blade row or in the presence of vortices.

(3) Parabolized Navier-Stokes (PNS) equation/space marching techniques: The assumption made in this technique is similar to the boundary layer assumption, but the technique allows for transverse and normal pressure gradients. The streamwise pressure gradient is prescribed from an inviscid code, and can be continuously updated to capture the flow physics. All of the techniques which utilize single pass spatial marching are included in this category. A second type of inviscid approximation (with the same viscous approximation as above) does not employ any approximations for the pressure gradient term, and instead approximates the convective terms in the cross (y, z, or η, ζ) momentum equations by decomposing the velocity into potential, rotational, and viscous terms.

(4) Thin Layer (TLNS)/Reduced Navier-Stokes Equation (RNS): In TLNS, the streamwise diffusion term is neglected and as the name implies, this is valid for thin viscous layers. It is also a useful simplification on computational grids that are too coarse to resolve the streamwise diffusion terms. In reduced Navier-Stokes equations, the viscous terms in the equation normal to a surface are neglected.

(5) Full Navier-Stokes solution: There are two types of solutions. In the first type, the entire equation is solved in either the steady or the unsteady form. In the second approximation, parabolic assumptions are made initially, and the pressure is updated in subsequent iterations or passes. The latter technique is not the PNS solution described earlier, but rather an initial approximation to this pressure field, which is updated to satisfy the entire Navier-Stokes equations. Therefore, the converged solution satisfies the full Navier-Stokes equations, even though the final stage was achieved through several intermediate approximations.

(6) Zonal technique: The solution of the full Navier-Stokes equation in the entire domain can be expensive. Hence zonal techniques, where several zones are identified and the corresponding (inviscid, boundary layer, parabolic) solutions are obtained and patched and integrated to obtain a composite solution. These are described in detail later and are accurate, but are much less expensive techniques.

Many regions of the flow may have a weak pressure field with a thin boundary layer and without any influence of curvature and rotation. It is not economical or efficient to solve the full Navier-Stokes equation in the entire region. Full Navier-Stokes solutions are exact, with the exception of modelling for the transition, turbulence, differencing scheme and the level of convergence. The solution of complex flow with a Navier-Stokes solver is expensive due to complex geometry and the flow field, both of which require fine mesh. Therefore, it is desirable to match the flow regions with a suitable approximation and to solve that region with the most efficient equation and technique. For example, viscous flow through a two-dimensional cascade with subsonic attached flow can be most accurately predicted using one of the inviscid techniques (e.g., panel code or solution of potential equations), combined with a good boundary layer code. It is unnecessary and inefficient to solve the full Navier-Stokes equations for this flow. Likewise, swirling flow through diffusers and ducts with large boundary layer growth can be best handled by making suitable approximations to reduce the Navier-Stokes equations to a parabolic form. A spatial marching solution should provide reasonably good results for most practical purposes. The boundary layer code is nearly two orders of magnitude more efficient, and the space-marching code is about one order of magnitude more efficient (in computer time) than a corresponding full Navier-Stokes solution. Boundary layer and space-marching codes are valuable tools in design, as they enable a large number of calculations to be made in a reasonable time. For many flows, such as the ones mentioned earlier, the accuracy of the solution from any of these techniques is about the same.

Some turbomachinery flows are dominated by inviscid effects such as flow turning, blade thickness, blunt leading edge, lean and skew, etc. It is not necessary to solve such flows by full Navier-Stokes equations, as it is prohibitively expensive. The major physics are captured by Euler equations, and viscous effects are estimated from a boundary layer code for nonseparated zones. Inviscid and viscous regions are identified and the corresponding equations are solved, and the boundary between the zones is iterated until a converged solution is obtained. On the other hand, viscous dominated flow, such as a flow in a transonic compressor with strong three-dimensional shocks and associated boundary layers, is best resolved by solving the Navier-Stokes equation in the entire region.

The techniques for viscous flow mentioned in this section are tabulated in Fig. 3. One must clearly distinguish between the approximations which involve physical phenomena and the mathematical approximations for numerical analysis such as finite difference, finite volume, finite element, etc. The error involved in solution can be classified as (1) those arising due to physical approximation, (2) those arising from discretization such as order of discretization, grid size, method of solution, control point, geometry and boundary representation, factorization error, linearization, etc., (3) those arising from iterative solution of algebraic equations (ADI, SOR, SLOR, etc.). The classification is based on the physical approximation (e.g., boundary layer, parabolized Navier-Stokes, etc.).

5 Assessment of Computational Techniques for Inviscid Flows, Quasi-Viscous Flows

The computational techniques available for inviscid flows in turbomachinery can be classified as follows:

(1) Method of singularity—panel method. (2-D cascade flows)

(2) Two-dimensional and three-dimensional potential flow solutions.

(3) Two-dimensional, quasi three-dimensional, stream function equations and their solutions.

(4) Two-dimensional and three-dimensional Euler solutions.

(5) Secondary flow theories.

The techniques used for the solution of the Euler and the Navier-Stokes equations are usually the same. These techniques and their assessments will be covered together in a later section.

The validity of potential flow solutions to turbomachinery flows is restricted to two-dimensional cascade flows. The three-dimensional flows are almost invariably rotational and the existence of potential flow is an exception in this case. In view of this, the treatment of potential flows in cascades has been kept deliberately brief. The panel method is valid for irrotational and incompressible flows. Attempts have been made to include corrections for compressibility effects (McFarland, 1982). For low to moderate subsonic, inviscid two-dimensional, irrotational cascade flow, this technique is most suitable. The pressure distribution can be predicted accurately. The technique is the most efficient and economical, and it is unnecessary to resort to any other technique if the interest lies only in the pressure distribution. This method can be coupled to a boundary layer code to predict viscous effects and losses.

Some of the most widely used quasi-three-dimensional and inviscid techniques in industry are based on the concept of S_1 and S_2 stream surfaces introduced by Wu (1952). Two sets of stream surfaces, one covering hub-to-tip (S_2) surfaces, and the other covering blade-to-blade (S_1) surfaces, are defined. The most common choice is the axisymmetric throughflow surface for S_2 and the surface of revolution (blade-to-blade) for S_1. On each of these surfaces, a stream function is defined, and the governing equations (based on the inviscid form of Eq. (1)) are developed. The source terms in each of these sets of partial differential equations are the variables from the other set of stream surfaces. Hence, these equations are solved iteratively until convergence is achieved. Many of these techniques and codes are highly mature and are routinely used in a day-to-day design mode. The effects of viscosity can be included approximately in the quasi-three-dimensional formulation through empirical loss correlations or entropy gradients. The effects of secondary flow and annulus wall boundary layer growth can also be included (Lebeouf, 1986).

There are two techniques which utilize this concept. In the first technique, an average hub-to-tip stream surface is defined and combined with several blade-to-blade surfaces. This only approximates (in an average fashion) the three-dimensional effects. The second technique is to solve for several S_1 and S_2 surfaces. The numerical techniques employed include both finite element (Krimmerman and Adler, 1978 and Hirsch and Warzee, 1979) and finite difference methods (e.g., Wang et al., 1985 and Katsanis and McNally, 1968, 1977) as well as the streamline curvature technique.

The concept of S_1 and S_2 surfaces have been used by Schultz (1988), Schultz and Kueny (1986), and Kueny and Desclaux (1989) to compute the cavitating characteristics of mixed-flow

pumps and rocket pump inducers. The blade-to-blade calculation includes a formulation for the cavity. A finite element technique was used. The cavity geometry is obtained by a nonlinear iterative technique. The departure point and length of the cavity are fixed. Constant pressure and slip boundary conditions are imposed on the cavity boundary, and the analysis is for inviscid flow. They show good agreement with the measured cavity length for a mixed flow pump (Schultz, 1988) and inducer (Kueny and Desclaux, 1989). Cooper (1967) carried out a similar analysis, based on an approximate quasi-three-dimensional analysis for both gaseous and liquid phase.

For subsonic flow, all of these two-dimensional and quasi-three-dimensional equations are elliptic and are solved by standard procedures (Anderson et al., 1984). If there are supersonic patches as in a transonic cascade, some special treatment is necessary to capture the shock formation.

The techniques available for the solution of potential and stream function equations for transonic cascades (mixed subsonic, transonic and supersonic flow) can be classified as follows: (*a*) strongly implicit procedure, (*b*) type-dependent scheme, (*c*) rotated difference scheme, (*d*) artificial time concept, (*e*) artificial compressibility concept. Most of these techniques are for stabilizing the solution in the supersonic region. In the type-dependent scheme, central differencing cannot be used, as all information in this case comes from upstream. Thus, a special backward or upwind differencing scheme is used in the supersonic region. In the rotated difference scheme, the coordinates are aligned in the direction of the resultant velocity.

The artificial-compressibility and artificial-viscosity techniques are developed to stabilize the solution in a supersonic zone through the local generation of artificial dissipation. As indicated earlier, there is no difficulty in solving these equations in the subsonic region. Instability occurs in the supersonic region and during shock formation. Some dissipative terms (nonphysical) are essential to damp these instabilities. The artificial compressibility and artificial viscosity techniques generate artificial dissipation in the locally supersonic region by modifying the density. Very few authors have produced satisfactory solutions from $S_1 - S_2$ surface technique for shocked flows. Even those who have tried produced fairly good results in the shock-free and moderate-Mach-number regions and poor predictions near sonic and shock conditions. Hence, for transonic and supersonic turbomachinery, this technique is not recommended. Instead, time-marching solutions of the Euler equations are the best approach.

Many authors have successfully computed the flow field in subsonic turbomachinery using Katsanis and McNally's quasi-three-dimensional technique and code (1968, 1977). Pouagare et al. (1983) predicted the flow field in a low speed axial compressor and showed excellent agreement with the data at the exit and good agreement at most passage locations with the exception of the viscous regions. The viscous effects are not included in this code. On the contrary, the flow in a centrifugal compressor, dominated by three-dimensional and viscous effects, is not captured well. A comparison between predictions (Wang and Yu, 1988) and data (Eckhardt, 1976) indicates that the agreement is reasonably good up to mid-chord, beyond which the comparison is poor. Beyond mid-chord, the effects of low aspect ratio, Coriolis force, secondary flow and high turbulence cause the technique to be invalid in these regions. It is not surprising that an inviscid code is not able to capture the jet-wake structure of the separated flow near the exit of an impeller.

The quasi-three-dimensional techniques are suitable for predicting three-dimensional inviscid flows. For such a case, this technique, even though more cumbersome to code, is computationally very efficient. The inviscid solution of S_1 and S_2 surfaces provide a great insight into the nature of flows and the pressure gradient, which can be helpful in the design process to derive an optimum blade shape. When radial velocities become large, the coupling between various S_1 and S_2 surfaces becomes strong and iterative methods are slow to converge.

There have been several attempts to incorporate viscous effects through loss correlation (using the equation $T\nabla S = \nabla h - \nabla P/\rho$). Quasi-viscous methods have found wide application in the design process, but they are of little value in predicting the local flow properties. For example, the viscous loss distribution from hub-to-tip is included in the mean S_2 surface equation to define gross effects of viscosity on the hub-to-tip flow field, which is then used in the analysis of the S_1 surface. Such an approach fails for fully 3-D flows, as S_2 and S_1 surfaces which are highly warped; coupling the two solutions becomes difficult, if not impossible. A detailed assessment of the Katsanis (1968) and Katsanis and McNally's (1977) code, modified to include boundary layer growth, has been carried out by Povinelli (1984). The prediction of outlet angle and loss was good for rectilinear and annular cascades. The loss and outlet angle predictions for endwall flow and rotor were poor.

Mention should be made of successful development of secondary flow theories to predict flow fields in the endwall region of turbomachinery. Very accurate prediction of flow field can be obtained through the combination of 2D inviscid (e.g., panel code), boundary layer and secondary flow theories. For example, Pouagare and Lakshminarayana (1982) predicted the transverse velocity and flow turning angle in the endwall region of Langston's (1977) cascade, using secondary flow theories; the results are as accurate as those predicted by Hah (1984) using the full Navier-Stokes code. If the requirements are overall performance (e.g., pressure rise, outlet angle, etc.), then the quasi-three-dimensional theories and secondary flow analyses are more than adequate. If the interest lies in local properties, then a full Euler/Navier-Stokes solution is necessary.

In summary,

(1) The S_1 and S_2 surface techniques are useful for moderate three-dimensional flows, subsonic flows, and are extremely useful in the design process. The quasi-three-dimensional viscous technique with one mean hub-tip surface and several S_1 surfaces with loss correlations included in the S_2 surface equations is widely used in the design and analysis procedure in industry. It will remain as a design tool for the foreseeable future as these are well-developed codes and incorporate a wide array of loss correlations. They can also easily be modified to include new loss correlations.

(2) The quasi-three-dimensional, (both viscous and inviscid) solutions are not valid for transonic or supersonic rotor flows. The potential solution methods are restricted to cascade flows.

(3) Good predictions for blade pressure distributions and reasonable predictions of overall performance are obtained. The technique is not suitable for capturing the endwall flows, tip clearance effects, or the blade-to-blade viscous effects.

(4) Secondary flow theories provide good predictions for outlet angles, especially in compressor cascades and rotors.

6 Assessment of Boundary Layer Solutions

In many instances, the boundary layers on turbomachinery blades are thin, and interaction effects between the viscous region and the inviscid region are small enough to be negligible. Under these circumstances, an inviscid solver can be combined with a boundary layer code to predict the entire flow field and losses. This approach is valid in regions away from the endwalls, as viscous-inviscid coupling is large in the shroud wall (with or without tip clearance) and hub wall regions. Moreover the boundary layer solutions, which assume the pressure gradient normal to the walls to be zero, are not valid in these regions.

The boundary layer approximation involves neglect of streamwise diffusion terms and retention of only the dominant

viscous terms (i.e., $\partial^2/\partial y^2$, where y is the direction normal to the wall). The pressure is prescribed at the edge of the boundary layer and is assumed to be constant across the viscous layer. There are two approaches for the solution of the boundary layer equations. In the momentum integral approach, where the interest lies in global features, the equations are integrated from wall to freestream, yielding differential equations for the growth of boundary layer momentum thickness.

Anand and Lakshminarayana (1978), and Lakshminarayana and Govindan (1981) developed a three-dimensional momentum integral technique using Head's entrainment equation for closure. A comparison between the measured and the computed momentum thickness for the Penn State low-speed rotor showed good agreement, and indicated the usefulness of these techniques in evaluating the gross performance of turbomachinery, especially the profile losses, blockage effect, etc. The profile losses estimated from the predicted blade boundary layer momentum thickness agree well with the experimental data (Pouagare et al., 1985; Lakshminarayana and Popovski, 1987). Thus, an inviscid computation technique combined with a viscous boundary-layer code can resolve most of the flow features away from endwalls, and is adequate for the prediction of blade pressure distribution, pressure rise and the profile losses for subsonic rotors.

There are many excellent textbooks and reviews dealing with the numerical solutions of two-dimensional boundary layers (e.g., Bradshaw et al., 1981). Even though a large class of external flow problems have been solved, the application of these numerical solutions to turbomachinery flows has not found widespread use. The boundary layer equations are parabolic or hyperbolic. Some of the widely used schemes for the numerical solution of the boundary layer equations are the Crank-Nicholson scheme, the Keller box scheme, the shifted box scheme, the double shifted box scheme, the zig-zag difference scheme, the characteristic difference scheme and the two-step method. (For details see Smith (1982), Keller (1978), Wang (1971), Cebeci et al., (1977), and Bradshaw et al. (1981).) One of the widely used codes in turbomachinery for the computation of two-dimensional boundary layers (with heat transfer) is due to Crawford and Kays (1976).

Most of the schemes are valid for unidirectional flow. It is not uncommon in turbomachinery applications to encounter reversal in a radial component of velocity within a three-dimensional boundary layer. Cousteix (1986) has reviewed the calculation methods for three-dimensional boundary layers. The method due to Vatsa (1985) is probably the most suitable technique available for turbomachinery flows. He employs a first-order formulation for spatial derivatives and an upwind scheme in the radial direction (to capture flow reversal in the cross flow direction only). The resulting linear algebraic equations are solved using a block tridiagonal solver. This earlier code (Vatsa, 1985; Anderson, 1987) utilized an algebraic eddy viscosity model. This was modified by Zhang and Lakshminarayana (1990) to include a coupled $k - \epsilon$/ARSM model described earlier and obtained good predictions for the three-dimensional boundary layer on a rotor blade, as shown in Fig. 2. This illustrates the ability of boundary layer codes to predict complex three-dimensional boundary layers. Thus an inviscid solution of the flow field coupled with a boundary layer solution can resolve most features of the three-dimensional flow in subsonic blade rows.

Assessment of boundary layer solutions:

(1) The technique is not valid when boundary layers are thick and normal pressure gradients as well as streamwise and radial diffusion (viscous), are substantial. This limits the application to non-separated, shock-free flows. Boundary layer solutions are not valid for transonic and supersonic rotors, where appreciable shock boundary layer interactions and three-dimensionality are present.

(2) These techniques and codes are restricted to axial-flow turbines and compressors where the boundary layers are relatively thin. The boundary layers in centrifugal compressors are thick and the entire passage is affected by the viscous flow; the boundary layer codes are not valid for such flows.

(3) The resolution of the leading-edge flow is a problem as the boundary layer thickness is very small there. It is best to interface the boundary layer code with an analytical solution in this region.

(4) Boundary layer solutions are not valid when the flow is separated, as in a corner between the endwall and the blade. It is not valid in the shroud wall region where the blade boundary layer, endwall boundary layer, horseshoe vortex, and leakage flow can interact to produce a complex flow field. Caution should be exercised in attempting to capture both the radial inward and the outward flow.

Despite these limitations, boundary layer techniques offer some unique advantages over Navier-Stokes codes. They include:

(1) The grid resolution and computational time restrict the accurate solution of wall layers using Navier-Stokes codes. Since boundary layer codes are computationally more efficient, the wall layers, including skin friction, heat transfer, and profile losses can be resolved accurately through large numbers of grid points in the normal direction.

(2) An efficient way to resolve both the viscous and the inviscid effects in turbomachinery with three-dimensional boundary layers is to couple an Euler code with a three-dimensional boundary layer code. This is all that is needed for subsonic blade rows with thin boundary layers. The blade pressure distribution is predicted well, and the performance predictions are reasonable.

Description and assessment of coupled inviscid/boundary layer solutions are given under the section heading "zonal methods." These methods have been used successfully to predict flow field in cascades and rotors (e.g., Barnett et al., 1990; Calvert, 1982; Singh, 1982).

7 Single-Pass Space-Marching Methods

In many instances, the boundary layer approximations are not valid, but the flow is not complex enough to necessitate a full Navier-Stokes solution. The situations in which the boundary layer approximations are not valid were listed earlier. The common feature of all of these cases is the presence of the pressure gradient normal to the wall. This does not necessarily mean that one must resort to the full Navier-Stokes equations. If the steamwise pressure gradient is large and the streamwise diffusion is substantial, then a full Navier-Stokes solution is the only approach to take. In many instances, the flow can be resolved with some approximations to the Navier-Stokes equations, resulting in a substantial savings in computational time and storage. The Navier-Stokes equation can be "parabolized" and "space-marched" to resolve the flow field. The parabolization of the equations results in a substantial improvement in CPU time required over the time marching technique or the relaxation technique for a class of flows in which streamwise pressure gradients are small, or known from the inviscid solution. Fewer terms in the approximated equations result in a substantial reduction in the amount of computer storage. This technique has been successfully used for many internal flows such as ducts, cascades, and rotor/stator passages. Unlike boundary layer techniques, this technique retains the normal (to the wall) pressure gradient and normal (to the wall) momentum equations. This is an essential requirement in solving thick or three-dimensional boundary layers.

One of the approximations made is to parabolize the Navier-Stokes equation in one of the coordinate directions so that a marching type of computational scheme can be implemented

in that direction. This approximation is well suited to internal flows, most of which have a dominant flow direction. The viscous diffusion terms in the streamwise direction are small in comparison to the diffusion in the transverse directions, and can be dropped from the equations. Intuitively, one would expect that the equations would behave as an initial-value problem due to the lack of second derivatives in the streamwise direction. However, the pressure terms have an elliptic influence in subsonic flows, and special care needs to be taken to handle them in a marching solution algorithm. Methods of treating the pressure terms differs among the many parabolic marching methods available in the literature.

There are three basic approaches used for the solution of the "parabolized" Navier-Stokes equations. In the first and earliest approach, an approximation is made for the pressure, and the governing equations are solved in an uncoupled fashion, with coupling enforced through iterative steps. In the second approach, the equations are solved in a coupled fashion, utilizing the numerical techniques (time marching) developed for the hyperbolic equations, and the solution is advanced along a predominant flow direction. In the third approach, the velocity is split into primary and secondary components.

In the first two approaches, a bulk pressure correction $P_m(x)$ (where x is the dominant flow direction), is introduced into the streamwise momentum equation, and is assumed to be uniform over the cross section. The value of $P_m(x)$ is corrected in subsequent steps to satisfy the global mass in the cross section. The cross flow pressure retains a separate correction $P_c(y, z)$, which is allowed to vary in the cross section. The streamwise momentum equation is parabolic, and the cross flow equations are elliptic. Patankar and Spalding (1972) derive a two-dimensional elliptic equation for pressure correction using a transverse momentum equation, while Briley (1974) utilized two elliptic equations in the cross plane, one for potential function and the other for P_c. Both of these methods use the uncoupled approach, where equations are solved in a sequential manner. The technique due to Govindan and Lakshminarayana (1988) is a coupled approach, where all equations are solved simultaneously. In the third approach due to Briley and McDonald (1984), and Govindan et al. (1991), a small scalar potential approximation is made, and the velocity is resolved into primary and secondary velocities. The secondary velocity potential is resolved into a scalar potential and a vector potential. The vector potential defines the streamwise vorticity and the large secondary velocity component associated with the streamwise vorticity. No approximation is introduced for the pressure. These decoupled equations are solved sequentially using an implicit numerical algorithm. Govindan et al. (private communication) have successfully solved a large class of flows including tip vortex flows, and flow over marine vehicles, and claim space marching codes achieved the same accuracy as Navier-Stokes for some of the complex cases in about 1/30 of CPU time required for a full Navier-Stokes solution.

Some of the drawbacks of this technique are in satisfying the local continuity in the entire flow field. A further drawback is the separation of governing equations into individual equations, with an iterative scheme to couple the equations. In addition to error due to discretization, error due to approximation in flow physics is introduced. Furthermore, stability problems are encountered, especially in situations for which the approximations employed are not valid.

In a flow field with strong secondary flow and transverse pressure gradients, the coupling of the pressure field and the transverse velocity would slow the convergence of the solution. The decoupling of equations cannot be avoided because of the different types of equations that are solved. These disadvantages led Govindan and Lakshminarayana (1988), and Pouagare and Lakshminarayana (1986) to develop a single-pass space-marching technique and to solve all of the equations in a coupled fashion for subsonic flow. This is an extension of a method developed for supersonic flows by Schiff and Steger (1980). Internal flows of the type found in turbomachinery blade rows are marked by three-dimensionality, pressure gradient, and turbulence effects. Since the transverse flow is strongly coupled to the longitudinal flow, it is best resolved using a "coupled" approach whereby all of the equations are solved simultaneously. Govindan and Lakshminarayana utilized the implicit algorithm due to Briley and McDonald (1976).

Many complex flows were predicted using this technique (Govindan and Lakshminarayana, 1988; Lakshminarayana et al., 1989). Among them are viscous laminar and turbulent flows through a 90 degree bend; viscous flow over a wing body junction; viscous flow through a cascade (Pouagare, et al., 1986); and endwall flow through a cascade. The flow in the endwall region of a cascade, measured by Flot and Papailiou (1975) is compared with prediction by Kirtley et al. (1986) in Fig. 4. The cascade consists of NACA 65-12-A10 airfoils, with a space chord ratio of 0.8, stagger angle at 15 degrees and 41.2 degrees deflection. The prediction of both the mainstream velocity and the secondary velocity is good. A comparison between the solution obtained from a single-pass space-marching code and the results from a pseudo-compressibility time marching code is shown compared with the data for Flot and Papailiou's cascade. The grids and computer were identical for both computations. The space-marching algorithm requires a pressure field which was obtained from a panel code. The time-marching code computes the pressure field. The overall CPU time was an order of magnitude lower for the space marching code. The streamwise velocity profiles are almost identical, but there is some discrepancy between the two predicted cross flow profiles. The space-marching code seems to capture the wall region better than the time marching code, while the outer region (the inviscid effect due to the pressure gradient) is more accurately predicted by the time marching code. An attempt to predict the flow through the Langston et al. (1977) cascade, which has a much higher turning angle, was not successful, as elliptic effects due to the horseshoe vortex were substantial and its presence or effect could not be captured.

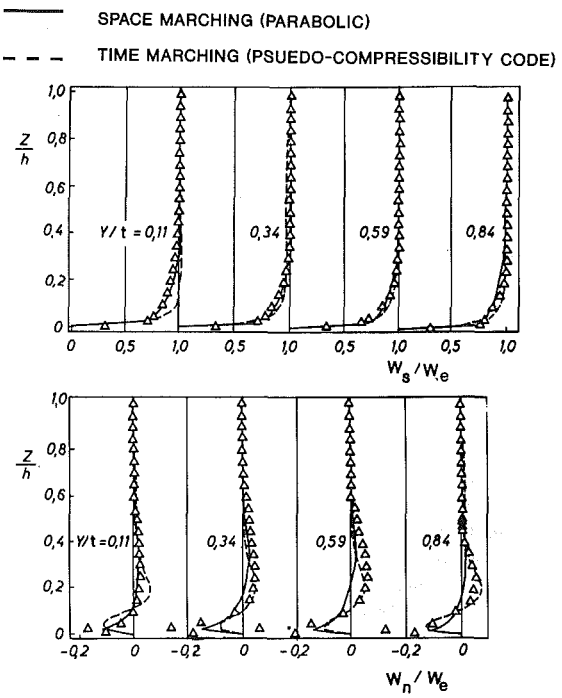

Fig. 4 Turbine endwall flow field near the trailing edge (data: Flot and Papailiou, 1975; Computation: Kirtley et al., 1986)

Extensions of this computational technique have been carried out by Pouagare and Lakshminarayana (1986), who developed a technique for incompressible flow, and by Kunz et al. (1988), who employed a finite-volume formulation to solve the parabolized equation. They have shown that the single-pass solution of PNS equations can be achieved in approximately one order of magnitude less time than a full Navier-Stokes (FNS) solution. Excellent agreement is achieved with the benchmark data for curved and S ducts.

Assessment of Space-Marching Techniques

(1) It should be emphasized that all of the methods described in this section are single-pass where the corrected pressure is not utilized to update the velocities. These techniques are useful for ducts and cascades where the pressure field is known or assumed and is close to its actual value. Since only a single sweep is employed, this should be about one order of magnitude faster than solutions described in the next section. The method is applicable to nonseparated flows.

(2) The technique can be used to predict subsonic flow through a rotor with thin boundary layers, if the approximate pressure field is known from an inviscid code. The endwall flow can be captured, provided the turning is not large or there is no corner flow separation. The requirement of positive streamwise velocity for stable marching limits the applicability of the equations to unseparated flows.

(3) The space-marching techniques are unsuitable for an endwall region with high turning, cascades with thick leading edges, corner flow separation, or in the presence of a horseshoe vortex. Furthermore, the space-marching technique requires an H grid, hence high stagger angles, high turning (or high camber) cascades with thick leading edges are unsuitable for space-marching codes due to grid restrictions. The omission of the streamwise diffusion terms limits the application to regions away from the vicinity of a leading edge. The method is limited to subsonic flows.

(4) The flow field can be resolved as accurately as with a full Navier-Stokes solution in a small fraction of time. This technique is also most suitable in the design mode in view of its computational efficiency.

(5) Upstream influence arising from the strong viscous-inviscid interaction cannot be captured by using this procedure.

(6) The space-marching code can be integrated with Euler or Navier-Stokes code to develop an efficient zonal code described later.

(7) In both the space-marching and the full Navier-Stokes solutions, the discretization error provides an approximate solution. The order of this error is usually well defined. However, with uncoupled space-marching techniques, an additional source of error is introduced in the way equations are decoupled and iterated. Since the equations are nonlinear, a converged solution to the uncoupled equation is only an approximate solution to the original discretized equations. The order of that approximation may be hard to quantify. This problem is overcome in coupled space-marching solutions.

8 Overview of Euler and Navier-Stokes Solutions

As indicated earlier, the techniques typically used for the solution of the Euler and Navier-Stokes equations are the same, even though there are some major differences in the behavior of the technique with and without the viscous terms. Therefore, all techniques used for Euler and Navier-Stokes equations are treated together. The classification of numerical techniques is shown in Fig. 3. The approximations to Navier-Stokes equations are many. One must clearly distinguish between the approximations to the equations (which neglect some of the physical phenomena) and approximations used in the discretization.

The approximations to the Navier-Stokes can be classified as Thin Layer Navier-Stokes (TLNS), Partially Parabolic Navier-Stokes (PPNS), and Reduced Navier-Stokes (RNS), as explained earlier. These approximations are based on the nature and physics of the flow. For example, TLNS neglects streamwise diffusion terms in the equations, and is valid when the viscous layer is thin compared to a characteristic length (e.g., spacing or chord length of a blade). The RNS equations are derived from an order of magnitude analysis or perturbation analysis of the Navier-Stokes equations applicable to high Reynolds number flows with a dominant direction. The RNS models neglect the viscous term in the normal momentum equation (normal to the body). Therefore, both TLNS and RNS are valid strictly for thin shear layers near the surface with a dominant flow direction. The equations are elliptic or hyperbolic and are accurate for most flows; exceptions are separated flows and near wakes regions where the neglected effects may be important. The RNS model can be utilized to solve the full Navier-Stokes equations where the neglected terms can be retained and solved by a deferred corrector approach. In the Partially Parabolic Navier-Stokes (PPNS) technique, the pressure is assumed initially and updated continuously through a pressure equation. The final converged solution in this case does represent the full Navier-Stokes, even though the solution was achieved through initial approximations. These are usually called the parabolic marching methods; the word "parabolic" is misleading, as the final solution has all the elliptic effects.

Here is a major classification of techniques employed for Euler and Navier-Stokes equations.

Pressure-Based Methods. This is an extension of the single-pass space-marching technique described earlier. In this technique, the assumed pressure is updated using an auxiliary equation for pressure, and a multi-pass procedure is adapted to converge both the pressure field and the velocity field.

Time-Dependent Methods. In these techniques, which may be either explicit or implicit, the unsteady terms in the Euler or Navier-Stokes equations are retained, even though only the steady solution may be of interest. The unsteady form of the system of compressible (subsonic, transonic, and supersonic) continuity, Navier-Stokes and energy equations is hyperbolic and, therefore, efficient techniques available for hyperbolic systems are employed to derive the steady state solution.

Pseudo-Compressibility Technique for Incompressible Flow. The incompressible Navier-Stokes equations are elliptic, and only relaxation solutions are applicable to this class of flows. One of the more efficient means of solving these equations is to introduce artificial time derivatives in the continuity equation, thus transforming the elliptic equations into a hyperbolic system. Any of the time-dependent methods can then be used to solve the set of equations.

Zonal Techniques. The principal feature of zonal techniques is to utilize the most appropriate equations in regions of interest and iterate between zones to derive an accurate solution. The motivation is to reduce computer time and storage.

Description and assessment of these techniques are given in Sections 9 through 14.

9 Pressure-Based Methods (Multi-Pass)

In the pressure-based methods, the equations are approximated with an assumed pressure field, which is continuously updated using an auxiliary pressure equation. The converged solution satisfies the fully elliptic Navier-Stokes equations; therefore, most of the pressure-based methods use relaxation techniques to solve the finite difference equations.

Most of the pressure-based methods (referred to by various

authors as multi-pass parabolic methods, partially parabolic methods, or partially elliptic methods) are extensions of the single-pass pressure correction (uncoupled) methods described earlier. In the single-pass technique, the corrected pressure P_m is not used to update the velocity or iterated until the correction is zero. This requires streamwise sweeps (or multi-pass). In the multi-pass technique, the domain is swept, both in the transverse and in the marching directions, until all variables are converged. The technique of updating the pressure and reducing the pressure correction is where the major difference between these techniques lies.

Pressure Correction and Substitution Method. One of the widely used pressure-based methods is the Pressure Correction Method (PCM), a technique similar to that outlined in Section 7, modified to include a multi-pass or a feedback mechanism, coupling the velocity and pressure fields. This technique was originally suggested by Chorin (1967, 1968). A review is given by Patankar (1988), and a step-by-step numerical approach for turbomachinery flows is described by Moore (1985).

In the PCM technique, a separate equation for pressure correction is developed for both the bulk pressure correction $P_m(x)$ and the pressure correction in the transverse momentum equation ($P_c(y, z)$), relating the source term in the Poisson equation to the divergence of the velocity field through the continuity equation. This pressure correction requires a staggered grid (pressure is solved on a different grid point than the velocity field) to eliminate oscillations in the solution of the pressure correction equation. This was one of the main disadvantages of the earlier efforts, which were restricted by Cartesian coordinates. Patankar (1988) and Hobson (1990) have provided a review of parabolic methods. A summary of these techniques follows.

In the pressure correction method (PCM), the pressure is expressed as $p = p^* + p'$, where p^* is the initial guess (or estimate) and p' is the pressure correction in the momentum equation and the velocity $\underline{W} = \underline{W}^* + \underline{W}'$, where $\underline{W}'$ is the change in velocity component due to change in pressure. These are substituted into the momentum equation and discretized. The divergence of momentum equation provides the Poisson equation for pressure correction. Detailed derivation of equations and the methodology can be found in Patankar (1980). The semi-implicit method for pressure-linked equations (SIMPLE) algorithms due to Patankar and Spalding (1972), consists of the following predictor-corrector steps.

(1) Guess the initial pressure p^*. This could be derived from a panel code.

(2) Solve the momentum equations in discretized form for $\underline{W}^*$, using assumed p^*.

(3) Solve the Poisson equation for p', and determine $p = p^* + p'$.

(4) Correct the velocity field ($\underline{W}'$) using the pressure correction (p').

(5) Solve any additional scalar transport equations (e.g., energy, $k - \epsilon$, etc.)

(6) Using the updated values of p and $\underline{W}$, go to step 2 and determine the new velocity components and repeat this procedure until convergency is achieved.

Both finite-difference and finite-volume techniques are used in solving the equations governing the fluid flow. In the finite-volume method, the equations are integrated over a finite volume and transformed into surface integrals. The dependent variables on control volume faces are approximated by finite-difference methods. Many of the investigators (Hah, 1984; Chan and Sheedy, 1990) use a second-order upwind scheme to discretize the convective terms. The fluxes are interpolated from the two nearest neighboring nodes. Chan et al. (1988) use a seven-point finite difference scheme for three-dimensional flows. A preconditioned conjugate gradient method is used to solve the matrices.

In the earlier PCM techniques, a pressure-correction equation was employed for p_m which was partially converged through a multi-pass sweep of the flow field. Patankar (1980) introduced the SIMPLER method, in which an extra equation was solved for the evaluation of the pressure. The SIMPLEST procedure was developed by Spalding (1980), who recommend an explicit treatment of the convection and implicit treatment of diffusion in the momentum equations. Another variant is the SIMPLEC procedure described by Von Doormal and Raithby (1984) which uses a consistent under-relaxation of the momentum and pressure corrections. Connell and Stow (1986) used higher order approximations to develop procedures and showed improvement over the SIMPLE scheme. Issa (1985) proposed a method called pressure-implicit split-operator (PISO), which like SIMPLER also solves an additional equation, but the implicit solution of the pressure is split between the double correction steps. Multigrid methods can be used to increase the efficiency of both implicit and explicit schemes.

The coupling between the velocities and pressure can be enhanced by solving them simultaneously at a grid point. For a point-by-point explicit scheme, the convergence is very slow, especially for fine grids. Vanka (1986) has used the multi-grid method with a coupled solution. This procedure was used to solve the discretized equations on a staggered grid. An explicit smoothing technique called Symmetrical Coupled Gauss-Seidel (SCGS) was proposed to update all four of the velocities at the faces of the computational control volume. An improvement on both convergence and CPU time was quoted.

Most earlier techniques utilized a staggered grid system. For a curvilinear coordinate system, which is most suited for turbomachinery flows, this staggered grid arrangement is extremely sensitive to grid smoothness. Chan and Sheedy (1990) overcame this problem by storing all dependent variables at the centroid of the control volume. The velocity components are linearly integrated from the discretized momentum equations in the neighboring node prints. Chan and Sheedy (1990) claim that this nonstaggered scheme provides sufficient ellipticity to maintain stability. On the other hand, Rhie and Chow (1983) used a weighting scheme to calculate mass flux at the cell centroids and the mass fluxes on the control volume faces are derived from linear interpolation. In this procedure, the linear interpolation introduces fourth order dissipation but does not alter the second order accuracy.

Very few investigators have carried out a systematic study of the various options in the pressure-based method, the effects of numerical diffusion caused by inadequate grid resolution, comparison of various turbulence models and the effect of wall functions or treatment of turbulence equations near the wall.

Application of these techniques to turbomachinery flows and subsequent modifications to improve accuracy and efficiency have been carried out by Moore and Moore (1986, 1990), Hah (1984), Hah and Krain (1990), Rhie (1985, 1986), and Hobson and Lakshminarayana (1990a, 1990b), Stow (1989), and others.

Moore and Moore's (1986) technique is similar to Pratap and Spalding (1976). They used a two-dimensional correction procedure on the cross-stream plane, which was not coupled to the longitudinal pressure gradient. A three-dimensional correction was employed to remove the local force residues after each sweep. A control volume with pressure corrections located at the center of the control volume was used. The turbulence is represented by an algebraic eddy viscosity model. In a later development, Moore et al., 1990 claim that no smoothing was employed. They computed a wide variety of flows, including flow through a varying area curved duct, centrifugal compressor, turbine cascade and rocket pump inducer. Stow (1989) successfully used this code in the computational design of compressors and turbines. One typical computation by Moore and Moore is the three-dimensional viscous flow in a rocket

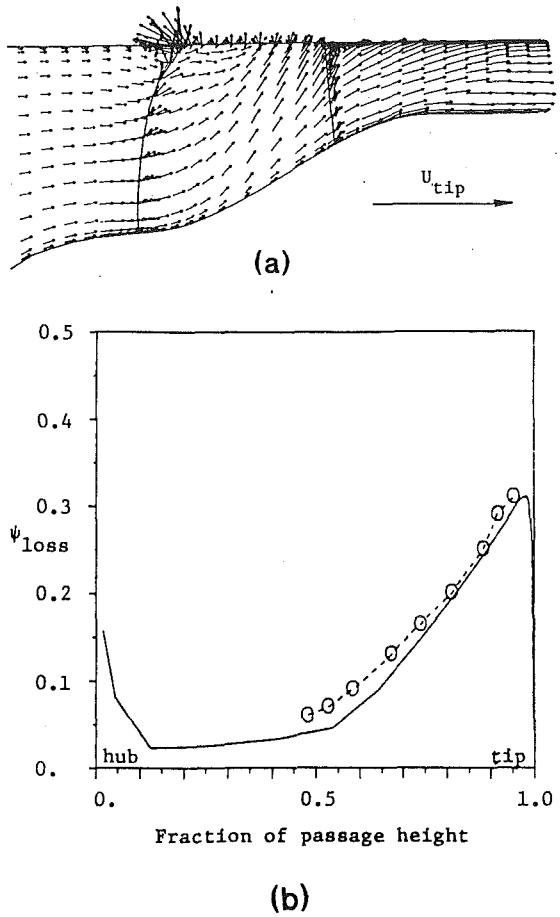

Fig. 5 Rocket pump inducer flow field (non cavitating peformance) (○ data: Bario et al., 1989; ——— computation; Moore et al., 1990) (*a*) velocity vectors near pressure side, 1 percent of pitch; (*b*) pitch averaged loss coefficient at blade exit. (Mass flow 0.2109 kg/s, N = 10,000 rpm, axial velocity/blade tip speed = 0.084, $R_N = \rho U_t D/\mu_t = 1.13 \times 10^6$, 4 bladed)

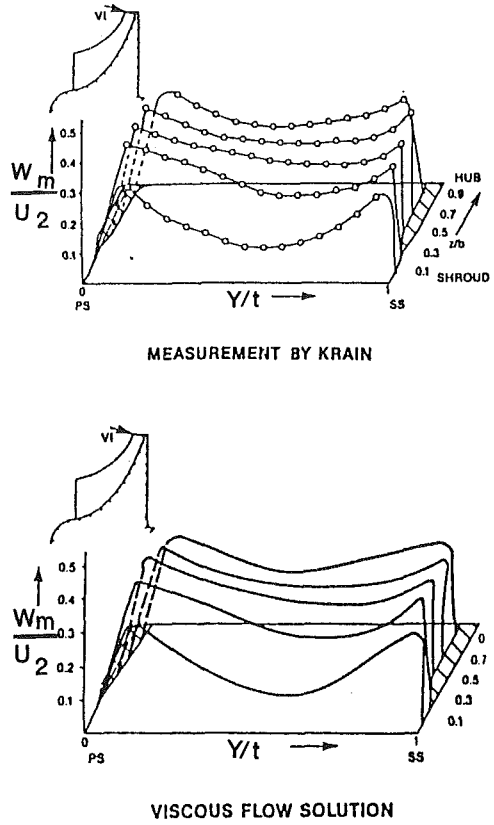

Fig. 6 High speed centrifugal compressor exit flow field (*z/b*-nondimensional blade height) (data: Krain, 1988; computation: Hah and Krain, 1990)

pump inducer, shown in Fig. 5. Large radial outflow near blade surfaces as well as very high flow losses are predicted well. It should be noted here that the inducer operating at low flow coefficient has one of the most complex flow fields, including very high losses as measured by Lakshminarayana and Gorton (1977). It is encouraging that present-day codes are able to capture such flows.

Hah (1986) solved the uncoupled equations on a staggered grid. A general coordinate transformation was used to represent the turbomachinery geometry, with skewed upwind differencing. He used higher-order discretization for the convection term to reduce numerical diffusion; the quadratic upstream differencing by Leonard (1979) and skew-upwind differencing by Raithby (1976) were extended and incorporated. The skew upwinding scheme is aimed primarily at reducing the error due to the streamline-to-grid skewness. Hah utilized one semi-implicit predictor step and two semi-implicit corrector steps and achieved third-order spatial accuracy. The code is capable of capturing both low speed and high speed shocked flows. Hah computed a wide variety of turbomachinery flows (Hah, 1984, 1986; Hah, et al., 1988; Hah and Krain, 1990) such as diffuser flows, turbine endwall flows, centrifugal compressor flow fields and tip leakage flows as well as transonic compressor flow. A comparison between the predicted and the measured relative velocity profiles at the exit of a high-speed centrifugal compressor is shown in Fig. 6. The data were taken using a laser two-focus velocimeter system in a 30 degree backswept impeller with a tip diameter of 400 mm, and design pressure ratio of 4.7, at a maximum stage efficiency of 94 percent. The predictions indicate that the tip clearance has a major influence on the flow field and should be included to capture the three-dimensional effects. A contour of constant relative flow angle shown in Hah and Krain (1990) indicates that the vortex structure near the tip (where the angle changes from 27 degrees to 59 degrees) as well as other features, are captured well. The exit relative velocity profile is predicted well (Fig. 6). Most of the emphasis in recent years has been to develop techniques and codes to predict the flow field. The recent trend is toward utilization of these codes for design, as well as for simulation to understand a particular phenomenon. One of the interesting examples is the use of Hah's code by Leylek and Wisler (1990) to simulate spanwise and cross-flow mixing phenomena in compressors. They were able to conclude qualitatively several sources causing spanwise mixing and confirm the observations made through flow visualization. This is a prime example of maturity and confidence in CFD codes and mutual interaction of CFD and data to understand complex flow features in turbomachinery.

Rhie and Chow (1983) used a pressure weighted method to suppress pressure oscillations and developed a differencing scheme for a curvilinear coordinate system on a nonstaggered grid. The technique still employs PCM to couple the momentum and continuity equations. Rhie (1986) recently extended his earlier scheme to employ the Pressure-Implicit Split-Operator (PISO) concept with a multi-grid procedure to enhance convergence. During the pressure correction iteration, the density was treated implicitly for the mass flow balance. Numerical diffusion was introduced to damp instabilities associated with central differencing of convective terms. Rhie and his group (1984, 1985, 1986) and Bansod and Rhie (1990) utilized the pressure-based method and computed a wide class of turbomachinery flows. This is a finite-volume formulation, with a

collocated grid and a central difference scheme for the basic equations. The pressure oscillations due to nonstaggered grid are suppressed by the use of a fourth-order pressure dissipation term. They state that this term acts as a mass flux term and does not alter the second-order accuracy of the continuity equation; they computed the flow through a three-dimensional duct (Rhie, 1985), and centrifugal compressors, with and without tip clearance (Bansod and Rhie, 1990). One of the complex cases computed by Bansod and Rhie (1990) is the centrifugal compressor tip loss mechanism as well as the entire passage flow. The blade tip was cusped and the Navier-Stokes code was run for different tip clearances. The results for the decrement of efficiency agree well with the measured data even with very coarse grid (within the tip clearance region), but the details of the flow field in the clearance region is predicted only qualitatively. It should be remarked here that all these computations were done with a $k - \epsilon$ turbulence model and hence, the complex features of tip vortex formation and jet-wake structure cannot be resolved as indicated earlier (e.g., see Fig. 1). However, the inviscid features of the flow, such as wall static pressure and meridional relative Mach numbers away from blade surfaces, are captured well.

Chan's group (1987, 1988, 1990) has a recent entry to PCM based techniques for turbomachinery. Their method is similar to Rhie (1985) and utilizes a second-order upwind scheme, a preconditioned conjugate gradient/method for acceleration and employs no user defined smoothing function. They have computed the flow field in a turbine endwall region, the space shuttle main engine return duct and rocket pumps. The code is used for both design and analysis.

Hobson and Lakshminarayana (1990a, 1990b) developed a pressure substitution method where the solution for the entire pressure instead of the pressure correction is obtained. The technique is similar to those outlined for the pressure correction methods, but differs in the formulation of Poisson equation for pressure. The new formulation, based on a pressure weighted method, incorporates p instead of p' in the Poisson equation for pressure. The strategy for this technique is as follows:

(1) Determine a new velocity field, at iteration level $k + 1$, from an assumed field at k, by solving the linearized form of momentum equations from the previous values of the velocity to determine the coefficients of the momentum equations.

(2) Solve the pressure field (p instead of p') and set this equal to the new assumed pressure field at iteration level $k + 1$.

(3) Solve any additional scalar transport equations.

(4) Check for convergence. If the solution is not converged, repeat the above, from steps 1 to 3.

It is evident that this algorithm is of the predictor type, with no correction step. A logical extension of this would be to solve the transport equations and the pressure equation in a coupled fashion. Block solution of the equations would then be possible with the probable increase in the coupling of the momentum and continuity equations. Improved convergence is obtained by the pressure substitution method (Hobson and Lakshminarayana, 1990b). It should be remarked here that PCM and PSM performed equally well in simple flows (e.g., cavity flows), but PSM shows improved convergence in more complex cases such as a cascade. Further research is necessary to evaluate its performance in 3-D flows. Hobson and Lakshminarayana computed a wide variety of flows using the pressure substitution method for two-dimensional flows and the pressure correction method for the three-dimensional case using a low Reynolds number form of $k - \epsilon$ model. The suction side velocity profile, predicted and measured in separated cascade flow, shows good agreement even in the separated region (Fig. 7). The skin friction coefficient is predicted accurately (Hobson and Lakshminarayana, 1990b) on the suction surface,

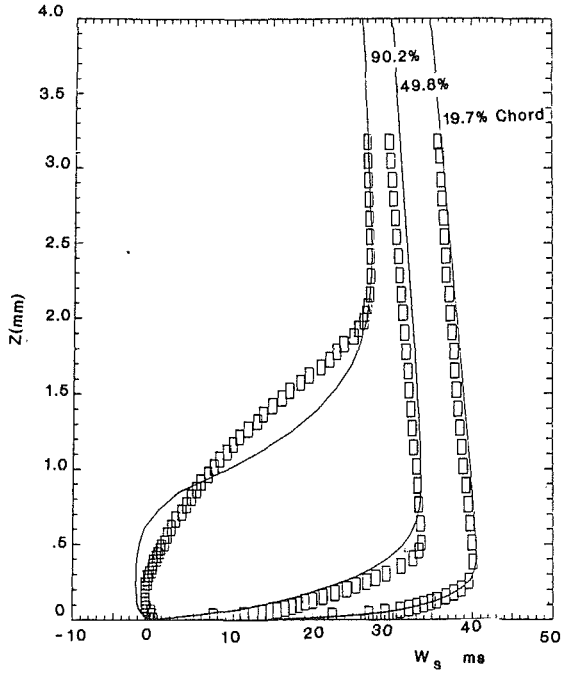

Fig. 7 Suction surface boundary layer profiles on a cascade blade (□ data: Zierke and Deutsch, 1989; _____ computation: Hobson and Lakshminarayana, 1990b).
(Solidity 2.14, λ = 20.5 deg, A = 1.61, C = 228.6 mm, camber = 65 deg, $R_N = 5.0 \times 10^5$, $i = -1.5$ deg.)

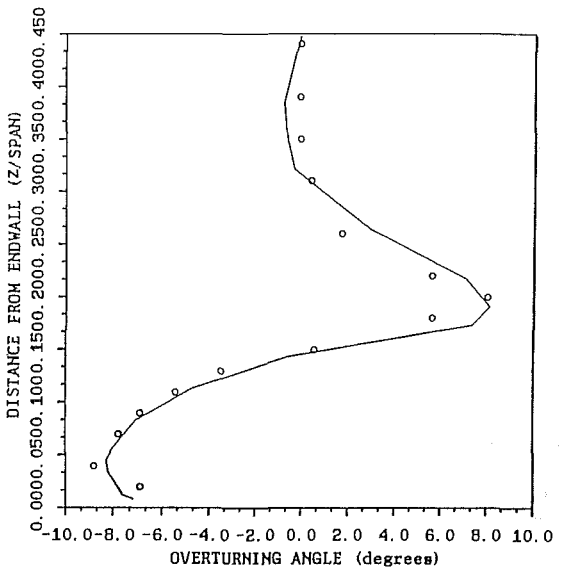

Fig. 8 Overturning and underturning angle distribution in the turbine endwall region
(○ data: Gregory-Smith, 1989; _____ computation: Hobson and Lakshminarayan, 1990a)
(C = 216 mm, S = 191 mm, h = 229 mm, $R_N = 5 \times 10^5$, α_1 = 42.75 deg, $\alpha_2 = -66.6$ deg)

where the boundary layer is thick, and not so accurately on the pressure side, where it is very thin. Both the experimental and the computational accuracy is poor on the pressure surface near the leading edge due to the very thin boundary layer.

Hobson and Lakshminarayana (1990a) also predicted the three-dimensional flow in the endwall region of a turbine cascade. The prediction shown in Fig. 8 shows that the size and strength of the large secondary vortex is captured well. The underturning and overturning angles are also predicted well.

Coupled Pressure-Based Method. In the techniques described earlier, the momentum, continuity and pressure equations are solved in an uncoupled manner, and the solutions are updated. This may result in convergence problems, especially in situations where the gradients of flow variables are large (e.g., leading and trailing edges, etc.). Kirtley and Lakshminarayana (1988) developed a coupled pressure-based method where all the equations were solved simultaneously. The continuity equation was modified with the introduction of a pressure-correction term, somewhat analogous to the pseudo-compressibility technique described later. The modified continuity equation is coupled to the momentum equation and solved using a spatial integration procedure.

As in other pressure-based methods, the streamwise viscous diffusion in the momentum equation is neglected. The method differs from those of others in the manner in which the streamwise pressure gradient is handled. The various methods that have proved to be successful in computing internal incompressible flow have relaxed some conditions during the iterative process. In the techniques described in the previous section, the procedure involves relaxing the continuity constraint by lagging the solution of the continuity equation. In the pseudo-compressibility technique, which utilizes a time marching method, an extra term is introduced in the continuity equation. Kirtley and Lakshminarayana (1988) developed a new technique by introducing an additional term in the continuity equation and solving the entire set of equations as a coupled system. The additional term in the converged solution goes to zero. This is an implicit technique and utilizes the approximate factorization scheme due to Briley and McDonald (1976) and Beam and Warming (1978) described later. The solution is advanced in the streamwise direction instead of time.

If the discretized equations are solved using the LBI scheme for time marching procedures, developed by Briley and McDonald (1976), the resulting factorization error significantly reduces the overall accuracy of the method. The error, unlike that of time marching methods, is multiplied by the streamwise change in Δq, which does not go to zero, unlike that in a time marching method. This error will accumulate in each streamwise step. A new scheme was developed to reduce this factorization error. The method has good convergence characteristics, but the computational efficiency has not been compared with other techniques. A wide variety of flows have been computed using these codes, including flow in a 90-duct, S duct, cascade wakes, endwall flows, and compressor rotor passage flow, including the blade boundary layer (Kirtley and Lakshminarayana, 1988).

Assessment of the Pressure-Based Method. The pressure-based methods have been in existence longer than any other scheme, hence considerable development effort has been expended on this technique. Furthermore, turbulence modelers have used these techniques in testing and developing new models. Thus these methods have reached a high level of maturity and are widely used in industry and academia. They have also been used to incorporate and test a wide variety of turbulence models (algebraic eddy viscosity to full Reynolds stress) and have been utilized to predict a wide variety of mostly internal flows. Recent developments include nonstaggered grids, highly skewed and highly nonuniform grids, multi-grid, coupled-solution, upwind differences, and extension to compressible and shocked flows. Many investigators claim that the computation can be done without smoothing. The method has found widespread use in the industrial design and analysis systems used by Pratt & Whitney Aircraft, General Electric Co., Rolls Royce, Rocketdyne, and Ingersoll Rand.

There are not many published attempts to evaluate various schemes, discretization and grid sensitivity for pressure-based methods for turbomachinery. Chan et al. (1988) carried out such a systematic analysis and some of their results are presented here. First and second-order discretization schemes for convective terms were tried and the results (Fig. 9) show a major influence on the pressure distribution. The convergence history for several solution schemes is shown in Fig. 10. A comparison between ADI, SIPSOL (Stone's, 1968, Strongly Implicit Procedure), and Preconditioned Conjugate Gradient Scheme (CGS, Kershaw, 1978) shows the improved performance with CGS. The convergence rate for both ADI and SIPSOL was very rapid for the initial 20 iterations and slowed considerably after this. Chan et al., (1988) claim that CGS is the more suitable scheme in a highly stretched grid system (as in a turbine case) which results in an ill-conditional matrix system. Likewise, they showed (Hadid et al., 1988) that the PISO scheme provides a much faster convergence than a SIMPLE algorithm.

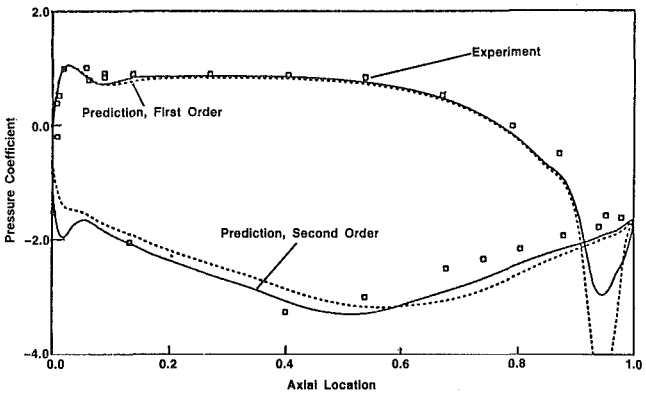

Fig. 9 Turbine cascade blade pressure distribution (58 × 35 grid) (data: Langston et al., 1977; computation: Chan et al., 1988) (C = 281.3 mm, A = 1, solidity = 0.95, λ = 35 deg, turning angle = 110 deg, α_1 = 45.3 deg)

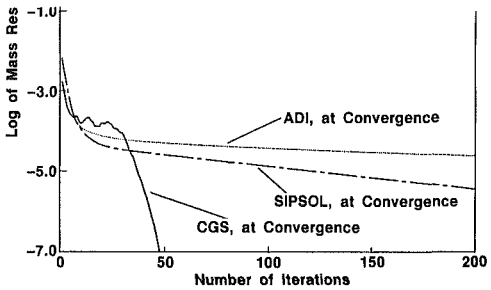

Fig. 10 Convergence history of various techniques for Langston's (1977) cascade (Chan et al., 1988)

One of the dramatic differences between various computations using the pressure-based methods is the loss distribution for Langston's cascade is shown in Fig. 11. This leads to an apparent dilemma as to the ability of various codes to predict losses and sensitivity to grid and turbulence models. The loss computations with finer grids (Chan and Sheedy, 1990) resulted in improved prediction. But Moore's computations with an algebraic eddy viscosity model apparently show the best agreement with the data.

It is evident from these discussions that the computation is very sensitive to grid, discretization and solution scheme as well as turbulence models. It is important to predict local properties and losses. In many instances (Hobson and Lakshminarayana, 1990a), the passage-averaged losses are predicted well, even though the local properties (e.g., location and strength of the loss core) in a turbine cascade are not predicted well.

As indicated earlier, very efficient codes are available for computation of the inviscid flow field for incompressible and subsonic flows, especially in 2-D cascades. For example, the

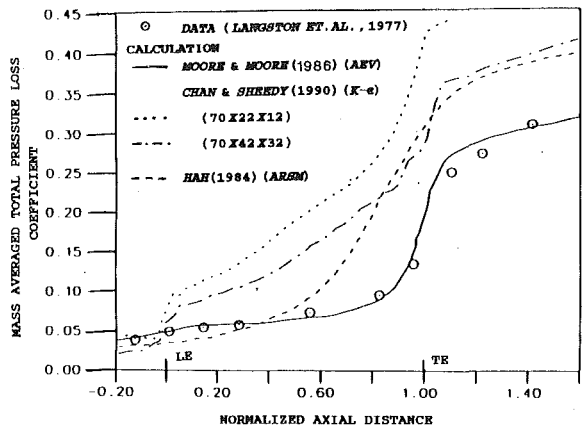

Fig. 11 Comparison of mass averaged loss distribution from various codes for turbine cascade
(C = 281.3 mm, A = 1, solidity = 0.95, λ = 35 deg, turning angle = 110 deg, α_1 = 45.3 deg)

panel method can handle two-dimensional flows as well as quasi-3-D flows. These codes are about 2–3 orders of magnitude more efficient compared to Euler or Navier-Stokes codes. Hence, the pressure field can be resolved to good accuracy except in the regions where viscous effects are large (e.g., suction surface near trailing edge regions). Availability of such codes makes PCM and PSM very attractive, and provides a quick and accurate estimate of the input pressure field for these Navier-Stokes codes. In a coupled time-marching scheme, the pressure is resolved as part of the solution, and convergence of pressure is slower than the velocity field. Since the equations are solved sequentially in the pressure-based method, only the inversion of a scalar matrix is required. This can result in significant reduction in memory and storage as compared to coupled systems (pseudo-compressibility and time marching solutions). Since convective velocity components are frozen at each iteration, and coefficients of the discretized equations are the same for all three momentum equations, the calculations can be distributed on three separate central processing units, thus taking advantage of parallel processors. This can provide a significant reduction in computational time.

The pressure-based method has been applied successfully to incompresible, compressible, laminar, turbulent, low and high Reynolds number flows for a large class of geometries. The grid system may be orthogonal or nonorthogonal. The method is flexible; either the finite difference or finite volume formulation can be employed. The technique has not been widely used for the computation of flows with shocks, even though many recent attempts (Rhie and Stowers, 1987; Hah and Wennerstrom, 1991 and Moore and Moore, 1989) indicate that shocked flows can be successfully computed and the method is as attractive as the time-marching technique described later.

Some of the major disadvantages are as follows: The convergence may be slow when large pressure gradients are present (e.g., leading edge region or large camber), and this technique has not been explored or used to compute inviscid flows. The effect of dropping viscous terms on stability of the scheme has not been investigated.

In conclusion, it is recommended that a systematic investigation on the accuracy of the solution to grid, artificial smoothing functions, and turbulence models be carried out. An investigation to evaluate this technique against others in CPU time, storage, sensitivity to grid, and convergence is also needed. The major problem with the pressure-based method is the solution of Poisson equation. Improvements in solution of this equation as well as boundary condition/specification are needed to further enhance the efficiency of this technique. The possibility of improved coupled solution should be explored. Nevertheless, the pressure-based methods are efficient and have reached a high level of sophistication; they are highly recommended for incompressible and subsonic turbomachinery flows.

10 Time-Marching Techniques

In this technique, the time derivatives in the Euler/Navier-Stokes equations are retained, thus making the equations hyperbolic in nature. Very efficient techniques have been developed to solve these hyperbolic equations for external and internal flows. The advantages of these time-iterative (or time-dependent or time-marching) techniques are as follows:

(1) The same code/algorithm is used for the solution of all flow regimes, low subsonic to hypersonic; viscous and inviscid equations.

(2) The technique is easy to implement and vectorize to take advantage of supercomputing capabilities. The equations are solved as a coupled system. The pressure, velocities, density, enthalpy, entropy, and temperature are solved simultaneously.

(3) The code/technique is flexible and the same code can be employed (with modification to boundary conditions) for external as well as a variety of internal flows; 2-D cascade, 3-D turbomachinery blade row and multi-stage turbomachinery flows, 3-D unsteady rotor and stator interaction problems.

(4) Extensive development work has been spent on these techniques by external aerodynamists and hence, the techniques are mature with considerable user experience in handling all flow situations and geometries.

(5) For complex flow geometries and flow fields, the technique is comparable in computational efficiency with pressure-based methods.

The major disadvantages are as follows:

(1) Since the technique is time-iterative and often requires very small time steps, the computational efficiency is low. This has been overcome, to some extent, by resorting to acceleration schemes such as local time stepping, multi-grid, and vectorization of the code, etc.

(2) The technique is not suitable for incompressible or very low Mach number flows. The pseudo-compressibility technique described later overcomes this problem by introduction of a time derivative.

There are two classes of methods of solving the time-dependent hyperbolic equations: explicit and implicit. Explicit methods, where spatial derivatives are evaluated using the known conditions at the old time level, are simpler and more easily vectorizable. The implementation of the boundary conditions is easier. The coding can be easily extended to include time-accurate solution. Their major disadvantages lie in the conditional stability dictated by a CFL limit, in which the numerical domain of dependence must contain the physical domain of dependence for hyperbolic equation. Unless the interest lies only in the steady-state solution, the convergence is usually slower and requires more computational time than an implicit method. Implementation of multi-grid and vector processing improves convergence and lowers computational time.

Implicit methods, where the unknown variable is derived from a simultaneous solution of a set of equations, on the other hand, usually allow for larger time steps and faster convergence and are attractive for both steady and unsteady flows. Direct solutions involve inversion of a block pentadiagonal matrix (2D) or block septadiagonal matrix (3D). This is computationally prohibitive, so approximate factorization is often employed to convert this into a block tridiagonal system. This in turn introduces a factorization error and may lead to stability problems.

Nevertheless, both explicit and implicit schemes are widely

employed in the computation of turbomachinery flows. Both of these techniques are undergoing development, and some of the disadvantages of both these techniques have been overcome. Some of the earlier methods utilized the explicit techniques exclusively. Later developments involved the implicit schemes, and recently the explicit schemes have been revived for both steady and the unsteady flow computation.

11 Explicit Time-Marching Methods

In the explicit schemes, the spatial derivatives are evaluated using known conditions at the old time level. The explicit schemes used widely for the computation of turbomachinery flows are as follows.

(1) The Lax-Wendroff scheme (1964) is second-order accurate in time and space. This scheme has the advantage of simplicity and robustness and the flow variables need to be stored only at a single time level.

(2) The predictor-corrector method due to MacCormack (1969) is a modified version of the Lax-Wendroff scheme and has been in use by external aerodynamicists for a long time. Many early turbomachinery computations were performed with this scheme, which is also second-order accurate in time and space and involves a two-step procedure. Hence, the variables have to be stored in two time steps. The method is less complex than the Lax-Wendroff technique and requires reasonable storage. The CFL limit is one for both these schemes.

(3) The Runge-Kutta type schemes (Jameson et al., 1981) have found wide application in both the internal and external flows. The four-stage scheme permits a maximum CFL number of $2\sqrt{2}$ and is a considerable improvement over the two methods listed above. This technique is likely to be explored widely for both the time-accurate (unsteady) and the steady-state solutions.

The advantage and disadvantage of the explicit versus implicit technique depend on the computational efficiency, i.e., the computer time required to achieve a converged and accurate solution. Let us examine this aspect. The total stability criterion for convection, pressure and diffusion terms in a two-dimensional flow is given by

$$\Delta t\left[\frac{|V_x|}{\Delta x}\left(1+\frac{2}{(R_c)_x}\right)+\frac{|V_y|}{\Delta y}\left(1+\frac{2}{(R_c)_y}\right)\right] + a\sqrt{\frac{1}{(\Delta x)^2}+\frac{1}{(\Delta y)^2}} \le 1 \quad (8)$$

where $(R_c)_x$ is the cell Reynolds number given by $(R_c)_x = \dfrac{\rho|V_x|\Delta x}{\mu}$

Outside the viscous region, viscous diffusion is not significant, and grid spacings (Δx, Δy) are chosen to resolve only the convection and pressure terms ($V_x/\Delta x$ etc.), moderate time steps can be taken. Inside the viscous layer and near the solid surface, diffusion terms dominate and the fine resolution of the viscous layer can only be resolved with a fine mesh, and small time steps are required in this region for turbulent flow, where the cell Reynolds number could be very small. The terms such as $(2/Rc_x)$ may dominate the criterion for the time step in the viscous and turbulent regions. This is one of the major drawbacks of the explicit methods, which require small time steps to resolve the viscous layer as well as the inviscid shock layers. In earlier computations, a constant time step was used in the entire region, but this is not necessary. If the interest lies only in steady-state solution, the scheme can be accelerated by using the time step consistent with the local CFL number for each grid point. Hence, $\Delta t_{i,j,k}$ can be chosen to vary to keep the CFL number constant over the grid. This procedure is called "variable time step" and significantly increases the convergence rate on highly stretched grids.

There is very little information available on the comparison between finite differences and finite volume methods. Since the integration of conservation variables are carried over a control volume in the finite volume technique, the error in conserving momentum fluxes should be lower than in the finite-difference techniques. Hirsch (1990) lists other advantages such as direct discretization in physical space, utilization of arbitrary mesh configuration and elimination of explicit computation of metric coefficients.

Lax-Wendroff Scheme and Its Variants. One of the most widely used class of schemes is the Lax-Wendroff (1960, 1964) technique. Even though these techniques are developed for linear equations, many modifications have been made to make them applicable to nonlinear, viscous flow in complex situations. An excellent treatment of these methods, including various modifications, stability and convergence characteristics and boundary treatment is given by Hirsch (Vol. 2, 1990).

The basic Lax-Friedrichs scheme can be written as (for two-dimensional inviscid form of Eq. (1), in Cartesian co-ordinates)

$$(\partial Q/\partial t = \partial E/\partial x + \partial F/\partial y)$$

$$Q_{i,j}^{n+1} = \frac{1}{4}(Q_{i+1,j}^n + Q_{i-1,j}^n + Q_{i,j+1}^n + Q_{i,j-1}^n) - \frac{\Delta t}{2\Delta x}(E_{i+1,j}^n - E_{i-1,j}^n) - \frac{\Delta t}{2\Delta y}(F_{i,j+1}^n - F_{i,j-1}^n) \quad (9)$$

This scheme is mildly dissipative (which may improve robustness), but does not introduce enough dissipation to capture shock correctly or even to prevent odd-even coupling on moderately stretched grids.

One of the earliest applications of this explicit scheme to turbomachinery is due to McDonald (1971), who computed inviscid flows through transonic cascades. He employed a finite-volume technique, writing the continuity, momentum and energy equations in time-dependent integral form, for a hexagonal grid (finite area) system. He modified the scheme by automatically adjusting the damping (artificial dissipation) to provide a proper balance between accuracy and stability, and the value of artificial dissipation decreased as the steady state was approached. He showed good agreement with the measured pressure distribution for a turbine cascade. This technique was extended to 3-D Euler flows by Denton (1975, 1982). The earlier technique developed by Denton in 1975 has undergone many changes. These efforts were mainly directed at the solution of 2-D and 3-D Euler equations for turbomachinery.

McDonald (1971) and Denton's (1975) method employs a finite-volume approach. The grid is set up and the equations are solved in the physical plane. Denton (1975) solves for the absolute flow variables in a rotating coordinate system. If the flow field is divided into a finite number of control volumes ΔV, then continuity, axial, tangential and radial momentum equations and energy equations (Eq. 1) in the conservative forms for inviscid flow are given, respectively, by

$$\Delta t\Sigma(\rho W_z dA_z + \rho W_\theta dA_\theta + \rho W_r dA_r) = \Delta V \cdot \Delta\rho \quad (10)$$

$$\Delta t\Sigma[(p+\rho W_z^2)dA_z + \rho W_\theta W_z dA_\theta + \rho W_z W_r dA_r] = \Delta V \cdot \Delta(\rho W_z) \quad (11)$$

$$\Delta t\Sigma[(\rho W_z r W_\theta dA_z + (p+\rho W_\theta^2) r dA_\theta + \rho W_r r W_\theta dA_r)] - \Delta t(2\Omega r \rho W_r)\Delta V = \Delta V \cdot \Delta(\rho r W_\theta) \quad (12)$$

$$\Delta t\Sigma[\rho W_r W_z dA_z + \rho W_\theta W_r dA_\theta + (P+\rho W_r^2)dA_r] + \Delta t p \cdot \frac{\Delta V}{r} + \Delta t \rho \frac{V_\theta^2}{r} \cdot \Delta V = \Delta V \cdot \Delta(\rho W_r) \quad (13)$$

$$\Delta t\Sigma(\rho W_z I dA_z + \rho W_\theta I dA_\theta + \rho W_r I dA_r) = \Delta V \cdot (\rho E)$$
$$I = H_O - \Omega r(V_\theta) = H_{OR} - U^2/2 = C_p T_{OR} - U^2/2 \quad (14)$$

In the above equations W_r, W_θ, W_2 are relative velocities, ΔV is the volume of the element and dA_r, dA_θ, dA_2 are the projected areas of the control volume in r, θ, z coordinate directions, respectively. Denton (1975) employed cuboids for the finite volume, with the node at each center. The fluxes through all sides of the control volume are calculated using the average flow properties at the four corners of the face. For stability reasons, it is necessary to provide under relaxation in the scheme. Denton uses the following under relaxation

$$\phi_{\text{new}} = (1 - SF)\phi_{\text{old}} + SF(\phi)_s$$

where $SF = 0.005$, and ϕ is the variable under consideration. He found that an order of magnitude increase in SF is necessary before the physics of the solution are affected.

A large number of computations have been carried out using this technique. In many instances the component codes are used izn quasi-three-dimensional and quasi-viscous iterations. McDonald et al. (1981) computed the flow in a transonic compressor (Dunker et al., 1977) using an axisymmetric streamline curvature calculation followed by blade-to-blade solutions using the technique just described (McDonald et al., 1971). The blade-to-blade flow calculation uses input data from a through flow calculation in the form of inlet Mach number and angle, exit angle, static pressure ratio, meridional streamline angle, and stream tube height distribution. The profile loss is modeled by using a skin friction correlation. This is a prime example of how an inviscid, two-dimensional time-marching code can be integrated with existing quasi-three-dimensional iteration techniques to predict and design the flow path. The results indicate excellent agreement with the data from 18 to 68 percent span of a transonic compressor, but the presence of complex shock structures near the tip (89 percent) is not captured well. This region may need a full Navier-Stokes solver to accurately predict the interaction between the end wall and the blade-to-blade flow field. Povinelli (1984) carried out a detailed assessment of Denton's inviscid code and its ability to predict turbine rotor flows. The code gave reasonable agreement with outlet temperature distribution but poor agreement with outlet angle distribution; it did not predict the significant underturning at mid-span rotor position, due to strong secondary flows present in the low-aspect-ratio blades. He concluded that "development of a three-dimensional viscous analysis for the rotor flow fields appear necessary."

Similar computations have been carried out by Denton (1982). The viscous corrections were applied using the displacement thickness calculated from a momentum integral technique (Singh, 1982). This involves a fully three-dimensional Euler calculation with viscous corrrections applied through boundary layer global parameters. Hence, this technique has less empiricism than the McDonald et al. (1981) code. The results were compared with LDV data for transonic fan by Pierzga and Wood (1985).

The local time step approach can be used to accelerate the scheme. Since most of the applications of this technique are for the Euler equations, the improvements are not substantial and depend on grid stretching. The most successful acceleration scheme for the Euler equation is the multi-grid scheme. In the multi-grid technique, a sequence of coarser grids is used to damp the low frequency error component of the solution. In the classical multi-grid technique, (e.g., Brandt, 1979 and Jameson and Baker, 1984), a forcing function is added to insure that the coarse-grid solutions maintain fine-grid accuracy. In Ni's (1982) multi-grid scheme, the coarse-grid equations are written in delta form, so that if the scheme converges, the coarse-grid does not affect the fine-grid accuracy. Denton (1982) was able to accelerate the computation by a factor of three through the use of multi-grid.

Ni (1982) used a one-step Lax-Wendroff type of technique to predict the inviscid flow field in cascades and turbomachinery rotors. This is a finite-volume, explicit technique with the cell-centered solution algorithm and with multi-gridding to improve convergence. The scheme is second-order accurate in time and space. Ni has extended this technique to a time-accurate solution (Ni and Bogoian, 1989 and Ni and Sharma, 1990). The finite volume equations are similar to Eqs. (10)–(14) and the procedure consists of two steps. In the first step, a finite-volume spatial approximation of the governing equation is applied to non-overlapping flow cells. The corrections to each cell node are determined by the distribution formulas, to provide the effect of upwind differencing to ensure the proper domain of dependence. As explained earlier, the computational efficiency of explicit methods is dictated by CFL numbers, and hence these techniques tend to be expensive. The computation can be accelerated by using local time stepping and multi-gridding, both of which were incorporated by Ni. In the multi-grid technique developed by Ni (1982), the solution on the fine grid is obtained by cycling the numerical procedure between the fine and the coarse grids. The coarse grid is used to propagate the corrections on the fine grid rapidly throughout the flow field, thus improving the convergence rate. The multi-grid technique can have several levels, as many levels as one can divide the grid evenly in half. Ni employs two levels, one coarse grid and the other fine grid. The coarse grid is obtained by removing every other fine grid point. In Ni's scheme, one iteration cycle consists of solution on the fine grid, and one application of coarse grid procedure to each level of progressively coarser meshes. Details of the transfer formulation and the technique can be found in Ni (1982). Ni and Bogoian (1989) utilized these techniques, developed a three-dimensional Euler code and obtained good predictions for a turbine blade. They showed excellent agreement between the data and the predictions for blade pressure distributions. A saving of 70 percent CPU time was achieved with the multi-grid procedure as compared to an all-fine-grid solution. Huber and Ni (1989) later used the code for an advanced turbine design.

The above technique has been extended to solve the Navier-Stokes equation by Chima and Johnson (1985), Chima, 1985, and Davis et al. (1987, 1988, 1989). The viscous stress terms and conduction terms are calculated by Davis et al. (1987) using central differences and stored at the computational nodes and, as such, are included in the integration step to calculate first-order changes in the flow variables at the cell center. Viscous effects are included by integrating the Navier-Stokes equation around a secondary control volume, consisting of cell centers of adjoining primary cells. The flow variables are updated according to Ni distribution formulae and the multi-grid scheme. The Baldwin-Lomax (1978) algebraic turbulence model is used for closure. Barnett et al. (1990) used Davis's (1988) code to predict flow field in a transonic compressor cascade ($M_1 \sim 0.73$, $M_2 = 0.49$, $\alpha_1 = 40$ deg, $\alpha_2 = 91$ deg, $\text{Re} = 9 \times 10^5$). The results are shown compared with data in Fig. 12(*a*). The Navier-Stokes solver and the zonal method (described later) provide better agreement with the data than the Euler solution. The scheme has successfully predicted the losses, as well as onset of separation, as shown in Fig. 12(*b*).

Cambier and Veuillot (1985, 1986, 1988) and Vuillez and Veuillot (1990) used a two step Lax-Wendroff scheme (explicit, cell-centered, finite volume). This is second-order-accurate in the inviscid zone and only first-order-accurate in the viscous regions, as dissipative terms are computed only once per iteration. The stability is ensured by second-order nonlinear and fourth-order linear artificial viscosity terms. Both local time stepping and multi-grid techniques are utilized for accelerating the convergence to steady state. Good agreement with data is shown for a supersonic cascade and wide chord supersonic fan.

Another modified version of the Lax-Wendroff technique is the hopscotch method, which combines positive features of both the explicit and the implicit schemes. The explicit and implicit schemes are combined at alternate points in a com-

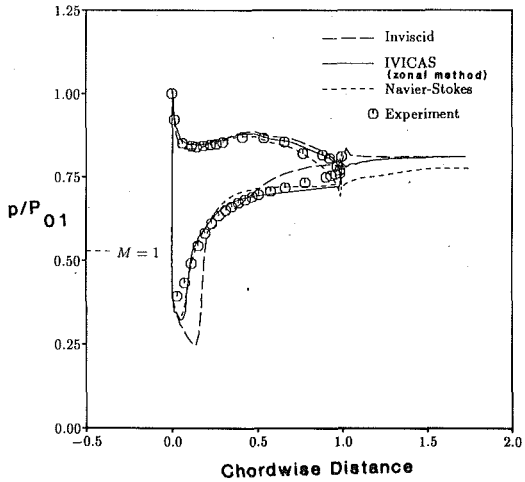

Fig. 12(*a*) Blade pressure distribution for a supercritical cascade at 7 deg incidence (data: Stephen and Hobbs, 1979; computation: Barnett, et al., 1990)

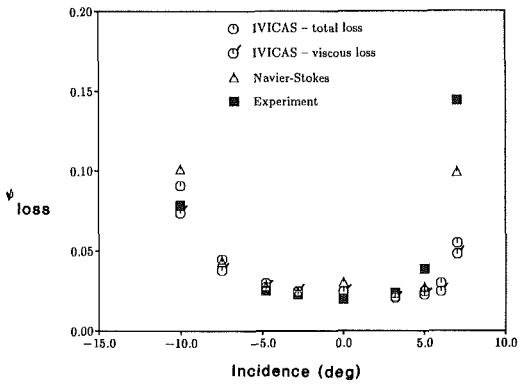

Fig. 12(*b*) Predicted loss versus incidence for a supercritical transonic compressor cascade (data: Stephen and Hobbs, 1979; computation: Barnett et al., 1990)

putational mesh to obtain improvement over previous explicit schemes. Gourlay and Morris (1972) were the first to apply the hopscotch technique to hyperbolic systems. This is a two-step scheme employing central differences for the spatial derivatives and backward differences for the time derivatives. The first sweep is equivalent to a single, linear extrapolation in time for the dependent variable. This scheme has been modified by Delaney (1983) and Sheih and Delaney (1987) and has been used to develop a 3-D Euler code for turbomachinery, with the first sweep ($i+j+n$-even) the same as Eq. (9) and the second sweep ($i+j+n$-odd) given by

$$Q_{i,j}^{n+1} = Q_{i,j}^{n} - \frac{\Delta t}{2\Delta x}[E_{i+1,j}^{n+1} - E_{i-1,j}^{n+1}] - \frac{\Delta t}{2\Delta y}[F_{i,j+1}^{n-1} - F_{i,j-1}^{n+1}] \quad (15)$$

For a repetitive application of this two-sweep process, the first sweep is equivalent to a simple linear extrapolation in time of the dependent variable.

$$Q_{i,j}^{n+1} = 2Q_{i,j}^{n} - Q_{i,j}^{n-1}$$

This simplification, they observe, results in a two-fold increase in the speed of the algorithm. The three time-level process indicated in the above equation requires only two time-level computer storage, since $Q_{i,j}$ can be overwritten with $Q_{i,j}^{n}$. The hopscotch method is first-order accurate in time, which is sufficient for the steady state solution.

Delaney (1983) and Sheih and Delaney (1987) used this technique with the boundary conditions and the CFL conditions described earlier, as well as an "O" grid to predict two and three-dimensional inviscid flows. The 3-D predictions are for a flared wall turbine cascade. Excellent agreement between the measured and the predicted pressure distribution, critical velocity ratio and the flow angle is shown. The efficiency of the hopscotch method as compared to other explicit techniques and implicit techniques are not yet known.

The results from these Euler codes (which employ Lax-Wendroff family of scheme) for compressor flows indicate very good shock capturing ability at both the peak efficiency and the peak pressure rise conditions. The 3-D Euler code with a simple boundary-layer correction scheme (Singh, 1982) or a 2-D Euler scheme combined with axisymmetric solution (McDonald et al., 1981) were able to predict the complex flow features in a transonic compressor and this demonstrates the utility of these codes in the analysis and design of turbomachinery. Some of the deviations between the computed and the measured flow field in the tip and trailing edge regions and in the shock boundary-layer region indicate the need for a full Navier-Stokes solution in these regions.

Predictor-Corrector Method. The predictor-corrector method proposed by MacCormack (1969) is a two-step procedure based on the Lax-Wendroff scheme, and is widely used for both internal and external flows. The method is second-order accurate in both time and space. It can be used for both steady and unsteady compressible flow, as well as viscous and inviscid flows.

Consider the inviscid form of the governing equations (Cartesian system of Eq. (1)) to illustrate the technique. Since a solution is sought for variable Q, and E, F are nonlinear terms, $E_{i,j}^{n+1} = E(q_{i,j}^{n+1})$ has to be evaluated. In the procedure suggested by MacCormack, an iterative approach and intermediate value $\overline{Q_{i,j,k}^{n+1}}$ is obtained by a predictor step, and $Q_{i,j,k}^{n+1}$ is obtained by a corrector step. The predictor step written for the 2-D inviscid equations in Cartesian (x, y) system is given by

$$\overline{Q_{i,j}^{n+1}} = Q_{i,j}^{n} - \frac{\Delta t}{\Delta x}[E_{i+1,j}^{n} - E_{i,j}^{n}] - \frac{\Delta t}{\Delta y}[F_{i,j+1}^{n} - F_{i,j}^{n}] \quad (16)$$

It should be emphasized here that this step provides only an approximate value for Q^{n+1}, and this can be corrected or updated using the following corrector step

$$Q_{i,j}^{n+1} = \frac{1}{2}\left\{ Q_{i,j}^{n} + \overline{Q_{i,j}^{n+1}} - \frac{\Delta t}{\Delta x}[\overline{E_{i,j}^{n+1}} - \overline{E_{i-1,j}^{n+1}}] - \frac{\Delta t}{\Delta y}[\overline{F_{i,j}^{n+1}} - \overline{F_{i,j-1}^{n+1}}] \right\} \quad (17)$$

In the "predictor" equation, a forward difference is used for E, F, and G, while in the "corrector" step, a backward difference is used for the same variables. This procedure is typically reversed in the next time step to symmetricize truncation errors. If the equations are linear, the MacCormack scheme is identical to the Lax-Wendroff scheme (1960). It can be proved that this scheme is second-order accurate in both space and time. Inadequate mesh size in regions of large gradients (e.g. shocks) result in numerical oscillations giving rise to instabilities in the code. MacCormack and Baldwin (1975) added an additional viscosity or dissipation term (source term) of the form $\epsilon(\Delta x)^4 \frac{\partial}{\partial x}\left[\frac{|V_x| + a}{4p}\left|\frac{\partial^2 p}{\partial x^2}\right|\frac{\partial V_x}{\partial x}\right]$ in the Navier-Stokes equation. This provides the necessary stability of the code. It affects the accuracy near the shock when $\partial^2 p/\partial x^2$ is large, its effect is small elsewhere.

It should be emphasized that the technique is slow without the modifications (local time step, multi-grid, etc.) mentioned earlier, as the time steps are limited by the CFL number of one. For high-Reynolds-number turbulent flows, the viscous regions (which require small time steps) are small and a locally variable time step has to be adapted to make the technique

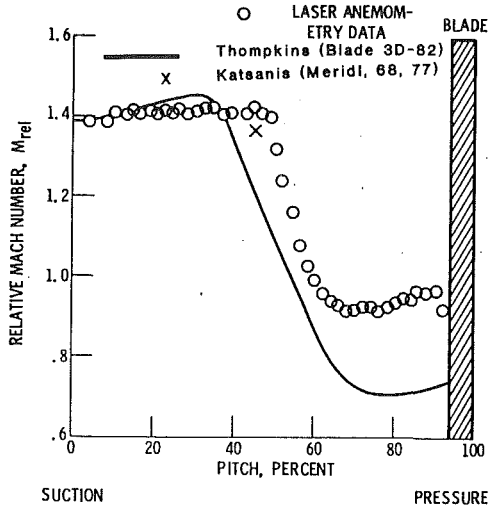

Fig. 13(*a*) Circumferential distribution of relative Mach number 15 percent of span from Tip at 23 percent of chord (through passage shock)-near-stall point (Chima and Strazisar, 1983)

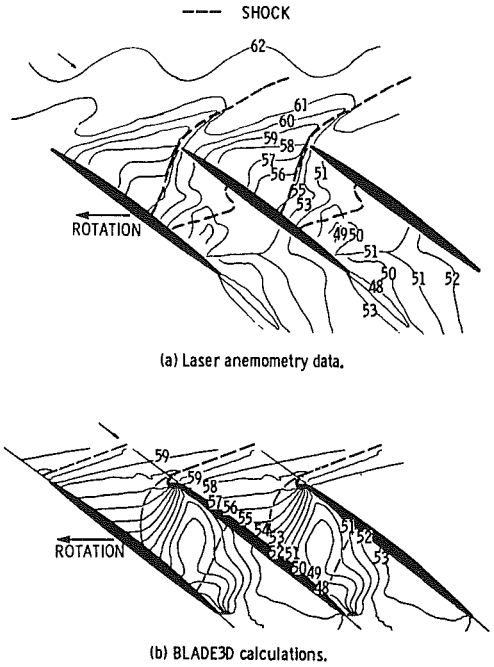

Fig. 13(*b*) Blade-to-blade contours of relative flow angle 50 percent of span from tip-maximum-flow point (Chima and Strazisar, 1983)

attractive. The efficiency of the scheme can be enhanced by vectorization.

Most of the early Euler and Navier-Stokes codes for the prediction of turbomachinery flows were based on the MacCormack scheme; both the finite-difference form and the finite-volume formulation have been employed using this technique. One of the earliest applications of the MacCormack scheme (finite difference) to turbomachinery is due to Gopalakrishna and Bozzola (1971), who predicted the inviscid transonic flow through 2-D turbine cascades. Kurzrock and Novick (1975) provided predictions for a three-dimensional blade row, including the viscous effects in an approximate manner. Thompkins (1982) and Haymann-Haber and Thompkins (1981) applied the MacCormack scheme for the Euler equation in the cylindrical coordinate system and showed qualitative comparison with the measured shock structure. Chima (1985) employed the multi-grid technique, variable time step, and a vectorized code to solve the viscous flow through cascades. The two acceleration schemes reduced the CPU time for this cascade by a factor of seven.

A comprehensive validation of explicit codes was carried out by Chima and Strasizar (1983). Laser Doppler Velocimeter measurements in a transonic compressor rotor (tip radius = 254 mm, 52 blades, tip chord = 44.5 mm, tip speed 16,100 rpm) were compared with the predictions from a 3-D Euler code developed by Thompkins (1982) and the quasi 3-D code (MERIDL/TSONIC) developed by Katsanis (1968, 1977) described earlier. The results shown in Figs. 13(*a*) and 13(*b*) indicate that the flow predictions are reasonably good, considering that the viscous effects are neglected. The Mach number, flow angle and shock structure as well as the average flow properties from hub-to-tip are predicted reasonably well. The authors had considerable difficulty in specifying the downstream boundary condition, which is based on the specification of static pressure on the hub surface. The specification of measured static pressure produced erroneous mass flows and losses as the measured static pressure include the viscous effects not accommodated in the code. The authors suggested use of an axisymmetric through flow code (example Katsanis and McNally, 1977) as a consistent and computationally efficient tool for choosing the downstream boundary.

Fourmaux and LeMeur (1987) and LeMeur (1988) used a predictor-corrector method to compute unsteady flows in turbomachinery, but showed no comparison with measured data. A novel approach was used to compute the flow field in a stage where the blade numbers are unequal. The computational domain contained k_1 and k_2 channels, where k_1/k_2 is as close as possible to the ratio of number of blades in the stator to those in the rotor. The computation of the exact geometry involves solution of flow field in almost all passages, which is prohibitively expensive. Giles (1990) utilized Ni's (1982) formulation of the Lax-Wendroff scheme and incorporated "time-inclined" computational planes to compute cases for which the ratio of stator and rotor pitches is not a simple integer. He predicted forty percent variation in lift due to unsteady shocks. The code and technique have been validated mostly against analytical solutions.

Runge-Kutta Technique. One of the most recent advances is the use of Runge-Kutta, multi-stage methods, similar to those used for the numerical solution of ordinary differential equations. Jameson et al. (1981) developed and implemented this technique for the Euler equations. This technique has received widespread acceptance for both external and internal flows, including turbomachinery flows.

An expression for a four stage Runge-Kutta method applied to a system of the form ($[Q_t = -R(Q,t)]$ can be written as

$$Q^1 = Q^n - \frac{1}{4}\Delta t R(Q^n)$$

$$Q^2 = Q^n - \frac{1}{3}\Delta t R(Q^1)$$

$$Q^3 = Q^n - \frac{1}{2}\Delta t R(Q^2)$$

$$Q^{n+1} = Q^n - \Delta t R(Q^3) \tag{18}$$

$Q^1 \ldots Q^4$ are provisional values at the new time step. The spatial derivatives are typically discretized central differences.

Martinelli (1987) carried out an analysis to include both convection and diffusion terms in the stability analysis of the numerical scheme. Kunz and Lakshminarayana (1991) carried out a stability analysis of the discrete, coupled system of equations (including the $k-\epsilon$ equations) in rotating coordinates to ascertain the relative importance of grid stretching, rotation and turbulence terms and the effective diffusivity on the stability of the scheme. They have demonstrated that the coupled

Navier-Stokes with $k-\epsilon$ and ARSM models are stable, and that rotation terms in the Navier-Stokes equation and source terms in $k-\epsilon$ equation do not affect the stability of the scheme. They further concluded that there is no advantage to numerically couple the $k-\epsilon$ equations in regard to convergence and stability, but these schemes are easily vectorizable, amenable to convergence acceleration schemes, and can be easily extended to unsteady flow computations in a straightforward manner.

Various groups have developed both 2-D and 3-D viscous codes as well as time accurate viscous codes to predict the flow field in cascades and rotors. Chima (1987) and Subramanian and Bozzola (1985, 1987) have successfully employed a multigrid technique. Some of the salient features of the techniques are as follows:

(1) The standard four-stage scheme is fourth-order accurate in time for a linear equation and only second-order accurate for nonlinear equations. The second-order central differences are used for the spatial derivatives.

(2) Often viscous and source terms are evaluated prior to the first stage for computational efficiency. This renders the scheme first-order accurate in time. Convective terms are computed at every stage. Typically, flux vectors, $\hat{E}$ and $\hat{F}$ (Eq. (1)), are computed at mid-points between nodes in a finite volume method. For viscous fluxes, this scheme incorporates information from all the nine points in the differencing molecule.

(3) To accelerate the solution to a steady state, locally varying time steps are computed based on a linear stability analysis of the discretized Navier-Stokes equations. The four-stage Runge-Kutta method allows a maximum CFL number of $2\sqrt{2}$, based on such an analysis.

(4) Central difference schemes that do not inherently damp high wave number disturbances require the addition of artificial dissipation when applied to hyperbolic system. Even for viscous flow calculations, artificial dissipation must be introduced into the scheme because the physical viscous terms are only effective in damping frequencies at higher wave numbers that can be resolved on practical grids. The fourth order operators are included to damp high wave number errors, and the second-order operators are included to improve shock capturing (Jameson et al., 1981).

(5) Implicit residual smoothing can be used to introduce some implicit character, and for increasing the maximum operational CFL number. This has the effect of smoothing the high frequency variations of the residual. The smoothing can be applied at alternate stages. Detailed discussions can be found in Jameson and Baker (1984) and Hirsch (1990, Vol. 2, p. 336).

The technique has been tested against a wide variety of flows including turbine rotors and endwall flows, supersonic and subsonic compressor cascades, subsonic compressor rotor flows, high-speed centrifugal compressors, and hydraulic turbines. The technique has also been extended to compute rotor-stator interactions.

The following list contains the applications and assessment of the method:

(1) The method has been used successfully to predict inviscid flow inside a Francis Water Turbine (Saxer and Felici, 1987; Thibaud et al., 1989).

(2) The method has been used successfully to predict two-dimensional viscous flows in cascades, quasi three-dimensional flows in turbomachinery and endwall flows in turbines (Chima et al., 1987; Chima and Yokota, 1990; Liu and Sockol, 1989; Kunz and Lakshminarayana, 1991; Zimmerman, 1990).

(3) The technique has shown promise to predict compressor and turbine rotor flows (Subramanian, 1989; Kunz and Lakshminarayana, 1991a; Erickson, 1987; Erickson and Billadal, 1989; Subramanian and Buzzola, 1985, 1987, 1989; Adamczyk et al., 1991).

(4) The technique has been extended to include time accurate unsteady flows and flows in multi-stage turbomachinery, but the validation has not been done (Jorgenson and Chima, 1989; Kirtley, Beach, and Adamczyk, 1990; Hall and Delaney, 1991, 1991a).

Kunz and Lakshminarayana (1991) computed the flow in a cascade tested at DFVLR by Schreiber (1988) at an inlet Mach number of 1.5. This precompression blade was designed especially to investigate shock boundary-layer interaction with separation. At the test free stream Mach number, a standoff leading-edge shock forms, which gives rise to a separated shock boundary layer interaction aft of mid-chord on the suction surface of the adjacent passage. This cascade operates at a "unique incidence" condition. This phenomenon, as well as the complex wave interaction field within the passage and shock-boundary-layer interaction, provides a challenging test case for both numerical schemes and the turbulence models. The predicted isentropic blade surface Mach number is plotted against the experimental values in Fig. 14. The calculation and experiment show fairly good agreement. The features labelled A, B, and C in Fig. 14 correspond to local compression regions where the bow shock impinges on the suction surface, and where the Mach reflection and the passage shock impinge on the pressure surface. Similar good agreement is also obtained for the flow downstream including the wake, and the shock boundary-layer interaction regions. In addition, good agreement is shown with the measured and computed profile losses (including shock losses at various Mach numbers).

Subramanian and Bozzola (1985, 1987, 1989) computed the three-dimensional viscous flow through turbine cascades, turbine stators, and transonic compressors. They were able to capture the endwall flow phenomena, including the presence of a horseshoe vortex, saddle point, and secondary flow. They computed the flow field for the NASA transonic compressor (designated as NASA Rotor 67) for which detailed flow data (LDV) is available (Pierzga and Wood, 1985). The design pressure ratio was 1.629 at a tip relative Mach number of 1.38 with an aspect of 1.56. The computed Mach numbers at 30 percent of span are shown compared with the measured values in Fig. 15. Also shown in this figure is the Mach number distribution of mid-passage at 30 percent span from the tip, compared with Denton's (1982) explicit-finite volume (inviscid technique), and the viscous code based on the Runge-Kutta method. The shock location, as well as Mach number distributions, is predicted well by the 3-D viscous code; the inviscid code predicted the shock location further downstream. The inviscid analysis predicts a sudden jump in properties, while the viscous code captures the physics of the flow near the shock more accurately. The inviscid codes are fairly accurate in the shock free region upstream, but it is essential to employ viscous solutions to capture shock location, shock smearing, and shock boundary-layer interaction effects.

Similar conclusions have been drawn by Erickson and Billadal (1989), who computed the flow field in a high speed centrifugal compressor (Eckhardt, 1976), using both the Euler and Navier-Stokes version of their 3-D code based on the Runge-Kutta method. This impeller is similar to Krain's impeller, whose results were shown earlier (Fig. 6). A dramatically different secondary flow pattern was observed when viscous effects were neglected in the computation. The Euler solution does not capture the exit flow for a centrifugal impeller, where the "jet-wake" flow field makes it one of the most complex flow fields encountered in turbomachinery. Even the Navier-Stokes predictions are at best qualitative. Hah and Krain (1990) seem to have resolved this flow more accurately using the pressure-based method (Fig. 6). This is not a reflection on the accuracy of the Runge-Kutta method, but on the grids and the turbulence models employed in this investigation.

The 3-D code developed by Kunz and Lakshminarayana (1991a) includes a low Reynolds number form of the $k-\epsilon$ model. This enabled them to capture the viscous flow field

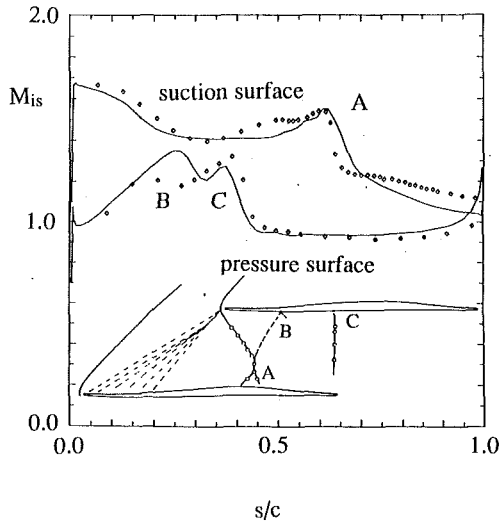

Fig. 14 Isentropic blade surface Mach numbers for the supersonic cascade
(◇ data: Schreiber, 1988; _____computation: Kunz and Lakshminarayana, 1990)
The insert shows wave pattern deduced from flow visualization and L2F measurements.

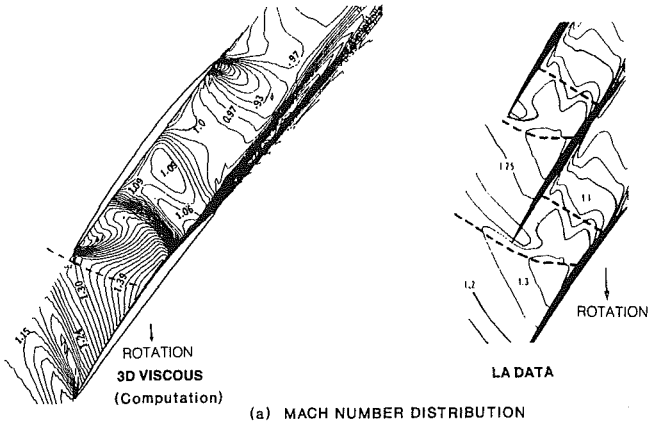

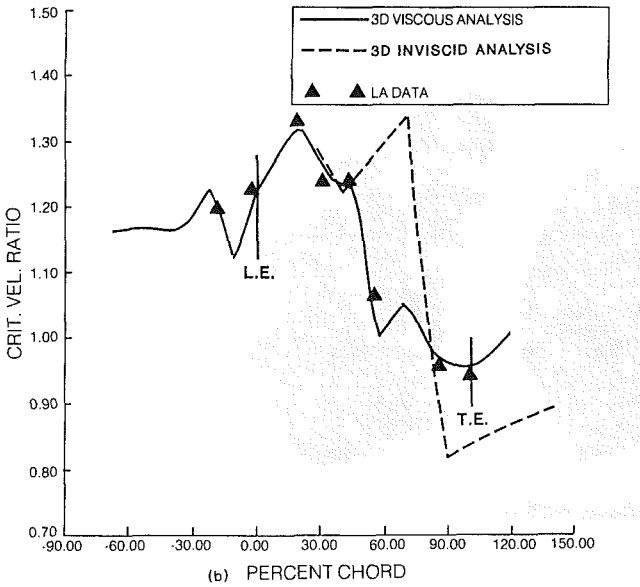

Fig. 15 Flow field in a transonic compressor
(data: Pierzga and Wood, 1985; Computation: Subramanian and Bozzola, 1987)

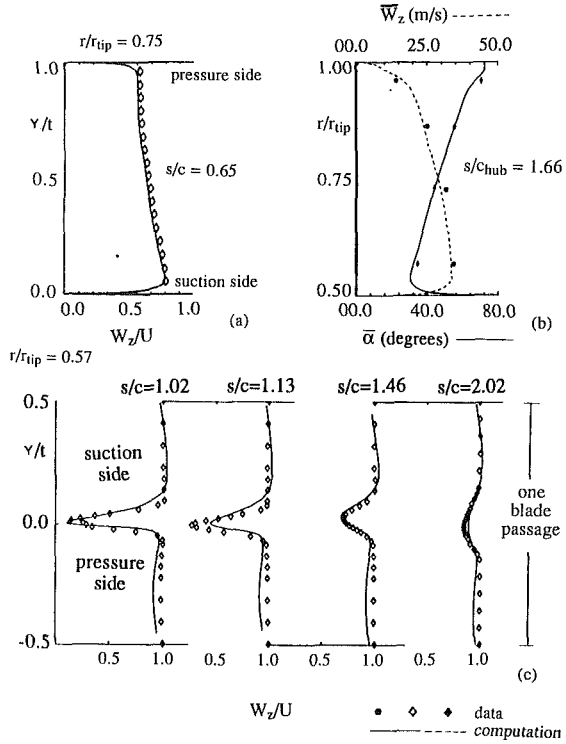

Fig. 16 Flow field in a subsonic axial flow compressor
(data: Popovoski and Lakshminarayana, 1986; Prato, 1990; computation: Kunz and Lakshminarayana, 1991a). See Fig. 2 caption for details of the compressor.
(*a*) blade-to-blade axial velocity distribution;
(*b*) radial distribution of passage averaged flow distribution;
(*c*) wake profiles at r/r_t = 0.57.

accurately, including viscous regions, boundary layers and wakes, and the spanwise mixing effects downstream of the Penn State compressor. The blade-to-blade distribution of properties, the wake, and the far downstream distribution of properties shown in Fig. 16 indicate good agreement with the measured values. This provides considerable confidence in the ability of these codes to capture important flow physics in these rotor passages.

Dawes (1987) developed an algorithm consisting of a two-step explicit and one-step implicit scheme derived as a preprocessed simplification of the Beam and Warming (1978) algorithm. It is called "preprocessed" as it involves Beam and Warming's classical implicit method and premultiplying the implicit algorithm gives it an explicit character. Hence the terminology "preprocessed." The scheme is similar in implementation to a two-step Runge-Kutta method with implicit residual smoothing. This method is hybrid in character, with both implicit and explicit schemes, and is very similar to the schemes described in this section. Dawes (1991) has recently developed a four-stage Runge-Kutta method with a solution-adaptive mesh methodology and predicted the secondary flow and the corner stall in a transonic compressor cascade. Goto (1990) has provided a comprehensive validation (Dawes, 1987 code) for a mixed-flow impeller. The Euler head rise was predicted well at four different tip clearance values. The actual head rise prediction was reasonable. The head loss coefficient ($\psi_{actual} - \psi_{Euler}$), shown in Fig. 17, indicates general agreement with the measured values. The details of the tip vortex (location, diameter) are not predicted well. As indicated earlier (see Section 3), it is essential to include higher order turbulence models to capture the physics of tip vortex. In the present method, the authors use an algebraic eddy viscosity. Nevertheless, the ability of these Navier-Stokes codes to capture the overall features of the flow field is encouraging. The jet-wake flow pattern at the exit has been captured qualitatively. Future

efforts should be directed toward improving turbulence models and grid resolution.

Zimmerman (1990) employed the four-stage Runge-Kutta scheme and carried out a detailed simulation of turbine endwall flow, including the formation of a corner vortex, horseshoe vortex and secondary vortex and their eventual roll-up. The loss distribution for high speed flow (M = 0.7, 0.9, and 1.1) shows major differences in flow losses as the Mach number is increased. The agreement between the data and experiment is not good, the authors attribute this to the turbulence model used (Baldwin-Lomax). The shock boundary-layer interaction and its effect on the flow field is not captured well.

There are instances where viscous effects may be small and an Euler code should be able to predict the flows accurately. Saxer and Felici (1987) and Thibaud et al. (1989) used a Runge-Kutta method and computed the flow field inside and at the exit of a Francis runner using an Euler code. Their results are shown in Fig. 18. The flow properties at the exit are predicted accurately, except near the outer wall. The results also indicate the sensitivity of predictions to grid density; over-refining the grids do not necessarily provide better predictions.

Hall and Delaney (1991, 1991a) used a four-stage Runge-Kutta method and implicit residual smoothing and developed a time accurate 3-D viscous code. The prediction of the suction surface static/total pressure ratio for two-bladed SR7 prop fan operating in steady flow is shown in Fig. 19. The predictions agree well with the experimental data (see Hall and Delaney, 1991a for detailed comparison). The leading edge vortex path is indicated by the region of low pressure bending across the suction surface from approximately 30 percent span toward the airfoil tip. The experimental data suggest that the leading edge vortex remains attached to the leading edge (indicated by

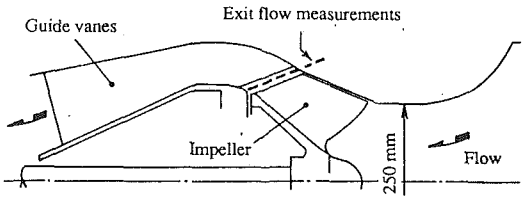

(a) Mixed-flow pump geometry. (Unshrouded case)

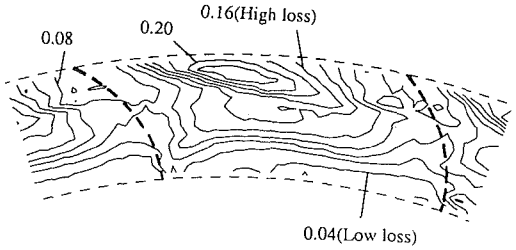

(b) Measurement Goto (1990)

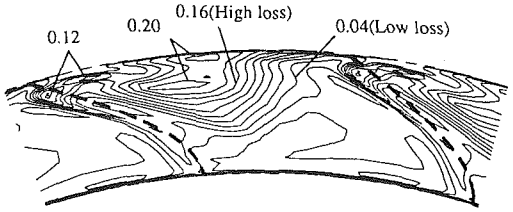

(c) Prediction Goto (1990) Dawes Code

Fig. 17 Predicted and measured loss coefficient contours at the exit of a mixed flow pump (Goto, 1990) (Design flow rate 8.7 m^3/min, head = 7.0 m H_2O, speed 800 rpm, tip clearance = 1.5 mm)

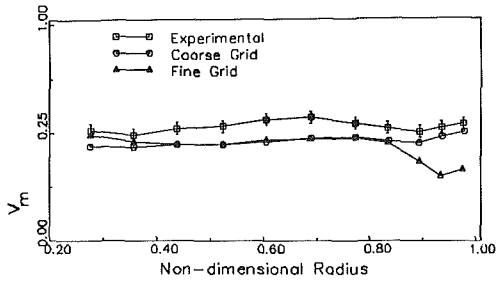

Fig. 18 Exit velocity distribution for the Francis Turbine (Saxer and Felici, 1987)

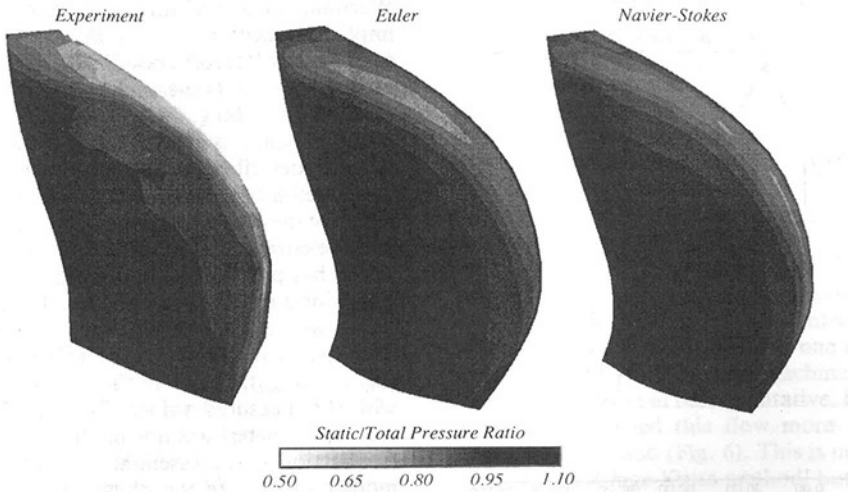

Fig. 19 Static/total pressure ratio distribution on suction side of SR7 prop fan
(data: Bushell, 1988; computation: Hall, et al., 1991a)
(M_∞ = 0.2, dia = 2.75 m, advance ratio = 0.881, 2 blades).
SR7 is designed for M_∞ = 0.8, operating with 8 blades

very low suction pressures), while both the Euler and the Navier-Stokes solution suggest that the vortex drifts further off axially of the blade. Hall and Delaney (1991a) suggest grid resolution as a potential source of error. The plot also indicates that the viscous effects are small (with the exception of leading edge vortex region) and an Euler code should resolve the blade pressures fairly accurately for this particular configuration. But the performance prediction (efficiency, losses, state) would need a Navier-Stokes solver.

In a recent investigation, Kirtley et al., (1990) utilized Adamczyk's (1984, 1989) passage-averaged equations and a Runge-Kutta technique to predict the steady-state performance of a space shuttle main engine turbine. The results indicate a complex pressure field dominated by tip leakage flow, especially in the second stator. More important, the predicted overall temperature and pressure drop agree well with the design values.

Assessment Summary for Explicit Schemes. The preceding discussion indicates that the explicit techniques are highly successful in predicting complex flow field in turbomachinery. The choice between an Euler solution and a Navier-Stokes solution depends on the type of flows and the machinery. Centrifugal machinery and high speed compressor flows are best resolved with a Navier-Stokes solution. The hydraulic turbine flow field can be captured with an Euler code. This should be combined with boundary layer codes to predict the efficiency and losses.

Among the explicit methods, all the techniques seem to perform well for viscous flow through turbomachinery. The two-step formulation of Ni, Lax-Wendroff schemes, and Runge-Kutta method, all perform well. The Runge-Kutta method allows for a larger time step than that of other schemes. All of these schemes provide inherent artificial dissipation due to truncation error. The Runge-Kutta schemes are somewhat less dissipative at high wave numbers than other formulations when applied to convection problems. For this reason, artificial dissipation must be purposefully added to these schemes, usually after each stage in the update procedure. This may provide the user with better control over levels of artificial dissipation present in a solution. The Runge-Kutta method has been widely used and is currently undergoing major development. The Runge-Kutta method is especially attractive if implemented with implicit residual smoothing, local time stepping, multigrid and in finite volume formulation. These and other techniques can be vectorized, and accuracy can be improved with velocity scaling for artificial dissipation. Moreover, all these techniques, especially the Runge-Kutta method, are attractive for unsteady flow.

12 Implicit Time-Marching Methods

One of the major disadvantages of explicit methods is that the size of the time step is limited by CFL conditions. This led to widespread use of implicit techniques which can be unconditionally stable for all time steps. In the implicit method, the calculation of an unknown variable requires the solution of a set of simultaneous equations. A review of various implicit techniques used in computational fluid dynamics can be found in Anderson et al. (1984) and Hirsch (1990). Only the techniques that are widely used in turbomachinery flow computations are discussed here.

Approximate Factorization. One of the most widely used implicit techniques is that due to Briley and McDonald (1976) and Beam and Warming (1978). This technique is widely used, with modifications, to predict viscous flow fields in cascades, stators, and rotors. Linear stability analysis provide that the schemes are unconditionally stable in two dimensions. Operational CFL numbers in the order of 10 appear to provide the best error damping properties. There is no CFL limit, even though there are some constraints on the time step. Most authors use the Baldwin-Lomax turbulence model. As in the explicit techniques, both finite-volume and finite-difference formulations are employed; these are briefly summarized in this section. The scheme for the two-dimensional inviscid form of Eq. (1) in Cartesian coordinates can be written as

$$\left(I+\frac{\Delta t}{2}\frac{\partial}{\partial x}A^n\right)\Delta Q^* = -\Delta t\left[\frac{\partial E}{\partial x}+\frac{\partial F}{\partial y}\right]$$

$$\left(I+\frac{\Delta t}{2}\frac{\partial}{\partial y}B^n\right)\Delta Q^n = \Delta Q^* \tag{19}$$

where I is the identity matrix and

$$Q^{n+1} = Q^n + \Delta Q^*,\ A=\frac{\partial E}{\partial Q},\ B=\frac{\partial F}{\partial Q}.$$

The major computational effort is expended in inverting the block tridiagonal matrix system that arise. Even though large time steps are allowed (for steady state problems), the additional effort involved in the inversion of these matrices and large amounts of storage make the two methods (explicit and implicit) comparable in computational effort. Hence, there is no clear advantage of one method over the other. The increased stability bounds for the implicit schemes offer some advantages. Other improvements include diagonalization of the blocks in implicit operators, pressure velocity split, grid refinement, improved boundary conditions, implicit treatment of artificial viscosity terms, variable time step, and multi-gridding. These can be found in Pulliam (1986).

Most investigators use the ADI scheme, each factorized step requiring inversion of a block tridiagonal matrix. For three dimensions, one of the ways to improve the computational efficiency is to implement LU (lower and upper diagonal) factoring. In this method, the matrix coefficient in the discretized algebraic equations are split into two matrices. The lower and upper diagonals are derived from the original matrix through the Gauss elimination procedure and this scheme is called LU decomposition. LU decomposition reduces storage requirements. Such a scheme has been implemented by Jameson and Turkel (1981) and incorporated into an internal flow code by Buratynski and Caughey (1986). Yakota (1990) has developed an implicit LU method with a multi-grid scheme for turbomachinery and computed turbine stator endwall flow.

Several attempts have been made to employ this factored implicit technique to predict flow field in cascades and turbomachines. Some of the earlier computations were done by Steger et al. (1980) and Shamroth et al. (1982) and were confined mostly to cascade flows. Only qualitative trends were shown. Recent application of these techniques to turbomachines include turbomachinery rotor and stator blade rows. Knight and Choi (1989), Choi and Knight (1989, 1988) employed the implicit approximate factorization method described, finite-volume formulation, second-order upwind differencing and a two-equation turbulence model. A cell-based finite-volume formulation was used for spatial discretization. The finite-volume discretization allows for flexibility in grid construction. Local time stepping was employed to accelerate the convergence. Knight and Choi (1989) computed many turbomachinery flows including the flow field in an Energy Efficient Engine (E^3) turbine vane. Their results are shown compared with data in Fig. 20. The flow field computation indicates the presence of a supersonic region at the exit. The losses and outlet angles are predicted reasonably well. The location of passage vortices (marked A and B in Fig. 20) is also predicted well. The underturning near the wall and a slight overturning away from the wall are also captured.

One of the interesting applications of CFD is the computation of flow fields in automotive torque converters. The passages in these devices are narrow, with very close pump-turbine-stator spacings all enclosed in a casing. The flow field

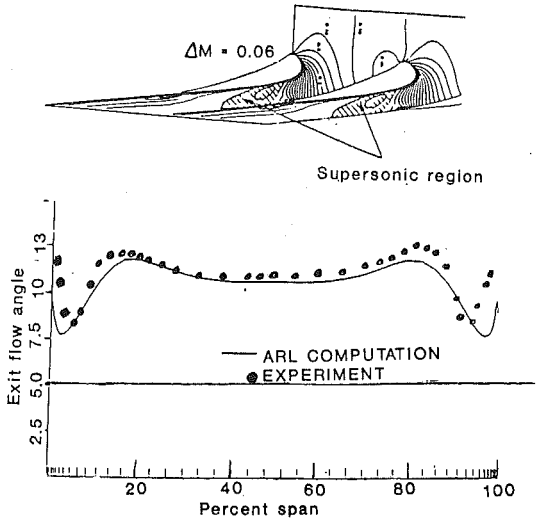

(a) Spanwise variation of mass-average flow angle at exit

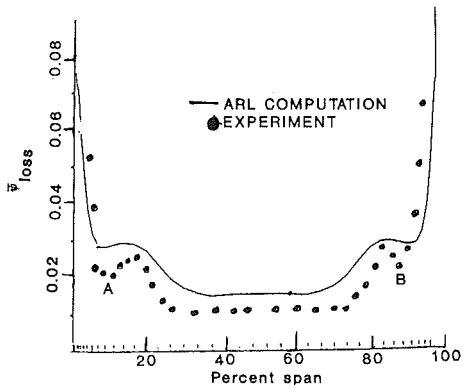

(b) Spanwise variation of passage averaged loss coefficient

Fig. 20 Flow field in energy efficient turbine nozzle (data: Kopper, et al., 1981; computation: Knight and Choi, 1989) (C = 9 cm, t = 8.46 cm, A = 0.513, α_1 = 90 deg, M_1 = 0.109, M_2 = 0.85)

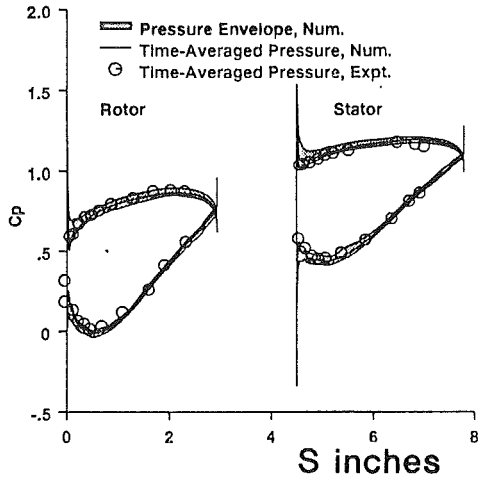

(a)

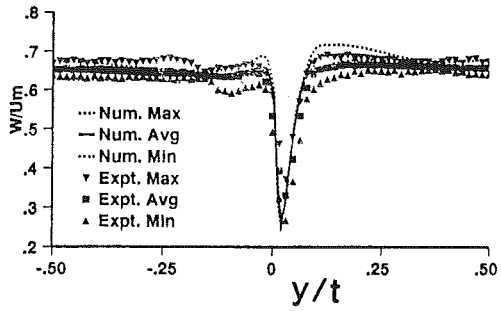

(b)

Fig. 21(*a*) Time averaged blade pressure and (*b*) rotor wake in a multi-stage compressor (data: Joslyn et al., 1989; computation: Gundy-Burlet, et al., 1990) (dia = 1.52 m, hub/tip ratio = 0.8, U_m = 46.7 m/s, no. of blades 44 in all rows, axial velocity/mean blade speed ratio = 0.510)

is very complex. Fujitani et al. (1988) discretized the Navier-Stokes equation using a first-order Euler implicit scheme for the convection term. Since no detailed flow data are available in these torque converters, it is difficult to access the code's capability to capture details of the local flow field. But the major interest in automotive torque converters is the torque ratio and the efficiency; these were predicted reasonably well. The efficiency prediction under cruise conditions is not good. Here again, it is doubtful whether a laminar flow solution with coarse grid can provide the detailed flow resolution needed to improve torque converter performance and design.

Nakahashi (1989) and Matsunaga et al. (1990) developed an LU implicit scheme and predicted turbine endwall flow. This code has been used to design an efficient bowed turbine vane. Weber and Delaney (1991) have developed a 3-D code based on Beam and Warming's scheme (1978) and predicted flow field for a NASA 67 compressor with both C and H grids and concluded that C grids provide better resolution of flow field.

Upwind Schemes. The conventional techniques described earlier, both explicit and implicit, use artificial viscosity terms, which must be specifically chosen and tuned for a particular problem. If strong shocks are present, employment of large numerical dissipation may obscure the real physics. One of the recent developments to overcome this problem is the development of upwind schemes (Osher and Solomon, 1982). This has been applied to both explicit (Chakravarthy and Osher, 1983) and implicit techniques (Rai and Chakravarthy, 1986). Upwind schemes are attractive since they provide a rational mathematical framework for adding dissipation to a scheme. They may be more robust than schemes with artificial viscosity. They do not usually have operator prescribed constants.

Most earlier techniques use conservative central difference schemes to capture shocks, requiring arbitrary smoothing parameters (artificial dissipation) to stabilize the calculation. The upwind difference schemes are used to capture strong shocks without requiring arbitrary parameters, which may alter the physics of the problem. The flux evaluation is numerically more intensive in upwind schemes; the scheme is more complicated to code and requires more computational time. This technique is still in the development stage.

This technique has also been extended to compute time accurate flows, and the major feature of the unsteady effects (unsteady pressures) has been captured (Rai, 1987, 1989). Rai was one of the first ones to predict viscous rotor-stator interaction in 2-D and 3-D flows. His work prompted considerable interest in the field. Gundy-Burlet et al. (1990) have used Rai's code to predict the quasi-steady and unsteady flow in a low-speed multi-stage compressor using a zonal grid system (alternately moving and stationary grids) and Rangawalla and Rai (1990) attempted prediction of rotor-stator interaction noise. The time-averaged pressure as well as the time-averaged

wakes are predicted well for Joslyn and Dring's multi-stage compressor (1989) (Fig. 21). The prediction of unsteady pressure distribution (Rai, 1987, 1989) is qualitative. This is an extremely complex case to compute, and recent advances made in this direction are noteworthy. What is needed now are improvements in transition and turbulence modeling in unsteady flow. Very little is known about the applicability of the turbulence models developed for steady flow to unsteady flows. The author's experience is that many of the important physical features are not captured by algebraic eddy viscosity models.

Assessment of Implicit Schemes. Implicit techniques for steady 3-D Euler and 3-D Navier-Stokes have reached a high level of maturity and are widely used in turbomachinery flow field computation. The techniques enable large time steps, but may introduce factorization error. Combined with local time stepping, multi-grid, and the LU scheme, they are as attractive as explicit codes. A wide variety of turbomachinery flows have been computed, including incompressible turbomachinery flow fields. Future directions will involve incorporation of higher order turbulence models and parallel processor implementation.

One of the comprehensive assessments of Rai's code for unsteady flow in turbomachinery has been carried out by Griffin and McConnaughey (1989). The aerodynamic and thermal data from Dring et al. (1986) were compared against Rai's code, and Katsanis and McNally's code (1977) combined with a boundary layer code (STAN 5-Crawford and Kays, 1976). The predictions from both codes for Dring's rotor (time-averaged heat transfer), are shown in Fig. 22. Both approaches yield similar agreement with the heat transfer data. Rai's code required six CPU hours and Katsanis and McNally's code, including the boundary layer calculation, required eight CPU minutes on a Cray XMP. Griffin and McConnaughey conclude that if the interest lies only in the time-averaged quantities, a conventional method is the better approach, as it requires much less computational time. If the interest lies in characterization of unsteady flow (e.g., viscous wakes and unsteady boundary layers), then the Navier-Stokes approach may be better. Even here, one has to qualify this statement. If the interest lies only in unsteady pressure on the blade, the linearized theories (see Platzer and Carta, 1987 for a review) can provide satisfactory results. For example, Chen and Eastland (1990), used Lakshminarayana and Davino's (1980) wake correlation and a linearized potential flow analysis to predict accurately the unsteady blade pressures measured by Dring et al. (1986) in a small fraction of computer time required by the unsteady Navier-Stokes code. The usefulness of the unsteady Navier-Stokes code lies in resolving the passages of wakes, unsteady flow field including boundary layers, and off-design performance in a multi-stage blade row.

Explicit Versus Implicit Time-Iterative Techniques. Both explicit and implicit techniques are widely used, with explicit techniques more commonly used in industry. Both techniques can incorporate local time stepping. The maximum time step (CFL) for a four-stage Runge-Kutta method is 2.8, and typical CFL numbers for the implicit LU scheme and ADI schemes are 5 to 10, respectively (Hall, 1989). But ADI schemes have more operations per iteration, and harder to vectorize. Hence, there is no great advantage in ADI over Runge-Kutta, maybe a factor of 2 at best. Rai (1987, 1989) uses much higher CFL numbers in his upwind scheme. Multi-grid is extensively and successfully used in explicit schemes, with some success in implicit schemes. The implicit residual smoothing is an attractive feature in the Runge-Kutta method. Both techniques are sensitive to grid stretching and skewness, and turbulence models. Explicit methods are easier to code, vectorize and adapt to massively parallel computers.

One of the extensive comparisons of various explicit and implicit techniques is due to Hall (1989) and Hall et al. (1990).

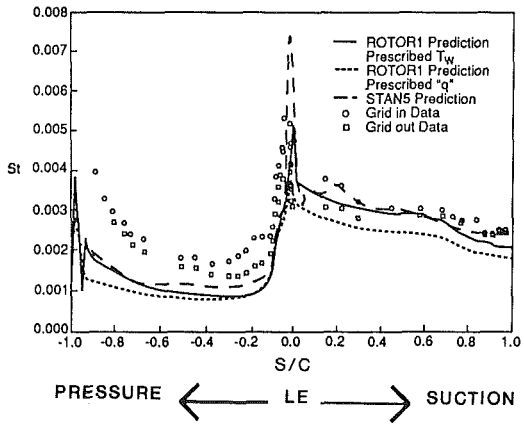

Fig. 22 Heat transfer on a turbine stator blade (data: Dring, et al., 1986; computation: Griffin and McConnaughey, 1989) — (ROTOR 1-Rai's Code, STAN 5-Boundary Layer Code) (dia = 1.52 m, hub/tip ratio = 0.8, aspect ratio = 1, 22 stator vanes, 28 rotor blades)

They have made a systematic (same grid, turbulence model, and computer) comparison of the explicit Hopscotch and Runge-Kutta scheme, implicit Beam and Warming's Approximate Factorization Linear Block Implicit Scheme (AFLBI) and the upwind generalized conjugate gradient total variation diminishing (GCGTVD) scheme for the following cases of 1) Inviscid flow over a cylinder; 2) Steady viscous/inviscid flow through a turbine cascade; 3) Unsteady viscous flow over an impulsively started cylinder.

The results for a turbine cascade indicate that all techniques/codes provide nearly identical pressure distribution; major differences lie in the CFL number and CPU seconds for convergence, as shown in Table 1. It is evident that for viscous flows, explicit methods require appreciably less computer time, even though this is not significant in terms of new developments that may occur in computer architecture. Hall (1989) concludes "that the choice of explicit versus implicit technique and the time accuracy of a given algorithm may have less to do with the accuracy of the predicted results than the nature of numerical damping and application grid." All of the schemes can predict most of the complex flow field in turbomachinery as indicated in earlier sections. But, the Runge-Kutta method shows somewhat superior performance as the artificial viscosity is introduced and controlled by the user; it is easy to code and vectorize and has received wide acceptance by the turbomachinery community.

Liu et al. (1991) have provided a comparison of the explicit (Subramanian and Bozzola, 1987) and implicit (Dawes, 1987) codes described earlier for the three-dimensional viscous flow in a high work turbine stator using identical grids and turbulence models. The flow field, losses, and outlet angles predicted are nearly identical. The authors have not provided any details on the computational efficiency.

13 Pseudo-Compressibility Technique for Incompressible Flow

Since a large number of turbomachines (especially liquid handling pumps and turbines) operate in the low speed range, incompressible flow prediction capability is important to the efforts of researchers to improve analysis and design techniques for these turbomachines.

The pressure-based methods solve a Poisson equation for pressure and the momentum equations in an uncoupled manner, iterating until a divergence-free flow field ($\nabla \cdot \underline{V} = 0$) is satisfied. On the other hand, it is evident from the material presented in the earlier section, very efficient and accurate algorithms have been developed for solving hyperbolic systems

Table 1 Comparison of various techniques, Hall (1989)

Viscous high-turning turbine cascade CPU time comparison

Method	CFL number	Iterations for convergence	CPU seconds for convergence	CPU seconds grid point/it.
Hopscotch	0.7	4043	224.70	$1.18\times10(-5)$
Runge-Kutta	1.5	3100	365.03	$2.50\times10(-5)$
AFLBI	3.0	1745	616.42	$7.50\times10(-5)$
GCGTVD	5.0	1497	706.50	$10.02\times10(-5)$

Impulsively started cylinder flow CPU time comparison, Re = 3000

Method	CFL number	Iterations for convergence	CPU seconds for convergence	CPU seconds grid point/it.
Hopscotch	$5.0\times10(-6)$	25,000	1759.00	$1.968\times10(-6)$
Runge-Kutta	$1.0\times10(-5)$	12,500	1799.00	$5.033\times10(-6)$
AFLBI	$2.5\times10(-5)$	5,000	2500.00	$2.798\times10(-5)$
GCGTVD	$2.5\times10(-5)$	5,000	3600.00	$4.029\times10(-5)$

governing compressible flow using time-iterative methods. Prediction of incompressible flow (very low M) using these techniques is not efficient and is not recommended. Furthermore, the energy equation in Eq. (1) has to be decoupled from the momentum equation for isothermal flows. Hence, there is a need for efficient techniques for solving incompressible flow. One approach involves recasting the incompressible flow equations (which are elliptic in steady state) as hyperbolic systems. One of the techniques which is finding wide use is the psuedo-compressibility technique due to Chorin (1967, 1968). To make the governing equations behave like a hyperbolic system, Chorin manipulated the continuity equation by adding a time derivative of a pressure term. In the steady state, these equations and solutions are exactly those of steady incompressible flow, even though the temporal solutions are not accurate. The continuity equation in this formulation is written as

$$\frac{1}{\beta}\frac{\partial p}{\partial t}+(\nabla\cdot\underline{V})=\frac{1}{\beta}\frac{\partial p^*}{\partial t} \tag{20}$$

where β is a psuedo compressibility parameter (as $1/\beta\ \partial p/\partial t$ behaves like $\partial\rho/\partial t$ term in the compressible formulation). p^* is the value of p at the previous iteration. This modification results in a hyperbolic system of equations. For example, in Eq. (1), the modifications include

$$Q=[p/\beta,\ W_r,\ W_\theta,\ W_z]^T$$
$$E=[W_r,\ (W_r^2+p/p-\tau_{rr}),\ (W_rW_\theta-\tau_{r\theta}),\ (W_rW_z-\tau_{rz})] \tag{21}$$

and similarly the vectors F, G, S are modified.

The formulation given by Eq. (20) introduces spurious pressure waves of finite speed into the fluid through the psuedo-compressibility parameter β. When $\beta\gg1$, the transient effect on the solution is minimized, but the artificial terms drop out at steady state. A detailed discussion of psuedo-compressibility technique, including a stability analysis, can be found in Kwak et al. (1986). Kwak et al. show that for turbulent flow, a lower bound for β should not be approached due to the retarding effects on convergence speed, accuracy, and stability. This criterion is given as

$$\beta\gg\left[1+\frac{1}{\mathrm{Re}_t}\left(\frac{X_{\mathrm{ref}}}{X_\delta}\right)\left(\frac{X_L}{X_{\mathrm{ref}}}\right)\right]^2-1$$

where Re_t is the Reynolds number based on the eddy viscosity and X_δ, X_L, and X_{ref} are characteristic lengths for vorticity waves, pressure waves, and geometry, respectively. The basic laminar psuedo-compressibility code developed at NASA Ames Research Center (Kwak et al., 1986) was modified by Warfield and Lakshminarayana (1989) for turbomachinery configuration to include rotation and turbulence models, to compute the flow in a low-speed compressor rotor. The psuedo-compressibility formulation is linearized, using a truncated Taylor series and discretized using a two-point central difference in the spatial directions. The solution technique is the standard implicit approximate factorization scheme described earlier. Constant explicit and implicit smoothing were utilized to facilitate stability and convergence of the solution. Convergence acceleration was implemented in the form of a variable time step (constant local CFL number).

It should be remarked here that any of the explicit and implicit techniques can be used to solve Eq. (1) with psuedo-compressibility formulation. Kwak et al. (1986) and Warfield and Lakshminarayana (1989) used the implicit technique due to Beam and Warming described earlier. Merkle and Tsai (1986) have employed the Runge-Kutta method. The technique described under pressure-based methods (Kirtley and Lakshminarayana, 1988) utilized the psuedo-compressibility concept, but solves the equations using the pressure-based methods.

The psuedo-compressibility technique has been utilized to predict the turbulent flow field in a 90 deg turning duct, cascade, rotating channel (Warfield and Lakshminarayana, 1987), and the Penn State compressor (Warfield and Lakshminarayana, 1989, and Suryavamshi and Lakshminarayana, 1991) at two different operating conditions with good agreement with the measured data. Extensive data are available for the Penn State compressor rotor, including the entire inviscid flow field, blade boundary layer, hub wall boundary layers and tip clearance flow. This is a low speed compressor with a 21 blade rotor, and a hub-to-tip ratio of 0.5. The operating conditions were a flow coefficient of 0.56 and a loading coefficient of 0.4884. The blade boundary layer and the complete flow field are predicted at the peak pressure rise coefficient, where the boundary layer growth is substantial. This is a severe test case for checking the validity of a three-dimensional Navier-Stokes code. The blade-to-blade flow, including the growth of the boundary layer along the blade, is predicted well (Fig. 23). Furthermore, the development of the wake, the spanwise mixing effects and radial distribution of losses are also predicted well (Suryavamshi and Lakshminarayana, 1991).

Assessment of PCT and Comparison With PBM. The psuedo-compressibility technique (PCT) utilizes well developed time and iterative techniques, but the stability and convergence are sensitive to the value of the parameter β. This value varies with configuration and flow regime (laminar, turbulent). Once an optimum value of β is achieved, the technique is more efficient than a corresponding compressible-flow formulation. This technique is suitable for pumps, hydraulic turbines, and other low speed turbomachinery. It is suitable for flows with separation, and the technique can be extended to unsteady flows (Rodgers et al., 1989). A wide variety of geometries and flows (cascade endwall flow, low speed compressor, S and 90 deg bends, space shuttle main engine hot gas manifold, rocket pump inducer, artificial heart pump) have been computed.

Recent developments on this technique include the use of a diagonal scheme for the inversion of the equations at each iteration (Rodgers et al., 1987), extension of unsteady flow

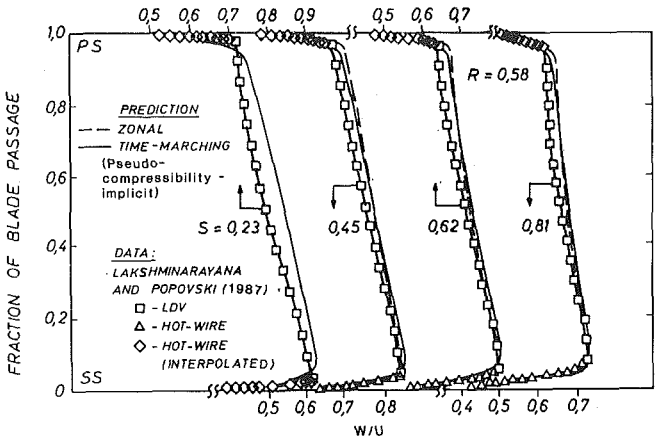

Fig. 23 Flow field in a subsonic single stage axial compressor (Warfield and Lakshminarayana, 1989)

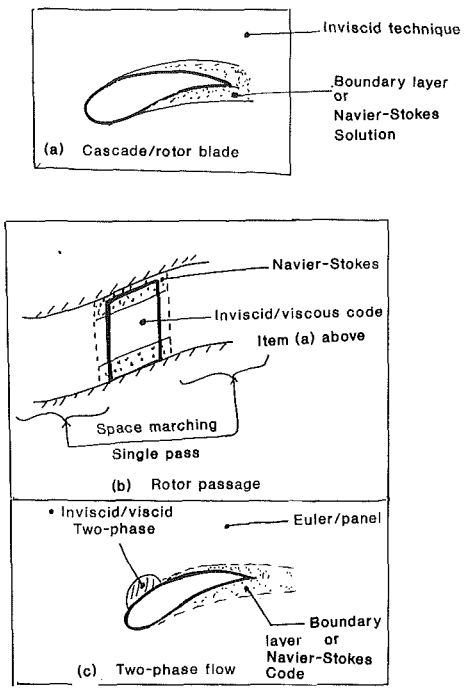

Fig. 24 Examples for zonal technique

(Rodgers et al., 1989), acceleration by introducing artificial bulk viscosity to dissipate the sound waves rapidly (Ramshaw and Mousseau, 1990), and preconditioned upwind method to accelerate the scheme by steady state (Hsu et al., 1990). These techniques are still in the development stage and have not been applied to turbomachinery flows. When these are incorporated, the technique and code may compete effectively with the pressure-based methods described earlier.

With regard to the pressure-based method (PBM) versus the psuedo-compressibility technique (PCT), PBM is well established, widely used and user friendly, and has lower storage requirements than PCT. It is easier to implement $k-\epsilon$ and ARSM models in the PBM. In situations where large pressure gradients exist (leading edge, large chamber, etc.), PBM convergence slows down in an uncoupled approach. In PCT, the pressure is solved in a coupled fashion, and this may have some advantage. The PCT requires large storage and an experienced user to choose an optimum value of β. The PCT can be further developed to become more attractive. Incorporation of multi-grid, an LU scheme (implicit) or Runge-Kutta scheme (explicit) could enhance its efficiency.

14 Zonal Techniques

It is evident from the various techniques presented in this paper that the solution of the Navier-Stokes equations by iterative techniques require a large amount of computer storage and time for three-dimensional turbulent flows. Future application of these techniques to the entire blade row, single stage and multi-stage turbomachinery, flows will challenge the computing power of present and future computers. Utilization of these techniques on a day-to-day basis for design in industry requires efficiency and cost effectiveness. As indicated earlier, the Navier-Stokes equations can be reduced to the Euler equations, potential equations, boundary layer equations, and parabolized Navier-Stokes equations. These are some of the approximations made to reduce the equations to forms amenable to efficient computation. Unfortunately, these equations do not provide solutions to the flow in the entire region. On the other hand, the solution of Navier-Stokes equations in the entire region is prohibitively expensive and challenges the computing power in terms of storage and cost. The zonal techniques overcome this problem. Instead of using one equation system in the entire region, several zones are identified and the solution is obtained by using the appropriate equations (Euler, PNS, BL code) and patching and integrating these regions. For example, one of the widely used techniques is a cascade solution consisting of potential equations in the inviscid region and boundary-layer equations in the viscous region, with interaction of these two regions to update the pressure and velocity fields due to boundary layer growth. The efficiency, cost, accuracy, and robustness of a code are important for repetitive runs for design and analysis of blade geometry. Duct flows are generally parabolic and can be resolved through a combination of inviscid codes and PNS codes.

Furthermore, the boundary-layer codes or space-marching codes are computationally very efficient and finer grid could be used near the surface to capture the viscous layers accurately. Examples where such zonal techniques are useful are ducts and inter-blade row, cascades and inviscid dominated subsonic rotors and multi-stage turbomachinery, where Navier-Stokes solutions are expensive. Some examples of zonal approach are given in Fig. 24.

An additional point is that even though the Navier-Stokes equations are universally valid, for certain classes of flows, reduced forms are actually more appropriate. For example, many boundary layer and duct flows are parabolic flows where downstream boundary conditions (which are necessary for Navier-Stokes solutions) can be difficult to determine. These situations actually make the Navier-Stokes system difficult to apply. The principal motivation behind zonal equation methods is to decrease the computation time and computer storage necessary to compute the solution for flows which exhibit localized regions of ellipticity. These regions inhibit the use of parabolized methods but are small enough to make a full iterative NS solution seem inefficient. The zonal techniques can be interactive or noninteractive depending on the requirement, and use of the most efficient techniques in each region.

A brief review of various zonal techniques is given in Warfield and Lakshminarayana (1987). These can be classified as: 1) Viscous/Inviscid Techniques, 2) Supersonic/Subsonic Techniques, and 3) Viscous/Viscous Techniques. Some of the current zonal techniques are shown schematically in Fig. 25.

Coupled Inviscid/Boundary Layer Solutions and Assessment. Normally this is an interactive procedure, with the inviscid solution feeding the boundary layer edge information to the viscous solver, while the viscous solution feeds displacement thickness information to the inviscid solver. The interaction is complete when a converged boundary layer solution

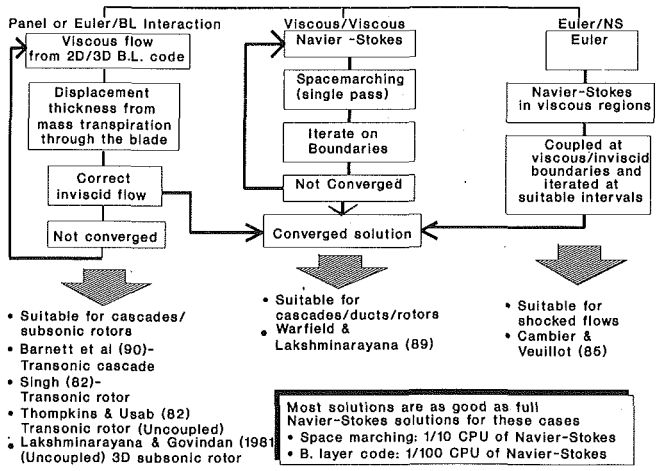

Fig. 25 Classification of zonal techniques

and the inviscid solution are reached. The boundary layer equations, being the appropriate equation set within the boundary layer, are normally solved either in differential or integral form for the viscous effects. The inviscid solution is achieved through Euler or potential solvers or both.

A general procedure can be outlined as follows: (Calvert et al., 1982, and Barnett, 1990)

(1) The inviscid flow field is computed from any of the techniques listed above, depending on the flow regime and geometry. For example 2-D incompressible flow is best handled by a panel method, supersonic and high-subsonic flows by an Euler equation, and subsonic flows by either a potential or a stream function solver.

(2) A boundary-layer code is used with the prescribed pressure (from item 1) to predict the local properties or the global properties (integral technique).

(3) If viscous effects are small (very thin boundary layer), the computation can be terminated here. If the viscous effects are substantial, the displacement thickness is calculated and the blade profile is modified to recompute the inviscid flow field. The viscous displacement effect is represented by a mass transpiration through the surfaces of the blades, and by a jump in the normal velocity component along the wake streamlines. These are specified so that the inviscid streamlines are displaced to conform to the effective displacement, which includes the blade profile plus the displacement thickness. The transpiration velocity is given by

$$\rho v|_s = \frac{d}{ds}(\rho_e U_e \delta^*) \tag{22}$$

where δ^* is the displacement thickness.

(4) The inviscid and viscous equations are coupled through the appropriate boundary conditions on the blade surface and the wake edge. The solution of the complete flow is obtained by "global" iteration between the viscous and the inviscid solutions, varying the displacement thickness parameter until the viscous-layer edge velocity matches with the corresponding inviscid velocity. Inverse or semi-inverse coupling or fully coupled techniques are needed to ensure convergence.

Barnett et al. (1990) utilized Ni's (1982) multi-grid Euler solver described earlier to resolve the inviscid flow. The boundary layer code utilized is that due to Carter (1978) which is a finite-difference formulation of a compressible stream function approach. They computed the viscous flow fields in a transonic cascade (Stephen and Hobbs, 1979) and a subsonic cascade and found good agreement with experimental data. The predicted blade pressure distribution is shown compared with data in Fig. 12(*a*). The loss distribution is also shown in Fig. 12(*b*). The turbulence model used in this analysis is due to Baldwin and Lomax (1978). A comparison between the inviscid code (Ni, 1982), Navier-Stokes analysis (Davis et al., 1988) and the results based on interaction of the inviscid/boundary layer code is also shown in Fig. 12. Substantial improvement over the inviscid solution is obtained by incorporating the displacement thickness due to the boundary layer. Furthermore, the prediction from the zonal and Navier-Stokes codes is almost identical. The incorporation of viscous effects through the transpiration model need not have to be carried out at every time step as $\partial\delta/\partial t$ is not large. Hence the inviscid solution can be updated every 30–50 time steps depending on the geometry and the problem. The inviscid boundary layer interaction code can provide very accurate results (at least for cascades) in a fraction of the computer time needed for a full Navier-Stokes solution. The shock boundary layer interaction regions may need more frequent updating than the unseparated boundary layers. None of the codes were able to predict the losses in stall regions with positive incidence.

Singh (1982) and Calvert (1982) incorporated a boundary-layer integral technique for compressible flow in a finite volume explicit procedure due to Denton (1975) and computed the shock boundary-layer interaction effects on inviscid flow. Singh showed considerable enhancement in the quality of flow computations for a transonic compressor rotor. This is an injected mass technique, (similar to the one described above), which allows fluid to pass through the walls in proportion to the rate of growth of the boundary layer thickness. The velocity normal to the wall is given by Eq. (22). Pierzga and Wood (1985) employed this code to predict the flow field in a NASA transonic rotor for which laser-doppler velocimeter data are available. The static pressure rise and exit tangential velocities were predicted more accurately with the inclusion of blockage in an Euler code, but no improvement was observed in detailed flow field predictions. Thompkins and Usab (1982) adopted a similar procedure and incorporated a differential 3-D boundary layer code in their explicit time-marching finite-difference inviscid code described earlier. The two solutions were not coupled; hence, the effect of a boundary layer on an inviscid flow was not computed, but the effect of an inviscid flow on the boundary layer was resolved.

It should be remarked here that all the inviscid/boundary layer interaction techniques described above resolve the global effects of viscous flow on the inviscid pressure, but the local effects are not computed accurately. Furthermore, convergence may be slow in separated flows, including shock boundary layer interaction regions. An assessment of a coupled inviscid/boundary layer technique is similar to assessment of boundary layer solutions described in Section 6.

There have been techniques developed to resolve the interaction effects more accurately through the use of Euler equation in the inviscid region, and Navier-Stokes equations in the viscous regions and couple these two techniques through an overlapping grid, where both equations are solved. The procedure used by Cambier and Veuillot (1985, 1986) can be summarized as follows.

(1) About five zones are incorporated in a cascade passage: three inviscid zones in the core regions of the flow (one above the suction surface, one above the pressure surface, one upstream) and two viscous zones (one near the suction surface, one near the pressure surface, including downstream wake).

(2) The explicit technique due to MacCormack is used.

(3) A compatibility condition (all variables have to be identical) is enforced in the overlapping zone between the inviscid and viscous regions.

Using this procedure, Cambier and Veuillot (1985, 1986) were able to resolve the inviscid pressure flow field as well as the boundary layers, wakes and shock boundary layer regions in a transonic cascade. This procedure showed substantial improvement in CPU time required for computing the flow in a

cascade over the full Navier-Stokes equations in the entire domain.

The inviscid/viscous techniques are also used in supersonic/subsonic flows. For example, the supersonic external flow may have subsonic viscous layers. The solution at supersonic speeds can be accomplished by a space-marching technique, while an iterative procedure is necessary in subsonic viscous regions. If these regions are thin, they can be treated by a single-pass space-marching Navier-Stokes procedure described earlier. Such a procedure for supersonic flows was developed by Schiff and Steger (1980). The supersonic/subsonic zonal approach has been used for both potential (Shankar et al., 1985) and for Navier-Stokes (Lombard et al., 1984) formulations in predominately supersonic flows with embedded subsonic zones. These methods are employed primarily in external flows at the present time. They are attractive for turbomachinery analysis and design due to large savings in computer time. The use of the space-marching technique in supersonic regions results in decreased computer storage.

Viscous/Viscous Techniques. Unlike the supersonic/subsonic zonal method, the streamwise pressure gradient in the incompressible flow equations needs special treatment to create a full parabolized formulation. The change in the character of the elliptic or time-hyperbolic Navier-Stokes equations to parabolic form creates an opportunity for significant improvement in computation time. A zonal technique for turbomachinery was developed by Warfield and Lakshminarayana (1989). The incompressible flow equations in rotating coordinates are solved for a turbomachinery rotor using the pseudo-compressibility technique in the elliptic regions of the flow and a space marching technique in the parabolic or nearly parabolic regions. The zonal technique developed is flexible, valid for three-dimensional flows, allows for zonal interaction, arbitrary zone location, and has potential for adaptive zone location. The technique has been applied to Penn State compressor rotor flow with a 69 percent saving in computation time over the full Navier-Stokes solution.

The basic principle on which the zonal technique is based is shown in Fig. 26. The purpose of the partial convergence (approximately 10 percent of computer time) of the time-marching code over the entire field is to establish an initially assumed pressure for the space-marching code and also to establish the location and extent of the elliptic boundaries. Two ellipticity parameters derived (Warfield and Lakshminaryana, 1987) are utilized to facilitate the placement of the boundaries between the elliptic and parabolic zones.

The zonal method for a compressor rotor application consisted of an elliptic zone extending from the inlet plane to the 25 percent chord location. The parabolic zone continued from the 25 percent chord location to the outflow plane. Both zones extended from blade-to-blade and from hub-to-tip. Only one sweep of the zonal method was utilized; the combination of zones with the elliptic zone upstream and the parabolic zone downstream reduces the need for multiple zonal sweeps due to the inability of the parabolic solution to influence the upstream elliptic solution. A comparison between the zonal technique and the full Navier-Stokes solution for the Penn State compressor is shown in Fig. 23. The overall features of the flow were predicted very well by both the Navier-Stokes and the zonal technique. This means that both the techniques capture these features. The solution for the entire rotor (including upstream and downstream of the blade row) was obtained in 31 percent of the time needed for the full Navier-Stokes solution.

The zonal technique combines the efficiency of the space-marching technique with accuracy of the time-iterative methods. The application of these techniques to the multi-stage compressor flow field is promising. The zonal techniques could be improved with an adaptive buffer zone, and could possibly include analytical solutions or the passage-averaged equations (Adamczyk, 1984) in some regions of the flow field. The improvement in zonal techniques also depends on improvements in component codes. As new and efficient techniques become available, they can be incorporated to provide improvements in zonal techniques.

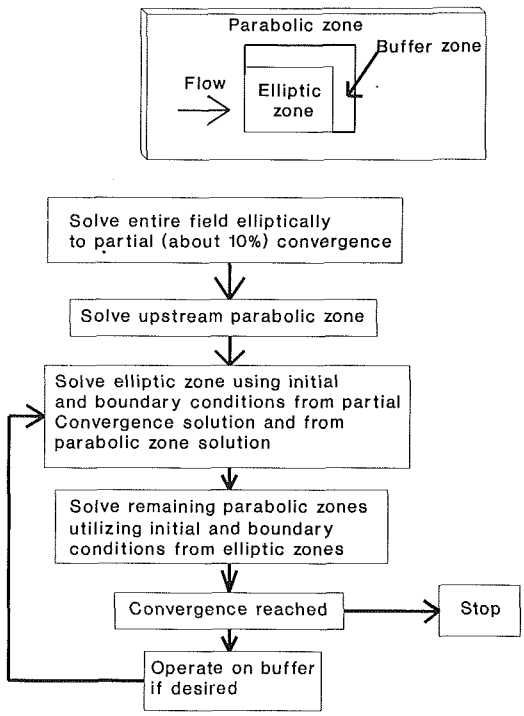

Fig. 26 Example of viscous/viscous zonal method

Assessment of Zonal Techniques.

(1) The zonal techniques, especially the inviscid/viscous techniques, are widely used in industry for design/analysis. The Navier-Stokes code is mainly used in the final iteration/research mode.

(2) Zonal techniques with embedded analytical solutions (i.e., tip clearance flow, leading edge laminar solutions), loss correlations (secondary and tip clearance losses), and quasi viscous representation (shear forces) are most attractive for turbomachinery.

(3) Zonal techniques save substantial computer time, but require experienced personnel and are difficult to code/operate.

(4) This is one of the attractive techniques for multi-stage turbomachinery.

(5) The technique can resolve overall performance, efficiency, blade pressure distribution, boundary layer and wake profiles, losses, and spanwise mixing accurately.

(6) Since space-marching and boundary-layer codes are very efficient, a very fine grid can be used in the viscous/near wall regions to resolve these flows more accurately than Navier-Stokes codes.

(7) Choice of component codes is critical. Overall efficiency and accuracy of zonal techniques depend on the efficiency and accuracy of component codes.

(8) Interaction between component zones is arbitrary at the present time. Systematic investigation is needed.

(9) Zonal techniques are not valid in endwall and tip clearance regions.

15 Computational Design

Major advances will take place in the use of powerful computational techniques in the design of turbomachinery flow

systems. Many industries have already updated their preliminary design codes with the computational design/analysis system. In a recent AGARD (1989) lecture series, some authors described a comprehensive state-of-the-art design methods for blading; compressors (Stow, Meauze), turbines (Bry, Hourmouziadis), 2D blading (Starken), etc. Howard et al. (1987) presented a comprehensive description of the design system used for the aerodynamic and the thermal design of turbines. Nojima (1988) provides a similar description for industrial centrifugal compressors. In view of these reviews, the treatment of computational design in the present paper has been kept brief. The methods solely based on empiricism, analytical or iterative analytical methods at arriving blade shape are not covered. The design methodology depends on the application, geometry, type of industry, etc. and there is no unified approach.

The inverse design technique, where the blade profile is derived from a prescribed velocity or pressure in the flow path, is restricted to two dimensions at the present time. If the flow is irrotational, a hodograph method (Sanz, 1983 and Leonard, 1990) can be used to transform the equations into the hodograph plane and the potential equation is solved using computational techniques to derive the blade geometry. Dulikravich and Sobieczky (1983) use a fictitious gas concept to design a cascade of airfoils. Both these methods have been very successful, especially in the design of shock free airfoils. A good example of this is shown in Fig. 27 taken from Stow's paper in AGARD (1989). Stow employed mixed mode blading codes. He specified the initial geometry and calculated the blade pressure distribution. This is the analysis mode. The pressure distribution is then specified over part of the chord to eliminate the shock and an inverse design technique was used to derive a new (or design) blade shape. The benefit of this technique is that they are often manufacturing limitation on leading and trailing edge thicknesses, so that the geometry is partially fixed. It should be remarked here that these designs are strictly valid for the design condition, with performance deterioration at off design conditions.

One of the interesting applications of inverse design techniques was carried out by Favre et al (1987). They developed an inverse calculation method, based on the panel technique, to reduce suction peaks at the suction side of the leading edge of a Francis turbine. This reduced the inlet and leading edge cavitation over an extended range, thus improving the performance. Furthermore, inverse design techniques can be made to interact with the boundary layer calculations to optimize for boundary layer growth and to minimize flow separation.

If the flow is rotational, an Euler technique has to be adopted; a first guess of the geometry is essential for this calculation. The initial geometry is modified during the flow calculation (Zanetti and Larocca, 1990). The most commonly used technique is the iterative inverse method, where the inverse and analysis methods are used in a suitable combination to derive an optimum blade shape, and geometry of the annulus. These techniques are reviewed by Leonard (1990).

Most industries now have some iterative schemes for the design of blading and flow path (Stow, 1988, 1989; Karadimas, 1990; Worth and Plehn, 1990; Nojima et al., 1988; Howard et al., 1987; Leylek and Wisler, 1990; Tyner and Sullivan, 1990). Most aircraft engine companies are beginning to iterate the design with Euler and Navier-Stokes codes. A typical system used successfully by Nojima et al. (1988) to design high performance industrial compressors is shown in Fig. 28. The design specification includes the pressure distribution and the desired overall performance. In the preliminary design system, the main dimensions of the impeller and diffuser are generated. A first approximation of the impeller and diffuser shape are generated by the program for succeeding detailed design. Optimization of the geometry is then carried out to achieve maximum efficiency. The analysis system consists of blade-to-blade

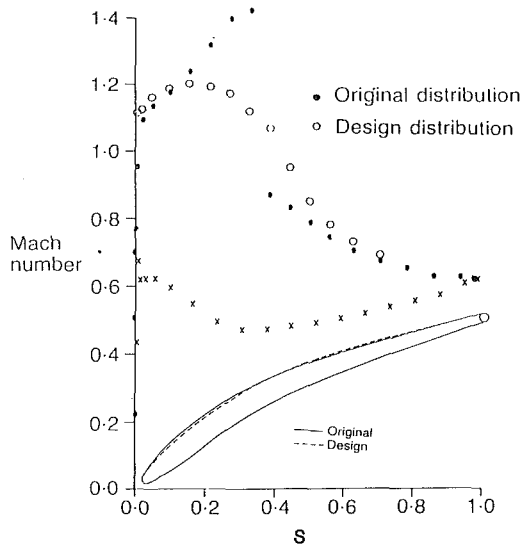

Fig. 27 Shock free supercritical compression blade derived from inverse design technique (Stow, 1989)

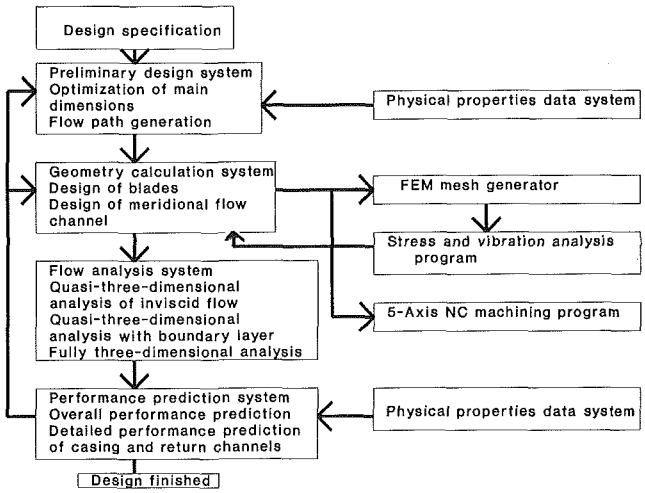

Fig. 28 Structure of centrifugal compressor aerodynamic design system compred-S (Nojima et al., 1988)

calculation, boundary layer computation, and three-dimensional time marching (Denton, 1982) techniques which were described earlier. The geometry and flow path are modified to achieve the desired velocity/pressure distribution along the flow path. The data base (loss correlations, etc.) are then used to carry out performance prediction. This step could be replaced by a Navier-Stokes solver. Nojima et al. (1988) were thus able to achieve very high efficiency of a family of centrifugal compressors, and this was verified by measurements.

Hourmouziadas (AGARD, 1989) describes a similar system for low pressure turbines, with optimization to achieve minimum boundary-layer growth, minimum trailing-edge thickness, no flow separation, highest blade pitch, and high acceleration on the suction side and delayed transition. Tyner and Sullivan (1990) designed a small high-performance, low-aspect-ratio, high-reaction compressor using a quasi 3-D and 3-D design system similar to that shown in Fig. 28. The high performance achieved by this compressor is attributed partly to a 3-D design system based on Ni's (1982) explicit Euler technique described earlier. Stow (1988) provides a more general description of the design system with emphasis on compressors, including through-flow calculation, blade section design using inverse and analysis methods, and blade section

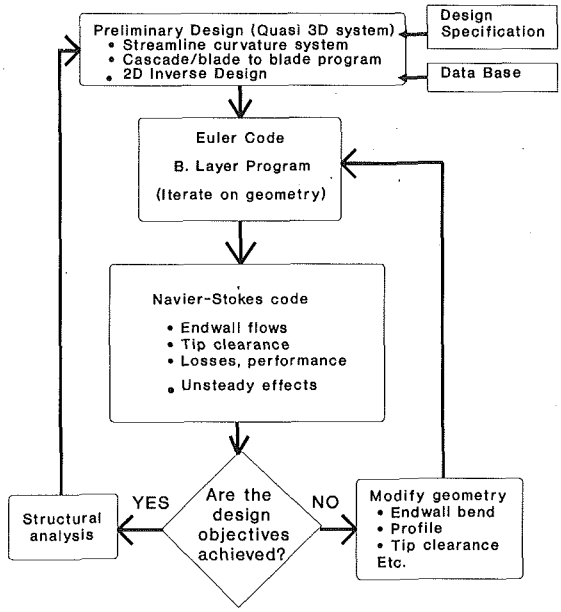

• Three-dimensional viscous codes should be employed in early stages of design to locate problem areas and to check validity of loss correlations

Fig. 29 Turbomachinery design: a suggested approach

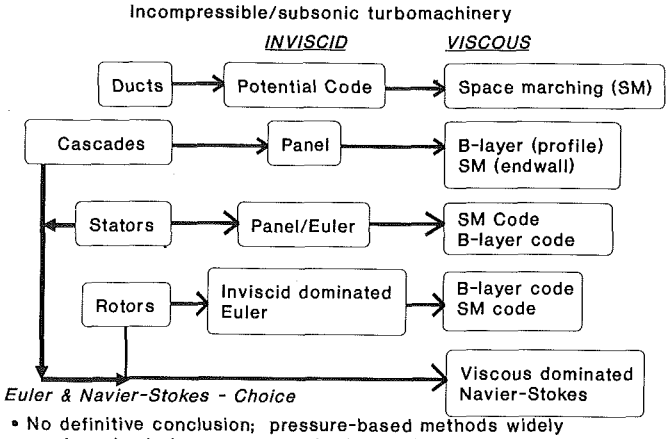

• No definitive conclusion; pressure-based methods widely used; easier to incorporate cavitation, turbulence, tip clearance models, etc.
• Advances in acceleration schemes may make explicit RK, implicit AFLBI, pseudo-compressibility techniques attractive

Fig. 30 Summary recommendations for incompressible subsonic turbomachinery

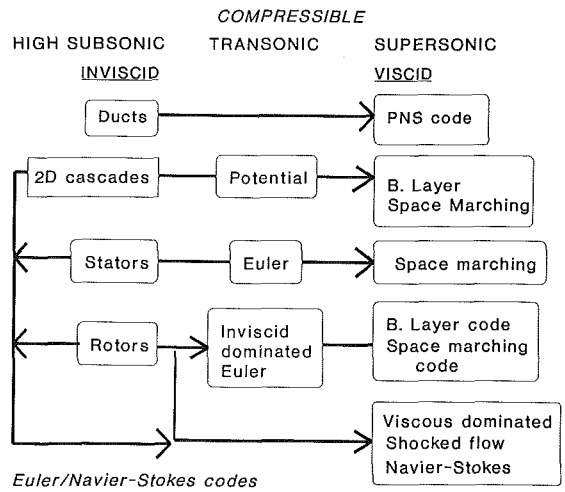

• No definitive conclusion; pressure-based methods, RK explicit widely used
• Advances in LU scheme may make implicit attractive
• None of the Navier-Stokes codes has resolved end wall flow, tip clearance flow field, shock - B.L. iteration regions satisfactorily

Fig. 31 Summary recommendations for high speed turbomachinery

stacking. The emerging role of the Navier-Stokes code is also emphasized.

A suggested approach for turbomachinery design is shown in Fig. 29. The design specifications include velocity and pressure field, desired efficiency, and losses. The data base include the profile loss correlations, tip clearance model, endwall loss correlations, deviation angle, spanwise mixing model and other correlations developed for that particular family of turbomachinery. For axial flow turbomachinery, the cascade inverse design technique (such as Sanz, 1983) or Favre et al. (1987) inverse panel code could be used to generate blade profiles from hub-to-tip. An Euler code is then used to iterate on the geometry in a coupled fashion. The desired hub-to-tip, blade-to-blade, and leading-to-trailing edge flow is achieved through iteration. The final step involves analysis of the blade row to detect high loss, separation, shock boundary layer interaction region, etc. If the design objectives are not met the procedure is repeated until the desired performance and blading is achieved. The choice of technique and code for the analysis is based on the assessment carried out earlier. For example, the liquid handling machinery is best handled with a pressure based method or pseudo-compressibility technique.

16 Summary — Recommendations

The technique to be employed for the computation of flow field in turbomachinery depends on the geometry and flow regime. The full Navier-Stokes code is most suitable for the final stage of design and analysis and has yet to be adapted on a day-to-day basis for analysis and design. This situation will change as advances are made in the computer architecture and the cost of computation is reduced. The recommendation made here refers to the cost-effective computation to capture the flow field accurately. These recommendations are summarized in Fig. 30 for incompressible/subsonic turbomachinery and in Fig. 31 for the high speed turbomachinery. If the interest lies only in the pressure distribution, the inviscid codes are most appropriate provided the viscous regions are small. If, for example, the flow field in a constant area duct has large viscous regions, a space-marching code can capture most of the flow physics.

For incompressible flow and moderate subsonic cascades, the most suitable approach would be to use a panel code, followed by a Keller-box type finite difference scheme for the boundary layer. The high subsonic flow case can be best resolved by a potential code integrated with a boundary layer code. The transonic and supersonic case, with shock/boundary layer separation and interaction, is best handled by an Euler/boundary layer code or a Navier-Stokes code depending on the extent of flow separation. Likewise, incompressible and subsonic rotor flows can be resolved with a quasi three-dimensional technique and a boundary layer code, with empirical correlations or secondary flow analysis in the endwall regions. Transonic and supersonic rotor flows are best resolved by a Navier-Stokes code. The viscous dominated regions such as the endwall, shock-boundary layer interaction regions are most accurately resolved through the solution of the full Navier-Stokes method. If the majority of the flow field is viscous or dominated by shocks, the full Navier-Stokes solution would be the most appropriate route to take.

The flow in a hydraulic turbine, some pumps, and other subsonic turbomachinery, where inviscid flow dominates, is best resolved with an Euler code in the inviscid region and a boundary layer code or a single-pass space-marching code in the viscous regions. On the other hand, low-aspect ratio turbomachinery are dominated by endwall effects with a large viscous loss core. This as well as transonic axial compressor and centrifugal compressor flow fields are better resolved with a full Navier-Stokes code.

17 Concluding Remarks

Techniques for turbomachinery flow computations have reached a high level of maturity. A wide variety of flows have been computed: the Francis Runner, mixed flow pumps, automotive torque converter, incompressible to supersonic compressors and turbines, propellers and prop fans, hydraulic, steam and gas turbines, rocket pumps, including inducers. However, the design is still based on classical techniques such as the through-flow method and correlation, even though some companies are now beginning to do the final analysis/design iteration using 3-D Navier-Stokes codes. The potential for resolving the complex flow physics in turbomachinery is recognized. Improvements in physical approximations and models (e.g., turbulence, transition), numerical and or artificial dissipation, stability, convergence rate, computational efficiency, are needed before Navier-Stokes method can be used extensively in the analysis and design phase. Ideally, the codes should be independent of user specified constants (e.g., psuedo-compressibility factor β, artificial dissipation, or constants in various turbulence models).

Furthermore, there is a need for calibration and validation of these codes before they are adapted for production runs. The calibration should be based on an exact analytical solution and validation should be based on benchmark-quality data for complex geometries and flow fields. For example, it is necessary to validate turbulence quantities predicted against data to check the accuracy of turbulence modelling. Benchmark quality data are scarce in the area of turbomachinery. This issue should be addressed before complete confidence in these codes can be achieved.

It should be remarked here that potential codes and panel codes are limited to cascade flows. The technique is not applicable for turbomachinery rotor flows. The Euler codes have matured and are routinely used in the design and the analysis of turbomachinery flows. The choice of Euler code/technique depends on the flow regime. The pressure-based methods and the psuedo-compressibility techniques are attractive for low speed and the explicit Runge-Kutta method and the pressure-based methods are widely used for steady high speed shocked flows. Similar conclusions can be made for Navier-Stokes. One of the most efficient computational techniques is the zonal method, especially in the design mode. The inviscid-boundary layer code is efficient, accurate and is widely used. The interactive Euler-Space marching technique is attractive. The other zonal techniques (Euler-Navier Stokes, Euler-Space marching, Navier-Stokes-space marching) are very attractive, but have not received wide acceptance.

The Navier-Stokes analyses are most useful for application where viscous flows dominate (e.g., centrifugal compressor and low aspect ratio turbomachinery). Even though great progress has been made in this area, the codes have not been able to capture the flow physics associated with tip clearance flow, secondary flow and endwall flows accurately. There has not been any satisfactory prediction of annulus-wall and hub-wall boundary layers in rotors.

There is a tendency among the new generation of turbomachinery computors to ignore the early advances made in the analysis of turbomachinery flows (e.g., boundary layer solutions, secondary and leakage flow theories, etc.). This led to widespread misuse of Navier-Stokes solvers. In some cases, for example, a panel code combined with boundary layer and secondary flow or other linearized solutions can provide predictions which are as good as Navier-Stokes solutions, but carried out in a fraction of time it takes to compute with full Navier-Stokes equation. The computors should be aware of these and incorporate these analyses in their codes for cost effective computation. Navier-Stokes is an overkill for some flows which may be as much as 95 percent inviscid. In addition, the designers should be willing to accept Navier-Stokes solutions and eliminate or update design correlations (e.g., blockage coefficient, loss correlations, deviations, etc.) using these solutions.

There has been no progress made in computing cavitating flows. It should be relatively easy to start by extending the Euler codes for cavitating flows.

18 Recommendations for Future Research

Some of the recommendations for future research are as follows:

(1) Develop improved acceleration schemes to reduce computational time, which will enable widespread use of these techniques in design and analysis of turbomachinery.

(2) Detailed evaluations of grid sensitivity, effect of artificial dissipation on the flow physics, accuracy, stability, convergence, CPU time and memory requirements for 3-D Euler and Navier-Stokes codes are needed.

(3) Comparison of various Euler/Navier-Stokes techniques is scarce. A need exists to evaluate various codes/techniques, turbulence models on identical turbomachinery geometry, grid, computer, and compare finite-difference, finite-volume and finite-element formulations. (See AGARD AR-275, 1990 for test cases for internal flows, cascades, rotors, etc.).

(4) Develop zonal methods; it is not necessary to solve Navier-Stokes where it is not needed. Zonal techniques should include analytical regions (i.e., boundary layer solutions near the leading edge, tip clearance flow, etc.). The zonal technique based on Euler or Navier-Stokes/space-marching (PNS) codes should be further developed.

(5) Improve Navier-Stokes code efficiency by embedding boundary layer calculations/solvers in near wall regions.

(6) One of the major problems with the pressure-based method is the solution of Poisson equation for pressure. Improved solution techniques to achieve faster convergence are needed. The possibility of coupled solution in the pressure-based method should be explored.

(7) Adapt codes to massively parallel computers to reduce computational time.

(8) Develop turbulence models to account for heat transfer, two-phase flow, compressibility, and unsteady flow.

(9) No adequate transition model is available for turbomachinery flow. Systematic experimental investigation is needed to evaluate the effects of freestream turbulence, rotation, heat transfer, pressure gradient, and curvature.

(10) Extend Euler/Navier-Stokes codes to cavitating flows using equations valid for two-phase flows.

(11) Develop artificial intelligence to automate the whole procedure.

(12) Develop 3-D Euler inverse method for cavitating and noncavitating flows; develop profile boundary layer optimization technique; develop optimization of blade shape using Navier-Stokes (iterative mode) for secondary flow, endwall flow, tip clearance, and boundary layer shock interaction losses.

(13) Validation experiment: Most of the turbomachinery flow data available for CFD validation are either incomplete (for example, inlet properties and turbulence quantities are missing) or have no uncertainty band. Benchmark quality data are needed for the following cases: (*a*) Integrated flow and

heat transfer data in turbines; (*b*) Cavitation data (cascades, rotors); (*c*) Flow physics associated with 3-D shock boundary layer interaction in rotors; (*d*) Endwall and blade boundary layer and wake data for high speed and low speed turbomachinery; (*e*) Liquid handling machinery has the least validation data—high quality data in pumps, turbines, and torque converters are needed; (*f*) Steady and unsteady flow, heat transfer, and turbulence data in multi-stage turbomachinery.

Acknowledgments

The preparation of this review and the lecture were made possible by the ASME Freeman Scholar Program in Fluids Engineering. The author is grateful to the Freeman Scholar committee, Drs. J. Dussourd, R. Arndt, and J. Hoyt for providing him with this opportunity. Many of the techniques and codes developed by the author's group were sponsored by NASA grants, with P. Sockol as the grant monitor. His comments and suggestions are gratefully acknowledged. The U.S. Navy sponsored the author's work on pressure-based methods, with D. Fuhs as the grant monitor.

Many individuals read the draft copies of the paper and made critical comments: R. Chima, R. Delaney, T. R. Govindan, M. A. Howard, K. Kirtley, R. Kunz, C. Rhie, J. Schwab, P. Stow, and D. Telionis. A very thorough and critical review of the paper by these individuals greatly enhanced the quality of the paper and the accuracy of assessments. Jennifer Wellar typed several drafts of this paper and her excellent typing skill is very much appreciated.

References

Adamczyk, J. J., 1984, "Model Equations for Simulating Flows in Multistage Turbomachinery," ASME Paper 85-GT-226.

Adamczyk, J. J. et al., 1989, "Simulation of 3D Viscous Flow Within a Multistage Turbine," ASME Paper 89-GT-152.

Adamczyk, J. J., Celestina, M. L., and E. M. Greitzer, 1991, "The Role of Tip Clearance in High Speed Fan Stage," ASME Paper 91-GT-83.

Adler, D., 1980, "Status of Centrifugal Impeller Internal Aerodynamics, Part I: Inviscid Flow Prediction Methods," ASME *Journal of Engineering for Power*, pp. 728–737; Part II: Experiments and Influence of Viscosity, ASME *Journal of Engineering for Power*, pp. 738–746.

AGARD, 1989, "Blading Design for Axial Flow Turbomachines," AGARD LS 167.

Anand, A. K., and Lakshminarayana, B., 1978, "Three Dimensional Turbulent Boundary Layer in A Rotating Helical Channel," ASME, JOURNAL OF FLUIDS ENGINEERING, Vol. 97, No. 2, pp. 197–210 (also see NASA CR 2888, 1977).

Anderson, D. A., Tannenhill, J. C., and Pletcher, R. H., 1984, "*Computational Fluid Mechanics and Heat Transfer*," Hemisphere Publishing Company.

Anderson, O. L., 1987, "Calculation of Three-Dimensional Boundary Layers on Rotating Turbine Blades," ASME JOURNAL OF FLUIDS ENGINEERING, Vol. 109, pp. 41–50.

Baldwin, B., and Lomax, H., 1978, "Thin Layer Approximations and Algebraic Model for Separated Flow," AIAA Paper 78-0257.

Bansod, P., and Rhie, C. M., 1990, "Computation of Flow Through a Centrifugal Impeller with Tip Leakage," AIAA Paper 90-2021.

Bario, F., Barral, L., and Bois, C., 1989, "Air Test Flow Analysis of the Hydrogen Pump of the Vulcan Type," *Pumping Machinery*, ASME FED Vol. 81, pp. 149–155.

Barnett, M., Hobbs, D. E., and Edwards, D. E., 1990, "Inviscid-Viscous Interaction Analysis of Compressor Cascade Performance," ASME GT-90-15.

Beam, R. M., and Warning, R. F., 1978, "An Implicit Factored Scheme for the Compressible Navier-Stokes Equations," *AIAA J.*, Vol. 16, No. 4, P. 393–402.

Bradshaw, P., Cebeci, T., and Whitelaw, J. H., 1981, *Engineering Calculation Methods for Turbulent Flow*, Academic Press.

Brandt, A., 1979, "A Multi-Level Adaptive Computation in Fluid Dynamics," AIAA Paper 79-1455.

Briley, W. R., 1974, "Numerical Method for Predicting Three-Dimensional Steady Viscous Flows in Ducts," *Journal of Computational Physics*, Vol. 14, No. 1, pp. 8–28.

Briley, W. R., and McDonald, H., 1984, "Three Dimensional Viscous Flow With Large Secondary Velocity," *Journal of Fluid Mechanics*, Vol. 144, pp. 47–77.

Briley, W. R., and McDonald, H., 1976, "Solution of the Multidimensional Compressible Navier-Stokes Equations by a Generalized Implicit Method," *Journal of Computational Physics*, Vol. 24, p. 372.

Buratynski, E. K., and Caughey, D. A., 1986, "An Implicit LU Scheme for the Euler Equations Applied to Arbitrary Cascades," *AIAA Journal*, Vol. 24, No. 1.

Bushell et al., 1988, "Measurement of Unsteady Blade Surface Pressure on a Single Rotation Large Scale Advanced Prop-Fan With Angular and Weak Inflow at M = 0.02 to 0.7," NASA CR 182123.

Calvert, W. J., 1982, "An Inviscid-Viscous Interaction Treatment to Predict Blade-to-Blade Performance of Axial Compressors with Leading Edge Shocks," ASME 82-GT-135.

Cambier, L., and Veuillot, J. P., 1988, "Computation of Cascade Flows at High Reynolds Number by Numerical Solution of the Navier Stokes Equation," AIAA Paper 88-0364.

Cambier, L.,and Veuillot, J. P., 1985, "Application of a Multi-Domain Approach to the Computation of Compressible Flows in Cascades," *Proc. Int. Sym. Air Breathing Engines*, Sept. 2–6, 1985 (published by AIAA).

Cambier, L., Escande, B. and Veuillot, J. P., 1986, "Calcul d'ecoulement internes a grand nombre de Reynold par resolution numerique des equations de Navier Stokes," AGARD CP 401.

Carter, J. E., 1978, "Inverse Boundary-Layer Theory and Comparison with Experiment," NASA TP-1208.

Cebeci, T., Kaups, K., and Ramsey, J. A., 1977, "A General Method for Calculating Three Dimensional Compressible Laminar and Turbulent Boundary Layers," NASA CR 2777.

Chakravarty, S. R., and Osher, S., 1983, "Numerical Experiments with the Osher Upwind Scheme for the Euler Equations," *AIAA Journal*, Vol. 21, No. 9, p. 1241.

Chan, D. C., and Sheedy, K. P., 1990, "Turbulent Flow Modelling of a Three-Dimensional Turbine," AIAA 90-2124.

Chan, D. C., Sindhir, M. M., and Gosman, A.D., 1987, "Numerical Simulation of Passages with Strong Curvature and Rotation Using a Three Dimensional Navier Stokes Solver," AIAA Paper 87-1354.

Chan, D. C. et al., 1988, "On the Development of a Reynolds Averaged Navier Stokes Equation Solver for Turbomachinery," *2nd Int. Sym. on Transport Phenomena*, Honolulu, Hawaii.

Chen, S. C., and Eastland, A. H., 1990, "Forced Response on Turbomachinery Blades Due to Passing Wakes," AIAA Paper 90-2353.

Chima, R. V., 1987, "Explicit Multigrid Algorithm for Quasi Three Dimensional Viscous Flows in Turbomachinery," *J. Propulsion and Power*, Vol. 3, No. 5, pp. 1556–1563.

Chima, R. V., 1985, "Inviscid and Viscous Flows in Cascades with an Explicit Multi-Grid Scheme," *AIAA Journal*, Vol. 23, No. 10, pp. 1556–1563.

Chima, R. V., and Yokota, J. W., 1990, "Numerical Analysis of Three-Dimensional Viscous Internal Flows," *AIAA Journal*, Vol. 28, No. 4, p. 798.

Chima, R. V., and Strazisa, A. J., 1983, "Comparison of Two and Three Dimensional Flow Computations with Laser Anemometer Measurements in a Transonic Compressor Rotor," ASME *Journal of Engineering for Power*, Vol. 105, p. 596.

Chima, R. V., and G. M. J. Johnson, 1985, "Efficient Solution of the Euler and Navier-Stokes Equations with a Vectorized Multi-Grid Algorithm," *AIAA Journal*, Vol. 23, No. 1, p. 23.

Chima, R. V., Turkel, E., and Schaffer, S., 1987, "Comparison of Three Explicit Multigrid Methods for the Euler and Navier-Stokes Equations," *NASA TM 88878.*

Choi, D., and Knight, C. J., 1988, "Computation of Three Dimensional Viscous Linear Cascade Flows," *AIAA Journal*, Vol. 26, 12, pp. 14–77.

Choi, D., and Knight, C. J., 1989, "Computations of 3D Viscous in Rotating Turbomachinery Passages," AIAA Paper 89-0323.

Chorin, A. J., and 1967, "A Numerical Method for Solving Incompressible Viscous Flow Problems," *J. Comp. Phys.*, 2, pp. 12–26.

Chorin, A. J., 1968, "Numerical Solution of the Navier-Stokes Equations," *Mathematics of Computation*, Vol. 22, pp. 745–762.

Connell, S. D., and Stow, P., 1986, "The Pressure Correction Method," *Computers and Fluids*, Vol. 14, No. 1, p. 1.

Cooper, P., 1967, "Analysis of Single and Two Phase Flows in Turbopump Inducers," ASME *Journal of Engineering for Power*, Vol. 89, pp. 577–588.

Cousteix, J., 1986, "Three Dimensional Boundary Layers—Introduction to Calculation Methods," AGARD R 471.

Crawford, M. E., and Kays, W. M., 1976, "A Program for Numerical Computation of Two Dimensional Internal and External Boundary Layers," NASA CR 2742.

Davis, R. L., Ni, R. H., and Carter, R. E., 1987, "Cascade Viscous Flow Analysis Using Navier Stokes Equation," *AIAA Journal of Propulsion*, Vol. 3, No. 5, pp. 406–414.

Davis, R. L., and Dannenhoffer, J. F., 1989, "Adaptive Grid Embedding Navier-Stokes Technique for Cascade Flows," AIAA Paper 89-0204.

Davis, R. L., Hobbs, D. E. and Weingold, H. D., 1988, "Prediction of Compressor Cascade Performance Using a Navier-Stokes Technique," ASME *Journal of Turbomachinery*, Vol. 110, No. 4, p. 520.

Dawes, W. N., 1987, "A Numerical Analysis of Viscous Flow in a Transonic Compressor Rotor and Comparison with Experiment," ASME *Journal of Engineering for Gas Turbine and Power*, Vol. 109, No. 1, p. 83.

Dawes, W. N., 1991, "The Simulation of Three-Dimensional Viscous Flow in Turbomachinery Geometries Using a Solution Adaptive Unstructured Mesh Methodology," ASME 91-GT-124.

Delaney, R. A., 1983, "Time-Marching Analysis of Steady Transonic Flow in Turbomachinery Cascades Using Hopscotch Method," ASME *Journal of Engineering for Power*, Vol. 105, No. 2.

Denton, J. D., "Solution of Euler Equations for Turbomachinery Flows," *Thermodynamics and Fluid Mechanics of Turbomachinery*, ed. by A. S. Ucer

et al., Martinas, Ni, Jhoff Publishers, Netherlands (also see ASME Paper 82-GT-239, 1982).

Denton, J. D., 1975, "A Time Marching Method for Two- and Three-Dimensional Blade-to-Blade Flow," Aeronautical Research Council R&M 3775.

Denton, J. D., 1982, "An Improved Time-Marching Method for Turbomachinery Flow Calculation," ASME Paper 82-GT-239.

Dring, R. P., et al., 1986, "Effects of Inlet Turbulence and Rotor/Stator Interactions on the Aerodynamics and Heat Transfer of a Large Rotating Turbine Model," Vol. 1, NASA CR 4079, Vols. III & IV (NASA CR 179469).

Dulikravich, G. S., and Sobieczky, H., 1983, "Design of Shock Free Compressor Cascades Including Viscous Boundary Layer Effects," ASME Paper 83-GT-134.

Dunker, R. J., Strinning, P. E., and Weyer, W. B., 1977, "Experimental Study of Flow Field in a Transonic Compressor Rotor by Laser Velocimetry and Comparison with Through Flow Calculations," ASME Paper 77-GT-28.

Eckhardt, D., 1976, "Detailed Flow Investigations Within a High Speed Centrifugal Impeller," ASME JOURNAL OF FLUIDS ENGINEERING, Vol. 98.

Erickson, L. E., 1987, "Simulation of Transonic Flow in Radial Compressors," *Computer Methods in Applied Mechanics and Engineering*, Vol. 64, pp. 95–111.

Erickson, L. E., and Billadal, J. T., 1989, "Validation of 3-D Euler and Navier-Stokes Finite Volume Solver for Radial Compressor," AGARD CP-437.

Escudier, M. P., Bornstein, J., and Zhender, N., 1980, "Observations with LDA Measurements of a Confined Vortex Flow," *J. Fluid Mechanics*, Vol. 98, p. 49.

Favre, J. N., Avellan, F., and Rhyming, I. L., 1987, "Cavitation Performance Improvement by Using a 2D Inverse Method for Hydraulic Runner Design," Int. Conf. Inverse Design Concepts and Optimization in Engineering Science, Penn State University.

Flot, R., and Papailiou, K., 1975, "Couches Limites et Effects D'Extremeties dans les Turbomachines," *Metraflu*, contract DRME 73/373, Lyon, France.

Fourmaux, A., and LeMeur, A., 1987, "Computation of Unsteady Phenomena in Transonic Turbines and Compressors," ONERA (France), TP No. 1987-131.

Fujitani, K., Himerno, R., and Takagi, M., 1988, "Computational Study of Flow Through a Torque Converter," SAE Paper 881746.

Galmes, J. M., and Lakshminarayana, B., 1984, "Turbulence Modelling for Three Dimensional Turbulent Shear Flows Over Curved Rotating Bodies," *AIAA Journal*, Vol. 22, No. 1, pp. 1420–1428.

Giles, M. B., 1990, "Stator/Rotor Interaction in a Transonic Turbine," *J. Propulsion and Power*, Vol. 6, pp. 621–627.

Goldman, L. J., and Seaholtz, R. G., 1982, "Laser Anemometer Measurements in Annular Turbine Cascade of Core Turbine Vanes and Comparison with Theory," NASA TP 2018.

Gopalakrishna, S., and Bozzola, R., 1971, "A Numerical Technique for the Calculation of Transonic Flows in Turbomachinery Cascades," ASME Paper 71-GT-41G, Also see ASME Paper 72-GT-31, ASME Paper 73-GT-5T.

Goto, A., 1990, "Study of Internal Flows in Mixed Flow Pump Impeller at Various Tip Clearance Using 3D Viscous Flow Calculations," ASME Paper 90-GT-36. (to be published in ASME *Journal of Turbomachinery*).

Gourlay, R. A., and Morris, J. L., 1972, "Hopscotch Difference Method for Non-Linear Hyperbolic Systems," *IBM J. Res. Dev.*, Vol. 16, No. 6, pp. 349–353.

Govindan, T. R. and Lakshminarayana, B., 1988, "A Space Marching Method for the Computation of Viscous Internal Flows," *Computer & Fluids*, Vol. 16, No. 1, pp. 21–39.

Govindan, T. R., Briley, W. R., and McDonald, H., 1991, "Generalized Three Dimensional Viscous Primary/Secondary Flow Equations," *AIAA Journal*, Vol. 29, No. 3, p. 36.

Gregory-Smith, D. G., 1989, "Private Communication," (also see ASME *Journal of Turbomachinery*, Vol. 110, 1988, p. 479).

Griffin, L. W., and McConnughey, H. V., 1989, "Prediction of Aerodynamic Environment and Heat Transfer for Rotor-Stator Configurations," ASME Paper 89-GT-89.

Gundy-Burlet, K. L., et al., 1990, "Temperature and Spatiality Resolved Flow in a Two-Stage Axial Compressor," ASME Paper 90-GT-299.

Hadid, A. H., et al, 1988, "Convergence and Accuracy of Pressure Based Finite Difference Schemes for Incompressible Viscous Flow Calculations in a Non-Orthogonal Co-ordinate System," AIAA Paper 88-3529.

Hah, C., and A. Wennerstrom, 1991, "Three-Dimensional Flow Fields Inside a Transonic Compressor With Swept Blades," ASME *Journal of Turbomachinery*, Vol. 113, p. 241.

Hah, C., 1984, "A Navier Stokes Analysis of Three-Dimensional Turbulent Flows Inside Turbine Blade Rows at Design and Off Design Conditions," ASME *Journal of Engineering for Power*, Vol. 106, pp. 421–429.

Hah, C., and Krain, H., 1990, "Secondary Flows and Vortex Motion in a High Effeciency Backswept Impeller at Design and Off Design Conditions," ASME *Journal of Turbomachinery*, Vol. 112, p. 7.

Hah, C., and Lakshminarayana, B., 1980a, "Numerical Analysis of Three Dimensional Turbulent Wakes of Rotors in Axial Flow Turbomachinery," ASME JOURNAL OF FLUIDS ENGINEERING, Vol. 102, No. 4, pp. 462–472.

Hah, C., and Lakshminarayana, B., 1980b, "The Prediction of Two and Three Dimensional Asymmetric Turbulent Wakes—A Comparison of Performance of Three Turbulent Models for the Effects of Curvature and Rotation," *AIAA Journal*, Vol. 18, No. 80, p. 1196.

Hah, C., Bryans, A. C., Moussa, Z., and Tomsho, M. E., 1988, "Application of Viscous Flow Computations for the Aerodynamic Performance of a Backswept Impeller at Various Operating Conditions," ASME *Journal of Turbomachinery*, Vol. 110, pp. 303–311.

Hall, E. J., Delaney, R. A., and Pletcher, R. H., 1990, "Simulation of Time Dependent Viscous Flows Using Central and Upwind-Biased Finite Difference Techniques," AIAA Paper 90-3012-CP.

Hall, E. J., Delaney, R. A.,and J. L., Bettner, 1991a, "Investigation of Advanced Counter Rotation Blade Configuration Concepts for High Speed Turbo Systems," Part II—"Unsteady Ducted Prop Fan Analysis," NASA CR 187106.

Hall, E. J., 1989, "Simulation of Time Dependent Compressible Viscous Flows Using Central and Upwind Biased Finite Difference Techniques, "Ph.D. thesis, Iowa State University.

Hall, E. J., and R. A. Delaney, 1991, "Time Dependent Aerodynamic Analysis of Ducted and Unducted Prop Fans at Angle of Attack," ASME Paper 91-GT-190.

Haymann-Haber and Thompkins, W. T. Jr., 1981, "Comparison of Experimental and Computation Structure in Transonic Compressor Rotor," ASME *Journal of Engineering for Power*, Vol. 103, p. 79.

Hirsch, C., 1990, "*Numerical Computation of Internal and External Flows*," Vols. 1 and 2, John Wiley, Inc.

Hirsch, C., and Warzee, G., 1979, "An Integrated Quasi-3-D Finite Element Calculation Program for Turbomachinery Flows," ASME *Journal of Engineering for Power*, Vol. 101, p. 141.

Hobson, G. V., 1990, "Fully Elliptic Calculations of Incompressible Viscous Turbomachinery Flows," Ph.D. thesis, Department of Aerospace Engineering, The Pennsylvania State University.

Hobson, G. V., and Lakshminarayana, B., 1990a, "A Computation of Turbine Flow Fields with a Navier Stokes Code," AIAA Paper 90-2122.

Hobson, G. V., and Lakshminarayna, B., 1990b, "Prediction of Cascade Performance Using an Incompressible Navier-Stokes Technique," ASME Paper 90-GT-261 (to be published in ASME *Journal of Turbomachinery*).

Howard, M. A., Walton, J. H., and Uppington, D. C., 1987, "Computer System for Aerodynamic and Thermal Design of Turbines," Inst. Mech. Engrs., London, Paper C33/187.

Hsu, C. H., Chen, Y. M., and Liu, C. H., 1990, "Preconditioned Upwind Methods to Solve 3D Incompressible Navier Stokes Equations for Viscous Flows," AIAA Paper 90-1496.

Huber, F. W., and Ni, R. H., 1989, "Application of a Multistage 3D Euler Solver to the Design of Turbines for Advanced Propulsion Systems," AIAA Paper 89-2578.

Hutchings, B., and Iannuzzeli, R., 1987, "Taking the Measure of Fluid Dynamic Software," *Mechanical Engineering*, Vol. 109, No. 5, p. 72.

Issa, R. I., 1985, "Solution of the Implicitly Discretized Fluid Flow Equations by Operator Splitting," *J. Comp. Phy.*, Vol. 62, pp. 40–65.

Jameson, A., Schmidt, W., and Turkel, E., 1981, "Numerical Solutions of the Euler Equations by Finite Volume Methods Using Runge-Kutta Time Stepping Schemes," AIAA Paper 81-1259.

Jameson, A., and Turkel, E., 1981, "Implicit Schemes and the LU Decompositions," *Mathematics* and *Computation*, Vol. 37, pp. 385–390.

Jameson, A., and Baker, T. J., 1984, "Multigrid Solutions of Euler Equations for Aircraft Configurations," AIAA Paper 84-0093.

Jones, W. P., and Launder, R. E., 1972, "The Prediction of Laminarization with a Two Equation Model of Turbulence," *Int. J. Heat and Mass Transfer*, Vol. 15, p. 301.

Jorgensen, P. C. E., and Chima, R. V., 1989, "An Unconditionally Stable Runge Kutta Method for Unsteady Flows," AIAA Paper 89-205.

Joslyn, H. D., et al., 1989, "Multi-stage Compressor Airfoil Aerodynamics," *J. Propulsion*, Vol. 5, p. 457.

Karadimas, G., 1989, "Application of Computational Systems to Aircraft Engine Components Development," *Ninth Int. Symp. on Airbreathing Engines*, Greece.

Katsanis, T., 1968, "Computer Program for Calculating Velocities and Streamlines on a Blade-to-Blade Surface of a Turbomachine," NASA TNS 4525 (also see NASA TND 5427, 1969).

Ktasanis, T., and McNally, W. D., 1977, "Fortran Program for Calculating Velocities and Streamlines on the Hub-Shroud Mid Channel Flow Surface of an Axial- or Mixed Flow Turbomachine," Vol. I and II, NASA TN D 8430 and TN D 8431.

Keller, H. B., 1978, "Numerical Methods in Boundary Layer Theory," *Ann. Rev. Field Mechanics*, Vol. 10, p. 417–433.

Kershaw, D. S., 1978, "The Incomplete Conjugate Gradient Modeling for the Iterative Solution of Linear Equations," *J. Comp. Physics*, Vol. 26.

Kirtley, K., and Lakshminarayana, B., 1988, "Computation of Three Dimensional Turbulent Flow Using a Coupled Parabolic Marching Method," ASME *Journal of Turbomachinery*, Vol. 110, p. 549.

Kirtley, K., Warfield, M., and Lakshminarayana, B., 1986, "A Comparison of Computational Methods for Three Dimensional Turbulent Turbomachinery Flows," AIAA Paper 86-1599, (Synoptic in *J. Propulsion*, Vol. 4, No. 3, May 1988).

Kirtley, K., Beach, T. A., and Adamczyk, A., 1990, "Numerical Analysis of Secondary Flow in a Two Dimensional Stage Turbine," AIAA Paper 90-2356.

Knight, C. J., and Choi, D., 1989, "Development of a Viscous Cascade Code Based on Scalar Implicit Factorization," *AIAA Journal*, Vol. 27, No. 5, p. 581.

Kopper, F. C. et al., 1981, "Experimental Investigation of Endwall Profiling in a Turbine Vane Cascade," *AIAA Journal*, Vol. 19, pp. 1033–1044.

Krain, H., 1988, "Swirling Impeller Flow," ASME *Journal of Turbomachinery*, Vol. 110, pp. 122–128.

Krimmerman, Y., and Adler, D., 1978, "The Three Dimensional Flow Field in Turbo Impellers," *J. Mech. Eng. Sci.*, Vol. 20, No. 3.

Kueny, J. L., and Desclaux, J., 1989, "Theoretical Analysis of Cavitation in Rocket Engine Inducers," "Pumping of Machinery, " (ed. P. Cooper), ASME FED, Vol. 8.

Kunz, R., and Lakshminarayana, B, 1991, "Stability of Explicit 3D Navier Stokes/k_ϵ Procedures in Complex Internal Flow Calculations," AIAA Paper 91-0018.

Kunz, R., and Lakshminarayana, B., 1991a, "Three-Dimensional Navier Stokes Computation of Turbomachinery Flows Using an Explicit Numerical Procedure and a Coupled k_ϵ-Turbulence Model," ASME 91-GT-146, (to be published ASME *Journal of Turbomachinery*, 1991).

Kunz, R., and Laksminarayan, B., 1990, "Computation of Supersonic and Low Subsonic Cascade Flows Using an Explicit Navier-Stokes Technique and the k-$_\epsilon$ Turbulence Model," CFD Aeropropulsion Conference, NASA Lewis Res Center (to be published in *AIAA Journal*, 1991).

Kunz, R., Rhie, C. M., and Malecki, R. E., 1988, "Calculation of Internal Flow Using a Single Pass Parabolized Navier-Stokes Analysis," AIAA Paper 88-3005.

Kurzrock, J. W., and Novick, A. S., 1975, "Transonic Flow Around Rotor Blade Elements," ASME JOURNAL OF FLUIDS ENGINEERING, p. 598.

Kwak, D., Chang, J. L. C., Shanks, S. P., and Chakravarty, S. R., 1986, "A Three-Dimensional Incompressible Navier-Stokes Flow Solver Using Primitive Variables," *AIAA Journal*, Vol. 24, pp. 390–398.

Lakshminarayana, B., 1986, "Turbulence Modelling for Complex Flows," *AIAA Journal*, Vol. 24, No. 12, pp. 1900–1917.

Lakshminarayana, B., and Gorton, C. A., 1977, "Three Dimensional Flow Field in Rocket Pump Inducers," ASME JOURNAL OF FLUIDS ENGINEERING, Vol. 99, No. 1, pp. 176–186.

Lakshminarayana, B., and Govindan, T. R., 1981, "Analysis of Turbulent Boundary Layer on Cascade and Rotor Blades of Turbomachinery," *AIAA Journal*, Vol. 19, pp. 1333–1341.

Lakshminarayana, B., and Popovski, P., 1987, "Three-Dimensional Boundary Layer on a Compressor Rotor Blade at Peak Pressure Rise Coefficient," ASME *Journal of Turbomachinery*, Vol. 109, pp. 91–98.

Lakshminarayana, B., Kirtley, K. R., and Warfield, M., 1989, "Computational Techniques and Validation of 3D Viscous/Turbulent Codes for Internal Flows," *Sadhana*, Indian Aca. Sci. Proc. Engineering Science, Vol. 14, Part 2, pp. 59–91 (also in AGARD CP 437, 1988).

Lakshninarayana, B., and Davino, R., 1980, "Mean Velocity and Decay Characteristics of the Wake of an Axial Flow Compressor Guide Vane and Stator Blade," ASME *Journal of Engineering Power*, Vol. 102, p. 50.

Langston, L. S., Nice, M. L., and Hooper, R. M., 1977, "Three Dimensional Flow Within a Turbine Passage," ASME *Journal of Engineering Power*, Vol. 99, p. 21–26.

Lax, P. D., and Wendroff, B., 1960, "Systems of Conversation Laws," *Comm. Pure. App. Math.*, Vol. 13, pp. 217–237.

Lax, P. D., and Wendroff, B., 1964, "Difference Schemes for Hyperbolic Equations with High Order Accuracy," *Comm. Pure. App. Math.*, 17, pp. 381–398.

Launder, B. E., Reece, B. J., and Rodi, W., 1976, "Progress in the Development of a Reynolds Stress Turbulence Closure Model," *J. Fluid Mech.*, Vol. 52, p. 609.

Launder, B. E., Tselepidakis, D. P., and Younis, B. A., 1987, "A Second Order Closure Study of Rotating Channel Flow," *J. Fluid Mech.*, Vol. 183, pp. 63–75.

Lebeouf, F., 1986, "Secondary Flows and End Wall Boundary Layers in Axial Turbomachines," Von Karman Inst. Lecture Series 84-05.

LeMeur, A., 1988, "Three Dimensional Unsteady Flow Computation in a Transonic Axial Turbine Stage," ONERA (France), TP No. 1988-2.

Leonard, D., 1990, "Subsonic and Transonic Cascade Design," Von Karman Institute, Lecture Series, 90-8.

Leonard, B. P., 1979, "A Stable and Accurate Convective Modeling Procedure Based on Quadratic Upstream Interpolation," *Comp. Meth. in App. Mech. and Engineering*, Vol. 19, p. 59.

Leylek, J. H., and Wisler, D. C., 1990, "Mixing in Axial-Flow Compressors: Conclusions Drawn from 3D Navier-Stokes Analysis and Experiments," ASME Paper 90-GT-333 (to be published, ASME *Journal of Turbomachinery*, 1991).

Liu, J. S., Sockol, P. N., and Prahl, J. M., 1989, "Navier-Stokes Cascade Analysis with a Stiff k_ϵ Turbulence Solver," AIAA Paper 88-0594.

Liu, J. S. Zedan, M., and Buzzola, R., 1991, "A Comparison Between Two Three Dimensional Codes and Experimental Results for High Work Turbine," AIAA Paper 91-0341.

Lombard, C. K., Venkatapathy, E., and Bardina, J., 1984, "Universal Single Level Implicit Algorithm for Gas Dynamics," AIAA Paper 98-1533.

Lumley, J. L., 1980, "*Prediction Methods for Turbulent Flows*," ed. W. Kollman, Hemisphere Publishing Co.

Maccormack, R. w., 1969, "The Effect of Viscoscity in Hypervelocity Impact Catering," AIAA Paper 69-345.

MacCormack, R. W., and Baldwin, B. S., 1975, "A Numerical Method for Solving the Navier-Stokes Equations with Application to Shock-Boundary Layer Interactions," AIAA Paper 75-1.

Martinelli, L., 1987, "Calculation of Viscous Flows with Multigrid Methods," Ph.D. thesis, MAE Department, Princeton University.

Matsunaga, K. et al., 1990, "Application of 3D Navier Stokes Computation to Bowed Stacking Turbine Design," AIAA Paper 90-2129.

Mayle, R E., 1991, ASME IGTI Scholar Lecture, Gas Turbine Conference, Orlando. ASME paper 91GT261.

McDonald, P. W. et al., 1981, "A Comparison Between Measured and Computed Flow Fields in a Transonic Compressor Rotor," ASME *Journal of Engineering for Power*, Vol. 104.

McDonald, P. W. et al., 1971, "The Computation of Transonic Flow Through Two Dimensional Gas Turbine Cascades," ASME Paper 71-GT-89.

McFarland, E. R., 1982, "Solution of Plane Cascade Flow Using Surface Singularity Method," ASME *Journal of Engineering for Power*, Vol. 104, pp. 668–674.

McNally, W. D., and Sockol, P., 1981, "Computational Methods for Internal Flows with Emphasis on Turbomachinery," NASA TM 82764 (condensed version in *J. Fluids Engineering*, Vol. 107, 1985).

Merkle, C. L., and Tsai, P. Y. L., 1986, "Application of Runge Kutta Schemes in Compressible Flows," AIAA Paper 86-0553.

Moore, J. et al., 1988, "Flow and Heat Transfer in Turbine Tip Gaps," ASME Paper 88-GT-188.

Moore, J. G., 1985, "An Elliptical Procedure for 3D Viscous Flow," in "3D Computation Techniques Applied to Internal Flows in Propulsion Systems," AGARD, LS-140.

Moore, J., and Moore, J. G., 1986, "Performance Evaluation of Linear Turbine Cascade Using Three-Dimensional Viscous Flow Calculation," ASME *Journal of Engineering for Gas Turbines and Power*, Vol. 108.

Moore, J., and Moore, J. G., 1989, "Shock Capturing and Loss Prediction for Transonic Turbine Blade," *Int. Symp. Air Breathing Engines*, Athens, Greece.

Moore, J., LeFur, T., and Moore, J. G., 1990, "Computational Study of 3D Turbulent Air Flow in a Helical Rocket Pump Inducer," AIAA Paper 90-2123.

Nakahashi, K., 1989, "Navier-Stokes Computation of Two and Three Dimensional Cascades Flow Fields," *J. Propulsion*, Vol. 5, No. 3, p. 320.

Naraimha, R., 1985, "The Laminar-Turbulent Zone in the Boundary Layer," *Prog. Aerospace Sci.*, Vol. 22, p. 29.

Ni, R. H., 1982, "A Multiple Grid Scheme for Solving the Euler Equations," *AIAA Journal*, Vol. 20, No. 11, pp. 1565–1571.

Ni, R. H., and Bogoian, J., 1989, "Prediction of 3D Multi-Stage Turbine Flow Field Using a Multiple Grid Euler Solver," AIAA Paper 89-0203.

Ni, R. H., and Sharma, O., 1990, "Using 3D Euler Simulations to Assess Effects of Periodic Unsteady Flow Through Turbines," AIAA Paper 90-2357.

Nojima et al., 1988, "Development of Aerodynamic Design System for Centrifugal Compressors," Mitsubishi Heavy Industries, Tech. Review, Vol. 25, No. 1.

Osher, S., and Salomon, F., 1982, "Upwind Schemes for Hyperbolic Systems of Conservation Laws," *Mathematics of Computation*, Vol. 38, p. 339.

Patankar, S. V., 1980, "*Numerical Heat Transfer and Fluid Flow*," Hemisphere, New York.

Patankar, S. V., 1988, "Recent Developments in Computational Heat Transfer," ASME *Journal Heat Transfer*, Vol. 110, p. 1037.

Patankar, S. V., and Spalding, D. B,. 1972, "A Calculation Procedure for Heat, Mass, and Momentum Transfer in Three-Dimensional Parabolic Flows," *International Journal of Heat and Mass Transfer*, Vol. 15, pp. 1787–1806.

Patel, V. C., Rodi, W., and Scheuerer, G., 1985, "A Review and Evaluation of Turbulence Models for Near Wall and Low Reynolds Number Flows," *AIAA Journal*, Vol. 23, pp. 1308–1319.

Pierzga, M. J., and Wood, J. R., 1985, "Investigations of the Three Dimensional Flow Field within a Transonic Compressor Rotor," ASME *Journal of Engineering for Gas Turbines and Power*, Vol. 107, p. 437.

Platzer, M. F., and Carta, F. O., (eds.), 1987, "AGARD Manual on Aeroelasticity of Turbomachines," Vol. 1, Unsteady Turbomachinery Aerodynamics, AGARD-AG-298.

Popovski, P., and Lakshminarayana, B., 1986, "Laser Anemometer Measurements in a Compressor Rotor Flow Field at Off-Design Conditions," *AIAA J.*, Vol. 24, pp. 1337–1345.

Pouagare, M., and Lakshminarayana, B., 1982, "Development of Secondary Flow and Vorticity in Ducts, Cascades, and Rotors, Including Effects of Viscosity and Rotation," ASME JOURNAL OF FLUIDS ENGINEERING, Vol. 104, p. 505.

Pouagare, M., and Lakshminarayana, B., 1986, "Computation of Viscous Flows in Turbomachinery Cascades with a Space Marching Method," *J. Propulsion and Energy*, Vol. 2, p. 266.

Pouagare, M., and Lakshminarayana, B., 1986, "A Space Machining Method for Viscous Incompressible Internal Flows," *J. Comp. Phy.*, Vol. 64, No. 2.

Pouagare, M., Galmes, J. M., and Lakshminarayana, B., 1985, "An Experimental Study of the Compressor Rotor Blade Boundary Layer," ASME *Journal of Engineering for Gas Turbines and Power*, Vol. 107, pp. 364–373.

Pouagare, M., Murthy, K. N. S., and Lakshminarayana, B., 1983, "Three Dimensional Flow Field Inside the Passage of a Low Speed Compressor," *AIAA Journal*, Vol. 21, No. 12, p. 1679.

Pourahamadi, F., and Humphrey, J. A. C., 1983, "Prediction of Curved Channel Flow with Extended k_ϵ Model of Turbulence," *AIAA Journal*, Vol. 21, p. 1365.

Povinelli, L., 1984, "Assessment of Three-Dimensional Inviscid Codes and Loss Correlations for Turbine Aerodynamics," ASME Paper 84-GT-187.

Pratap, V. S., and Spalding, D. B., 1976, "Fluid Flow and Heat Transfer in Three-Dimensional Ducts," *Int. J. Heat & Mass Transfer*, Vol. 19, p. 1183.

Prato, J., 1990, "Effects of Blade Loading on the Wake Characteristics of a Compressor Rotor Blade," M.S. thesis, The Pennsylvania State University.

Pulliam, T., 1986, "Efficient Solution Methods for the Navier-Stokes Equations," *Numerical Techniques For Viscous Flow Computations in Turbomachinery Bladings*, VKI LS-86.

Rai, M. M., 1987, "Navier-Stokes Simulation of Rotor/Stator Interaction Using Patched and Overlaid Grids," *Journal of Propulsion and Power*, Vol. 3, pp. 387–396.

Rai, M. M., 1989, "Unsteady Three-Dimensional Navier-Stokes Simulations of Turbine Rotor-Stator Interaction," Parts I and II, *J. Propulsion*, Vol. 5, No. 3, p. 305.

Rai, M. M., and Chakravarthy, S. R., 1986, "An Implicit Form for the Osher Upwind Scheme," *AIAA Journal*, Vol. 24, No. 5, p. 735.

Raithby, G. D., 1976, "Skew Upstream Differencing Schemes for Problems Involving Fluid Flow," *Computer Methods in Applied Mechanics and Engineering*, Vol. 9, pp. 153–164.

Raj, R., and Lakshminarayana, B., 1974, "On the Investigation of Cascade and Turbomachinery Wake Characteristics," NASA CR 134680.

Ramshaw, J. D., and Mousseau, V. A., 1990, "Accelerated Artifical Method for Steady State Incompressible Flow Calculations," *Computers and Fluids*, Vol. 18, pp. 361–367.

Rangawalla, A., and Rai, M., 1990, "A Kinematical/Numerical Analysis of Rotor-Stator Interaction Noise," AIAA Paper 90-0281.

Rhie, C. M., 1986, "A Pressure Based Navier-Stokes Solver Using the Multigrid Method," AIAA Paper 86-0207.

Rhie, C. M., 1985, "A Three Dimensional Passage Flow Analysis Method Aimed at Centrifugal Compressors," *Computers and Fluids*, Vol. 13, No. 4, pp. 443–460.

Rhie, C. M., and Chow, W. L., 1983, "Numerical Study of the Turbulent Flows Past an Airfoil With Trailing Edge Separation," *AIAA Journal*, Vol. 21, pp. 1525–1532.

Rhie, C. M., Delaney, R. A., and McKain, T. F., 1984, "Three Dimensional Viscous Flow Analysis for Centrifugal Impellers," AIAA-84-1296.

Rhie, J., and Stowers, S. T. 1987, "Navier-Stokes Analysis for High Speed Flows Using Pressure Correction Algorithm," AIAA Paper 87-1980.

Rodi, W., 1976, "A New Algebraic Relation for Calculating Reynolds Stress," *ZAMM*, Vol. 56, p. 219.

Rodi, W., and Scheurer, G., 1983, "Calculations of Curved Shear Layers with Two Equation Models," *The Physics of Fluids*, Vol. 26, p. 1422.

Rodgers, S. E., Kwak, D., and Kiris, C., 1989, "Numerical Solution of Incompressible Navier-Stokes Equations for Steady State and Time Dependent Problems," AIAA Paper 89-0463 (also see NASA TM 102183).

Rodgers, S. E., Chang, J. L. C., and Kwak, D., 1987, "A Diagonal Algorithm for the Method of Psuedo-Compressibility," *J. Comp. Phy.*, Vol. 73, pp. 364–379.

Sanz, J. M., 1983, "Design of Supercritical Cascades with High Solidity," *AIAA Journal*, Vol. 21, No. 9, pp. 1289–1293 (also see NASA TP2676, 1987).

Saxer, A., and Felici, H., 1987, "Etude Numerique D'Ecoulements Interes Incompressibles et Stationnaires Par Les Equations D' Euler," IMHEF Report T 87-4, Ecole Polytechnique Federale De Lausanne, Switzerland.

Schiff, L. B., and Steger, J. L., 1980, "Numerical Simulation of Steady Supersonic Viscous Flow," *AIAA Journal*, Vol. 18, No. 12, pp. 1421–1430.

Schrieber, H. A., 1988, "Experimental Investigations on Shock Losses of Transonic and Supersonic Compressor Cascades," AGARD CP-401, Paper No. 11.

Schultz, J. L., 1988, "Modelization De La Cavitation Partielle Dans Les Pompes," Doctoral thesis, Institut National Polytechnique de Grenoble.

Schultz, J. L., and Kueny, J. L., 1986, "Partial Cavitation on Pump Blades," *Proc. Fluid Dynamics and Space*, Von Karman Institute, ESA SP 265.

Scott, J. N., 1985, "Numerical Solution of the Navier-Stokes Equations for 3D Internal Flows," AGARD LS140.

Shamroth, S. J., McDonald, H., and Briley, W. R., 1982, "Application of Navier-Stokes Analysis to Transonic Cascade Flow Fields," ASME *Journal of Engineering for Power*.

Shang, J., 1985, "An Assessment of Numerical Solution of the Compressible Navier Stokes Equations," *J. Aircraft*, Vol. 22, p. 353.

Shankar, V., Kuo, Y., and Osher, S., 1985, "Treatment of Supersonic Flows with Embedded Subsonic Regions," *AIAA J.*, Vol. 23, No. 1, p. 41.

Sheih, L. F., and Delaney, R. A., 1987, "An Accurate and Efficient Euler Solver for Three Dimensional Turbomachinery Flows," ASME *J. Turbomachinery*, Vol. 109.

Shih, T. G., and Lumley, J. L., 1986, "Second Order Modeling of Near Wall Turbulence," *Phys. Fluids*, Vol. 29, pp. 971–975.

Singh, U. K., 1982, "Computation and Comparison with Measurements of Transonic Flow in an Axial Compressor Stage with Shock Boundary Layer Interactions," ASME *Journal of Engineering for Power*, Vol. 104, pp. 510–515.

Smith, P. D., 1982, "Numerical Computation of Three Dimensional Boundary Layers," *Three Dimensional Turbulent Boundary Layers*, ed. H. H. Fernolz and E. Krause, Springer-Verlag.

Spalding, D. B., 1980, "A Mathematical Modelling of Fluid Dynamics, Heat Transfer and Mean Transfer Processes," Imperial College (London) Report HTS/8011.

Speziale, C. G., Raj, R., and Gatski, T. B., 1990, "Modeling the Dissipation Rate in Rotating Turbulent Flows," ICASE Report No. 90-88, NASA CR 187485.

Steger, J. L., Pulliam, T. H., and Chima, R. V., 1980, "An Implicit Finite Difference Code for Inviscid and Viscous Cascade Flow," AIAA Paper 80-1427, AIAA 13th Fluid and Plasma Dynamics Conference, Snowmass.

Stephen, H. E., and Hobbs, D. E., 1979, "Design and Performance Evaluation of Supercritical Air Foils for Axial Flow Compressors," NAVAIR Report FT-11455.

Stone, H. L., 1968, "Iterative Solution of Implicit Approximations of Multidimensional Partial Differential Equations," *SIAM J. Num. Analysis*, Vol. 5, pp. 530–555.

Stow, P., 1989, "Development of Advanced Computational Methods for Turbomachinery Design," *Int. J. Num. Methods in Fluids*, Vol. 9, p. 921.

Stow, P., 1988, "Turbomachinery Blade Design Using Advanced Calculation Methods," In "Advanced Flow Calculations for Internal Flow and Turbomachinery," Cranfield Fluids Engineering Course (England).

Subramanian, S. V., 1989, "Three Dimensional Multi-Grid Navier-Stokes Computations for Turbomachinery Applications," AIAA Paper 89-2453 (also see AIAA Paper 89-1818).

Subramanian S. V., and Bozzola, R., 1987, "Numerical Simulation of Three Dimensional Flow Fields in Turbomachinery Blade Rows Using the Compressible Navier Stokes Equations," AIAA Paper 87-1314.

Subramanian, S. V., and Bozzola, R., 1985, "Application of Runge-Kutta Time Marching Scheme for the Computation of Transonic Flows in Turbomachines," AIAA Paper No. 85-1332.

Suryavamshi, N., and Lakshminarayana, B., 1991, "Numerical Prediction of Wakes in Cascades and Compressor Rotors Including the Effects of Mixing," Part I (ASME 91-GT-225), Part II (ASME Paper 91-GT-222).

Thompkins, W. T., 1982, "A FORTRAN Program for Calculating Three-Dimensional, Inviscid, Rotational Flows with Shock Waves in Axial Compressor Blade Rows, User's Manual," NASA CR 3560.

Thompkins, W. T., and Usab, W. J., Jr., 1982, "A Quasi-Three Dimensional Blade Surface Boundary Layer Analysis of Rotating Blades," ASME *Journal of Engineering for Power*, Vol. 104, p. 439.

Thibaud, F., Drost, A., and Sottas, G., 1989, "Validation of Euler Code for Hydraulic Turbine," AGARD CP-437.

Tyner, T. M., and Sullivan, J. P., 1990, "Design and Performance of a Small High Speed Axial Compressor," AIAA Paper 90-1911.

Vanka, 1986, "Block Implicit Multigrid Calculation of the Two Dimensional Recirculating Flow," *Computer Methods in App. Mech. and Engineering*, Vol. 59, pp. 29–48.

Vatsa, V. N., 1985, "A Three-Dimensional Boundary Layer Analysis Including Heat Transfer and Blade Rotation Effects," Paper presented at the Third Symposium on Numerical and Physical Aspect of Aerodynamic Flows, Long Beach, CA.

Von Doormal, J. P., and Raithby, G. D., 1984, "Enhancement of the SIMPLE Method for Predicting Incompressible Fluid Flow," *Num. Heat Transfer*, Vol. 67, p. 147.

Vuillez, C., and Veuillot, J. P., 1990, "Quasi 3D Viscous Flow Computations in Subsonic and Transonic Turbomachinery Blading," AIAA Paper 90-2126.

Wang, K. C., 1971, "On the Determination of Zones of Influence and Dependence for Three Dimensional Boundary Layer Equations," *Journal of Fluid Mechanics*, Vol. 48, Part 2, pp. 397–404.

Wang, Q., Zhu, B., and Wu, C. H., 1985, "Quasi Three Dimensional and Full Three Dimensional Rotational Flow Calculations in Turbo-machines," ASME *Journal of Engineering for Gas Turbines and Power*, Vol. 107, p. 277.

Wang, A., and Yu, H., 1988, "A Unified Solution Method for the Flow Calculations About S_1 and S_2 Surfaces Used for the Computer Aided Design of Centrifugal Compressor," ASME Paper, 88-GT-237.

Warfield, M., and Lakshminarayana, B., 1987, "Calculation of Three-Dimensional Locally Elliptic Flow with a Zonal Equation Method, Hawaii, AIAA Paper 87-1141CP (Synoptic, *AIAA Journal*, Feb. 1991).

Warfield, M., and Lakshminarayana, B., 1987a, "Computation of Rotating Turbulent Flow with an Algebraic Reynolds Stress Model," *AIAA Journal*, Vol. 25, No. 7, pp. 957–964.

Warfield, M., and Lakshminarayana, B., 1989, "Calculation of Three Dimensional Turbomachinery Rotor Flow Using Psuedo Compressibility and Zonal Techniques," *Z. Flugwiss WelTraum Forsch*, Vol. 13, p. 31.

Weber, K. F., and Delaney, R. F., 1991, "Viscous Analysis of Three-Dimensional Turbomachinery Flows Using an Implicit Solver," ASME 91-GT-205.

White, F., 1991, *Viscous Fluid Flow*, McGraw-Hill.

Worth, E., and Plehn, N., 1990, "Application of 3D Viscous Code in the Design of a High Performance Compressor, AIAA Paper 90-1914.

Wu, C. H., 1952, "A General Theory of Three Dimensional Flow in Subsonic and Supersonic Turbomachine in Radial, Axial and Mixed Flow Types," NACA TN 2604.

Yakota, J. W., 1990, "Diagonally Inverted Lower-Upper Factored Implicit Multi-grid Scheme for the Three-Dimensional Navier-Stokes Equations," *AIAA Journal*, Vol. 28, No. 9, p. 1642.

Zannetti, L., and Larocca, F., 1990, "Inverse Design Methods for Internal Flows," Von Karman Institute Lecture Series, 90-8.

Zhang, J., Lakshminarayana, B., 1990, "Computation and Turbulence Modelling for Three Dimensional Turbulent Boundary Layers Including Turbomachinery Rotor Blades," *AIAA Journal*, Vol. 28, No. 11, pp. 1861–1969.

Zierke, W. C., and Deutsch, S., 1989, "The Measurement of Boundary Layers on a Compressor Blade in Cascade: Part 4—Flow Fields for Incidence Angles of -1.5 and -8.5 Degrees," ASME 89-GT-72.

Zimmerman, H., 1990, "Calculation of Two- and Three-Dimensional Flow in a Transonic Turbine Cascade with Particular Regard to the Losses," AIAA Paper 90-1542.

A Finite-Element Perturbation Approach to Fluid/Rotor Interaction in Turbomachinery Elements. Part 1: Theory

E. A. Baskharone
Associate Professor.
Mem. ASME

S. J. Hensel[1]
Mem. ASME

Department of Mechanical Engineering,
Texas A&M University,
College Station, Texas 77843

The vibrational characteristics of a rotor that is in contact with a fluid in an annular clearance gap, as dictated by the fluid forces in the gap, are investigated. The "rotor" here is a general term that may refer to the shaft segment within the housing of an annular seal, on the simple end of the application spectrum, or the shroud-seal assembly in a shrouded-impeller stage of a turbomachine, on the complex end. The disturbance under consideration involves the axis of rotation, and includes a virtual lateral eccentricity, together with a whirling motion around the housing centerline. Uniqueness of the computational model stems from the manner in which the rotor eccentricity is physically perceived and subsequently incorporated. It is first established that the fluid reaction components arise from infinitesimally small deformations with varied magnitudes which are experienced by an assembly of finite elements in the rotor-to-housing gap as the gap becomes distorted due to the rotor virtual eccentricity. The idea is then cast into a perturbation model in which the perturbation equations emerge from the flow-governing equations in their discrete finite-element form as opposed to the differential form, which is traditionally the case. As a result, restrictions on the rotor-to-housing gap geometry, or the manner in which the rotor virtual eccentricity occurs are practically nonexisting. While the emphasis in this paper is on the theoretical model, a representative application of the model and assessment of the numerical results are the focus of a companion paper that is being published concurrently.

Introduction

Reliable modeling of the rotordynamic characteristics of fluid-encompassed elements in turbomachines, such as the annular seal rotor in Fig. 1, started fairly recently. The bulk-flow model devised by Childs (1983) is an example of some widely used predictive tools in this area. This technique was used to compute both the direct and cross-coupled rotordynamic coefficients for an annular seal (Childs, 1985) and further extended by Nelson (1985) to account for the flow compressibility and the seal taper. However, the accuracy of this model would naturally decline in the case of a generally shaped annular flow passage, such as the secondary passage of the shrouded impeller in Fig. 2, where lateral (rotor-to-housing) flow stresses become comparable to those at the solid walls. Besides, the analysis is conceptually incapable of simulating the effects of flow separation and recirculation in such a complex flow passage, but has been remarkably successful otherwise (Childs, 1989).

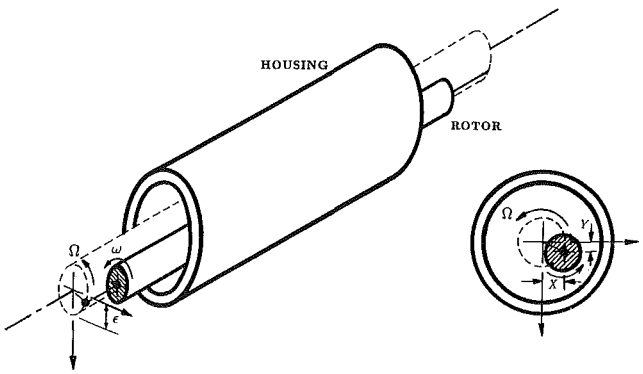

Fig. 1 Cylindrical whirl of a rotor inside a housing

Recently, a more rigorous finite difference-based perturbation model was developed by Dietzen et al. (1987) and applied to an annular seal. The distorted seal annulus for the displaced shaft configuration, in this case, was mapped into a fictitious frame of reference, reducing the problem into that of a centered shaft rotation. A traditional hypothesis was then made that perturbations of the flow variables vary sinusoidally with the tangential coordinate around the circumference in the

[1]Graduate Research Assistant, currently a Senior Engineer at Westinghouse Savannah River Laboratory, Aiken, South Carolina.

Contributed by the Fluids Engineering Division for publication in the JOURNAL OF FLUIDS ENGINEERING. Manuscript received by the Fluids Engineering Division March 27, 1990.

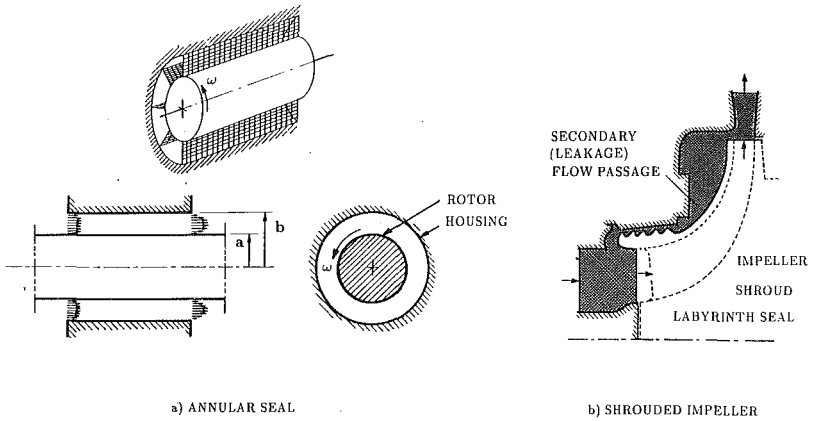

a) ANNULAR SEAL b) SHROUDED IMPELLER

Fig. 2 Two representative problems of turbomachinery rotating elements

fictitious space, with only the first harmonic wave taken into account. Based on this assumption, a perturbation analysis of Navier-Stokes equations was then performed and the rotordynamic coefficients, in the end, obtained. Despite the apparent generality and complex nature of this analysis, it involves geometry-related restrictions and is limited to a uniform lateral eccentricity of the rotor axis. Other existing models for annular and labyrinth seals, e.g., those by Dietzen and Nordmann (1988) and Hensel (1986), do not utilize the perturbation concept and are therefore tedious as well as costly, for they require solution of the fully three-dimensional Navier-Stokes equations in the distorted flow domain.

In this paper, a new finite element-based perturbation model is presented. The model introduces what may be referred to as the "virtually deformable" finite element concept, as a means of determining the fluid-exerted forces in the rotor-to-housing gap, and whether such forces would sustain or suppress a rotor whirling motion of the cylindrical type, as depicted in Fig. 1 for a simple annular seal. Originality and versatility of the new model both stem from the fact that the perturbation equations emerge from the discrete finite-element flow equations as opposed to the flow-governing equations in their differential form as is traditionally the case.

Analysis

The governing equations are grouped as pertinent to the fundamental rotordynamics basis, the flow kinetics in the undisturbed operation mode and, finally, the perturbation model. In all phases, reference is made to a general fluid domain with which the rotor is in contact. Two examples of such domain, namely that of an annular seal and shrouded pump impeller (Fig. 2), are given.

Definition of the Rotordynamic Coefficients. Evaluation of the force coefficients is initialized by considering the rotor lateral eccentricity "ϵ" coupled with a circular whirling motion around the housing centerline (Fig. 1). The locus of the rotor axis, in this case, can parametrically be described as follows:

$$X=\epsilon\sin(\Omega t), Y=\epsilon\cos(\Omega t) \tag{1}$$

where "X" and "Y" are the eccentricity components of the rotor axis (Fig. 1), "Ω" is the whirl frequency and "t" refers to time. Noting that the direction of "Ω" in Fig. 3(a) is negative, the rotor equation of motion can be written as follows:

$$-\begin{Bmatrix}\delta F_x\\ \delta F_y\end{Bmatrix}=\begin{bmatrix}K & -k\\ k & K\end{bmatrix}\begin{Bmatrix}X\\ Y\end{Bmatrix}+\begin{bmatrix}C & -c\\ c & C\end{bmatrix}\begin{Bmatrix}\dot{X}\\ \dot{Y}\end{Bmatrix}+\begin{bmatrix}M & -m\\ m & M\end{bmatrix}\begin{Bmatrix}\ddot{X}\\ \ddot{Y}\end{Bmatrix} \tag{2}$$

where

δF_x, δF_y are the incremental changes in the rotor force components as a result of the rotor disturbance,
K, k are the direct and cross-coupled stiffness coefficients of the fluid/structure system,
C, c are the damping coefficients,
M, m are the inertia (or added mass) coefficients,

Assuming cylindrical whirl around the housing centerline at

Nomenclature

$[A]$, $[a]$ = global and elemental matrices of influence coefficients in the finite element equations
$\{B\}$, $\{b\}$ = global and elemental load vectors in the finite element equations
F, G, H, I, J, K = linear operators defined in the element local frame of reference
K, k, C, c, M, m = direct and cross-coupled stiffness, damping and inertia coefficients
$M_i(\zeta, \eta, \xi)$ = linear shape function associated with the ith corner node of a finite element
$N_i(\zeta, \eta, \xi)$ = quadratic shape function associated with the ith corner or midside node of a finite element
p = static pressure
u, v, w = velocity components in the cartesian frame of reference
W_i = weight function in the Petrov-Galerkin weighted-residual analysis
x, y, z = cartesian coordinates
ϵ = lateral eccentricity of the rotor axis
ζ, η, ξ = coordinates in the element local frame of reference
ν = kinematic viscosity
ρ = density
$\{\Phi\}$, $\{\phi\}$ = global and elemental vector of unknown velocity components and pressure
Ω = whirl frequency
ω = rotor operating speed

Other Symbols

overbar = perturbation in a quantity due to the rotor eccentricity
$(\hat{\ })$ = a quantity that is known from a previous iteration or an initial guess

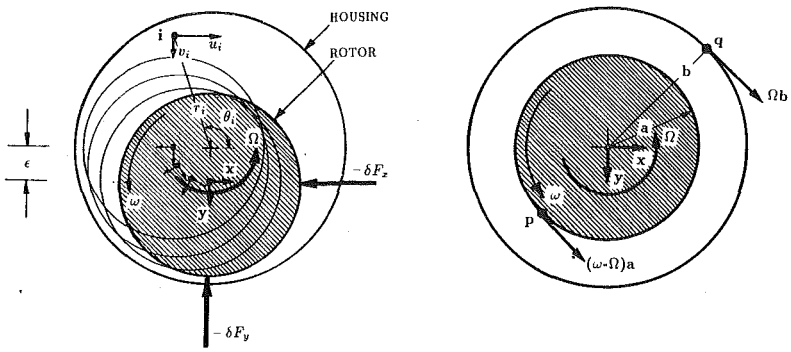

a) ECCENTRIC ROTOR b) CENTERED ROTOR

Fig. 3 Definition of the rotating-translating axes and solid-wall boundary conditions

a constant whirl frequency "Ω", and refering to Fig. 1, consider the position of the rotor axis that is vertically underneath the housing centerline. The axis location, linear velocity and acceleration at this position are:

$$X=0 \quad Y=\epsilon$$
$$\dot{X}=\Omega\epsilon \quad \dot{Y}=0$$
$$\ddot{X}=0 \quad \ddot{Y}=-\Omega^2\epsilon$$

Substituting these into the expanded form of the matrix Eq. (2), and taking the limit as "ϵ" tends to zero, the following equations are obtained:

$$\frac{\partial F_x}{\partial \epsilon}=\lim_{\epsilon\to 0}\left(\frac{\delta F_x}{\epsilon}\right)=k-\Omega C-\Omega^2 m \tag{3}$$

$$\frac{\partial F_y}{\partial \epsilon}=\lim_{\epsilon\to 0}\left(\frac{\delta F_y}{\epsilon}\right)=-K-\Omega c+\Omega^2 M \tag{4}$$

Determination of the rotordynamic coefficients in Eqs. (3) and (4) requires computation of the derivatives $\frac{\partial F_x}{\partial \epsilon}$ and $\frac{\partial F_y}{\partial \epsilon}$ at a minimum of three different values of the whirl frequency "Ω." Interpolation of these two derivatives as parabolic expressions of "Ω," using curve fitting techniques, leads to the rotordynamic coefficients by simply equating the different terms in these expressions to those on the right-hand sides of Eqs. (3) and (4). It is therefore clear that the fundamental problem here is that of computing the rate (with respect to the virtual eccentricity "ϵ") at which the fluid reaction forces are developed on the whirling rotor (Fig. 1). The procedure is initialized by solving the flow-governing equations in the undisturbed rotation mode as presented next.

Choice of the Coordinate Axes. The flow equations are cast in a frame of reference that is consistent with the annular gap geometry in the disturbed-rotor operation mode. As shown in Fig. 3(*a*), the reference axes are attached to the displaced rotor and are, therefore, of the rotating-translating, or simply whirling, type. The rotational speed, in this case, is numerically equal to the whirl frequency "Ω" and the translation is identical to that of the rotor axis. As seen, the clearance gap flow field, viewed in this frame of reference, is now steady at all times, despite the apparent time dependency of the absolute flow field when viewed in a stationary frame of reference.

Motion of the coordinate axes, in the general manner just described, takes place only after the rotor has entered its eccentric operation mode. However, it is only the axes rotation that prevails in the centered-rotor mode (Fig. 3(*b*)), in which case "Ω" is to be viewed as an arbitrary frequency.

The choice of a rotating-translating frame of reference does not imply the need to solve the flow-governing equations in the physically distorted clearance gap (e.g., Dietzen et al., (1987). The fact, however, is that this choice, despite the complex nature of the flow equations it produces (as will be seen next), makes it easier to develop the perturbation model as it ensures consistency of the unperturbed and perturbed flow fields, with the difference between the two fields being a result of only the rotor eccentricity (Fig. 3). Note that this consistency requirement can alternately be ensured by solving the simple axisymmetric flow field in the undistorted passage (Baskharone and Hensel, 1991) and then casting this "zeroth-order" solution in the frame of reference defined above (Hensel, 1990). This procedure was implemented during execution of the computer code for the substantial reduction in the core and CPU time consumption it provides.

Flow-Governing Equations. The swirling flow in the undistorted rotor-to-housing gap (Fig. 3(*b*)) is assumed adiabatic, incompressible and generally turbulent. The momentum and mass conservation equations can therefore be expressed in the rotating frame of reference (noting that "Ω" in Fig. 3(*b*) is negative) as follows:

$$\hat{u}\frac{\partial u}{\partial x}+\hat{v}\frac{\partial u}{\partial y}+\hat{w}\frac{\partial u}{\partial z}+2\Omega v-\Omega^2 x=-\frac{1}{\rho}\frac{\partial p}{\partial x}+\nu_e\nabla^2 u$$
$$+2\frac{\partial \nu_t}{\partial x}\frac{\partial u}{\partial x}+\frac{\partial \nu_t}{\partial y}\left(\frac{\partial u}{\partial y}+\frac{\partial v}{\partial x}\right)+\frac{\partial \nu_t}{\partial z}\left(\frac{\partial u}{\partial z}+\frac{\partial w}{\partial x}\right) \tag{5}$$

$$\hat{u}\frac{\partial v}{\partial x}+\hat{v}\frac{\partial v}{\partial y}+\hat{w}\frac{\partial v}{\partial z}-2\Omega u-\Omega^2 y=-\frac{1}{\rho}\frac{\partial p}{\partial x}+\nu_e\nabla^2 v$$
$$+2\frac{\partial \nu_t}{\partial y}\frac{\partial v}{\partial y}+\frac{\partial \nu_t}{\partial x}\left(\frac{\partial u}{\partial y}+\frac{\partial v}{\partial x}\right)+\frac{\partial \nu_t}{\partial z}\left(\frac{\partial v}{\partial z}+\frac{\partial w}{\partial y}\right) \tag{6}$$

$$\hat{u}\frac{\partial w}{\partial x}+\hat{v}\frac{\partial w}{\partial y}+\hat{w}\frac{\partial w}{\partial z}=-\frac{1}{\rho}\frac{\partial p}{\partial z}+\nu_e\nabla^2 w$$
$$+2\frac{\partial \nu_t}{\partial z}\frac{\partial w}{\partial z}+\frac{\partial \nu_t}{\partial x}\left(\frac{\partial u}{\partial z}+\frac{\partial w}{\partial x}\right) \tag{7}$$

$$\frac{\partial u}{\partial x}+\frac{\partial v}{\partial y}+\frac{\partial w}{\partial z}=0 \tag{8}$$

where

u, v, w are the relative velocity components
p is the static pressure
Ω is the rotational frequency of the coordinate axes (to be set equal to the rotor whirl frequency once the rotor eccentricity prevails)
ν_t, ν_e are the eddy and effective coefficients of kinematic viscosity, respectively

with the symbol (^) designating values that are carried over from a previous iteration or an initial guess for the purpose of successively linearizing the momentum equations. As seen, the axes rotational frequency "Ω" is part of these equations, which is a result of including the centripetal and Coriolis acceleration effects in this case.

Turbulence Closure. Simulation of the flow turbulence is based on the algebraic eddy-viscosity turbulence model by Baldwin and Lomax (1978). However, an adjustment in this vorticity-based model was implemented whereby the relative, as opposed to the absolute, vorticity was used to calculate the mixing length in the fluid layer that is adjacent to a solid surface. Equally important in implementing the turbulence model was the analysis of the near-wall zone which was conceptually based on the approach by Benim and Zinser (1985). Further details of the turbulence closure and the near-wall flow analysis are covered by Baskharone and Hensel (1991).

Boundary Conditions. The major difference between the two problem configurations in Fig. 2 is in the multiple entry/departure nature of the flow domain associated with the centrifugal impeller case. Uniqueness of the solution, under such circumstances, was described and attained by Baskharone and Hensel (1989) through a specific set of boundary conditions over the flow-permeable segments of the domain boundary. Boundary conditions pertaining to the annular seal problem include known profiles of inlet velocity components and zero streamwise diffusion of the exit velocity vector. The latter replaces a zero velocity gradient exit condition which would imply a fully developed flow at this station and may, in this sense, be accurate only for sufficiently long seals.

The last category of boundary conditions concerns the rotor and housing surfaces and is created by the rotation of the coordinate axes. Referring to Fig. 3(*b*), the housing surface to an observer in the rotating frame of reference, will no longer appear stationary, but will rather possess a relative velocity component "Ωb" as indicated in the figure, where "b" is the housing radius. Considering the case of what would amount to forward whirl (as the rotor axis becomes eccentric), the rotor surface in Fig. 3(*b*) would appear to the same observer as rotating at an angular speed that is less than the rotor operating speed "ω" by the amount "Ω." The rotor surface velocity in this case is $(\omega - \Omega)a$, where "a" is the rotor radius.

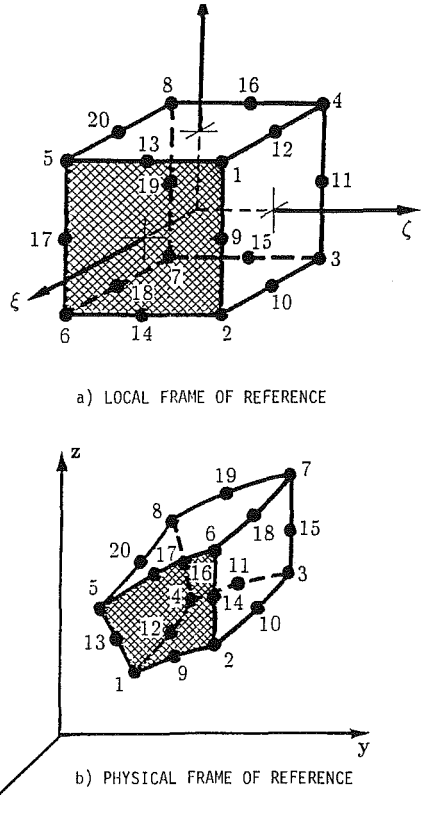

Fig. 4 Quadrilateral curve-sided isoparametric finite element

Finite-Element Formulation. The finite-element model is constructed with the twenty-node quadrilateral element in Fig. 4 as the discretization unit. The procedure is initiated by creating the finite-element discretization model corresponding to the centered-rotor operation mode as shown in Fig. 5(*a*) for a generally-shaped rotor. Within a typical "undistorted" finite element in this figure, let the cartesian-to-local spatial coordinate mapping (Fig. 4) be defined as follows:

$$x = \sum_{i=1}^{20} N_i x_i, \quad y = \sum_{i=1}^{20} N_i y_i, \quad z = \sum_{i=1}^{20} N_i z_i \tag{9}$$

where N_i are quadratic "shape" functions (Zienkiewicz, 1971) of the local coordinates ζ, η, and ξ (Fig. 4). Conversion of the spatial derivatives is, in this case, defined as follows:

$$\begin{Bmatrix} \frac{\partial}{\partial x} \\ \frac{\partial}{\partial y} \\ \frac{\partial}{\partial z} \end{Bmatrix} = [T] \begin{Bmatrix} \frac{\partial}{\partial \zeta} \\ \frac{\partial}{\partial \eta} \\ \frac{\partial}{\partial \xi} \end{Bmatrix} \tag{10}$$

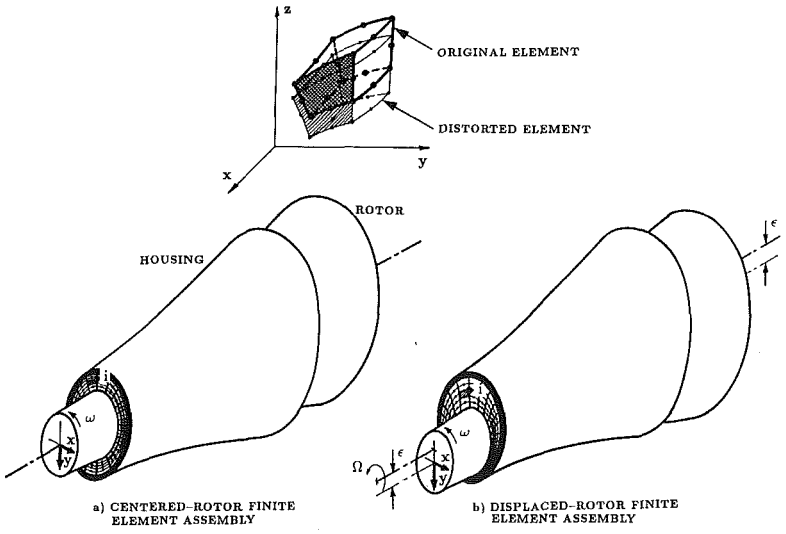

Fig. 5 Distortion of the finite elements as a result of the rotor eccentricity in a general fluid/rotor interaction problem

where the components of the matrix $[T]$ are as follows:

$$T_{11}=\frac{1}{|J|}\left(\sum_{i=1}^{20}\frac{\partial N_i}{\partial\eta}y_i\sum_{i=1}^{20}\frac{\partial N_i}{\partial\xi}z_i-\sum_{i=1}^{20}\frac{\partial N_i}{\partial\xi}y_i\sum_{i=1}^{20}\frac{\partial N_i}{\partial\eta}z_i\right)$$

$$T_{12}=\frac{1}{|J|}\left(\sum_{i=1}^{20}\frac{\partial N_i}{\partial\xi}y_i\sum_{i=1}^{20}\frac{\partial N_i}{\partial\zeta}z_i-\sum_{i=1}^{20}\frac{\partial N_i}{\partial\zeta}y_i\sum_{i=1}^{20}\frac{\partial N_i}{\partial\xi}z_i\right)$$

$$T_{13}=\frac{1}{|J|}\left(\sum_{i=1}^{20}\frac{\partial N_i}{\partial\zeta}y_i\sum_{i=1}^{20}\frac{\partial N_i}{\partial\eta}z_i-\sum_{i=1}^{20}\frac{\partial N_i}{\partial\eta}y_i\sum_{i=1}^{20}\frac{\partial N_i}{\partial\zeta}z_i\right)$$

$$T_{21}=\frac{1}{|J|}\left(\sum_{i=1}^{20}\frac{\partial N_i}{\partial\xi}x_i\sum_{i=1}^{20}\frac{\partial N_i}{\partial\eta}z_i-\sum_{i=1}^{20}\frac{\partial N_i}{\partial\eta}x_i\sum_{i=1}^{20}\frac{\partial N_i}{\partial\xi}z_i\right)$$

$$T_{22}=\frac{1}{|J|}\left(\sum_{i=1}^{20}\frac{\partial N_i}{\partial\zeta}x_i\sum_{i=1}^{20}\frac{\partial N_i}{\partial\xi}z_i-\sum_{i=1}^{20}\frac{\partial N_i}{\partial\xi}x_i\sum_{i=1}^{20}\frac{\partial N_i}{\partial\zeta}z_i\right)$$

$$T_{23}=\frac{1}{|J|}\left(\sum_{i=1}^{20}\frac{\partial N_i}{\partial\eta}x_i\sum_{i=1}^{20}\frac{\partial N_i}{\partial\zeta}z_i-\sum_{i=1}^{20}\frac{\partial N_i}{\partial\zeta}x_i\sum_{i=1}^{20}\frac{\partial N_i}{\partial\eta}z_i\right)$$

$$T_{31}=\frac{1}{|J|}\left(\sum_{i=1}^{20}\frac{\partial N_i}{\partial\eta}x_i\sum_{i=1}^{20}\frac{\partial N_i}{\partial\xi}y_i-\sum_{i=1}^{20}\frac{\partial N_i}{\partial\xi}x_i\sum_{i=1}^{20}\frac{\partial N_i}{\partial\eta}y_i\right)$$

$$T_{32}=\frac{1}{|J|}\left(\sum_{i=1}^{20}\frac{\partial N_i}{\partial\xi}x_i\sum_{i=1}^{20}\frac{\partial N_i}{\partial\zeta}y_i-\sum_{i=1}^{20}\frac{\partial N_i}{\partial\zeta}x_i\sum_{i=1}^{20}\frac{\partial N_i}{\partial\xi}y_i\right)$$

$$T_{33}=\frac{1}{|J|}\left(\sum_{i=1}^{20}\frac{\partial N_i}{\partial\zeta}x_i\sum_{i=1}^{20}\frac{\partial N_i}{\partial\eta}y_i-\sum_{i=1}^{20}\frac{\partial N_i}{\partial\eta}x_i\sum_{i=1}^{20}\frac{\partial N_i}{\partial\zeta}y_i\right)$$

with $|J|$ being the Jacobian of transformation.

Next the flow variables are interpolated within the typical element in a similar fashion. Guided by the Ladyshenskaya-Babuska-Brezzi compatibility requirements (Carey and Oden, 1986), as applied to the current problem, the velocity components and pressure are expressed as follows:

$$u=\sum_{i=1}^{20}N_iu_i,\quad v=\sum_{i=1}^{20}N_iv_i,$$

$$w=\sum_{i=1}^{20}N_iw_i,\quad p=\sum_{k=1}^{8}M_kp_k \tag{11}$$

where the interpolants "M_k" appearing in the pressure expressions are the linear shape functions associated with the finite element corner nodes (Zienkiewwicz, 1971).

The error functions produced by the unperturbed flow governing equations as a result of the interpolation expressions above, are then made orthogonal to a special set of weight functions W_i throughout the finite element. In constructing these functions, the so-called error consistency criterion of Hood and Taylor (1974) is implemented, whereby the element linear shape functions, M_i, are used in conjunction with the continuity equation. The weight functions used with the momentum equations, on the other hand, are of the upwind form (Baskharone and Hensel, 1991) when applied to the convection terms, and are identical to the element quadratic shape functions "N_i" for all other terms.

The orthogonality conditions stated above constitute the elemental set of finite element equations, which can be written as follows:

$$[a_1]\{u\}+[a_2]\{v\}+[a_3]\{w\}+[a_4]\{p\}=\{b_1\} \tag{12}$$

$$[a_5]\{u\}+[a_6]\{v\}+[a_7]\{w\}+[a_8]\{p\}=\{b_2\} \tag{13}$$

$$[a_9]\{u\}+[a_{10}]\{v\}+[a_{11}]\{w\}+[a_{12}]\{p\}=\{b_3\} \tag{14}$$

$$[a_{13}]\{u\}+[a_{14}]\{v\}+[a_{15}]\{w\}=0 \tag{15}$$

where:

$$a_1)_{i,j}=\int_{V^{(e)}}\{\hat{\nu}_e[\mathbf{F}(N_i)\mathbf{F}(N_j)+\mathbf{G}(N_i)\mathbf{G}(N_j)+\mathbf{H}(N_i)\mathbf{H}(N_j)]$$
$$-N_i[\mathbf{G}(\hat{\nu}_t)\mathbf{G}(N_j)+\mathbf{H}(\hat{\nu}_t)\mathbf{H}(N_j)+2\mathbf{F}(\hat{\nu}_t)\mathbf{F}(N_j)]$$
$$+W_i[\hat{u}\mathbf{F}(N_j)+\hat{v}\mathbf{G}(N_j)+\hat{w}\mathbf{H}(N_j)]\}dV$$

$$a_2)_{i,j}=\int_{V^{(e)}}-N_i[\mathbf{G}(\hat{\nu}_t)\mathbf{F}(N_j)-2\Omega N_j]dV$$

$$a_3)_{i,j}=\int_{V^{(e)}}-N_i\mathbf{H}(\hat{\nu}_t)\mathbf{F}(N_j)dV$$

$$a_4)_{i,k}=\int_{V^{(e)}}\frac{1}{\rho}N_i\mathbf{F}(M_k)dV$$

$$a_5)_{i,j}=\int_{V^{(e)}}-N_i[\mathbf{F}(\hat{\nu}_t)\mathbf{G}(N_j)+2\Omega N_j]dV$$

$$a_6)_{i,j}=\int_{V^{(e)}}\{\hat{\nu}_e[\mathbf{F}(N_i)\mathbf{F}(N_j)+\mathbf{G}(N_i)\mathbf{G}(N_j)+\mathbf{H}(N_i)\mathbf{H}(N_j)]$$
$$-N_i[\mathbf{F}(\hat{\nu}_t)\mathbf{F}(N_j)+\mathbf{H}(\hat{\nu}_t)\mathbf{H}(N_j)+2\mathbf{G}(\hat{\nu}_t)\mathbf{G}(N_j)]$$
$$+W_i[\hat{u}\mathbf{F}(N_j)+\hat{v}\mathbf{G}(N_j)+\hat{w}\mathbf{H}(N_j)]\}dV$$

$$a_7)_{i,j}=\int_{V^{(e)}}-N_i\mathbf{H}(\hat{\nu}_t)\mathbf{G}(N_j)dV$$

$$a_8)_{i,k}=\int_{V^{(e)}}\frac{1}{\rho}N_i\mathbf{G}(M_k)dV$$

$$a_9)_{i,j}=\int_{V^{(e)}}-N_i\mathbf{F}(\hat{\nu}_t)\mathbf{H}(N_j)dV$$

$$a_{10})_{i,j}=\int_{V^{(e)}}-N_i\mathbf{G}(\hat{\nu}_t)\mathbf{H}(N_j)dV$$

$$a_{11})_{i,j}=\int_{V^{(e)}}\{\hat{\nu}_e[\mathbf{F}(N_i)\mathbf{F}(N_j)+\mathbf{G}(N_i)\mathbf{G}(N_j)+\mathbf{H}(N_i)\mathbf{H}(N_j)]$$
$$-N_i[\mathbf{F}(\hat{\nu}_t)\mathbf{F}(N_j)+\mathbf{G}(\hat{\nu}_t)\mathbf{G}(N_j)+2\mathbf{H}(\hat{\nu}_t)\mathbf{H}(N_j)]$$
$$+W_i[\hat{u}\mathbf{F}(N_j)+\hat{v}\mathbf{G}(N_j)+\hat{w}\mathbf{H}(N_j)]\}dV$$

$$a_{12})_{i,k}=\int_{V^{(e)}}\frac{1}{\rho}N_i\mathbf{H}(M_k)dV$$

$$a_{13})_{k,j}=\int_{V^{(e)}}M_k\mathbf{F}(N_j)dV$$

$$a_{14})_{k,j}=\int_{V^{(e)}}M_k\mathbf{G}(N_j)dV$$

$$a_{15})_{k,j}=\int_{V^{(e)}}M_k\mathbf{H}(N_j)dV$$

$$b_1)_i=\int_{S^{(e)}}\hat{\nu}_eN_i(\mathbf{n}\cdot\nabla u)dS+\Omega^2\int_{V^{(e)}}N_i\left(\sum_{l=1}^{20}N_lx_l\right)dV$$

$$b_2)_i=\int_{S^{(e)}}\hat{\nu}_eN_i(\mathbf{n}\cdot\nabla v)dS+\Omega^2\int_{V^{(e)}}N_i\left(\sum_{l=1}^{20}N_ly_l\right)dV$$

$$b_3)_i=\int_{S^{(e)}}\hat{\nu}_eN_i(\mathbf{n}\cdot\nabla w)dS$$

where (e) refers to a typical finite element, $i=1,2,\ldots,20$, $j=1,2,\ldots,20$, $k=1,2,\ldots,8$, the superscript $(\hat{})$ refers to a value that is known from a previous iteration or an initial guess, dS is the differential element of surface area and $\mathbf{n}$ is the local unit vector normal to the boundary (Fig. 4). Also, the volume differential dV and the operators $\mathbf{F}$, $\mathbf{G}$, and $\mathbf{H}$ are defined as follows:

$$dV=|J|d\zeta d\eta d\xi$$

$$\mathbf{F}=T_{11}\frac{\partial}{\partial\zeta}+T_{12}\frac{\partial}{\partial\eta}+T_{13}\frac{\partial}{\partial\xi} \tag{16}$$

$$\mathbf{G} = T_{21}\frac{\partial}{\partial\zeta} + T_{22}\frac{\partial}{\partial\eta} + T_{23}\frac{\partial}{\partial\xi} \tag{17}$$

$$\mathbf{H} = T_{31}\frac{\partial}{\partial\zeta} + T_{32}\frac{\partial}{\partial\eta} + T_{33}\frac{\partial}{\partial\xi} \tag{18}$$

It should be pointed out that expanding the finite element equations in terms of the operators **F**, **G**, and **H**, defined above, is consistent with, and indeed simplifies, the procedure leading to the perturbed version of the flow equations, as will be seen later in this section.

Equations (12) through (15) can be rewritten in the following compact form:

$$[a]\{\phi\} = \{b\} \tag{19}$$

where the vector $\{\phi\}$ contains the nodal values of velocity components and static pressure that are associated with the typical element "e." The global form of the elemental set of Eqs. (19) is obtained by assembling all finite element contributions, and introducing the various boundary conditions, at which point the equations are expressible in the following form:

$$[A]\{\Phi\} = \{B\} \tag{20}$$

Perturbation Model. Referring to Eqs. (3) and (4), determination of the rotordynamic coefficients reduces to the fundamental problem of computing the rate (with respect to the virtual eccentricity "ϵ") at which the fluid forces are exerted on a cylindrically-whirling rotor. This objective is achieved through the perturbation analysis outlined next.

The current model is centered around the manner in which the finite-element Eqs. (20) are altered as a result of the rotor virtual eccentricity "ϵ" (Fig. 5). Under such eccentricity, each finite element will yield a perturbed set of equations. The assembled form of these equations can generally be written as follows:

$$([A] + \epsilon[\bar{A}])(\{\Phi\} + \{\delta\Phi\}) = (\{B\} + \epsilon\{\bar{B}\}) \tag{21}$$

where $\{\Phi\}$ is the global vector containing the nodal values of the velocity components and pressure. Combination of Eqs. (20) and (21) gives rise to the following:

$$\frac{\partial\{\Phi\}}{\partial\epsilon} = \lim_{\epsilon\to 0}\left\{\frac{\delta\Phi}{\epsilon}\right\} = [A]^{-1}(\{\bar{B}\} - [\bar{A}]\{\Phi\}) \tag{22}$$

Equation (22) reveals that the differential changes by which the flow variables, namely the velocity components and pressure, vary as a result of the rotor eccentricity can be achieved knowing the undisturbed flow solution vector $\{\Phi\}$ which is known at this point, a matrix $[\bar{A}]$ and a vector $\{\bar{B}\}$ with the latter two arrays representing, respectively, the effect of distorting the finite elements, and the changes in the flow kinematics as a result of the whirling motion of the coordinate axes (Fig. 3(a)). The arrays $[\bar{A}]$ and $\{\bar{B}\}$ are derived next as part of the procedure to compute the rotordynamic coefficients.

Consider a distorted finite element in the clearance gap corresponding to the eccentric-rotor operation mode (Fig. 5). To an observer in the whirling frame of reference, the typical node "i" of this element will now be displaced by an amount that is a function of the rotor virtual eccentricity "ϵ" and the node original location in the cross-flow plane. Referred to the displaced axes position in Fig. 5(b), the new nodal coordinates $\mathbf{x}_i$, $\mathbf{y}_i$, and $\mathbf{z}_i$ can be related to those prior to the rotor eccentricity as follows:

$$\mathbf{x}_i = x_i, \quad \mathbf{y}_i = y_i + \lambda_i\epsilon \quad \text{and} \quad \mathbf{z}_i = z_i$$

where λ_i is a fraction that varies from zero, for nodes on the rotor surface, to -1.0 for those on the housing surface, since the housing, to an observer in the whirling frame of reference, is the surface that undergoes the virtual displacement (note the positive direction of the y-axis in Fig. 4). The local-to-cartesian transformation Jacobian $|J|$ can correspondingly be written for a distorted finite element as $|J_1|$ where:

$$|J_1| = |J| + \epsilon|\bar{J}| \tag{24}$$

in which the Jacobian $|J|$ is that of the undistorted element, and $|\bar{J}|$ is as follows:

$$|\bar{J}| = \begin{vmatrix} \sum_{i=1}^{20}\frac{\partial N_i}{\partial\zeta}x_i & \sum_{i=1}^{20}\frac{\partial N_i}{\partial\zeta}\lambda_i & \sum_{i=1}^{20}\frac{\partial N_i}{\partial\zeta}z_i \\ \sum_{i=1}^{20}\frac{\partial N_i}{\partial\eta}x_i & \sum_{i=1}^{20}\frac{\partial N_i}{\partial\eta}\lambda_i & \sum_{i=1}^{20}\frac{\partial N_i}{\partial\eta}z_i \\ \sum_{i=1}^{20}\frac{\partial N_i}{\partial\xi}x_i & \sum_{i=1}^{20}\frac{\partial N_i}{\partial\xi}\lambda_i & \sum_{i=1}^{20}\frac{\partial N_i}{\partial\xi}z_i \end{vmatrix}$$

A new spatial derivative operator, that is equivalent to that in Eq. (10), can now be derived as follows:

$$\begin{Bmatrix} \frac{\partial}{\partial x} \\ \frac{\partial}{\partial y} \\ \frac{\partial}{\partial z} \end{Bmatrix} = ([T] + \epsilon[P]) \begin{Bmatrix} \frac{\partial}{\partial\zeta} \\ \frac{\partial}{\partial\eta} \\ \frac{\partial}{\partial\xi} \end{Bmatrix} \tag{25}$$

where the matrix $[T]$ is the same as described in conjunction with Eq. (10), while the matrix $[P]$ is defined as follows:

$$P_{11} = \frac{1}{|J|}\left(\sum_{i=1}^{20}\frac{\partial N_i}{\partial\eta}\lambda_i\sum_{i=1}^{20}\frac{\partial N_i}{\partial\xi}z_i - \sum_{i=1}^{20}\frac{\partial N_i}{\partial\xi}\lambda_i\sum_{i=1}^{20}\frac{\partial N_i}{\partial\eta}z_i\right) - \frac{|\bar{J}|}{|J|^2}T_{11}$$

$$P_{12} = \frac{1}{|J|}\left(\sum_{i=1}^{20}\frac{\partial N_i}{\partial\xi}\lambda_i\sum_{i=1}^{20}\frac{\partial N_i}{\partial\zeta}z_i - \sum_{i=1}^{20}\frac{\partial N_i}{\partial\zeta}\lambda_i\sum_{i=1}^{20}\frac{\partial N_i}{\partial\xi}z_i\right) - \frac{|\bar{J}|}{|J|^2}T_{12}$$

$$P_{13} = \frac{1}{|J|}\left(\sum_{i=1}^{20}\frac{\partial N_i}{\partial\zeta}\lambda_i\sum_{i=1}^{20}\frac{\partial N_i}{\partial\eta}z_i - \sum_{i=1}^{20}\frac{\partial N_i}{\partial\eta}\lambda_i\sum_{i=1}^{20}\frac{\partial N_i}{\partial\zeta}z_i\right) - \frac{|\bar{J}|}{|J|^2}T_{13}$$

$$P_{21} = -\frac{|\bar{J}|}{|J|^2}T_{21}$$

$$P_{22} = -\frac{|\bar{J}|}{|J|^2}T_{22}$$

$$P_{23} = -\frac{|\bar{J}|}{|J|^2}T_{23}$$

$$P_{31} = \frac{1}{|J|}\left(\sum_{i=1}^{20}\frac{\partial N_i}{\partial\eta}x_i\sum_{i=1}^{20}\frac{\partial N_i}{\partial\xi}\lambda_i - \sum_{i=1}^{20}\frac{\partial N_i}{\partial\xi}x_i\sum_{i=1}^{20}\frac{\partial N_i}{\partial\eta}\lambda_i\right) - \frac{|\bar{J}|}{|J|^2}T_{31}$$

$$P_{32} = \frac{1}{|J|}\left(\sum_{i=1}^{20}\frac{\partial N_i}{\partial\xi}x_i\sum_{i=1}^{20}\frac{\partial N_i}{\partial\zeta}\lambda_i - \sum_{i=1}^{20}\frac{\partial N_i}{\partial\zeta}x_i\sum_{i=1}^{20}\frac{\partial N_i}{\partial\xi}\lambda_i\right) - \frac{|\bar{J}|}{|J|^2}T_{32}$$

$$P_{33} = \frac{1}{|J|}\left(\sum_{i=1}^{20}\frac{\partial N_i}{\partial\zeta}x_i\sum_{i=1}^{20}\frac{\partial N_i}{\partial\eta}\lambda_i - \sum_{i=1}^{20}\frac{\partial N_i}{\partial\eta}x_i\sum_{i=1}^{20}\frac{\partial N_i}{\partial\zeta}\lambda_i\right) - \frac{|\bar{J}|}{|J|^2}T_{33}$$

Using the Jacobian of coordinate transformation and operator of spatial derivatives for the distorted element (Eqs. (24) and (25), respectively) as well as the general interpolation expressions (11), in the flow-governing Eqs. (5 through 8), and reapplying the weighted-residual procedure, the distorted element equations can be written (upon separation of terms containing "ϵ" and ignoring high order terms) as follows:

$$([a]+\epsilon[\bar{a}])(\{\phi\}+\{\delta\phi\})=(\{b\}+\epsilon\{\bar{b}\}) \tag{26}$$

where the matrix $\{\bar{a}\}$ and the vector $\{\bar{b}\}$ are produced by the distortion in the finite element shape, while the non-zero entries of the vector $\{\bar{b}\}$ are associated with some distortion-related entries which are explained later in this section. The vector $\{\bar{b}\}$ also contains the effect of an additional acceleration component that is created by the motion of the coordinate axes origin around the housing centerline. The vector $\{\delta\phi\}$ in Eq. (26) contains the differential changes in the nodal values of velocity components and pressure that are created by the virtual eccentricity.

Noting that the matrix $[\bar{a}]$ is similar, in construction, to $[a]$ in Eq. (19), the earlier can consistently be viewed as composed of submatrices $[\bar{a}_1]$ through $[\bar{a}_{15}]$, which correspond to those in Eqs. (12) through (15), and are defined as follows:

$$\begin{aligned}\bar{a}_1)_{i,j}=a_1^*)_{i,j}+\int_{V^{(e)}}\{&\hat{\nu}_e[\mathbf{F}(N_i)\mathbf{I}(N_j)\\&+\mathbf{I}(N_i)\mathbf{F}(N_j)+\mathbf{G}(N_i)\mathbf{J}(N_j)\\&+\mathbf{J}(N_i)\mathbf{G}(N_j)+\mathbf{H}(N_i)\mathbf{K}(N_j)+\mathbf{K}(N_i)\mathbf{H}(N_j)]-N_i[\mathbf{G}(\hat{\nu}_t)\mathbf{J}(N_j)\\&+\mathbf{J}(\hat{\nu}_t)\mathbf{G}(N_j)+\mathbf{H}(\hat{\nu}_t)\mathbf{K}(N_j)+\mathbf{K}(\hat{\nu}_t)\mathbf{H}(N_j)\\&+2\mathbf{F}(\hat{\nu}_t)\mathbf{I}(N_j)+2\mathbf{I}(\hat{\nu}_t)\mathbf{F}(N_j)]+W_i[\hat{u}\mathbf{I}(N_j)\\&+\hat{v}\mathbf{J}(N_j)+\hat{w}\mathbf{K}(N_j)]\}dV\end{aligned}$$

$$\bar{a}_2)_{i,j}=a_2^*)_{i,j}-\int_{V^{(e)}}N_i[\mathbf{G}(\hat{\nu}_t)\mathbf{I}(N_j)+\mathbf{J}(\hat{\nu}_t)\mathbf{F}(N_j)]dV$$

$$\bar{a}_3)_{i,j}=a_3^*)_{i,j}-\int_{V^{(e)}}N_i[\mathbf{H}(\hat{\nu}_t)\mathbf{I}(N_j)+\mathbf{K}(\hat{\nu}_t)\mathbf{F}(N_j)]dV$$

$$\bar{a}_4)_{i,k}=a_4^*)_{i,k}+\int_{V^{(e)}}\frac{1}{\rho}N_i\mathbf{I}(M_k)dV$$

$$\bar{a}_5)_{i,j}=a_5^*)_{i,j}-\int_{V^{(e)}}N_i[\mathbf{F}(\hat{\nu}_t)\mathbf{J}(N_j)+\mathbf{I}(\hat{\nu}_t)\mathbf{G}(N_j)]dV$$

$$\begin{aligned}\bar{a}_6)_{i,j}=a_6^*)_{i,j}+\int_{V^{(e)}}\{&\hat{\nu}_e[\mathbf{F}(N_i)\mathbf{I}(N_j)\\&+\mathbf{I}(N_i)\mathbf{F}(N_j)+\mathbf{G}(N_i)\mathbf{J}(N_j)\\&+\mathbf{J}(N_i)\mathbf{G}(N_j)+\mathbf{H}(N_i)\mathbf{K}(N_j)+\mathbf{K}(N_i)\mathbf{H}(N_j)]-N_i[\mathbf{F}(\hat{\nu}_t)\mathbf{I}(N_j)\\&+\mathbf{I}(\hat{\nu}_t)\mathbf{F}(N_j)+\mathbf{H}(\hat{\nu}_t)\mathbf{K}(N_j)+\mathbf{K}(\hat{\nu}_t)\mathbf{H}(N_j)\\&+2\mathbf{G}(\hat{\nu}_t)\mathbf{J}(N_j)+2\mathbf{J}(\hat{\nu}_t)\mathbf{G}(N_j)]+W_i[\hat{u}\mathbf{I}(N_j)\\&+\hat{v}\mathbf{J}(N_j)+\hat{w}\mathbf{K}(N_j)]\}dV\end{aligned}$$

$$\bar{a}_7)_{i,j}=a_7^*)_{i,j}-\int_{V^{(e)}}N_i[\mathbf{H}(\hat{\nu}_t)\mathbf{J}(N_j)+\mathbf{K}(\hat{\nu}_t)\mathbf{G}(N_j)]dV$$

$$\bar{a}_8)_{i,k}=a_8^*)_{i,k}-\int_{V^{(e)}}\frac{1}{\rho}N_i\mathbf{J}(M_k)dV$$

$$\bar{a}_9)_{i,j}=a_9^*)_{i,j}-\int_{V^{(e)}}N_i[\mathbf{F}(\hat{\nu}_t)\mathbf{K}(N_j)+\mathbf{I}(\hat{\nu}_t)\mathbf{H}(N_j)]dV$$

$$\bar{a}_{10})_{i,j}=a_{10}^*)_{i,j}-\int_{V^{(e)}}N_i[\mathbf{G}(\hat{\nu}_t)\mathbf{K}(N_j)+\mathbf{J}(\hat{\nu}_t)\mathbf{H}(N_j)]dV$$

$$\begin{aligned}\bar{a}_{11})_{i,j}=a_{11}^*)_{i,j}+\int_{V^{(e)}}\{&\hat{\nu}_e[\mathbf{F}(N_i)\mathbf{I}(N_j)\\&+\mathbf{I}(N_i)\mathbf{F}(N_j)+\mathbf{G}(N_i)\mathbf{J}(N_j)\\&+\mathbf{J}(N_i)\mathbf{G}(N_j)+\mathbf{H}(N_i)\mathbf{K}(N_j)+\mathbf{K}(N_i)\mathbf{H}(N_j)]-N_i[\mathbf{F}(\hat{\nu}_t)\mathbf{I}(N_j)\\&+\mathbf{I}(\hat{\nu}_t)\mathbf{F}(N_j)+\mathbf{G}(\hat{\nu}_t)\mathbf{J}(N_j)+\mathbf{J}(\hat{\nu}_t)\mathbf{G}(N_j)\\&+2\mathbf{H}(\hat{\nu}_t)\mathbf{K}(N_j)+2\mathbf{K}(\hat{\nu}_t)\mathbf{H}(N_j)]+W_i[\hat{u}\mathbf{I}(N_j)\\&+\hat{v}\mathbf{J}(N_j)+\hat{w}\mathbf{K}(N_j)]\}dV\end{aligned}$$

$$\bar{a}_{12})_{i,k}=a_{12}^*)_{i,k}+\int_{V^{(e)}}\frac{1}{\rho}N_i\mathbf{K}(M_k)dV$$

$$\bar{a}_{13})_{k,j}=a_{13}^*)_{k,j}+\int_{V^{(e)}}M_k\mathbf{I}(N_j)dV$$

$$\bar{a}_{14})_{k,j}=a_{14}^*)_{k,j}+\int_{V^{(e)}}M_k\mathbf{J}(N_j)dV$$

$$\bar{a}_{15})_{k,j}=a_{15}^*)_{k,j}+\int_{V^{(e)}}M_k\mathbf{K}(N_j)dV$$

where

$$dV=|J|d\zeta d\eta d\xi$$

In the these expressions, a matrix entry with an asterisk has the same form as that in Eqs. (12) through (15), with the exception that the Jacobian $|J|$ is now replaced by $|\bar{J}|$ as defined in conjunction with Eq. (24). The vector $\{\bar{b}\}$ in Eq. (26) can similarly be defined by the subvectors $\{\bar{b}_1\}$ and $\{\bar{b}_2\}$, as in Eqs. (12) through (15), as follows:

$$\bar{b}_1)_i=\Omega^2\int_{V^{(e)}}N_i\left(\sum_{l=1}^{20}N_lx_l\right)|\bar{J}|d\zeta d\eta d\xi$$

$$\bar{b}_2)_i=\Omega^2\int_{V^{(e)}}N_i\left(\sum_{l=1}^{20}N_ly_l\right)|\bar{J}|d\zeta d\eta d\xi$$

$$-\Omega^2\int_{V^{(e)}}N_i\left(\sum_{l=1}^{20}N_i\lambda_l\right)dV+\Omega^2\int_{V^{(e)}}N_idV$$

$$\bar{b}_3)_i=0$$

where i and j vary from 1 to 20, while k varies from 1 to 8. With the operator **F**, **G**, and **H** being those defined by Eqs. (16) through (18), the new operators **I**, **J**, and **K** are defined as follows:

$$\mathbf{I}=P_{11}\frac{\partial}{\partial\zeta}+P_{12}\frac{\partial}{\partial\eta}+P_{13}\frac{\partial}{\partial\xi} \tag{27}$$

$$\mathbf{J}=P_{21}\frac{\partial}{\partial\zeta}+P_{22}\frac{\partial}{\partial\eta}+P_{23}\frac{\partial}{\partial\xi} \tag{28}$$

$$\mathbf{K}=P_{31}\frac{\partial}{\partial\zeta}+P_{32}\frac{\partial}{\partial\eta}+P_{33}\frac{\partial}{\partial\xi} \tag{29}$$

The matrix $[P]$ is the same as defined in conjunction with Eq. (25). Of particular interest here is the construction of $\bar{b}_1)_i$, $\bar{b}_2)_i$ and $\bar{b}_3)_i$ above, as compared to that of $b_1)_i$, $b_2)_i$ and $b_3)_i$ in Eqs. (12) through (14). First, it is noted that the perturbations of the surface integrals in $b_1)_i$ and $b_2)_i$ are nonexisting in $\bar{b}_1$ and $\bar{b}_2$ since these surface integrals would have nonzero values only in the case where a nonzero normal derivative of, respectively, "u" or "v" is prescribed as a boundary condition, a situation which is not encountered in formulating the undisturbed-flow problem. Secondly, it is due to the centripetal acceleration of the rotating axes origin around the housing centerline that the last term in the $\bar{b}_2)_i$ is produced, while the other terms, in $b_1)_i$ and $b_2)_i$, result from infinitesimally-small distortions in the finite element shape as a result of the rotor eccentricity.

Calculation of the Rotordynamic Coefficients. Equation (22) can be rewritten in the following detailed form:

$$\frac{\partial\{\Phi\}}{\partial\epsilon}\equiv\frac{\partial}{\partial\epsilon}\begin{Bmatrix}\{U\}\\\{V\}\\\{W\}\\\{P\}\end{Bmatrix}=[A]^{-1}(\{\overline{B}\}-[\overline{A}]\{\Phi\}) \tag{30}$$

where $\{U\}$, $\{V\}$, $\{W\}$, and $\{P\}$ are vectors containing the nodal values of the velocity components and static pressure, respectively, with the overbars signifying quantities that are associated with the perturbation in the rotor-to-housing flow field. Of all the pressure nodal values in the vector $\{P\}$ above, define a subvector $\{\mathcal{P}\}$ as composed of the pressure values at the rotor surface nodes, i.e.,

$$\{\mathcal{P}\}=\{p_i, i=1,N_s\}\subset\{P\} \tag{31}$$

where N_s is the total number of corner nodes existing on the rotor surface. It is true, in this case, that $\left\{\frac{\partial\mathcal{P}}{\partial\epsilon}\right\}=\left\{\left(\frac{\partial p}{\partial\epsilon}\right)_i, i=1, N_s\right\}$ is but a subvector of the already computed global vector $\left\{\frac{\partial\Phi}{\partial\epsilon}\right\}$ in Eq. (30) and is, therefore, known as this computational step.

Next, consider the finite element face "s" in Fig. 6 which exists on the rotor surface in its displaced position. The pressure derivative $p^{(s)}_{,\epsilon}$ over this surface element can now be interpolated in terms of the known pressure derivatives at the four corner nodes of "s" as follows:

$$p^{(s)}_{,\epsilon}=\sum_{i=1}^{4}M_i(1,\eta,\xi)\left(\frac{\partial p}{\partial\epsilon}\right)_i \tag{32}$$

Summation of $p^{(s)}_{,\epsilon}$, as contributed by all finite elements sharing faces with the rotor, over the entire rotor surface yields the rate (with respect to "ϵ") at which the fluid force is exerted on the rotor. This can be resolved in the "x" and "y" directions to produce the derivatives $\frac{\partial F_x}{\partial\epsilon}$ and $\frac{\partial F_y}{\partial\epsilon}$ as follows:

$$\frac{\partial F_x}{\partial\epsilon}=\sum_{i=1}^{N_s}\int_{-1}^{+1}\int_{-1}^{+1}n_x(\eta,\xi)p_{,\epsilon}(\eta,\xi)G(\eta,\xi)d\eta d\xi \tag{33}$$

$$\frac{\partial F_y}{\partial\epsilon}=\sum_{i=1}^{N_s}\int_{-1}^{+1}\int_{-1}^{+1}n_y(\eta,\xi)p_{,\epsilon}(\eta,\xi)G(\eta,\xi)d\eta d\xi \tag{34}$$

where n_x and n_y are the components of the local unit vector that is normal to the rotor surface (Fig. 6). Also, the parameter $G(\eta, \xi)$ is a Jacobian-like function for cartesian-to-local area transformation, and was previously derived by Baskharone (1979) as follows:

$$G(\eta,\xi)=\left[\left(\frac{\partial y}{\partial\eta}\frac{\partial z}{\partial\xi}-\frac{\partial y}{\partial\xi}\frac{\partial z}{\partial\eta}\right)^2+\left(\frac{\partial x}{\partial\xi}\frac{\partial z}{\partial\eta}-\frac{\partial x}{\partial\eta}\frac{\partial z}{\partial\xi}\right)^2+\left(\frac{\partial x}{\partial\eta}\frac{\partial y}{\partial\xi}-\frac{\partial x}{\partial\xi}\frac{\partial y}{\partial\eta}\right)^2\right]^{1/2}$$

where the derivatives on the right-hand side are evaluated using the interpolation expressions (9) for a "ζ" value of 1.0 (Fig. 6). Having computed the force derivatives (Eqs. (33) and (34) above), the requirements for computing the force coefficients (K, k, C, c, M, m) are, by reference to Eqs. (3) and (4), complete.

Concluding Remarks

The virtually deformable finite element concept introduced in this paper offers a new and powerful tool with which the fluid/structure interaction effects can be captured. Versatility of the computational model was illustrated through two typical problem categories where a cylindrically whirling rotor was analyzed. In this, and all similar disturbance modes, the object of the perturbation analysis is the finite-element equivalent of the flow governing equations in the rotor-to-housing gap.

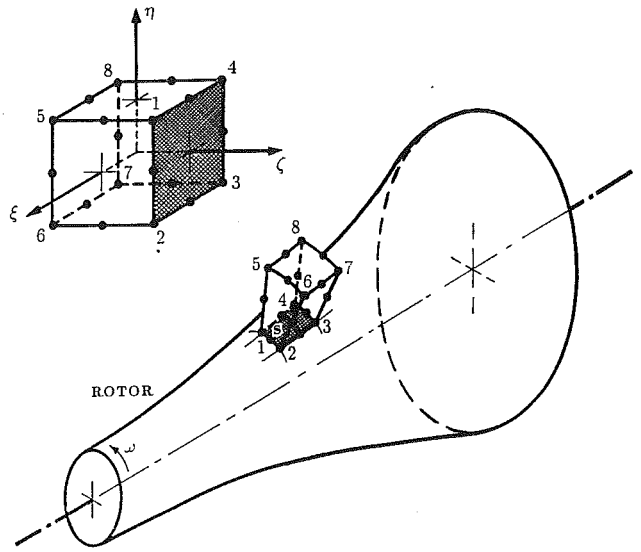

Fig. 6 Pressure integration segment over the surface of a generally shaped rotor

Sample results of the current analysis are contained in a companion paper (Baskharone and Hensel, 1991). Under focus in this paper is the rotordynamic coefficient of an annular seal under a cylindrical type of rotor whirl. It is undoubtedly clear, at this point, that tilting-related, or simply moment, coefficients of a conically-whirling rotor would equally be calculable using the virtual finite-element distortion concept developed in the current study. Utilization of the concept in this case would lead to the differential changes in the fluid forces along the rotor axis which, in turn, exert differential moments around two perpendicular axes at the center of the tilting motion. The moment coefficients are eventually computed by integrating these moments along the axis and relating the outcome to the rotor angular displacement and its time derivatives. It is further emphasized that the same concept is potentially applicable to other modes of fluid-induced vibrations. An example of these modes is the axial oscillation of the impeller-shroud assembly of the centrifugal pump to which reference was made in this paper. The oscillatory motion is, in this case, caused by the fluid forces on the front (or shroud) side of the impeller as well as the back face of the impeller disk. An equally detailed computational model that is capable of analyzing such vibration modes is currently non-existing in the open literature.

Acknowledgment

This study was funded by NASA-Marshall Space Flight Center (Huntsville, Alabama), contract no. NAS8-37821, NASA monitor: James Cannon. Partial funding was also provided by the Houston Advanced Rsearch Center (The Woodlands, Texas), grant no. 88-025.

References

Baldwin, B. S., and Lomax, H., 1978, "Thin Layer Approximation and Algebraic Model for Separated Turbulent Flow," AIAA Paper No. 78-257.

Baskharone, E., 1979, "A New Approach in Turbomachinery Flow Analysis Using the Finite Element Method," Ph.D. dissertation, University of Cincinnati.

Baskharone, E. A., and Hensel, S. J., 1989, "A New Model for Leakage Prediction in Shrouded-Impeller Turbopumps," ASME JOURNAL OF FLUIDS ENGINEERING, Vol. 111, pp. 118–123.

Baskharone, E. A., and Hensel, S. J., 1991, "A Finite-Element Perturbation

Approach to Fluid/Rotor Interaction in Turbomachinery Elements. Part 2: Application," ASME JOURNAL OF FLUIDS ENGINEERING, published in this issue, pp. 362-367.

Benim, A. C., and Zinser, W., 1985, "Investigation into the Finite Element Analysis of Confined Turbulent Flow Using a k-ϵ Model of Turbulence," *Computer Methods in Applied Mechanics and Engineering*, Vol. 51, pp. 507-523.

Carey, G. F., and Oden, J. T., 1986, "Finite Elements: Fluid Mechanics," *The Texas Finite Element Series*, Vol. IV, Prentice-Hall.

Childs, D. W., 1983, "Finite Length Solutions for Rotordynamic Coefficients of Turbulent Annular Seals," ASME *Journal of Lubrication Technology*, Vol. 105, pp. 437-445.

Childs, D. W., 1989, "Fluid-Structure Interaction Forces at Pump-Impeller-Shroud Surfaces for Rotordynamic Calculations," ASME *Journal of Vibration, Stress and Reliability in Design*, Vol. 111, pp. 216-225.

Childs, D., and Kim, C. H., 1985, "Analysis and Testing for Rotordynamic Coefficients of Turbulent Annular Seals with Different Homogeneous Surface Roughness Treatment for Rotor and Stator Elements," ASME *Journal of Tribology*, Vol. 107, pp. 296-306.

Dietzen, F. J., and Nordmann, R., 1987, "Calculating Rotordynamic Coefficients of Seals by Finite Difference Techniques," ASME *Journal of Tribology*, Vol. 109, pp. 388-394.

Dietzen, F. J., and Nordmann, R., 1988, "A 3-Dimensional Finite-Difference Method for Calculating the Dynamic Coefficients of Seals," Presented at the Workshop on Rotordynamic Instability in High Performance Turbomachinery, Texas A&M University.

Hensel, S. J., 1986, "Rotordynamic Forces on Labyrinth Seals," M.S. thesis, Texas A&M University.

Hensel, S. J., 1990, "A New Method for Determining Rotordynamic Forces on Liquid Annular Seals," Ph.D. dissertation, Texas A&M University.

Hood, P., and Taylor, C., 1974, "Navier-Stokes Equations Using Mixed Interpolation," *Proceedings of the International Symposium on Finite Element Methods in Flow Problems*, University of Wales, Swansea, United Kingdom.

Nelson, C. C., 1985, "Rotordynamic Coefficients for Compressible Flow in Tapered Annular Seals," ASME *Journal of Tribology*, Vol. 107, pp. 318-325.

Zienkiewicz, O. C., 1971, *The Finite Element Method in Engineering Science*, McGraw-Hill.

A Finite-Element Perturbation Approach to Fluid/Rotor Interaction in Turbomachinery Elements. Part 2: Application

E. A. Baskharone
Associate Professor.
Mem. ASME

S. J. Hensel[1]
Mem. ASME

Department of Mechanical Engineering,
Texas A&M University,
College Station, Texas 77843

A newly devised perturbation model for the fluid-induced vibration of turbomachinery rotating elements is used to compute the rotordynamic coefficients of an annular seal. First, the finite element-based solution of the flow field in the centered-rotor operation mode is verified and its grid dependency tested for different seal configurations. The rotordynamic behavior of a hydraulic seal with a clearance gap depth/length ratio of 0.01, as a representative case, is then analyzed under a cylindrical type of rotor whirl and several running speeds. The direct and cross-coupled rotordynamic coefficients dictating the rotor instability mechanism in this case are compared to experimental and analytical data, and the outcome is favorable. The numerical results are also used to discuss the validity of a common assumption in existing computational models in regard to the circumferential distribution of the perturbed flow variables in the eccentric rotor operation mode.

Introduction

Fluid-induced vibration of turbomachinery rotating components is often a result of today's high performance demands. These, among others, include excessively tight clearances, high speeds, and highly loaded blades in the primary-flow passages. While these design trends intendingly maximize the overall efficiency, they may also lead to forced vibration of the rotating components. This potentially dangerous situation can also be the result of fluid/solid interaction mechanisms in secondary-flow passages such as seals, dampers and bearings. Of these, the problem of seal rotordynamics has been the focus of extensive research in recent years.

Although the primary function of seals is leakage control, they evidently influence the overall stability of turbomachines. While nonsmooth seals, of the grooved, labyrinth and honeycomb types (Diewald and Nordmann, 1988; Childs and Scharrer, 1987; Childs, 1988) are known to produce minimum leakage, it is not established with certainty that they provide better rotordynamic characteristics when compared to smooth untapered seals. It is established, however, that the instability in all cases are dependent upon such parameters as the clearance depth (Childs and Scharrer, 1987), the flow preswirl (Childs, 1988) and other geometry-related variables. The latter includes the taper angle, in the case of an annular seal (Nelson, 1984) and whether the seal is of the "look-through" or the stepped type (Scharrer, 1988) in the class of labyrinth seals.

Recent advances in the seal rotordynamics area have established the computational fluid dynamics tool as a strong modeling foundation. The first and foremost contribution in this field was that by Dietzen and Nordmann (1987), where a finite-difference formulation of Navier-Stokes equations was used in conjunction with a perturbation model to compute the rotordynamic coefficients of incompressible-flow annular seals (Fig. 1). The significance of that study lies in the departure it advocated from the bulk-flow model (Childs, 1983) in which details of the rotor-to-housing flow field were significantly simplified. A common assumption in the study by Dietzen and Nordmann (1987), as well as that of Childs (1983), has involved a single-harmonic sinusoidal variation of the flow properties in the tangential direction.

It is the purpose of this paper to validate a comprehensive finite element-based perturbation model which the authors have recently devised (Baskharone and Hensel, 1991). The model conceptually deviates from the traditional perturbation analyses (Dietzen and Nordmann, 1987; Childs, 1983) in that the perturbation equations emerge from the flow-governing equations in their discrete, finite-element form as opposed to the differential form in all existing models. The perturbation in the flow field, in this case, is physically perceived as a result of virtual distortions in an assembly of finite elements that is occupying the rotor-to-housing gap. The computational approach, as such, makes it potentially possible to analyze different rotor vibration modes which may not necessarily involve a uniform rotor eccentricity (which leads to a cylindrical rotor whirl), as well as imparts the versatility and adaptability of the finite-element method to this class of engineering applications.

In view of the substantial versatility of the current model,

[1]Graduate Research Assistant, currently a Senior Engineer at Westinghouse Savannah River Laboratory, Aiken, South Carolina.

Contributed by the Fluids Engineering Division for publication in the JOURNAL OF FLUIDS ENGINEERING. Manuscript received by the Fluids Engineering Division March 27, 1990.

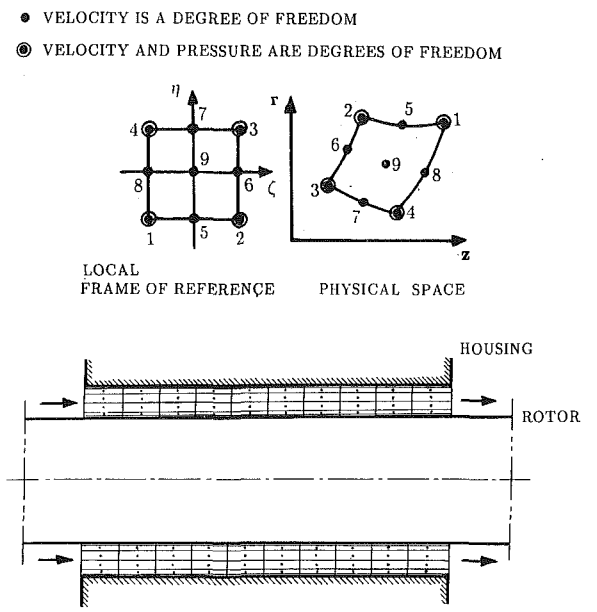

Fig. 1 Finite-element discretization model of the centered-rotor clearance gap

it may appear that cylindrically whirling rotors of annular seals do not represent a sufficiently challenging problem, owing to the extensive amount of existing data that virtually covers all aspects of this problem. However, it is precisely the availability of these data that led to selecting this sample case. As demonstrated by Baskharone and Hensel (1991), the new perturbation model offers a conceptual deviation from all existing fluid-induced vibration models. Although the originality here is indeed rotordynamics-related, it is also the application of the finite-element technique to such excessively narrow gaps with a considerable magnitude of flow turbulence and inertia domination, that is hardly verified in the literature. Since analysis of the zeroth-order and perturbed flow fields are both based on this technique, the availability of experimental data to verify the finite-element flow solution was a primary criterion in the selection process. As a result, the numerical investigation in this paper asserts, among others, the finite-element method as a reliable means of securing the narrow-gap zeroth-order flow solution, with which the perturbation analysis is initiated. The investigation, therefore, goes beyond the objective of simply validating the final outcome of the perturbation model.

Centered-Rotor Flow Field

The axisymmetric flow analysis corresponding to this rotor position provides the zeroth-order solution in the perturbation model (Baskharone and Hensel, 1991). Presented here, however, is an assessment of the stability, smoothness and accuracy aspects of the numerical solution as strongly tied to the level of nonlinearity in the flow equations, the latter being implied by the Reynolds number, and the manner in which the flow turbulence and near-wall flow structure are analyzed. One of two example cases under investigation is a hydraulic annular seal with the following dimensions and operating conditions:

Rotor radius (a) = 31.0 mm

Clearance (s) = 0.294 mm

Length (L) = 200.0 mm

Through-Flow Reynolds number ($\mathrm{R_e}$) = 10^4

Tangential Reynolds number ($\mathrm{R_{e,\omega}}$) = 2.5×10^4

where the through-flow Reynolds number is based on the inlet through-flow velocity and the tangential Reynolds number is based on the circumferential velocity of the rotor surface, with the characteristic length being the seal clearance in both cases. Experimental measurements concerning this seal configuration were reported by Yamada (1962) in the form of a seal "resistance" parameter (λ), which is defined as follows:

$$\lambda = \frac{\Delta p}{\rho V_{z_i}^2} \tag{1}$$

where:

Δp is the static pressure drop across the seal,
ρ is the fluid density,
V_{z_i} is the seal-inlet through-flow velocity.

Turbulence Closure and Near-Wall Flow Zone. An algebraic eddy viscosity model by Baldwin and Lomax (1978) is used to simulate the flow turbulent behavior. According to this model, the effective kinematic viscosity is viewed as composed of two, molecular and eddy, components as follows:

$$\nu_e = \nu_l + \nu_t \tag{2}$$

In calculating the eddy component, ν_t, the procedure assumes the presence of two, inner and outer, layers. In the inner layer, the Prandtl-van Driest formulation yields the following expression:

$$\nu_{t,i} = l^2 |\omega'| \tag{3}$$

where the subscript i refers to the inner layer. The mixing length l in expression (3) is defined as follows:

$$l = \kappa y \left[1 - \exp\left(\frac{-y^+}{A^+} \right) \right], \quad y^+ = \frac{\sqrt{\rho_w \tau_w}}{\mu_w} y$$

where:

y is the distance normal to the nearest wall
τ_w is the wall shear stress
ω' is the local vorticity

The model switches from Van Driest formulation to that of the outer region at the smallest value of y for which the inner and outer values of the eddy kinematic viscosity are equal. The formulation for the outer layer is given by:

$$\nu_{t,o} = KC_{cp} F_{\max} y_{\max} F_{KLEB} \tag{4}$$

where:

Nomenclature

a = rotor radius
b = housing radius
C, c = direct and cross-coupled damping coefficients
K, k = direct and cross-coupled stiffness coefficients
L = seal length
l = mixing length
M, m = direct and cross-coupled inertia coefficients
p = static pressure
Re = Reynolds number
s = clearance gap width
y = distance from the wall
β = grid refinement factor
λ = dimensionless seal resistance (defined in Eq. (1))
μ = viscosity coefficient
ν = kinematic viscosity coefficient
ρ = density
τ = shear stress
Ω = whirl frequency
ω = shaft running speed
ω' = vorticity

Subscripts

i = seal inlet station
R = relative flow property
r = radial component
w = value at the wall
z = axial component
θ = tangential component

$$F_{max} = y_{max} |\omega'| \left[1 - \exp\left(\frac{-y^+}{A^+} \right) \right]; \text{ and}$$

$$F_{KLEB} = \left[1 + 5.5 \left(C_{KLEB} \frac{y}{y_{max}} \right)^6 \right]^{-1}$$

with y_{max} referring to the value of y at which F_{max} occurs. The various constants in Baldwin-Lomax model are as follows:

$$A^+ = 26,\ \kappa = 0.4,\ K = 0.0168,\ C_{cp} = 1.6; \text{ and } C_{KLEB} = 0.3$$

It is important to point out that in applying this turbulence model, which was devised for two-dimensional flow applications, the vorticity and wall shear stress calculations were modified in such a way that the tangential velocity component is taken into account. This was necessary since the flow in the rotor-to-housing passage is generally that of the swirling type.

The authors experience with the foregoing turbulence closure during the course of this study has proven that, regardless of any "practical" level of mesh refinement near solid boundary segments, accurate values of the near-wall eddy viscosity were unachievable at high Reynolds numbers. The focus then was on the annular seal described above, for which the flow resistance, as measured by the static pressure drop across the seal, was persistently overestimated. Further investigation revealed that the high velocity gradients in the near-wall zone were improperly depicted. The situation was conclusively remedied by utilizing the universal law of the wall concept in computing the wall shear stress "τ_w" appearing in the expression of the dimensionless distance y^+ above.

Computation of the wall shear stress, that is associated with a typical node "i" (Fig. 2), is based on the near-wall zone treatment proposed by Benim and Zinser (1985). The assumption here is that the universal law of the wall at any wall location is extendible, across the wall element width, to the grid node "j" (Fig. 2) at this axial location. Referring to the distance of node "j" from the wall by y_{min}, the following expression for the wall shear stress is then obtained:

$$\tau_w = \begin{cases} \dfrac{\nu_l \rho V_{min}}{y_{min}} & \text{for } y^+_{min} < 11.6 \\ \dfrac{\kappa C_D^{1/4} \rho V_{min} k_{min}^{1/2}}{\ln\left(E C_D^{1/4} y_{min} \dfrac{k_{min}^{1/2}}{\nu_l} \right)} & \text{for } y^+_{min} \geq 11.6 \end{cases} \quad (5)$$

where: $k_{min} = \dfrac{\tau_w}{\rho C_D^{1/2}}$, $C_D = 0.09$, $\kappa = 0.4$, $E = 9.0$

with V_{min} referring to the magnitude of velocity, with the tangential component taken into account, at the interior node and ν_l being the molecular coefficient of kinematic viscosity. Referring to Eq. (5) above, note that the outcome of this equation in the case where $y^+_{min} \geq 11.6$ is a recursive relationship since τ_w now appears on both sides of the equation. An iterative procedure is executed, in this case, to compute τ_w. Noteworthy is also the fact that the node "j" (Fig. 2) in the Benim and Zinser model is replaced by the corner node "k" which is consistent with their choice being a four-noded bilinear finite element. In reality, however, neither one of these nodes would be sufficiently close to the wall, in view of the steep velocity gradient in this region. An alternate choice of this near-wall point was, in this case, adopted as part of the accuracy enhancement process discussed next.

Numerical implementation of the preceding turbulence closure, including the near-wall model, is achieved with the aid of an array of points that is different from the primary set of computational nodes. Figure 2 shows an enlarged segment of the computational domain near a solid wall, in which the primary nodes in the finite-element discretization model are identified by hollow circles, while the points used in the eddy viscosity computations at the typical node "i" are solid circles.

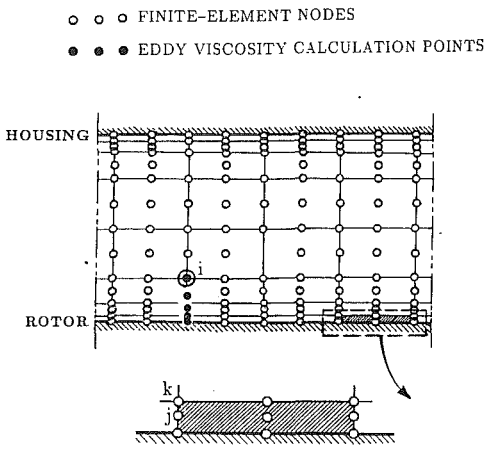

Fig. 2 Refinement of the near-wall region for accurate prediction of the eddy viscosity

The objective here was twofold; to estimate the cut-off location between the inner and outer layer with sufficient accuracy, and to capture the steep gradients of the flow variables near the solid wall. A substantial enhancement of the solution was, as a result, observed during the preliminary testing phase. This, for the major part, was due to the excellent accuracy with which the wall shear stress was computed, for it was generally possible to compute the stress at a point where the dimensionless wall coordinate (y^+) was acceptably small.

A modification to the Baldwin and Lomax turbulence closure was made in the current study to accommodate the angular motion of the rotor surface. Referring to the definition of the inner-layer kinematic eddy viscosity (Eq. (3)), and considering the case in which the layer is attached to this rotating surface, the vorticity and wall shear stress were both defined on the basis of the relative velocity ($\mathbf{V}_R$) as opposed to the absolute velocity ($\mathbf{V}$), where:

$$\mathbf{V}_R = \mathbf{V} - \omega a \mathbf{e}_\theta \quad (7)$$

where:

ω is the rotor spinning speed

a is the rotor radius

$\mathbf{e}_\theta$ is the unit vector in the positive tangential direction

In this case, the absolute vorticity (ω'_R) is expressible in terms of the absolute velocity (ω') as follows:

$$\omega'_R = \omega' - 2\omega \quad (8)$$

Calculation of the eddy viscosity in the outer layer (Eq. (4)) as pertaining to the rotating surface was consistently performed using the relative flow properties.

Introduction to the Upwinding Technique. Adoption of the conventional Galerkin's method in deriving the finite-element equivalent of the flow governing equations was, perhaps expectedly, unsuccessful. This was a result of the high Reynolds number which caused the flow field to be inertia-dominated. Surprisingly, the "wiggles" appearing in the streamwise pressure distribution in this case were not entirely eliminated even when full upwinding of the equations of motion, in the manner devised by Heinrich and Zienkiewicz (1977), was implemented. In fact, the large magnitude of false numerical diffusion that was imparted to the flow field in this case also made it practically impossible to achieve a numerical solution in the neighborhood of the experimental data. The situation was further worsened by the large aspect ratio of the rotor-to-housing gap (defined as the gap length/clearance ratio) which, in turn, produced high aspect-ratio finite elements. This had an adverse numerical effect, especially near the rotor and housing surfaces where the need for high resolution of the flow structure led to excessively narrow elements in this region.

Corrective measures included deviation from the full up-

winding strategy and optimization of the elemental aspect ratio. First, in implementing the weighted-residual method (Zienkiewicz, 1971), terms in the error functions which result from the momentum equations were weighed differently in the process of deriving the finite element equations. In this case, the weight functions proposed by Heinrich and Zienkiewicz (1977), being applicable to the current axisymmetric flow problem, were used in conjunction with only the convection terms in the momentum equations. On the other hand, the element shape functions were used with all other terms. This is consistent with the well-known practice in the area of finite-difference modeling, where backward differencing is exclusively utilized when approximating the convection terms. Optimization of the element aspect ratio, on the other hand, contributed to the smoothness of the flow variables as will be discussed in the grid dependency section of the numerical results.

Grid Dependency and Accuracy Assessment. Sensitivity of the numerical solution to the size of the finite-element discretization model, and the level of field resolution it provides, was first investigated. In all cases considered, the number of cross-flow stations between the seal inlet and exit stations was fixed at 48, while the number of grid lines between the inner and outer walls, referred to as N_r, was varied from 7 to 11. The latter family of grid lines was constructed with varying increments in the radial direction. To better quantify this variation, the growth of the increments from either wall to the mean radius was made to be of the geometric sequence type with a common ratio "β." Illustrated in Fig. 3 is the geometrical effects of varying "β" from 1.0, which yields equal increments, to a value of 1.5 for the case where N_r is fixed at 11. Note the drastic change in the width of the wall elements as a result.

Shown in Fig. 4 is a comparison between the computed seal resistance "λ," corresponding to different discretization patterns, and the experimental value of Yamada (1962). Examination of this figure reveals that the accuracy of the seal resistance, which is largely influenced by the precision of the computed eddy viscosity, is generally improved by refining the finite-element grid near the walls, be that the result of increasing "N_r" or "β." It was in view of these results, that an optimum grid with $N_r = 9$ and $\beta = 1.5$ was permanently fixed thereafter.

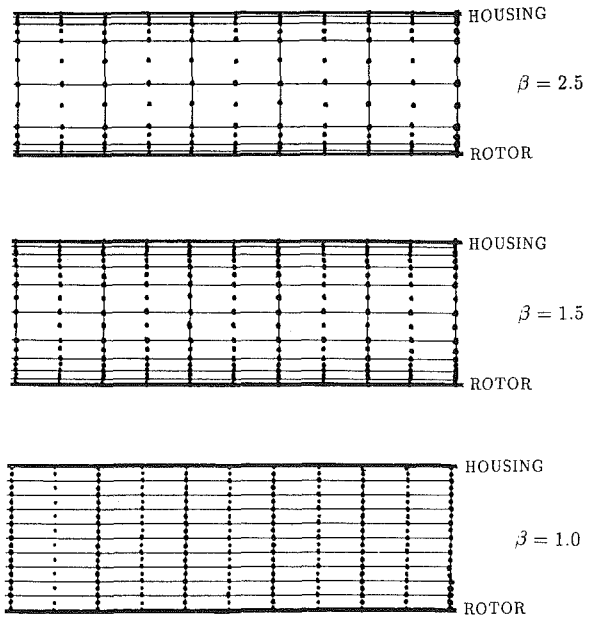

Fig. 3 Geometrical effects of varying the refinement factor (β) on the finite-element discretization model

Accuracy of the centered-rotor flow field was further investigated, with the emphasis being on the cross-flow velocity profiles through the seal. Evaluation of the finite-element solution in this case was made in light of the flow measurements of Morrison et al. (1988) for an annular seal with a gap width/length ratio of 0.034. Development of the through-flow and tangential velocity profiles along this seal were measured by Morrison et al. under a high preswirl/inlet through-flow velocity ratio of 4.2, and a Reynolds number, based on the clearance width and inlet velocity, of 13,280. Figure 5 shows the set of measured through-flow and tangential velocity profiles at non-dimensional axial length ratios of 25, 50, and 75 percent, together with the computed profiles for comparison. As seen in the figure, the computed velocities seem to depict the experimental profiles with reasonable accuracy. Note that the peak point of the through-flow velocity profiles, particularly in the computed profiles, corresponds to radii which are higher than the mean radius due to the radial shifting of the flow particles as a result of the high circumferential velocity which, in turn, is caused by the high rotational speed of the

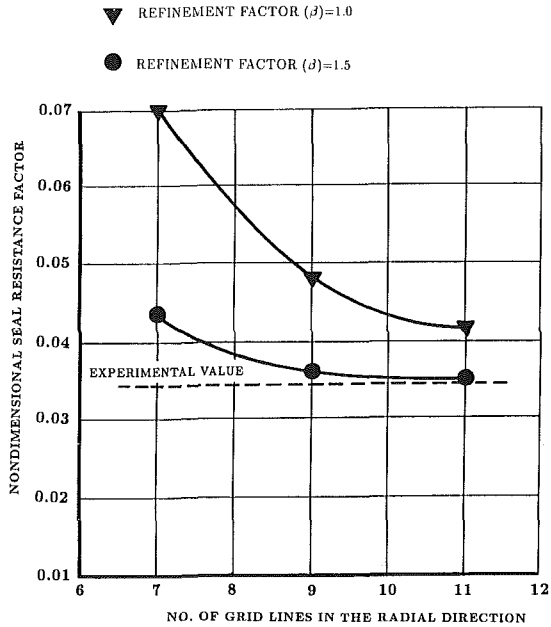

Fig. 4 Seal resistance as a function of the finite-element model size and near-wall refinement

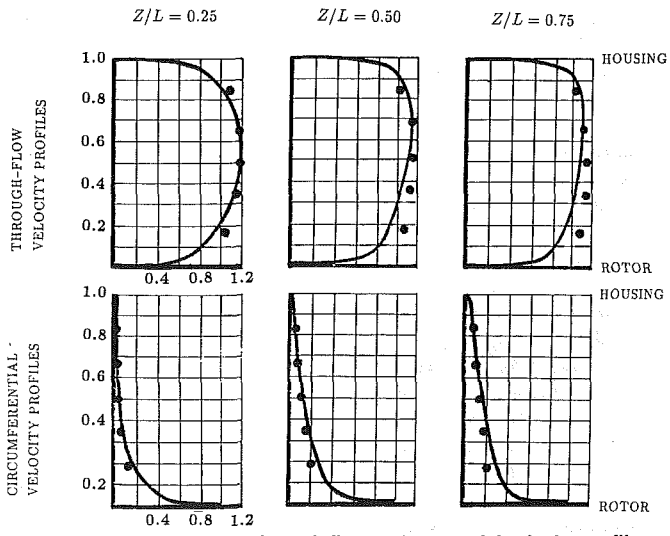

Fig. 5 Comparison of the through-flow and tangential velocity profiles at three axial locations with experimental data (experimental data in solid circles)

seal inner wall. Development of the computed tangential velocity along the seal in this figure seems to also be in close agreement with the flow measurements.

Perturbation Analysis and Rotordynamic Coefficients

The newly devised perturbation analysis (Baskharone and Hensel, 1991) was applied to a representative case of annular seal for which experimental and analytical rotordynamic data exist (Dietzen and Nordmann, 1987). Under focus here was the variation of the direct and cross-coupled stiffness, damping and inertia coefficients (K, k, C, c, M, and m) of the fluid/rotor interaction system. Of these, only the stiffness and damping coefficients were reported by Dietzen and Nordmann (1987), and are used in the present study for verification purposes. The analytical data by Dietzen and Nordmann (1987) is the outcome of a traditional finite difference-based perturbation analysis in which sinusoidal variations of the field variables around the circumference were assumed, as opposed to circumferential variations that are totally unrestricted in the current model.

Of particular interest in assessing the new perturbation model were the stability-related rotordynamic coefficients of which experimental and analytical data were reported by Dietzen and Nordmann (1987) for a typical hydraulic seal. These are the cross-coupled stiffness and direct damping coefficients "k" and "C," respectively, which dictate the fluid-exerted tangential force and, subsequently, the rotor whirl. The seal under investigation had a clearance/length ratio of 0.0085, a rotor radius of 23.5 mm, and a Reynold's number (based on the clearance and inlet through-flow velocity) of 4700. Operating speeds of 2000, 4000, and 6000 rpm were considered, together with inlet preswirl/through-flow velocity ratios 0.04, 0.10 and 0.17, respectively.

The three-dimensional grid used to analyze the distorted clearance gap (Baskharone and Hensel, 1991) was first optimized. In this case, the number of tangential stations "N_θ" in this gap (Fig. 6) was varied, while maintaining the axial and radial station counts, as well as the near-wall refinement level, unchanged. Figure 6 shows the variation of the error in the computed force derivatives, $\partial F_x/\partial\epsilon$ and $\partial F_y/\partial\epsilon$, where "$\epsilon$" is the rotor virtual eccentricity, as a result. The error in this figure is defined as the dimensionless difference between the force derivative and that corresponding to an N_θ value of 12, and the force derivatives are those associated with a zero whirl frequency. Based on the asymptotic shape of both curves in Fig. 6, the number of tangential stations was chosen to be 12. As a result, the RAM and CPU time consumption, regardless of the whirl frequency magnitude, were roughly 1220 K. bytes and 12 minutes, respectively, on the SX2 supercomputer, per each whirl frequency.

Shown in Fig. 7 is a comparison of the computed rotordynamic coefficients with those reported by Dietzen and Nordmann (1987). The latter data set contained measurements of the direct and cross-coupled stiffness coefficients, but only the direct damping coefficient. Also contained in this set were the numerical results obtained by Dietzen and Nordmann, for all four of the stiffness and damping coefficients, using a traditional perturbation analysis in which the finite-difference method was utilized. As seen in this figure, the computed results are generally in close agreement with the experimental and analytical data as far as the cross-coupled stiffness and direct damping coefficients are concerned. These two coefficients, as discussed earlier, are representative of the fluid-induced tangential force perturbation and, as such, dominate the mechanism of rotor instability. The cross-coupled stiffness coefficient "k" is, by reference to Fig. 7, positive, therefore destabilizing, and increases with the rotor speed. The direct damping coefficient "C," on the other hand, provides a stabilizing effect which, according to the computed results, increases slightly with the operating speed. Examination of Fig. 7 reveals, however, that the predicted values of the direct stiffness coefficient "K" and cross-coupled damping coefficient "c" are significantly different from those computed by Dietzen and Nordmann (1987). This, for the major part, is caused by differences in the unperturbed flow fields including, in particular, the radial profiles of the flow properties along the seal axis as explained next.

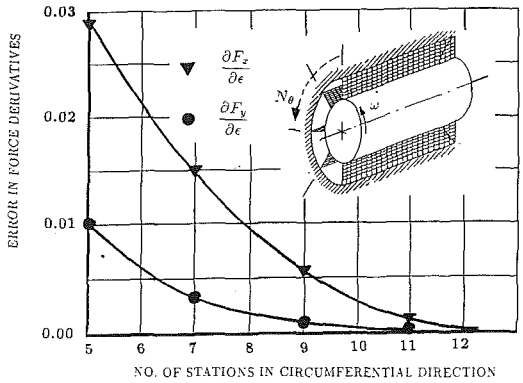

Fig. 6 Sensitivity of the force derivatives to the number of grid planes around the circumference

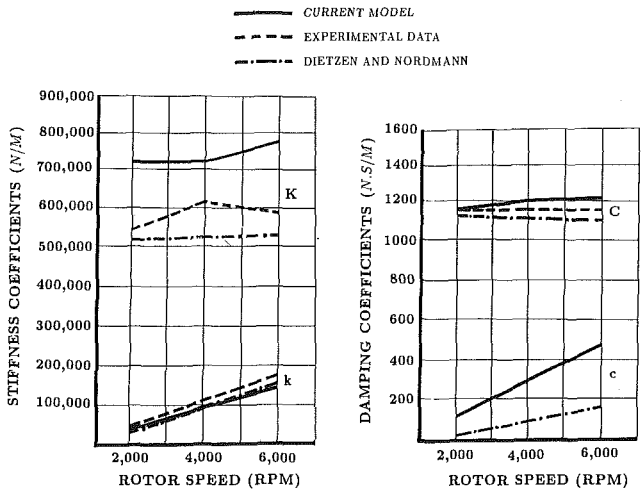

Fig. 7 Comparison of the direct and cross-coupled rotordynamic coefficients with experimental and analytical data

Evolution of the direct stiffness and cross-coupled damping coefficients in Fig. 7 can be traced back (Baskharone and Hensel, 1991) to a single source, namely the radial component of the fluid reaction force on the rotor. As reported by Hensel (1990) for the same seal, this force component is highly sensitive to the inlet through-flow velocity profile including, in particular, the inlet boundary layer thickness. For instance, Hensel reported an average reduction of nearly 21 percent in the direct stiffness coefficient "K" as a result of arbitrarily reducing the inlet boundary layer thickness, on both the rotor and housing surfaces, from 15 percent of the clearance width to 7.5 percent, which is the current value, with the cross-coupled stiffness and direct damping coefficients remaining practically unchanged. Such sensitivity would naturally be anticipated in seals, such as the present, where the axial length is too small to permit a fully developed flow even at the exit station. It is therefore true that the computed values of "K" in Fig. 7 are primarily dependent on the inlet boundary layer thickness assumption which, in turn, was necessary since no measured thickness was available. On the other hand, there is no clear evidence that this assumption had any significant effect on the trend of "K" with the rotor speed in Fig. 7. Nevertheless, it should be noted, in reference to this figure, that the experimentally-determined peak of "K" at a rotor speed of 4000 rpm is as absent in the

results of Dietzen and Nordmann (1987) as it is in the current results despite the major difference in simulating the flow turbulence in both studies.

Versatility Assessment of the Current Perturbation Model. Thorough examination of the current numerical results for the simple annular seal under consideration appeared, as anticipated, to confirm the validity of the single-wave sinusoidal forms of flow perturbations around the circumference. The flow variable under focus was the rotor-surface pressure perturbation ($\partial p_i/\partial \epsilon$) at the middle seal section which, through use of the computed nodal pressures, was cast in the following Fourier series form:

$$\frac{\partial p_i}{\partial \epsilon} = a_0 + \sum_n a_n \cos(n\theta) + \sum_n b_n \sin(n\theta) \tag{9}$$

where the subscript "i" refers to the inner (or rotor) radius and "θ" is the angular coordinate. The number of sine and cosine waves "n" in expression (9) was arbitrarily set equal to five. The ratios (a_n/a_1) and (b_n/b_1) were then computed. All of these ratios came to be less than 0.5 percent for $2 \leq n \leq 5$ regardless of the whirl frequency/spinning speed ratio. This simply means that the common form of field variable perturbation, namely:

$$\mathcal{P} = \mathcal{P}_c \cos\theta + \mathcal{P}_s \sin\theta \tag{10}$$

where $\mathcal{P}$ stands for the perturbation of any flow variable, is seemingly as accurate as can be. This functional form is recognizably a built-in assumption in any existing perturbation model in this rotordynamics area (e.g., Dietzen and Nordmann, 1987; Childs, 1983).

Complex clearance gaps and/or vibration modes, however, are where approximations of the type indicated above may become inapplicable. Consider, for instance, the problem of a shrouded pump impeller (e.g., Baskharone and Hensel, 1989) where the rotor, being the shrouded impeller in this case, undergoes a conical type of whirl as a result of an angular eccentricity of the rotor axis. As indicated by the authors (Baskharone and Hensel, 1991), it is this problem configuration to which the virtual finite-element distortion concept, being the foundation of the current perturbation model, is uniquely applicable. In this case, deformations of the finite elements, due to the angular rotor eccentricity, will give rise to differential changes in the rotor surface pressure which, in the end, produce fluid-exerted moments M_x and M_y around the center of conical whirl. Future application of the current analysis to this type of rotor eccentricity may indeed make it possible to assess the validity of the simple sinusoidal distribution (indicated above) under such circumstances. The authors suspect that such simple distribution would probably be unrealistic in the tooth-to-tooth gap of the labyrinth seal which may very well be part of the leakage passage (e.g., Baskharone and Hensel, 1989), as well as other subdomains where flow separation and recirculation occur. Stated differently, it is in critical subdomains, such as these, that the coefficients "a_n" and "b_n" in expression (9) may not be necessarily zero for $n > 1$ as is generally assumed to be the case in virtually all existing perturbation models of fluid-rotor interaction.

Concluding Remarks

The intention in this paper was to verify a new and categorically different methodology in the area of fluid-induced vibration, as well as validate its fluid mechanics foundation. Both tasks were successfully accomplished using representative annular seal configurations. The direct and cross-coupled rotordynamic coefficients, which comprise the ultimate goal of the study, were in close agreement with available experimental and analytical data, particularly those which are directly linked to the rotor instability. While the strategy in the current perturbation model was clearly different from all existing perturbation models in this field, an effort to assess the versatility of the new model, by comparison, was made and the fundamental differences identified. Since limitations on the rotor-to-housing clearance gap in the model are practically nonexisting, it is presently the plan to apply the model to shrouded impellers of the Space Shuttle Main Engine turbopumps for which the destabilizing forces are developed in the shroud-to-housing secondary-flow gap. Release of the computer code, as part of an upcoming NASA contractor report, will take place upon completion of this final research phase.

Acknowledgment

This study was funded by NASA-Marshall Space Flight Center (Huntsville, Alabama), contract no. NAS8-37821, NASA monitor: James Cannon. Partial funding was also provided by the Houston Advanced Research Center (The Woodlands, Texas), grant no. 88-025.

References

Baldwin, B. S., and Lomax, H., 1978, "Thin Layer Approximation and Algebraic Model for Separated Turbulent Flows," AIAA Paper No. 78-257.

Baskharone, E. A., and Hensel, S. J., 1989, "A New Model for Leakage Prediction in Shrouded-Impeller Turbopumps," ASME JOURNAL OF FLUIDS ENGINEERING, Vol. 111, pp. 118–123.

Baskharone, E. A., and Hensel, S. J., 1991, "A Finite-Element Perturbation Approach to Fluid/Rotor Interaction in Turbomachinery Elements. Part 1: Theory," ASME JOURNAL OF FLUIDS ENGINEERING, published in this issue, pp. 353–361.

Benim, A. C., and Zinser, W., 1985, "Investigation of the Finite Element Analysis of Confined Turbulent Flows Using a k–ϵ Model of Turbulence," *Computer Methods in Applied Mechanics and Engineering*, Vol. 51, pp. 507–523.

Childs, D. W., 1983, "Finite Length Solutions for Rotordynamic Coefficients of Turbulent Annular Seals," ASME *Journal of Lubrication Technology*, Vol. 105, pp. 437–445.

Childs, D. W., and Scharrer, J. K., 1987, "Theory Versus Experiment for the Rotordynamic Coefficients of Labyrinth Gas Seals: Part II-A Comparison to Experiment," *ASME Rotating Machinery Dynamics*, Vol. 2, pp. 427–434.

Childs, D. W., 1988, "Annular Honeycomb Seals: Test Results for Leakage and Rotordynamic Coefficients; Comparison to Labyrinth and Smooth Configurations," *Proceedings of the Fifth Workshop on Rotordynamic Instability Problems in High-Performance Turbomachinery*, Texas A&M University.

Dietzen, F. J., and Nordmann, R., 1987, "Calculating Rotordynamic Coefficients of Seals by Finite Difference Techniques," ASME *Journal of Tribology*, Vol. 109, pp. 388–394.

Diewald, W., and Nordmann, R., 1988, "Influence of Different Types of Seals on the Stability Behavior of Turbopumps," *Proceedings of the Fifth Workshop on Rotordynamic Instability Problems in High-Performance Turbomachinery*, Texas A&M University.

Heinrich, J. C., and Zienkiewicz, O. C., 1977, "Quadratic Finite Element Schemes for Two-Dimensional Convective-Transport Problems," *Int. J. Num. Meth. Eng.*, Vol. 11, pp. 1831–1844.

Hensel, S. J., 1990, "A New Method for Determining Rotordynamic Forces on Liquid Annular Seals," Ph.D. dissertation, Texas A&M University.

Morrison, G. L., Johnson, M. C., and Tatterson, G. B., 1988, "3-D Laser Anemometer Measurements in an Annular Seal," ASME Paper No. 88-GT-64.

Nelson, C. C., 1984, "Analysis for Leakage and Rotordynamic Coefficients of Surface Roughened Tapered Annular Seals," *Proceedings of the Third Workshop on Rotordynamic Instability Problems in High-Performance Turbomachinery*, Texas A&M University.

Scharrer, J. K., 1988, "Rotordynamic Coefficients for Stepped Labyrinth Gas Seals," *Proceedings of the Third Workshop on Rotordynamic Instability Problems in High-Performance Turbomachinery*, Texas A&M University.

Yamada, Y., 1962, "Resistance of Flow Through an Annulus with an Inner Rotating Surface," *Bulletin of JSME*, Vol. 5, No. 18, pp. 302–310.

Zienkiewicz, O. C., 1971, *The Finite Element Method in Engineering Science*, McGraw-Hill.

Navier-Stokes Calculations of Transonic Flows Past Cavities

S. Srinivasan
Former Graduate Student.

O. Baysal
Associate Professor.

Mechanical Engineering and Mechanics Department, Old Dominion University, Norfolk, VA 23529-0247

Presented in this paper is a computational investigation of subsonic and transonic flows past three-dimensional deep and transitional cavities. Simulations of these self-induced oscillatory flows have been generated through time-accurate solutions of the Reynolds averaged, full Navier-Stokes equations, using the explicit MacCormack scheme. The Reynolds stresses have been included through the Baldwin-Lomax algebraic turbulence model with certain modifications. The computational results include instantaneous and time averaged flow properties. The results of an experimental investigation have been used not only to validate the time-averaged results, but also to investigate the effects of varying the Mach number and the incoming boundary-layer thickness. Time series analyses have been performed for the instantaneous pressure values on the cavity floor and compared with the results obtained by a predictive formula. While most of the comparisons have been favorable, some discrepancies have been observed, particularly on the rear face. The present results help understanding the three-dimensional and unsteady features of the separations, vortices, the shear layer, as well as some of the aeroacoustic phenomena of compressible cavity flows.

Introduction

There are several types of researchers who study flows past cavities. Aerodynamicists, such as, Stallings and Wilcox (1987), Plentovich (1988), are concerned with the drag due to a cavity, which may serve as a bay for weapons or special cameras, or a landing gear well on an aircraft. Aeroacousticians, such as, Rossiter (1966) and Shaw (1986), however, study the sound waves generated by the self-induced oscillations of the flow inside a cavity, which can affect the avionics and the people on board. Fluid dynamicists, such as Baysal and Stallings (1988a), Baysal et al. (1988b), Srinivasan (1988), are interested in the complex structure of the flow in a cavity in addition to the other concerns. Stallings and Wilcox (1987), Plentovich (1988), Rossiter (1966), and Shaw (1986) have investigated two and three dimensional rectangular cavities using experimental techniques. These flowfields have been computationally simulated by Baysal and Stallings (1988a), Baysal et al. (1988b), Srinivasan (1988), Rizzeta (1988), and Suhs (1987). Although work has been conducted from the subsonic to hypersonic regimes, most of the effort has been concentrated on the supersonic speed regime. In the subsonic and transonic regime, static pressure data have been sparse. Currently, there is no report that displays the complex transonic flow features inside the cavity. Also, because of renewed interest in high maneuverability and less radar detection signatures, which require internal carriage of weapons and stores, this research effort has been pursued.

As in the supersonic regime, there exist two distinct types of cavity flows when the approaching flow is transonic (Stallings and Wilcox, 1987, and Plentovich, 1988). The first occurs when the cavity is deep, and it is called an open cavity flow. In the case of an open cavity flow, the shear layer "bridges" the cavity opening. The other type of cavity flow is for shallow cavities, and it is termed a closed cavity flow. In the case of a closed cavity flow, the flow separates at the front face and reattaches on the cavity floor. The flow remains attached until it undergoes separation due to high pressures ahead of the rear face. Therefore, the flow in a shallow cavity resembles that of the flow behind a rearward facing step followed by the flow ahead of a forward facing step. The parameter used to indicate the deepness or the shallowness of a cavity is its length-to-depth ratio, L/D (Fig. 1).

There is a gradual change from closed to open cavity flow as the L/D ratio is decreased, which is called a transitional cavity flow. Stallings and Wilcox (1987) have found that a transitional flow occurs for L/D between 10 and 13 for supersonic free-stream conditions. They also have shown that there are hysteresis effects in this L/D region. Although a similar study has not been conducted for the subsonic and transonic regimes, it is conceivable that the same trends exist in these flow regimes.

Karamcheti (1955) has found that periodic pressure fluctuations are accompanied by strong acoustic radiation from the cavity. The frequency of these pressure fluctuations is found to increase with air speed and decrease as the cavity length is increased. In very deep cavities ($L/D < 3$), the pressure fluctuations are mainly periodic, but as the cavity depth is decreased, the fluctuations become random in character. For shallow cavities ($L/D > 10$), the spectrum is smooth and covers a broad band of frequencies showing that the pressure fluctuations are random in character. As the depth of the cavity is increased, peaks occur in the spectra indicating that periodic pressure fluctuations are superimposed upon the random levels.

Contributed by the Fluids Engineering Division for publication in the JOURNAL OF FLUIDS ENGINEERING. Manuscript received by the Fluids Engineering Division June 6, 1989.

A steady state solution does not exist for high speed cavity flows. The flow goes through a sequence of physical phenomena (cycle) such as mass ingestion and egestion, but this cycle is non-periodic (does not have a fixed time period). This is primarily due to the compressibility effects and the presence of the "feedback loop" (Shaw, 1986) associated with the wave propagation.

The results of Plentovich's (1988) experimental investigation are used for comparison as well as to expand the database and knowledge of the flowfield in the cavities over the transonic regimes. These experiments have been conducted at the 7-by-10-Foot Transonic Tunnel of David Taylor Naval Ship Research and Development Center. The computations have been performed on the CYBER-205 (VPS-32) computer at NASA Langley Research Center.

Governing Equations

The governing equations used in the computational analysis are the three-dimensional, time-dependent, compressible, full Navier-Stokes equations in terms of Reynolds averaged variables. These equations can be written in Cartesian coordinates as follows:

$$(\partial Q/\partial t)+(\partial F/\partial x)+(\partial G/\partial y)+(\partial H/\partial z)=0 \tag{1}$$

$$Q=\begin{bmatrix}\rho\\ \rho u\\ \rho v\\ \rho w\\ \rho E\end{bmatrix} \quad F=\begin{bmatrix}\rho u\\ \rho uu-\tau_{xx}+p\\ \rho uv-\tau_{xy}\\ \rho uw-\tau_{xz}\\ \rho(E+p)u-k_1\end{bmatrix}$$

$$G=\begin{bmatrix}\rho v\\ \rho uv-\tau_{xy}\\ \rho_{vv}-\tau_{yy}+p\\ \rho vw-\tau_{yz}\\ \rho(E+p)v-k_2\end{bmatrix} \quad H=\begin{bmatrix}\rho w\\ \rho uw-\tau_{xz}\\ \rho vw-\tau_{yx}\\ \rho ww-\tau_{zz}+p\\ \rho(E+p)w-k_3\end{bmatrix} \tag{2}$$

The expressions for k_1, k_2, k_3, the shear stresses and the heat fluxes can be written in tensoral shorthand notation (l, m, n are dummy indices) as,

$$k_m=u_n\tau_{x_nx_m}-q_{x_m} \tag{3}$$

$$\tau_{x_nx_m}=\mu[(\partial u_m/\partial x_n)+(\partial u_n/\partial x_m)-2/3(\partial u_l/\partial x_l)\delta_{mn}] \tag{4}$$

$$q_{x_m}=-K(\partial T/\partial x_m) \tag{5}$$

The perfect gas law,

$$p=(\gamma-1)[\rho E-\rho(u^2+v^2+w^2)/2] \tag{6}$$

and the Sutherland's laminar viscosity law have been used to complete the system of equations. δ denotes the Kronecker delta. For turbulent flow, the viscosity coefficient is defined as the sum of laminar viscosity (μ_l) and the turbulent eddy viscosity (μ_t). The governing equations (Eqs. (1-6)) have been transformed into generalized curvilinear coordinates in order to facilitate the stretched computational grids used in this study (Fig. 2).

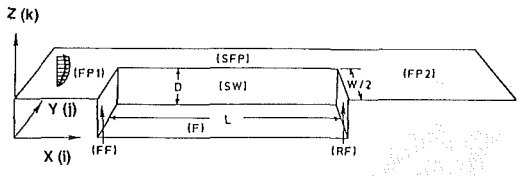

Fig. 1 Schematic of a rectangular half-span cavity

Numerical Procedure

The numerical scheme for the current problem is required to be time-accurate, highly vectorizable, and simple to code. The explicit MacCormack (1969) scheme satisfies these conditions. This predictor-corrector explicit algorithm is summarized below in generalized coordinates, where ($\hat{}$) indicates a quantity written in these coordinates.

Predictor Step:

$$\hat{Q}^{\overline{n+1}}=\hat{Q}^n-\Delta t[\Delta_\xi\hat{F}^n+\Delta_\eta\hat{G}^n+\Delta_\zeta\hat{H}^n] \tag{7}$$

Corrector Step:

$$\hat{Q}^{n+1}=\frac{1}{2}(\hat{Q}^n+\hat{Q}^{\overline{n+1}})-\frac{\Delta t}{2}[\nabla_\xi\hat{F}^{\overline{n+1}}+\nabla_\eta\hat{G}^{\overline{n+1}}+\nabla_\zeta\hat{H}^{\overline{n+1}}] \tag{8}$$

Δ denotes a forward spatial difference and ∇ denotes a backward spatial difference. This two-step process (predictor-corrector) consists of evaluating derivatives by one-sided differences taken in opposite directions during alternate steps for symmetric calculations. As in any other centrally differenced scheme, fourth-order damping terms are included explicitly. This scheme is second order accurate both spatially and temporally.

Cavity flows have been assumed symmetric with respect to the longitudinal center plane. Hence, the grids have been generated for a half-span cavity (Figs. 1, 2). A two-dimensional Cartesian grid has been generated for the symmetry plane (x-y plane), with clustering of nodes near walls and in the shear layer region. This symmetry plane grid has been stacked in the z-direction, with clustering of these planes near the sidewall. The grid size for the $L/D=4.4$ cavity is $(111\times71\times28)$, and that of the $L/D=11.7$ cavity is $(121\times71\times28)$, in the longitudinal, normal, and lateral directions, respectively. Each grid has 15 nodes in the boundary layer at the front lip of the cavity. The computational zone is swept by the code plane-by-plane in the z-direction with vectorization done in each x-y plane. To ensure the longest possible data vectors, neither the overlapped grids (Suhs, 1987), nor the body fitted curvilinear grids (Baysal and Stallings, 1988a), which would allow the mapping of the cavity surface to the $\zeta=0$ plane, are used;

Nomenclature

c_p = pressure coefficient
D,L,W = depth, length, and width of the cavity, respectively
E = total energy
FF = front face
FP1,FP2 = front and rear flat plates
J = Jacobian of coordinate transformation
K = coefficient of thermal conductivity
M = Mach number
n = time index
p = static pressure
Pr = Prandtl number
R = universal gas constant
Re = Reynolds number
SFP = side flat plate
SW = side wall
T = static temperature
t = time
t = turbulent value index
t_c = characteristic time
RF = rear face
u,v,w = Cartesian velocity components
x,y,z = Cartesian coordinates
γ = ratio of specific heats
δ = boundary-layer thickness
μ = viscosity coefficient
μ_t = eddy viscosity coefficient
ξ,η,ζ = generalized coordinates
ρ = density

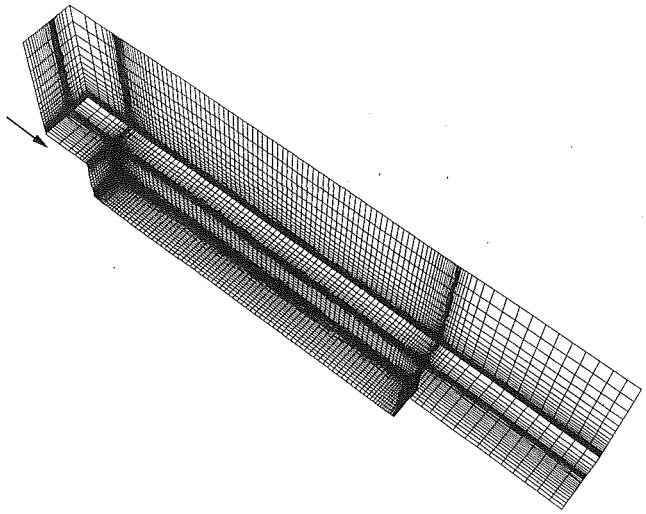

Fig. 2 Three-dimensional grid structure for a half-span rectangular cavity

instead dummy points have been created for the regions under FP1, SFP, and FP2, from the $y=0$ plane to the $y=D$ plane. Such a data vector structuring and fully vectorizing the code has resulted in a processing rate of five microseconds per grid point per time step using 32-bit arithmetic on the CDC CYBER 205 of NASA Langley Research Center. This Fortran-200 code of the solution algorithm has been developed by Kumar (1985).

Turbulence Model. The modeling of the stresses resulting from the Reynolds averaging of the governing equations is complicated by the fact that several length scales exist which control the generation, transport, and dissipation of turbulent kinetic energy. Therefore, the standard two-layer algebraic turbulence model of Baldwin and Lomax (1978) has been modified and used herein. It is based on the Boussinesq approximation of modeling the Reynolds stresses by an eddy viscosity, μ_t.

Three specific modifications have been made to the standard Baldwin-Lomax model to account for: (*a*) vortex-boundary layer interaction and separation, (*b*) presence of multiple walls, and (*c*) turbulent memory effects in addition to the local equilibrium for the shear layer. The details of these modifications are given by Baysal et al. (1988b), Srinivasan (1988), Baysal and Yen (1990).

Initial and Boundary Conditions. The entire flowfield above the cavity has been initialized with the inflow conditions. The flow velocities within the deep cavity are much lower than that of the freestream. Therefore, the velocity components inside the cavity have been specified as 10 percent of their freestream values. Since the shear layer impinges on the floor of the shallow cavity, an approximate velocity profile close to the inflow velocity profile has been specified within the cavity. The pressure and temperature within both cavities have been set to their freestream values.

No-slip boundary condition has been used on solid surfaces. These solid surfaces have been considered to be adiabatic. The pressures at the solid surfaces have been obtained from an extrapolation of the interior point values of pressure in the direction normal to the wall (i.e., zero normal gradient).

The values of u, v, w, and T at the inflow boundary have been specified by a profile generated using the two-dimensional boundary layer equations. The density in this region, however, is extrapolated from the computation zone. This ensures the information to propagate upstream. The flow variables at the downstream boundary, with the exception of pressure, have been obtained by zeroth-order extrapolation from the computation zone. The static pressure in this region has been specified to be at its freestream value. The outer boundary conditions have been specified by zeroth-order extrapolation for outflow, and as freestream conditions for inflow. The pressure values have always been assumed to be freestream value at this boundary since the normal flow has always been subsonic. The symmetry of the flow at the plane of symmetry ($z=0$) has been ensured by setting the z-component of velocity to zero and applying zeroth-order extrapolation for the other flow variables.

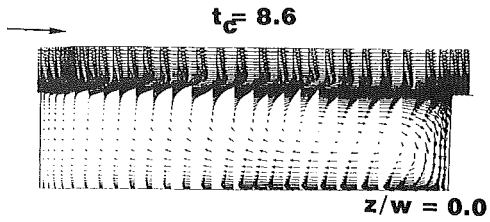

Fig. 3 Instantaneous streamwise velocity vectors of Case 1

Results and Discussion

The results of an experimental investigation have been used in this report for comparison purposes. The cavity flow model has been tested by Plentovich (1988). A flat plate has been chosen as the parent body to simulate a generic aircraft configuration and to allow a well defined flow to develop ahead of the cavity. The cavity has been sized to be approximately one-quarter scale, with a cavity length of 3.5 ft, a width of 0.8 ft, and a maximum depth of 0.8 ft. The floor of the cavity could also be moved to a cavity depth of 0.3 ft. The cavity L/D values tested have been 4.4 for the deep configuration ($D=0.8$ ft) and 11.7 for the shallow configuration.

In order to establish a measure of time for this unsteady analysis, a characteristic time, t_c, has been loosely defined as the time it would take a fluid particle to travel the length of the cavity at the freestream velocity.

Case 1: $M=0.9$, $Re/ft=1.6\times10^6$, $L/D=4.4$. The computer program has been run approximately 8.6 characteristic times (t_c). One t_c is 3.57 milliseconds (ms). The computational time for this case has been 15.5 CPU hours on the CYBER-205. The instantaneous velocity vectors at the plane of symmetry ($Z/W=0.0$) are shown in Fig. 3. As expected of deep cavities, the shear layer bridges the cavity opening. The organized behavior of the shear layer is evident. A large vortex encompasses the entire cavity. Shown in Fig. 4 are the instantaneous streamlines within the cavity at three spanwise planes moving from the plane of symmetry toward the sidewall ($Z/W=0.117$, 0.294, 0.353). As observed in the velocity vector plots, it is seen that the flow interacts with the rear face and forms a large vortex structure. As the sidewall is approached, the vortex structure changes its shape and size, and the core of the vortex moves towards the cavity opening. In addition to the main vortex structure, secondary vortices are visible near the corners. At $Z/W=0.353$, a secondary separation is seen at the cavity floor close to the front face.

In order to depict the physical behavior of mass expulsion and ingestion, which in turn causes the unsteady behavior, the density contours at two instants of time and at two spanwise planes have been displayed in Fig. 5. At $t_c=7.2$, the shear layer is deflected up, and mass is being expelled from the cavity at the rear face. The external flow is compressed as it negotiates this deflection. There is a large region of separation and a vortex on FP2 caused by the expansion at the sharp corner of the rear face. At the front face, the shear layer is deflected down into the cavity, causing the external flow to expand. At $t_c=8.6$, mass is being entrained into the cavity. Due to the deflection of the shear layer into the cavity at the rear face, the external flow expands and then undergoes compression in this region. At the rear lip, which is exposed to the external

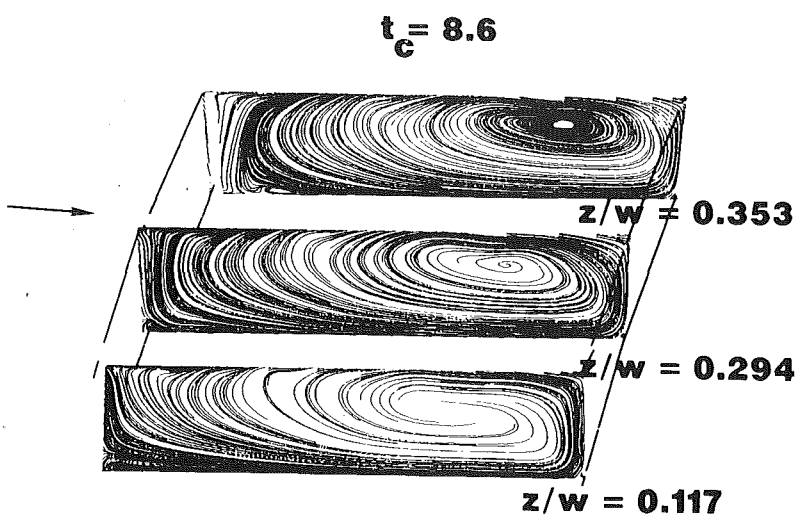

Fig. 4 Instantaneous streamlines of Case 1 at three spanwise planes

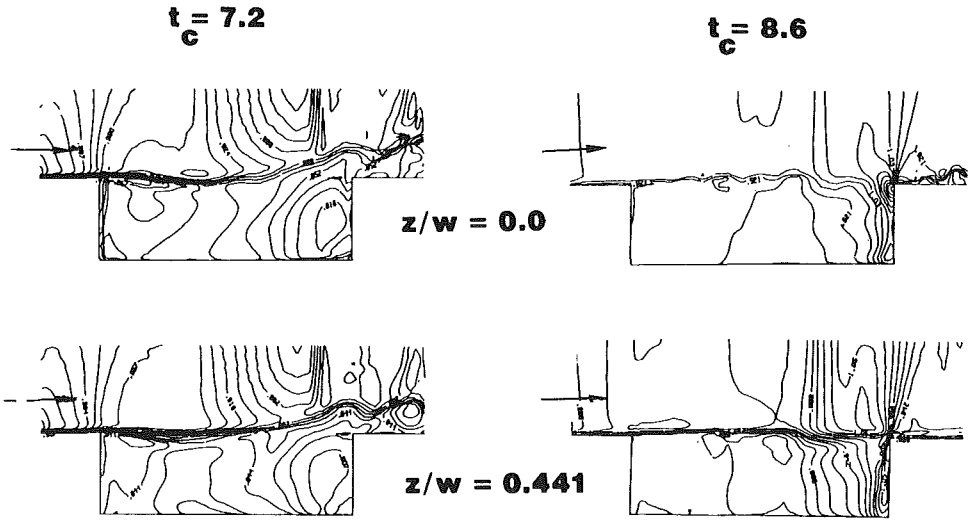

Fig. 5 Instantaneous density contours of Case 1 at two spanwise planes and two time instants

flow, the flow has to negotiate the 90 deg turn, thereby undergoing an expansion which is seen in the density contours. At the front face, the shear layer is parallel to the flat plate. Therefore, the incoming flow does not undergo any expansion or compression. Also, in the upstream lip region of the cavity, a sequence of compressions and expansions produced by the wavy structure of the shear layer can be observed. The unsteady nature of the flow is clearly indicated in Fig. 5.

Shown in Fig. 6 are the instantaneous cross flow velocity vectors at two axial locations ($X/L = 0.725, 0.978$). Notice that the direction of the cross flow is different at various axial locations (leaving or entering the cavity). Also, vortices are generated or dissipated at different cross sections.

The mean streamwise surface pressure coefficient distribution along the plane of symmetry are shown in Fig. 7. The averaging has been started after running the program for 2 t_c, and it has been performed over 6 t_c thereafter. The experimental measurements have been averaged over one second. Good agreement between the present computational results and Plentovich's (1988) experimental results has been obtained on the floor, the rear face, and the downstream flat plate (FP2). The numerical results seem to be slightly overpredicting the pressure on the rear face towards the cavity floor. Spanwise C_p distributions on the rear face at 25 percent, and 62.5 percent depth are shown in Fig. 7(*d*). There is an increase in pressure towards the side wall, because the fluid is compressed as it

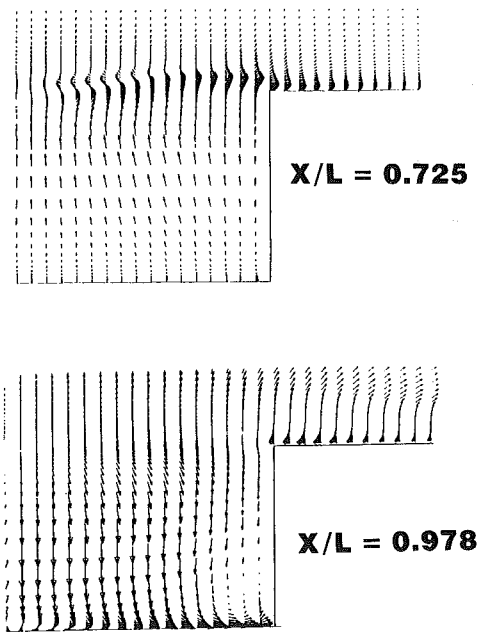

Fig. 6 Instantaneous ($t_c = 8.6$) cross flow velocity vectors at two axial locations of Case 1

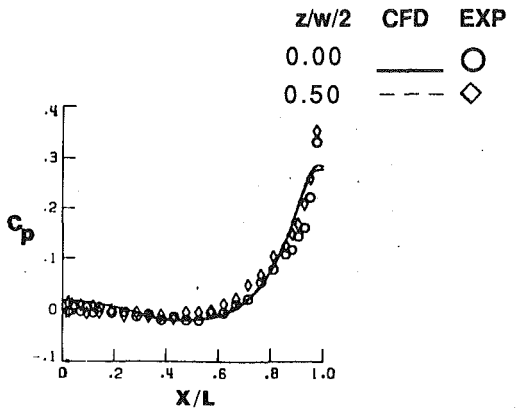

Fig. 7(*a*)

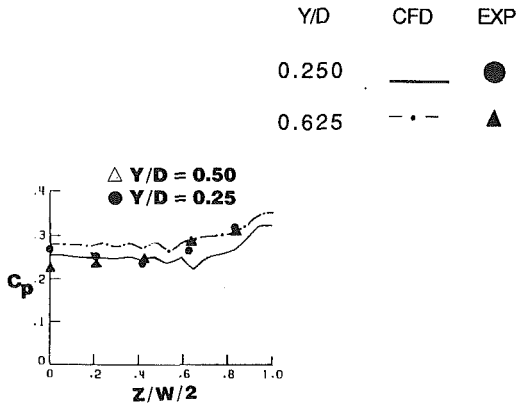

Fig. 7(*c*)

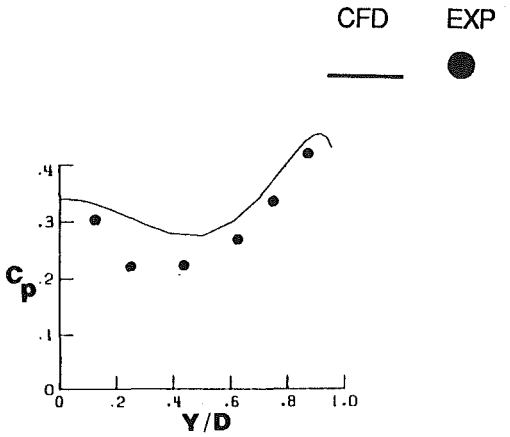

Fig. 7(*b*)

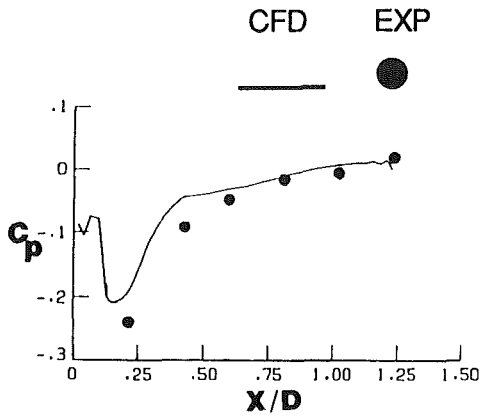

Fig. 7(*d*)

Fig. 7 Time-averaged surface pressure coefficient distributions of Case 1 (*a*) on the floor, (*b*) along the centerline of RF, (*c*) along the centerline of FP2, (*d*) spanwise on RF (experiments by Plentovich, 1988)

reaches the rear face/sidewall intersection. Differences between the numerical solution and experimental data are notable on the rear face, where the magnitude of the fluctuating pressure is greatest and thus most sensitive to numerical inaccuracy. Also, the extent of separation has been slightly underpredicted on the aft section of the flat plate. The discrepancy between the computational and experimental results can be attributed to several reasons: (*a*) use of a relatively simple turbulence model, (*b*) relatively coarser mesh than necessary for better turbulent resolution, (*c*) explicit addition of artificial damping needed to smooth the numerical oscillations, and (*d*) averaging of the wall pressures have been done for a relatively shorter period of time in comparison with the experiments.

The instantaneous limiting streamline pattern on the cavity floor is shown in Fig. 8(*a*). The corresponding shear stress vectors on the cavity floor are shown in Fig. 8(*b*). The limiting streamlines qualitatively follow the same trends as the skin friction lines. Close to the front face, the streamlines from opposite directions converge on to a line of instantaneous separation. This separation causes the main vortex structure in the streamwise plane within the cavity. In addition to the main separation, a secondary closed type separation region is seen near the sidewall. Close to the rear face, the flow reattaches. Similar reattachment region is visible very close to the front face.

The frequency spectra at a point on the cavity floor is shown in Fig. 9. It has been obtained by transforming the pressure histories from the time domain into the frequency domain (units in Hz) through fast Fourier transformations. Also, the pressure values have been converted from Pascals to decibels (dB) of sound pressure levels (SPL). Since no experimental

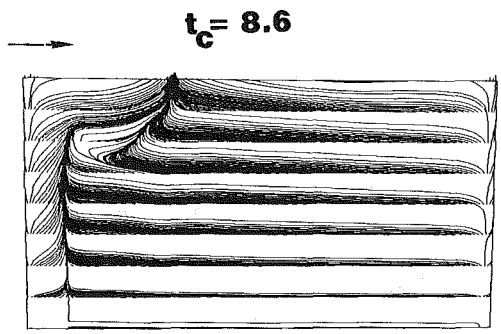

Fig. 8(*a*)

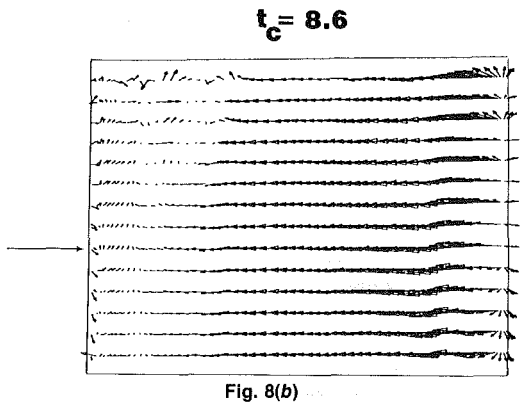

Fig. 8(*b*)

Fig. 8 Instantaneous (*a*) limiting streamlines (*b*) shear stress vectors, of Case 1 on the cavity floor

results are available for this case, a comparison is made with the Rossiter's (1966) prediction formula. The Rossiter's formula predicts the fundamental, second, and third harmonics to be $f_1 = 78$ Hz, $f_2 = 183$ Hz, and $f_3 = 312$ Hz, respectively. The fundamental and second harmonics computed herein agrees with the Rossiter's prediction within ± 5Hz. The third harmonic is smeared out, presumably due to numerical dissipation. It also should be noted, that ideally about 10 data points are needed under the first harmonic. Nonetheless, even with about one-third of ideal number of data points, the salient features of the aeroacoustic environment are captured and compared favorably with the Rossiter's formula.

Case 2: $M = 0.58$, $Re/ft = 1.52 \times 10^6$, $L/D = 11.7$. The computer program has been run approximately for 6 t_c. One

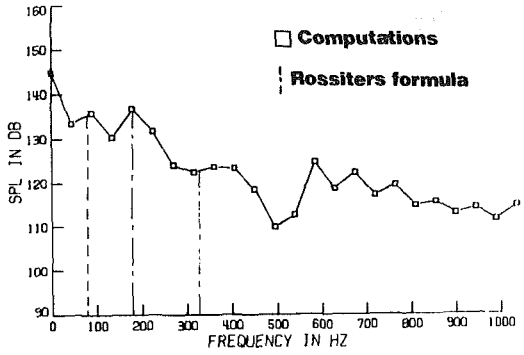

Fig. 9 Frequency spectra of sound pressure levels (SPL) on the cavity floor at $X/L = 0.30$ of Case 1 (Rossiter's formula from Rossiter, 1966)

t_c corresponds to 5.47 ms for this flow. The computational time for this run has been 15.0 CPU hours on the CYBER-205. Instantaneous velocity vectors in the streamwise plane at $Z/W = 0.353$ and at two instants of time ($t_c = 5.2$ and 6.0) are shown in Fig. 10. For clarity, vectors are displayed at every other grid point in the streamwise direction. The shear layer in the front half of the cavity shows a tendency to bridge the cavity opening. Halfway through the cavity opening, the shear layer deflects into the cavity towards the floor. The boundary layer on the floor grows from the point of reattachment toward the rear face. Due to the compression of the fluid near the rear face, the adverse pressure gradient causes the flow to separate and the shear layer deflects out of the cavity. Then the flow negotiates a 90 deg turn and separates on FP2. The velocity vectors show that in the front half on the cavity, the flow resembles an open cavity flow, and the rear half exhibits the trends of a closed cavity flow. This explains the reason for calling it a transitional cavity.

The instantaneous streamline plots at five spanwise locations are shown in Fig. 11. As indicated in these plots also, the flow in the front half of the cavity resembles a deep cavity flow and then the shear layer impinges on the cavity floor. Beyond the point of impingement, the flow portrays the shallow cavity features. The point of reattachment moves closer to the front face as the sidewall is approached. The presence of the sidewall influences the reattachment point due to the crossflow. In addition, the vortex structure changes from the plane of symmetry towards the sidewall. The instantaneous ($t_c = 6$) Mach contours at two spanwise planes ($Z/W = 0.0$, 0.47) are shown in Fig. 12. The shear layer is deflected out of the cavity at the rear face and the flow separates on FP2. The separation region

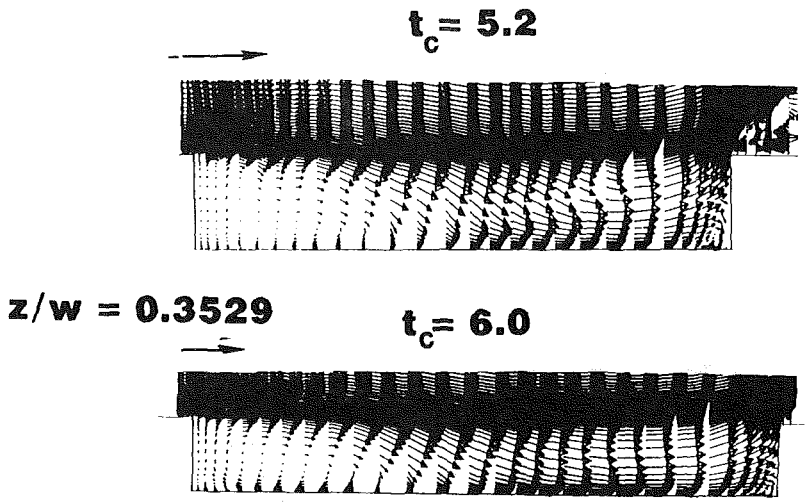

Fig. 10 Streamwise distribution of velocity vectors at two time instants of Case 2

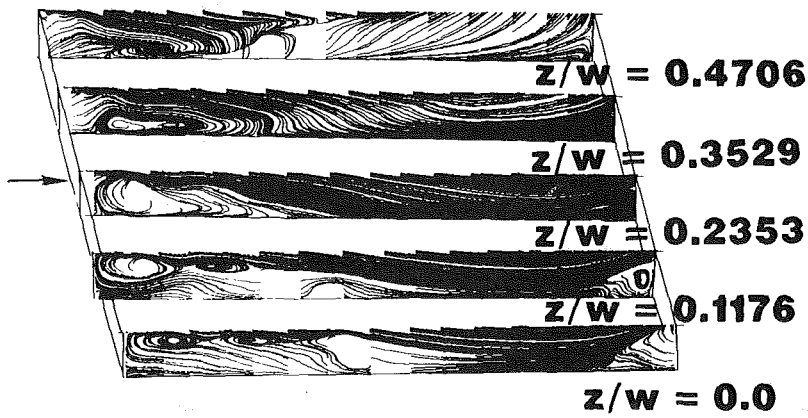

Fig. 11 Instantaneous ($t_c = 6.0$) streamlines at five spanwise planes of Case 2

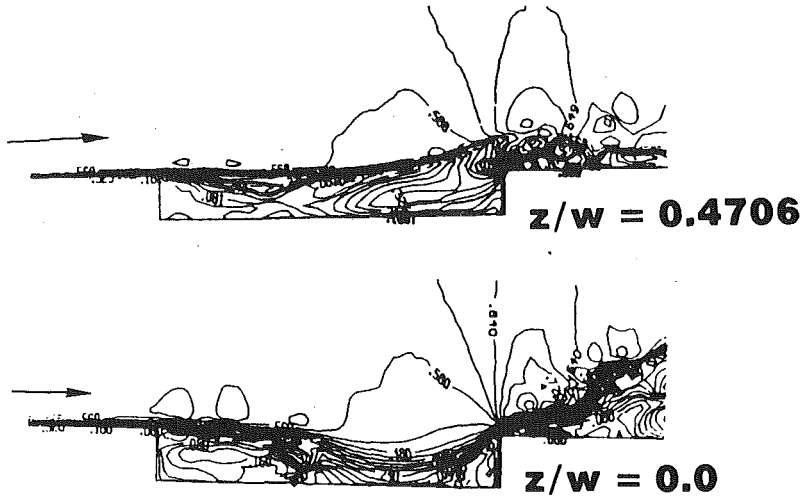

Fig. 12 Instantaneous ($t_c = 6.0$) Mach number contours at two spanwise planes of Case 2

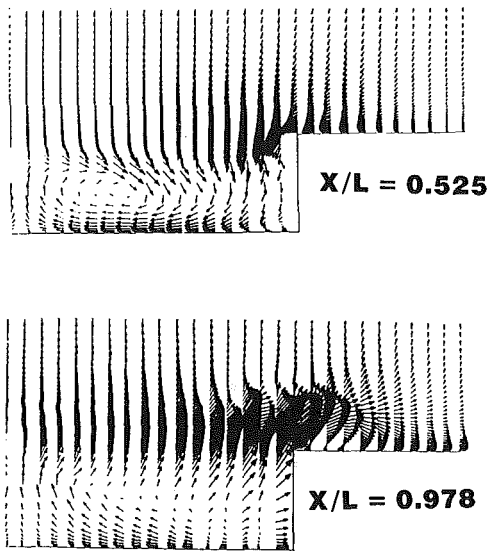

Fig. 13 Instantaneous ($t_c = 6.0$) cross flow velocity vectors at two axial planes of Case 2

shrinks in size as the side wall is approached. A presentation of the crossflow structure is provided in Fig. 13, where instantaneous ($t_c = 6$) cross flow velocity vector plots within the cavity are shown at two axial locations. The most prominent feature observed in these figures is the vortex structure which is caused by the cross flow mass ingestion from the lateral outboard at $X/L = 0.525$. This vortex structure moves from the cavity centerline towards the side wall at $W/L = 0.978$.

The mean wall pressure coefficients along the cavity centerline are shown in Fig. 14. The averaging has been started after running the program for 2 t_c, and it has been performed over 4 t_c thereafter. The experimental measurements have been averaged over one second, which is approximately 183 t_c. A comparison of this figure and Fig. 7 indicates the significant differences in the pressure fields of a deep cavity and a transitional cavity. The computed C_p distribution on the cavity floor shows similar trends as observed experimentally, however, the reattachment point has been underpredicted by the computations. The discrepancies in the results for the floor and the rear face can be attributed to the same reasons explained for the previous case.

The instantaneous limiting streamline pattern on the cavity floor is shown in Fig. 15(*a*). The corresponding shear stress vectors on the cavity floor are shown in Fig. 15(*b*). The observed separation patterns are rather complex. Close to the front face, the streamlines from opposite directions converge on to the separation line. In addition to the main separation, secondary closed separation can be observed. This separation flow reattaches on the cavity floor indicated by the reattachment line. From the point of reattachment, the flow remains attached to the floor until it reaches the rear face region. The flow separates in the streamwise and spanwise directions close to the sidewall. Within the main separation, a secondary horseshoe type separation structure is visible.

Shown in Fig. 16 are the frequency spectra contributing to the overall sound pressure level at two positions along the cavity centerline. Both of the pressure pickup points have been located on the cavity floor. From Shaw's (1986) experimental observations, it is known that there are no frequency modes which are excited for a closed cavity, and slightly more variations in the spectrum occur for a transitional cavity. This is attributed to the deflection of the shear layer attaching on the floor of the cavity, which partially prevents the feed-back mechanism for the pressure waves from occurring. This feature is displayed in the computational predictions.

The discussions in the next subsections are based not only on the computational results of this report, but also on the results of Stallings and Wilcox (1987), Plentovich (1988), Baysal and Stallings (1988a), Baysal et al. (1988b), and Srinivasan (1988).

Mach Number Effects. Cavity flows with various freestream Mach numbers have been compared at a Reynolds number range from 1.0×10^6 to 1.9×10^6 in Plentovich's (1988) experimental investigation. It has been observed that, in the case of deep cavities Mach number has only a little effect on the cavity wall pressures over the Mach number range from 0.60 to 1.05. In comparison with the supersonic flow case for a deep cavity (Baysal et al., 1988b), it has been observed that the values of C_p on the cavity floor toward the rear face and on the rear face decrease slightly from their values at low Mach numbers. It has also been observed that as the Mach number decreases in the subsonic and transonic regimes, a separation bubble exists on the flat plate downstream of the cavity (FP2).

The C_p distribution on the transitional cavity floor shows a plateau region (Fig. 14(*d*)), indicating the shear layer impingement on the floor in the lower Mach number (0.3 to 0.6) range. This trend is similar to the C_p distribution on the floor of a shallow cavity. As the Mach number increases, this plateau region slowly disappears and C_p distribution on the floor shows a monotonic increase. This is typical of a transitional cavity. The increase in Mach number affects the critical L/D ratio. The critical L/D refers to a particular ratio beyond which the flow behaves completely as a closed cavity flow, and below

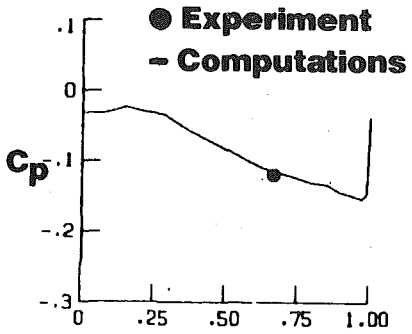

Fig. 14(*a*)

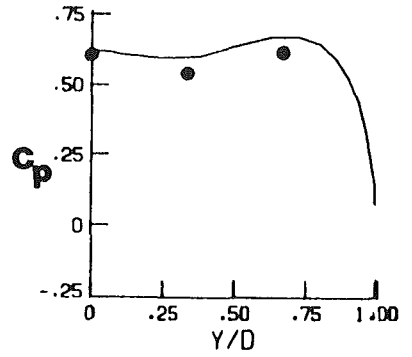

Fig. 14(*b*)

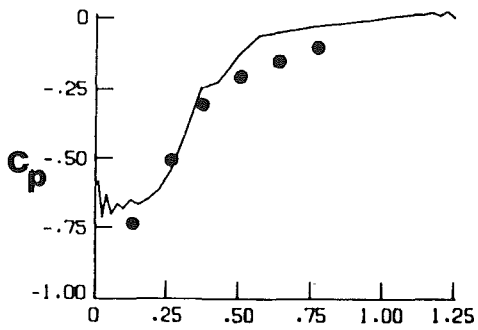

Fig. 14(*c*)

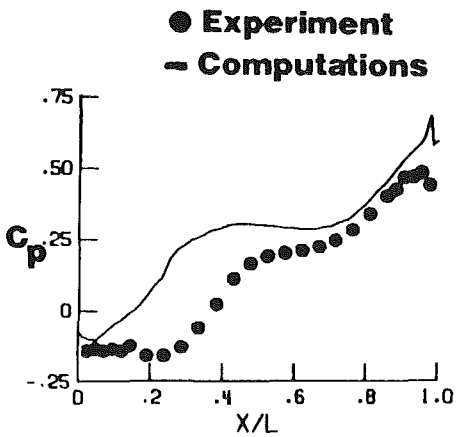

Fig. 14(*d*)

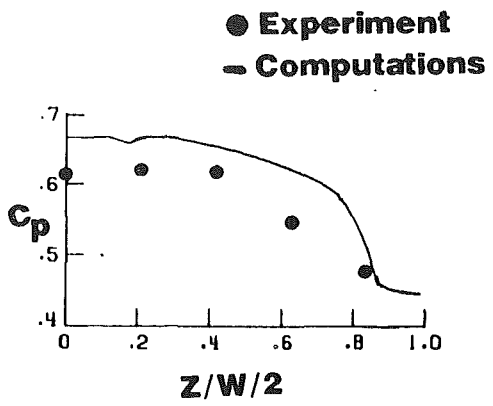

Fig. 14(*e*)

Fig. 14 Time-averaged surface pressure coefficient distributions of Case 2 along the centerline of, (*a*) FF, (*b*) RF, (*c*) FP2, (*d*) floor, and (*e*) spanwise variation on the rear face at $Y/D = 0.5$ (experiments by Plentovich, 1988)

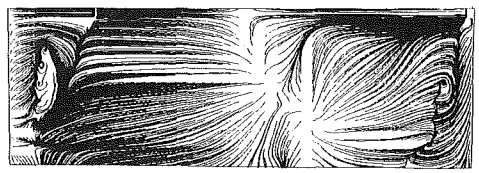
Fig. 15(*a*)

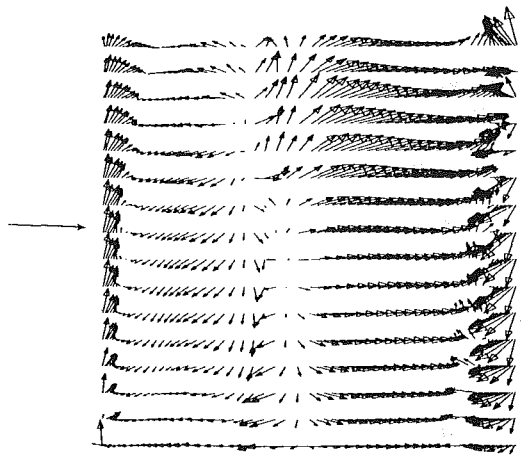
Fig. 15(*b*)

Fig. 15 Instantaneous (*a*) limiting streamlines, (*b*) shear stress vectors, on the cavity floor of Case 2 ($t_c = 6.0$)

which it behaves as an open cavity flow. Therefore, the same trends as observed in the case of supersonic flows by Stallings and Wilcox (1987), Baysal and Stallings (1988a) and Baysal et al. (1988b), are also seen in the subsonic and transonic flow cases.

Shaw's (1986) parametric study indicates that the sound pressure levels increase monotonically for deep and shallow cavities over a Mach number range of 0.6 to 1.0 for the first three frequency modes. However, for Mach numbers from 1.0 to 1.2, these levels either gradually drop or remain unchanged.

Effect of Boundary Layer Thickness. The effect of varying the ratio of the incoming boundary layer thickness to the cavity depth at the cavity lip is reported by Stallings and Wilcox (1987) for supersonic flows. For a constant boundary layer thickness, when the cavity depth is increased (the ratio δ/D decreases), pressures on the rear face and aft region of the cavity floor also increase. This trend is observed in this computational study for subsonic and transonic flows. In the transonic flow case ($L/D = 4.4$ and $M = 0.9$), the ratio δ/D is 0.105. Whereas, in the supersonic flow cases ($L/D = 6.0$ and $M = 1.5$) reported by Baysal and Stallings (1988a) and Baysal et al. (1988b), this ratio is 0.25. Since the δ/D is smaller in the

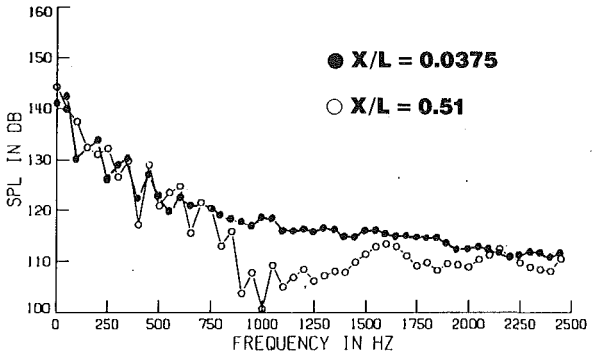

Fig. 16 Frequency spectra of sound pressure levels (SPL) on the cavity floor at two axial locations of Case 2

transonic deep cavity flow case, the pressures on the rear face and the aft region of the floor are observed to be higher.

A comparison of C_p distributions on the cavity rear face for a transitional cavity ($L/D = 11.7$ and $M = 0.58$) and a shallow cavity from Baysal et al. (1988b) ($L/D = 16$ and $M = 1.5$) has also been made. The δ/D ratio of the shallow cavity case is 0.25 and that of the transitional case is 0.22. The same trend observed for the deep cavities has been seen for the shallow and transitional cavities. That is, the C_p distribution on the rear face of the shallow cavity (larger δ/D) is slightly less than that of the transitional case (smaller δ/D).

Conclusions

Transonic flows past deep and transitional cavities have been computationally simulated. The results have provided the computational visualization of this class of flows as well as the analysis of the three-dimensional unsteady separations on the cavity walls. A parametric study based on the current investigation as well as the previous computational and experimental investigations has been conducted to investigate the effects of varying the Mach number and the ratio (δ/D). Both time averaged and instantaneous solutions have been obtained. Time averaged C_p has been compared with the experimental data reported by Plentovich (1988). While most of this comparison has been favorable, discrepancies in the computational results occur on the floor and rear face of the cavity. These discrepancies have been attributed to several reasons: (*a*) use of a relatively simple turbulence model, (*b*) relatively coarser mesh than necessary for better turbulent resolution, (*c*) explicit addition of artificial damping needed to smooth the numerical oscillations, and (*d*) averaging of the wall pressures have been done for a relatively shorter period of time in comparison with the experiments.

Two-dimensional analyses, such as those reported by Baysal and Stallings (1988a) and Rizzeta (1988) could also yield some of the cavity flow features, such as, the simulation of the flow in the symmetry plane and the aeroacoustic information. One of the motives of this research effort, however, has also been studying the three-dimensional effects. The present simulation has captured additional feature, such as, the crossflow separation, three-dimensional shear layers and vortices inside the cavity and on the side edge. Another reason for pursuing a three-dimensional analysis as such has been the follow-up extension of this analysis to include an object, such as a missile, placed inside the cavity.

Acknowledgment

This work has been supported under NASA Cooperative Agreement NCC1-121.

References

Baldwin, B. S., and Lomax, H., 1978, "Thin-Layer Approximation and Algebraic Model for Separated Turbulent Flows," AIAA Paper 78-257.

Baysal, O., and Stallings, R. L., Jr., 1988a, "Computational and Experimental Investigations of Cavity Flowfields," *AIAA Journal*, Vol. 26, No. 1, pp. 6–7.

Baysal, O., Srinivasan, S., and Stallings, R. L., Jr., 1988b, "Unsteady Viscous Calculations of Supersonic Flows Past Deep and Shallow Three-Dimensional Cavities," AIAA Paper 88-0101.

Baysal, O., Yen, G. W., 1990, "Implicit and Explicit Computations of Flows Past Cavities With and Without Yaw," AIAA Paper No. 90-0049.

Karamcheti, K., 1955, "Sound Radiation From Rectangular Cutouts," NACA-TN-3487.

Kumar, A., 1985, "Numerical Simulation of Flow Through Scramjet Inlet Flowfield Using the 3-D Navier-Stokes Code," AIAA Paper 85-1664.

MacCormack, R. W., 1969, "The Effect of Viscosity in Hypervelocity Impact Cratering," AIAA Paper 69-354.

Plentovich, E. B., 1988, "Study of Three-Dimensional Cavity Flow at Transonic Speeds," AIAA Paper 88-2032.

Rizzeta, D. P., 1988, "Numerical Simulation of Supersonic Flow Over a Three-Dimensional Cavity," *AIAA Journal*, Vol. 26, No. 7, pp. 799–807.

Rossiter, J. E., 1966, "Wind Tunnel Experiments on the Flow Over Rectangular Cavities at Subsonic and Transonic Speeds," RAE-ARC-R&M 3438.

Shaw, L. L., 1986, "Supersonic Flow Induced Cavity Acoustics," 56th Shock and Vibration Symposium, Monterey, CA, Oct. 1985. Also, *Shock and Vibration Bulletin*, Part 2.

Srinivasan, S., 1988, "Numerical Simulation of Turbulent Three-Dimensional Cavity Flows," Ph.D. Dissertation, Old Dominion University, Norfolk, Virginia.

Stallings, R. L., and Wilcox, F. J., 1987, "Experimental Cavity Pressure Distributions at Supersonic Speeds," NASA-TP-2683.

Suhs, N. E., 1987, "Computations of Three-Dimensional Cavity Flow at Subsonic and Supersonic Mach Numbers," AIAA Paper 87-1208.

Oscillating Flow Past a Rigid Circular Cylinder: A Finite-Difference Calculation

Xuegeng Wang

Charles Dalton

Department of Mechanical Engineering,
University of Houston,
Houston, TX 77204-4814

A finite-difference study of the sinusoidally oscillating flow past a fixed circular cylinder is made using vorticity and stream function as the dependent variables. Calculations are performed for conditions which lead to both a symmetric wake and an unsymmetric wake. The Reynolds number ranges from 100 to 3000 and the Keulegan-Carpenter number ranges from 1 to 12. A hybrid differencing scheme is introduced to provide a stable for large values of the parameters. Good comparison to flow visualization results and calculated force coefficients is found. The results are given a physical interpretation for the various vortex patterns observed.

Introduction

An oscillating flow past a fixed circular cylinder has been the subject of several recent experimental and computational studies. A physical problem for which this flow is a two-dimensional model is a water wave acting on a vertical leg of an offshore platform. A knowledge of the force resulting from the interaction is important for the adequate design of offshore structures.

There have been four recent studies (Sarpkaya, 1985; Williamson, 1985; Obasaja et al., 1988; Tatsuno and Bearman, 1990) which examined the oscillating flow problem. These studies have begun to the relate the motion of the vortices to the force acting on the cylinder. In addition, the vortex motions are explained in terms of the relevant dimensionless parameters, i.e., the Reynolds number (Re) and the Keulegan-Carpenter number (KC). The Keulegan-Carpenter number is defined as the product of the maximum oscillatory velocity and the period of oscillation divided by the cylinder diameter. For a sinusoidal oscillation, KC is $2\pi a/d$, where a is the oscillation amplitude and d is the cylinder diameter. The velocity in Re is also the maximum oscillatory velocity. Sarpkaya (1985) reviewed the current state of knowledge concerning vortex formation and its relationship to the instantaneous force acting on a cylinder. He discussed two different flow regimes; KC < 8 and 8 < KC < 12. For KC < 8, the wake vortices are observed to remain symmetric and oscillate with the sinusoidal flow, with a new pair of symmetric vortices forming in each half cycle of oscillation. For 8 < KC < 12, the wake vortices become asymmetric and, as the oscillating flow continues, are swept primarily to one side of the cylinder due to the effects of induced velocity; thus a vortex street transverse to the oscillating flow is developed. Williamson (1985) also explained the transverse vortex street behavior in terms of the induced velocity generated by the individual vortices. Obasaja et al. (1988) also presented oscillating flow results for a fixed circular cylinder. Their results produced observations that agreed with Sarpkaya and Williamson regarding vortex formation and induced velocities. Tatsuno and Bearman (1990) performed flow visualization studies for oscillating flows and found "a fascinating set of flow patterns." These four flow visualization studies have provided the basis for comparison in the prediction of oscillating flows past fixed cylinders.

Baba and Miyata (1987) were the first to present a comprehensive finite-difference solution with a body-fitted coordinate system for the oscillating flow problem. They presented computational results of their analysis for Re = 1000 and KC = 5 and Re = 700 and KC = 7. The solutions showed reasonable agreement with the results expected from the discussions presented by Sarpkaya (1985) and Williamson (1985). Their Figs. 15–17 and 19 show instabilities in the vorticity contours which were also found in these results, but which we eliminated by use of a hybrid differencing scheme (to be discussed later) for the convective terms.

The only other finite-difference study which addresses the problem of oscillating flow past a fixed circular cylinder has been conducted by Murashige et al. (1989) who used an upwind MAC method. This study was a direct numerical simulation with a body-fitted coordinate system at Re = 10^4 with KC = 5, 7, and 10. Murashige et al. claim their calculations have produced the transverse vortex street at KC = 10, but it is not at all evident from the limited computational output presented that this result was obtained. In spite of this criticism of the work of Murashige et al., their study represents a significant step forward in the computation of oscillating flows past a fixed circular cylinder.

The purpose of this study is to continue the examination of the oscillating flow past a circular cylinder. We pursue numerical solutions for situations which were not studied previously. We also employ a simulation model which has not been previously applied to the oscillating flow problem.

Contributed by the Fluids Engineering Division for publication in the JOURNAL OF FLUIDS ENGINEERING. Manuscript received by the Fluids Engineering Division May 1, 1990.

Analysis

We represent the time-dependent flow of a viscous incompressible fluid past a stationary circular cylinder as a two-dimensional flow with dominant viscous stresses. There are obvious Reynolds number limitations to these assumptions; these will be addressed as the results are presented. The governing equations are the vorticity transport equation,

$$\frac{\partial \omega}{\partial t}-\frac{1}{r}\left[\frac{\partial}{\partial r}\left(\omega\frac{\partial \Psi}{\partial \theta}\right)-\frac{\partial}{\partial \theta}\left(\omega\frac{\partial \Psi}{\partial r}\right)\right]=\nu\nabla^2\omega, \tag{1}$$

and the equation relating the vorticity to the stream function,

$$\nabla^2\Psi=\omega \tag{2}$$

where

$$\nabla^2=\frac{\partial^2}{\partial r^2}+\frac{1}{r}\frac{1}{\partial r}+\frac{1}{r^2}\frac{\partial^2}{\partial \theta^2}.$$

In Eqs. (1) and (2), ω is the two-dimensional vorticity, Ψ is the two-dimensional stream function with r, θ the polar coordinates, t is time, and ν is the kinematic viscosity. The fluid velocities are found from

$$u=-\frac{1}{r}\frac{\partial \Psi}{\partial \theta} \text{ and } v=\frac{\partial \Psi}{\partial r}. \tag{3}$$

The boundary conditions on the cylinder surface are

$$\Psi=\frac{\partial \Psi}{\partial r}=0 \text{ on } r=R, \tag{4}$$

where R is the radius of the cylinder.

The far-field boundary condition for the oscillating flow is that the flow remains undisturbed as r becomes large. The far field boundary conditions are given by

$$\Psi=U_1(r-R^2/r)\sin\theta \tag{5a}$$

and

$$\omega=0 \tag{5b}$$

both as $r\rightarrow\infty$ with

$$U_1=U_m\sin(2\pi t/T),$$

where U_m is the maximum oscillatory velocity and T is the period of oscillation. The actual distance at which the far-field condition is applied depends on the Reynolds number, the elapsed time in the calculation, and the parameter, a, in the coordinate transformation to be applied.

Since the major velocity gradients in the flow appear near the cylinder surface, it is necessary to find a coordinate transformation which will concentrate the mesh spacing near the surface. This is accomplished by setting

$$r/R=e^{a\xi} \text{ and } \theta=a\eta. \tag{6}$$

In Eq. (6), a is the transformation parameter which is taken to be π for this study, and ξ and η are the transformed variables. This is the logarithmic straining approach of Braza et al. (1986). We now define $\tau=t/T$, $\mathrm{Re}=2RU_m/\nu$, $\tilde{\Psi}=\Psi/RU_m$, $\tilde{\omega}=\omega R/U_m$, $\tilde{u}=u/U_m$, $\tilde{U}_1=U_1/U_m$, and $\tilde{v}=v/U_m$. Equations (1) and (2) become

$$g(\xi)\frac{\partial \tilde{\omega}}{\partial \tau}-\frac{\partial}{\partial \xi}\left(\frac{\partial \tilde{\Psi}}{\partial \eta}\tilde{\omega}\right)+\frac{\partial}{\partial \eta}\left(\frac{\partial \tilde{\Psi}}{\partial \xi}\tilde{\omega}\right)=\frac{2}{\mathrm{Re}}\nabla^2\tilde{\omega} \tag{7}$$

and

$$\nabla^2\tilde{\Psi}=g(\xi)\tilde{\omega}, \tag{8}$$

with

$$\nabla^2=\frac{\partial^2}{\partial \xi^2}+\frac{\partial^2}{\partial \eta^2} \text{ and } g(\xi)=a^2e^{2a\xi}.$$

The velocities are given by

$$\tilde{u}=U/\sqrt{g(\xi)} \text{ and } \tilde{v}=V/\sqrt{g(\xi)}, \tag{9}$$

where

$$U=-\frac{\partial \tilde{\Psi}}{\partial \eta} \text{ and } V=\frac{\partial \tilde{\Psi}}{\partial \xi}.$$

The boundary conditions are now given by

$$\tilde{\Psi}=\frac{\partial \tilde{\Psi}}{\partial \xi}=0 \text{ on } \xi=0, \tag{10}$$

and

$$\tilde{\Psi}=2\tilde{U}_1\,sinh(a\xi_\infty)\sin(a\eta) \text{ and } \tilde{\omega}=0 \text{ at } \xi=\xi_\infty. \tag{11}$$

This now completes the system of governing equations and boundary conditions. Hereafter, we will omit the $\sim$ above the dimensionless variables and understand that we are working with dimensionless quantities.

Numerical Solution

Equation (7) will be solved by a predictor-corrector finite-difference scheme while Eq. (8) will be solved by a subroutine (FPS2H), available from the IMSL mathematical package, for solving Poisson equations. The subroutine FPS2H is based on representing the elliptic (Poisson) equation in finite-difference form using a method developed by Lynch and Rice (1978) and known as the HODIE (High Order Difference approximation with Identity Expansion) method. The resulting system of linear algebraic equations is solved using fast Fourier transform techniques (see Boisvert, 1984). This particular fast Poisson solver has the restriction that the mesh spacing is the same in the two coordinate directions. This restriction is not related to the method but is imposed by IMSL. The transformed coordinate system selected to represent the problem is convenient for the fast Poisson solver in that it is easy to accommodate the equal mesh spacing requirement. Equation (7) in finite-difference form becomes

$$\begin{aligned} g(\xi)\frac{\partial \omega_{i,j}}{\partial \tau}=&-\left(\frac{U_{i,j+1}\,\omega_{i,j+1}-U_{i,j-1}\,\omega_{i,j-1}}{2\Delta\xi}\right)\\ &-\left(\frac{V_{i+1,j}\,\omega_{i+1,j}-V_{i-1,j}\,\omega_{i-1,j}}{2\Delta\eta}\right)\\ &+\frac{2}{\mathrm{Re}}\left[\frac{\omega_{i,j+1}-2\omega_{i,j}+\omega_{i,j-1}}{\Delta\xi^2}+\frac{\omega_{i+1,j}-2\omega_{i,j}-\omega_{i-1,j}}{\Delta\eta^2}\right]. \end{aligned} \tag{12}$$

In Eq. (12), the subscripts i, j represent the i, j mesh point in the η, ξ coordinates, respectively, and the truncation error is $O(\Delta\eta^2, \Delta\xi^2)$. Note that the convective terms in Eq. (7) have been replaced by central-difference approximations. For a range of parameters, the central-difference representation is found to be adequate. However, when both Re and KC become large enough, the central-difference representation becomes inadequate and upwinding must be included to obtain a stable solution. The particular form of upwinding which is suggested is a second-order accurate scheme described by Leonard (1981). The use of the second-order upwind scheme is, however, not without disadvantage; the time step required for the method is considerably less than that required for the central-difference approximation. In order to take advantage of the benefits of both central differencing and upwinding on the nonlinear terms, a hybrid scheme evolved where central differences were used for $r \leq 1.6$ R and second-order upwinding was used for $r > 1.6\ R$. This hybrid scheme was able to utilize the relatively large time step of the central-difference approximation and retain the corrective characteristics of the second-order upwind procedure. In Eq. (12), we set

$$U_{i,j}=-\frac{\Psi_{i+1,j}-\Psi_{i-1,j}}{2\Delta\eta} \text{ and } V_{i,j}=\frac{\Psi_{i,j+1}-\Psi_{i,j-1}}{2\Delta\xi}. \tag{13}$$

Equation (12) is now written as

$$\frac{\partial \omega_{i,j}}{\partial \tau} = f_{i,j}, \tag{14}$$

where the right-hand side is divided by $g(\xi_j)$ and becomes $f_{i,j}$.

A two-step, three-level, finite-difference, predictor-corrector scheme is used. The predictor is based on the second-order Adams-Bashforth method,

$$\omega^*_{i,j} = \omega^n_{i,j} + \frac{\Delta\tau}{2}(3f^n_{i,j} - f^{n-1}_{i,j}), \tag{15}$$

where n indicates the nth time step and * refers to the predicted ω value at the $n + 1$ time step. The corrector equation is

$$\omega^{n+1}_{i,j} = \omega^n_{i,j} + \frac{\Delta\tau}{12}(5f^*_{i,j} + 8f^n_{i,j} - f^{n-1}_{i,j}). \tag{16}$$

Note that the calculation of f^* involves not only ω^* but U^* and V^* also. The corrector gives a third-order value for $\omega^{n+1}_{i,j}$. Since Eqs. (15) and (16) require information at the $(n-1)$ time step, the Euler Forward method is used to calculate the vorticity at the first time step,

$$\omega^*_{i,j} = \omega^1_{i,j} + \Delta\tau f^1_{i,j}. \tag{17}$$

The corrector is given by

$$\omega^2_{i,j} = \omega^1_{i,j} + (f^*_{i,j} + f^1_{i,j})\Delta\tau/2. \tag{18}$$

These two equations provide for second-order accuracy at the first time step.

A von Neumann linear stability analysis was performed for Eq. (12). The vorticity $\omega^n_{i,j}$ was expanded in a Fourier series as

$$\omega^n_{i,j} = \sum_k \sum_l A^n_{kl} \exp(2\pi k\hat{i}\xi_j) \exp(2\pi l\hat{i}\eta_i), \tag{19}$$

and substituted into Eq. (12). The stability of the scheme requires that the Fourier modes do not increase with time. This yields

$$\left| \left(1 + \frac{13}{12}\lambda_{kl} + \frac{5}{8}\lambda^2_{kl}\right) \pm \sqrt{\left(1 + \frac{13}{12}\lambda_{kl} + \frac{5}{8}\lambda^2_{kl}\right) - \left(\frac{5}{6}\lambda^2_{kl} + \frac{1}{3}\lambda_{kl}\right)} \right| < 2, \tag{20}$$

where

$$\lambda_{kl} = \frac{\Delta\tau}{g(\xi_j)}\left[\frac{U_{ij}\hat{i}\sin(2\pi k\Delta\xi)}{\Delta\xi} + \frac{V_{ij}\hat{i}\sin(2\pi l\Delta\eta)}{\Delta\eta} + \frac{4}{\mathrm{Re}}\left(\frac{1-\cos(2\pi k\Delta\xi)}{(\Delta\xi)^2} + \frac{1-\cos(2\pi l\Delta\eta)}{(\Delta\eta)^2}\right)\right] \tag{21}$$

Setting $\Delta\xi = \Delta\eta$ and transforming back to the physical plane yields

$$\lambda_{kl} = -\hat{i}\frac{\Delta\tau}{\Delta\tilde{r}}\left[u_{ij}\sin\left(\frac{2\pi k\Delta\tilde{r}}{a\tilde{r}_j}\right) + v_{ij}\sin\left(\frac{2\pi l\Delta\tilde{r}}{a\tilde{r}_j}\right)\right] - \frac{4\Delta\tau}{\mathrm{Re}(\Delta\tilde{r})^2}\left[2 - \cos\left(\frac{2\pi k\Delta\tilde{r}}{a\tilde{r}_j}\right) + \cos\left(\frac{2\pi l\Delta\tilde{r}}{a\tilde{r}_j}\right)\right] \tag{22}$$

where a has been previously set equal to π and $\tilde{r} = r/R$.

The mesh-size influence has been examined extensively for this solution technique as applied to the problem of the impulsively started and decelerated flow past a circular cylinder. The details and the results are given in Wang and Dalton (1991) where excellent agreement with other calculations and flow visualization results is cited. The mesh-size/time-step was conducted as follows: Four different dimensionless mesh sizes were examined to determine the appropriate mesh size for a physically correct solution at Re = 550 for an impulsive start. The mesh sizes used were $\Delta\xi = \Delta\eta = 1/32$, 1/50, 1/64, and 1/100. The solutions for 1/64 and 1/100 were the same and yielded remarkably good comparison with flow visualization and other computational results. The results from calculations for 1/50 and 1/32 showed increasingly distinct differences from the 1/64 results. Three different dimensionless time steps (0.02, 0.01, and 0.005) were used; the results were indistinguishable for a mesh spacing of 1/64. Thus, the results presented herein are exclusively for a constant mesh spacing of $\Delta\xi = \Delta\eta = 1/64$. A time step of $(t/T) = 0.001$ was chosen for compatibility with the stability analysis described by Eq. (22).

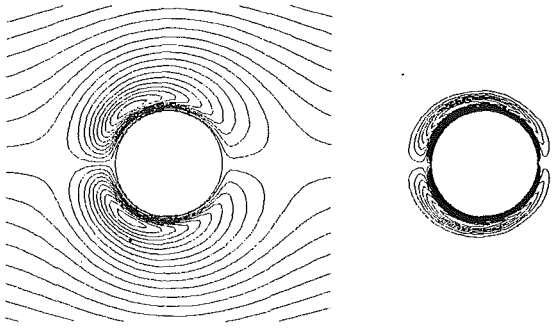

Fig. 1 Streamlines and vorticity contours for KC = 1, Re = 100 at $t/T = 5.0$

The computational effort for KC = 10 and Re = 1000 serves as an example of the time required to represent one period of oscillation. For a time step of 0.0005 and a mesh system 81 × 129, the CPU time was 2.31 seconds per time step. Thus, to complete one period of oscillation requires 2000 time steps, or 77 minutes of CPU time on a VAX 11/780.

Results for Sinusoidal Oscillations With a Symmetric Wake

For KC < 8 and Re < 1000, the wake behind a cylinder in an oscillating flow is expected to be symmetric. The initial wake vortices are symmetric and each successive pair of vortices is also symmetric. The motion of these vortices as the flow reverses is symmetric. Based on experimental studies, the controlling parameter appears to be KC because the wake behavior seems to depend more on KC than on Re. This apparently is because Re is relatively low. Flow visualization results show that the symmetric wake vortices move around the cylinder in the direction of the sinusoidally oscillating flow. The velocity of each vortex, upon flow reversal, is actually greater than the oscillatory flow velocity because each vortex has added to the oscillatory velocity, the velocity induced on it by the other vortex (or vortices). This process repeats itself cyclically as the undisturbed fluid continues to oscillate.

Results for very small KC, KC = 1 and 2, are shown at Re = 100 and 1000. The mesh sizes are $\Delta\xi = \Delta\eta = 1/64$, the mesh system is 65 × 129, the time step is $\Delta(t/T) = 0.001$ and the outside boundary is located at $\xi_\infty = 1.0$ ($r_\infty = 23R$). The same mesh size, time step and outside-boundary location are used throughout the calculations discussed in this section. The calculated streamlines and vorticity contours are given in Fig. 1 for KC = 1, Re = 100 and in Fig. 2 for KC = 1, Re = 1000, both at $t/T = 5.0$. The flow pattern is observed to change very little at like times in different periods for these conditions. From Fig. 1, at Re = 100, we find that the vorticity is restricted to a very small region around the cylinder and the flow pattern has little change after one cycle of flow oscillation. When Re is increased by a factor of 10, i.e., Re = 1000, the flow pattern, see Fig. 2, is quite similar to that at Re = 100. The vorticity is more concentrated near the cylinder and the flow pattern has little change in this case also. The Reynolds number influence on the flow pattern at such a small KC(KC = 1) is to concentrate the vorticity near the cylinder surface.

The calculated flow patterns at KC = 2, Re = 100 (not shown) are similar to those shown in Figs. 1 and 2. The vorticity

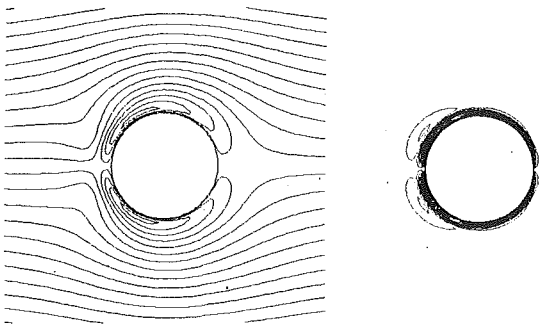

Fig. 2 Streamlines and vorticity contours for KC = 1, Re = 1000 at t/T = 5.0

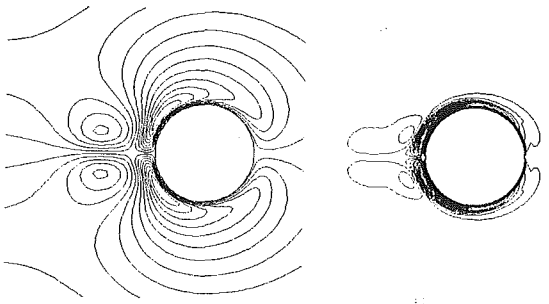

Fig. 3 Streamlines and vorticity contours for KC = 2, Re = 1000 at t/T = 2.0

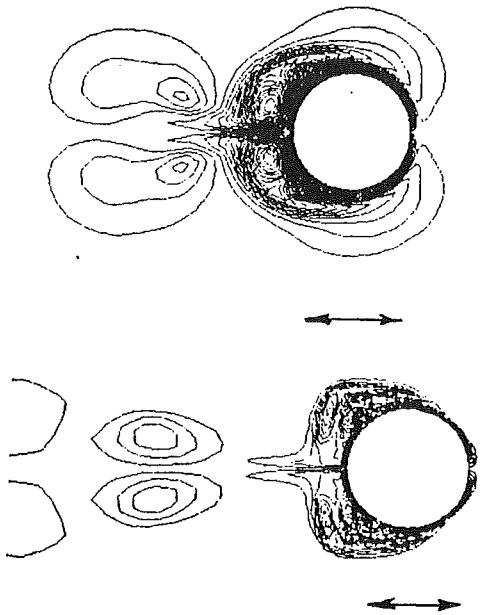

Fig. 4 Vorticity contours for KC = 5 and t/T = 2.0. (*a*) Re = 200, (*b*) Re = 1000

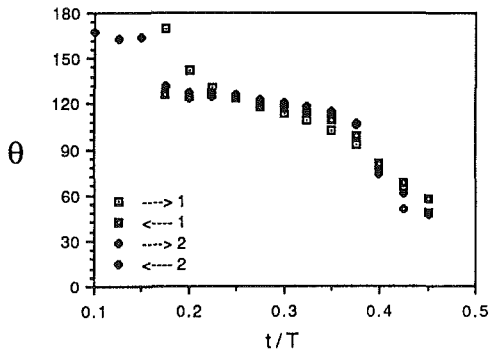

Fig. 5 Time variation of separation points at Re = 200, KC = 5

is slightly stronger and extends farther away from the surface of the cylinder, but still produces a recirculation region which is attached to the cylinder. The flow pattern also seems to repeat itself after one cycle of flow oscillation in this case. However, as we increase Re to 1000, an apparent flow-pattern change is noticed (see Fig. 3 for t/T = 2.0). The recirculation region formed in the previous half cycle moves to the opposite side of the cylinder as the freestream flow reverses and is no longer attached to the cylinder. Two pairs of vortices can clearly be seen on the streamline plots in Fig. 3. The flow patterns are basically the same for one and two cycles of flow oscillation even though the former is not shown. It is also noted that KC has a stronger influence on flow patterns at higher Re than at lower Re, see Figs. 2 and 3 for comparison.

For KC = 5, solutions are calculated for Reynolds numbers up to 1000. The same mesh sizes, time steps and outside boundary are used as in the previous oscillating flow calculations. The influences of Re can easily be observed as shown in Fig. 4. At the end of the first half cycle, a pair of vortices is formed and is attached to the surface of the cylinder. As the flow reverses its direction, the vortices generated in the previous half cycle move very quickly in the direction of the oscillating flow because the induced velocities generate motion in the same direction as the incident flow velocity. This process stimulates the growth of the new wake vortices which are much larger and stronger in the second half cycle than in the first half cycle. At the end of the first cycle, two pairs of vortices are observed in both cases. This pattern of two pairs of vortices remains for the case of Re = 200 at the end of the second cycle, see Fig. 4; only the vortices formed in the current and previous half cycles have observable influence on the flow pattern at this Reynolds number. However, for Re = 1000, viscous diffusion is much weaker and the vortices generated in the previous half cycles still have strong influences on the current flow pattern. The time variation of the separation points (zero shear stress) is also calculated at different half-cycles and plotted in Fig. 5 for the case of Re = 200. Separation starts at t/T = 0.17 and ends at t/T = 0.45 in the first half cycle and the location of these points begins to become coincident with the previous half-cycle (counted from the incident flow direction) after one complete cycle.

Comparison to the flow visualization results of Heinzer and Dalton (1969) at KC = 2π is presented by Wang and Dalton (1990) in a symposium presentation of results of this calculation procedure. The comparison of the streamlines was shown at different points through a cycle of oscillation and the agreement was excellent.

Results for Sinusoidal Oscillations With an Unsymmetric Wake

When KC reaches about 8 and Re is large enough, the wakes should be asymmetric. Perturbations of the outside boundary are applied to generate the wake asymmetry. The value of the outer-boundary stream function is increased by 0.5 percent on the upper half plane and decreased by the same amount on the lower half plane. The perturbation is applied only at the first cycle, i.e., $0 \leq t/T \leq 0.5$. For these calculations, the mesh sizes are $\Delta\xi = \Delta\eta = 1/64$, the mesh system is 81 × 129, the time step is $\Delta(t/T) = 0.0005$, and the outside boundary is given by $\xi_\infty = 1.25$ ($r_\infty = 51R$).

In the first group of cases, Re = 100 and KC = 8, 10, and 12, the results are calculated and shown in Fig. 6. For this example, several cycles of flow oscillations have been calculated. The wake vortices have moved much farther away from

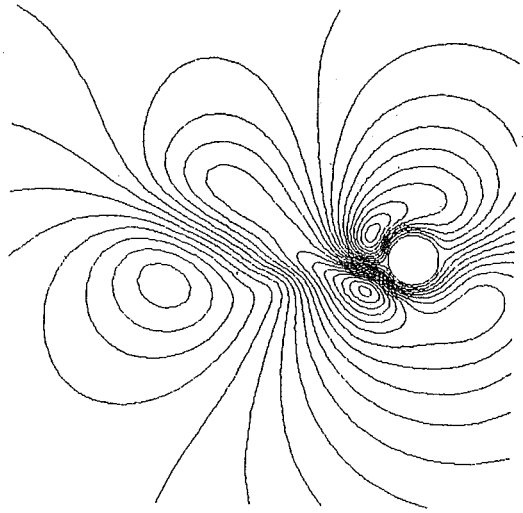

Fig. 6(*a*)

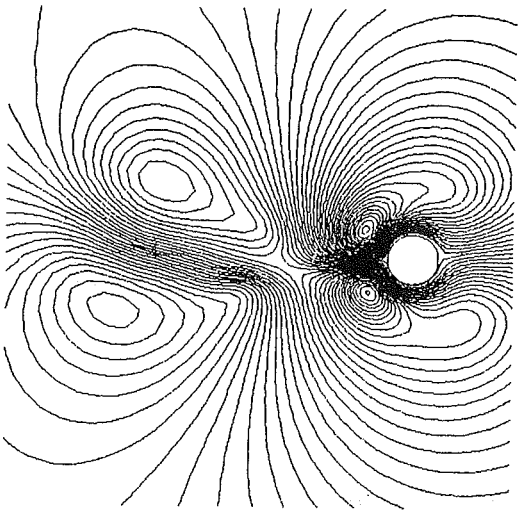

Fig. 6(*b*)

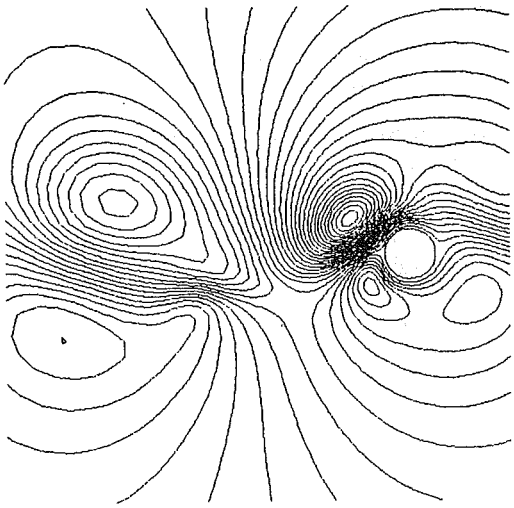

Fig. 6(*c*)

Fig. 6 Streamlines at Re = 100 at t/T = 4.0. (*a*) KC = 8, (*b*) KC = 10, (*c*) KC = 12

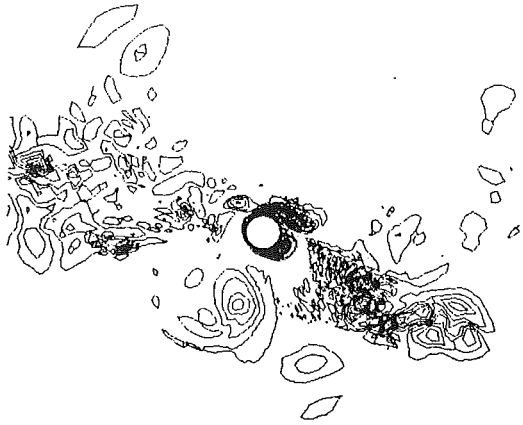

Fig. 7(*a*)

Fig. 7(*b*)

Fig. 7 Numerical instability and its elimination at Re = 1000 and KC = 10 (*a*) central differences (*b*) mixed upwind scheme

the cylinder than in the case of symmetric wakes. However, at low Re, these vortices are still located near the x-axis and the asymmetry of the wake does not seem to grow with time. The viscous diffusion is so strong that the vortices generated in the previous cycles decay quickly and the flow pattern starts to repeat itself after a few cycles of motion. It is also noted that the flow patterns shown in Fig. 6 are quite similar at this Reynolds number, the Keulegan-Carpenter number doesn't seem to have too strong an influence.

Carrying the calculations to higher values of Re and KC produced a computational difficulty as can be seen in vorticity results in Fig. 7 (a) at Re = 1000 and KC = 10. The calculated stream-function and vorticity fields produced irregular patterns; a form of vortex disintegration due to computational effects occurred. The difficulty was traced to the central-differencing technique on the convective terms (Gupta and Manohar, 1978). An upwinding scheme was employed to eliminate the problem. However, this required a smaller time step and produced a convergence failure in the second half-cycle of oscillation. A hybrid technique, utilizing a combination of both central-differencing and upwind schemes, was attempted and was found to eliminate the vortex disintegration shown in Fig. 7 (a). The vorticity results from the hybrid scheme for Re = 1000 and KC = 10 are shown in Fig. 7 (b) with a very obvious improvement in the vorticity field. The hybrid scheme retains the central-differencing technique near the cylinder surface but, for $r > 1.6R$, the second-order upwinding scheme of Leonard (1981) is used. This approach is used for all of the remaining calculations and completely eliminated the vortex disintegration problem.

The results at Re = 2000 at KC = 8 are shown in Fig. 8 at several different times. These flow patterns are quite different from the results at Re = 100 and the same KC as shown in Fig. 6. The wakes are more asymmetric and irregular than for the lower Reynolds number solutions. Vortex shedding can be identified at this Reynolds number. The vortices, shed from the cylinder, start moving away from the cylinder not only in

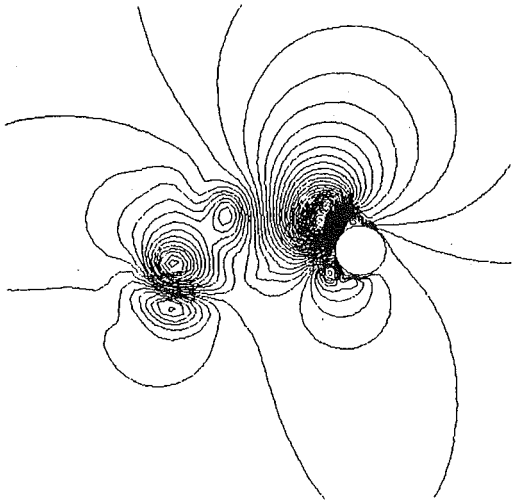

Fig. 8(*a*)

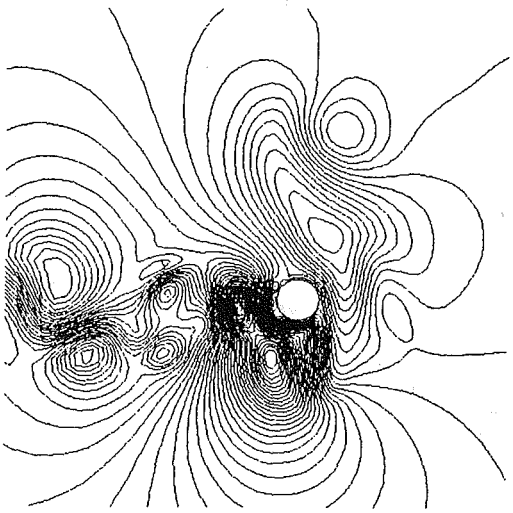

Fig. 8(*b*)

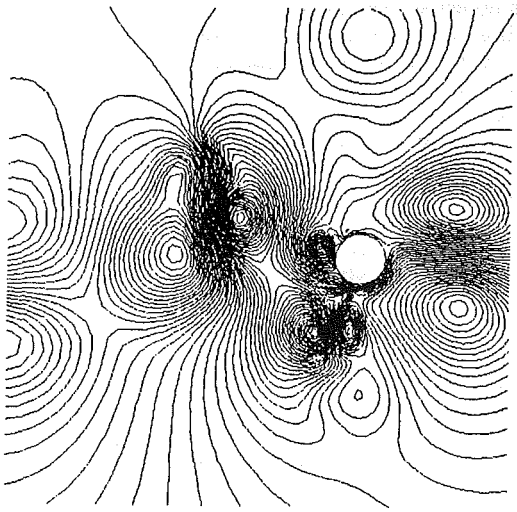

Fig. 8(*c*)

Fig. 8 Streamlines at Re = 2000 and KC = 8. (*a*) t/T = 1, (*b*) t/T = 3, and (c) t/T = 5.0

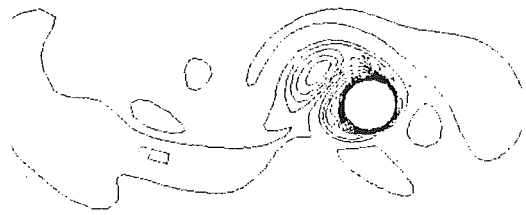

Fig. 9(*a*)

Fig. 9(*b*)

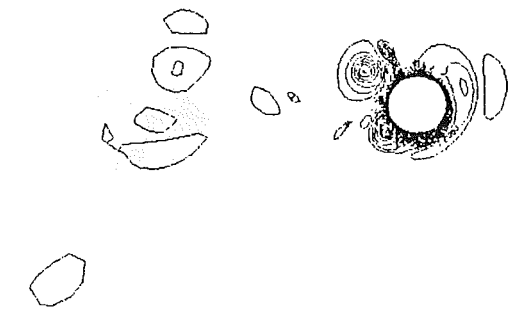

Fig. 9(*c*)

Fig. 9 Vorticity contours at KC = 10 and t/T = 2.0. (*a*) Re = 200, (*b*) Re = 1000, (*c*) Re = 3000.

the flow-oscillation direction but also in the transverse direction, see Figs. 8(*a*) through 8(*c*). The flow pattern becomes increasingly asymmetric as time increases and the newly shed vortices in each half cycle start moving in the transverse direction instead of the flow-oscillation direction.

Another case examined here is for KC = 10, where a half transverse vortex street is observed in flow visualizations for Re = 3000. The Reynolds number examples are at Re = 200, 1000, and 3000, and the calculated results are shown in Fig. 9. From Fig. 9(*a*), we find that, at this value of KC, the flow patterns do not change much from those in the previous cycle for Re ≤ 400 after a few cycles of oscillation. The shed vortices start moving away from the oscillation axis, but still stay very close to this axis. For Re = 1000, see Fig. 9(*b*), we find that the wakes becomes more asymmetric than in the cases of lower Reynolds number (Re = 200). More vortices are located on the upper and lower sides of the cylinder (off the line-of-oscillation direction) than the front and the rear of the cylinder as the Reynolds number increases. The newly formed vortices at the end of each cycle are all located on the lower half plane. For the case of Re = 3000, transverse vortex shedding becomes more apparent. When the flow reverses at the beginning of the fifth period of oscillation, a pair of vortices is found at the lower half plane and moves from left to right. This pair of vortices moves downward while continuing to move to the

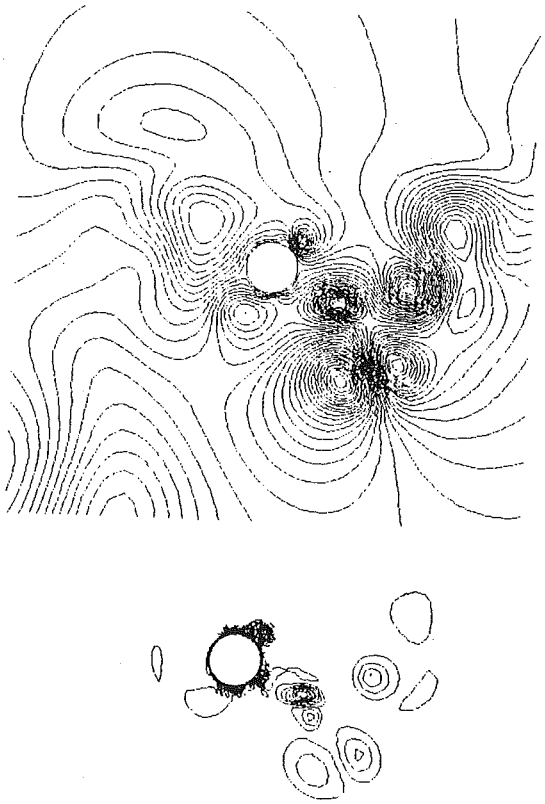

Fig. 10 Streamlines and vorticity contours at KC = 10, Re = 3000 at t/T = 4.5

right, which is seen at the right-lower corner of the vortices plot at t/T = 4.5 (see Fig. 10). This pair of vortices moves from right to left and continues to move downward when the flow reverses its direction again at the second half cycle of the fifth period of flow oscillation. At the end of the fifth period (t/T = 5), this pair of vortices has been shed transversely toward the lower side of flow oscillation. However, the half transverse vortex street is not observed for all the Reynolds numbers examined. The explanation for not reproducing the same results as seen in the limited flow visualization studies, i.e., the half transverse vortex street at Re = 3000, in the numerical simulations is as follows: (*a*). The half transverse vortex street flow pattern is extremely unstable and has been observed only under very carefully conducted experiments and this flow pattern can easily change to other type of flow patterns under very small flow perturbations (Sarpkaya, 1985). (*b*) In the case of an oscillating flow past a cylinder, the flow reverses its direction at the end of every half cycle; thus, the perturbation has a long-term influence and the flow takes a relatively longer time to converge to its physical pattern if the artificial perturbation is different from the natural perturbation.

The root-mean-square values of the tin-line forces (CF RMS) are calculated and plotted in Fig. 11. The experimental data, at β = 451 ($\beta \equiv$ Re/KC), by Bearman et al. (1979) are also shown in this figure. The β values in the present calculations are in the range of 200 to 300. From Fig. 11, it is noted that the present calculated results are in very good agreement with the experimental data by Bearman et al.

Conclusions

We have used a predictor-corrector finite-difference method to solve the unsteady vorticity transport equation with the

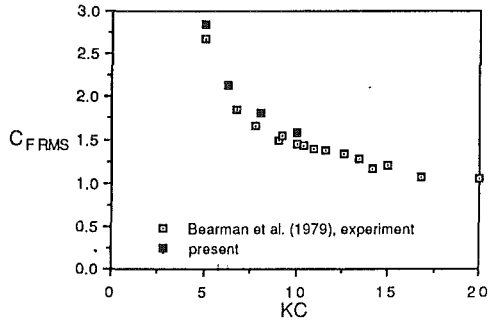

Fig. 11 Comparison of calculated and experimental $C_{F,\,RMS}$

stream-function/vorticity equation being solved by a fast Poisson solver (FPS2H) from the IMSL mathematical subroutines. Accurate solutions of the oscillating fluid flow past a fixed cylinder have been obtained. A hybrid scheme for the convective terms of the vorticity transport equation was developed to overcome an erratic and unphysical vorticity behavior. We feel that these results demonstrate the utility of this computational scheme. To find the long time behavior of the vortex pattern would require more cycles of oscillation than we have examined here. Including either three-dimensional viscous effects or even a two-dimensional wake-turbulence model greatly complicates the computational effort. Thus, it is clear that viscous solution for more than several cycles or with three-dimensional wake effects or turbulence modeling should require significantly more computational effort.

References

Baba, N., and Miyata, H., 1987, "Higher-Order Accurate Difference Solutions of Vortex Generation from a Circular Cylinder in an Oscillatory Flow," *Journal of Computational Physics*, Vol. 69, pp. 362–369.

Boisvert, R., 1984, "A Fourth-Order Accurate Fast Direct Method for the Helmholtz Equation," *Elliptic Problem Solvers II*, ed. by G. Binkhoff and A. Schoenstadt, Academic Press, pp. 35–44.

Braza, M., Chassaing, P., Ha Minh, H., 1986, "Numerical Study and Physical Analysis of the Pressure and Velocity Fields in the Near Wake of a Circular Cylinder," *Journal of Fluid Mechanics*, Vol. 165, pp. 79–130.

Heinzer, A. J., and Dalton, C., 1969, "Wake Observations for Oscillating Cylinders," ASME *Journal of Basic Engineering*, Vol. 91, pp. 850–852.

Leonard, B. P., 1981, "A Survey of Finite Differences with Upwinding for Numerical Modelling of the Incompressible Convective Diffusion Equation," *Computational Techniques in Transient and Turbulent Flow*, Pineridge Press Ltd., Vol. 2, pp. 1–35.

Lynch, R. E., and Rice, J. R., 1978, "High Accuracy Finite Difference Approximations to Solutions of Elliptic Partial Differential Equations," *Proceedings National Academy of Science*, Vol. 75, pp. 2541–2544.

Murashige, S., Kinoshita, R., and Hinatsu, M., 1989, "Direct Calculations of the Navier Stokes Equations for Forces Acting on a Cylinder in Oscillatory Flow," *Proceedings of the Eighth International Conference on Offshore Mechanics and Arctic Engineering*, the Hague, pp. 411–418.

Obasaja, E. D., Bearman, P. W., and Graham, J. M. R., 1988, "A Study of Forces, Circulation, and Vortex Patterns Around a Circular Cylinder in Oscillating Flow," *Journal of Fluid Mechanics*, Vol. 196, pp. 467–494.

Rumsey, C. L., 1988, "Details of the Computed Flowfield over a Circular Cylinder at Reynolds Number 1200," ASME JOURNAL OF FLUIDS ENGINEERING, Vol. 110, pp. 446–452.

Sarpkaya, T., 1985, "Past Progress and Outstanding Problems in Time-Dependent Flows about Ocean Structures," *Proceedings of the International Symposium on Separated Flow Around Marine Structures*, Trondheim, Norway.

Tatsuno, M., and Bearman, P. W., 1990, "A Visual Study of the Flow Around an Oscillating Circular Cylinder at Low Keulegan-Carpenter Numbers and Low Stokes Numbers," *Journal of Fluid Mechanics*, Vol. 211, pp. 157–182.

Wang, X,. and Dalton, C., 1990, "Oscillating Flow Past a Circular Cylinder," ASME International Symposium on Nonsteady Fluid Dynamics, FED-Vol. 92, Toronto, 23–31.

Wang, X., and Dalton, C., 1991, "Numerical Solutions for Impulsively Started and Decelerated Viscous Flow Past a Circular Cylinder," *International Journal for Numerical Methods in Fluids*, Vol. 12, pp. 383–400.

Williamson, C. H. K., 1985, "Sinusoidal Flow Relative to Circular Cylinders," *Journal of Fluid Mechanics*, Vol. 155, pp. 141–174.

Vortex Shedding From a Bluff Body Adjacent to a Plane Sliding Wall

M. P. Arnal

D. J. Goering

J. A. C. Humphrey

University of California at Berkeley,
Berkeley, Calif. 94720

The characteristics of the flow around a bluff body of square cross-section in contact with a solid-wall boundary are investigated numerically using a finite difference procedure. Previous studies (Taneda, 1965; Kamemoto et al., 1984) have shown qualitatively the strong influence of solid-wall boundaries on the vortex-shedding process and the formation of the vortex street downstream. In the present study three cases are investigated which correspond to flow past a square rib in a freestream, flow past a rib on a fixed wall and flow past a rib on a sliding wall. Values of the Reynolds number studied ranged from 100 to 2000, where the Reynolds number is based on the rib height, H, and bulk stream velocity, U_b. Comparisons between the sliding-wall and fixed-wall cases show that the sliding wall has a significant destabilizing effect on the recirculation region behind the rib. Results show the onset of unsteadiness at a lower Reynolds number for the sliding-wall case ($50 \leq Re_{crit} \leq 100$) than for the fixed-wall case ($Re_{crit} \geq 100$). A careful examination of the vortex-shedding process reveals similarities between the sliding-wall case and both the freestream and fixed-wall cases. At moderate Reynolds numbers ($Re \geq 250$) the sliding-wall results show that the rib periodically sheds vortices of alternating circulation in much the same manner as the rib in a freestream; as in, for example, Davis and Moore [1982]. The vortices are distributed asymmetrically downstream of the rib and are not of equal strength as in the freestream case. However, the sliding-wall case shows no tendency to develop cycle-to-cycle variations at higher Reynolds numbers, as observed in the freestream and fixed-wall cases. Thus, while the moving wall causes the flow past the rib to become unsteady at a lower Reynolds number than in the fixed-wall case, it also acts to stabilize or "lock-in" the vortex-shedding frequency. This is attributed to the additional source of positive vorticity immediately downstream of the rib on the sliding wall.

1 Introduction

The viscous flow past a two-dimensional bluff body and the resulting recirculation region behind it have been the focus of numerous investigations. These studies have been motivated by the desire to understand the fundamental physics of such flows as well as their practical importance in industry. This study shows that, as in the case of a fixed wall, the presence of a sliding wall in contact with a bluff body has a pronounced influence on the stability of the resulting flow and its dynamical characteristics.

From the practical point of view, the flow past a bluff body near a sliding wall has been of interest for several years in the automotive industry, particularly to reduce drag for more fuel-efficient vehicles. More recently, a strong interest in such flows has arisen in relation to magnetic disc-storage devices in the computer-peripherals industry. The flow past a bluff body fixed on a solid wall is also of interest to the electronics cooling industry and has been the focus of several fundamental studies on transition to turbulence and vortex generation.

In this study we investigate the two-dimensional, unsteady flow past a bluff body of square cross-section and the effects on this flow due to an adjacent wall which is either fixed or sliding at the bulk fluid velocity. A sketch of the three cases of interest is given in Fig. 1.

1.1 Previous Work. The literature relevant to the present study can be broadly divided into two groups: one concerning bluff-body flows far from any bounding walls and one concerning flows past bluff bodies near a plane wall. The latter group can be further subdivided depending on whether the plane wall is fixed or sliding with respect to the bluff body.

For those studies focussing on bluff-body flows far from any solid wall boundaries the unsteady features of the vortex-shedding process are of particular interest. The review by Berger and Wille (1972) provides much of the information and background for the current understanding of such flows. Several additional detailed studies of the vortex-shedding process behind a bluff body have appeared since the publication of that review.

Contributed by the Fluids Engineering Division for publication in the JOURNAL OF FLUIDS ENGINEERING. Manuscript received by the Fluids Engineering Division July 31, 1989.

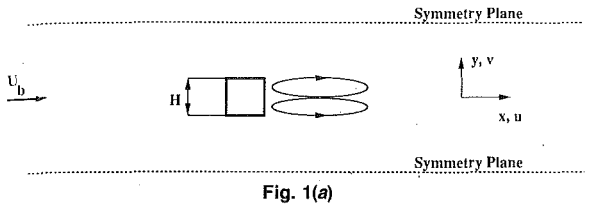

Fig. 1(*a*)

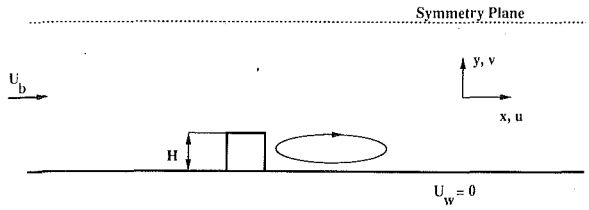

Fig. 1(*b*)

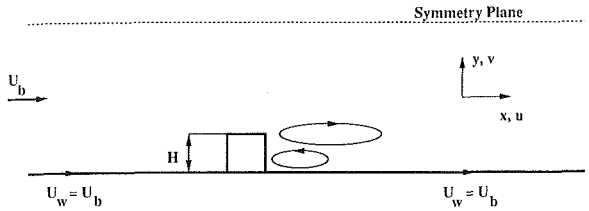

Fig. 1(*c*)

Fig. 1 Schematics of the flow configurations showing dimensions, coordinate system and velocity components. (*a*) Rib in a freestream; (*b*) rib on a fixed wall; (*c*) rib on a sliding wall.

Davis and Moore (1982) calculated the shedding process behind a rectangular cylinder in a freestream. The authors used a finite difference procedure similar to that employed in the present study to explore the effects of the Reynolds number, flow angle of attack and body aspect ratio on the shedding process. Plots of the time variation in the lift and drag on the cylinder show evidence of cycle-to-cycle variations similar to those observed in the present study. Such cycle-to-cycle variations are also observed in the experimental study of flow past rectangular cylinders by Okajima (1982). In both of these studies evidence of irregularity in the shedding process was mentioned but the origins and subsequent development of the irregularity were not discussed.

Braza et al. (1986) have computed the vortex shedding process in the near-wake region for incompressible flow past a circular cylinder using a second-order accurate velocity-pressure formulation. The authors discuss the interaction between the unsteady pressure and velocity fields for a range of Reynolds numbers, $100 \leq Re \leq 1000$, similar to that of the present study. Inter-cycle variations of the lift and drag coefficients were observed at high Reynolds numbers but were not discussed. The vortex shedding process was initiated by applying a physical perturbation, as in the free-stream case of the present study.

The influence of plane walls on vortex-shedding from bluff bodies is of special interest to this study. An extensive literature review of flows relevant to vehicle aerodynamics is given by Bearman (1980). The flows past obstacles near stationary and moving walls are discussed in detail. The majority of the studies cited are experimental, the flows being mostly turbulent, strongly three-dimensional and unsteady. Although no time-dependent data are presented, time-averaged lift and drag coefficients are provided.

Taneda (1965) reported qualitative observations of the flow around a circular cylinder towed through water past a plane wall. At Re = 170 and for small gaps between the wall and the cylinder, Taneda observed a single row of vortices shed downstream. For gaps greater than one cylinder diameter, a strong regular vortex street appeared. A related investigation of the flow past a fixed cylinder near a plane wall was carried out by Bearman and Zdravkovich (1978). Of special interest to the present study was the finding that the influence of the plane wall on the vortex shedding was to make it a more highly-tuned process as the gap was reduced. For small but non-zero gap widths the jet of fluid passing through the gap creates a flow similar to the sliding wall case of the present studies.

Kamemoto et al. (1984) visualized the flow past bluff bodies of rectangular and triangular cross-sections near fixed and sliding walls over a range of Reynolds numbers, $100 \leq Re \leq 37{,}000$. For the sliding wall case vortex shedding was observed for $Re \geq 130$ even for small gap widths. By contrast, for the fixed-wall case with a turbulent boundary layer thickness approximately equal to the bluff body dimension, vortex shedding was suppressed. At higher Reynolds numbers, the authors did not observe regular vortex shedding for either the fixed- or sliding-wall cases, although the flow visualization pictures indicate the presence of vortical structures downstream. The influence of the upstream turbulence on the vortex-shedding process and the determination of the shedding frequency were not discussed.

Sethian and Ghoniem (1988) and Ghoniem and Cagnon (1987) employed the discrete vortex method to study the dynamics of the recirculation zone behind a backward-facing step in a channel. The range of Reynolds numbers explored, based on the step height, was $50 \leq Re \leq 5000$. Long time averages of the calculations yield mean flow profiles and statistics in good qualitative agreement with existing experimental data. The authors also found evidence of eddy shedding for Reynolds numbers as low as Re = 125. This seems to suggest that flow unsteadiness can occur at much lower Reynolds numbers than indicated in experimental studies and is in agreement with the findings of the present investigations where unsteady behavior was observed in the case of a rib on a fixed or sliding wall at similar Reynolds numbers.

1.2 Objectives of This Study. While previous studies have demonstrated the influence of a fixed plane bounding wall on vortex shedding from a bluff body, no detailed investigation has been conducted on the influence of the wall's sliding motion on the shedding process. This situation is redressed in the present investigation which focusses on the influence of a flat wall on the transition to unsteady flow for the case of a bluff body in the shape of a rib of square cross-section located adjacent to the wall. In particular, the effect of wall sliding motion on the onset and development of the unsteady vortex-shedding process, and the relation of this flow to the fixed-wall case, are investigated. The time-dependent, two-dimensional flow was simulated numerically using a finite-volume differencing scheme second-order accurate in space and first-order accurate in time. The numerical procedure was tested extensively to determine the spatial and temporal accuracy which could be expected of the calculations as a function of space- and time-increments. Some of the results of this testing are discussed for completeness. The three flow configurations calculated correspond to:

1. flow past a rib in a freestream (Fig. 1(*a*));
2. flow past a rib located on a fixed wall (Fig. 1(*b*));
3. flow past a rib located on a sliding wall (Fig. 1(*c*)).

For each of these cases, calculations corresponding to Re = 100, 500, and 1000 were performed. A selection of the results is presented and discussed here The complete set of results is available in Arnal et al. (1990).

2 Governing Equations and Boundary Conditions

2.1 The Equations. The conservation equations describing the flows are the time-dependent, two-dimensional Navier-Stokes equations for a constant property fluid. They are given here in non-dimensional conservative form:

Continuity:

$$\frac{\partial u}{\partial x}+\frac{\partial v}{\partial y}=0 \tag{1}$$

Momentum:

$$\frac{\partial u}{\partial t}+\frac{\partial}{\partial x}(uu)+\frac{\partial}{\partial y}(uv)=-\frac{\partial P}{\partial x}+\frac{1}{\mathrm{Re}}\left(\frac{\partial^2 u}{\partial x^2}+\frac{\partial^2 u}{\partial y^2}\right) \tag{2}$$

$$\frac{\partial v}{\partial t}+\frac{\partial}{\partial x}(uv)+\frac{\partial}{\partial y}(vv)=-\frac{\partial P}{\partial y}+\frac{1}{\mathrm{Re}}\left(\frac{\partial^2 v}{\partial x^2}+\frac{\partial^2 v}{\partial y^2}\right) \tag{3}$$

where the following dimensionless variables are defined:

$$x=\frac{\tilde{x}}{H},\quad y=\frac{\tilde{y}}{H},\quad t=\frac{\tilde{t}U_b}{H}$$

$$u=\frac{\tilde{u}}{U_b},\quad v=\frac{\tilde{v}}{U_b},\quad P=\frac{\tilde{P}}{\rho U_b^2},\quad \mathrm{Re}=\frac{U_b H}{\nu}$$

The tilde denotes a dimensional variable and the u and v velocity components correspond to the x- and y-directions of the Cartesian coordinate system, shown in Fig. 1. The kinematic viscosity of the fluid is denoted by ν, and the dynamic pressure by P. The various terms in the equations are nondimensionalized using the fluid density, ρ, the height of the square rib, H, and U_b, the uniform bulk velocity upstream of the rib. The time, $\tilde{t}$ has been normalized with the convective time scale, $T=H/U_b$. Relative to the viscous time scale, $T_\nu=H^2/\nu$, the convective time scale was always at least two orders of magnitude smaller for the flows of interest here ($\mathrm{Re}\geq 100$).

2.2 The Boundary Conditions. The recirculating viscous flow past a bluff body poses an elliptic problem requiring boundary conditions at all the boundaries of the calculation domain. In addition, since the flows of concern are known to be time dependent beyond a critical Reynolds number, an initial condition is required. One of the following two initial conditions was employed in the present calculations: (i) a uniform velocity field with an impulsive start at $t = 0$; or, (ii) the results of a previous calculation at a different Reynolds number, which often shortened the time required to reach a steady state or steady periodic flow behavior.

At the inlet plane of the flow domain, located five rib-heights ($5H$) upstream of the rib, the velocity was prescribed for all three cases studied. This choice of entry length was fixed by the fact that larger entry lengths did not significantly change the character of the flow a distance $5H$ upstream of the rib. For all the results presented here, a uniform-flow profile was fixed at the inlet:

$$u=U_b,\quad v=0 \tag{4a}$$

The boundary conditions used at a solid wall surface were those of impermeability and no-slip:

$$v_\perp=0,\quad v_\parallel=v_{\mathrm{wall}} \tag{4b}$$

where $v_\perp$ and $v_\parallel$ are the velocities perpendicular and parallel to the wall, respectively, and v_{wall} is the speed at which the wall slides along the x axis in its own plane. These conditions apply to the wall adjacent to the rib in the wall-bounded flows, as well as to the surfaces of the rib itself. v_{wall} is set to zero on the surfaces of the rib for all cases considered. For the sliding-wall case $v_{\mathrm{wall}} = U_b$ at the lower bounding wall. For the fixed-wall case $v_{\mathrm{wall}} = 0$ at the lower bounding wall downstream of the rib and $v_{\mathrm{wall}} = 0$ or U_b at this wall upstream of the rib. Whether the lower wall boundary condition upstream of the rib is sliding or fixed has a significant impact on the resulting flow downstream of the rib. Further discussion of this point is given in the results.

For the freestream case, zero shear boundaries were specified 6 rib heights above and below the rib centerline. For the wall-bounded flows the same condition was specified along the upper boundary of the calculation domain, located 8 rib heights above the lower wall. Thus at these boundaries:

$$v=0,\quad \frac{\partial u}{\partial y}=0 \tag{4c}$$

Because of the elliptic nature of the flow fields investigated, the outlet boundary condition will have some influence on the development of the upstream flow. Two alternative conditions were used at the outlet plane in the present study. The first was to set the normal gradient of all dependent variables at the outlet plane equal to a constant ($\neq 0$). This is equivalent to requiring that the second derivative of any dependent variable be zero and results in less artificial smoothing than the fully-developed flow condition. Using this condition the numerical procedure was stable and convergent for those flows which eventually reached a steady-state result. However, for the periodic flows which are of primary interest here, this condition often led to instabilities in the numerical procedure and yielded diverging results. In addition, at the outlet plane it also caused distortion of vortices generated by the obstacle in the flow domain.

For these reasons, the open boundary condition described by Han et al. (1983) was used for the unsteady calculations. This condition allows the shear-induced flow structures created in the flow domain to pass through the exit plane without reflecting waves at that boundary. The open-boundary condition is based on the Sommerfeld radiation condition:

$$\frac{\partial \phi}{\partial t}+c\frac{\partial \phi}{\partial x}=0 \tag{5}$$

where ϕ is any dependent variable and c is the local wave speed of the ϕ wave ($c\geq 0$), calculated from the values of ϕ immediately ahead of the exit boundary. Preliminary tests were conducted to determine the influence of the outlet condition on the flow field development. The same flow (Re = 250, sliding-wall case) was calculated twice with the outlet plane located $15H$ and $25H$ downstream of the rib, respectively. The results showed that the outlet condition did not influence time-dependent quantities, such as the vortex-shedding frequency, or the spatial distribution of waves passing through the outlet plane. (The little distortion that did arise resulted from ignoring diffusive effects in this region, but it did not extend more than one rib height upstream of the exit plane.)

3 Numerical Procedure

The calculation procedure used in this study is essentially the primitive variable formulation described in LeQuere et al. (1981), modified as explained below. Following Harlow and Welch (1965), a staggered-grid system is employed in which the main grid nodes are the storage locations for pressure. Velocity components are stored at points midway between the main grid nodes. The finite difference forms of the governing equations are obtained by integrating the partial differential equations over elemental rectangular control volumes or cells. The resulting set of algebraic difference equations is then solved iteratively, using the modified, strongly-implicit (MSI) procedure of Schneider and Zedan (1981). A single iteration consists of the sequential solution of: (i) a Poisson-type equation for pressure, using the velocity field from the previous iteration; (ii) the u,v momentum equations using the new pressure field; and (iii) the pressure correction (continuity) equation, used to update the velocity field so that continuity is satisfied. This iterative scheme goes by the acronym SIMPLER (SIMPLE-Revised) and is due to Patankar (1981). For the flows of interest to this study, the method for determining the pressure field directly in the SIMPLER algorithm has represented a significant improvement over SIMPLE in terms of both computational cost and numerical stability. This is because the effectiveness of the SIMPLER solution procedure does not

depend on the goodness of the initial guess for the pressure field.

The above iteration sequence is repeated until converged velocity and pressure fields are obtained. The convergence criterion is that the least of the normalized residuals for mass and momentum, summed over all the control volumes in the grid, should be less than a prescribed value, usually 10^{-5}. For unsteady flows, this entire procedure is repeated at each time step.

The terms in the finite difference equations approximating the spatial derivatives were determined using Leonard's (1979) third-order accurate QUICK scheme for the convective terms, and the standard central-differencing scheme for the diffusion terms. The particular form of the QUICK scheme used here is due to Freitas et al. (1985) and assures the diagonal dominance of the resulting matrix of coefficients. Since the central-differencing scheme used for the diffusion terms is second-order accurate, the overall accuracy of the spatial difference terms is second order. The unsteady terms were approximated using a first-order accurate, fully-implicit backward time discretization. This discretization is stable and convergent for all time-step sizes although the accuracy of the solution degrades with increasing time-step size.

For steady flows, all the flow-field variables were stored when a converged solution was obtained. For unsteady flows, the flow-field variables were stored every 1 or 2 time scale intervals in order to follow the progress of the flow development. A few quantities were monitored at each time step in order to characterize the time-dependent nature of the flows. These included the lift and drag coefficients for the forces acting on the rib as well as the cross-stream velocity at two points in the rib wake. The drag and lift coefficients (C_D, C_L) were both determined considering the viscous and pressure forces acting on the rib. They were calculated from their respective definitions:

$$C_D = \frac{F_D}{1/2\rho U_b^2 H} \tag{6}$$

$$C_L = \frac{F_L}{1/2\rho U_b^2 H} \tag{7}$$

where F_D and F_L are the integrated drag and lift forces respectively, acting on the rib. These forces were determined from the following dimensional expressions:

$$F_D = \int_0^H (\tau_{wT}(x) + \tau_{wB}(x))dx + \int_0^H (P_U(y) - P_D(y))dy \tag{8}$$

$$F_L = \int_0^H (\tau_{wU}(y) + \tau_{wD}(y))dy + \int_0^H (P_T(x) - P_B(x))dx \tag{9}$$

where $\tau_w(x)$ is the shear stress acting on the horizontal surfaces of the rib and $\tau_w(y)$ is the shear stress acting on the vertical surfaces. Subscripts U and D denote the vertical, upstream and downstream sides of the rib, while subscripts T and B denote the horizontal, top and bottom sides. In all cases, the viscous drag was never more than a few percent of the form drag acting on the body. This was also true for the lift force, the viscous lift never being more than 3 percent of the lift due to pressure forces.

From the time variations in these quantities the frequencies of events such as the vortex-shedding process could be determined. The frequencies were non-dimensionalized using the characteristic convective time scale, $T = H/U_b$, to form a Strouhal number:

$$\mathrm{St} = \frac{fU_b}{H} \tag{10}$$

where f is the frequency of oscillation of a given quantity in the flow field. The frequencies reported in the present study were determined by averaging the frequencies of oscillation in the lift and drag coefficients and the cross-stream velocity in the rib wake. These values were always within a few percent of one another.

3.1 Testing of the Numerical Procedure. The computational procedure was extensively tested before calculating the three flow configurations of concern to this work. The results of the spatial and temporal refinement studies are reported in Arnal et al. (1990). We present here a summary of their findings.

3.1.1 Spatial Grid Refinement. The laminar flow through a two-dimensional sudden expansion was calculated for different Reynolds numbers using three different (x,y) grids (60 $\times$ 20, 90 $\times$ 30, and 120 $\times$ 40 nodes). The grids were non-uniform in the streamwise direction and uniform in the cross-stream direction. Comparisons were made with respect to the measurements and calculations performed in this flow configuration by Armaly et al. (1983), and the calculations performed by Mansour et al. (1983). Care was taken to implement the boundary conditions provided by the authors for each case.

The finest grid calculations for the case of Armaly et al. underpredicted the measured reattachment length by 10 percent at a Reynolds number Re = 400 and by 23 percent at Re = 800; where Re = HU_b/ν, H being the height of the expansion step. However, the small differences between reattachment length predictions on the successively refined grids employed with the present scheme (provided in Arnal et al.), lead us to conclude that finer grids will not account for the discrepancies observed. By contrast, very good agreement was found with respect to the reattachment length predictions of Mansour et al.

Underprediction of the sudden expansion reattachment length has been the experience of other investigators including Armaly et al. and Mansour et al. The two reasons cited most often for this are that: (*a*) Flow three-dimensionality lengthens the reattachment length. (See Armaly et al. for evidence of flow three-dimensionality for Re>400.); and, (*b*) The reattachment length varies as a result of flow unsteadiness. (Evidence for this is given in the numerical study by Ghoniem and Cagnon (1987) for Re<250, and at higher Re in the experimental work discussed by Eaton and Johnston (1981).)

Additional numerical verification was performed with respect to Case 1 of this study, corresponding to a rib in a freestream. For this, grids of the following $x-y$ sizes were employed: 40 $\times$ 45, 60 $\times$ 69 and 119 $\times$ 137. Computational costs restricted calculations on the most refined grid to a limited number of selected cases. Transient calculations were performed for Re = 500 in two ways. The first allowed the asymmetries in the numerical solution procedure to trigger the unsteady eddy shedding process observed. The second was based on a deliberately imposed perturbation as described in Section 4.1 to accelerate the appearance of eddy shedding. Briefly, this consisted in allowing the top wall of the rib to move with the flow temporarily. While the transients of these two approaches necessarily differed, the long-term unsteady features of the flow were not significantly different.

Table 1 provides a summary of the grid refinement comparisons for Case 1. It shows that the difference between the medium and most refined grid calculations was less than 16 percent for the mean drag coefficient, and less than 1 percent for the Strouhal number. Plots of time-variations of the lift and drag coefficients for the two most refined grids (not shown

Table 1 Grid refinement study for Case 1

Grid	$C_{D\,\mathrm{av}}$	$C_{D\,\mathrm{rms}}$	$C_{L\,\mathrm{rms}}$	St
119×137	2.20	0.379	1.35	0.142
60×69	1.85	0.170	0.823	0.143
40×45	1.80	0.076	0.462	0.173

here) were also in good qualitative agreement. Subsequent processing of these and other time records from which corresponding spectra were derived showed frequency differences among them no larger than those displayed by the two most refined grid calculations of the Strouhal number, listed in Table 1.

These and related considerations led us to conclude that the bulk of the calculation cases could be computed on the medium-sized grid. Numerical predictions of the reattachment length on successively refined grids using the present procedure were within 10 percent of each other for the Reynolds numbers considered. As a result of these and the additional refinement tests discussed above for Case 1, we conclude that spatial resolution on the medium-sized grid was sufficiently accurate for the purposes of this study.

3.1.2 Temporal Grid Refinement. The accuracy of the time-differencing scheme was evaluated by calculating the vortex-shedding frequency for the flow past a square obstacle in a freestream and comparing with experimental results. The Strouhal number was determined for Reynolds numbers of 100, 500, and 1000 and compared with the experiments of Davis and Moore (1982) and Okajima (1982). For the case of Re = 500 three different time-step sizes were used (0.1T, 0.05T, 0.025T), where T is the convective time scale defined earlier.

Although there is scatter in the experimental data, the numerical results using the present code were within 10 percent of the data for the Reynolds number range chosen. The scatter in the experimental data, particularly the differences between the two sets of experiments, are an indication of the difficulties that arise in trying to perform such experiments. In a related study by Gerrard (1978), concerning unsteady flows past circular cylinders, the author comments on the sensitivity of the St-Re relation to the effects of three-dimensionality and fluctuations in the flow upstream of the cylinder. Variations of 10 percent in the measured Strouhal number for a given Reynolds number were shown for the circular cylinder flow. In the present study, the predicted Strouhal number increased moderately with decreasing time step size. Time steps of 0.05T gave Strouhal numbers within a few percent of the experimental average for the three Reynolds numbers investigated. Time histories of the lift and drag coefficients were also calculated using different time step sizes.

3.1.3 Summary of Refinement Tests. As a result of the above refinement studies, time steps between 0.02T and 0.03T (corresponding to 33–50 time steps per time scale) were used for the unsteady calculations of the three flow configurations considered. Three grids were used for the spatial resolution of these flows. The results reported here for Case 1, a rib in a freestream, were obtained with a 60×69 grid, while results for the wall bounded flows (Cases 2 and 3) were obtained with either a 113×37 or 131×37 grid. In each case the grids were highly non-uniform, expanding in each direction away from the rib. The rib itself was discretized with 10×10 nodes. Use of the staggered-grid topology helps to avoid difficulties at sharp corners because velocity and pressure nodes are not located at these points. With this spatial and temporal resolution the maximum Courant number, based on the inlet velocity and spatial and temporal grid sizes, was always less than unity.

In concluding this section we note that the flow developing along the surface of a rib facing the oncoming flow generates a boundary layer of thickness δ with $\delta/H = 0\ (\mathrm{Re}^{-1/2})$. For Re = 100 and 1000, the values of δ/H are of order 0.10 and 0.03 respectively. Even with the unevenly distributed grids used, we were unable to fully resolve this boundary layer. A cumulative measure of this deficiency is obtained by comparing the mean drag and lift coefficients, as well as their rms values, for successively refined grids. Table 1 shows the results for Case 1 when Re = 500. While C_L averaged out to zero for all grids, there is a 16 percent difference between the medium and refined grid calculations of C_D. The corresponding differences in rms values of C_L and C_D are 39 percent and 55 percent, respectively. Notwithstanding this rather severe surface-integrated error measure, the tests performed on a rib in a free stream showed that all important qualitative and quantitative features of that flow were correctly predicted. The situation described has also been the experience of Davis and Moore (1982) employing a grid resolution comparable to ours. We conclude, therefore, that the bulk of the results for a rib on a sliding wall are not significantly affected by this lack of computational detail.

All our calculations were performed on the Berkeley campus CRAY-XMP computer. Computation times were typically one CPU hour for 30 time scales of flow simulation on the finest grids used. This is equivalent to two CPU minutes for every time scale of simulation, or approximately two CPU seconds required for every time step. Generally, between one and three hours of CPU time were required to obtain steady periodic vortex shedding when using the results of a previous calculation as initial conditions.

4 Results

Numerical solutions for the three flow configurations corresponding to Fig. 1 are presented in this section. Case 1 is that of a square rib in a freestream and corresponds to one of the test cases discussed in the previous section. In Case 2 the flow past a square rib adjacent to a fixed wall is considered. Case 3 is identical to Case 2 except that the wall slides in the downstream direction at the same speed as the inlet freestream fluid. Extensive calculations were performed for each of these geometries at Reynolds numbers of 100, 500, and 1000. The results show that the presence of a fixed or sliding wall has a substantial influence on the characteristics of the resulting flow. A comparison of the solutions obtained for each of these geometries is given in the discussion section.

4.1 Case 1. Rib in a Freestream. In addition to helping to establish the accuracy of our numerical calculation procedure, the freestream case provides an excellent basis for assessing the influence of the wall which is present in the other two flow configurations. For the freestream situation unsteady solutions were obtained at all three Reynolds numbers. The solutions consisted of eddy shedding behind the rib followed by vortex street development downstream. Since the main interest was in the unsteady behavior of the flow configurations, no attempt was made to find steady, symmetric low Reynolds number solutions. Consequently, an asymmetric cross-stream condition was always used to begin each of the calculations in order to trigger asymmetric eddy shedding from the rib. This was accomplished in the following way. At the beginning of the unsteady simulation which was carried out at Re = 500, the symmetric flow field was perturbed by allowing the top wall of the rib to slide with the flow temporarily. This condition was maintained for five time scales. The resulting unsteady asymmetric flow was then used as the starting field condition for the calculations at Re = 100 and 1000.

Time histories of the lift and drag coefficients and their Fourier transforms are presented in Figs. 2 and 3, respectively. The lift and drag time records for Re = 100 show that the solution approaches a periodic shedding cycle after the initial transients die out at about 20 time scales. The temporal integration was terminated at 60 time scales and a plot of the instantaneous vorticity field at that point in time is shown in Fig. 4(*a*). This figure shows a wake which develops symmetrically in the downstream direction, with the structures originating from the top and bottom of the rib being out of phase by exactly one-half of a shedding cycle.

The steady limit cycle to which the Re = 100 solution converges consists of the shedding of one pair of eddies from the

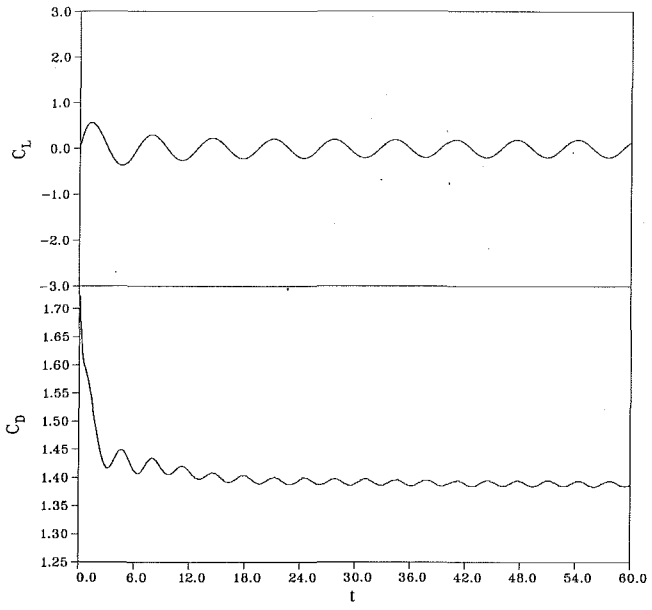

Fig. 2(*a*)

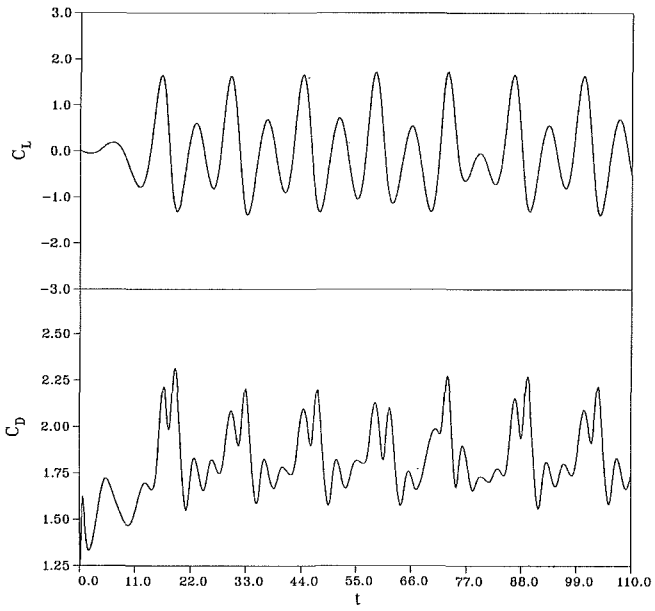

Fig. 2(*b*)

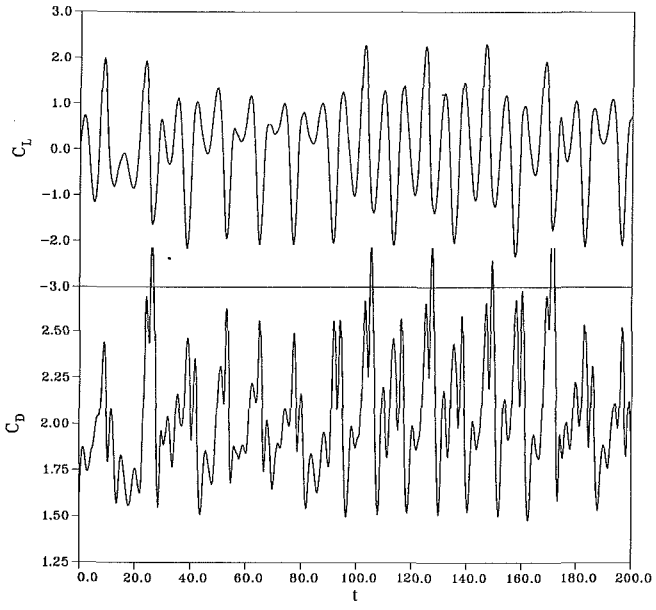

Fig. 2(*c*)

Fig. 2 Case 1: Flow past a rib in a freestream. Unsteady lift and drag coefficients for (*a*) Re = 100, (*b*) Re = 500, (*c*) Re = 1000.

rib. The base shedding frequency can be obtained by measuring the frequency of the lift oscillation. It is apparent from Fig. 2(*a*) that the drag coefficient oscillates at twice the frequency of the lift coefficient. This is explained by the fact that the drag on the rib is not sensitive to the asymmetry of the shedding process and, therefore, goes through a full cycle each time one eddy is shed. The lift, however, completes a full cycle only after a pair of eddies has been shed. The Fourier transform of each of these time histories consists of a single dominant peak at a Strouhal number of 0.07 for the drag and 0.14 for the lift.

Lift and drag histories for Re = 500 are presented in Fig. 2(*b*). At this Reynolds number the time histories are no longer purely sinusoidal but the base shedding period is still discernible as the distance between local maxima or minima in the lift coefficient record. The records now contain oscillations at frequencies other than the harmonics and subharmonics of the base shedding frequency. Corresponding Fourier transforms of the lift and drag records are shown in Fig. 3(*a*). The large peak in the lift spectrum corresponds to the base shedding frequency of 0.143. A second peak is located at one-half of this value and corresponds to the inter-cycle variation which is apparent in the time history of the lift. The spectrum of the drag coefficient shows a peak at twice the base frequency. This peak corresponds to single eddies leaving the rib. The dominant peak in the drag spectrum is at one half of the base shedding frequency. This low frequency peak is absent from the drag signal at a Re = 100.

An interesting feature of the time histories obtained at Re = 500 is that they do not reach a steady periodic cycle during the length of the temporal integration performed. In contrast with the solution obtained for Re = 100, the cycle-to-cycle variations do not decay completely at Re = 500. Figure 4(*b*) shows instantaneous vorticity profiles at 110 time scales. The development of the wake displayed in the figure is no longer symmetric. Based on the current data it is difficult to say whether this is due to very long transients or some more complicated behavior of the flow as the Reynolds number is increased. Similar behavior is evident in some of the numerical data presented by Davis and Moore. We also note that for the similar flow past a circular cylinder, the periodic vortex shedding breaks down for Re > 200.

Figures 2(*c*) and 3(*b*) show the time histories and spectra for the solution obtained at Re = 1000. These time histories display a behavior similar to that observed at Re = 500. Even though the temporal integration was longer for this case, the solution still does not converge to a fully periodic shedding cycle. Cycle-to-cycle variations arise in the lift time history. Relative minima occur in the lift record when eddies are shed from the top of the rib and, conversely, relative maxima occur when they are shed from the bottom. Vorticity contours at $t = 180$ are shown in Fig. 4(*c*). Examination of these contours reveals that much of the cycle to cycle variation is due to variations in the strengths of the eddies that are shed; relatively larger maxima or minima corresponding to larger eddies.

Careful examination of the time histories at Re = 1000 in Fig. 2(*c*) reveals some very interesting patterns. First, the flow seems to settle down by $t = 100$ to display a pattern with a wavelength three times the shedding cycle. This behavior is repeated twice in almost identical fashion. The first cycle occurs between $t = 100$ and $t = 122$ while the second occurs between $t = 122$ and $t = 144$. Streamline data show a slight waviness in the wake during this portion of the time integration with a

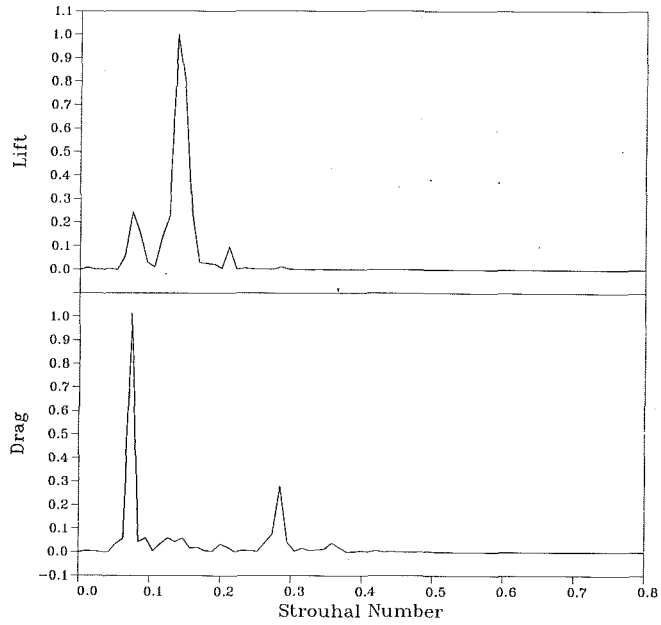

Fig. 3(*a*)

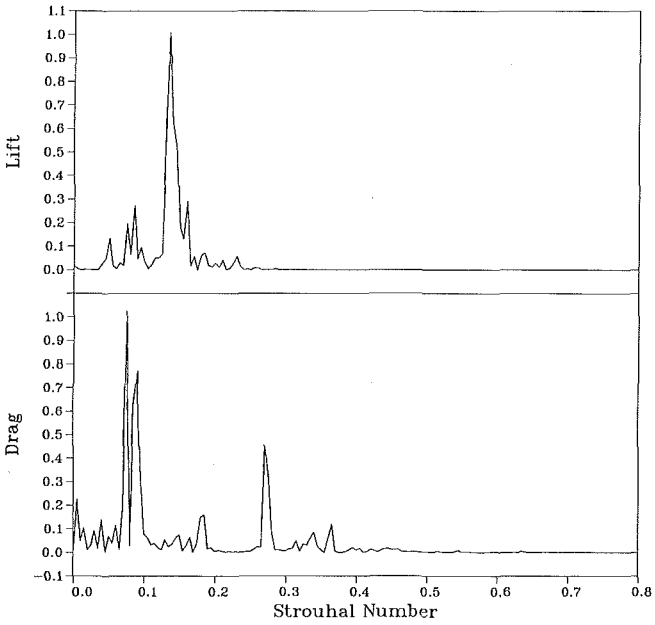

Fig. 3(*b*)

Fig. 3 Case 1: Flow past a rib in a freestream. Spectra for lift and drag time histories, (*a*) Re = 500, (*b*) Re = 1000.

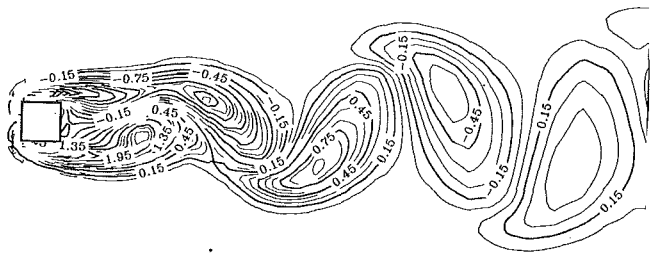

Fig. 4(*a*)

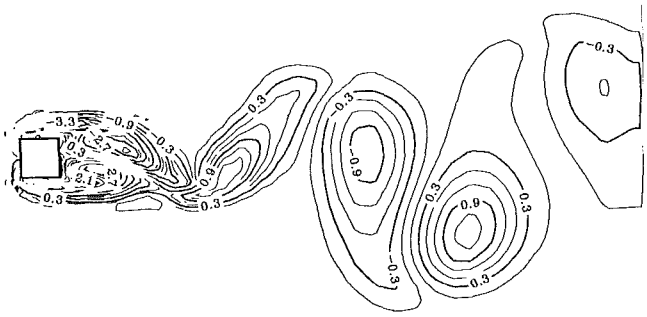

Fig. 4(*b*)

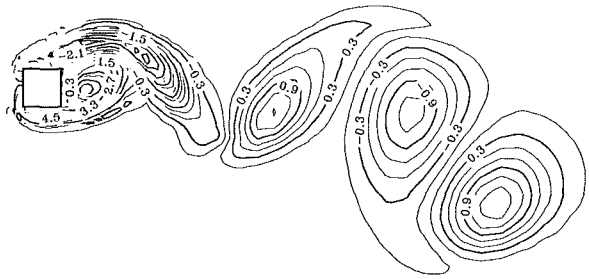

Fig. 4(*c*)

Fig. 4 Case 1: Flow past a rib in a freestream. Instantaneous vorticity contours for (*a*) Re = 100, *t* = 60; (*b*) Re = 500, *t* = 110; (*c*) Re = 1000, *t* = 180.

wavelength of three shedding cycles. Another interesting feature is that the behavior of the time records starting at $t = 20$ appears to be repeated starting at $t = 165$. The correspondence is not exact, and from the present data it is not possible to say whether the entire history between $t = 20$ and 165 will be repeated or whether similarity will break down. Of course, in a real flow situation the vortex shedding process may be affected by three-dimensionality at this Reynolds number as well as free-stream turbulence which might be present. Neither of these effects can be reproduced in the present two-dimensional calculations.

4.2 Case 2. Rib on a Fixed Wall. The geometry which corresponds to this case is shown in Fig. 1(*b*). All results presented here were obtained with the wall fixed downstream of the rib (e.g., $v_{wall} = 0$). Upstream of the rib, two different boundary conditions were used at the wall. In one case (Case 2A) the upstream wall was allowed to slide with the incoming flow (e.g., $v_{wall} = U_b$), whereas in the other case (Case 2B) the upstream wall was fixed. At the lowest Reynolds number investigated (Re = 100), a steady solution was obtained for both geometries by marching in time until the transient behavior died away. Following this development period, no changes in the flow field variables were observed. Figures 5(*a*) and 5(*b*) show streamline plots of the results for Case 2A and 2B, respectively. In Fig. 5(*a*), the flow field is dominated by a single large eddy behind the rib, which is 30.8 rib heights in length. Figure 5(*b*) reveals a much smaller recirculation region for Case 2B. In comparing the two flow fields, it is also apparent that the upstream boundary layer separation and resulting recirculation bubble upstream of the rib in Case 2B is absent from the flow field in Case 2A. The absence of the upstream separation in Case 2A results in increased upward momentum of the fluid as it travels over the rib and induces the larger downstream recirculation shown in Fig. 5(*a*). An additional, very small, counter-clockwise rotating eddy was also predicted near the downstream corner of the rib for both cases. This eddy is induced by the larger one which forms the main recirculation zone behind the rib.

At Re = 500 calculations were again performed with both sliding and fixed walls upstream of the rib. The steady solutions with Re = 100 were used as initial conditions. Marching in time did not produce steady solutions for either case at this Reynolds number. Instead, in both cases a time-varying flow developed consisting of structures periodically shed from behind the rib and which moved downstream. While this was true for both Case 2A and 2B, further examination of the data revealed that the unsteadiness was very weak for Case 2B and only minor

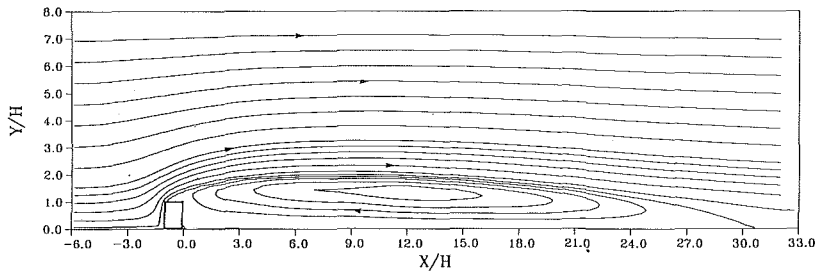

Fig. 5(*a*) Case 2A: Flow past a rib on a wall which is fixed downstream and sliding upstream. Streamlines for steady flow at Re = 100.

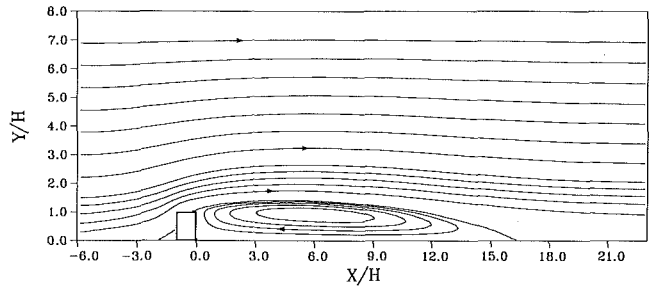

Fig. 5(*b*) Case 2B: Flow past a rib on a wall which is fixed upstream and downstream. Streamlines for steady flow at Re = 100.

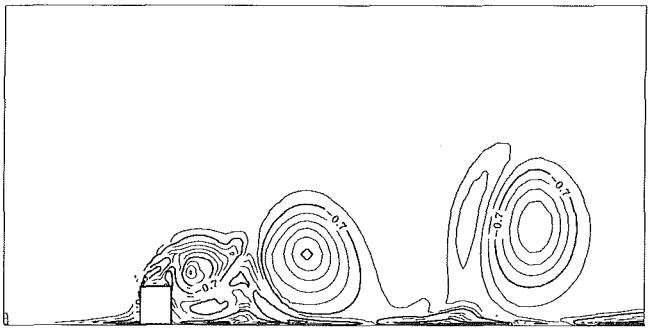

Fig. 6 Case 2: Flow past a rib on a fixed wall. Instantaneous vorticity contours for the unsteady flow case, Re = 500

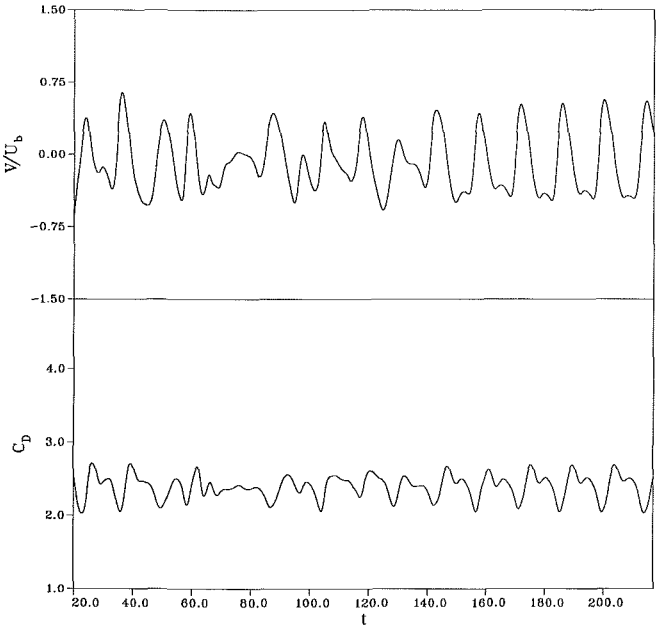

Fig. 7 Case 2: Flow past a rib on a fixed wall. Drag coefficient and cross-stream velocity fluctuations, Re = 500.

fluctuations in the lift and drag (on the order of 1 percent) were produced for this geometry. For Case 2A, much stronger unsteady fluctuations were observed. The different behavior is due to the existence of the upstream boundary layer separation and recirculation bubble caused by the fixed upstream wall in Case 2B. As with the Re = 100 results, upstream recirculation tends to reduce the upward momentum of the fluid as it passes the rib, thereby diminishing the disturbance caused by the rib. Upstream recirculation bubbles are not found in Case 1, Case 3, or Case 2A. In order to facilitate comparison of all the results, the remainder of this section and following sections will focus on Case 2A (henceforth referred to as Case 2) because of its greater similarity to Case 1 and Case 3.

A plot of the instantaneous vorticity contours for Case 2 with Re = 500 is shown in Fig. 6 for t = 46.1. In the figure, two recirculating eddies (with negative vorticity) are clearly seen downstream of the rib. A third eddy with the same sense of circulation grows on top of the rib and moves behind it. Between this third vortex and the one previously shed is a weaker counter-rotating (positive) vortex which also moves downstream. An earlier positive vortex can also be seen between the two large negative vortices downstream of the rib. It should be noted that the positive vortices are always much weaker than the dominant negative vortices generated by shearing of the flow by the rib.

A very long "transient" period in which the vortex shedding occurred aperiodically was observed for Re = 500 and Re = 1000. In Fig. 7 the fluctuations in the rib drag coefficient are plotted for Re = 500. The figure also shows the time variation of the cross-stream velocity component very close to the downstream upper corner of the rib. In both plots the oscillations settle down to a periodic variation after approximately 120 time scales of elapsed time. However, even after this transient, some cycle to cycle variations occur, although the variations are small.

The time evolution of the flow at Re = 1000 is similar to that at Re = 500, with some noteworthy differences. First, the amplitude of the fluctuations is larger in the time histories of both the velocity and drag coefficient for the higher Reynolds number flow. Second, for this case there is an even longer transient time-period of at least 170 time scales before the fluctuations start to appear periodic. However, although the base frequency was established at that point in time, higher frequency variations continued to occur for the entire length of the simulation (nearly 240 time scales).

The Fourier transforms of the drag coefficient and velocity fluctuations for Re = 500 are shown in Fig. 8. In this figure only the period following the initial transient time ($t > 140$) was transformed. The transform of the entire time sequence shows a large number of peaks in addition to the dominant frequencies.

For the higher Reynolds number flow, the cycle-to-cycle variations which occur yield a Fourier transform which shows many more peaks than the Re = 500 case. Even when the long initial transient region is not included and a regular base frequency can be picked out, the transform shows secondary peaks at a variety of frequencies.

4.3 Case 3. Rib on a Sliding Wall. The flow past a rib on a sliding wall was calculated for eight different Reynolds numbers in the range $50 \leq Re \leq 2000$. The results for $Re = 100$, 500 and 1000 are presented in this section. They were chosen for comparison with the two cases presented previously and, among them, they illustrate all the basic features which arise at higher Reynolds numbers.

Singularities in the velocity field occur on the sliding wall where it meets with the upstream and downstream walls of the rib. In the regions very close the singularities, the flow is diffusion dominated and in a low Reynolds number (creeping-flow) regime. A closed-form solution can be obtained for the biharmonic equation which is the governing equation for the stream function of this flow. In the present investigation, the singularities presented no stability problems for the numerical method employed. (This is due to the use of a staggered grid methodology which avoids the singular points at the base of the rib.) The streamline pattern and flow field solution approached those of the low Reynolds number closed-form solution in these regions.

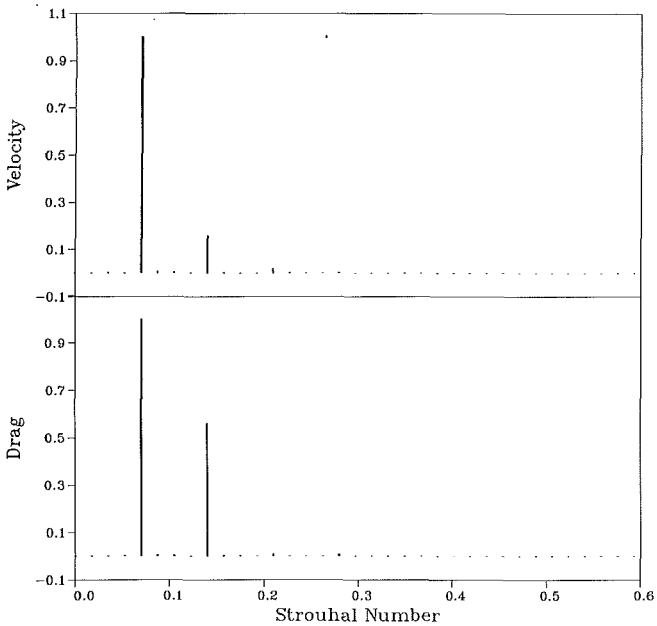

Fig. 8 Case 2: Flow past a rib on a fixed wall. Spectra for drag and velocity time histories, Re = 500. Transformation of the time sequence following the initial transient period.

At the lowest Reynolds number investigated ($Re = 50$) a steady state solution was obtained for this configuration. However, for all higher Reynolds numbers investigated, $Re \geq 100$, the solutions obtained were unsteady in nature. The unsteadiness which occurred at $Re = 100$ was markedly different from that which occurred at $Re = 500$ and $Re = 1000$. Unlike the higher Reynolds number flows, no periodic vortex shedding occurred. Instead, after the initial transients died away, a "quasi-steady" solution developed in which two vortices of opposite sign remained attached to the rib. Although no vortex shedding occurred, some small amplitude waviness was present in the wake region. Because this waviness was not visible in the plots of the flow field, and because no vortex shedding occurred, this case is termed "quasi-steady." In contrast, at lower Reynolds numbers ($Re \leq 50$) a truly steady solution developed in which no unsteadiness was observed.

The main features of the $Re = 100$ flow are illustrated in Figs. 9(*a*) and 9(*b*) which show streamlines and vorticity contours for this case. A uniform velocity profile equal in speed to the wall speed (U_b) impinges on the rib and is forced over it. This induces a clockwise rotating (negative) recirculation region behind the rib. The sliding wall behind the rib induces a second counter-rotating (positive) recirculation zone immediately above this wall. The result is for a recirculating flow,

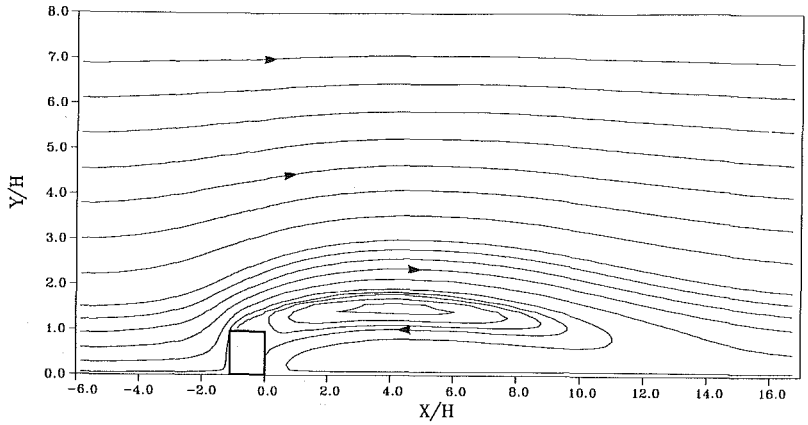

Fig. 9(*a*) Case 3: Flow past a rib on a sliding wall. Streamlines for quasi-steady flow at Re = 100

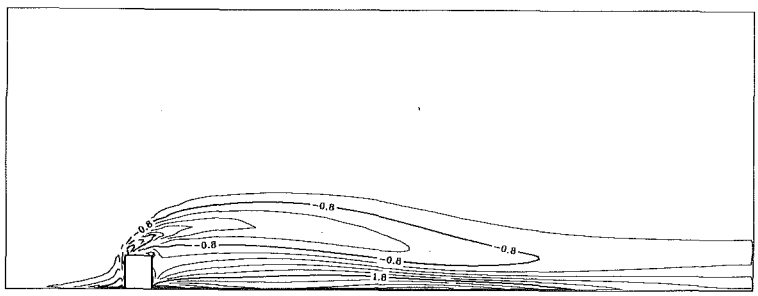

Fig. 9(*b*) Case 3: Flow past a rib on a sliding wall. Vorticity contours for quasi-steady flow at Re = 100

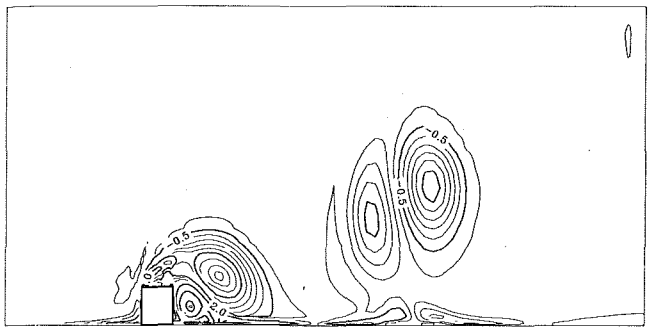

Fig. 10 Case 3: Flow past a rib on a sliding wall. Instantaneous vorticity contours for the unsteady flow case, Re = 500

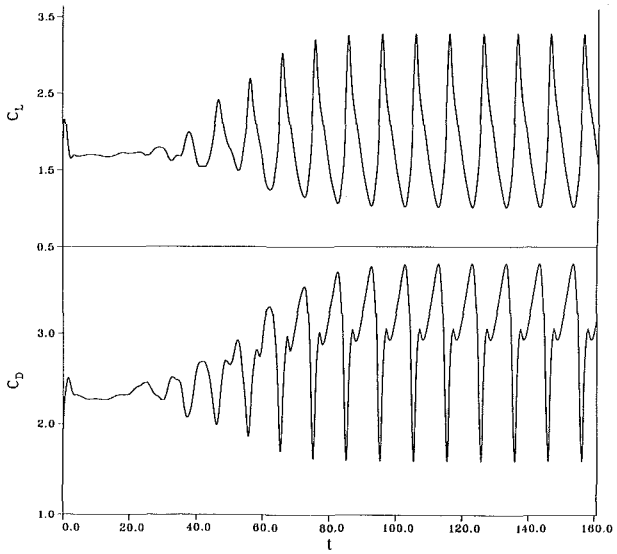

Fig. 11 Case 3: Flow past a rib on a sliding wall. Unsteady lift and drag coefficients for Re = 500. Initial condition for the calculation is the quasi-steady solution at Re = 100.

consisting of two distorted counter-rotating vortices, to develop behind the rib. A smaller, barely visible positive vortex also appeared in the steady fixed-wall calculations at Re = 100; see Fig. 5(*a*). The sliding wall condition acts to lengthen and strengthen this secondary vortex under the primary, negative vortex, quite considerably.

For flows with Re ≥ 250, the flow behavior was distinctly different from that at Re = 100 downstream of the obstacle. Periodic shedding of positive and negative vortices occurred. A typical plot of the instantaneous vorticity contours is shown in Fig. 10. The vortex pair developing behind the rib is clearly visible. The large peak in positive vorticity (+7.5) which occurs in this configuration is much stronger than that which occurs in Case 2. A second vortex pair which was shed earlier has moved downstream and away from the wall.

Figure 11 illustrates the periodic behavior of the lift and drag coefficients due to the forces acting on the rib at Re = 500. In this case the flow was started with the quasi-steady solution for Re = 100 and the vortex shedding was allowed to develop. The first 50 time scales show evidence of initial transients, but the regular periodicity of both the lift and drag are well established after $t = 80$. This is in contrast with the situation in Case 2 where regular periodicity without cycle-to-cycle variations did not occur even after 200 time scales. The periodicity of the lift and drag coefficients is illustrated in Fig. 12 which shows their Fourier transforms. The secondary peaks in the plots are higher harmonics of a single base frequency which has been identified as the vortex-pair shedding frequency.

Calculations of the drag and lift coefficients for Re = 1000, using the steady periodic solution at Re = 250 as the initial

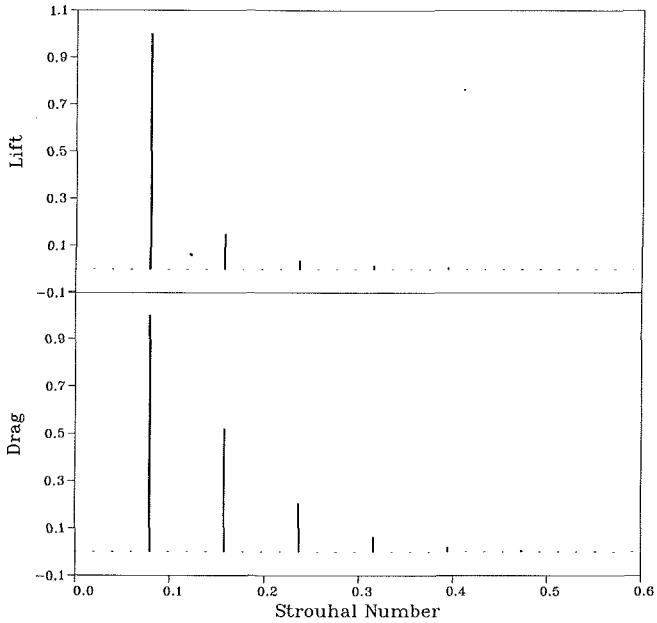

Fig. 12 Case 3: Flow past a rib on a sliding wall. Spectra for lift and drag time histories, Re = 500.

condition, yielded steady periodic behavior by $t \approx 20$. The corresponding spectra were essentially identical to those shown in Fig. 12.

4.4 Comparison of the Cases. In this section the vortex-shedding process in the sliding-wall case is described and compared with the other two flow configurations. The shedding process can be identified with one period in the drag cycle, starting and ending at the point of maximum drag. A comparison of the lift and drag in Fig. 11 shows that the peak lift occurs when the drag on the rib is a minimum and vice versa. The periodicity of the drag coefficient is not a simple sine curve even at low Reynolds numbers. Between the minimum and maximum values of C_D a localized maximum and minimum occur. The local maxima become more pronounced at higher Reynolds numbers.

Figure 13(*a*) shows a vortex pair immediately behind the rib at the instant of maximum drag in the drag coefficient cycle, also corresponding to the largest streamwise pressure drop across the rib. Fluid impinging on the front of the rib is forced over it and the attached recirculation zone. This creates a region of low pressure directly behind the rib where the two vortices are located. The vortices attain their maximum strength (+7.0, −5.5) and are close to their maximum size before being shed. A pair of vortices shed earlier can be seen moving downstream and away from the wall. The vortices are shed in pairs and are of opposite sign and approximately equal strength.

In Fig. 13(*b*), four time scales later in the cycle, the negative vortex has been shed while a new negative vortex grows on top of the rib. The positive vortex behind the rib has reached its maximum size before being shed. The negative vortex is generated at the front top corner of the rib and moves behind the rib as it grows. This front corner of the rib and the front of the rib itself are the primary sources of negative vorticity in the flow. The source of positive vorticity is the lower downstream corner of the rib near the sliding wall. The situation shown in the figure corresponds to the minimum in the drag cycle. Fluid flowing over the rib is forced down behind the rib by the growing vortex on the rib top. This raises the pressure behind the rib and, as a result, lowers the drag force acting on it.

At this point in the cycle, just after being shed from behind the rib, the vortices move downstream at about 30 percent of

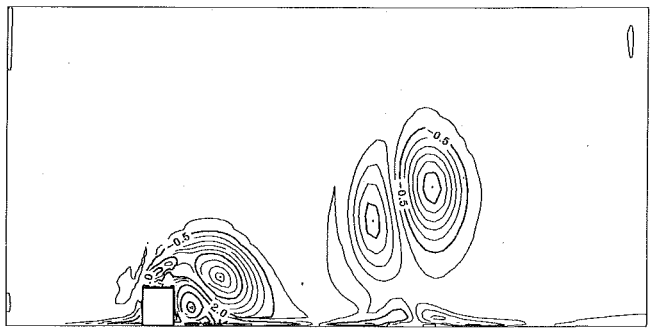

Fig. 13(*a*) Case 3: Flow past a rib on a sliding wall. Instantaneous vorticity contours illustrating vortex shedding sequence, $t = 42$. Re = 500. Configuration at the time of maximum drag.

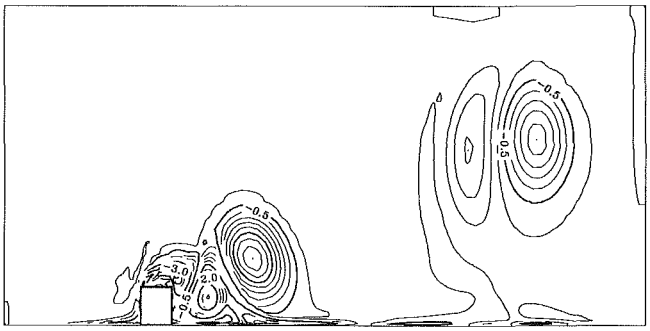

Fig. 13(*b*) Case 3: Flow past a rib on a sliding wall. Instantaneous vorticity contours illustrating vortex shedding sequence, $t = 46$. Re = 500. Configuration at the time of minimum drag.

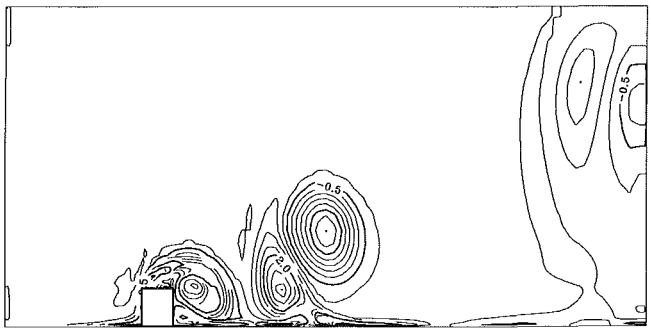

Fig. 13(*c*) Case 3: Flow past a rib on a sliding wall. Instantaneous vorticity contours illustrating vortex shedding sequence, $t = 50$. Re = 500. Configuration at the time of the local minimum in drag cycle.

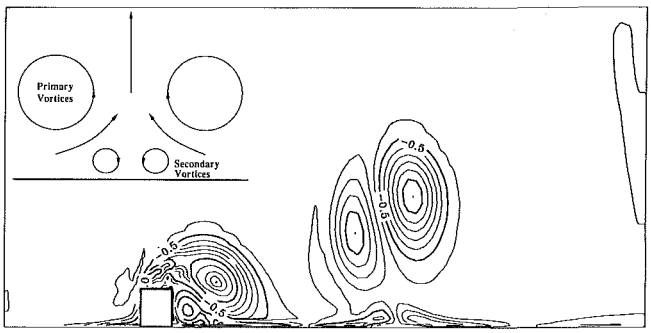

Fig. 13(*d*) Case 3: Flow past a rib on a sliding wall. Instantaneous vorticity contours illustrating vortex shedding sequence, $t = 54$. Re = 500. Configuration just prior to maximum drag.

the bulk fluid velocity ($0.3U_b$). As they move downstream of the rib and into the freestream their velocity gradually increases to the freestream velocity (U_b). For example, the vortex pair which was shed earlier is approximately 10 rib heights downstream and already moving at the freestream velocity.

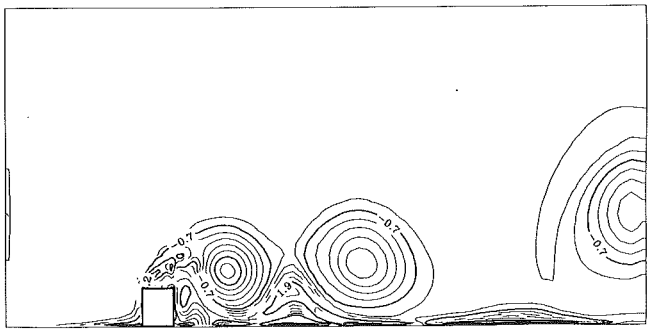

Fig. 14 Case 2: Flow past a rib on a fixed wall. Instantaneous vorticity contours for the unsteady flow case, Re = 500

As the vortices grow at their locations behind the rib, the pressure on the downstream side of the rib gradually decreases as the fluid upstream is forced over the rib and this vortex pair. A competing effect, which acts to raise the downstream pressure, is illustrated in Fig. 13(*c*). As the positive vortex closest to the sliding wall grows, a jet forms between it and the primary negative vortex. This jet acts to push fluid back towards the rib and raise the pressure, and is responsible for the local minimum in the drag cycle. However, as the two vortices continue to grow the jet is forced up into the freestream, allowing the pressure to decrease and the drag to increase.

In the final illustration of the shedding cycle, Fig. 13(*d*), the new vortex pair grows behind the rib while the pair which has just been shed moves downstream and away from the wall. The pair moves away from the wall because of the mutually induced motion of one vortex upon the other. The flow between vortices in a vortex pair is away from the wall and intense. It is responsible for inducing a secondary pair of counter-rotating vortices near the wall and directly underneath the primary vortex pair. The motion of the vortices away from the wall and the secondary, induced vortices are illustrated in the insert in Fig. 13(*d*). The behavior of the counter-rotating vortex pair downstream of the rib is similar to that found by Doligalski and Walker (1984) in their studies of induced boundary layers by convected vortices near a wall. In particular, these authors found that for all convection rates of a vortex near a fixed wall, an induced boundary layer will grow which eventually erupts from the wall in the region behind the vortex. In the present study a similar effect was observed in the region between the vortex pair near the sliding wall after the pair had been shed. This is the region where the induced vortices near the wall actually develop. In addition, a corresponding stagnation region occurs ahead and behind the vortex pair. Similar separation and stagnation regions also appear between the vortices which are shed in the fixed wall case.

The shedding cycle for Case 2, where the wall is fixed behind the rib instead of sliding, differs in a couple of important aspects from the sliding-wall case. First, the positive vortex which forms in the downstream lower corner of the rib is much weaker when the downstream wall is fixed than when it is moving. The formation of the positive vortex behind the rib in the fixed-wall case is dependent on the motion induced by the strong negative vortex in the downstream corner. Without the sliding wall as an additional source of positive vorticity, the positive vortex which is formed is much weaker and dies out more quickly downstream. Figure 14 shows the vorticity contours at Re = 500 for Case 2 with the fixed wall. The region of positive vorticity near the downstream corner of the rib can be compared with the sliding wall case in Fig. 13(*c*). In Fig. 13(*d*), the maximum vorticity contour just behind the rib is +7, for the sliding-wall case. The corresponding maximum vorticity contour in Fig. 14 is +1.8, just behind the rib near the fixed bottom wall.

This figure also illustrates the second major difference between the two wall-bounded cases. Once the vortices are shed in Case 2, the much weaker positive vortex does not induce much of an upward motion on the stronger, negative vortex as it moves downstream. As a result, this vortex remains relatively close to the wall and essentially "rolls" downstream as time progresses. As it moves downstream it picks up speed but only reaches 75 percent of the bulk velocity ($0.75U_b$). This is in contrast to the sliding-wall situation where the vortices attain the freestream velocity approximately 10 rib heights downstream of the rib. This effect of the fixed wall can be explained in the following way. As the negative vortex moves downstream, it remains in the wake of the rib longer without the upward motion induced by the positive vortex. Further downstream a boundary layer type flow will develop. In both regions the fluid surrounding the vortex moves slower than the bulk velocity and acts to retard the vortex.

The effect of the fixed wall can also be understood in terms of the influence of image vortices reflected at the wall. Image vortices are used in inviscid flow theory to enforce the zero normal velocity condition at a wall in potential flow, when studying the behavior of vortices near walls. In the fixed-wall case, a positive image vortex acts to retard the downstream motion of the real negative vortex shed from the rib. This results in a velocity which is less than the freestream flow velocity.

The shedding process in the freestream case (Case 1) also differs from the wall-bounded flows (Cases, 2, 3) in a couple of significant ways. In the freestream case, positive and negative vortices are shed alternately from behind the rib, rather than being shed as a pair. In the wall-bounded flows, vortices of opposite sign grow behind the rib and are shed together. In addition, the vortices shed in Case 1 are generally similar in strength to each other, but much smaller and weaker than in the wall-bounded flows. However, there are some similarities between the flow past a rib near a sliding wall and the flow past an obstacle in a freestream at an angle of attack. The latter flow geometry was one of the cases considered in the study by Davis and Moore (1982). In both flows the front stagnation region on the obstacle moves downward off center, while the rear stagnation region moves upwards. This is because more of the fluid impinging on the front is forced over the top of the obstacle. The rib near a sliding wall is in fact a limiting case, where all the fluid is forced over the top. This results in a pair of vortices forming downstream which do not behave in a symmetrical way. In both cases the behavior of the lift and drag coefficients is modified accordingly, to account for the unequal behavior of the two vortices. The shedding of the negative vortex leads to a small local minimum in the drag coefficient while the shedding of the positive vortex leads to a large decrease in the drag. Further distinctions between the freestream and the wall-bounded flows are discussed in the next section.

The mean drag coefficient for the three cases is plotted as a function of Reynolds number in Fig. 15. In all three cases, the mean C_D increases with increasing Re over the Reynolds number range studied. The fixed-wall case (Case 2) shows the smallest dependence on Reynolds number variations. The mean drag in Case 1 (freestream) was always less than the wall-bounded flows of Cases 2 and 3. At the lowest Reynolds number (Re = 100), the drag is approximately the same for Case 2 and 3. This indicates that for the wall-bounded flows, where no periodic vortex shedding was observed, the sliding wall has no significant influence on the drag. For higher values of Re, where shedding does occur, the effect of the sliding wall is to increase the mean drag as well as the amplitude of the fluctuations in C_D. For example, at Re = 500, for Case 2 the range of the drag coefficient was $2.04 \leq C_D \leq 2.69$ while for the sliding-wall case (Case 3) the range was $1.58 \leq C_D \leq 3.78$.

The variation in the nondimensional shedding frequency, or

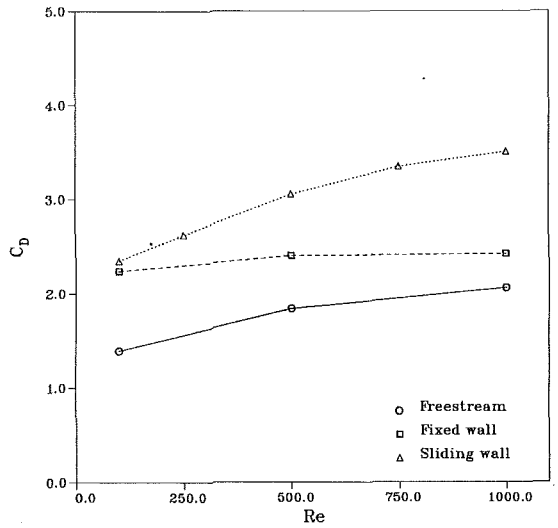

Fig. 15 Mean drag coefficient variation with flow Reynolds number for the three flow configurations under consideration

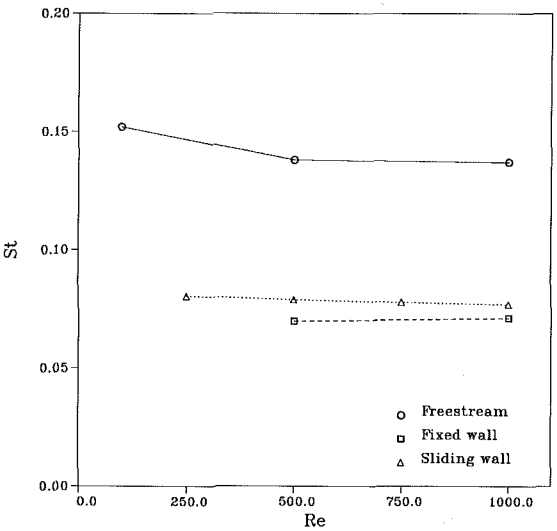

Fig. 16 Strouhal number variation with flow Reynolds number for the three flow configurations under consideration

Strouhal number, is plotted as a function of Reynolds number for the three cases in Fig. 16. The frequency used to determine the Strouhal number is the frequency at which a pair of vortices is shed from behind the rib. In all three cases, the Strouhal number is only a weak function of the Reynolds number. This relative insensitivity of the shedding frequency to Reynolds number has been observed in other studies and holds over a large Reynolds number range extending well into the turbulent flow regime; see, for example, Durao et al. (1988) and Davis and Moore (1982). Although the Strouhal number varies only slightly with Reynolds number, it is quite different for Case 1, where the rib is not adjacent to a wall. The wall-bounded flows have Strouhal numbers approximately 50 percent lower than the values for the freestream case where vortex shedding occurs. This distinction is discussed in the following section along with some questions regarding the stability of bluff body flows and the influence of the neighboring wall on such flows.

5 Discussion

Although it was not the intention of this study to accurately determine the conditions marking transition from steady to unsteady flow for the three cases investigated, some comments can be made regarding their relative stability. In this section we discuss this point and various issues raised in the previous section.

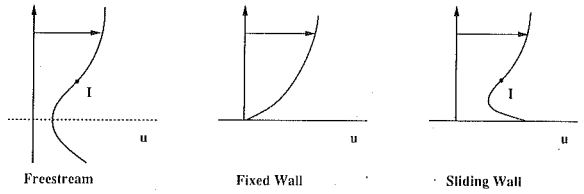

Fig. 17 Sketches of the streamwise velocity profiles downstream of the rib for the three cases under consideration. (*a*) Case 1, rib in a freestream; (*b*) Case 2, rib on a fixed wall; (*c*) Case 3, rib on a sliding wall.

We first summarize the results of the previous section regarding the stability of the three flows. For Case 1, the rib in a freestream, all three Reynolds numbers (Re = 100, 500, 1000) yielded unsteady solutions in which vortex shedding occurs. It is well known that the transition from steady recirculating flow to a flow with periodic vortex shedding occurs at approximately Re = 50 for a bluff body in a freestream. For Case 2, the rib on a fixed wall, a steady state solution was obtained at Re = 100 while at the higher Reynolds numbers (Re = 500, 1000) periodic vortex shedding occurred. For Case 3, the rib on a sliding wall, a steady solution was obtained at a Reynolds number of Re = 50. For the flows discussed in the present study, all three Reynolds numbers yielded unsteady solutions. However, we described the flow at Re = 100 for Case 3 as quasi-steady since, although waviness occurred in the wake, no vortex shedding developed. At higher Reynolds numbers (Re > 250) the flow was unsteady and periodic with regular vortex shedding. From this brief summary it is apparent that the transition to a periodic shedding flow occurs at the lowest Reynolds number (Re ≈ 50) for Case 1; at an intermediate Reynolds number (50 < Re < 100) for Case 3 and at the highest Reynolds number (Re > 100) for Case 2. We now attempt to understand why the freestream and sliding-wall cases are more unstable than the fixed-wall flow.

Consider the steady solutions which develop at low Reynolds numbers for all three cases. Intuitively, one would expect a sliding wall near a bluff body to be a destabilizing influence on the wake region. In this configuration a mechanism is available for removing relatively stagnant fluid from behind the rib. This mechanism is not available when the wall is fixed. The moving wall also provides a mechanism for the generation of a strong counter-rotating (positive) vortex. This vortex interacts with the negative vortex which develops as a result of forcing the oncoming flow over the rib. The structure of the flow behind the rib in Case 3 for which the wall is sliding, is very similar to the flow behind the rib in a freestream. In both cases, two vortices of opposite sign and roughly equal strength are present behind the rib. Also, in both cases, the absence of a fixed wall downstream of the rib makes flow reattachment impossible. Instead, the zero velocity point is free to move in the wake of the rib.

This argument, based on observation, can be strengthened by referring to Fig. 17 which presents sketches of the streamwise velocity profiles downstream of the rib for the three cases, when the flow is steady. We evaluate these profiles in light of the inviscid stability of nearly parallel flows. According to Rayleigh's point-of-inflection theorem:

A necessary (but not sufficient) condition for inviscid instability is that the basic velocity profile has a point of inflection.

A related theorem which gives a slightly stronger criterion for stability is Fjortoft's theorem:

If y_0 is the position of a point of inflection in the basic profile, $u(y)$, and $u_0 = u(y_0)$, then a necessary but not sufficient condition for inviscid instability is that

$$\frac{d^2u}{dy^2}(u-u_0)<0$$

must be true somewhere in the flow.

In Fig. 17, points of inflection are marked (I) where they arise. By both Rayleigh's theorem and Fjortoft's theorem, the profiles in Cases 1 and 3 are possibly unstable. Case 2, which has no inflection points in the profile, should be stable to inviscid perturbations. It should be noted that downstream of the recirculation region in Case 2 the velocity profile develops quickly into a boundary-layer-like flow, and it is well known that the Blasius boundary layer is stable to inviscid disturbances. The similarity between the profiles of Cases 1 and 3 is more noticeable if the freestream profile below the symmetry plane is included for comparison as drawn in the figure.

Thus, based on careful observation and appealing to inviscid stability theory, we conclude that the flow past a rib near a fixed wall (Case 2) is the most stable of the three flow configurations. This conclusion is supported by the findings of the present study which determined unsteady solutions for the freestream (Case 1) and sliding-wall (Case 3) configurations at lower Reynolds numbers than for the fixed-wall geometry.

We turn now to a comparison of the freestream and sliding-wall flows and note that in the freestream case the transition Reynolds number is about half that for the sliding-wall case. In comparing the two flows when they are steady, there are two features which are distinctly different. First, the stagnation point on the upstream side of the rib is close to the wall for Case 3 since all the fluid has to pass over the top of the rib. In Case 1 the stagnation point is close to the midpoint of the rib and only half of the fluid impinging on the rib passes over the top, the remaining half of the fluid passing underneath.

The second feature distinguishing the two flows is the difference in the conditions governing the locations of their respective stagnation points upstream of the rib. When the flow goes unsteady in the sliding-wall case, the position of the stagnation point remains fixed at the lower upstream corner of the rib. For the freestream flow the stagnation point is not constrained to remain on the geometric symmetry plane but is free to move. In the freestream flow the velocity normal to the geometrical symmetry plane (v-component) is not constrained to be zero. Indeed, after vortex shedding develops, the cross-stream velocity is often not zero. However, for the sliding-wall flow, the cross-stream velocity is constrained to be zero at the stagnation point and all along the wall upstream of the rib and downstream as well. In contrast, note that the streamwise velocity conditions on the symmetry plane in Case 1 and on the sliding wall in Case 3 are not so different. In the freestream case the streamwise velocity is not constrained on the symmetry plane, while in the sliding-wall case it is forced to acquire the wall velocity by the no-slip condition.

It seems reasonable to assume that the freestream flow becomes unstable at a lower Reynolds number than in the sliding-wall geometry because it is susceptible to perturbations which break the symmetry of the steady flow. This allows non-zero cross-stream velocities on the symmetry plane and permits the upstream stagnation point to oscillate about a mean position. Similar perturbations are not permitted in the region near the upstream stagnation point in the sliding-wall flow because the cross-stream velocities are forced to zero by the boundary conditions imposed at the wall. As a result, the stagnation point is not free to oscillate about a mean position but is, instead, constrained to remain fixed.

Examination of the time histories presented in the previous section indicates that the sliding wall of Case 3 also has a substantial influence on the type of unsteady behavior which is observed. For this case the unsteady simulations always resulted in a short transient followed by a perfectly periodic shedding cycle. This was true not only at Re = 500 and 1000, but also at Re = 1500 and 2000, for which we have not presented time histories. At Re = 500 the calculation was started impulsively and fully periodic shedding was observed at approximately 80 time scales, (Fig. 11). The initial condition for the

Re = 1000 calculation was taken from the periodic solution at 250. In this case a short transient is observed with periodic shedding following at about $t = 20$. The shedding cycles observed in each of these simulations were repeated exactly to within the resolution of our calculations. None of the simulations which were performed for Cases 1 or 2 resulted in perfect periodicity at these Reynolds numbers. The solution for Case 2 at Re = 500 appears to be approaching a fully periodic state (Fig. 11) but still has not reached one after 220 time scales. Computational costs limited our ability to perform longer time integrations for these flows and, consequently, based on the current data it is difficult to say whether any of the solutions for Cases 1 or 2 will ultimately attain a fully periodic state. Nevertheless, the data does illustrate that the unsteady flow solution is much more strongly attracted to a fully periodic state when the sliding wall is present.

The periodic behavior of Case 3 is very likely the result of the interaction of the sliding wall with the fluid in the region immediately behind the rib. Fluid is drawn into the corner formed by the back of the rib and the wall, and then pulled out as the wall slides downstream. Very near the corner, where viscous effects are dominant, an analytical solution for the steady flow can be obtained. The form of this solution suggests that this corner acts as a source of positive vorticity. The corner continually injects positive vorticity into the flow immediately behind the rib, regardless of the freestream flow conditions. Neither Case 1 nor 2 have an analogous source of vorticity in the recirculation region. In contrast with Case 3, velocity variations occurring close to the walls downstream of the rib for Cases 1 or 2 are imposed by the unsteady outer flow. For Case 2 the corner flow solution contains a hierarchy of positive and negative vortices in the region very near the corner. However, in neither Case 2 or Case 1 does the wall stress boundary condition induce fluid motion as it does in the sliding wall case.

The shedding cycle which is observed for Case 3 consists of a period during which a vortex pair grows behind the rib, followed by a shedding of this pair into the freestream. Growth of the negative vortex is promoted by shearing of the freestream fluid with that in the recirculation region. In this case the growth of the positive vortex is aided by the vorticity generation at the corner. Even though the positive vortex is the smaller of the pair, it plays an important role in the shedding event by forcing the negative vortex further into the freestream and thereby promoting shedding. The initiation and growth of the positive vortex are of key importance to the shedding process. The influx of positive vorticity from the corner appears to be the seed for this vortex which is independent of the outer freestream flow. Such an independent mechanism for initiation of the corner vortex is absent from Cases 1 and 2 and is believed to be responsible for the strongly periodic nature of the flow in the presence of a sliding wall.

Figure 16 shows clearly the interesting result that the presence of a wall, whether sliding or fixed, reduces the shedding frequency dramatically. The Strouhal numbers for Cases 2 and 3 are approximately half the value obtained for the freestream flow. Even though the presence of a sliding wall increases the tendency to a periodic flow condition, it seems to have only a minor influence on the value of the shedding frequency itself. Apparently, it is the constraint on the normal velocity at the wall which causes a decrease in the Strouhal number. A closer examination of this phenomenon reveals some interesting characteristics of the vortex-shedding process.

The presence of a wall affects the flow near the rib in several ways. One of the more significant of these is that the wall forces all the fluid which approaches from upstream to flow over the top of the rib. The interaction of this flow with the rib generates negative vorticity which then collects in the recirculation region in the form on a large clockwise-rotating vortex. The amount of negative vorticity generated should scale with the amount of upstream fluid diverted over the rib. When the wall is present the amount of fluid diverted over the rib is proportional to H, whereas for the freestream case it is proportional to $H/2$. This argument suggests that the size of the negative vortices should scale with H for Cases 2 and 3 and with $H/2$ for Case 1. Examination of the vorticity contours supports this contention. The negative vortices which are shed in Case 1 are approximately half as strong as those shed when a wall is present. This can be confirmed by checking the minimum vorticity values and the size of the vortices in relation to the rib size (Figs. 4(*a*), 4(*b*), and 4(*c*)). It is also interesting to note that very little positive vorticity is generated in Case 2 and that the positive vorticity present in Case 3 is the result of the sliding wall. This is a consequence of the fact that there is no upstream fluid flowing under the rib in either of these cases.

The preceding discussion suggests that the appropriate length scale to use when considering vortex dynamics is different for the freestream and wall-bounded cases. Using a length scale of $H/2$ for Case 1 and H for Cases 2 and 3, Strouhal numbers of 0.069, 0.070, and 0.079 are obtained for the base shedding frequencies of Cases 1, 2, and 3, respectively, at Re = 500. Thus, using these length scales, the Strouhal numbers differ considerably less, clustering about an average value of 0.072, approximately.

6 Conclusions

The effect of a sliding or fixed wall on the flow near a square bluff body has been investigated numerically. The boundary conditions imposed by the wall on the normal and tangential velocity components are shown to affect the flow in different ways. The types of solutions which were obtained included steady recirculation, quasi-steady recirculation, periodic vortex shedding, and aperiodic vortex shedding. The characteristics of these solutions have been summarized in terms of time records of lift and drag coefficients and their Fourier transforms, instantaneous streamline plots, instantaneous vorticity contours, and relative comparisons of the shedding frequencies and average drag among the cases investigated.

Results indicate that the presence of a wall and the streamwise shear induced by it strongly affect the stability of the flow and the type of vortex shedding which is observed. In fact, the geometry and spatial boundary conditions influence the vortex shedding and type of wake that are observed to a greater extent than the Reynolds number. As is the case for other bluff body flows (Okajima 1982, Durao et al. 1988), the frequency of vortex shedding is only a weak function of the Reynolds number. This trend is expected to extend into the higher Reynolds number turbulent flow regime and it is possible that shedding of coherent structures with properties similar to those observed in this study will also occur at these Reynolds numbers.

Comparison with results from the freestream simulation show that the presence of a wall stabilizes the flow and increases the critical Reynolds number at which the flow becomes unsteady. The stabilizing influence was more pronounced when the wall was stationary. The presence of the wall was also shown to reduce the Strouhal number at which vortex shedding occurred. This has been explained by a simple scaling argument.

A particularly interesting finding of the current study is that the presence of a wall which slides at the freestream velocity results in vortex shedding which is strongly periodic. For this case, perfectly repeatable vortex shedding was observed at Reynolds numbers ranging from 250 to 2000. This phenomenon is attributed to the generation of positive vorticity which arises at the wall, in the wall-rib corner immediately behind the rib, when the wall slides.

Acknowledgments

The authors wish to express their thanks to the IBM Corporation for a grant to support this study and to the Cray Research, Inc. for their support in the form of grants for time on the U. C. Berkeley campus Cray computer. The first author also thanks the IBM Corporation for its support through an IBM fellowship. The authors' names are listed in alphabetical order.

References

Armaly, B. F., Durst, F., Pereira, J. C. F., and Schoenung, B., 1983, "Experimental and Theoretical Investigation of Backward-Facing Step Flow," *J. Fluid Mech.*, Vol. 127, p. 473.

Arnal, M., Goering, D., and Humphrey, J. A. C., 1990, "On the Influence of a Solid Boundary On Vortex Shedding from a Bluff Body," CML Report No. 90-013, Department of Mechanical Engineering, University of California at Berkeley.

Bearman, P. W., 1980, "REVIEW-Bluff Body Flows Applicable to Vehicle Aerodynamics," ASME JOURNAL OF FLUIDS ENGINEERING, Vol. 102, p. 265.

Bearman, P. W., and Zdravkovich, M. M., 1978, "Flow Around a Circular Cylinder Near a Plane Boundary," *J. Fluid Mech.*, Vol. 89, Part 1, p. 33.

Berger, E., and Wille, R., 1972, "Periodic Flow Phenomena," *Ann. Rev. Fluid Mech.*, Vol. 4, p. 313.

Braza, M., Chassaing, P., and Ha Minh, H., 1986, "Numerical Study and Physical Analysis of the Pressure and Velocity Fields in the Near Wake of a Circular Cylinder," *J. Fluid Mech.*, Vol. 165, p. 79.

Davis, R. W., and Moore, E. F., 1982, "A Numerical Study of Vortex Shedding From Rectangles," *J. Fluid Mech.*, Vol. 116, p. 475.

Doligalski, T. L., and Walker, J. D. A., 1984, "The Boundary Layer Induced by a Convected Two-Dimensional Vortex," *J. Fluid Mech.*, Vol. 139, p. 1.

Durao, D. F. G., Heitor, M. V., and Pereira, J. C. F., 1988, "Measurements of Turbulent and Periodic Flows Around a Square Cross-Section Cylinder," *Experiments in Fluids*, Vol. 6, p. 298.

Eaton, J. K., and Johnston, J. P., 1981, "A Review of Research on Subsonic Turbulent Flow Reattachment," *AIAA*, Vol. 19, No. 9, p. 1093.

Freitas, C. J., Street, R. L., Findikakis, A. N., and Koseff, J. R., 1985, "Numerical Simulation of Three-Dimensional Flow in a Cavity," *Int. J. Num. Meth. in Fluids*, Vol. 5, p. 561.

Gerrard, J. H., 1978, "The Wakes of Cylindrical Bluff Bodies at Low Reynolds Number," *Proc. Royal Soc.*, Series A, 288 p. 29.

Ghoniem, A. F., and Cagnon, Y., 1987, "Vortex Simulation of Laminar Recirculating Flow," *J. Comput. Phys.*, Vol. 68, p. 346.

Han, T. Y., Meng, J. C. S., and Innis, G. E., 1983, "An Open Boundary Condition for Incompressible Stratified Flows," *J. Comp., Physics*, Vol. 49, p. 276.

Harlow, F. H., and Welch, J. E., 1965, "Numerical Calculation of Time-Dependent Viscous Incompressible Flow of Fluid with Free Surface," *Phys. of Fluids*, Vol. 8, No. 12, p. 2182.

Kamemoto, K., Oda, Y., and Aizawa, M., 1984, "Characteristics of the Flow Around a Bluff Body Near a Plane Surface," *Bulletin of JSME*, Vol. 27, No. 230, p. 1637.

Leonard, B. P., 1979, "A Stable and Accurate Convective Modeling Procedure Based on Quadratic Upstream Interpolation," *Comput. Meths. Appl. Mech. Eng.*, Vol. 19, p. 59.

LeQuere, P., Humphrey, J. A. C., and Sherman, F. S., 1981, "Numerical Calculation of Thermally Driven Two-Dimensional Unsteady Laminar Flow in Cavities of Rectangular Cross Section," *Num. Heat Trans.*, Vol. 4, p. 249.

Mansour, N. N., Kim, J., and Moin, P., 1983, "Computation of Turbulent Flows Over a Backward-Facing Step," NASA tech. mem. 85851.

Okajima, A., 1982, "Strouhal Numbers of Rectangular Cylinders," *J. Fluid Mech.*, Vol. 123, p. 379.

Patankar, S. V., 1981, "A Calculation Procedure for Two-Dimensional Elliptic Situations," *Num. Heat Trans.*, Vol. 4, p. 409.

Schneider, G. E., and Zedan, M., 1981, "A Modified Strongly Implicit Procedure for the Numerical Solution of Field Problems," *Num. Heat Trans.*, Vol. 4, p. 1.

Sethian, J. A., and Ghoniem, A. F., 1988, "Validation Study of Vortex Methods," *J. Comput. Phys.*, Vol. 74, p. 283.

Taneda, S., 1965, "Experimental Investigation of Vortex Streets," *J. Phys. Soc. Japan*, Vol. 20, No. 9, p. 1714.

Velocity Profiles for Turbulent Boundary Layers Under Freestream Turbulence

J. A. Hoffmann
Professor.

K. Mohammadi
Graduate Student.

Aeronautical Engineering Department,
California Polytechnic State University,
San Luis Obispo, Calif. 93407

Correlations for changes of skin friction coefficients (Δc_f) and wake parameters ($\Delta\Pi$), relative to the low freestream turbulence condition, are presented for the case of turbulent boundary layers under freestream turbulence with zero and adverse pressure gradients. The turbulent boundary layers were evaluated on a plate in a wind tunnel using a monoplane rod set turbulence generator; comparisons were also made using the data of several other investigators. The results, which define the velocity profiles within the boundary layers, were found to collapse for a large range of the pressure gradient parameter.

Introduction

There are many engineering examples of boundary layers which experience FST. In systems which utilize compressors and turbines, the boundary layers over the blades of these components generally experience a highly turbulent external flow and a pressure gradient. In order to design these blades for both good aerodynamic and thermal performance, it is important to know how the viscous and thermal boundary layers around the blades are affected by the FST.

Several recent studies have documented the influence of FST on boundary layers. The effect of isotropic FST on a fully turbulent boundary layer in a zero pressure gradient flow field has been studied by Hancock and Bradshaw (1983). They correlated the increase in skin friction and decrease in the boundary-layer shape factor to a FST parameter, $u'/U_\infty/(L_x/\delta + 2)$. Castro (1984) found that this correlation was dependent upon Reynolds number for low Reynolds numbers. Blair (1983) studied the case of boundary layers with a zero pressure gradient and found that the transition Reynolds number is weakly sensitive to acceleration and is dependent upon the FST intensity, with larger FST intensities resulting in lower transition Reynolds numbers. He also found that the Stanton number/skin friction coefficient ratio increased slightly with increasing FST intensity. Arnal (1977) studied the turbulent boundary layer over a plate with mild and significant adverse pressure gradients for conditions both with and without FST. For the significant adverse pressure gradient condition, he found that boundary-layer separation occurred without FST, whereas the boundary layer remained attached with FST. Hoffmann et al. (1988a), (1989) also evaluated the effect of FST on turbulent boundary layers with zero and mild adverse pressure gradients, and attributed the incrase in boundary-layer strength (a resistance to flow separation as exhibited by a decrease of the shape factor of the boundary layer) which occurs with adverse pressure gradients and FST to improved fluid mixing. The improved fluid mixing which results in a transfer of momentum from the free-stream to the boundary layer occurs as a result of a decrease of L_x/δ and to vortex stretching of the turbulent eddies in the freestream. The decrease of L_x/δ occurs primarily due to the increase in δ for boundary layers with adverse pressure gradients.

Evans (1985a) evaluated turbulent boundary layers on the suction surface of an airfoil in a compressor cascade. Using an integral method developed by Hirst and Reynolds (1968), Evans and Horlock (1974) predicted boundary-layer parameters and related the wake parameter for turbulent boundary layers to the FST intensity (Evans, 1985b).

In two-dimensional diffuser studies, improvements of pressure recovery coefficients of 24 percent have been obtained by Hoffmann (1981) with highly anisotropic and high intensity inlet FST, resulting in delayed separation and a reduction of flow distortion within the diffuser (Hoffmann and Gonzalez, 1984). Anisotropic inlet FST has been shown to be significantly more effective at improving pressure recovery coefficients relative to near isotropic inlet FST (Hoffmann and Fang, 1988b).

It is the purpose of this study to identify and to present the interrelationship between important boundary layer and FST parameters, which will define the velocity profiles and corresponding shape parameters of turbulent boundary layers under FST for the case of adverse pressure gradient conditions. Once this interrelationship is documented, engineers may use this information in the design of systems with FST; it will be useful for both aerodynamic and thermodynamic considerations.

Experimental System and Procedure

The turbulent boundary layers on a flat plate were evaluated using the experimental system illustrated in Fig. 1. The plate, which spans the entire height of the test section, was positioned in the draw-thru wind tunnel described by Hoffmann et al. (1989). The cross-sectional dimensions of the wind tunnel are

Contributed by the Fluids Engineering Division of the THE AMERICAN SOCIETY OF MECHANICAL ENGINEERS and presented at the ASME/JSME Joint Fluids Engineering Conference, Portland, OR, June 23-27, 1991. Manuscript received by the Fluids Engineering Division April 13, 1990.

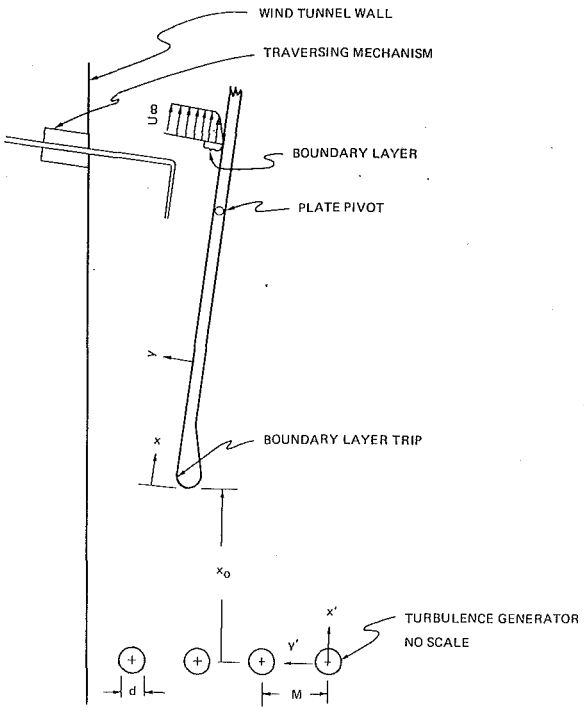

Fig. 1 Experimental system

0.88 m × 1.18 m; experimentation was performed holding the velocity upstream of the turbulence generators constant at 24.1 m/s.

Without turbulence generators, the FST intensity in the test section (u'/U_∞) is 0.25 percent. To generate FST, the same rod set used by Hoffmann et al. (1989) a monoplane set of parallel rods with a solidity (d/M) of 0.32 and a mesh size (M) of 6.67 cm, was positioned at two locations upstream of the leading edge of the flat plate, Xo = 0.67 m and 1.13 m.

The flat plate with a length of 1.52 m was constructed from 1.90 cm plywood and was varnished and sanded to obtain a smooth surface. The plate pivots at x = 0.63 m to obtain various angles of incidence to the freestream flow. The distance from the tunnel wall to the surface of the flat plate at the location of the pivot is 0.32 m. The plate was first positioned to obtain a zero static pressure gradient—the α = 0 deg position; for α = 0 deg, the plate and tunnel wall formed a diffuser with a 1.5 deg total included divergence angle. The plate was then adjusted to obtain adverse pressure gradients with α = 2.6, α = 5.2, and 6.8 deg, inclined from the α = 0 deg position. In order to prevent flow separation near the leading edge of the plate (observed with tufts), the radius of the leading edge of the plate was changed from 2.5 cm for α = 0, 2.5, and 5.2 deg to 3.8 cm for α = 6.8 deg. To trip the boundary layer, masking tape (2.5 cm wide) was centered at the intersection of the leading edge of the plate and the plate itself.

At two x locations along the flat plate (x = 0.56 m and x = 0.94 m), the plate is instrumented with static pressure taps located near the centerline of the plate, two Preston tubes of different diameter (d = 0.52 mm and d = 0.82 mm), and four fixed total pressure probes with d = 0.82 mm located at various y positions were used to determine velocities near the surface. In order to determine velocities above the plate at any y position, a total pressure probe (d = 0.82 mm) was attached to a remote-controlled model B2509WIJ Velmex Inc. electric traversing mechanism. The voltage output of the mechanism, proportional to y, was measured using the HP model 3466A digital multimeter. The velocity pressure at each location was fed into a Celesco Model P15D ± 0.1PSID pressure transducer, and then through a Model CD 10 Carrier Demodulator into a TSI model 1076 multimeter, to obtain a ten second time average of the velocity pressure. A curve fit of the velocity pressures and velocities was obtained using a CAD system, resulting in values of c_f, δ, δ^*, θ, and H for the boundary layers.

FST intensity measurements were obtained using a TSI model 1050 anemometer, a TSI model 1052 linearizer, and a TSI model 1076 voltmeter; boundary-layer turbulence measurements were not obtained. Wire calibration was achieved using a TSI model 1125 calibrator. Measurements were obtained at

Nomenclature

A, C, κ = constants for turbulence decay, law of the wall and law of the wake equations
c_f = boundary-layer skin friction coefficient
Δc_f = change in c_f with FST compared to the low FST condition at the same Re_θ and dP/dx, = $c_f - c_{f0}$
d = diameter
FST = freestream turbulence
H = boundary-layer shape factor, = δ^*/θ
K = constant, c_{f0} (experimental)/c_{f0} (empirical)
L_x = dissipation length scale
M = mesh size of turbulence generators
n = exponent for turbulence decay equation
P = static pressure
q' = total rms freestream turbulence fluctuation, = $\sqrt{(u'^2 + v'^2 + w'^2)/3}$
R_x = freestream autocorrelation coefficient
Re_θ = Reynolds number based on θ, = $U_\infty\theta/\nu$
T = freestream turbulence parameter, = $100\ u'/U_\infty/(L_x/\delta + 2)$
u', v', w' = freestream RMS turbulence components in the x, y, and z directions, respectively
U_∞ = freestream time averaged velocity
$\bar{u}$ = time averaged velocity
u_* = shear velocity, = $U_\infty\sqrt{c_f/2}$
x, y, z = coordinate system relative to leading edge of flat plate
x', y' = coordinate system relative to rods
X_0 = distance from rods to leading edge of flat plate
α = angle of incident of flat plate relative to the zero pressure gradient case
β = pressure gradient parameter, = $(\delta^*/\tau_0)(dP/dx)$
Λ = integral length scale of turbulence, = $\int_0^\infty R_x dx$
δ, δ^*, θ = boundary-layer thickness when $\bar{u}$ = 0.995 U_∞, displacement thickness and momentum thickness, respectively
ν = kinematic viscosity
τ_0 = wall shear stress
Π = wake parameter
$\Delta\Pi$ = change in Π with FST compared to the low FST condition at the same β, = $\Pi - \Pi_0$

Subscript

0 = low freestream turbulence condition

two streamwise locations above the flat plate ($x = 0.56$ m and $x = 0.94$ m) using a single wire normal to the flow and wire inclined at 45 deg to the flow.

Results and Discussion

Velocity profiles and FST measurements were obtained at two x locations along the flat plate at each α for the case of low FST and with the rod set located at two positions upstream from the plate. The results of the FST and the turbulent boundary layer measurements are presented below; they include some results previously reported by Hoffmann et al. (1988a), (1989). An analysis of results presented by other authors is also included.

Freestream Flow. The turbulence generator used to produce FST, the same rod set previously used by Hoffmann et al. (1989) produced relatively large turbulence intensities ($3.1 \leq u'/U_\infty$ (%) ≤ 4.8); length scales (L_x/δ) varied from 0.8 to 2.5. Equation (1) was used to describe the turbulence decay using turbulence measurements at two x locations at each α. This decay was used in Eq. (2) to obtain the freestream dissipation length scale. The pressure gradient parameter, β, was obtained using the freestream velocity measurements at two x locations along the flat plate at each α along with a potential flow solution. All results are presented in Table 1.

$$u'^2 = Ax'^n \tag{1}$$

$$U_\infty d(u'^2)/dx' = -(u'^2)^{3/2}/L_x \tag{2}$$

The FST was found to be somewhat anisotropic. The degree of anisotropy varied weakly with the angle of incidence of the plate and was found to be essentially independent of position (x) for the range of x investigated. Anisotropy ratios (v'/u' and w'/u') were approximately equal in magnitude and varied from 0.96 at $\alpha = 0$ deg to 1.01 at $\alpha = 6.8$ deg. Uberoi and Wallis (1967) and Gad-el-Hak and Corrain (1974) independently studied zero pressure gradient flows downstream of grids and a monoplane rod set with $d/M = 0.37$; anisotropy ratios (v'/u' and w'/u') ranged from 0.86 to 0.91 and were found to be approximately equal in magnitude and independent of x for both the grid sets and the monoplane rod set. In the present study, larger values of U_∞ occur over the plate relative to the velocities upstream of the plate, caused by plate blockage in the test section; this acceleration of the freestream flow accounts for the larger isotropy ratios measured (closer to unity), relative to those obtained by Uberoi and Wallis (1967) and Gad-el-Hak and Corrain (1974). The flow at the plane normal to the leading edge of the plate exhibits broadband FST, as represented by autocorrelation and spectral distribution curves. Some of the v' and w' results presented by Hoffmann et al. (1988a), (1989) were found to be incorrect as a result of improper probe alignment. The results of this study were obtained with the probe positioned parallel to the flow, with flow direction determined using an X-wire probe. All of the boundary layer and other FST results reported by Hoffmann et al. (1988a), (1989) were found to agree with results presented in this study within the repeatability limits of the data. The uncertainty of the turbulence measurements (20:1 odds) is ±5 percent.

Boundary-Layer Results. The values of c_f presented were obtained by fitting the velocities near the surface to the law of the wall, Eq. (3), with $\kappa = 0.41$ and $C = 5.2$ as recommended by Hancock and Bradshaw (1983). Values of c_f obtained using the Preston tube results and the calibration table of Head (13) were found to agree with these values to within 4 percent.

$$\bar{u}/u_* = 1/\kappa \ln u_* y/\nu + C \tag{3}$$

In this study, all values of c_f for the case with FST were subtracted from the values of c_{f0} holding Re_θ and dP/dx constant. The values of c_f, with and without FST, were compared

Table 1 Summary of results

Rod Set X_0 α	x (m)	v'/U_∞ %	U_∞ (m/s)	L_x/δ	$\frac{u'/U_\infty}{L_x/\delta + 2}$ (%)	β	δ (cm)	$\frac{U_\infty \theta}{\nu}$	H	Cf x10^3	ΔCf x10^3	Π	$-\Delta\Pi$
A 0.67m 0°	0.56	4.83	26.3	1.570	1.35	0.000	2.36	2582	1.326	3.930	0.553	-0.214	0.690
	0.94	3.92	26.1	1.310	1.18	0.000	3.00	3972	1.322	3.500	0.492	-0.027	0.503
A 0.67m 2.6°	0.56	4.67	29.2	1.581	1.30	0.260	3.15	4082	1.318	3.520	0.659	-0.122	0.773
	0.94	4.23	27.6	1.204	1.32	0.430	4.90	6185	1.302	3.130	0.648	0.008	0.750
A 0.67m 5.2°	0.56	4.63	32.4	1.018	1.53	0.600	3.75	6499	1.302	3.190	0.556	0.008	0.851
	0.94	4.16	29.5	0.816	1.48	0.940	5.50	9108	1.305	2.800	0.638	0.240	0.812
A 0.67m 6.8°	0.56	4.67	33.0	1.150	1.48	0.719	4.15	6683	1.297	3.147	0.466	-0.013	0.941
	0.94	4.40	29.8	0.890	1.52	1.249	6.65	10437	1.294	2.775	0.592	0.168	1.049
A 1.13m 0°	0.56	3.55	25.7	2.500	0.79	0.000	2.26	2718	1.347	3.730	0.377	-0.046	0.522
	0.94	3.20	25.6	2.120	0.78	0.000	2.95	3978	1.343	3.390	0.383	-0.078	0.554
A 1.13m 2.6°	0.56	3.38	29.7	1.650	0.93	0.270	3.23	4207	1.310	3.380	0.543	-0.034	0.692
	0.94	3.32	27.7	1.370	0.99	0.480	4.58	6478	1.321	2.970	0.534	0.190	0.598
A 1.13m 5.2°	0.56	3.19	32.5	1.353	0.95	0.650	3.82	6380	1.311	2.990	0.333	0.182	0.706
	0.94	3.10	29.8	1.121	1.00	1.030	5.55	9352	1.324	2.640	0.511	0.408	0.693
A 1.13m 6.8°	0.56	3.22	32.9	1.311	0.97	0.679	4.03	7157	1.315	2.985	0.392	0.155	0.750
	0.94	3.16	30.2	1.076	1.03	1.206	5.90	10894	1.330	2.590	0.461	0.432	0.762

at the same x locations at each α, where essentially the same values of U_∞ and dU_∞/dx (or dP/dx) exist. Since the values of Re_θ for c_f and c_{f0} were as much as 21 percent different, empirical corrections were made to determine the value of c_{f0} at the Re_θ for the case with FST. This empirical correction was obtained by numerical integration of the modified von Doenhoff and Tetervin equations (Eqs. (7) and (8) and Clauser's formula (Eq. (10)) for $dP/dx = 0$, and the Ludwieg and Tillmann formula (Eq. (9)) for $dP/dx > 0$. These equations, presented in the Appendix, resulted in a maximum change in c_{f0} of 12 percent.

The velocity profiles of the boundary layers were fit to a formula suggested by Dean (1976), and Hancock and Bradshaw (1983), for conditions both with and without FST, Eq. (4). The first two terms on the right side of Eq. (4) represent the law of the wall, Eq. (3), whereas the last term represents the deviation from the law of the wall (the wake function) and becomes significant in the wake region of the boundary layers. Values of Π were obtained by evaluating Eq. (4) at $y = \delta$ (the last term of Eq. (4) then becomes $2\Pi/\kappa$ and the left side of the equation becomes $\sqrt{2/c_f}$).

$$\bar{u}/u_* = 1/\kappa \ln u_* y/\nu + C + 1/\kappa[(1+6\Pi)(y/\delta)^2 - (1+4\Pi)(y/\delta)^3] \tag{4}$$

In this study, values of Π for the case with FST are subtracted from the values of Π_0 for boundary layers with low FST, holding β constant. The data obtained for $\Pi_0 = f(\beta)$ are presented in Fig. 2 and are shown to correlate reasonably well with the equation presented by White (1974), Eq. (5); correspondingly, values of Π_0 for this study were obtained using Eq. (5) evaluated at the β corresponding to the case with FST. $\Pi_0 - \beta$ relationships corresponding to the results of many authors have been formulated by Das and White (1986) for a large range of β.

$$\Pi_0 = 0.8(\beta + 0.5)^{0.75} \tag{5}$$

Values of Δc_f and $\Delta\Pi$ are presented as a function of Hancock's FST parameter in Fig. 3. The values of Δc_f and $\Delta\Pi$

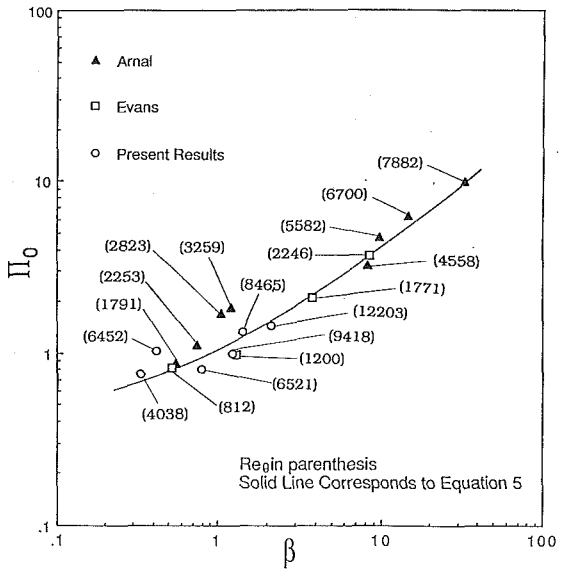

Fig. 2 Π_0 versus β

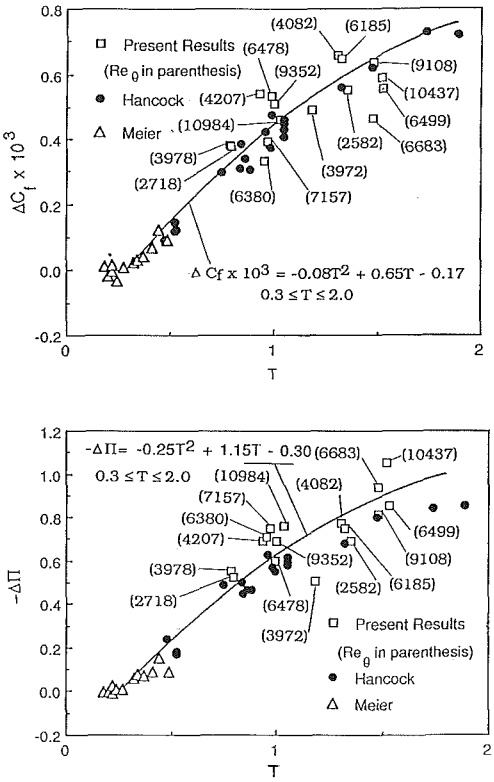

Fig. 3 Δc_f and $\Delta\Pi$ versus T for $0 \le \beta \le 1.25$

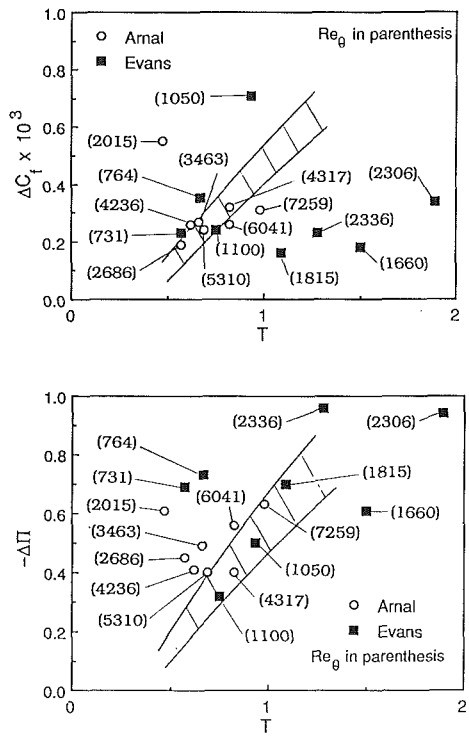

Fig. 4 Δc_f and $\Delta\Pi$ versus T for $0.5 \le \beta \le 8.5$. Crosshatched region represents range of results for $0 \le \beta \le 1.25$ from Fig. 3.

obtained by Hancock and Bradshaw (1983) for the case of $dP/dx = 0$ and the present results for zero and mild adverse pressure gradients ($0 \le \beta \le 1.2$) collapse quite well. The value of Π_0 used for Hancock's results was 0.55, shown by Cebeci and Smith (1974) to be valid when $dP/dx = 0$ and $Re_\theta > 2000$. Values of Δc_f and $\Delta\Pi$ have been presented for the results of Meier et al. (1987) at low L_x/δ ($0.23 \le L_x/\delta \le 0.66$) for $dP/dx = 0$. The data of Meier indicate that a threshold magnitude of the FST parameter of approximately 0.25 percent is required before any change in the boundary layer occurs.

As shown in Figs. 2 and 3, no trends of the Π_0, Δc_f or $\Delta\Pi$ data occurs with Re_θ for the range studied ($2500 < Re_\theta < 11{,}000$), and the scatter is attributed to the uncertainty of the measurements. For the zero pressure gradient case, Cebeci and Smith (1974) have shown that Π_0 is not a function of Re_θ for $Re_\theta > 2000$, and the results of Castro (1984) and Hancock and Bradshaw (1983) have shown that Δc_f is not a function of Re_θ for $Re > 2000$. For the case with pressure gradients, White (1974) states that Π_0 is only a function of β when equilibrium boundary layers exist.

Arnal (1977) investigated the turbulent boundary layer at several streamwise locations on a flat plate at two angles of incidence producing mild and high adverse pressure gradient conditions ($0.7 \le \beta \le 7.0$) for conditions with grid generated FST. The freestream eddy size range (L_x/δ) varied from 4.4 to 7.5, and the Re_θ range varied from 2000 to 7200. Arnal's data from the last three measurement stations along the plate have been ignored; at these locations, values of c_{f0} and u' for the low FST condition increased with increasing x, indicating possible interference to the freestream from flow over adjacent and/or opposite walls, affecting the boundary layer over the plate. The measured values of c_{f0} were close to those predicted by the Ludwieg and Tillmann formula (1949) (±9 percent); correspondingly, the Ludwieg and Tillmann formula was used to evaluate c_{f0} at the Re_θ corresponding to each condition with FST, and the von Doenhoff and Tetervin equations were used to obtain H at that Re_θ. Values of Π_0 were obtained using White's equation, Eq. (5); Fig. 2 shows a reasonably good agreement of Arnal's results with those of White. The values of Δc_f and $\Delta\Pi$ are presented in Fig. 4 and show more scatter compared to the present results.

Evans (1985a) investigated the turbulent boundary layer at various locations along the suction surface of a blade in a compressor cascade. The boundary layers experienced moderate to large adverse pressure gradients ($0.5 \le \beta \le 8.5$) and were evaluated with two levels of grid generated freestream turbulence with a L_x/δ range from 0.5 to 5.8. Values of the dissipation length scale were calculated using Eq. (2) assuming that u'/U_∞ is constant for each grid set, shown to be approximately true in the adverse pressure gradient flows of Arnal (1977) and Hoffmann et al. (1989). Values of Π_0 were obtained using White's equation, Eq. (5), and are shown to agree well

with Evan's low FST values of Π_0 in Fig. 2. Values of c_{f0} were corrected imposing the condition of constant Re_θ using the modified von Doenhoff and Tetervin, and Ludwieg and Tillmann equations, as described earlier for the present results. Corrections for the low Re_θ for Evans results ($700 \leq Re_\theta \leq 2300$) were obtained using Castro's results (1984), and corrections for the high low FST condition of Evans results ($u'/U_\infty = 0.68$ percent and $0.1 < L_x/\delta < 0.8$) were obtained using results of Meier et al., (1987). The results of Δc_f and $\Delta\Pi$ presented in Fig. 4 show more scatter relative to those of the present study. All four of Evans data points for Δc_f that fall to the right of the crosshatched region were obtained at the two most downstream measurement stations, and may be low due to possible flow interference to the free-stream, affecting the boundary layer (increasing c_{f0}), as observed with the results of Arnal. Also, these four data points have relatively large values of $\delta^* d\beta/dx$ ($0.18 \leq \delta^* d\beta/dx \leq 0.68$), indicating highly nonequilibrium boundary layers. The values of $\delta^* d\beta/dx$ for Evans other data points with FST ranged from 0.01 to 0.05, while those of the present results and those of Arnal ranged from 0 to 0.02.

In the present study, along with those of Evans (1985a) and Arnal (1977), values of Π_0 are reasonably close to the results of White (1974), developed for equilibrium boundary layers. It can be expected that the results presented in Fig. 3 may not be applicable for nonequilibrium boundary layers with large values of $\delta^* d\beta/dx$. The scatter of the results of Evans and Arnal presented in Fig. 4 may be a result of a larger uncertainty caused by the high adverse pressure gradient flows and associated unsteadiness. The results do not show a clear trend with Re_θ. The scatter of the results of Evans and Arnal generally center around the present results and extends the apparent applicability of Fig. 3 to a large range of β ($0 \leq \beta \leq 8.4$ for boundary layers with FST).

Integrity of Results. The FST parameter used in this study, $u'/U_\infty/(L_x/\delta + 2)$, is based on u' rather than q' which results in a reduction in its uncertainty; the uncertainty of q'/U_∞ is $\pm$ 9 percent (three turbulence measurements are required) while that of u'/U_∞ is $\pm$ 5 percent (only one turbulence measurement is needed). The magnitude of u' is not significantly different compared to that of q'; values of q'/u' for this study varied from 0.97 to 1.02. The FST parameter also incorporates the dissipation length scale rather than the integral length scale; this allows comparison of the present results to those of others who have not measured integral length scales. The boundary layer parameter, $\Delta c_f/c_{f0}$, used by Meier et al. (1987) and Hancock and Bradshaw (1983) for $dP/dx = 0$, approaches infinity as c_{f0} approaches zero and is therefore not applicable for boundary layers with adverse pressure gradients. Values of Δc_f and $\Delta\Pi$ are presented by Mohammadi (1989) as a function of $u'/u_*/(L_x/\delta + 2)$, a FST parameter based on u_* as suggested by Bradshaw (1974), and $u'/U_\infty/\Lambda/\delta$ used by Hoffmann et al. (1988a), (1989), but neither of these resulted in as good a collapse of the data. The repeatability of values of Δc_f was generally $\pm$ 0.06 $\times$ 10^{-3} and that of $\Delta\Pi$ was $\pm$ 0.15. To assess the integrity of the experiment, the values of c_{f0} obtained were compared to values obtained using Clauser's formula presented by Harleman and Daily (1973) for $\beta = 0$ and the Ludwieg and Tillmann formula (1949) for $\beta > 0$; a maximum 5 percent difference occurred. In order to check the validity of the equations used to correct c_{f0}, the integral method of Head presented by Cebeci and Bradshaw (1977) was also used to determine the values of c_{f0} at the Re_θ for the conditions with FST; the resulting values of Δc_f were within 2 percent of those presented. The maximum deviation of values of Π_0 compared to those obtained by White's equation was 0.18 for eleven data points with low FST; only one data point fell outside this limit. Generally, scatter of the data increased with increasing β. The present results for $\beta = 0$ and those of Hancock and Bradshaw (1983) for $\beta = 0$ show the least scatter; the present results for $0.3 \leq \beta \leq 1.2$ show more scatter, while those of Evans (1985a) for $0.5 \leq \beta \leq 8.4$ and Arnal (1977) for ($0.7 \leq \beta \leq 7.0$) show even more scatter. The best fit curves for Δc_f and $\Delta\Pi$ for $\beta > 0$ generally coincide with those for $\beta = 0$ case.

Velocity Profile Prediction With FST. Several velocity profiles are presented in Fig. 5, and they show a very good agreement compared to those obtained using Eq. (4). Generally, it is desirable to predict the velocity profiles under FST. It is assumed that the low FST boundary-layer solution (c_{f0}, $\Pi_0 = f(x)$), the potential flow solution (U_∞, $dP/dx = g(x)$) and the FST ($u' = h(x)$) relationships are known. The procedure presented in the following can be used to predict the velocity profiles.

A first-order solution can be obtained by using Fig. 3 to obtain Δc_f and an estimate for c_f at each x location. This c_f is evaluated at the dP/dx and the Re_θ corresponding to the low FST case, while the second order solution will obtain c_f at the Re_θ corresponding to the case with FST. To estimate β with FST, δ^* can be estimated by using an equation presented by Hancock and Bradshaw (1983) for $dP/dx = 0$ and constant Re_θ, Eq. (6), the definition of H, and the assumption that $\theta = \theta_0$. Equation (6) has been shown to be valid for $dP/dx \geq 0$ by Mohammadi (1989), and the results of Hancock and Bradshaw (1983), Evans (1985a), and others have shown that $\theta \simeq \theta_0$. The Π-β relationship is known since the FST parameter is known at each x, and Fig. 3 can be used to obtain $\Delta\Pi$ and Π. To obtain δ, Eq. (4) may be evaluated at $y = \delta$. Equation (4) may now be integrated to obtain δ^* and θ.

$$\Delta H/H_0 = -0.47\Delta c_f/c_{f0} \tag{6}$$

To obtain a second order solution for c_{f0} at the Re_θ corresponding to the condition with FST, the von Doenhoff and Tetervin, and Ludwieg and Tillmann equations can be used for the low FST case, integrating with respect to θ holding dP/dx constant. Figure 3 is now used to obtain a corrected c_f. Using δ^* from the first-order solution and the corrected c_f, the β with FST and the corresponding $\Delta\Pi$ and Π for the condition with FST can now be obtained.

Conclusions

A single equation, composed of the law of the wall and the

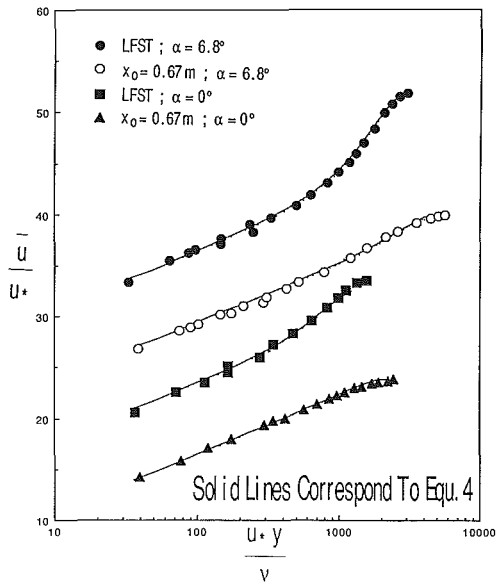

Fig. 5 Velocity profiles at x = 0.94 m. Ordinate scale refers to lowest profile.

law of the wake, is presented which defines the mean velocity profiles of turbulent boundary layers under freestream turbulence (FST) for conditions with zero and adverse pressure gradients. For use of this equation, correlations for skin friction coefficients and the wake parameters, relative to low FST condition, are presented as a function of Hancock's FST parameter. The present results for the case of zero and mild adverse pressure gradient boundary layers collapse very well with the results of Hancock and Meier for the zero pressure gradient case, while more scatter exists when the present results are compared with those of Evans and Arnal for the high adverse pressure gradient case. The correlations presented were obtained for fully turbulent boundary layers with large Reynolds numbers ($2000 \leq \mathrm{Re}_\theta \leq 11{,}000$), for conditions with near isotropic and near homogeneous FST. The correlations may only be applicable for turbulent boundary layers with low values of $d\beta/dx$ (near constant β), and are expected to be valid to the point of boundary layer separation for the low FST condition. The results will be useful for the development of integral methods for the prediction of system performance when turbulent boundary layers experience FST, and can also be used for comparison with results from CFD studies.

Acknowledgments

The authors gratefully acknowledge the quality work of student assistants Scott Ashbaugh, Nora Galloway, Shannon Lewis, and Heather Miller.

References

Arnal, Daniel, 1977, "Influence De La Turbulence De L'Ecoulement General Sur Les Couches Limites Turbulentes En Fluide Incompressible," European Space Agency Technical Translation ESA TT—411, Sept.

Blair, M. F., 1983, "Influence of Free-Stream Turbulence on Turbulent Boundary Layer Heat Transfer and Mean Profile Development, Part II—Analysis of Results," ASME *Journal of Heat Transfer*, Vol. 105, pp. 41–46.

Bradshaw, P., 1974, "Effect of Free-Stream Turbulence on Turbulent Shear Layers," I. C. Aero Report 74-19, Aeronautical Research Council 35 648, F.M. 4520, Oct.

Castro, I. P., 1984, "Effects of Free-Stream Turbulence on Low Reynolds Number Boundary Layers," ASME JOURNAL OF FLUIDS ENGINEERING, Vol. 106, Sept.

Cebeci, T., and Smith, A. M. O., 1974, *Analysis of Turbulent Boundary Layers*, Academic Press.

Cebeci, T., and Bradshaw, P., 1977, *Momentum Transfer in Boundary Layers*, Hemisphere Publishing.

Das, D. K., and White, F. M., 1986, "Integral Skin Friction Prediction for Turbulent Separated Flows," ASME JOURNAL OF FLUIDS ENGINEERING, Vol. 108, Dec.

Dean, R. B., 1976, "A Single Formula for the Complete Velocity Profile in a Turbulent Boundary Layer," ASME JOURNAL OF FLUIDS ENGINEERING, Dec., pp. 723–727.

Evans, R. L., 1985a, "The Effect of Free-Stream Turbulence on the Profile Boundary Layer and Losses in a Compressor Cascade," *International Journal of Turbo and Jet Engines*, Vol. 2, pp. 107–113.

Evans, R. L., 1985b, "Free-Stream Turbulence Effects on Turbulent Boundary Layers in an Adverse Pressure Gradient," *AIAA Journal*, Vol. 23, No. 11, Nov., pp. 1814–1816.

Evans, R. L., and Horlock, J. H., 1974, "Calculation of the Development of Turbulent Boundary Layers With a Turbulent Free-Stream," ASME JOURNAL OF FLUIDS ENGINEERING, Dec., pp. 348–352.

Gad-el-Hak, M., and Corrsin, S., 1974, "Measurement of the Nearly Isotropic Turbulence Behind a Uniform Jet Grid," *Journal of Fluid Mechanics*, Vol. 62, Part 1, pp. 115–143.

Hancock, P. E., and Bradshaw, P., 1983, "The Effect of Free-Stream Turbulence on Turbulent Boundary Layers," ASME JOURNAL OF FLUIDS ENGINEERING, Vol. 105, Sept., p. 284.

Harleman, D. R. F., and Daily, J. W., 1973, *Fluid Dynamics*, Addison-Wesley.

Head, M. R., and Rechenberg, I., 1962, "The Preston Tube as a Means of Measuring Skin Friction," *Journal of Fluid Mechanics*, Vol. 14.

Hoffmann, J. A., 1981, "Effects of Free-Stream Turbulence on Diffuser Performance," ASME JOURNAL OF FLUIDS ENGINEERING, Vol. 103, Sept., pp. 385–390.

Hoffmann, J. A., and Gonzalez, G., 1984, "Effects of Small Scale, High Intensity Inlet Turbulence on Flow in Two Dimensional Diffuser," ASME JOURNAL OF FLUIDS ENGINEERING, Vol. 106, June, pp. 121–124.

Hoffmann, J. A., and Kassir, S. M., 1988a, "Effects of Free-Stream Turbulence on Turbulent Boundary Layers with Mild Adverse Pressure Gradients," AIAA Paper 88-3757-CP, 1st National Fluid Dynamics Congress, Cincinnati, Ohio, July 25–28.

Hoffmann, J. A., and Fang, Liang-Wei, 1988b, "Observations of the Structure of Inlet Free-Stream Turbulence on Diffuser Performance," AIAA Paper 88-3673-CP, presented at The First National Fluid Dynamics Congress, July 24–28.

Hoffmann, J. A., Kassir, S. M., and Larwood, S. M., 1989, "The Influence of Free-Stream Turbulence on Turbulent Boundary Layers with Mild Adverse Pressure Gradients," NASA Contractor Report 177520, Feb.

Hurst, E. A., and Reynolds, W. C., 1968, "An Integral Prediction Method for Turbulent Boundary Layers Using the Turbulent Kinetic Equation," Rept. MD-21, Thermosciences Division, Stanford University, June.

Ludwieg, H., and W. Tillmann, 1949, "Investigations of the Wall-Shearing Stress in Turbulent Boundary Layers," Nat. Advisory Comm. Aeron., Tech. Memo. 1285 (1950); Transl. from Z. Angew. Math. Mech., 29.

Meier, H. U., Michel, U., and Kreplin, H. P., 1987, "The Influence of Wind Tunnel Turbulence on the Boundary Layer Transition," International Symposium on Perspectives in Turbulent Studies, DFVLR Research Center, Gottingen, May 11–12, pp. 26–46.

Mohammadi, K., 1989, "Free-Stream Turbulence Effects on Turbulent Boundary Layers with Favorable, Zero, and Mild Adverse Pressure Gradients," Master of Science Thesis, Aero Engr. Dept., Cal Poly, San Luis Obispo, CA 93420, Sept.

Uberoi, M. S., and Wallis, S., 1967, "Effect of Grid Geometry on Turbulence Decay," *The Physics of Fluids*, Vol. 10, No. 6, pp. 1216–1223.

White, F. M., 1974, *Viscous Fluid Flow*, McGraw-Hill, New York.

APPENDIX

Equations used to correct c_{f0} for changes in Re_θ

Modified von-Doenhoff and Tetervin equations from Hurst and Reynolds (1968):

$$d\theta/dx = c_{f0}/2 - (H_0+2)(\theta/U_\infty)dU_\infty/dx \tag{7}$$

$$dH_0/dx = e^{4.68(H_0-2.975)}[-(2/U_\infty)(dU_\infty/dx) \times [5.89\ \log 4.075\mathrm{Re}_\theta]^2 - 2.035(H_0-1.286)/\theta] \tag{8}$$

Ludwieg and Tillmann equation (used for $dP/dx > 0$) from Ludwieg and Tillmann (1949):

$$c_{f0} = 0.246K/(10^{0.678H_0}\mathrm{Re}_\theta^{0.268}) \tag{9}$$

Clauser's formula (used for $dP/dx = 0$) from Harleman and Daily (1973):

$$c_{f0} = K/(3.96\ \log\ H_0\mathrm{Re}_\theta + 3.04)^2 \tag{10}$$

Three-Dimensional Vortex Structure in a Leading-Edge Separation Bubble at Moderate Reynolds Numbers

Kyuro Sasaki
Assistant Professor,
Department of Mining Engineering,
Mining College,
Akita University,
Akita, 010 Japan

Masaru Kiya
Professor,
Department of Mechanical Engineering,
Hokkaido University,
Sapporo, 060 Japan

This paper describes the results of a flow visualization study which concerns three-dimensional vortex structures in a leading-edge separation bubble formed along the sides of a blunt flat plate. Dye and hydrogen bubbles were used as tracers. Reynolds number (Re), based on the plate thickness, was varied from 80 to 800. For 80 < Re < 320, the separated shear layer remains laminar up to the reattachment line without significant spanwise distortion of vortex filaments. For 320 < Re < 380, a Λ-shaped deformation of vortex filaments appears shortly downstream of the reattachment and is arranged in-phase in the downstream direction. For Re > 380, hairpin-like structures are formed and arranged in a staggered manner. The longitudinal and spanwise distances of the vortex arrangement are presented as functions of the Reynolds number.

1 Introduction

Flows with separation and reattachment have long been subjects of fluids engineering research. Previous studies on the separation-reattachment flows (hereinafter referred to as a "separation bubble") have demonstrated that the flows are highly unsteady and are dominated by large-scale vortices in the separated shear layer (Kiya and Sasaki, 1983 and 1985; Kiya, 1989; Cherry et al., 1984). Bradshaw and Wong (1972) and Sigurdson (1986) give excellent reviews of the flow in this category.

Observations of vortices in the separation bubble formed by boundary-layer separation at the leading edge of a blunt flat plate are reported by Lane and Loehrke (1980), Ota et al. (1981), Kiya (1989), and Sigurdson and Roshko (1984) at low and moderate Reynolds numbers. Cherry et al. (1984) present instantaneous smoke flow visualizations synchronized with pressure fluctuation wave forms at high Reynolds numbers. Kiya and Sasaki (1985) suggest a three-dimensional U-shape vortex structure in the reattachment region on the basis of conditionally-averaged velocity fluctuations. Kiya (1989) shows an aspect of the three-dimensional flow patterns at moderate Reynolds numbers. Sigurdson (1986), Sigurdson and Roshko (1984), and Kiya et al. (1983) reported that the vortex loops are sometimes arranged in a staggered pattern. However, the deformation process of three-dimensional vortices and their arrangements in the separation bubble are not well understood. The relation between bubble length and Reynolds number is reported by Lane and Loehrke (1980) and Ota et al. (1981) at low and moderate Reynolds numbers.

Three-dimensional vortex structures in turbulent shear flows have been reported by many authors. Head and Bandyopadhyay (1981) showed by flow visualizations that turbulent boundary layers at high Reynolds numbers appear to consist of closely packed hairpin vortices or vortex pairs which incline with an angle in the downstream direction. Perry et al. (1981) observed Λ-shape vortices in a flow behind a vibrating trip wire.

The purpose of this work is to describe the results of a flow visualization study on the development and arrangement of three-dimensional vortex deformation and on arrangement of large scale vortices in the leading edge separation bubble at moderate Reynolds numbers.

Symbols are defined in Fig. 1. The Cartesian coordinates x, y, z are defined in such a way that the x-axis is in the longitudinal direction, the y-axis is vertically outward from the side, and the z-axis is normal to the x- and y-axes to form a right-handed system. The origin is located at the separation edge of the plate, whose thickness is denoted by $2H$. The longitudinal and spanwise distances between the large-scale vortices are denoted by l_x and l_z, respectively. The velocity at infinity upstream is denoted by U_∞. The time-mean bubble length is written as x_R.

2 Experimental Apparatus and Methods

2.1 Water Channel. Visualizations were performed in a recirculating open water channel as shown in Fig. 2. The rectangular shaped test section of the channel had dimensions of 200 mm in width, 250 mm in depth, and 800 mm in length.

Contributed by the Fluids Engineering Division for publication in the JOURNAL OF FLUIDS ENGINEERING. Manuscript received by the Fluids Engineering Division July 24, 1990.

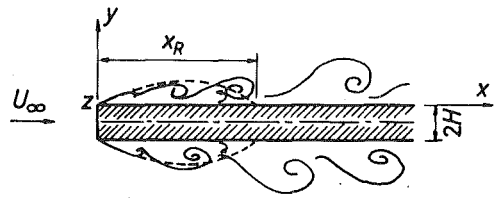

Fig. 1 Configuration of flow and definition of symbols

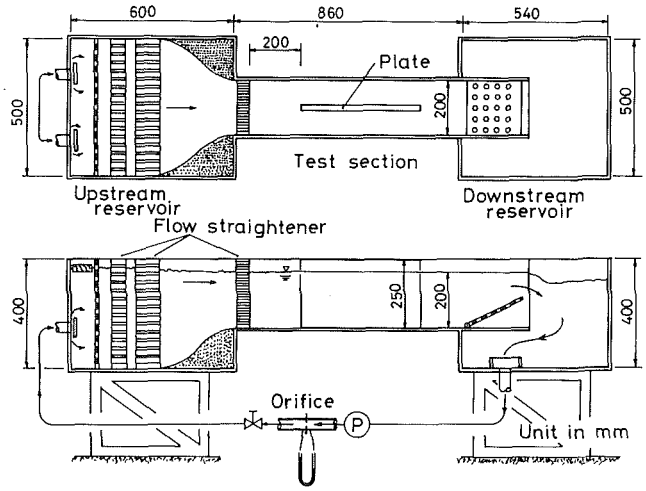

Fig. 2 Recirculating open channel (dimensions in mm)

No appreciable waves were observed on the free surface during the experiments. Most parts of the channel consisted of 10 mm thick transparent acrylic-resin plates for the purpose of flow visualization. The vortex structures were observed through the free surface and from the sides of the test section.

The water was circulated by a small centrifugal pump. The velocity in the test section was controlled by a throttle valve in a return pipe. The water was passed through two screens, a series of honeycombs (4 mm in cell size) and a bell entrance before flowing into the test section. The depth of water in the test section, controlled by an inclined plate at the entrance of the downstream reservoir, was 200 mm.

2.2 Measurements of Mean Velocity of the Uniform Flow. The time-mean velocity of the main flow in the test section (U_∞) was obtained by measuring distances between two timelines of hydrogen bubbles. The timelines were produced by a pulsed voltage from a straight wire of 50 μm in diameter and 210 mm in length. The timelines were not completely straight because the hydrogen bubbles did not leave the wire simultaneously. The distances between two consecutive timelines were fairly constant in the spanwise and downstream directions; the uncertainty of the velocity measurement was estimated to be ± 2 percent. The longitudinal velocity profile was uniform within about ± 3 percent over the test section

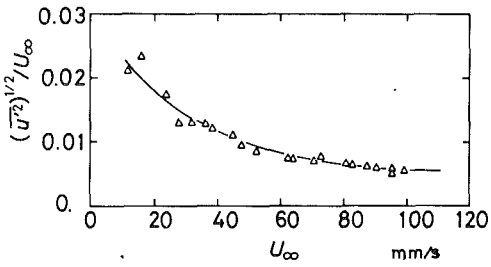

Fig. 3 Longitudinal turbulence intensity in main flow

except the boundary layers along the bottom and side walls in a range $U_\infty \approx$ 10–100 mm/s. The uncertainty in Re was ± 5 percent.

2.3 Measurements of Turbulence Intensity of Main Flow. The longitudinal turbulence intensity of the main flow was measured by a linearized constant-temperature hot-wire anemometer using a hot-film sensor 51 μm in diameter (produced by Thermo-System Inc.). The calibration curves were linear within ± 5 percent. A low-path filter (40 dec./oct., cut-off frequency = 40 Hz) to cut electronic noises of the constant temperature hot-film velocimeter. The equivalent turbulence level relating to the electronic noises was approximately 0.2–0.3 percent of the main flow velocity.

Figure 3 shows the turbulence intensity $(\overline{u'^2})^{1/2}/U_\infty$ where u' is the longitudinal velocity fluctuation as a function of U_∞. The higher the main-flow velocity, the lower is the turbulence intensity; for example, the turbulence intensity was approximately 0.6 percent at U_∞ = 80 mm/s.

2.4 Blunt Flat Plates. The blunt flat plates tested were made from smooth acrylic-resin. Three test plates of thicknesses $2H$ = 20, 10, and 5 mm were employed. The radius of the corner is less than 0.1 mm. The spanwise width of all the plates were 250 mm. Since the spanwise length of the plates immersed in water was 200 mm, their aspect ratio ranged from 10 to 40. The channel-wall blockage ratio ranged from 2.5 to 10 percent. No end plates were used. The plates were mounted vertically along the centerline of the test section. The length of the plates was 480 mm long enough to realize the leading-edge separation bubble of a semi-infinite blunt plate, because the maximum bubble length is not longer than 150 mm (Lane and Loehrke, 1980). The exact alignment of the plate was determined such that a bifurcation of the stagnation streamline visualized by the dye was symmetric.

2.5 Flow Visualization. The flow was visualized by two methods. The first was a dye tracer method using fluorescent natrium solution (specific gravity = 1.006); this was used to visualize the flow in xy-plane (Fig. 1). The dye was injected into the boundary layer along the front face through a 0.8 mm diameter hole located at the stagnation point in the midspan plane. The injection velocity of the dye as sufficiently low so as not to disturb the boundary layer along the front face. The dye was taken into the shear layer starting from the separation

Nomenclature

H = half thickness of plate
l_x = longitudinal distance between large-scale vortices
l_z = spanwise distance between large-scale vortices
Re = Reynolds number based on plate thickness, $2HU_\infty/\nu$
U_∞ = uniform velocity at infinity upstream
u' = fluctuating velocity of uniform flow
x = longitudinal coordinate along plate surface
x_R = bubble length
y = coordinate normal to plate surface
z = coordinate in spanwise direction
ν = kinetic viscosity

point. The second method used fine hydrogen bubbles to visualize the three-dimensional deformation of vortex filaments and the formation of large vortices. The hydrogen bubbles were continuously generated from a platinum wire 200 mm long and 50 μm in diameter placed on the side face 0.3 mm downstream of the separation line. The fine hydrogen bubbles concentrate into the vortex center. This is because the density of the hydrogen bubbles is much less than that of water so that the centrifugal force acting on the bubbles in a vortex is overcome by the pressure gradient. The voltage supplied to the bubble generator was controlled to produce hydrogen bubbles less than 0.1 mm in diameter.

The dye and the hydrogen bubbles were, respectively, made visible by a sheet of light inserted through the side wall of the channel and by a sheet of light reflected by a mirror located under the bottom of the channel. The light was produced by a 500 W slide projector. Photographs were taken with ASA-400 films and the exposure time of 1/60 s.

2.6 Measurement of Bubble Length. The time-mean bubble length x_R is defined as the distance between the leading edge and the time-mean reattachment line. The reattachment line was determined as follows: The hydrogen bubbles were generated from the platinum wire which was placed on the plate surface near the reattachment line and inclined at an angle of 30 deg with respect to the spanwise direction. Figure 4 shows a sketch of the observed motion of the hydrogen bubbles. Although the hydrogen bubbles have a tendency to rise up toward the free surface, their motion in the longitudinal direction clearly demonstrated an instantaneous reattachment position. The time-mean reattachment position was determined by observing the motion of the instantaneous reattachment with the aid of a range finder. The uncertainty of measured x_R was estimated to be $\pm 0.2H$. The measurements of reattachment point were made in a spanwise region $\pm 3H$ from the midspan. A difference in the bubble length in this region was less than $\pm 0.2H$.

3 Experimental Results and Discussion

3.1 Time-Mean Bubble Length. Figure 5 shows the time-mean bubble length x_R plotted against the Reynolds number $\mathrm{Re} = 2HU_\infty/\nu$ where ν is kinetic viscosity together with the results of Lane and Loehrke (1980) and Ota et al. (1981). Differences between the present and other authors' results are probably associated with different methods to determine x_R, plate lengths, methods of visualization, blockage ratios, aspect ratios, and main flow turbulence intensity.

In the present experiment the separation bubble appeared where $\mathrm{Re} > 80$, while Lane and Loehrke (1980) observed it in a range $\mathrm{Re} > 100$. The bubble length is seen to attain a maximum of about $13H$ at $\mathrm{Re} = 320$, agreeing with the results of the previous authors. If the bubble length in a range $80 < \mathrm{Re} < 320$ is shown in the log-log plot, the bubble length is approximately proportional to Re^2 in the same range of Re. Ota et al.'s (1981) results for blunt flat plates with various nose shapes do not have the same relation. Goldstein et al. (1970) and Back and Roschke (1972) showed that for a downward-facing step and for an abrupt circular pipe expansion, x_R increases linearly with Re up to $\mathrm{Re} \approx 500$ and 250 respectively.

The sudden decrease of x_R in a range $320 < \mathrm{Re} < 380$ is associated with the onset of rolling-up of the separated shear layer. For larger Reynolds numbers $\mathrm{Re} > 380$, x_R takes a constant value of approximately $9H$. Results by Lane and Loehrke (1980) seem to follow the same trend up to $\mathrm{Re} \approx 500$, while Ota et al.'s (1981) results show a gradual decrease up to $\mathrm{Re} \approx 1600$.

The above feature of x_R suggests an intimate connection between the bubble length and the vortex structure in the shear layer. Moreover, Fig. 5 suggests that the flow can be classified

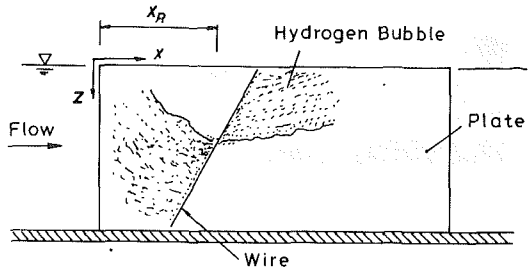

Fig. 4 Method to obtain reattachment point

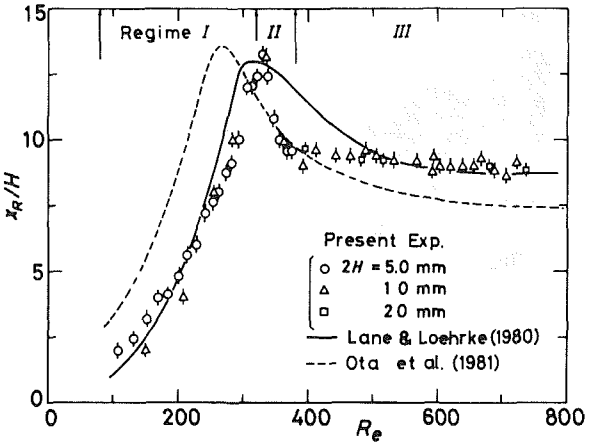

Fig. 5 Bubble length versus Reynolds number. (Uncertainty in boundaries of regime I-III = ±5 percent of Re)

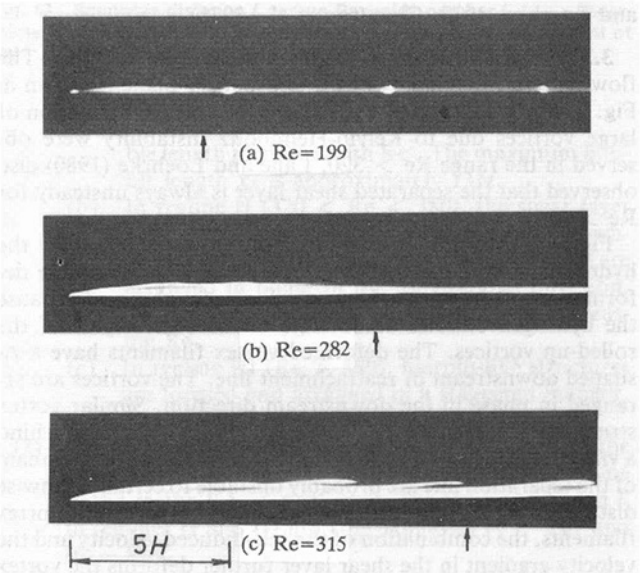

Fig. 6 Side view of separated shear layer in regime I (dye tracer, ↑; x_R)

into three regimes: regime I ($80 < \mathrm{Re} < 320$), regime II ($320 < \mathrm{Re} < 380$), and regime III ($\mathrm{Re} > 380$).

3.2 Vortex Structure in Regime I ($80 < \mathrm{Re} < 320$). The flow patterns in the midspan xy-plane, which were visualized by the dye, are shown in Fig. 6(a)-(c) for three Reynolds numbers in regime I. At low Reynolds numbers $\mathrm{Re} = 80 - 300$ (Fig. 6(a) and (b)), the shear layer remains laminar up to the reattachment line experiencing no rolling up; the spanwise distortion of the shear layer was also insignificant. An instability wave in the shear layer such as the one shown in Fig. 6(c) was observed near $\mathrm{Re} = 320$. The instability wave

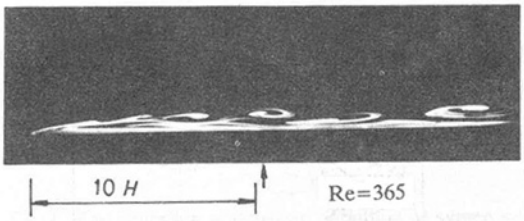

Fig. 7 Side view of vortices in regime II (dye tracer, ↑; x_R)

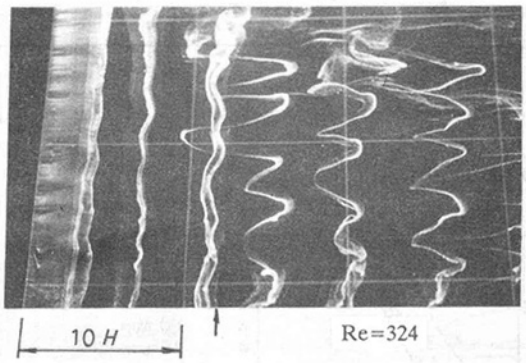

Fig. 8 Top view of vortices in regime II (hydrogen bubbles, ↑; x_R)

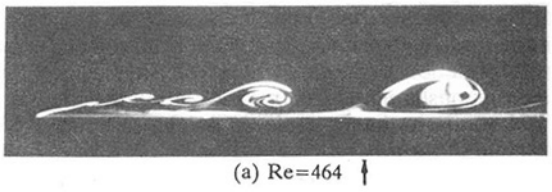

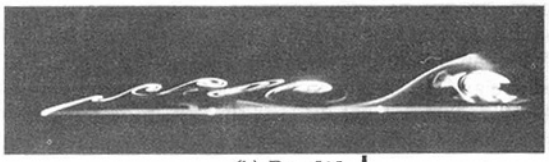

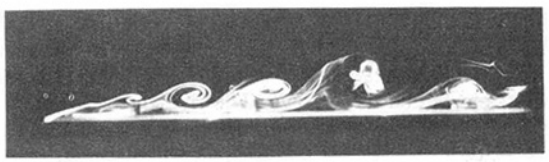

Fig. 9 Side view of vortices in regime III (dye tracer, ↑; x_R)

propagates downstream with no spanwise deformation; the shear layer does not roll up to form large vortices because the viscous force is yet dominant in the range Re < 320. The instability wave in the shear layer is also reported by previous authors (Lane and Loehrke, 1980; Goldstein et al., 1970; Back and Roschke, 1972; Cherdron et al., 1978).

3.3 Vortex Structure in Regime II (320 < Re < 380). The flow pattern in regime II in the midspan *xy*-plane is shown in Fig. 7. The rolling-up of the shear layer and the formation of large vortices due to Kelvin-Helmholtz instability were observed in the range Re > 320. Lane and Loehrke (1980) also observed that the separated shear layer is always unsteady for Re > 325.

Figure 8 shows the top view of the flow visualized by the hydrogen bubble method. The pseudo-periodic spanwise deformation of the vortex filaments is clearly observed because the hydrogen bubbles accumulate in the central part of the rolled-up vortices. The deformed vortex filaments have a Λ-shaped downstream of reattachment line. The vortices are arranged in phase in the downstream direction. Similar vortex structures are reported by Perry et al. (1981) for a flow behind a vibrating trip wire. The straight vortex filaments downstream of the separation line are probably unstable to certain spanwise disturbances. If such a disturbance slightly deforms the vortex filaments, the combination of the self-induced velocity and the velocity gradient in the shear layer further deforms the vortex filaments. The inherent wave length is probably dependent on the radius of core of the vortex filaments, and thus on the Reynolds number. The in-phase arrangement of the Λ-shape vortices will be referred to as "pattern A."

3.4 Vortex Structure in Regime III (Re > 380). Flow patterns in regime III in the *xy*-plane are shown in Fig. 9. The separated shear layer becomes thinner and thus the point where it begins to roll up is further upstream than that in regime II. The amalgamation of two or three rolled-up vortices is observed in the middle of the bubble ($0.3 < x/x_R < 0.8$); the amalgamation produces large-scale vortices with three dimensional structures. The number of the amalgamation increases with Re, thus the three-dimensional structure appears at a position further upstream. In Fig. 9(*c*), the dye indicates a three-dimensional twisting motion.

Figure 10 shows the top views in regime III at different values of Re. Hairpin-like structures are observed in Figs. 10(*a*) and (*b*). Their legs are enormously stretched in the longitudinal direction, so that the vortices looks like a vortex ring. The vortices are generally arranged in a staggered manner. The deformation of vortex filaments near separation line appears to be affected by a spanwise nonuniformity of the velocity field induced by the three-dimensional vortices located downstream. This induced velocity field might give rise to the staggered arrangement of the large vortices, illustrated in Fig. 11. The same arrangement is reported by previous authors (Sigurdson, 1986; Sigurdson and Roshko, 1984; Kiya et al., 1983). The staggered arrangement of the hairpin-like structures will be referred to as "pattern B."

As the Reynolds number increases, the shape and the arrangement of vortices become less regular shown in Fig. 10(*c*). This is because the amalgamation does not occur uniformly in the spanwise direction and disorders are thus superimposed at every amalgamation. These disorders may produce high-frequency random velocity fluctuations at high Reynolds numbers.

3.5 Longitudinal and Spanwise Distances Between Vortices. The longitudinal and spanwise distances between large vortices l_x and l_z were obtained in the region $0.6 < x/x_R < 2.0$. Values of l_x and l_z were obtained from the top view photographs and are shown in Figs. 12 and 13; the experimental uncertainty was less than $\pm 0.75H$. The distances l_x and l_z are almost the same and have values of approximately $l_x = l_z = (4 - 5)H$ for pattern A and $(6 - 8)H$ for pattern B. A wind tunnel experiment at a high Reynolds number $\mathrm{Re} = 2.6 \times 10^4$ (Kiya and Sasaki, 1985) suggests $l_x = (7 - 8)H$ and $l_z = (5 - 7)H$, which are close to the above results for pattern B.

4 Conclusions

Three-dimensional vortex structures in a leading-edge separation bubble formed along the sides of a blunt flat plate were studied by flow visualization techniques in a Reynolds number range 80 < Re < 800. Results can be summarized as follows:

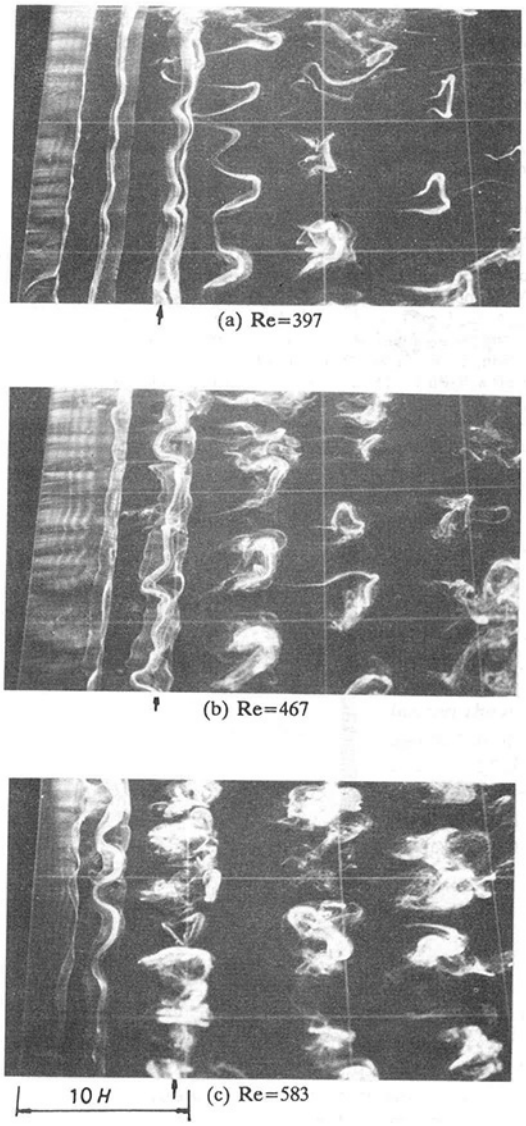

Fig. 10 Top view of vortices in regime III (hydrogen bubbles, ↑; x_R)

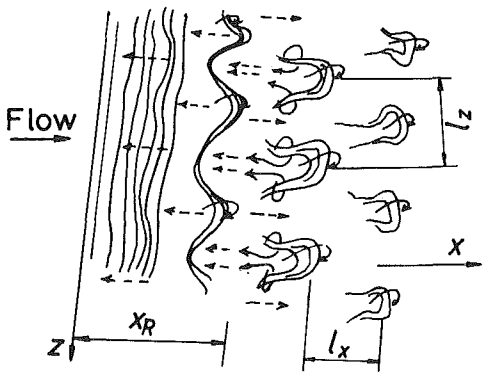

Fig. 11 Illustration of mechanism to generate staggered manner of vortices

(1) The time-mean bubble length is given as a function of Reynolds number.
(2) The vortex structure can be classified into three regimes.
   (*a*) In regime I (80 < Re < 320), the shear layer remains laminar up to the reattachment point without significant spanwise distortion. The bubble length increases with Re^2. The maximum bubble length x_R is approximately $13H$.
   (*b*) In regime II (320 < Re < 380), the shear layer rolls up to form Λ-shape vortices shortly downstream of the reattachment line; these vortices are arranged in phase in the longitudinal direction. The bubble length decreases sharply with increasing Re.
   (*c*) In regime III (Re > 380), hairpin-like structures are formed and arranged in a staggered manner. The bubble length is approximately constant.
(3) The longitudinal and spanwise distances l_x and l_z of the arrangement of the large vortices are almost the same in the region $0.6 < x/x_R < 2$. The values of l_x and l_z in regimes II and III are approximately $(4 - 5)H$ and $(6 - 8)H$.

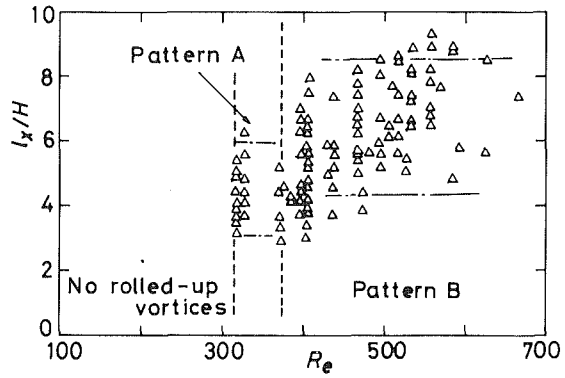

Fig. 12 Longitudinal distance l_x versus Reynolds number (— · —, uncertainty limit; uncertainty in boundaries of regime I-III = ±5 percent of Re)

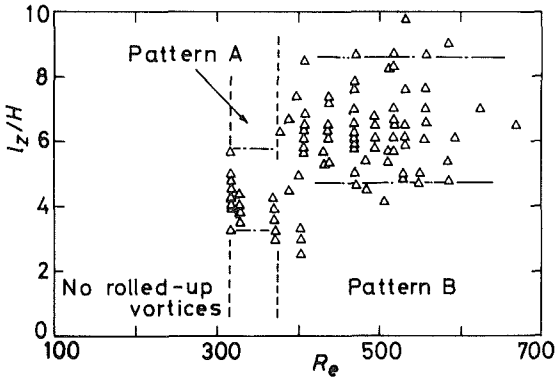

Fig. 13 Spanwise distance l_z versus Reynolds number (— · —, uncertainty limit; uncertainty in boundaries of regime I-III = ±5 percent of Re)

Acknowledgments

This work was supported by a grant-in-aid from the Taro Yamashita Memorial Scholarship Society (Akita, Japan). This paper was written while K. Sasaki was a visitor in the Department of Mechanical Engineering, University of Alberta, Canada. The authors would like to express their thanks to Mr. M. Yasukawa for his assistance in the flow visualization, and to Dr. S. Tamura (Hokkaido University), Dr. L. W. Sigurdson (University of Alberta), and Dr. K. C. Cheng (University of Alberta) for their helpful discussions.

References

Back, L. H., and Roschke, E. J., 1972, "Shear-Layer Flow Regimes and Wave Instabilities and Reattachment Lengths Downstream of an Abrupt Circular

Channel Expansion," ASME *Journal of Applied Mechanics*, Vol. 39, pp. 677–681.

Bradshaw, P., and Wong, F. Y. F., 1972, "The Reattachment and Relaxation of a Turbulent Boundary Layer," *Journal of Fluid Mechanics*, Vol. 51-2, pp. 113–135.

Cherdron, W., Durst, F., and Whitelaw, J. H., 1978, "Asymmetric Flows and Instabilities in Symmetric Ducts with Sudden Expansion," *Journal of Fluid Mechanics*, Vol. 84-1, pp. 13–32.

Cherry, N. J., Hillier, R., and Laughter, M. E. M. P., 1984, "Unsteady Measurement in a Separated and Reattaching Flow," *Journal of Fluid Mechanics*, Vol. 144, pp. 13–46.

Goldstein, R. J., Eriksen, V. L., Olsen, R. M., and Eckert, E. R. G., 1970, "Laminar Separation, Reattachment and Transition of the Flow Over a Downstream-Facing Step," ASME *Journal of Basic Engineering*, Vol. 92, pp. 732–741.

Head, M. R., and Bandyopadhyay, P., 1981, "New Aspects of Turbulent Boundary-Layer Structure," *Journal of Fluid Mechanics*, Vol. 107, pp. 297–338.

Kiya, M., 1989, "Separation Bubbles," *Theoretical and Applied Mechanics*, eds. Germain, P., Piau, M., and Caillerie, D., Elsevier Sci. Pub. (North-Holland), pp. 173–191.

Kiya, M., and Sasaki, K., 1983, "Structure of a Turbulent Separation Bubble," *Journal of Fluid Mechanics*, Vol. 137, pp. 83–113.

Kiya, M., and Sasaki, K., 1985, "Structure of Large-Scale Vortices and Unsteady Reverse Flow in the Reattaching Zone of a Turbulent Separation Bubble," *Journal of Fluid Mechanics*, Vol. 154, pp. 463–491.

Kiya, M., Sasaki, K., and Yasukawa, M., 1983, "Three Dimensional Structure of Leading Edge Separation Bubble," *Proc. of Annual Meeting in Hokkaido District of JSME*, No. 832-3, pp. 39–44 (in Japanese).

Lane, J. C., and Loehrke, R. I., 1980, "Leading Edge Separation From a Blunt Plate at Low Reynolds Number," ASME JOURNAL OF FLUIDS ENGINEERING, Vol. 102-11, pp. 494–496.

Ota, T., Asano, Y., and Okawa, J., 1981, "Reattachment Length and Transition of the Separated Flow Over Blunt Flat Plates," *Bulletin of the JSME*, Vol. 24-192, pp. 941–947.

Perry, A. E., Lim, T. T., and Teh, E. W., 1981, "A Visual Study of Turbulent Spots," *Journal of Fluid Mechanics*, Vol. 104, pp. 387–405.

Sigurdson, L. W., 1986, "The Structure and Control of a Turbulent Reattaching Flow," Ph.D. Thesis, California Institute of Technology.

Sigurdson, L. W., and Roshko, A., 1984, "The Large-Scale Structure of a Turbulent Reattaching Flow," *Bull. Am. Phys. Soc.*, 29(9), presented at the Annual Meeting of the Fluid Dynamics Division, Providence, RI, p. 1542.

Computation of Turbulent Flow in a Thin Liquid Layer of Fluid Involving a Hydraulic Jump

M. M. Rahman

A. Faghri

W. L. Hankey

Department of Mechanical and Materials Engineering,
Wright State University,
Dayton, Ohio 45435

Numerically computed flow fields and free surface height distributions are presented for the flow of a thin layer of liquid adjacent to a solid horizontal surface that encounters a hydraulic jump. Two kinds of flow configurations are considered: two-dimensional plane flow and axisymmetric radial flow. The computations used a boundary-fitted moving grid method with a k-ϵ model for the closure of turbulence. The free surface height was determined by an optimization procedure which minimized the error in the pressure distribution on the free surface. It was also checked against an approximate procedure involving integration of the governing equations and use of the MacCormack predictor-corrector method. The computed film height also compared reasonably well with previous experiments. A region of recirculating flow as found to be present adjacent to the solid boundary near the location of the jump, which was caused by a rapid deceleration of the flow.

Introduction

The free surface flow of a turbulent liquid layer has applications in civil, mechanical, and chemical engineering. The flow in a cooling tower or compact evaporator is often turbulent where a thin liquid film evaporates adjacent to a solid wall. A thin turbulent fluid film may be also encountered in gas absorption columns and condensers. The open channel flow in a river or water table is also turbulent in nature. To properly understand such natural or engineering phenomena, a detailed study of the turbulent flow field in a liquid layer is essential.

The previous research related to the present investigation can be categorized into two groups: the studies related to thin liquid films, where viscous effects are predominant and the flow may be laminar, wavy-laminar, or turbulent depending on the flow rate; and the studies related to an open channel, where the viscous resistance is small, but the flow is usually turbulent in nature. The wavy-laminar and turbulent flow in a falling liquid film was investigated, among others, by Chun and Seban (1971), Mills and Chung (1973), Seban and Faghri (1976, 1978), Hirshburg and Florschuetz (1982), Grossman and Heath (1984), and Faghri and Seban (1985, 1988). The fluid flow, as well as heat and mass transfer phenomena, were studied experimentally and theoretically. In a vertically falling film, however, no hydraulic jump is present. A jump may be encountered when the gravitational force acts across the thickness of the film. Watson (1964) analyzed the turbulent flow of a radially spreading thin film produced by the impingement of a vertical liquid jet onto a horizontal surface. A similarity solution was derived by solving the parabolic version of the governing transport equations assuming that viscous effects propagate all the way across the film and the eddy diffusivity remains constant. Even though the analysis predicted his experimental data, it had the drawback that the location of the hydraulic jump and the downstream film height could not be uniquely determined from the parabolic momentum equation. The flow, in reality, is elliptic in nature. Also, since the driving mechanism in this flow is the jet velocity and its diameter, the results cannot be applied to a flow where the film is produced by discharge from a slot in a pressurized container.

The laminar flow of a thin film emanating from a slot in a pressurized vessel under zero and normal gravity environments was studied recently by Thomas et al. (1990) and Rahman et al. (1990a, 1990b). In the investigation by Thomas et al. (1990), the flow was assumed to be one-dimensional in nature, and solved numerically using the MacCormack predictor-corrector method. Both upstream and downstream boundary conditions were imposed, and the algorithm marched explicitly in time and yielded the final steady-state solution. The resistance to the flow due to the solid wall was accounted for by assuming suitable expressions for the friction coefficient. The primary outcome of this study was the prediction of the film height distribution for a given flow rate and inlet and outlet Froude numbers.

Rahman et al. (1990a, 1990b) developed a full two-dimensional numerical solution procedure for laminar flow without any approximation for the friction coefficient. A curvilinear boundary-fitted coordinate system was used, where the irregular free surface conformed to one of the boundaries of the computation domain. Since the two-dimensional finite-difference method required the specification of the free surface for grid generation, whereas the surface geometry itself is dependent on other flow parameters, an iterative solution pro-

Contributed by the Fluids Engineering Division of THE AMERICAN SOCIETY OF MECHANICAL ENGINEERS and presented at the ASME/AIAA Thermophysics and Heat Transfer Conference, Seattle, WA, June 18–20, 1990. Manuscript received by the Fluids Engineering Division April 3, 1990.

cedure had to be adapted to arrive at the correct location of the free surface. The method used by Rahman et al. (1990a) is termed "pressure optimization method," where the free surface was assumed to be a frictionless solid wall with its geometry defined by an algebraic equation with two or more arbitrary constants. The values of these constants were optimized by using an exhaustive search technique that minimized the error on the free surface pressure distribution. In this method, the supercritical and subcritical flows were computed separately and the location of the jump was determined by taking into account the conservation of momentum at the jump itself. The method proposed by Rahman et al. (1990b) was an alternative iteration procedure where the free surface was assumed to be a porous wall allowing penetration of flow through it depending on the difference between the free surface and ambient pressures. Since an ideal free surface is required to satisfy the streamline and zero-penetration conditions, these two criteria were monitored during the iteration process to arrive at the final free surface height distribution.

All of the above studies on thin film flows adjacent to a horizontal surface as produced by fluid discharging through a slot considered only laminar flow. In reality, the flow is expected to be turbulent at high flow rates and film heights. No study has been yet devoted to address this kind of turbulent flow. On the other extreme, the turbulent flow in a thick liquid layer as seen in a water table or river has been studied extensively. The hydraulic jumps associated with such flows have been reviewed by Rajaratnam (1967). This review compiled experimental measurements as well as theoretical models for flow in the hydraulic jump. The separation of flow at the wall due to frictional resistance was studied by Leutheusser and Alemu (1979). Experimental data were taken for different values of Reynolds and Froude numbers. The surface profile of a hydraulic jump was measured by Sarma and Newnham (1973). The experimental data for a number of flow rates and inlet Froude numbers were reported covering the jump and subcritical regions. The turbulence characteristics at the jump were studied by Rouse et al. (1959) who performed a simulated experiment using an air duct of the shape of a hydraulic jump. The measurements of mean and fluctuating velocity components were taken using a hot film anemometer.

The present investigation is intended to understand the mean behavior of the flow during turbulent motion in a thin liquid layer. The one-dimensional and two-dimensional numerical solution procedures developed by Thomas et al. (1990) and Rahman et al. (1990a) for laminar flow will be extended to incorporate turbulent flow. Both plane and radially spreading flows will be considered. The film height distribution and details of the flow field will be presented for different values of Reynolds and Froude numbers. In addition to the fundamental understanding of the physics of the flow, the results are expected to be very useful in the design of process and heat exchange equipment.

Mathematical Model

Two different flow geometries, i.e., plane flow and radially spreading flow, are considered in the present investigation. In the case of plane flow, the fluid particles move in a two-dimensional fashion on a plane horizontal wall with no variation in the third direction. Radially spreading flow is where fluid is discharged at the center of a circular horizontal disk and spreads radially outward in an axisymmetric fashion. In both cases the gravitational body force acts perpendicular to the plate, i.e., across the thickness of the film.

The coordinate system shown in Fig. 1 is used in the computations. The r-axis is directed along the plate radius (or length, for plane flow) and the y-axis is directed perpendicular to the plate. This r-y system is used for the formulation of the one-dimensional computational scheme where the continuity and momentum equations are integrated out in the y-direction. For a complete two-dimensional solution, a boundary-fitted coordinate system is used. In this system, the coordinates are defined along lines connecting the centers of the adjacent grid

Nomenclature

a_k = von Kármán constant, 0.435
c_f = coefficient of friction, $T_w/(0.5\rho W^2)$
C_1 = turbulence model constant (Eq. (8)), 1.44
C_2 = turbulence model constant (Eq. (8)), 1.92
C_D = turbulence model constant (Eq. (13)), 0.1643
C_μ = turbulence model constant (Eq. (10)), 0.09
E = roughness factor, 9.0 for smooth wall
Fr = Froude number, $W/\sqrt{g\delta}$
g = acceleration due to gravity
G = rate of generation of turbulent kinetic energy, defined by Eq. (9)
k = turbulent kinetic energy, or index for wall location in z-direction
K = geometric factor, $\begin{cases}0, \text{ for plane flow}\\1, \text{ for radial flow}\end{cases}$
L = length of the plate
n = coordinate normal to surface
p = difference between fluid and ambient pressures
r = radial coordinate or coordinate along the plate for plane flow
r^+ = normalized distance along the plate, $\begin{cases}r/L, \text{ for plane flow}\\(r - r_{in})/(r_{out} - r_{in}), \text{ for radial flow}\end{cases}$
Re_δ = Reynolds number in terms of film thickness, $W\delta/\nu$
Re_L = Reynolds number in terms of plate length, WL/ν or $W(r_{out} - r_{in})/\nu$
Re_Δ = frictional Reynolds number, defined by Eq. (11)
t = time
v = component of velocity in y-direction
V = dimensionless velocity along the plate, defined by Eq. (15)
$\mathbf{V}$ = velocity vector
w = component of velocity along r- or z-direction
W = average velocity along the plate
y = coordinate normal to the plate
z = coordinate along the main flow direction
β = coefficient of artificial viscosity
δ = film thickness
δ^+ = dimensionless film thickness, defined by Eq. (15)
ϵ = rate of diffusion of turbulent kinetic energy
ν = kinematic viscosity
ν_T = Eddy diffusivity
ξ = dimensionless distance, defined by Eq. (15)
ρ = density
σ_k = diffusivity factor for turbulent kinetic energy, 1.0
σ_ϵ = diffusivity factor for rate of diffusion of turbulent kinetic energy, 1.3
τ = shear stress, or dimensionless time defined by Eq. (15)

Subscripts

in = condition at entrance
out = condition at exit
w = condition on solid wall
Δ = value at a small distance "Δ" away from the solid wall

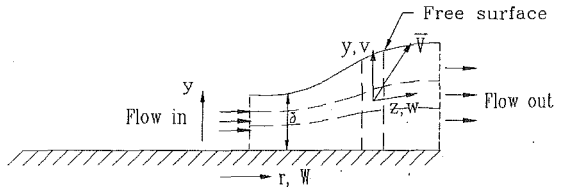

Fig. 1 The coordinate system for one and two-dimensional numerical computation

cells. The z-axis is located in the direction of the main flow and y-axis across the thickness of the liquid layer. Comparing the r-y and z-y system, we notice that the y-axis remains unaltered, whereas the z-coordinate is related to r by a geometrical factor.

The conservation of mass and momentum for incompressible flow of a Newtonian, constant-property fluid is given by

$$\nabla \cdot \mathbf{V} = 0 \tag{1}$$

$$\frac{Dv}{Dt} = -\frac{1}{\rho}\frac{\partial p}{\partial y} + \nabla \cdot [(\nu + \nu_T)\nabla v] - g \tag{2a}$$

$$\frac{Dw}{Dt} = -\frac{1}{\rho}\frac{\partial p}{\partial z} + \nabla \cdot [(\nu + \nu_T)\nabla w] \tag{2b}$$

The boundary conditions can be stated as:

at solid wall: $\mathbf{V} = 0$ (3)

at free surface: $\frac{\partial \mathbf{V}}{\partial n} = 0,\ p = 0$ (4)

at entrance: $\mathbf{V} = \mathbf{V}_{\text{in}},\ \delta = \delta_{\text{in}}$ (5)

at exit: $\frac{\partial \mathbf{V}}{\partial n} = 0,\ \delta = \delta_{\text{out}}$ (6)

Here "p" is the difference between the static pressure in the fluid and the ambient pressure. At the free surface, the stress-free condition requires a balance in the normal and shear stresses. In general, the balance of normal stresses relates the free surface pressure to that of the ambient via surface tension and other stresses. As discussed by Rahman et al. (1990b), the effects of surface tension and other stresses appear to be negligible in most regions of the flow at large values of Reynolds and Weber numbers, leading to the $p = 0$ condition on the free surface. For laminar flow, $\nu_T = 0$. For turbulent flow, ν_T can be determined by actually solving the equations for turbulent kinetic energy and its rate of dissipation. The conservation equations for these quantities are given by:

$$\frac{Dk}{Dt} = \nabla \cdot \left[\left(\nu + \frac{\nu_T}{\sigma_k}\right)\nabla k\right] + G - \epsilon \tag{7}$$

$$\frac{D\epsilon}{Dt} = \nabla \cdot \left[\left(\nu + \frac{\nu_T}{\sigma_\epsilon}\right)\nabla \epsilon\right] + C_{1\epsilon}\frac{G}{k} - C_2\frac{\epsilon^2}{k} \tag{8}$$

where

$$G = \nu_T\left[2\left(\frac{\partial v}{\partial y}\right)^2 + 2\left(\frac{\partial w}{\partial z}\right)^2 + \left(\frac{\partial v}{\partial z} + \frac{\partial w}{\partial y}\right)^2\right] \tag{9}$$

The constants appearing in these equations can be taken to be those proposed by Launder and Spalding (1974) for turbulent recirculating flows.

$$C_1 = 1.44 \quad \sigma_k = 1.0$$
$$C_2 = 1.92 \quad \sigma_\epsilon = 1.3$$

The generation term "G" is taken here to be ν_T times the rate of strain, which is true for flows involving negligible changes in fluid properties. ν_T is related to k and ϵ by the equation,

$$\nu_T = C_\mu \frac{k^2}{\epsilon} \tag{10}$$

where $C_\mu = 0.09$.

In order to solve these equations, suitable boundary conditions also need to be specified at the boundaries of the flow domain. The boundary conditions at the solid wall were computed from the logarithmic law of the wall as discussed by Rosten and Worrell (1988). The friction coefficient is given by

$$c_f = \begin{cases} \left\{\dfrac{a_k}{\ln(E \cdot \text{Re}_\Delta \cdot \sqrt{c_f})}\right\}^2, & \text{for } \text{Re}_\Delta > 132.5 \\ \dfrac{1.0}{\text{Re}_\Delta}, & \text{for } \text{Re}_\Delta \le 132.5 \end{cases}$$

where c_f = friction coefficient at the wall

$$\text{Re}_\Delta = \text{friction Reynolds number} = \frac{w_\Delta \cdot \Delta}{\nu} \tag{11}$$

w_Δ = the fluid velocity at a small distance Δ (typically one grid cell) away from the wall
a_k = von Kármán constant = 0.435
E = roughness factor = 9.0, for smooth wall

The values of k and ϵ at a small distance Δ from the wall are given by

$$k_\Delta = \frac{c_f w_\Delta^2}{\sqrt{C_\mu}} \tag{12}$$

$$\epsilon_\Delta = k_\Delta^{3/2}\frac{C_D}{a_k \Delta} \tag{13}$$

where $C_D = 0.1643$, a constant relating mixing length with k and ϵ. At the free surface, the gradients of k and ϵ were assumed to be zero. The value of k at the entrance section was estimated from the inlet velocity as $k_{\text{in}} = (f/4)W_{\text{in}}^2$ where f was assumed to be 0.018. The value for ϵ was estimated from the value of turbulent kinetic energy by assuming the mixing length to be $0.09\,\delta_{\text{in}}$, giving $\epsilon_{\text{in}} = C_D\, k_{\text{in}}^{3/2}/(0.09\,\delta_{\text{in}})$. At the exit plane, the gradients of k and ϵ were assumed to be zero.

Computational Procedure

One-Dimensional Solution. The one-dimensional computational procedure for the free surface flow of a turbulent liquid layer was developed using a method similar to that of Thomas et al. (1990) for a laminar flow. Since the thickness of the liquid layer is small compared to the length or radius of the plate and the fluid velocity normal to the plate is much smaller than the velocity along the plate, the governing transport Eqs. (1)–(2) can be easily simplified using scaling arguments. It can be shown that the flow is strongly parabolic and the pressure variation across the thickness of the film is hydrostatic in nature. The conservation equations can then be integrated from $y = 0$ to δ by assuming a suitable velocity profile. For turbulent flow, the velocity remains approximately uniform, except for the region very close to the wall. Therefore, a flat profile is assumed. The frictional resistance from the solid wall is assumed to be proportional to inertia. Therefore, the momentum equation in the radial (longitudinal, if plane flow) direction is

$$\frac{\partial}{\partial t}(W\delta) + \frac{\partial}{\partial r}\left(W^2\delta + \frac{1}{2}g\delta^2\right) = -K\delta\frac{W^2}{r} - c_f\frac{W^2}{2} \tag{14}$$

Here W is the average local velocity and K is the geometric parameter ($K = 0$ for plane flow, $K = 1$ for radial flow).

Since only the steady-state solution is desired, the time derivative term can be further simplified as

$$\frac{\partial}{\partial t}(W\delta) \approx \delta\frac{\partial W}{\partial t}$$

leading a quasi-steady formulation. Here it is assumed that the film thickness and shape of the control volume remains the same at an instant of time. The time is not entirely eliminated in order to devise an explicit marching algorithm described later.

The following parameters are defined in order to express the equation in nondimensional form.

$$\frac{W}{W_{\text{in}}}=V,\quad \frac{\delta}{\delta_{\text{in}}}=\delta^{+},\quad \frac{r}{\delta_{in}}=\xi,\quad t\frac{W}{\delta_{\text{in}}}=\tau,$$
$$\frac{W_{\text{in}}^2}{g\delta_{\text{in}}}=\text{Fr}_{\text{in}}^2,\quad \frac{W_{\text{in}}\delta_{\text{in}}}{\nu}=\text{Re}_{\delta,in} \quad (15)$$

After eliminating δ from Eq. (14) using the continuity relationship and the above parameters, the momentum balance can be expressed as

$$\frac{\partial V}{\partial \tau}+V\xi^{K}\frac{\partial}{\partial \xi}\left\{\frac{V}{\xi^{K}}+\frac{\xi_{\text{in}}^{K}}{2\text{Fr}_{\text{in}}^2}\left(\frac{1}{V\xi^{K}}\right)^2-\beta\frac{\partial V}{\partial \xi}\right\}$$
$$=-\frac{KV^2}{\xi}-\frac{c_f}{2}V^3\left(\frac{\xi}{\xi_{\text{in}}}\right)^{K} \quad (16)$$

The dimensionless initial and boundary conditions are given as

$$\tau=0: \quad V=1$$
$$\xi=\xi_{\text{in}}: \quad V=1$$
$$\xi=\xi_{\text{out}}: \quad V=V_{\text{out}}$$

These conditions correspond to a constant velocity across the fluid layer at the initial time and constant inlet and outlet velocities at all times.

The quantity β is termed as the coefficient of artificial viscosity. The term containing β is an extra term added to this equation in order to reduce the numerical oscillations in the solution. These oscillations are typical in the vicinity of a hydraulic jump or shock wave (Anderson et al., 1984). In the present computation $\beta = -0.001$ was used. The addition of this term does not affect the computed film height at any other location but reduces the fluctuations near the jump.

In order to solve Eq. (16), a value of c_f also needs to be specified. Since no suitable correlation is available for turbulent flow in a thin film or liquid layer, an approximate estimate can be obtained from boundary-layer theory adjacent to a flat horizontal surface (Kays and Crawford, 1980). For turbulent flow, an average friction coefficient can be written as

$$c_f=0.072\ \text{Re}_L^{-0.2} \quad (17)$$

where Re_L is the Reynolds number defined in terms of total flow length; i.e., length of the plate or difference between outer and inner radii. In general, one may use a better estimate of the friction factor, if available from experiment or the two-dimensional numerical solution described later in this paper. It is also quite possible and expected to have a variation of the friction coefficient along the plate. A nonuniform distribution can be also accommodated in the computation without any modification of Eq. (16). In fact, one may choose to use local values of the friction coefficient estimated from boundary layer theory. However, this was not done here since c_f obtained from boundary layer flow is only an approximation for thin film flow. It may also be noted here that the one-dimensional formulation does not require any information about k or ϵ, and the effect of turbulence is incorporated by specification of an appropriate friction coefficient.

The finite difference equations were derived by using the MacCormack predictor-corrector method. For each time step, the predicted solution first used forward differencing in both time and space and then improved the prediction using forward differencing in time but backward differencing in space. The corrected solution was taken as an arithmetic average of the past and predicted solutions. The details of the formulation were similar to those given by Thomas et al. (1990). The time step was chosen to be slightly less than the maximum that satisfies the convergence criterion for an explicit scheme (Carnahan et al., 1969). The converged solution was obtained within about 5000 iterations. The predicted film height was checked for accuracy by changing both $\Delta\tau$ and $\Delta\xi$. The effect of $\Delta\tau$ on the steady-state solution was found to be negligible. A time step of $\Delta\tau = 0.5$ was used. Reducing it by half produced an identical steady-state solution, but required twice as much time for convergence. The number of grids in the ξ-direction was 500, which produced a very good resolution in the film height distribution. Test runs with twice as many grids yielded solutions within 0.01 percent. This proved that the numerical solution presented here is independent of the choice of time step and grid size and accurate within 0.1 percent. Even though a parabolic version of the momentum equation was used, both upstream and downstream velocity boundary conditions were imposed by choosing both forward and backward differencing in space. This is essential in the computation of a hydraulic jump since both upstream and downstream conditions affect the location and structure of the jump.

Two-Dimensional Solution. The complete two-dimensional solution of the flow field was obtained using a boundary-fitted curvilinear coordinate system. As shown in Fig. 1, the local coordinates were defined along lines connecting the centers of the adjacent grid cells. The z-axis was taken in the direction of the primary motion of the fluid stream, and the y-axis pointed vertically upward from the plate. The grid cells were generated by algebraic interpolation between the boundaries of the computation domain, where the irregular free surface was taken as one of the boundaries. In general, the cell faces were nonorthogonal to each other. In the finite-difference formulation, the velocity and force vectors were resolved into covariant components; i.e., the components parallel to the cell faces. The primary physical variables were used directly without performing any nondimensional transformation. The energy equation was not solved here but can be added in the general solution algorithm to predict the heat transfer.

The finite-difference equations were derived by using the principle of conservation of mass and momentum at each cell. A staggered grid system was used, where the pressure, turbulent kinetic energy (k) and the dissipation rate (ϵ) were stored at the center of a cell, whereas velocities were present at the cell boundaries. The mass flux across a cell boundary was computed exactly from the scalar product of the velocity vector and the vector representing the area of the cell face. The momentum transport across a cell boundary included both convection and diffusion. The calculation of convective transport was exact where special attention was given to the change of orientation of the coordinate axes and the curvature of a cell face. In the calculation of diffusion, however, the cell boundaries were approximated to be locally orthogonal. Terms involving cell curvature and non-orthogonal orientation were neglected. This simplification is justified for the problems considered here since the transport is primarily convective. The relative importance of convection and diffusion was determined by examining the cell Peclet number. The hybrid difference scheme as demonstrated by Patankar (1980) was used. The finite-difference equations for k and ϵ were also derived in an analogous way, except for the linearization of the source term for ϵ. Using Eq. (10) the source term was written as

$$C_1\epsilon\frac{G}{k}-C_2\frac{\epsilon^2}{k}=\frac{C_2C_\mu k}{\nu_T}\left(\frac{C_1}{C_2}G-\epsilon\right)$$

The linearization is essential in order to preserve the stability of the computational scheme.

Table 1 Flow conditions and optimum free surface height distribution

Plane flow	
Case 1	
$Re_\delta = 6.5 \times 10^4$	Free surface:
$Fr_{in} = 4.0$, $Fr_{out} = 0.35$	$\frac{\delta}{\delta_{in}} = \left(1 + 12.37\frac{r}{L}\right)^{0.25}$, supercritical
$\delta_{in} = 0.03$ m, $L = 12.37$ m	$\frac{\delta}{\delta_{in}} = 5.27\left(1 - 0.93\frac{r}{L}\right)^{0.014}$, subcritical
Case 2	
$Re_\delta = 5000$	Free surface:
$Fr_{in} = 15$, $Fr_{out} = 0.44$	$\frac{\delta}{\delta_{in}} = \left(1 + 1.28\frac{r}{L}\right)^{2.5}$, supercritical
$\delta_{in} = 0.002255$ m, $L = 2.301$ m	$\frac{\delta}{\delta_{in}} = 12.42\left(1 - 0.7\frac{r}{L}\right)^{0.14}$, subcritical
Case 3	
$Re_\delta = 2000$	Free surface:
$Fr_{in} = 15$, $Fr_{out} = 0.44$	$\frac{\delta}{\delta_{in}} = \left(1 + 1.28\frac{r}{L}\right)^{4.6}$, supercritical
$\delta_{in} = 0.001224$ m, $L = 2.301$ m	$\frac{\delta}{\delta_{in}} = 15.04\left(1 - 0.7\frac{r}{L}\right)^{0.3}$, subcritical
Radial flow	
Case 4	
$Re_{\delta,in} = 5000$	Free surface:
$Fr_{in} = 20$, $Fr_{out} = 0.15$	$\frac{\delta}{\delta_{in}} = \left(\frac{r}{r_{in}}\right)^{-0.07}$, supercritical
$\delta_{in} = 0.001861$ m, $r_{in} = 0.05$ m, $r_{out} = 0.55$ m	$\frac{\delta}{\delta_{in}} = 7.89\left(\frac{r}{r_{in}}\right)^{-0.16}$, subcritical

The number of grids in the y-z plane was established from a grid independence test. A series of runs with a different number of grids in the y- and z-directions were made. In each run a fully converged solution of the flow field was established, and iterations were performed to determine the location of the free surface. It was found that the computed film height and mean velocity distribution changed negligibly if grids were refined beyond 25 cells in the y-direction and 50 cells in the z-direction. This was not surprising since the control volume formulation (Patankar, 1980) was used for discretization instead of Taylor series expansion where truncation error is dependent on the grid size. Comparing the results obtained using 25×50 cells and 40×100 cells, it was found that the film height as well as the magnitude of the velocity vectors were within 4 percent. Since the objective of the present investigation is to understand the steady mean flow behavior, and not the time-dependent fluctuating velocity or pressure distribution, 25×50 cells in the y-z plane appeared to be adequate to produce grid independent solutions accurate to within 5 percent and was used here for the computation.

For any given film height, the field equations were solved using the SIMPLEST algorithm introduced by Spalding (1980). The computation started by guessing a pressure field and turbulent viscosity, and then the momentum equations were solved to determine the velocity components. The values of turbulent kinetic energy and its dissipation rate were also determined by solving the corresponding conservation equations. The continuity equation was then used to solve for the pressure. Even though the continuity equation does not contain any pressure, it can be easily transformed to a pressure correction equation as shown by Patankar (1980). The solutions were assembled to determine pressure and other quantities to be used for the next iteration. The computation was continued until the residual for each equation dropped below 10^{-6}.

As mentioned before, the geometry of the free surface needs to be specified in order to generate the grid structure and to solve the flow field. On the other hand, the height of the free surface is a function of the velocity components and pressure, so an iterative procedure introduced by Rahman et al. (1990a) was used. An algebraic equation describing the geometry of the free surface was assumed. The piecewise function had two branches for the supercritical and subcritical regions connected by a straight line in the jump region. This function had a number of arbitrary constants that needed to be optimized to obtain the best possible free surface height distribution. The quantity to be minimized is the error in the difference between the free surface and ambient pressures. For an ideal free surface, the quantity p has to be zero everywhere along the plate. The average error was defined as

$$\text{Normalized RMS Error} = \frac{\sqrt{\frac{1}{n}\sum_{k=1}^{n}(p_k)^2}}{\left(\rho g \delta_{in} + \frac{\rho W_{in}^2}{2}\right)}$$

To start the solution process, each arbitrary constant (parameter) was assigned a value. Then only one parameter was changed at a time, keeping the others at their assigned values and the trend of the error was observed. The parameter was changed in both directions until the value corresponding to the minimum error was established. Another parameter was then changed in a similar fashion to determine its optimum value. This was continued for all parameters. Once the first round of search was complete, the first parameter was again changed to see whether further minimization was possible or not. The process was repeated for other parameters over cycles until an absolute minimum was established. The final solution of the free surface height distribution for the problems considered here is listed in Table 1.

The above procedure was used to establish the film height separately in the supercritical and subcritical regimes. An additional condition needed to be satisfied at the location of the jump. The film height before and after the jump are related by (Fox and McDonald, 1985)

$$\frac{\delta_2}{\delta_1} = \frac{1}{2}\left[\sqrt{1 + 8\text{Fr}_1^2} - 1\right]$$

This condition established the location of the jump in the flow domain. It can also be pointed out that both supercritical and subcritical film heights were calculated using the same flow rate, but for supercritical flow, the inlet height (or Froude number) was fixed, whereas in the subcritical region, the outlet

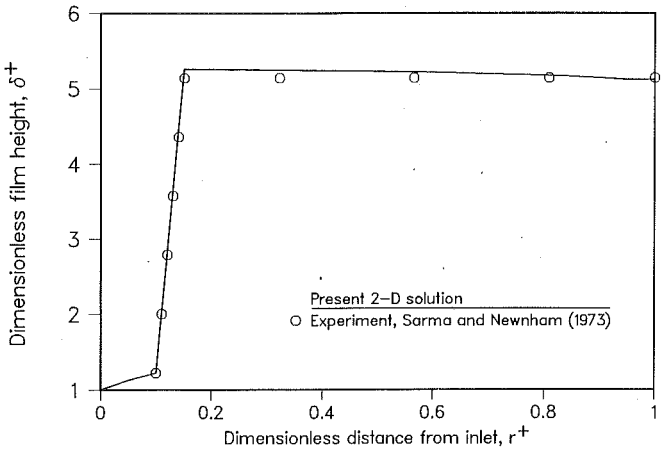

Fig. 2 Comparison of computed film height with experimental measurements of plane flow at $Re_\delta = 6.5 \times 10^4$, $Fr_{in} = 4.0$ and $Fr_{out} = 0.35$

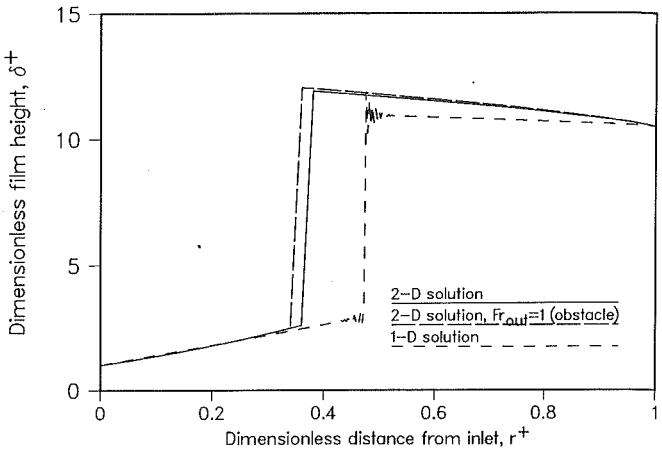

Fig. 3 Film height for plane flow at $Re_\delta = 5000$, $Fr_{in} = 15$ and $Fr_{out} = 0.44$

height (or Froude number) was fixed. Once the location of the jump was established, the slope of the jump was changed until an overall minimum in the normalized RMS error in pressure was determined.

Results and Discussion

Two different geometrical configurations were considered in the present investigation: plane flow, and radially spreading flow. For both configurations, the flow field and free surface height distribution were computed using the one-dimensional and two-dimensional solution algorithms developed here. For the two-dimensional computation the k-ϵ model has been used, which previously has been adequate for recirculating flows. For a thin film or liquid layer, the onset of turbulence is not very well defined. Two lengthscales are of significance here. In terms of the film height, the flow can be expected to be laminar for $Re_\delta \leq 1000$. This criterion was arrived at by comparing film flow with flow between parallel plates where a zero shear surface exists halfway between the plates. The other criterion may be derived by comparing thin film flow with a boundary layer flow where distance from the entrance is important. In this case, the laminar regime may be expected for $Re_L \leq 10^5$. Moreover, waves are present on the free surface that may trigger turbulence at an earlier location. In the absence of any well-established borderline, we considered only flows that were fully-turbulent for numerical simulation. We also assumed the flow to be turbulent in the entire computational domain.

The computed results for plane flow over a 12.4 m long plate with $Re_\delta = 6.5 \times 10^4$, $Fr_{in} = 4.0$ and $Fr_{out} = 0.35$ is shown in Fig. 2 (case 1 in Table 1). These conditions corresponded to the experimental measurements of Sarma and Newnham (1973) for jump heights at low Froude numbers. The measurements are also shown in the same figure and the agreement is excellent. Both the profile of the jump and subcritical film height were accurately predicted using the present algorithm. This gives some confidence in using the $k-\epsilon$ model for the prediction of turbulence in a free surface flow.

The computed film height for plane flow at $Re_\delta = 5000$ (case 2 in Table 1) is shown in Fig. 3. Here $Fr_{in} = 15.0$ and $Fr_{out} = 0.44$. In this situation, the liquid layer has a smaller thickness but larger entrance velocity. The film height increases monotonically in the supercritical region. A jump is encountered at an intermediate location of the computational domain, and thereafter the film height decreases gradually all the way to the exit. For plane flow, the Reynolds number is directly proportional to the flow rate. The Froude numbers are determined by the entrance and exit conditions in the flow. To create a jump in a water channel, the outlet is usually restricted by a partition so that the water height is elevated to form a smooth subcritical flow regime. In this situation, the outlet Froude number at the edge of the partition can have values up to unity if the fluid particles beyond the partition experience a free fall and surface tension is negligible. A numerical simulation of this situation keeping the same flow rate and inlet Froude number but a partition with $Fr = 1$ at the edge is also shown in Fig. 3. The outlet film height is still the same as the previous problem. It appears that the supercritical and subcritical film heights are not affected significantly by the presence of the partition. The location of the jump, however, moves slightly upstream due to the accumulation of the stagnant fluid on the upstream side of the partition. It may be expected that the effects of the partition will be dominant in the immediate vicinity of it, but do not appreciably influence the flow behavior further upstream.

Figure 3 also shows the film height predicted by using the one-dimensional computational method for the same Reynolds number and inlet and outlet Froude numbers (case 2 in Table 1). It may be noticed that the supercritical film heights coincide with the two-dimensional solution, whereas the location of the jump moves further downstream and presents a smaller film height in the subcritical region. In the one-dimensional computation, the velocity of the fluid normal to the plate is entirely neglected, which is not valid in a real flow situation. Moreover, the estimation of frictional resistance is not very accurate. Keeping in mind these limitations, the one-dimensional solution appears to give a reasonable estimate of the film height and location of the jump.

A plot of the velocity profile for plane flow at $Re_\delta = 5000$ (case 2 in Table 1) is shown in Fig. 4 for three different locations in the flow field. The inlet and outlet Froude numbers are those used for the computation of film height; i.e., $Fr_{in} = 15$, and $Fr_{out} = 0.44$. At $r^+ = 0.24$, which corresponds to the supercritical flow regime, the film thickness is small and the magnitude of the velocity is large. The maximum velocity occurs at the free surface and gradually decreases as the solid wall is approached. In this region, the viscous effects are quite strong and encompass the thickness of the film. Even though the no-slip condition is met on the solid wall, the change of velocity near the wall is quite rapid as is typical for a turbulent flow. At $r^+ = 0.38$, which corresponds to a region just downstream of the jump, it is found that the flow separates from the solid wall and results in a backward circulation. This separation of the flow is due to the rapid rise of the fluid level at the jump and the associated deceleration of the flow. This phenomenon was seen previously in the laminar flow computation by Rahman et al. (1990b). In the present problem, the separation persisted for a small length of the flow (≈ 0.1

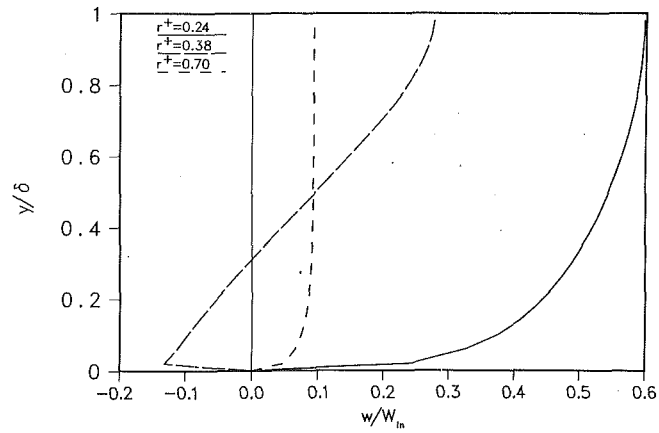

Fig. 4 Velocity profile for plane flow at Re_δ = 5000, Fr_{in} = 15 and Fr_{out} = 0.44

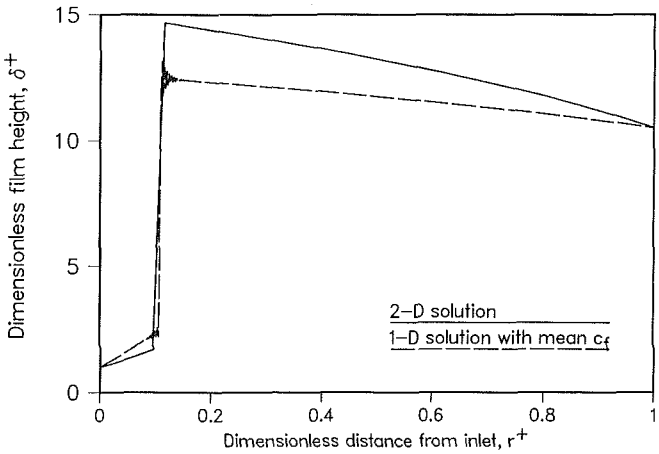

Fig. 5 Film height for plane flow at Re_δ = 2000, Fr_{in} = 15 and Fr_{out} = 0.44

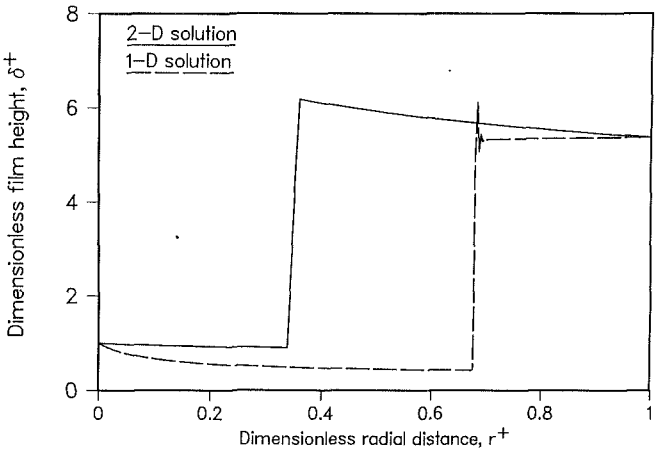

Fig. 6 Film height for radial flow at $Re_{\delta,in}$ = 5000, Fr_{in} = 20 and Fr_{out} = 0.15

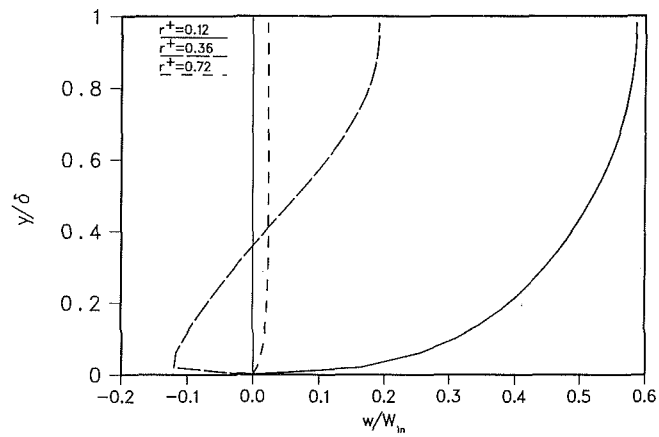

Fig. 7 Velocity profile for radial flow at $Re_{\delta,in}$ = 5000, Fr_{in} = 20 and Fr_{out} = 0.15

m) and thereafter the flow reattached to the surface. It may also be noticed here that changes in velocity near the wall are large even in the recirculation region because of the large magnitude of the velocity. At a further downstream location in the subcritical regime ($r^+ = 0.7$), it can be seen that the velocity profile is typical of a boundary layer flow. The velocity is uniform in most regions of the film and decreases close to the surface. The thickness of the viscous sublayer here is much smaller compared to the film height. Looking at the computed distribution of turbulent viscosity, it was found that ν_T becomes maximum in the jump region and gradually decreases both upstream and downstream. The sudden rise of the film height at the jump and the churning motion of fluid particles cause a rapid production of turbulence in that region. The effects of turbulence were smaller in other regions of the flow.

The results for plane flow at Re_δ = 2000 with Fr_{in} = 15 and Fr_{out} = 0.44 (case 3 in Table 1) are shown in Fig. 5. Analogous to the previous case, the film height increased monotonically in the supercritical region and decreased monotonically in the subcritical region. Here the jump occurred at an earlier location. Comparing with case 2, it can be noticed that when the Reynolds number decreased, the amount of inertia in the flow also decreased. Therefore, the supercritical regime cannot be sustained for a longer distance. With a decrease in flow rate, the jump is moved farther upstream maintaining only subcritical flow in a limiting situation. The opposite is also true. With an increase in flow rate, the jump moves downstream and can be swept away from the computational domain in the absence of any obstacle. The figure also shows a comparison with the one-dimensional solution where the average friction factor obtained from the two-dimensional solution has been used as an input. It can be noticed that the location of the jump is exactly predicted when the correct friction coefficient is used for the computation. However, there is some deviation in the prediction of the supercritical and subcritical film heights.

The flow where fluid is discharged at the center of a disk from a pressurized container and flows radially outward is also considered here. The computed film height for radial flow with $Re_{\delta,in}$ = 5000, Fr_{in} = 20 and Fr_{out} = 0.15 (case 4 in Table 1) is shown in Fig. 6. For this flow condition, the film height decreased in both the supercritical and subcritical regions. In radial flow, with an increase in radius, more cross-sectional area becomes available to the flow. Therefore, even though the velocity is decreased, the film height may increase or decrease depending on the flow conditions and radial location. Comparing the results of the one-dimensional and two-dimensional computations, it may be noticed that the one-dimensional solution predicted the jump farther downstream due to a somewhat smaller estimate of the friction coefficient.

The velocity profile for radial flow (case 4 in Table 1) is shown in Fig. 7 for three different locations in the flow field. The flow parameters used here are the same as those for the computation of the film height; i.e., $Re_{\delta,in}$ = 5000, Fr_{in} = 20 and Fr_{out} = 0.15. The distribution of the velocity for radial flow appears to be somewhat similar to that for the plane flow demonstrated in Fig. 4. In the supercritical region ($r^+ = 0.12$), the velocity profile is not flat; rather there is a monotonic

decrease from the maximum at the free surface to zero at the wall. A rapid change in velocity occurs near the wall. At a location just downstream of the jump ($r^+ = 0.36$), the flow separates from the surface due to a rapid change in film height. This type of separation was seen previously in the experimental work of Nakovyakov et al. (1978) for a radial hydraulic jump. The recirculation encompasses a large portion of the film thickness. Farther downstream in the subcritical region, the flow reattaches to the surface and develops to a well-ordered profile as seen in the plot corresponding to $r^+ = 0.72$. The profile here is similar to that in a turbulent boundary-layer flow over a flat plate. The velocity is uniform in most regions across the film thickness and changes occur over a small region near the solid wall. It can also be seen that the magnitude of the velocity decreases downstream somewhat more rapidly in radial flow than the plane flow. This is because more area is available to the flow as the radius increases.

Conclusions

The computational procedure for the free surface flow of a turbulent liquid layer is developed using both a one-dimensional approximate method and a fully two-dimensional method using a boundary-fitted coordinate system. The geometries considered include both plane and radially spreading flows. For plane flow, it was found that the film height increased monotonically in the supercritical region, and decreased monotonically in the subcritical region. The two regions were connected by a jump where a large change in film height took place. Just downstream from the jump, a recirculating flow was found to be present near the solid wall. This was caused by a rapid deceleration of the flow at the jump where inertia was overtaken by frictional resistance. In the subcritical regime, the velocity profile across the film thickness was found to be almost flat except for a small region adjacent to the solid wall. In the supercritical regime, however, the decrease of the velocity from the free surface to the solid wall was found to be somewhat gradual. In radial flow, the film height decreased gradually in both the supercritical and subcritical flow regimes for the flow condition considered here. In general, the supercritical film height may increase or decrease with distance depending on the flow rate and radial location. The distribution of the velocity for radial flow was found to be similar to that for plane flow, where recirculation occurred just downstream of the jump. The computed film height compared reasonably well with previous experimental data.

Acknowledgment

Funding for this research was provided by NASA Goddard Space Flight Center, Greenbelt, Maryland, under contract NAG 5-956.

References

Anderson, D. A., Tannehill, J. C., and Pletcher, R. H., 1984, *Computational Fluid Mechanics and Heat Transfer*, Hemisphere Publishing Corporation, N.Y., pp. 151–154.

Carnahan, B., Luther, H. A., and Wilkes, J. O., 1969, *Applied Numerical Methods*, Wiley, N.Y., pp. 432–433.

Chun, K. R., and Seban, R. A., 1971, "Heat Transfer to Evaporating Liquid Films," ASME *Journal of Heat Transfer*, Vol. 93, No. 4, pp. 391–396.

Faghri, A., and Seban, R. A., 1985, "Heat Transfer in Wavy Liquid Films," *Int. J. Heat Mass Transfer*, Vol. 28, No. 2, pp. 506–508.

Faghri, A., and Seban, R. A., 1988, "Heat and Mass Transfer to a Turbulent Liquid Film," *Int. J. Heat Mass Transfer*, Vol. 31, No. 4, pp. 891–894.

Fox, R. W., and McDonald, A. T., 1985, *Introduction to Fluid Mechanics*, Third Edition, Wiley, N.Y., pp. 540–543.

Grossman, G., and Heath, M. T., 1984, "Simultaneous Heat and Mass Transfer in Absorption of Gases in Turbulent Liquid Films," *Int. J. Heat Mass Transfer*, Vol. 27, pp. 2365–2376.

Hirshburg, R. I., and Florschuetz, L. W., 1982, "Laminar Wavy-Film Flow: Part I, Hydrodynamic Analysis," ASME *Journal of Heat Transfer*, Vol. 104, pp. 452–458.

Kays, W. M., and Crawford, M. E., 1980, *Convective Heat and Mass Transfer*, Second Edition, McGraw-Hill, N.Y., p. 175.

Launder, B. E., and Spalding, D. B., 1974, "The Numerical Computation of Turbulent Flows," *Comp. Methods in Appl. Mech. and Engr.*, Vol. 3, pp. 269–289.

Leutheusser, H. J., and Alemu, S., 1979, "Flow Separation Under Hydraulic Jump," *J. Hydraulic Research*, Vol. 17, No. 3, pp. 193–206.

Mills, A. F., and Chung, D. K., 1973, "Heat Transfer Across Turbulent Falling Films," *Int. J. Heat Mass Transfer*, Vol. 16, pp. 694–696.

Nakovyakov, V. E., Polusaev, B. G., and Troyan, E. N., 1978, "Impingement of an Axisymmetric Liquid Jet on a Barrier," *Int. J. Heat Mass Transfer*, Vol. 21, pp. 1175–1184.

Patankar, S. V., 1980, *Numerical Heat Transfer and Fluid Flow*, Hemisphere Publishing Corporation, N.Y., pp. 30–129.

Rahman, M. M., Faghri, A., Hankey, W. L., and Swanson, T. D., 1990a, "Computation of the Free Surface Flow of a Thin Liquid Film at Zero and Normal Gravity," *Numerical Heat Transfer*, Part A, Vol. 17, pp. 53–71.

Rahman, M. M., Faghri, A., and Hankey, W. L., 1990b, "New Methodology for the Computation of the Free Surface Flows Using a Permeable Wall," *Numerical Heat Transfer*, Part B, Vol. 18, pp. 23–41.

Rajaratnam, N., 1967, "Hydraulic Jumps," *Advances in Hydroscience*, Vol. 4, pp. 197–280.

Rosten, H. I., and Worrell, J. K., 1988, "Generalized Wall Functions for Turbulent Flow," *PHOENICS J. Comp. Fluid Dynamics and Applications*, Vol. 1, No. 1, pp. 81–109.

Rouse, H., Siao, T. T., and Nagaratnam, S., 1959, "Turbulence Characteristics of the Hydraulic Jump," *ASCE Transactions*, Vol. 124, pp. 926–966.

Sarma, K. V. N., and Newnham, D. A., 1973, "Surface Profiles of Hydraulic Jump for Froude Numbers Less Than Four," *Water Power*, Vol. 25, pp. 139–142.

Seban, R. A., and Faghri, A., 1976, "Evaporation and Heating with Turbulent Falling Liquid Films," ASME *Journal of Heat Transfer*, Vol. 98, No. 2, pp. 315–318.

Seban, R. A., and Faghri, A., 1978, "Wave Effects on the Transport to Falling Liquid Films," ASME *Journal of Heat Transfer*, Vol. 100, No. 1, pp. 143–147.

Spalding, D. B., 1980, "Mathematical Modelling of Fluid Mechanics, Heat Transfer and Chemical Reaction Processes," A Lecture Course, CFDU Reports, HTS/80/1, Imperial College, London.

Thomas, S., Hankey, W., Faghri, A., and Swanson, T., 1990, "One-Dimensional Analysis of the Hydrodynamic and Thermal Characteristics of Thin Film Flows Including the Hydraulic Jump and Rotation," ASME *Journal of Heat Transfer*, Vol. 112, No. 3, pp. 728–735.

Watson, E. J., 1964, "The Radial Spread of a Liquid Jet Over a Horizontal Plane," *J. Fluid Mechanics*, Vol. 20, Part 3, pp. 481–499.

M. J. Morris
Scientist,
McDonnell Douglas Research Laboratories,
McDonnell Douglas Corporation,
St. Louis, Mo. 63166

J. C. Dutton
Professor,
Department of Mechanical and Industrial Engineering,
University of Illinois at Urbana-Champaign,
Urbana, Ill. 61801

The Performance of Two Butterfly Valves Mounted in Series[1]

The results of an experimental investigation concerning the operating characteristics of two similar butterfly valves mounted in series are reported. Emphasis is given to the influence of the upstream valve disk angle, the downstream valve disk angle, the relative valve orientation, and the spacing between the valves. The dimensionless pressure drop, the mass flowrate coefficient, and the aerodynamic torque coefficient of each valve are used to characterize the system performance. The results show that the operating characteristics are strongly tied to the combined effect of the two valve disk angles. With noted exceptions, the valve disk orientation and spacing are secondary influences.

Introduction

A variety of fluid dynamic systems and processes use butterfly valves for many purposes. As a result, these valves can be found in endless piping geometries. These configurations range from somewhat simple ones (e.g., a straight section of pipe) to very complex combinations of elbows, valves, expansions, contractions, bulkheads, etc. Each of these geometries, in turn, has an influence on the performance characteristics of the valve included therein. Most investigations of butterfly valves have been conducted in a straight section of pipe, since this geometry minimizes both upstream and downstream influences on the valve performance. This basic geometry serves as a good base case for identifying the fundamental mechanisms controlling valve performance. Morris (1987) discusses and summarizes many of these findings. Unfortunately, this basic geometry is not often encountered in actual valve applications. The authors have previously reported the results of an investigation concerning the effects of an upstream elbow on the performance of butterfly valves (Morris and Dutton, 1991). When compared to valve performance in a straight section of pipe, the elbow strongly influenced the operating characteristics of the valve, especially at small valve/elbow spacings. These results can likely be generalized to somewhat different piping geometries, but the performance of the valve/elbow combination is unique. As a result, investigations of other specific valve/piping geometries are necessary to estimate accurately the performance of valves in more practical applications.

Two butterfly valves located in series have been used as a redundant safety shut-off system for nuclear containment purge systems. One valve is typically electrically actuated, and the second is usually pneumatically operated such that, in the event that one of the actuator systems fails, the containment vessel can still be isolated with the second system during an accident. This investigation was conducted to identify the performance characteristics resulting from the interaction of two butterfly valves mounted in series and close together. The parameters influencing the operating characteristics of a two-valve system include the relative valve orientation, the spacing between the valves, the upstream valve disk angle, the downstream valve disk angle, and the operating pressure ratio. Obviously, testing all possible combinations of these parameters would have been impractical, so the range of variables considered during the investigation was necessarily limited. Even so, the reduced test plan included over 400 combinations of test variables.

Experimental Parameters

A preliminary set of baseline experiments was conducted with one of the valve models mounted in a straight section of pipe. Sections of pipe twenty diameters long were located both upstream and downstream of the valve model. During these experiments, the stagnation pressure upstream of the test valve, P_{01}, was controlled as was the downstream static pressure, P_2. These pressure levels were adjusted such that the valve was exposed to a wide range of operating conditions, both choked and unchoked. The aerodynamic torque on the valve disk, the mass flowrate, and static and stagnation pressures across the valve were measured for a range of valve disk opening angles. These results were used for direct comparison with the two-valve experimental results.

The baseline experiments were followed by a series of experiments at similar operating conditions during which two valves were mounted in series. A schematic of the two-valve test apparatus is shown in Fig. 1. During these experiments, the valve models were mounted downstream of a straight section of pipe twenty diameters long and upstream of a section thirty diameters long. This arrangement was selected to isolate the test section from other influences.

These experiments were conducted using two similar butterfly valve models with flat plate disks. The experimental apparatus was designed such that the test valves could be separated with spacers of 2, 4, or 8 diameters. Since the results

[1]This work was conducted as unfunded independent research at the University of Illinois at Urbana-Champaign prior to the employment of M. J. Morris at McDonnell Douglas Research Laboratories.

Contributed by the Fluids Engineering Division for publication in the JOURNAL OF FLUIDS ENGINEERING. Manuscript received by the Fluids Engineering Division August 20, 1990.

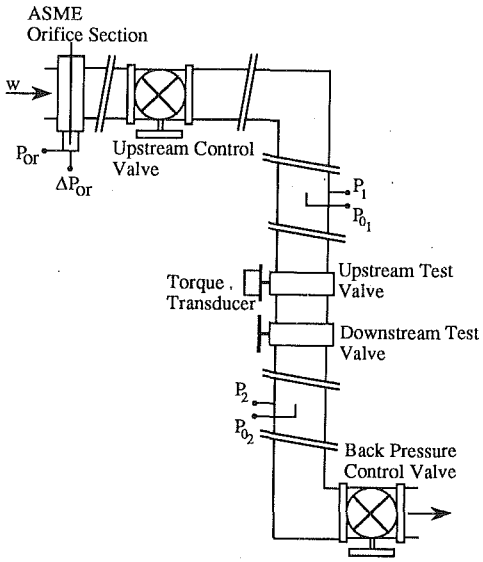

Fig. 1 Schematic of the experimental test section

of the valve/elbow experiments reported previously (Morris and Dutton, 1991) indicated that the interaction between the valves would be small for a spacing of 8 diameters, only spacings of 2 and 4 diameters were used in the present studies.

Besides valve spacing, the valves could also be rotated relative to each other. Figure 2 shows the three orientations of the two test valves that were used during these experiments. The combinations will be called Orientations A, B, and C, respectively. The valve shafts are parallel and both valves close in the same direction for Orientation A. For Orientation B, the downstream valve was rotated 180 deg so that the shafts were still parallel but the valves closed in opposite directions. In contrast, the valve shafts were perpendicular for Orientation C.

Most of the experiments were conducted to identify the combined influence of the two valve disk opening angles on the valve performance. In general, both valve disk angles were varied from a fully open position ($\alpha = 0$ deg) to a nearly closed position ($\alpha = 60$ deg) in increments of 10 deg. These angles were the same as those used in the single valve experiments. During the investigation, the range of the valve disk angles was sometimes reduced to eliminate combinations for which the valve-valve interaction was expected to be negligible.

The experiments were conducted over a range of back pressure-to-upstream stagnation pressure ratios of $0.25 < P_2/P_{01} < 0.78$. Compressibility was clearly an important factor in these studies (Addy et al., 1985 and Morris, 1987) since the flow through the test section was choked at pressure ratios below $P_2/P_{01} = 0.75$. For the results reported herein, the measured operating pressure ratios for the various combinations of valve angles are shown in Fig. 3 (all valve orientations and spacings). During experiments in which both test valves were near a fully open position, losses through the downstream piping system were large. As a result, the minimum achievable back pressure ratio for these cases was higher than for the other cases, as shown in Fig. 3. The flow was choked for all of these cases and the variation in back pressure ratio is not expected to influence the results as presented herein. The pipe Reynolds numbers for this range of operating conditions were approximately 3×10^4 to 7×10^5.

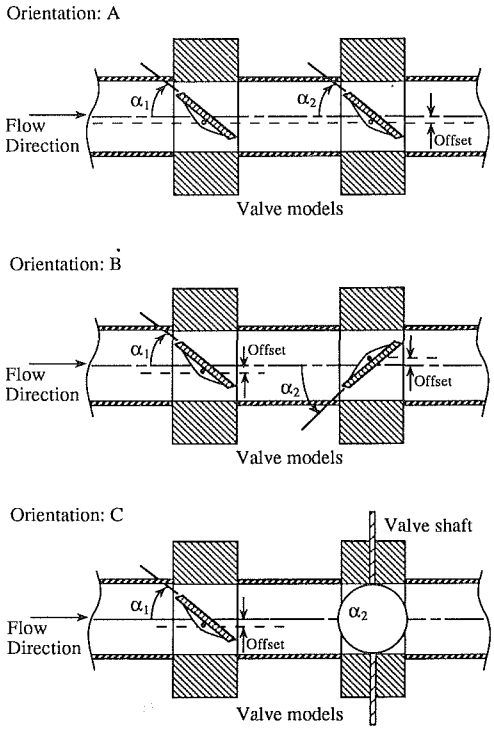

Fig. 2 The three relative valve orientations for the two test valves

Operating Characteristics

The operating characteristics of a butterfly valve are dependent upon the local flowfield through the valve. The flowfield and operating characteristics of these valves have been discussed in detail previously by the authors and others (Addy et al., 1985; Coers, 1983; Cohn, 1951; Hicks et al., 1952; Keller and Salzmann, 1936; Morris et al., 1982, 1987, 1989a, 1989b, 1991; Robinson, 1957). Most of this information is related to butterfly valves located in a straight section of pipe. Even for this basic application, the flow features are very complex, and the flowfield and related operating characteristics are strongly influenced by separation and reattachment phenomena. Com-

Nomenclature

C_f = dimensionless mass flow coefficient
C_T = dimensionless torque coefficient
D = nominal valve disk diameter
P = pressure
P_{or} = pressure at the ASME orifice
T = aerodynamic torque
w = mass flowrate
α_1 = upstream valve disk angle (0 deg is fully open)
α_2 = downstream valve disk angle (0 deg is fully open)
ΔP_{or} = differential pressure across the ASME standard measurement section

Subscripts

0 = stagnation properties of the air supply
01 = stagnation properties upstream of the test section
02 = stagnation properties downstream of the test section
1 = static properties upstream of the test section
2 = static properties downstream of the test section

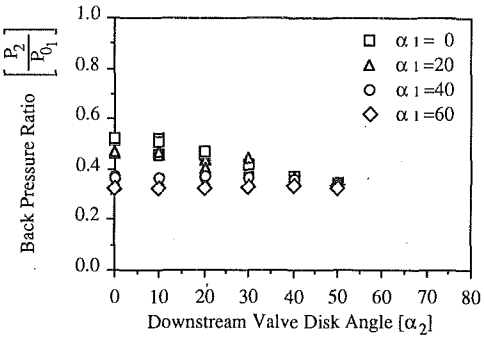

Fig. 3 Operating pressure ratio as a function of valve disk angles for all valve orientations and spacings and a stagnation pressure of 45 psia (Uncertainty in $P_2/P_{01} = \pm 1$ percent and in $\alpha = \pm 1$ deg)

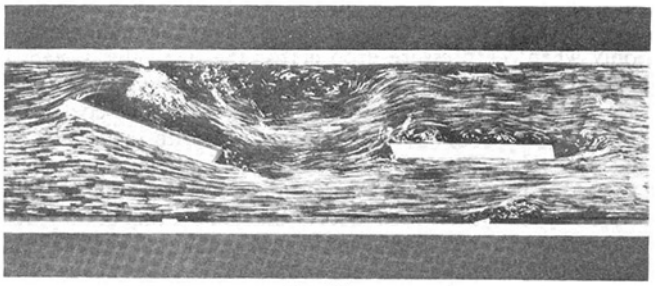

Fig. 4(*a*)

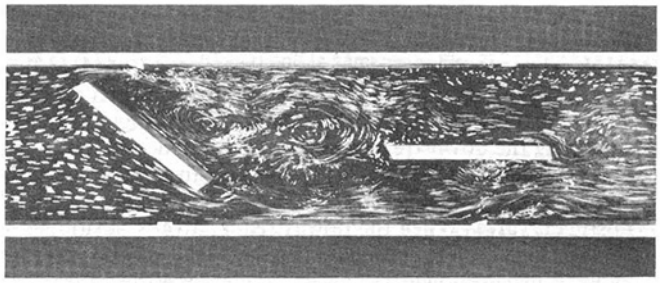

Fig. 4(*b*)

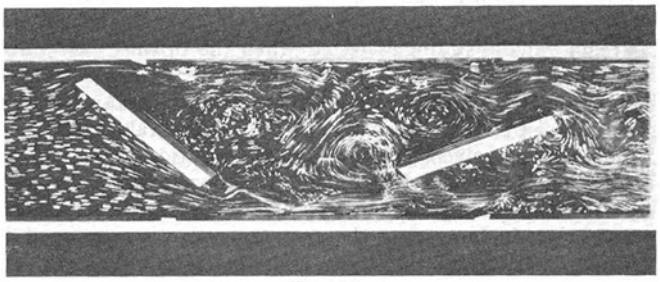

Fig. 4(*c*)

Fig. 4 Typical results from a water table investigation of two butterfly valves in series; (*a*) $\alpha_1 = 20$ deg, $\alpha_2 = 0$ deg, (*b*) $\alpha_1 = 40$ deg, $\alpha_2 = 0$ deg, (*c*) $\alpha_1 = 40$ deg, $\alpha_2 = 20$ deg

pressibility effects have also been shown to be significant even for relatively high operating pressure ratios ($P_2/P_{01} \approx 0.75$). These effects include phenomena associated with supersonic velocities such as choking, and both steady and unsteady shock waves and expansion waves.

The flowfield of two butterfly valves in series is similarly complex and will exhibit similar compressible phenomena. The proximity of the valves complicates the flowfield further and thereby modifies the operating characteristics. A water table simulation of this geometry by Morris et al. (1982) qualitatively characterized the flowfield. Typical results from this report are shown in Fig. 4. The flow is from left-to-right and the valve arrangement corresponds to Orientation B in which the valve disks close in opposite directions. The high speed flows accelerating around the upstream valve disk and the wake of the disk are seen to interact with the downstream valve. This interaction is primarily dependent upon the operating pressure conditions and upstream valve disk angle. With the upstream valve disk positioned at 20 deg, Fig. 4(*a*), the high velocity flows accelerating around this disk are shown to impinge on the fully open downstream valve disk. In contrast, when the upstream valve disk is at $\alpha_1 = 40$ deg and the downstream valve is fully open, Fig. 4(*b*), the downstream valve is shown to be bounded by the wake from the first valve. For some cases, such as in Fig. 4(*c*) at $\alpha_1 = 40$ deg and $\alpha_2 = 20$ deg, eddies shed from the upstream valve interact with the downstream valve. This interaction could be expected to result in an unsteady pressure field on the downstream valve disk. For all cases considered by Morris et al. (1982) (spacings up to four diameters), the separated, nonuniform flowfield of the upstream valve affected the downstream valve disk with the expectation that this circumstance could influence the system performance.

The investigation reported herein did not focus on the details of the flowfield. Rather the focus was on the resulting operating characteristics, primarily: the mass flowrate, the aerodynamic torque on each valve, and the static pressure drop across the test section. The mass flowrate through the test section was measured using an ASME orifice plate together with strain gauge pressure transducers. This result, reported as a flow coefficient (Addy et al., 1985), was defined as the ratio of the actual to ideal mass flowrate, $C_f = w_{\text{actual}}/w_{\text{ideal}}$.[2] The static pressure drop across the test section was also measured using strain gauge pressure transducers. It was nondimensionalized using the upstream static pressure. In addition, the aerodynamic torque on each test valve was of key interest. The valve models were equipped with a Lebow torque transducer to measure the torques. They are reported as dimensionless torque coefficients, $C_T = T/D^3(P_1 - P_2)$, where T is the aerodynamic torque, D is the nominal valve diameter, and $(P_1 - P_2)$ is the static pressure drop across the valve.

Experimental Results

The operating characteristics of the two valves mounted in series were strongly linked to the valve disk opening angles. Usually, the performance of the system was dictated by the valve that was most nearly closed. For some cases, the performance of an individual valve of the two-valve system was very similar to the performance of a single valve in a straight section of pipe (e.g., when the upstream valve was fully open and the downstream valve was in a nearly closed position, the effect of the upstream valve was small). For many cases, the interaction between valves was important to the overall performance of the two-valve test section. A somewhat unexpected finding was the lack of influence of the relative valve orientation. With exceptions to be noted later, in general, the results for orientations A, B, and C were similar. Consequently, only the results for orientation B will be presented in most of the figures. The results for valve spacings of two and four diameters were also quite similar and, for this reason, only the results for the two diameter spacing will be presented. The nominal operating pressure ratio for the experiments reported below is $P_2/P_{01} = 0.33$.

The static pressure drop across the two-valve test section can be directly compared to a single valve test section. In all cases both the static and the stagnations pressures were measured ten diameters upstream and downstream of the test section

[2] w_{ideal} is the ideal mass flowrate through a converging nozzle with the same nominal diameter and operating under the same pressure conditions as the test valve.

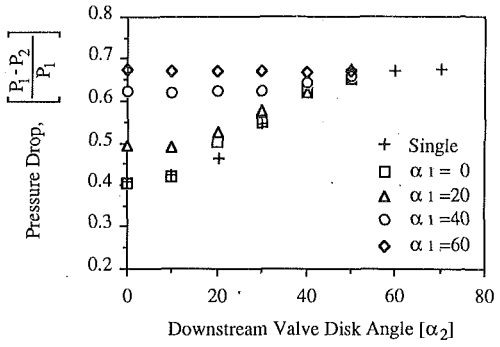

Fig. 5 Static pressure drop as a function of valve disk angles for Orientation B, a spacing of 2D, and a nominal pressure ratio of P_2/P_{01} = 0.33 (Uncertainty in $(P_1 - P_2)/P_1 = \pm 1$ percent and in $\alpha = \pm 1$ deg)

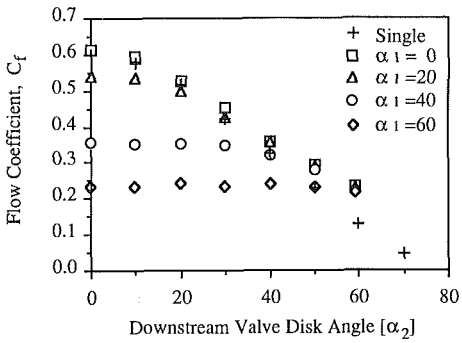

Fig. 6 Mass flow coefficient as a function of valve disk angles for Orientation B, a spacing of 2D, and a nominal pressure ratio of P_2/P_{01} = 0.33 (Uncertainty in $C_f = \pm 1$ percent and in $\alpha = \pm 1$ deg)

in a fully developed pipe flow. Figure 5 shows the dimensionless static pressure drop as a function of the two valve disk angles. A small value corresponds to low pressure losses and good pressure recovery. The results when both valve disk angles are small reflect a change in the effective back pressure ratio across the system, as discussed previously. The increased back pressure ratio leads to reduced losses and an improved pressure recovery for these cases. As can be seen in Fig. 5, the pressure drop across the test section for $\alpha_1 = 0$ deg is essentially identical with that of a single valve at the same valve disk angle as the downstream disk angle. The two-valve results for $\alpha_1 = 60$ deg are also seen to be the same as a single valve at a disk angle of 60 deg, independent of the setting of the downstream valve disk angle. Clearly, the pressure drop across the two-valve system is strongly linked to the larger of the two valve disk angles, as would be expected. Similar results were found for all valve orientations and both valve spacings.

The mass flowrate coefficient for two valves in series also can be compared directly to the single valve experiments as a fraction of the ideal mass flowrate through the valve system (i.e., using the mass flow coefficient, C_f). For an inviscid flow, the ideal mass flowrate through both the single and two-valve systems is the same. Figure 6 shows the mass flowrate coefficient for the two-valve system and the single valve system as a function of the disk angles. In most cases, the mass flowrate through the two-valve system is related to the larger of the two valve disk angles. When the upstream valve is fully open, $\alpha_1 = 0$ deg, the flow coefficient is approximately the same as that of the single valve experiment for most cases. The mass flowrate coefficient decreases for upstream valve disk angles of $\alpha_1 = 20$ and 40 deg, reflecting the additional losses introduced by closing the upstream valve.

With an upstream disk angle of 60 deg, the mass flowrate coefficient is nearly independent of the downstream angle and is approximately double that of the single valve experiment with $\alpha = 60$ deg. The same is true for upstream valve angles of $\alpha_1 = 0$, 20, and 40 deg and a downstream valve angle of $\alpha_2 = 60$ deg. The mass flowrate through the system is therefore *increased* by locating two valves in series for these cases. The choked mass flowrate is directly linked to the minimum *aerodynamic* cross section of the flow. The increase in the mass flowrate for the two-valve system may be related to a streamlining effect that the smaller angle valve flow imposes on the controlling, large angle valve flowfield which could increase the aerodynamic throat area. However, further investigation of this finding is required before a definitive statement can be made.

The aerodynamic torque was also measured on both valve models. The results are reported here as a torque coefficient which includes the pressure drop across both valves. In contrast, the single valve experiments use the pressure drop across only the test valve. As a result, a direct comparison of torque magnitudes between the one and two-valve experiments is valid only when the pressure drop across the two-valve system is primarily influenced by one of the two valves. For example, when the upstream valve is fully open, the torque coefficient for the downstream valve compares well with the results for a single valve. The actual dimensional torque on either of the two valve disks at a given opening angle and operating pressure ratio was always less than that for the same setting of the single valve experiments. Therefore, a means for reducing aerodynamic torque might be to use two valves in series instead of a single valve.

Figures 7 and 8 show the torque coefficients for the upstream and the downstream valves, respectively. The torque coefficient on the upstream valve is similar to that of the single valve result when the downstream valve angle, α_2, is 0 deg (fully open). With the downstream valve in this fully open position, a peak torque exists at an upstream valve disk angle of 20 deg. Changing the downstream valve angle to 20 deg decreases the torque coefficient by increasing the pressure drop across the system while also reducing the aerodynamic torque on the upstream valve. When the downstream valve is positioned at 20 deg, the peak torque angle shifted to 30 deg for the upstream valve. When the downstream valve angle was 40 deg, the torque coefficient for the upstream valve did not approach the single valve level until it was near a closed position of 50 deg. The torque coefficient was small and nearly constant for all upstream valve disk angles tested when the downstream valve angle was at 60 deg.

As shown in Fig. 8, the torque coefficient for the downstream valve is also similar to the results of the single valve case when the upstream valve is near a fully open position ($\alpha_1 = 0$ or 20 deg). The torque coefficient for the downstream valve also decreases as the upstream disk angle is increased to $\alpha_1 = 40$ or 60 deg. In fact, when the upstream valve is positioned at 60 deg, the downstream valve is immersed in its wake, resulting in a very small aerodynamic torque for all of the angles examined.

A notable interaction between the two valves occurs for an upstream valve disk angle of 20 deg. Comparison of the downstream valve torque coefficient results for orientations A, B, and C for this upstream disk angle are shown in Fig. 9. The results of the water table investigation, Fig. 4, showed that at $\alpha_1 = 20$ deg, the flow around the upstream valve impinged on the downstream valve. For Orientation B and downstream valve angles less than 20 deg, this interaction resulted in a reduced aerodynamic torque coefficient (in fact, torque reversal at $\alpha_2 = 0$ deg). In contrast, rotating the downstream valve to orientation A resulted in an increased torque coefficient (closing torque) at the small downstream disk angles. At the same valve angles, Orientation C (valve shafts perpendicular) produced torque coefficients for the downstream valve that are comparable to the single valve experiment.

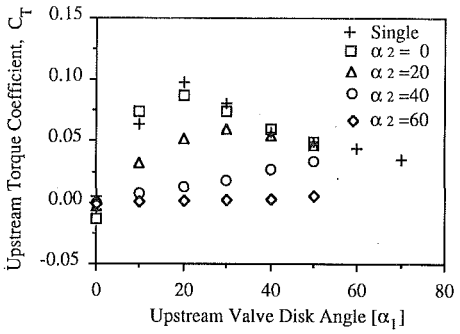

Fig. 7 Torque coefficient for the upstream valve disk as a function of disk angles for Orientation B, a spacing of 2D, and a nominal pressure ratio of P_2/P_{01} = 0.33. (Uncertainty in C_T = ±2 percent and in α = ±1 deg)

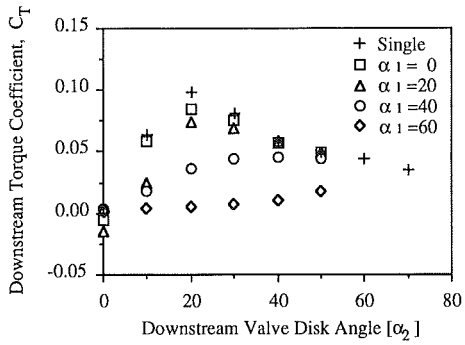

Fig. 8 Torque coefficient for the downstream valve disk as a function of disk angles for Orientation B, a spacing of 2D, and a nominal pressure ratio of P_2/P_{01} = 0.33 (Uncertainties same as in Fig. 7)

Conclusions

The interaction between two butterfly valves in series was found to modify the performance characteristics of the individual valves, but typically the effects were small. Neither the relative valve orientation nor the spacing between the valves was a dominant parameter. The interaction between the valves was strongest when the valve disk angles of the upstream and downstream valves were approximately the same. If one of the two valve disk angles was greater than the other, that particular valve dominated the performance of the two-valve system. In addition, if one of the two valves was in a fully open position, the second valve performance was similar to that of a single valve. On the other hand, the mass flowrate through nearly closed valves was increased by including a second valve at smaller disk angles. The reason for this increase is not presently clear and should be the focus of further investigation.

Locating two valves in series caused the valves to deviate from typical single valve aerodynamic torque performance.

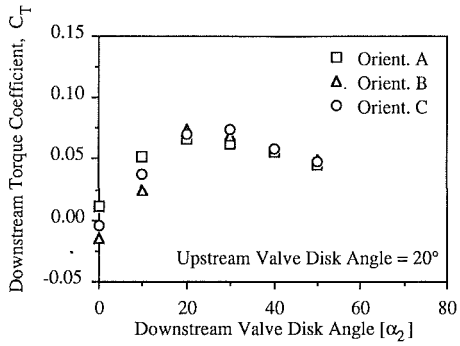

Fig. 9 Torque coefficient for the downstream valve disk for Orientations A, B, and C at α_1 = 20 deg and a nominal pressure ratio of P_2/P_{01} = 0.33 (Uncertainties same as in Fig. 7)

These deviations were observed as a reduction in peak torque and an increase in the peak torque angle as the disk angle of the other valve was increased. For all combinations of valve disk angles, the dimensional torque on either valve was less than that of a single valve at similar operating conditions. This result suggests that the aerodynamic torque on a given valve could be reduced by combining it with a second valve.

References

Addy, A. L., Morris, M. J., and Dutton, J. C., 1985, "An Investigation of Compressible Flow Characteristics of Butterfly Valves," ASME JOURNAL OF FLUIDS ENGINEERING, Vol. 107, No. 4, pp. 512–517.

Coers, B. A., 1983, "A Parametric Study of a Butterfly Valve Utilizing the Hydraulic Analogy," M.S. thesis, Department of Mechanical Engineering, Bradley University.

Cohn, S. D., 1951, "Performance Analysis of Butterfly Valves," *Instruments*, Vol. 24, pp. 880–884.

Hicks, H. H., Garby, L. C., Stohrer, A., and Reid, F. A., 1952, "Flow and Torque Characteristics of Butterfly Valves at Subcritical and Supercritical Pressure Ratios," Project M932 Report for Sverdrup and Parcel, Inc., Engineering Research Institute, University of Michigan, Ann Arbor.

Keller, C., and Salzmann, F., 1936, "Aerodynamic Model Tests on Butterfly Valves," *Escher Wyss News*, Zurich, Vol. IX, No. 1.

Morris, M. J., 1987, "An Investigation of Compressible Flow Through Butterfly Valves," Ph.D. thesis, Department of Mechanical and Industrial Engineering, University of Illinois at Urbana-Champaign, Urbana, Illinois.

Morris, M. J., and Dutton, J. C., 1989a, "Aerodynamic Torque Characteristics of Butterfly Valves in Compressible Flow," ASME JOURNAL OF FLUIDS ENGINEERING, Vol. 111, No. 4, pp. 392–399.

Morris, M. J., and Dutton, J. C., 1989b, "Compressible Flowfield Characteristics of Butterfly Valves," ASME JOURNAL OF FLUIDS ENGINEERING, Vol. 111, No. 4, pp. 400–407.

Morris, M. J., and Dutton, J. C., 1991, "An Experimental Investigation of Butterfly Valve Performance Downstream of an Elbow," ASME JOURNAL OF FLUIDS ENGINEERING, Vol. 113, No. 1, pp. 81–85.

Morris, M. J., Hurt, R. F., and Krist, S. E., 1982, "Water Table Investigation of a Two-Dimensional Scale Model of a 24-Inch CLOW Tricentric Butterfly Valve," Technical Report for CLOW Corporation.

Robinson, A. H., 1957, "Torque and Flow Characteristics of a Butterfly Valve Operating at Pressure Ratios Above the Critical," Memorandum No. M304, National Gas Turbine Establishment.

Dan D. Budny
Department of Freshman Engineering,
Purdue University,
West Lafayette, IN 47907

D. C. Wiggert

F. J. Hatfield

Department of Civil and
Environmental Engineering,
Michigan State University,
East Lansing, Mich. 48824

The Influence of Structural Damping on Internal Pressure During a Transient Pipe Flow

A four equation model of axial wave propagation with Poisson coupling which includes viscous damping to account for structural energy dissipation is evaluated. Comparison of the predictions with experimental data indicates that the model can satisfactorily predict fluid pressure and structural velocity. The results show that structural damping reduces the pressure peaks during a transient event by eliminating the high frequency components. For the conditions studied, this reduction was 20 to 25 percent for a piping system with no axial constraints. A saddle-type support increases the equivalent viscous damping, and this increased damping can be modeled as either distributed damping or as an external damper.

Introduction

The traditional technique for analysis of fluid-structure interaction during a transient event is to use Joukowski's (1904) modified bulk modulus in the equation of state and complete the fluid solution for the velocity and pressure. Once these values are obtained, the resultant pressure forces are input into a structural analysis model to determine the stresses and pipe motion. The liquid is typically represented in these structural models by its mass only, and energy dissipation is either neglected or approximated by assuming structural damping proportional to mass and stiffness to permit decoupling of the structural equations.

Various studies such as Jones and Wood (1972) and Wiggert et al. (1985) have shown that pipe motion can modify pressure surges to magnitudes significantly greater than those predicted by the traditional analysis, since the traditional models cannot predict modifications of pressure by pipe motion. Apparently, an accurate model of pressure surges in piping must include mechanical interaction of liquid and pipe. One form of interaction is Poisson, or strain-related coupling, which results from the transformation to axial strain of circumferential strain caused by internal pressure. The axial strain propagates within the pipe wall at the sonic velocity of the material, and produces an overpressure due to reduction in the pipe radius. Since the pipe material usually has a sonic velocity which is greater than that of the fluid, this overpressure wave usually travels ahead of the main pressure wave. Thus, Poisson coupling is also referred to as the precursor wave phenomenon.

Skalak (1956) extended Joukowski's analysis to include Poisson coupling. Walker and Phillips (1977) included radial equilibrium and continuity in the equations of motion for the fluid and pipe. Wiggert et al. (1985) simplified the equations of Walker and Phillips by assuming that radial inertia was negligible. Budny (1989) introduced viscous damping and Zielke's (1968) frequency-dependent fluid friction into the coupled equations and demonstrated that the model could satisfactorily predict fluid pressure and structural velocity. This study evaluates the effect that structural damping has on a transient pressure. The goal of this study is to use theoretical predictions along with comparisons of experimental data to determine the influence of structural damping, and to define the appropriate modeling technique.

Analytical Development

The following equations, in cylindrical coordinates, govern the fluid pressure and axial velocity, and the pipe axial stress and axial velocity. For the fluid motion, it is assumed that instantaneous pressure remains above vapor pressure, the fluid is linear homogeneous and isotropic, and the radial fluid velocity equals the radial pipe wall velocity. The structural equations are based on assumptions of axisymmetric, linear elastic pipe walls, small deformation, no buckling, plane stress, viscous damping, and negligible radial inertia.

Budny (1989) introduced the following four coupled, linear, first order, hyperbolic, partial differential equations to describe the behavior of the four dependent variables, P, V, σ, and $\dot{u}$, as functions of distance z and time t:

$$\frac{\partial V}{\partial t}+\frac{1}{\rho_f}\frac{\partial P}{\partial z}+g\sin\alpha+\frac{\tau_0\pi D}{A_f\rho_f}=0 \tag{1}$$

$$\frac{\partial \sigma_z}{\partial z}-\frac{C_z}{A_p}\dot{u}+\frac{\tau_0\pi D}{A_p}-\rho_p\frac{\partial \dot{u}}{\partial t}=0 \tag{2}$$

$$\frac{\partial P}{\partial t}-2\nu K^*\frac{\partial \dot{u}}{\partial z}+K^*\frac{\partial V}{\partial z}=0 \tag{3}$$

$$\frac{\partial \sigma_z}{\partial t}-E\frac{\partial \dot{u}}{\partial z}-\frac{\nu R}{e}\frac{\partial P}{\partial t}=0 \tag{4}$$

where

Contributed by the Fluids Engineering Division and presented at the Winter Annual Meeting, San Francisco, Calif., December 10–15, 1989 of THE AMERICAN SOCIETY OF MECHANICAL ENGINEERS. Manuscript received by the Fluids Engineering Division February 2, 1990.

$$K^* = K \Big/ \left[1 + \frac{2RK}{eE}(1-\nu^2) \right] \tag{5}$$

Poisson coupling is evident in Eq. (3), where the coupled fluid continuity equation includes a structural velocity gradient, and in the coupled structural constitutive relation, Eq. 4, where a pressure term is introduced. The energy dissipation terms appear as structural damping in Eq. (2), and fluid shear stress in Eqs. (1) and (2).

Fluid Friction and Structural Damping

The following wall shear stress equation developed by Zielke (1968) is used to represent the fluid friction

$$\tau_0 = \frac{4\rho_f \mu_f}{R} \tilde{V}(t) + \frac{2\rho_f \mu_f}{R} \int_0^t \frac{\partial \tilde{V}}{\partial t}(\beta) W(t-\beta) d\beta \tag{6}$$

Since the stress is evaluated at the wall, the fluid velocity in this equation must be the velocity relative to the wall. Thus, to account for the moving boundary condition the following relative fluid velocity is used

$$\tilde{V} = V - \dot{u} \tag{7}$$

Zielke developed Eq. (6) for the laminar flow regime. However, he stated that the fluid friction term is valid for laminar flow and only a criterion of the laminar-turbulent transition can describe the range of applicability of the theory. Thus, the acceptable limits for the use of this friction term are not well defined. For the experiments presented herein, initial flow rate conditions exceeding laminar flow were required to introduce significant structural motion. Thus, the first step of this study was to determine if Zielke's model could be extended into a higher range of Reynolds numbers. Budny (1989) has shown that it can be employed to predict a rapidly decelerating fluid transient in a pipe with an initial steady-state Reynolds number as high as 10,000.

Models to represent damping in the structural equations of motion have been widely reported in texts on structural dynamics (1981). The most commonly employed model is linear viscous damping, wherein damping takes the form of force proportional in magnitude to the structural velocity and acting in the opposite direction. The constant of proportionality is termed the viscous damping coefficient C. Other types of damping such as inertial, structural, or Coulomb can also be employed. However, usual practice is to equate the energy loss from these nonviscous types to that associated with viscous damping in order to represent the damping as equivalent viscous damping.

Since the coupled liquid-piping equations are given in terms of structural velocity, viscous and equivalent viscous damping are easily incorporated. However, damping coefficients are typically normalized and reported in terms of a damping ratio ξ. For this study the following normalization was employed:

$$\xi = \frac{C}{2m\omega} \tag{8}$$

where the natural frequency is

$$\omega^2 = \frac{K}{m} = \frac{AE}{mL} \tag{9}$$

Then a relation for the damping constant C per unit length can be obtained

$$C = 2m\omega\xi = 2\xi\sqrt{Km} = 2\xi A\sqrt{E\rho_p} \tag{10}$$

Compatibility Equations

The four partial differential equations are transformed into ordinary differential equations by the method of characteristics. Characteristic roots or eigenvalues and their eigenvectors are found, and compatibility relations are developed which are valid along the characteristic lines. The relation for the eigenvalues (wave speeds) is:

$$\lambda_i^2 = \frac{1}{2}\left(a_f^2 + a_p^2 + 2\nu^2 a_f^2 \frac{d}{b}\right) \pm \frac{1}{2}\sqrt{\left(a_f^2 + a_p^2 + 2\nu^2 a_f^2 \frac{d}{b}\right)^2 - 4a_f^2 a_p^2} \tag{11}$$

where $a_f^2 = \dfrac{K^*}{\rho_f}$, and $a_p^2 = \dfrac{E}{\rho_p}$.

When $i = 1$ or 2, λ represents the positive or negative axial pipe wave speed, and when $i = 3$ or 4, λ represents the positive or negative liquid wave speed. As noted by Stuckenbruck et al. (1985), if the second order Poisson term is dropped from the above equation, the classical fluid wave speed prediction (1982) for a pipe anchored throughout against axial motion is obtained. The four compatibility equations, for $i = 1,2,3$ and 4, have the form:

$$\frac{2\nu\lambda_i}{\rho_p(\lambda_i^2 - a_p^2)}\frac{d\sigma}{dt} - \frac{2\nu\lambda_i^2}{(\lambda_i^2 - a_p^2)}\frac{d\dot{u}}{dt} + \left(\frac{\lambda_i}{K^*} - \frac{2\nu^2 d\lambda_i}{\rho_p(\lambda_i^2 - a_p^2)}\right)\frac{dP}{dt} + \frac{dV}{dt} + \frac{2\nu\lambda_i^2}{b(\lambda_i^2 - a_p^2)}\left(\frac{\tau_0 \pi D}{\rho_f A_p} - \frac{C_z \dot{u}}{\rho_f A_p}\right) + g\sin\alpha + \frac{\tau_0 \pi D}{\rho_f A_f} = 0 \tag{12}$$

Nomenclature

A = cross-sectional area
a = wave speed
b = ratio of pipe density to fluid density
C = viscous damping coefficient
d = ratio of pipe radius and wall thickness
D = inside pipe diameter
E = Young's modulus of elasticity
e = thickness of pipe wall
g = acceleration due to gravity
K = fluid isothermal bulk modulus of elasticity, or stiffness
L = length of horizontal pipe
m = mass of system
P = fluid pressure at pipe centerline
R = pipe internal radius
Re = Reynolds number
t = time
u = displacement of pipe in axial direction
$\dot{u}$ = structural velocity
V = average velocity of fluid
W = weighting function used in friction term
α = angle of inclination of the pipeline with the horizontal
β = time used in convolution integral
ρ = mass density
ν = Poisson's ratio for the pipe material
μ = absolute viscosity
τ_0 = fluid shear stress at wall
σ = pipe axial stress
ξ = damping ratio
ω = circular frequency
λ = modified wave speed
Δt = time step in space time grid
Δz = distance associated with Δt in space time grid

Subscripts

c = critical
f = fluid
i = $i = 1$ or 2 implies pipe wave speed, 3 or 4 fluid wave speed
p = pipe
r, θ, z = principal cylindrical coordinate directions

Superscripts

$*$ = modified
$\sim$ = relative

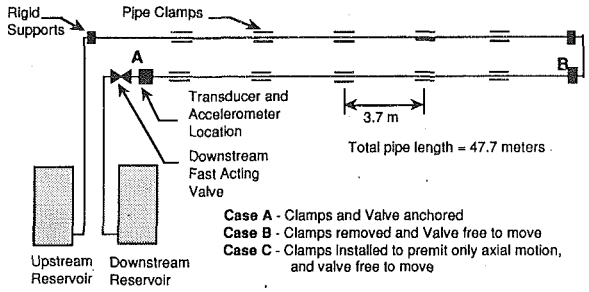

Fig. 1 Experimental apparatus

Each compatibility equation is integrated along its appropriate characteristic line, and algebraic equations are produced which are solved on a time-space grid. The algebraic equations must be solved for the dependent variables P, V, σ, and $\dot{u}$. However, the variation of energy dissipation terms are unknown a priori, so their evaluation requires an approximation. A first-order approximation where the variation is set equal to the value at the previous time step was investigated and found to give satisfactory results.

As long as the fluid and pipe wave speeds are multiples of each other, the numerical method of characteristics can be continued to any time duration without interpolation error. However, wave speeds that are not multiples necessitate the use of either interpolations or adjusted wave speeds, both of which introduce numerical errors in the solution. These procedures are described, for example, by Goldberg and Wylie (1983). For the piping used in this study, the fluid and structural wave speeds have a ratio of 2.95. Thus, a wave speed ratio of 3 is assumed to avoid the need for interpolation. This approximation will cause the computed and measured pressure traces to diverge as time progresses.

Description of the Experimental Apparatus

The piping system used in this study is shown in Fig. 1; the pipe is a 1 in US nominal diameter type L copper pipe, with a total length from the upstream reservoir to the downstream valve of 47.7 meters. PCB Quartz crystal dynamic pressure transducers, and a quartz accelerometer with a single integrating power unit were used to measure the fluid pressure within the pipeline and to monitor the pipe motion at the downstream fast acting valve. Water was used as the fluid medium, and excitation was produced by a rapid valve closure of the downstream valve. Unistrut model P2031 pipe clamps mounted approximately 3.7 meters apart were used as intermediate supports to maintain the pipe in a horizontal plane. In addition, a rigid support was connected to the pipe and then mounted to the wall at the elbows shown to eliminate all axial motion. The downstream valve support was designed such that the valve could be free to move in the axial direction, or it could be bolted to the wall to eliminate all axial motion.

Three configurations of the piping system were used in this study. Setup A is the rigidly-fixed system; all of the intermediate pipe clamps are tightened and the valve was anchored to the wall. Setup B, the free system, is similar except the intermediate supports are modified by replacing the clamps with wires which suspended the pipe and removed all axial constraints. In addition, the axial restraint at the valve was eliminated. This design produced the maximum axial motion of the pipe, especially in the reach between points A and B. In Setup C, the intermediate clamps were installed but not tightened, hence they maintained the pipe in the horizontal plane but did not prevent axial motion. This arrangement was designed to model a typical saddle support used on piping systems. The actual pipe support was accomplished by resting the un-tightened clamp on top of an additional support. This increased the damping from that of the free case, since Coulomb friction was now introduced between the un-tightened clamp and the pipe wall.

Experimental Uncertainty

The sources of experimental uncertainty associated with the transducer data include the inherent errors of each transducer, and the error in the conversion of the analog voltage to a digital format by the A/D converter. The pressure transducers have a linear error of 2 percent. The linearity of the error means the error is a constant 2 percent along the entire operating range of the transducer. Thus, a reading of 500 kPa would have an error of plus or minus 10.0 kPa. The output sensitivity for each transducer was determined in compliance with MIL-STD-45662, the approximate value as represented by the manufacture is 10 mVolts/psi. The error due to the A/D conversion is controlled by the 11 bit resolution of the input data. Since the A/D board is configured for bipolar inputs ± 10.0 volts, the 11 bit resolution is equivalent to an error of ± 9.7 millivolts. Therefore, the maximum experimental error associated with the pressure readings due to the propagation of both the transducer and conversion error based on rms estimate for a 500 kPa reading at a gain of 1.0 would be ± 12.0 kPa.

The maximum accelerometer error is based on which type of power unit is connected to the transducer. If a nonintegrating unit is used, the error in the measurement is that due to the transducer which is a linear error of 1 percent. However if one of the integrating units is used, the error is increased to the 5 percent error associated with the integration within the power unit.

The sources of error in modeling an experimental test are the piping and fluid parameters. The copper pipe was manufactured to a tolerance for the inside diameter and wall thickness of 0.4 percent (0.1 mm) and 3 percent (0.04 mm), respectively. The fluid temperature was measured with an accuracy of 0.5°C.

Experimental Results

To test the validity of the four equation model, and to measure the effect structural damping has on the fluid response, the free system (setup B) was used. Tests at Reynolds numbers from approximately 1000 to 11000 were studied. A typical result for this setup at an initial steady-state Reynolds number of 11400 is displayed in Figs. 2 and 6(a). The high Reynolds number data are used since it corresponds to the largest axial motion. Similar results were obtained for the entire range of Reynolds numbers. The pressure and structural velocity are recorded at the downstream valve. In Fig. 2, plot (a) is the experimental data for the free condition, plot (b) is the four equation model prediction using $\xi = 0$ percent, plot (c) is for $\xi = 2$ percent damping, and plot (d) is a combination of the measured results and the 2 percent damping model predictions. Figure 6(a) shows the comparison of the measured and computed structural velocities. As shown in these figures, the model can predict the fluid pressures, and the general trend in the structural velocity throughout the transient. These results indicate that the four equation model is valid, and therefore the structural viscous damping incorporated in the model is also valid. By comparing the $\xi = 0$ and 2 percent results in Fig. 2, it can also be concluded that the copper pipe studied has a damping ratio of about 2 percent, and this structural damping reduces the high frequency components of the fluid pressure wave form; that is, an additional 20–25 percent increase in the peak pressure response could be expected if structural damping were not present.

If damping can reduce these high frequency peaks, then what effect does reducing the motion of the pipe produce? Since setup A contains additional restrictions on the motion of the piping, the results from setup A should be different from those

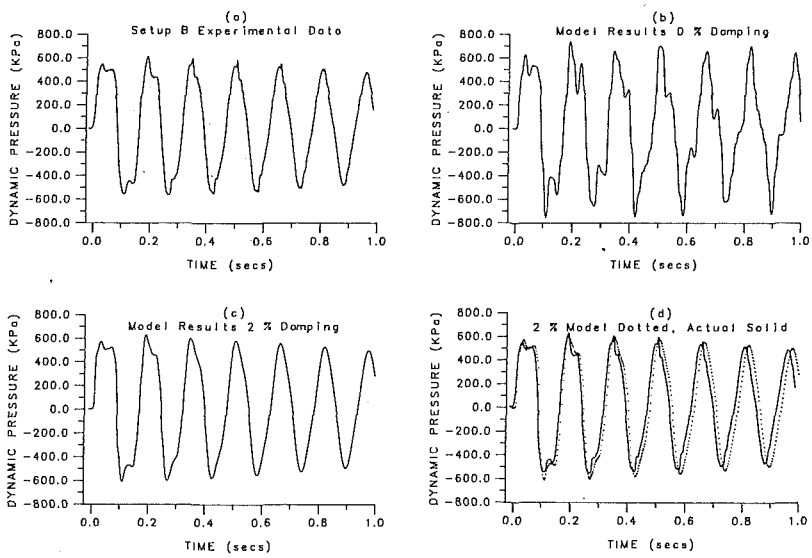

Fig. 2 Comparison of experimental and computer results, setup B; 0, and 2 percent damping; Re = 11400

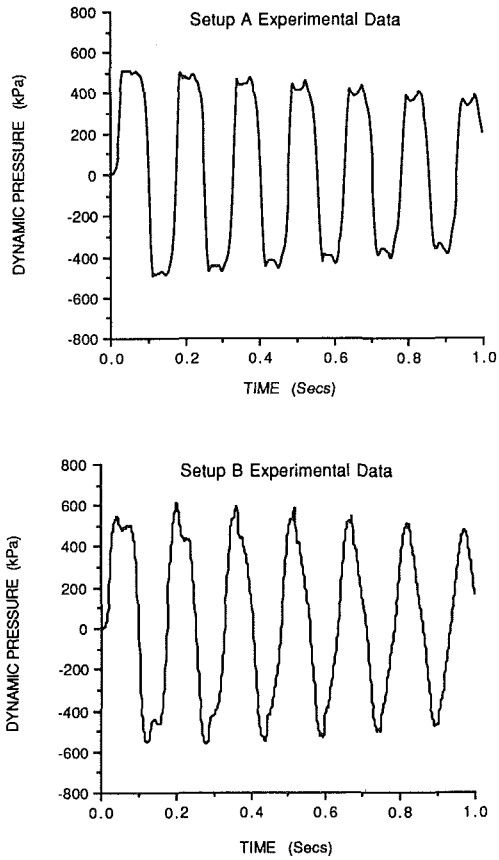

Fig. 3 Comparison of experimental results for setups A and B

of setup B. Figure 3 compares the results for setup A and B at an initial Reynolds number of 11000. The first observation made from these plots is that the wave form changes. The rigid system has a closer resemblance to a square wave. This results in a reduction in the higher frequency components of the fluid pressure, and produces peak pressure values in setup A much lower than the setup B. The reason for the differences in the results for setup A and B is that Poisson coupling is considerably less significant in setup A because the pipe motion is restrained. Stated differently, the high frequency components of the pressure rise which cause the distortion on the top of the fluid "square wave" are related to the structural motion. This is shown by the manner in which the top of the wave changes. Thus, structural motion increases the magnitude of the high frequency peaks. The results of Figs. 2 and 3 indicate that either damping or restricting this motion will reduce these peaks. However, do the supports only restrict the motion, or do they also act as additional damping?

This can be studied by analyzing the results of setup A. Figure 4 compares the four equation model results against the experimental data for setup A at a Reynolds number of 1800. The 1800 Reynolds number data are used for purposes of visual observation only similar results were obtained at the higher Reynolds numbers however the results are not as visually apparent. Since, the pipe motion is restricted in setup A, the 1800 Reynolds number data produces a condition where the magnitude of the pressure rise created by the stoppage of flow and the pressure rise created by the Poisson coupling is of the same order of magnitude. Thus, by using the lower Reynolds number data the effect of changing the damping within the model is visually detectable in the plotted data. Plot (*a*) is the measured pressure at the downstream valve, plot (*b*) is the result of the model with $\xi = 0$ percent, and plots (*c*) and (*d*) are for $\xi = 2$ and 5 percent damping respectively. Figure 4 shows that the peak pressures result in only an additional 6 to 9 percent increase over the peak pressure response when damping is not present. Also, notice how the "U" shaped appearance on the top of the wave in Fig. 4 is diminished and more closely resembles the experimental data as the damping of the structural motion is increased. Thus, the general shape of the results of Fig. 4 gives an indication that a damping ratio of 3 to 4 percent would fit analytic results to experimental observations. The major difference between setups A and B is the magnitude of axial motion permitted. Thus, the restriction of motion imposed by the supports appears to act as additional damping.

To verify this observation, setup C was installed. This should increase the damping from setup B, since Coulomb friction is now introduced between the supports and pipe wall. In Fig. 5, plot (*a*) compares the measured fluid pressure at the downstream valve for setups C and B, and plot (*b*) compares the data from setup C against the results predicted by the four equation model. Since the hypothesis is that the damping should be increased, the model uses a damping ratio of 5 percent. The setup C data in plot (*a*) has been offset by 5 ms and plotted as a dotted line to aid in viewing the data. Figure 6(*b*) compares

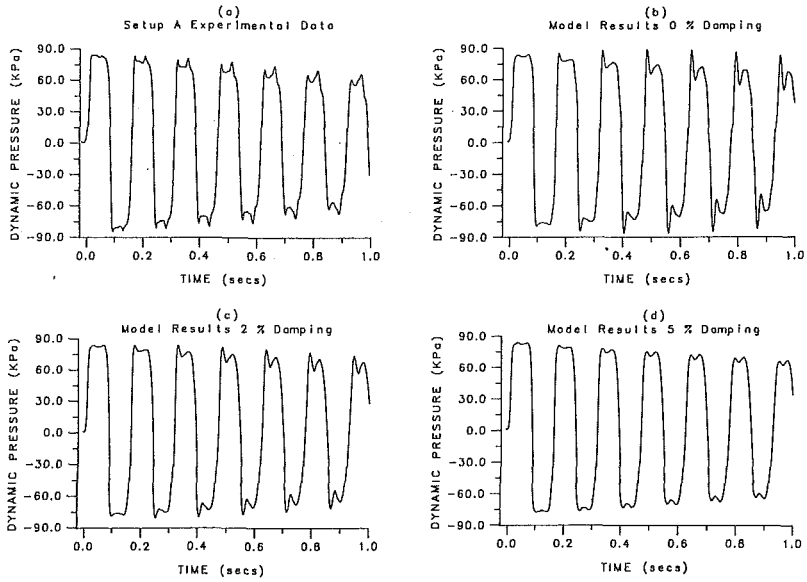

Fig. 4 Comparison of experimental and computer results, setup A; 0, 2 and 5 percent damping; Re = 1800

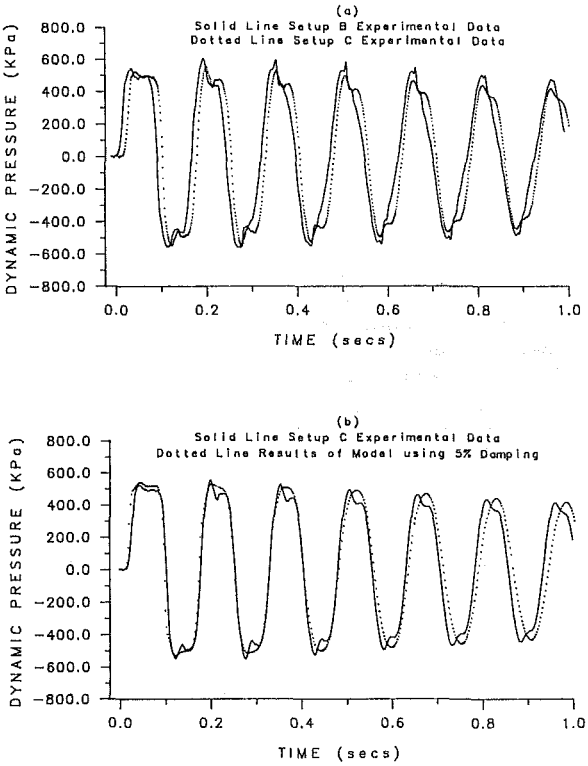

Fig. 5 Comparison of setup C data with setup B data and model results using 5 percent damping

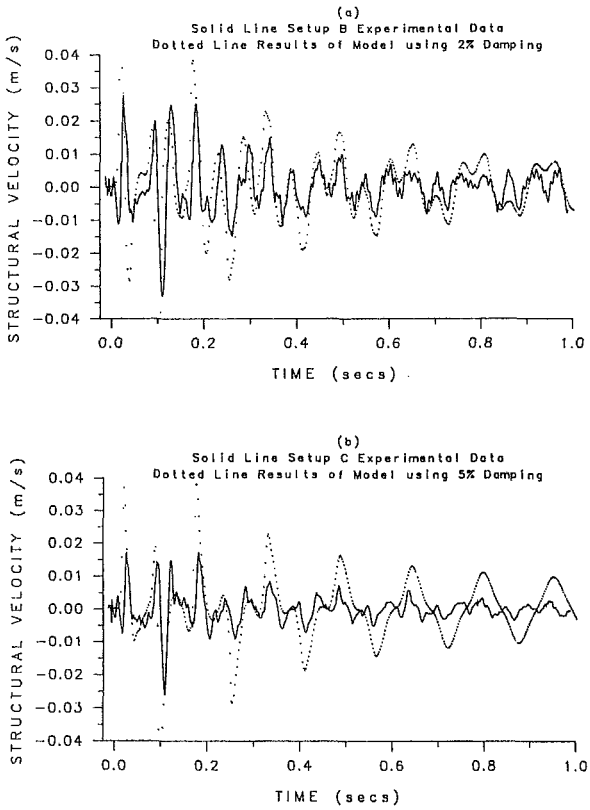

Fig. 6 Comparison of experimental velocities; setup B and C against model predictions

the measured structural velocity of the valve against the value predicted by the four equation model for setup C. As expected there is additional damping present in setup C caused by the Coulomb damping in the support. This is verified in Figs. 5 and 6 by the increase in the general pressure decay rate between setups B and C, the elimination of the steep peaks in the pressure response for setup C, and the change in the measured structural velocity between setups B and C. Also, note how the four equation model can predict the results of setup C with the additional damping.

The discrepancies between the model and experimental data in the setup C plots is caused by modeling the Coulomb friction as an equivalent viscous damping. Since this equivalence only produces a condition of equivalent energy dissipation, the damping model is not capable of maintaining the actual shape of the pressure or velocity response after a few cycles. However, it can predict the magnitude of each peak, and the gross decay rate.

As an alternative to distributing this Coulomb friction along the entire length of the pipe, the effect can also be modeled as a viscous damper located at the support. Figure 7 compares the measured pressure at the valve (*a*), and the structural ve-

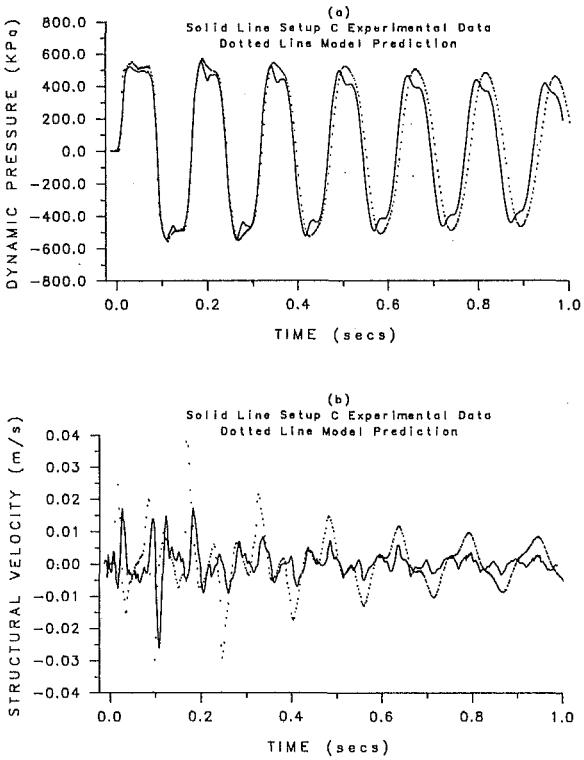

Fig. 7 Model predictions for setup C using 2 percent damping plus external dampers

locity of the valve (*b*) against the four equation model using 2 percent distributed damping and an additional external damper at each support. The four equation model is still capable of predicting the general pressure decay and structural velocity of the valve, but once again since the Coulomb friction is not related to the structural velocity it fails to match the data after a few cycles. Thus, a saddle type support will increase the general damping, and this increase in damping can be modeled by making the assumption that the Coulomb damping can be described as equivalent viscous damping. This equivalent viscous damping can be accounted for as either external dampers or additional distributed damping. However, since modeling Coulomb friction as an equivalent viscous damping only produces a condition of equivalent energy dissipation, the damping model is not capable of maintaining the actual shape of the pressure or velocity response after a few cycles. However, it can predict the magnitude of each peak, and the gross decay rate.

If distributed structural damping and incidental frictional damping at supports can reduce the resulting pressure, then externally mounted dampers should also be capable of changing the pressure response. To test this idea a damper was installed on the valve in setup B. Only a 2.5 percent pressure attenuation was observed with the addition of the damper. The problem encountered was that because of experimental constraints it was impossible to achieve large pipe motions without causing cavitation. Thus, the physical constraints and the minor pressure attenuation made it very difficult to reach a conclusion on the effectiveness of the external dampers. However, from a mathematical viewpoint, the four equation model was capable of predicting the results of this experiment. To further the study of external dampers it was necessary to design a new setup which would increase the structural displacement without causing cavitation. Budny (1990) performed such a study and verified that external dampers can have a significant effect on the fluid response.

Summary and Conclusions

Based on the experimental tests and comparison with theory, the following observations can be made:

1) The four equation model described by Eqs. (1)–(4), which incorporate a viscous damping model, is capable of accounting for the fluid-structure interaction, and predicting the fluid pressure and axial pipe velocity.

2) The effect of structural damping on a fluid transient is to reduce the pressure peaks by eliminating the high frequency structural components caused by the structural motion. Thus, it is possible by increasing the damping or reducing the resulting pipe motion to attenuate the high frequency components of the pressure.

3) For the pipe studied in this report, the pressure reduction produced by structural damping was 20–25 percent for a piping system with no intermediate supports and the axial constraints at the downstream valve removed.

4) The pipe studied in this report has an apparent viscous damping ratio of approximately 2 percent. By adding intermediate saddle type supports along the pipe length, the equivalent viscous damping ratio was increased to approximately 5 percent. This increased damping can be modeled as either additional distributed damping or as an external damper.

Acknowledgment

This work has been supported in part by the National Science Foundation, through Grant No. MEA-8401339.

References

Budny, D. D., Hatfield, F. J., Wiggert, D. C., 1990, "An Experimental Study on the Influence of Structural Damping on Internal Fluid Pressure During a Transient Flow," ASME *Journal of Pressure Vessel Technology*, Vol. 112, No. 3, pp. 284–290.

Budny, D. D., Wiggert, D. C., and Hatfield, F. J., 1989, "Energy Dissipation in Axially-Coupled Model for Transient Flow," *Proceedings 6th International Conference on Pressure Surges*, Cambridge, England, pp. 15–26.

Goldberg, D. E., Wylie, E. B., 1983, "Characteristics Method using Time-Line Interpolations," *Journal of Hydraulic Engineering*, ASCE, Vol. 109, No. 5, pp. 670–683.

Jones, S. E., and Wood, D. J., 1972, "The Effect of Axial Boundary Motion on Pressure Surge Generation," ASME *Journal of Basic Engineering*, Vol. 94, No. 2, pp. 441–446.

Joukowsky, N. E., 1904, translated by O. Simin as "Water Hammer," *Proceedings, American Water Works Association*, Vol. 24, pp. 341–424.

Skalak, R., 1956, "An Extension of the Theory of Water Hammer," *Trans. ASME*, Vol. 78, No. 1, pp. 105–116.

Stuckenbruck, S., Wiggert, D. C., and Otwell, R. S., 1985, "The Influence of Axial Pipe Motion on Acoustic Wave Propagation," ASME JOURNAL OF FLUIDS ENGINEERING, Vol. 107, No. 4, pp. 518–522.

Thomson, W. T., 1981, *Theory of Vibration with Applications*, 2nd Ed., Prentice Hill, Englewood Cliffs, N. J., pp. 13–92.

Walker, J. S., Phillips, J. W., 1977, "Pulse Propagation in Fluid Filled Tubes," ASME *Journal of Applied Mechanics*, Vol. 44, No. 1, pp. 31–35.

Wiggert, D. C., Otwell, R. S., Hatfield, F. J., 1985, "The Effect of Elbow Restraint on Pressure Transients," ASME JOURNAL OF FLUIDS ENGINEERING, Vol. 107, No. 3, pp. 402–406.

Wylie, E. B., Streeter, V. L., 1982, *Fluid Transients*, FEB Press, pp. 1–8.

Zielke, W., 1968, "Frequency Dependent Friction in Transient Pipe Flow," ASME *Journal of Basic Engineering*, Vol. 90, No. 1, pp. 109–115.

T. F. Swean, Jr.
Research Mechanical Engineer,
Center for Advanced Space Sensing,
Naval Research Laboratory,
Washington, D.C. 20375-5000

S. E. Ramberg
Director,
Ocean Engineering Division,
Office of Naval Research,
Arlington, VA 22217-5000

E. W. Miner
Mechanical Engineer,
Center for Advanced Space Sensing,
Naval Research Laboratory,
Washington, D.C. 20375-5000

Anisotropy in a Turbulent Jet Near a Free Surface

Laboratory measurements of the turbulent flow in a plane jet issuing at the free surface are reported and analyzed. Single point hot-film data were obtained for mean velocities and turbulent fluctuations of velocity and shear stress in the developing jet to $x_1/b_0 = 240$ with an emphasis on the near surface turbulent behavior. Anisotropy distributions indicate two layers within the jet. In a surface-influenced layer of thickness comparable to 1.5 times the local jet half-width, the vertical anisotropy is constant and the primary net energy transfer is from the streamwise component of turbulent kinetic energy to the spanwise component. In a near-surface layer of about 1/4 the local half-width, the vertical fluctuations decrease rapidly with a concomitant redistribution of energy to the horizontal components. Analysis of one-dimensional spectra reveal integral scales that are consistent with the anisotropy data and in qualitative agreement with analyses and experiments for isotropic turbulence near moving walls and free surfaces but differs by exhibiting a wider range of surface-influenced turbulent length scales.

Introduction

The turbulent flow below a gas-liquid interface plays an important role in diverse areas ranging from environmental flows and industrial mixing processes to the remote sensing of ship wakes. Transport processes at the interface are of primary concern in environmental and industrial applications, whereas remote sensing issues ultimately involve any surface motions which may be detectable. The remotely sensible surface events may be either generated or modified by the subsurface turbulent flow. The primary motivation for the present work stems from the remote sensing problem wherein various sensors appear to respond to the turbulent wake region of a surface ship. For example, the two most common and persistent features seen in synthetic aperture radar (SAR) images of ship wakes include bright "narrow-vees" and long dark "scars" which may be a result of surface Bragg wave generation or modification through interactions with near surface turbulence. Common to all of these problems is the need for a better understanding of the structure of turbulence below a free surface. The present study examines experimentally the turbulent structure below a free surface where the underlying flow is developing in the manner of a 2D planar jet. Surface deflections are minimized in order to isolate the kinematic effect of the free surface upon the turbulence below.

Background

The literature on bounded shear flows is extensive but almost exclusively directed at the wall boundary layer problem where the no slip boundary condition leads to steep velocity gradients very near to the boundary and a nonzero shear stress at the wall. A clean free surface with negligible velocities in the overlying gas phase cannot support a mean or fluctuating shear stress and therefore, unlike the wall boundary layer flow, turbulence production is negligible near the free boundary. The surface region acts to modify and to dissipate the impinging turbulence which has been generated below and advected to the surface. Under the assumption of small vertical surface motions, the free surface behaves like a rigid wall moving at the free-stream velocity, such that mean shear is zero. These conditions were employed by Hunt (1984) to extend a theory for a moving wall (Hunt and Graham, 1978) to the free surface problem. In this theory, isotropic decay of turbulence behind a grid is taken as the outer or farfield source of turbulence for interaction with a wall moving at the speed of the free stream. The theory describes a layer near the surface where vertical turbulent scales larger than the distance to the surface are "blocked" which produces an anisotropic redistribution of turbulent energy from the vertical (x_2) component to the two lateral components. The thickness of the redistribution layer is on the order of the farfield ($x_2 \rightarrow \infty$) turbulent integral scale, L_0.

Measurements of the grid turbulence in proximity to a moving wall by Thomas and Hancock (1977) and computations of a similar flow by Biringen and Reynolds (1981) are in general agreement with the theory. Related experiments for an oscillating grid below a rigid wall by McDougall (1979) and below a free surface by Brumley and Jirka (1987) also generally agree with the theory. The blocking of vertical scales as the surface is approached and the redistribution of turbulent energy from vertical to lateral components are observed in all of the above cases although not exactly as the theory predicts. Differences from the theory include greater anisotropy among turbulent components and a wider range of surface influenced turbulent scales. These differences have been ascribed to the modification of the finer scales of the turbulence by the larger surface-influenced scales, which is expected but not included in the theory.

Contributed by the Fluids Engineering Division for publication in the JOURNAL OF FLUIDS ENGINEERING. Manuscript received by the Fluids Engineering Division March 21, 1990.

All of the above literature is restricted to a farfield or source turbulent flow which is isotropic and therefore characterized by a single farfield integral scale. The present study was undertaken to examine a nonisotroic turbulent farfield in the presence of a free surface. The basic flow chosen for this investigation was a nominally two-dimensional planar jet issuing at a free surface, often termed a surface jet. Relatively little attention has been given to surface jets except for the hydraulic literature where the concern is for the influence of buoyancy on the spreading and mixing of outfalls that are generally warmer than the receiving fluid. A study by Chu and Baddour (1984) presents experimental results for a buoyant planar jet and contains a good review of that particular area of the literature. Rajaratnam and Humphries (1984) have reported experimental data for both planar and axisymmetric surface jets where it is shown that mean velocity profiles exhibit similarity based on the usual characteristic velocity and length scales. For the planar surface jet these scales vary in a manner closest to the planar wall jet where the jet issues tangent to the wall. Earlier results by Rajaratnam (1969) indicated that the surface jet synoptic scales behaved more like the free planar jet scales. Neither of these studies reported results for the turbulence statistics but rather concentrated on the evolution of the characteristic velocity and length scales.

Due to the apparent confusion about free surface jet characteristics and the sparsity of additional reference data for the nonbuoyant jet, the clarification of the mean behavior of the surface jet was a goal of the current effort. The results of that portion of the study have been reported by Swean et al. (1989). Those data show that the growth rates for the velocity and length scales are much lower than those found in the free jet, and similar to but remaining lower than those determined for planar wall jets at comparable Reynolds number. If the plane of the mean free surface is compared to the symmetry plane of a free jet, the lower growth rates in the surface jet can be explained by the absence of instantaneous momentum flux across the free surface. In addition the above study quantifies the subtle and pervasive influence of finite depth on jet evolution and determines that the conflicting information for nonbuoyant surface jets (and buoyant jets at low Richardson number) is likely due to restricted entrainment. The present study will concentrate on the turbulence characteristics near to the free surface.

Experimental Conditions

Facility. The experiments reported here were performed at one end of a long tow channel (Fig. 1) described by Ramberg and Fung (1982). The channel has nominal interior dimensions of 1 m in depth, 1.3 m in width, and 18 m in length. A temporary dividing wall was located 0.46 m from the near wall and extended downstream to 2.62 m. The still water level in the channel was maintained at 0.82 m by a steady supply of water at one end and an adjustable overflow drain at the opposite end. The jet flow was obtained by replenishing the jet reservoir with water from the far end of the channel. Both

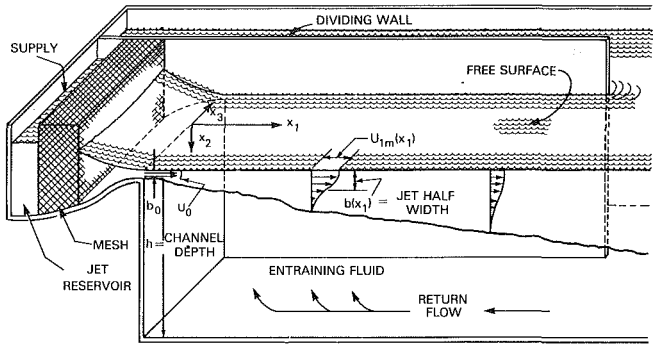

Fig. 1 Schematic of experimental arrangement showing nomenclature

flow rates were monitored along with the mean and still water depths over the jet lip ($x_1/b_0 = 0$). As a result of these precautions, the discharge height of the jet, b_0, and the depth of the jet lip relative to the surface elevation at large x_1 were maintained to within ± 0.1 mm at 7.6 mm and 6.7 mm, respectively. The jet exit velocity, U_0, was maintained at 340 ± 5 mm/s. Figure 1 also contains the nomenclature for describing the results. Subscripts are used to denote the three coordinate directions. The primary flow is in the "1" direction and the vertical down direction is "2," leaving "3" for the transverse or lateral direction in a right-handed coordinate system. Conditions at the jet inlet ($x_1 = 0$) are denoted by the subscript $(\ )_0$ and locally maximum values are designated by the subscript $(\ )_m$. The time-average of the ith-component of velocity is denoted by U_i and its velocity of fluctuation by u_i'. In the discussion that follows the primes will be omitted from the fluctuating velocities and mean values of turbulence quantities will be denoted simply by an overbar. We further use the shorthand notation $\overline{u_i}$ to denote $(\overline{u_i'^2})^{1/2}$.

Instrumentation. The data were obtained with a dual sensor (X-type) hot-film probe (DISA 55R62) connected to DISA 56C01 constant temperature anemometers. The anemometer output voltages were passed through DISA 56N21 linearizer then through DISA 56N20 signal conditioners where they were offset to ± 5v for acquisition by a QSI simultaneous sample digital tape recorder. Prior to recording, the signals were filtered through Rockland Wavetek Model 452 filters. The sensors were mounted on a vertical-horizontal traversing system operated by a Velmex Model 8300 controller, which was in turn mounted on one of the tow channel carriages. The elements were operated at an overheat ratio of 1.06 (sensor temperature = 42°C) to prevent bubble formation. Water impurities were kept to a minimum by constant filtration and recirculation during periods when a measurement was not in progress. In addition, a drain was positioned at the far end of the channel approximately 12 m from the downstream end of the test section. The height of the drain was adjustable and was typically positioned to slowly but constantly remove the free surface. Water velocities induced by this technique were too small to be measurable.

Nomenclature

a_{ij} = anisotropy tensor
A_2 = second anisotropy invariant
A_3 = third anisotropy invariant
b = local jet half width
F_i = wavenumber function of ith component of velocity
h = channel depth
k = wavenumber
L_i = longitudinal macroscale of ith component of velocity
q = turbulent kinetic energy
R_{ii} = autocorrelation function; $\overline{u_i(t)u_i(t+\tau)}/\overline{u_i^2}$
U_i = local mean velocity in ith direction
u_i' = local fluctuating velocity in ith direction
x_i = cartesian coordinate in ith direction

Subscripts

1, 2, 3 = axial, vertical, and lateral coordinate directions, respectively
0 = conditions at the jet origin
m = local maximum value

Measurements. Composite profiles were obtained at ten axial stations along the centerline of the developing jet ($x_3 = 0$ in Fig. 1). Spanwise measurements showed that the mean velocity variation was less than 5 percent over at least the middle 50 percent for all axial locations. At each station the sequence of vertical positions and dwell time for each were programmed into the traverse control. The sampling rates per channel and the record lengths varied with longitudinal position in the jet and ranged between 100–200 Hz and 45–120 s. The filters were operated between 40–80 Hz. Measurements were repeated at least twice for each sequence of each probe orientation so the streamwise velocities were realized at least eight times and the other two velocity components four times. The results are the averages of the individual realizations at each point.

Errors can arise from imperfect calibration and linearization, probe positioning and orientation, and sensitivity and repeatability limitations. Except in the low velocity intermittent region near the bottom edge of the jet, the maximum error in the mean velocity, U_1, is estimated at 4 percent (20:1 odds). For the turbulence quantities $\overline{u_1}$, $\overline{u_2}$ and $\overline{u_3}$, $\overline{u_1u_2}$ the estimated maximum errors at the same odds are 10 and 15 percent, respectively. These errors are due to sensitivity, repeatability and calibration limitations. Additional details of these measurements as well as other precautions taken to insure accuracy of measurement are described in the report by Ramberg et al. (1989).

Results and Discussion

Mean Flow Statistics. A number of preliminary experiments were performed with various geometries and jet flow rates in search of an arrangement where proper jet behavior could be maintained at the largest possible x_1/b_0. The results reported below are for jet number 10 of the study by Swean et al. (1989) for which the Reynolds number (U_0b_0/ν) was 2550. The ratio of channel depth to initial jet discharge height (h/b_0) was 108. For these conditions the characteristic scales of the jet are described by,

$$\left(\frac{U_0}{U_{1m}}\right)^2 = 0.047\left(\frac{x_1}{b_0}\right) + 0.04;\ 0 \le x_1/b_0 \le 160, \qquad (1)$$

and

$$\frac{b}{b_0} = 0.05\left(\frac{x_1}{b_0}\right) + 0.9;\ 0 \le x_1/b_0 \le 200, \qquad (2)$$

and are shown in Fig. 2. The local half-width dimensions were determined as the x_2 locations where the mean velocity had decreased to one half of its maximum value at the x_1 station in question. It should be noted that the breakdown in velocity scale due to facility constraints occurs prior to that for the length scale as discussed by Swean et al.

The profiles of the mean longitudinal velocity, U_1, are shown in Fig. 3 for the ten measurement stations when scaled by the local maximum, U_{1m}, and jet half-width, $b(x_1)$. This figure also contains the symbol table relevant to the next several figures to be discussed. The maximum velocity at any station always occurred at or very close to the free surface. The first two measurement stations ($x_1/b_0 \le 4$) were in the developing region of the jet and exhibit a nearly uniform potential flow above the spreading shear layer emanating from the solid lip of the jet origin. For the remaining measurement stations in the fully developed jet, traditional similarity in the mean velocity profiles is achieved based on the two scales, $b(x_1)$ and U_{1m}. The largest amount of scatter in the results is found near to the free surface and in the lower portions of each profile, particularly at the most distant stations downstream.

Some of the variance in the lower portions is attributable to the rectification of velocity fluctuations which are larger than the local mean at the edge of the jet. The hot-film anemometers cannot differentiate flow direction under these conditions and therefore indicate a larger mean velocity in proportion to the root-mean-square fluctuations. This is clearest in the third and fourth stations where the profiles never attain zero values deep into the entraining fluid. At the most downstream stations the jet is beginning to deform as it interacts with the reversed flow supplying fluid to the upstream jet flow. The scatter in mean velocities near to the surface is due to the difficulty in maintaining calibrations in that region and the influence of an intrusive measurement near to the surface. These measurements rarely exhibited any trend toward a zero mean velocity gradient at the surface except at very small x_1/b_0. A second measurement series was employed which sequenced the sensors in much smaller spatial increments up to and through the free surface. These measurements did usually exhibit a narrow region below the surface of approximately zero velocity gradient. Due to the high concentration of contaminants near the surface, the before-and-after probe calibrations for these measurements often differed widely. Within

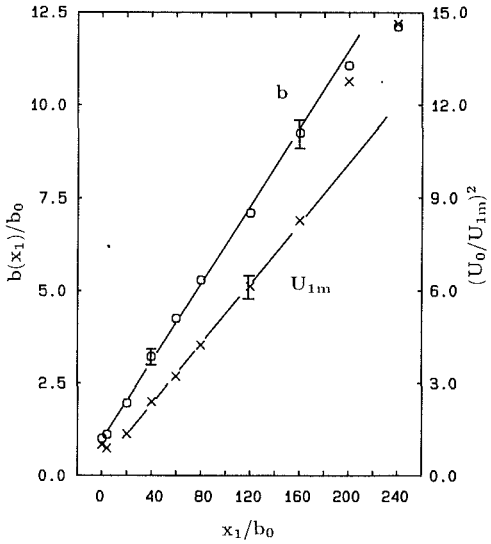

Fig. 2 Streamwise development of characteristic scales. Uncertainties: x_1/b_0: ±0.1; Scales: shown by vertical bars.

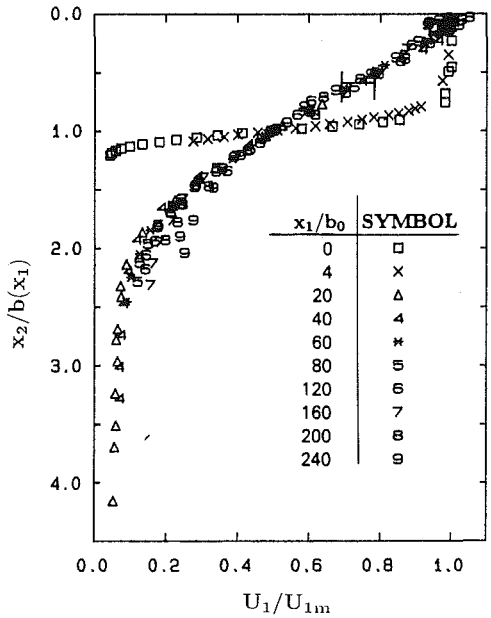

Fig. 3 Mean velocity distributions for $0 \le x_1/b_0 \le 240$. Uncertainties: x_2/b: ±0.05; mean velocity data: shown by horizontal bars.

the scatter of the data, however, we could not detect a boundary-layer region due to surface contamination, as discussed for example by Hunt (1984b). Due to the decreased reliability of the second measurement series the results presented in the following figures are based on the averages of the primary measurement series described in the previous section.

Turbulence Statistics. The averaged profiles of the turbulence intensities and the shear stress are shown in Figs. 4*a–d* where the symbols follow the table given in Fig. 3. In contrast to the mean velocity, the turbulence does not achieve self-similar distributions until $x_1/b_0 > 20$. Thereafter, the data collapse well until $x_1/b_0 \geq 200$ (symbols 8 and 9). At these stations the deviations from the collapsed profiles are particularly evident in the x_1 and x_3 fluctuating velocities. As shown in Fig. 2 the local velocity scale deviates from Eq. (2) beyond $x_1/b_0 = 160$ due to restricted entrainment. If the data are renormalized by the local mean velocity maximum obtained by the continuation of Eq. (2) beyond $x_1/b_0 = 160$, the profiles retain self-similarity within normal scatter. This is shown for example in Fig. 5.

Close inspection of Figs. 4(*a–d*) show that there is a trend for the data to be progressively shifted to the right as x_1/b_0 is increased. This pattern is particularly evident in Figs. 4(*a*) and 4(*c*) and appears to be largely confined in $x_2/b < 1$. The adjustment in velocity scale in Fig. 5 mitigates the trend to a degree but it remains clear for $x_1/b_0 < 160$ where the scales in Fig. 2 are well behaved. We have considered that this behavior may be due to low-frequency long waves in the channel. Inspection of Fig. 4(*b*), however, shows that for $\overline{u_2}/U_{1m}$ the trend is barely discernible, if at all. The same observation holds

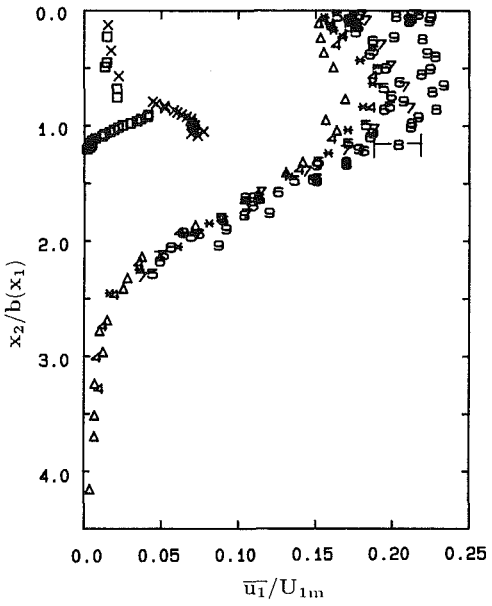

Fig. 4(*a*) longitudinal

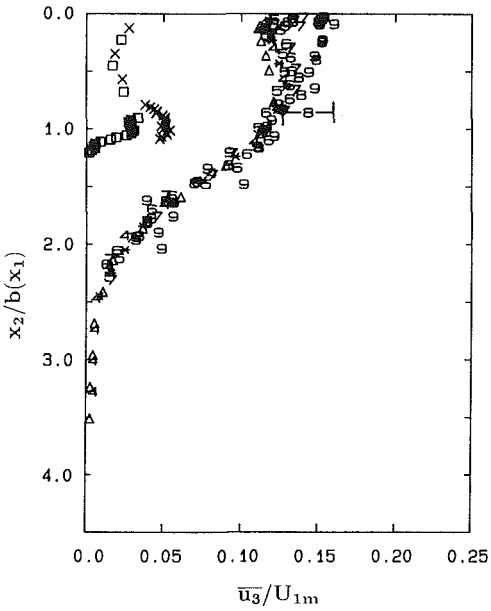

Fig. 4(*c*) lateral

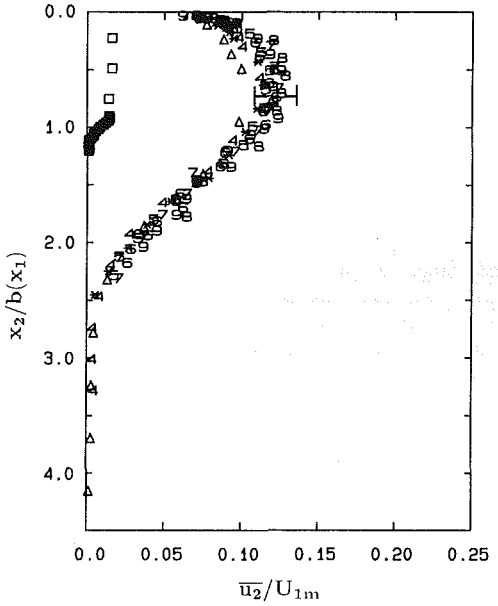

Fig. 4(*b*) vertical

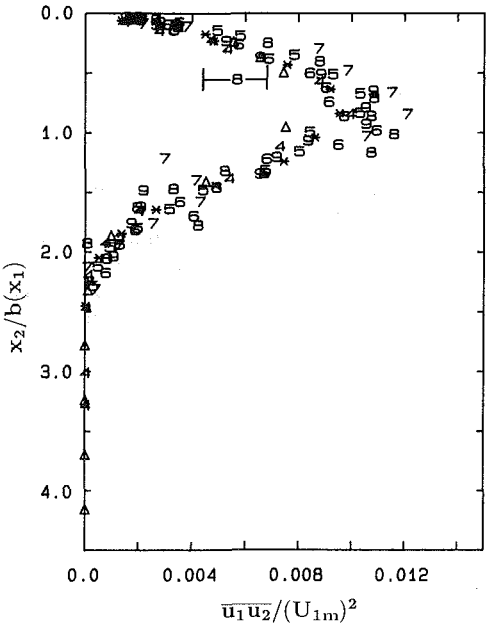

Fig. 4(*d*) Reynolds stress

Fig. 4 RMS velocities and Reynolds stress for $0 \leq x_1/b_0 \leq 240$ normalized by the local maximum mean velocity. Uncertainties: x_2/b: ±0.05; turbulence data: shown by horizontal bars.

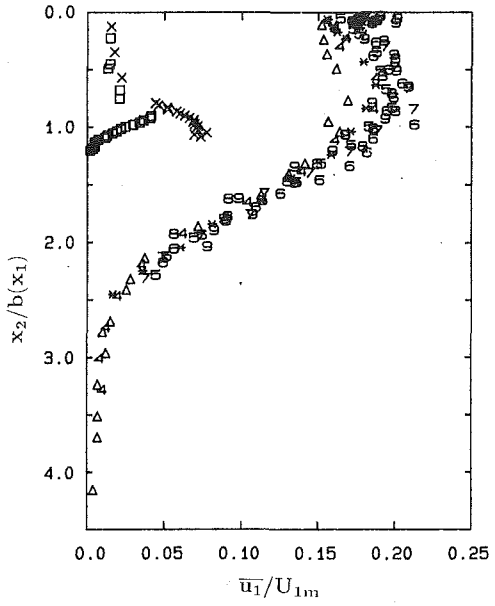

Fig. 5 Longitudinal RMS velocity normalized by mean velocity adjusted beyond $x_1/b_0 = 160$. Uncertainties: x_2/b: ±0.05; turbulence data: as in Fig. 4(*a*).

true for the shear stress in Fig. 4(*d*). Also the relative scatter in $\overline{u_2}$ and $\overline{u_1u_2}$ is smaller in a region near the free surface than in $\overline{u_1}$ or $\overline{u_3}$. This would indicate that the additional energy is not due to either long waves or the small wavelength randomly oriented waves created by the subsurface turbulence. Nor is it probable that probe noise is the cause since the identical probe was used in both orientations. While our data are certainly inconclusive on this point, we believe the additional energy in the x_1 and x_3 components of turbulence energy is most probably due to the existence of vertically oriented (at least very close to the surface) vortex tubes which intermittently contact the probe. The orientation of the instantaneous vorticity is the major structural characteristic which distinguishes the surface region of the surface jet from either the wall region of the wall jet or the symmetry plane of the free jet, the local vorticity field being one-dimensional, two-dimensional, or three-dimensional, respectively.

We observed during the course of our experiments these meandering structures whose signature at the free surface would be a local depression of perceptibly coherent and intense circulation. Dye injection during these experiments revealed the regular but low frequency production of spanwise oriented vortices originating at the jet lip. These vortex tubes may be the origin of coherent vertical structures at the free surface after a break-and-reconnect process similar to that discussed by Bernal and Kwon (1989). The vertical structures are also continuously produced in the channel side-wall boundary layers and may intermittently propagate into the measurement domain.

While this aspect of the free surface fluid dynamics has not been a major concern of the current study, the reconnection of random and coherent vorticity at a free surface is lately receiving increasing attention. Recent relevant studies include those of Madnia (1989) who experimentally investigated a submerged turbulent round jet flow issuing at various depths from the surface, and Leighton et al. (1991) who have performed a direct numerical simulation of low Reynolds number turbulent flow near a shear-free surface. Madnia reports flow visualization data which show that coherent vertically oriented vortex tubes are a frequent occurrence in the far field. In the calculation of Leighton, the turbulence was generated at the bottom wall of an open channel flow homogeneous in the x_1 and x_3 directions. Those results show that quasi-stable vortical structures are formed which originate in the buffer layer and are attached to the free surface. The downflow within these structures results in significant strain that moderates the viscous diffusion effects. Without nearby antiparallel image vorticity these structures do not dissipate quickly and contribute, out of proportion to the small area they occupy, to the energy balance averaged in the surface plane. Low frequency contact by the sensors with these slowly dissipating and nearly two-dimensional structures would explain the trends in Figs. 4(*a*) and 4(*c*).

The data of Figs. 4(*a–d*) illustrate the principal statistical characteristics that differentiate the surface jet from either the free jet or the wall jet. In the fully developed free jet there are clearly defined local minima in $\overline{u_1}$ and $\overline{u_3}$ in the symmetry plane since there is negligible turbulence production in the region. The vertical fluctuation, on the other hand, being closely correlated (negatively) with the static pressure distribution is found to be at a maximum in the symmetry plane. In the wall region of a wall jet, of course, all velocities approach zero. For the present case of a surface jet the distributions of the horizontal components appear to reach a local minimum near the surface but in a small region very near the surface there is a tendency for the horizontal components to increase in magnitude while at the same time the vertical component and the Reynolds shear stress rapidly approach zero. These behaviors are distinct from either of the classical jet configurations.

Anisotropy. In order to examine the anisotropy in the near surface region it is convenient to define an anisotropy tensor, $a_{ij} \equiv (\overline{u_iu_j} - 2q\delta_{ij}/3)/q$, where $q = (u_1^2 + u_2^2 + u_3^2)/2$ is the turbulent kinetic energy. The diagonal components of this tensor, as determined from the data, have been plotted in Fig. 6 for $x_1/b_0 \geq 20$. Far from the free surface the relative turbulence intensities are very low (Figs. 4(*a–c*)) and u_1^2 is the dominant contributor to the turbulent kinetic energy. As a result the streamwise anisotropy is near the positive limit of 4/3 while the vertical (note the shifted scale for a_{22}) and spanwise anisotropies are near the negative limit of $-2/3$. In the region above $x_2/b \sim 1.5$ there is a clear tendency for a_{33} and a_{11} to become equal. The vertical anisotropy, on the other hand, is very slowly varying and can well be approximated as constant, except for a thin region near the free surface. In this region there is a rapid (spatially) transfer of turbulent energy from the vertical component to the horizontal components.

The experimental data are incomplete for the purpose of constructing reliable energy balances for the u_i^2. Some of the processes (e.g., convection, viscous diffusion, production, and part of the turbulent transport) can be estimated from the data in Figs. 2–4 in conjunction with continuity considerations and assuming flow homogeneity in x_3. It is possible to obtain very crude estimates of the dissipation rates by resort to the frequency spectra for the various components but these estimates become progressively less valid as the free surface is approached. Since the processes of paramount importance near the free surface, pressure diffusion, pressure strain, and dissipation, can only be estimated by difference and cannot be separated from one another, energy balances are not included herein. It is clear, however, that the primary turbulence production for this flow, $-\overline{u_iu_k}\partial U_i/\partial x_k - \overline{u_ju_k}\partial U_j/\partial x_k$, is in the streamwise component. The production of u_2^2 is relatively much smaller, and for u_2^3 it is nominally zero. The major source for these components is the redistribution of energy from the streamwise component by pressure strain. In the absence of boundary influence one would expect energy transfer from u_1 into u_2 and u_3 at comparable rates. The lack of vertical development of the a_{22} component over a broad surface-influenced layer ($x_2/b < 1.5$) suggests that energy is blocked from the vertical component at the largest scales in the manner proposed by Hunt (1984). The narrower region near the free surface suggests that most of the vertical component of tur-

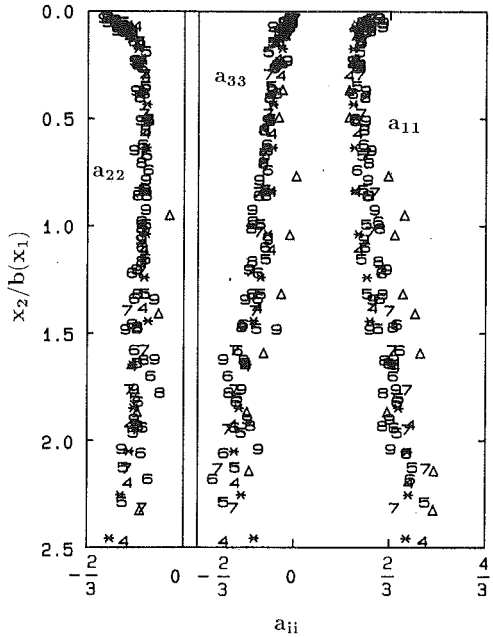

Fig. 6 Anisotropy distributions within the jet. Uncertainties: x_2/b: ±0.05; scatter in velocity components as shown in Fig. 4.

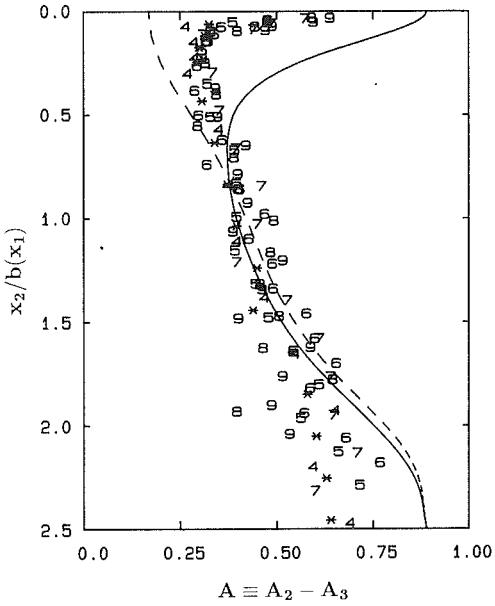

Fig. 7 Distribution of anisotropy tensor invariant factor $A = A_2 - A_3$; symbols: jet data; solid line: open channel simulation; dashed line: closed channel simulation

bulent kinetic energy approaching the surface from below is contained in eddies a fraction of the size of the local jet width. Most of the turbulence energy, of course, is in the horizontal components of the largest eddies.

Lumley (1978) has shown that the second ($A_2 \equiv a_{ij}a_{ji}$) and third ($A_3 \equiv a_{ij}a_{jk}a_{ki}$) invariants of the anisotropy tensor can be used to characterize the state of the turbulence. If one component of the velocity vanishes then the difference, $A \equiv A_2 - A_3$, becomes the constant value 8/9, irrespective of the distributions of the other two velocity components. The factor A, computed from the data, is shown in Fig. 7 where it is seen that this perspective of the data highlights the region of strong damping near the surface. For the purpose of comparing the anisotropy to that which would exist if the surface were not present, this figure also includes data from direct numerical simulations of turbulent open and closed channel flows (Swean et al., 1991). In the channel flow simulations the reference length, h, is the channel depth and half-height for open and closed flows, respectively. The difference in the numerical results at depths greater than $x_2/h \sim 0.5$ is primarily due to a difference in Reynolds numbers of approximately 10 percent and is not nearly as distinct, if plotted in wall (inner) variables. A comparison of the simulations indicates that a good quantitative measure of the domain of major influence of the free surface (near-surface layer) is given by the distance from the free surface such that $dA/dx_2 = 0$. For the jet data this region is apparently within $0.25b(x_1)$ of the free surface, a result that has obvious modeling consequences.

Spectra and Scales. In order to gain insight into the structure of the turbulence near to the free surface, estimates were obtained of the one-dimensional spectra along with the turbulent macroscales, L_i. Turbulent frequency spectrum estimates were computed from ensemble averages of FFT results for all blocks of time series data. Using Taylor's frozen turbulence hypothesis these spectral estimates were converted to wavenumber spectra ($k = 2\pi f/U_1$) using the local value of $U_1(x_2)$. The computed wavenumber function satisfies, $\int F_i(k)dk = \overline{u_i^2}$. The macroscale estimates were obtained by integrating the autocorrelation function, $L_i = U_1 \int R_{ii}(\tau)d\tau$ and L_i is thus a measure of the streamwise correlation length of u_i. Difficulties arose due to the autocorrelation curve oscillating about the t-axis at large values of time. In the data presented here the integrations were arbitrarily interrupted at the first zero crossing. As such the scale estimates derived from the process must be regarded as only being indicative of trends and not as quantitative. To assess the uncertainty in the scales several of the estimates were re-evaluated according to the process suggested by Nakagawa et al. (1975). In this procedure for example, $L_1 = (\pi/2\overline{u_1^2})F_1(k \to 0)$, and the Kármán interpolation formula, $F_1(k) = (2/\pi)\overline{u_1^2}L_1\{1 + (kL_1)^2\}^{-5/6}$, is used in the low wavenumber range to determine the scale which gave the best visual fit to the data. The scales determined in this manner retained the trends of those determined from the autocorrelation curves but differ in magnitude by as much as ±25 percent.

The scale estimates are shown in Figs. 8(*a–c*). The symbols, *a*, *b*, and *c*, used to plot the data points represent the distance below the surface of the measurements, and correspond to the depths 2.2, 5.8, and 7.6 mm, respectively. The jet half-width scale, $b(x_1)$, is included in the figures as the solid lines and the dashed lines represent the extent of the near-surface region, $x_2 = 0.25b(x_1)$, observed in Fig. 7. These data support the expected result that the scales are proportional to $b(x_1)$, with the L_2 and L_3 scales being of order $L_1/2$. The data show that $L_1 \sim 0.7b(x_1)$ but the scale deviates from the linear behavior beyond $x_1/b_0 = 160$, with a trend for the breakdown to occur nearer the origin as the depth of the measurement increases. This may indicate that the large-scale recirculation effects show up earlier in the turbulence than in the mean flow scale. The accelerated departure from linearity, however, is on the order of the uncertainty in the estimates and not so detectable in L_2 and L_3. There is the indication that proximity to the surface increases the L_1 and L_3 scales. Discounting the nonlinear region of the L_1 estimate the trend appears to be most significant in the L_3 evolution which is consistent with Hunt's (1984) theory. The vertical velocity scale is more clearly influenced by the free surface to the extent that much of the downstream development at depths *a* and *b* is suppressed and nearly uniform scale estimates are obtained. This is also in qualitative agreement with Hunt's theory. The L_2 values at these positions are on the order of the depth of the measurements. That this scale at depth *c* is approximately coincident with the line $0.25b(x_1)$ is remarkable, however, it should be remembered that all of the L_i values are estimates of the streamwise correlation lengths

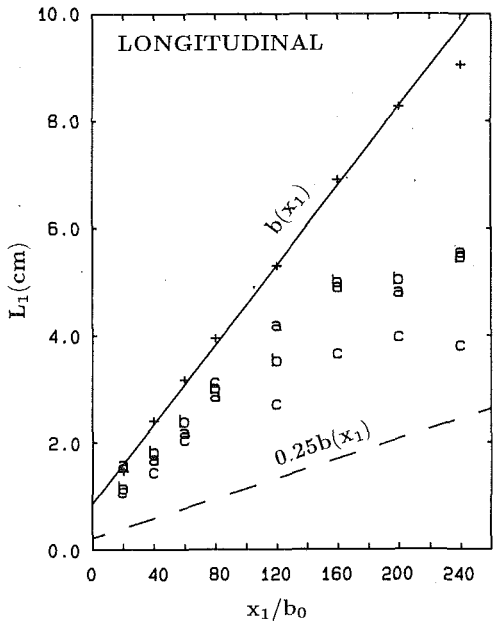

Fig. 8(a)

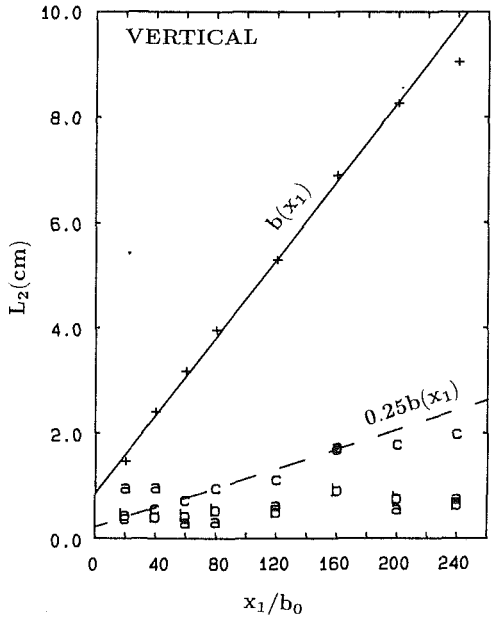

Fig. 8(b)

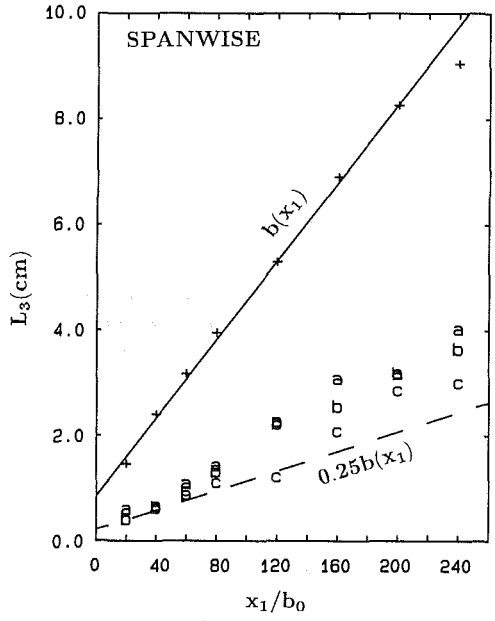

Fig. 8(c)

Fig. 8 Longitudinal variations of turbulent integral scale estimates. Uncertainties: $x_1/b_0 = \pm 0.1$; scale data: $\pm 25\%$; best estimates.

for the various components. The depth of point c, 7.6 mm, is about $0.1b(x_1)$ at large x_1/b_0 so the L_2 values are somewhat larger than the distance to the surface in this region.

Vertically spaced sequences of typical turbulence spectra are plotted in Figs. 9(a–b) representing the measuring stations at $x_1/b_0 = 40$ and $x_1/b_0 = 200$, respectively. Similar sequences of spectra for the remaining x_1/b_0 locations are contained in the report by Ramberg et al. (1989). The top four spectra in each stack correspond to the depths $x_2 = 2.2$, 4.0, 5.8, and 7.6 mm, respectively. The bottom spectrum in each stack is obtained at mid-depth locations closest to $x_2 = b(x_1)$ for comparison to the near-surface layer. Within each plot the symbols 1, 2, and 3 denote the three component directions. All of the spectra were integrated to insure that the total turbulent energy matched the earlier computations of $\overline{u_i^2}$.

The downstream development of the jet away from the surface is best illustrated by comparing the sequence beginning at the bottom spectra of each stack ($x_2 \sim b(x_1)$). For most of the higher wavenumber range, the three components of turbulent fluctuations are about the same in consequence of isotropy. As the jet develops downstream the spectra at depth evolve into the classical shape containing isotropic equilibrium and dissipation ranges with distinguishable and appropriate slopes in each range on the log-log plots. At the lowest wavenumbers the spectra exhibit anisotropy with greater energy in the longitudinal components as would be expected for this type of shear flow. The spectra of the vertical and lateral components are similar to each other at $x_2 \sim b(x_1)$ at all streamwise stations.

Within the upper layer of the fluid the following trends

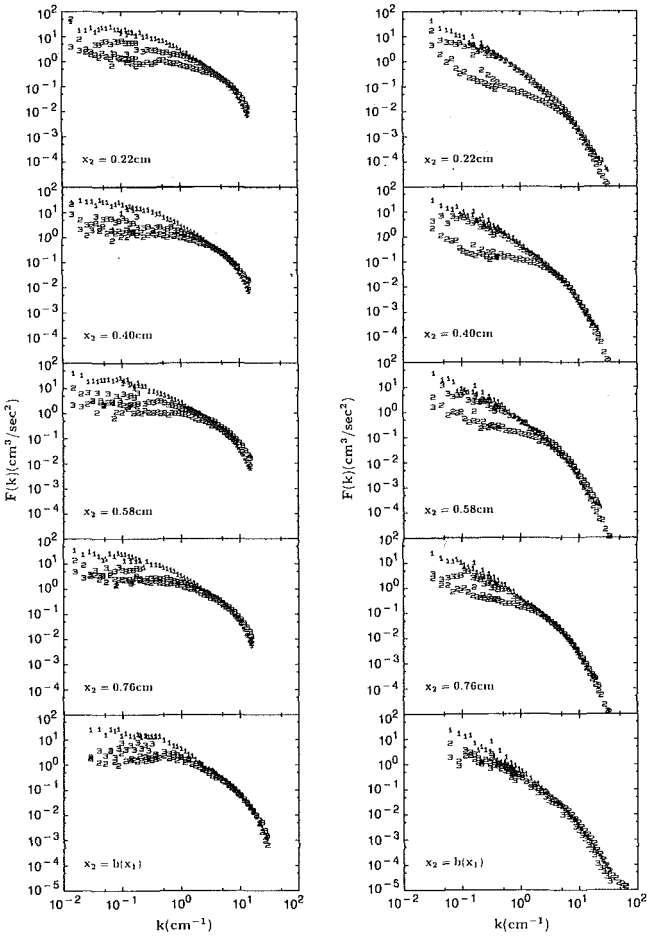

Fig. 9 Turbulent velocity fluctuation spectra. Uncertainties: x_2: 0.01 mm relative to local mean free surface level known to ±0.5 mm; integrals of spectra recover $\overline{u_i^2}$ to within 0.5 percent. (*a*) x_1/b_0 = 40; (*b*) x_1/b_0 = 200.

become apparent. As the jet develops downstream, a separation between the lateral and vertical spectra grows. More energy is found in the low wavenumbers of the lateral components, (symbol 3), at the expense of the vertical components, (symbol 2), as compared to the spectra at $x_2 \sim b(x_1)$. Eventually the lateral components approach the distribution of the longitudinal components. The longitudinal components appear relatively unaffected by surface proximity. This behavior is in qualitative agreement to the theoretical results of Hunt and Graham (1978) for the moving wall problem. However, that theory predicts a flat cutoff in the low wavenumber region $\overline{u_2}$ beginning at a wavenumber corresponding to the distance of the measurement from the interface. The u_2 spectra measured here are relatively flat at low wavenumbers if compared to the horizontal components but there is a trend for increasing energy in the vertical direction as wavenumber decreases. The cutoff wavenumber does appear to increase as the surface is approached in most of the vertical stacks, however, the variation in this wavenumber with distance from the surface does not match either the linear form or the magnitudes predicted by the theory. The most appropriate variation seems to be linear on these plots as they are displayed (e.g., Fig. 9(*a*)). Given that the wavenumber axis is logarithmic, these data do not support a linear variation with distance from the surface.

The additional energy in the vertical component above a flat spectral level cutoff for wavenumbers less than the cutoff could be attributable to the surface wave fluctuations. Very small wave amplitudes, on the order of those in the later stages of the jet, (~0.5 mm) could give rise to apparent turbulent fluctuations of the magnitudes observed here. These ought to be

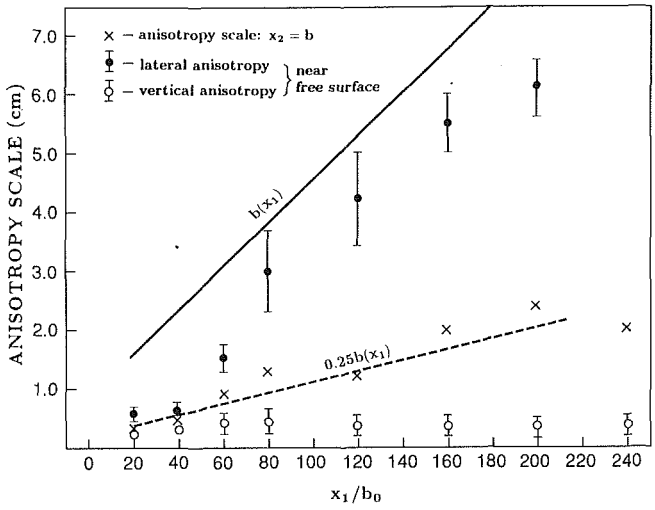

Fig. 10 Cutoff scales for isotropy in turbulent spectra. Uncertainties: x_1/b_0: ±0.1; vertical bars show ranges of values in interval 0.22 cm ≤ x_2 ≤ 0.76 cm.

greatly attentuated with depth in this range, however, and equally evident in each of the two horizontal components, assuming omnidirectional propagation of the waves. The proper depth attenuation is not evident in the data. Moreover, the magnitudes of the two horizontal components do not appear sufficiently larger than the $x_2 \sim b(x_1)$ distributions to contain an equal amount of wave fluctuation energy implied by the increase in the vertical component over a flat distribution. One must be careful to note the nearly order of magnitude difference between energy levels of the vertical fluctuations and the levels of the two horizontal components. It appears that the increase in $\overline{u_2}$ with decreasing wavenumber is a feature of the surface-influenced turbulent layer which is not captured by the moving wall theory. This may be a consequence of interactions between the intermediate turbulent scales near the surface which are not contained in the theory as noted by Hunt and Graham (1978).

The various scales (defined as $1/k$) at which anisotropy between components are observed from the spectra are plotted in Fig. 10. These data are derived directly from Figs. 9(*a–b*) and the additional data for $x_1/b_0 \leq 240$ contained in Ramberg et al. (1989). For reference, the scale corresponding to anisotropy at $x_2 \sim b(x_1)$ in the body of the jet is plotted as the crosses in the figure. This scale corresponds to the wavenumber where both the vertical and lateral components begin to diverge from the longitudinal component. This scale grows approximately linearly along the jet as one might expect for a shear flow of this nature. For reference the region defined by $x_2 = 0.25b(x_1)$ is shown as the dashed line and it is seen that the anisotropy scales far from the surface tend to lie below this line. The solid circles represent the average scale at which the longitudinal and lateral components begin to diverge under the influence of the free surface. The bars on each data point cover the range of values found in the measurements in the region $2.2 \leq x_2 \leq 7.6$. Note that this scale is $\sim 0.7b(x_1)$ and thus comparable to the L_1 estimates in Fig. 9(*a*). Clearly, the free surface has caused the two horizontal scales to become comparable at much larger scales (smaller wavenumbers) than in the body of the jet by an amount that grows with downstream distance. The free surface has rendered the horizontal turbulent motions nearly indistinguishable for all but perhaps the largest scales. The average scale corresponding to the cutoff wavenumber in the near-surface region for the vertical fluctuations is plotted as the open circles in the figure and the range of values is again indicated by the bars on each point. In this case the influence of the surface layer is to decrease the scale at

which the vertical component remains comparable to the other two. In other words, the free surface suppresses these fluctuations and therefore increases the difference. In conjunction with Figs. 6–7 the spectra and scales suggest that the vertical evolution of the turbulent structure is blocked within the jet at depths approaching 1–1.5 times the local mean flow scale, $b(x_1)$, or about twice the local streamwise integral scale, L_1. At large depths the longitudinal scales of the lateral and vertical velocities are comparable and about one-half of that for the streamwise velocity. As the free surface is approached from below, the growth of the u_2 integral scale is suppressed while the u_3 scale evolves unrestricted. In a narrow region near the free surface the u_2 scale is severely reduced while the u_3 scale becomes comparable to the u_1 scale. Since the at depth scales for u_3 and u_2 are comparable, this implies that the u_3 scale is amplified as much as the u_2 scale is reduced. This is consistent with the Hunt (1984) theory, which also predicts that the u_1 scale is unaffected by the interface. This is not inconsistent with visual inspection of the spectra, however, the crude scale estimates of Figs. 8 are inconclusive on this aspect.

Summary and Conclusions

The data indicate the existence of a thin region near the free surface in which the vertical velocity fluctuations are suppressed while the horizontal components are enhanced. The size of this region is on the order of 1/4 of the local jet width. In a larger surface-influenced layer of order 1–1.5 times the local jet width, the relative contribution of the vertical fluctuations to the turbulent kinetic energy is approximately constant and the primary net energy transfer among components is from the streamwise to the lateral. Estimates of the longitudinal integral scales of the various velocity components are consistent with the averaged velocity data in the sense that the horizontal velocity scales become comparable as the free surface is approached and the development of the vertical scale with distance from the jet origin is suppressed. These observations are in qualitative agreement with the theories of Hunt and Graham (1978) and Hunt (1984). The thickness of the surface-influenced layer appears to be of order 2 times the longitudinal integral scale rather than approximately equal in size as predicted by the theory. The vertical spectra near the surface tend to flatten in the low to moderate wavenumber range if viewed relative to the other spectra, however there remains a trend for increasing energy at wavenumbers which represent scales larger than the distance of the measurement point from the surface. This may be an indication of dynamics among the intermediate scales which are not accounted for by the theory. There are small but observable trends in the velocity data, particularly the horizontal components, and generally within one jet width of the free surface. Because of the particular characteristics of the trends, we do not consider it likely that these trends are induced by the typical irritants to this type of experiment, namely contamination, surface waves, and large-scale recirculation. Rather we speculate that it is more plausible the source is low-frequency contact with relatively coherent and slowly dissipating vertically oriented vortices. Additional multiple-point, nonintrusive measurements, coupled with conditional sampling techniques and simultaneous measurements of the surface waves, are necessary to further clarify the near surface dynamics.

Acknowledgments

This work was supported by the Naval Research Laboratory under the Fluid Dynamics Task Area. One author (SER) received support from the Office of Naval Research to complete this study. The contributions of Dave Andrews and Mary Barber in the execution of the experiments and reduction of the data are greatly appreciated. The authors are grateful to the referees for helpful suggestions.

References

Bernal, L. P., and Kwon, J. T., 1989, "Vortex Ring Dynamics at a Free Surface," *Physics of Fluids A*, Vol. 1, pp. 449–451.

Biringen, S., and Reynolds, W. C., 1981, "Large Eddy Simulations of the Shear Free Turbulent Boundary Layer," *Journal of Fluid Mechanics*, Vol. 103, pp. 53–63.

Brumley, B. H., and Jirka, G. H., 1987, "Near-Surface Turbulence in a Grid-Stirred Tank," *Journal of Fluid Mechanics*, Vol. 183, pp. 235–263.

Chu, V. H., and Baddour, R. E., 1984, "Turbulent Gravity Stratified Shear Flows," *Journal of Fluid Mechanics*, Vol. 138, pp. 353–370.

Hunt, J. C. R., 1984, "Turbulence Structure in Thermal Convection and Shear Free Boundary Layers," *Journal of Fluid Mechanics*, Vol. 138, pp. 161–184.

Hunt, J. C. R., 1984b, "Turbulence Structure and Turbulent Diffusion Near Gas-Liquid Interfaces," in *Gas Transfer at Air-Water Surfaces*, eds. W. Brutsaert and G. H. Jirka, D. Reidel Publishing Company.

Hunt, J. C. R., and Graham, J. M. R., 1978, "Free Stream Turbulence Near Plane Boundaries," *Journal of Fluid Mechanics*, Vol. 84, pp. 209–235.

Leighton, R. I., Swean, T. F., Jr., Handler, R. A., and Swearingen, J. D., 1991, "Interaction of Vorticity with a Free Surface in Turbulent Open Channel Flow," AIAA Paper No. 91-0236, 29th Aerospace Sciences Meeting.

Lumley, J. L., 1978, "Computational Modeling of Turbulent Flows," *Advances in Applied Mechanics*, Vol. 18, pp. 123–176.

Madnia, K., 1989, "Interaction of a Turbulent Round Jet with the Free Surface," Ph.D. thesis, The University of Michigan Program in Ship Hydrodynamics Technical Report No. 89-05, Ann Arbor, MI.

McDougall, T. J., 1979, "Measurements of Turbulence in a Zero Mean Shear Mixed Layer," *Journal of Fluid Mechanics*, Vol. 94, pp. 409–431.

Nakagawa, H., Nezu, I., and Ueda, H., 1975, "Turbulence of Open Channel Flow Over Smooth and Rough Beds," *Proceedings of Japan Society of Civil Engineers*, No. 241, pp. 155–168.

Rajaratnam, N., 1969, "Diffusion of a Supercritical Stream on a Stagnant Pool," *Transactions of the Engineering Institute of Canada*, Vol. 12, No. A-1.

Rajaratnam, N., and Humphries, J. A., 1984, "Turbulent Non-Buoyant Surface Jets," *Canadian Journal of Hydraulic Research*, Vol. 22, No. 2, pp. 103–114.

Ramberg, S. E., and Fung, Y. T., 1982, "A New Stratified Towing Channel at NRL," NRL Memorandum Report 4829, Naval Research Laboratory, Washington, D.C.

Ramberg, S. E., Swean, T. F., Jr., and Plesniak, M. W., 1989, "Turbulence in a Free Surface in a Plane Jet," NRL Memorandum Report 6367, Naval Research Laboratory, Washington, D.C.

Swean, T. F., Jr., Ramberg, S. E., Plesniak, M. W., and Stewart, M. B., 1989, "Turbulent Surface Jet in Channel of Limited Depth," *ASCE, Journal of Hydraulic Engineering*, Vol. 115, No. 12, pp. 1587–1606.

Swean, T. F., Jr., Leighton, R. I., Handler, R. A., and Swearingen, J. D., 1991, "Turbulence Modeling Near the Free Surface in an Open Channel Flow," AIAA Paper No. 91-0613, 29th Aerospace Sciences Meeting.

Thomas, S. M., and Hancock, P. E., 1977, "Grid Turbulence Near a Moving Wall," *Journal of Fluid Mechanics*, Vol. 83, pp. 481–496.

D. F. Elger
Assistant Professor.

E. T. McLam
Graduate Student.

S. J. Taylor
Graduate Student.

Mechanical Engineering Department,
University of Idaho,
Moscow, ID 83843

A New Way to Represent Jet Pump Performance

Researchers commonly represent jet pump performance with a Head-Ratio, Flow-Ratio curve (HR/FR curve). Our goals are to show that the HR/FR curve has several problems and to propose a new way to represent jet pump performance. Analysis shows that a HR/FR curve does not give enough information to predict the operating point of a system which includes a jet pump. Moreover, the way a HR/FR curve specifies data can force a designer to estimate head losses inside a jet pump and can make data acquisition very difficult. We propose using two curves to represent jet pump performance. Use of the two curves eliminates the problems of the HR/FR curve.

Introduction

Jet pumps are used to pump slurries, water from deep wells, water in nuclear reactors, and in other applications. The insets in Fig. 1 show the two most common jet pump geometries. A center-drive jet pump uses a high speed circular jet to entrain an annular suction flow. An annular-drive jet pump uses a high speed annular jet to entrain a central suction flow.

Figure 2 shows a system comprised of a jet pump, a centrifugal pump, and a piping network. We label this system a "pumping system." Figure 2 defines the subscripts used in this paper. Numerical subscripts refer to the location shown in Fig. 2, and letter subscripts s, j, and e reference the suction, jet and exit pipes, respectively.

As shown by reviews of jet pumps and ducted jets, there are over 400 technical papers related to jet pumps (Blevins, 1984; Bonnington and King, 1976). Every paper we are aware of presents jet pump performance with a curve, introduced by Gosline and O'Brien (1934), called a Head-Ratio, Flow Ratio curve (HR/FR curve). Figure 1 shows typical HR/FR curves for annular-drive and for center-drive jet pumps. A HR/FR curve gives the head ratio N as a function of the flow ratio M, where N and M are defined by

$$N=(H_{e4}-H_{s3})/(H_{j3}-H_{e4}), \tag{1}$$

and

$$M=Q_s/Q_j. \tag{2}$$

Q is fluid volume flow rate, and H the fluid total dynamic head is given by

$$H=P/\rho g+V^2/2g+z, \tag{3}$$

where P is fluid static pressure and V is average fluid velocity.

Our goals are to show that the HR/FR curve has several problems and to propose a new way to represent jet pump performance.

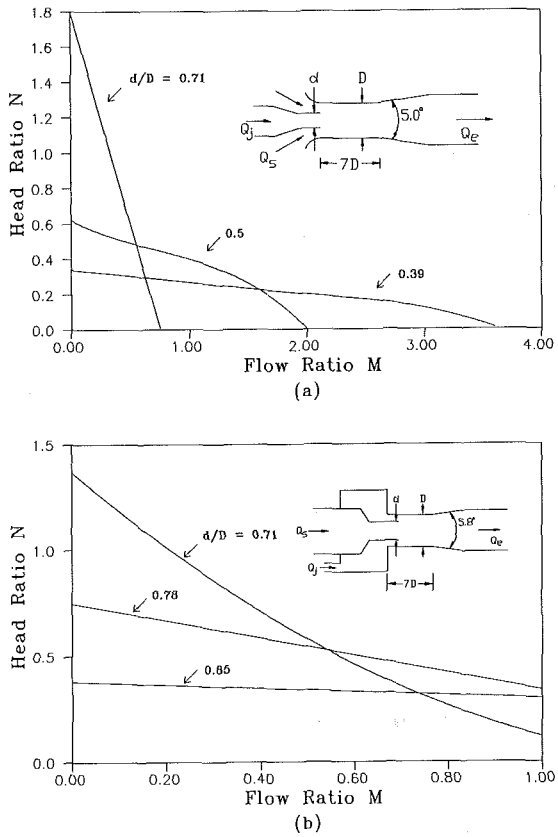

Fig. 1 HR/FR curves: (*a*) a center-drive jet pump; data from Silvester and Mueller (1968) and (*b*) an annular-drive jet pump; data from Shimizu et al. (1987)

Problems With the HR/FR Curve

We will first show that the HR/FR curve does not give enough information to characterize a jet-pump. Both dimensional analysis and modeling of a pumping system illustrate this point. Next we will show that the HR/FR curve specifies variables at inappropriate locations in a jet pump.

Contributed by the Fluids Engineering Division for publication in the JOURNAL OF FLUIDS ENGINEERING. Manuscript received by the Fluids Engineering Division September 25, 1990.

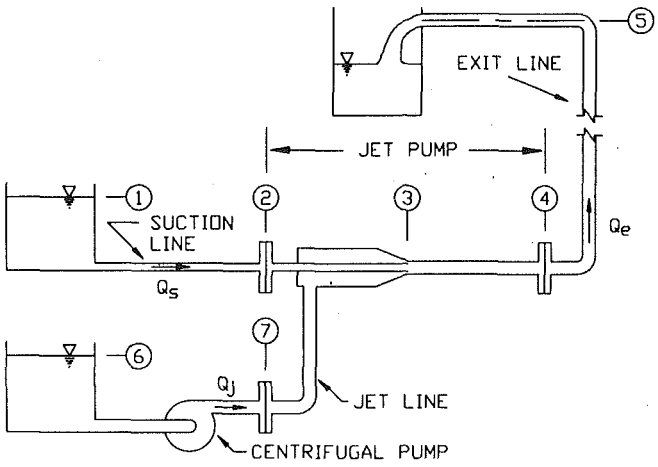

Fig. 2 A pumping system comprised of a jet pump, a centrifugal pump, and the associated piping network; the numbers define locations where variables are specified

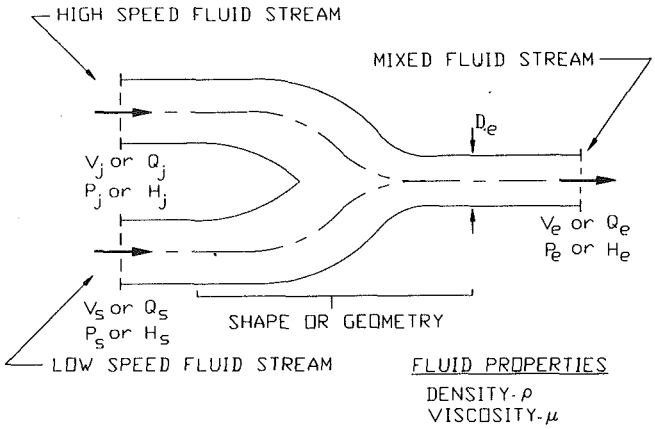

Fig. 3 A generic jet pump showing the independent and dependent variables which characterize the jet pump operating point

Dimensional Analysis. Dimensional analysis gives insight about the number of variables needed to quantify jet-pump performance. Figure 3 shows a jet pump in the simplest sense—a jet pump is any device which mixes high and low speed fluid streams to produce a combined fluid stream leaving the device. Assume (i) interior walls of the jet pump are smooth, (ii) a single fluid flows through the jet pump, (iii) elevations are known, (iv) cavitation does not occur, and (v) inlet fluid streams are fully developed.

Figure 3 shows the variables which define the operating point of the jet pump. Listing shape as a variable means the jet pump geometry is fixed. A shape and a fixed length scale D_e set all other jet pump dimensions. Listing two variables, for example P_j or H_j, means that either variable could be used, but not both of them. This occurs when the two variables are related by an equation, for example Eq. (4).

How many of the Fig. 3 variables can be selected before the operating point of the jet pump is fixed? One such selection is

$$\{(P_s-P_e) \text{ or } (H_s-H_e),\ (P_j-P_e) \text{ or } (H_j-H_e),\ V_e\} = f(\mu,\ \rho,\ V_s,\ V_j,\ D_e,\ \text{shape}), \quad (4)$$

where f indicates a functional relationship; the variables on the left side of Eq. (4) depend on the variables on the right side of Eq. (4). Since Eq. (4) has three dependent variables, three equations relate the dependent variables to the independent variables. One possible dimensionless form of the three equations is

$$\left(K_j \equiv \frac{(H_j-H_e)}{(V_e^2/2g)}\right) = f_1\left(\frac{Q_s}{Q_j},\ \mathrm{Re}=\frac{V_eD_e}{\nu},\ \text{shape}\right), \quad (5)$$

$$\left(K_s \equiv \frac{(H_s-H_e)}{(V_e^2/2g)}\right) = f_2\left(\frac{Q_s}{Q_j},\ \mathrm{Re}=\frac{V_eD_e}{\nu},\ \text{shape}\right), \quad (6)$$

$$\left(\frac{Q_e}{Q_s}\right) = f_3\left(\frac{Q_s}{Q_j},\ \mathrm{Re}=\frac{V_eD_e}{\nu},\ \text{shape}\right). \quad (7)$$

Equations (5) and (6) define the jet flow loss coefficient K_j and the suction flow loss coefficient K_s.

Equations (5) to (7) imply that a total of three equations are needed to characterize jet pump performance. Since continuity gives Eq. (7), we need two more equations to characterize a jet pump. The HR/FR curve, which has the form

$$\left(N=\frac{-K_s}{K_j}\right) = f\left(M=\frac{Q_s}{Q_j},\ \text{shape}\right), \quad (8)$$

gives only one equation, and so we are left one equation short.

Modeling of a Pumping System. Dimensional analysis showed that a HR/FR curve fails to give enough equations to characterize a jet pump. The result is that the operating point of a pumping system cannot be found. To illustrate this point, imagine a jet pump is being engineered into a pumping system, and the goal is to calculate all the flow rates and pressures in the system. Assume that (i) all pipe dimensions and elevations are known, (ii) the centrifugal pump has a known pump curve, (iii) the jet pump has a known HR/FR curve, (iv) the inlet heads H_1 and H_6 are known, and (v) the exit static pressure P_5 is known.

Conservation of mechanical energy between 1 and 3 in the suction pipe gives

$$H_1 = H_{s3} + HL_{13}, \quad (9)$$

Nomenclature

A = area = $\pi D^2/4$ (m^2)
D = diameter (m)
g = gravitational acceleration (m/s^2)
H = total head as defined in Eq. (3) (m)
HL = head loss (m)
K_j = jet flow loss coefficient as defined in Eq. (5) (dimensionless)
K_s = suction flow loss coefficient as defined in Eq. (6) (dimensionless)
L = length (m)
M = flow ratio = Q_s/Q_j (dimensionless)
N = head ratio as defined in Eq. (1) (dimensionless)
P = static pressure (Pa)
Q = volume flow rate (m^3/s)
V = average velocity = Q/A (m/s)
z = elevation (m)
μ = viscosity (kg m/s)
ν = kinematic viscosity (m^2/s)
ρ = density (kg/m^3)

Subscripts

e = exit pipe
j = jet pipe
s = suction pipe
1 to 6 = locations defined in Fig. 2

where HL_{13} is the head loss between 1 and 3. Summing head losses due to fluid friction and minor losses gives HL_{13}.

Conservation of mechanical energy between 6 and 3 in the jet pipe gives

$$H_6 + H_{cp} = H_{j3} + HL_{63}, \tag{10}$$

where H_{cp} is the head added by the centrifugal pump.

Conservation of mechanical energy between 4 and 5 in the exit pipe gives

$$H_4 = H_5 + HL_{45}. \tag{11}$$

The continuity equation across the jet pump gives

$$Q_e = Q_j + Q_s. \tag{12}$$

Finally the HR/FR curve gives

$$\frac{(H_{e4} - H_{s3})}{(H_{j3} - H_{e4})} = f\left(\frac{Q_s}{Q_j}\right). \tag{13}$$

Equations (9) to (13) form a system of five equations with six unknowns: Q_s or V_s, Q_j or V_j, Q_e or V_e, H_{s3} or P_{s3}, H_{j3} or P_{j3}, H_{e4} or P_4. Thus the system of equations does not have a unique solution; this means the operating point of the pumping system cannot be calculated without one additional equation. Thus, the jet pump should be characterized using two equations, not one as is done by the HR/FR curve. Some researchers have assumed $P_{j3} = P_{s3}$ to close the system of equations, but there are problems with this approximation; see Appendix A for more discussion.

Two Practical Problems With the HR/FR Curve. The common definition of head ratio causes two problems. While it is possible to avoid these problems by modifying the common definition (i.e., specifying variables at the bolt-in points of the jet pump—location 2, 7, and 4 in Fig. 2), this is not commonly done. In this section we describe the problems which occur when the common definition, Eq. (2), is used.

A HR/FR curve can force a designer to estimate head losses interior to a jet pump. Since the head ratio relates information between 3 and 4 in Fig. 2, a designer must estimate head losses between 2 and 3 and between 7 and 3. The complex geometries used in jet pumps can introduce high uncertainties into these estimates. Giving "bolt-in-data" which relates information between 2 and 4 and between 7 and 4 solves this problem.

Experimental determination of a HR/FR curve can require measurements at location 3; such measurements are extremely difficult. The velocity and pressure fields at 3 are not uniform in the radial direction. Thus, accurate head determination requires pointwise measurement of static pressure and velocity and integration of these variables over area 3. Also the precise direction of the fluid velocity is unknown. Thus fluid velocity should be measured with a transducer such as a pitch probe or a x-geometry hot-film probe. Alternatively, it is easy to measure heads at the bolt-in points 2, 4, and 7. Thus, using bolt-in data also makes experimental characterization of a jet pump much easier.

A Proposal—Two New Jet Pump Curves

We propose using two curves to represent jet pump performance. In equation form, the new jet pump curves are

$$\left(K_j \equiv \frac{(H_{j7} - H_{e4})}{(V_{e4}^2/2g)}\right) = f_1\left(\frac{Q_s}{Q_e}, \mathrm{Re} = \frac{V_{e4}D_{e4}}{\nu}, \text{shape}\right), \tag{14}$$

$$\left(K_s \equiv \frac{(H_{s2} - H_{e4})}{(V_{e4}^2/2g)}\right) = f_2\left(\frac{Q_s}{Q_e}, \mathrm{Re} = \frac{V_{e4}D_{e4}}{\nu}, \text{shape}\right). \tag{15}$$

In graphical form, the new jet pump curves are shown in Fig. 4.

The new jet pump curves show the jet flow loss coefficient K_j and the suction flow loss coefficient K_s plotted against the flow fraction Q_s/Q_e.

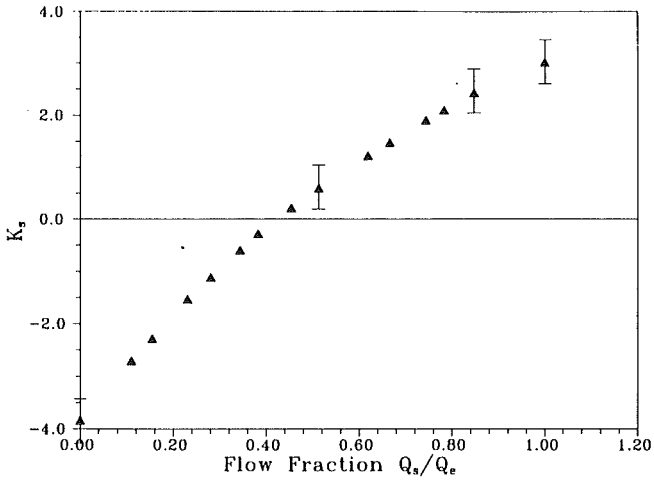

Fig. 4(*a*)

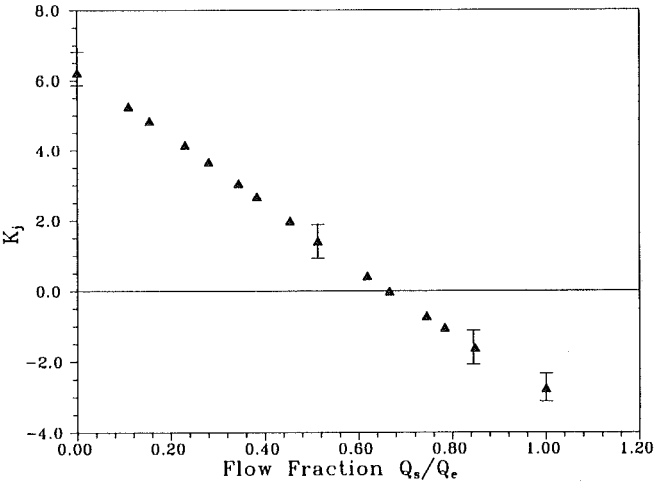

Fig. 4(*b*)

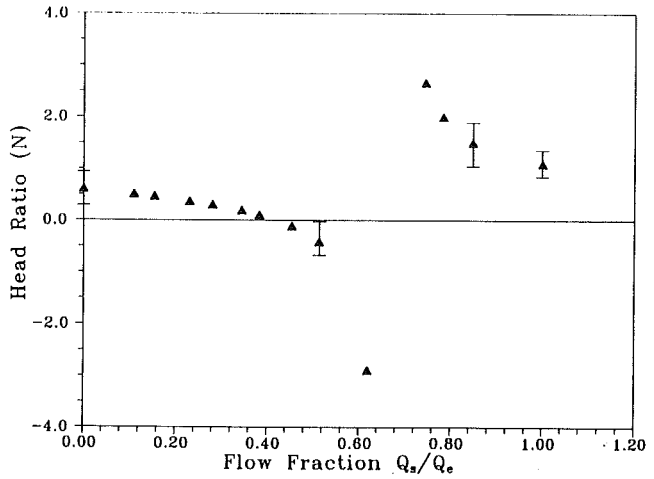

Fig. 4(*c*)

Fig. 4 Jet pumps curves for the jet pump shown in Fig. 5. (*a*) and (*b*) are the new jet pump curves; (*c*) is a head ratio curve; Reynolds number is 1.00×10^5; data from McLam (1990); error bars show estimated bias uncertainty; note that precision uncertainty is negligible compared to bias uncertainty

Each loss coefficient has a physical interpretation. The coefficient K_j when multiplied by $V_e^2/2g$ gives the total head lost by the jet fluid stream. Similarly, the coefficient K_s when mul-

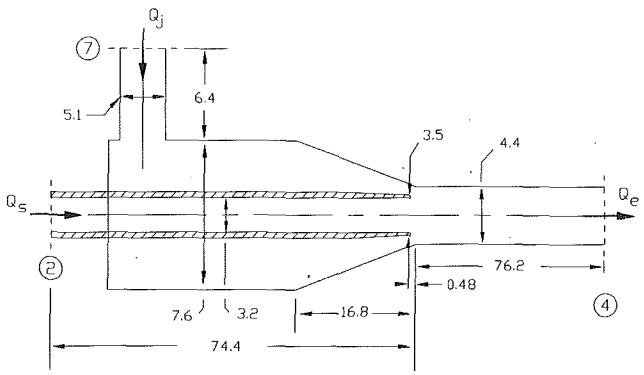

Fig. 5 Jet pump geometry for which the new jet pump curves shown in Fig. 4 apply; dimensions in centimeters

tiplied by $V_e^2/2g$ gives the total head lost by the suction fluid stream. Usually K_s is negative which means that the suction fluid stream gained head.

We recommend using the flow fraction Q_s/Q_e as the independent variable instead of the flow ratio Q_s/Q_j. This is because the flow ratio, which ranges from 0 to ∞, can compress results near low values of the flow ratio. The flow fraction, which ranges from 0 to 1, does not have this problem. Note that the flow ratio can be calculated from the flow fraction using conservation of mass.

Researchers should specify shape between the bolt-in points of the jet pump when presenting the new jet pump curves. Figure 5 shows the jet pump for which the pump curves in Fig. 4 apply.

Researchers should present Reynolds number information with any experimental jet pump curve. The performance of devices such as orifices, piping tees, and valves is independent of Reynolds number so long as the fluid flow is fully turbulent (i.e., at a high enough Reynolds number). While we expect a jet pump to have the same sort of Reynolds number independence, we do not know the Reynolds number required for fully turbulent flow. Until such a limit is established, Reynolds number information should be presented. Figure 4 was measured at a Reynolds number of 10,420.

Figure 4(*c*) shows head ratio calculated from the same data used to produce the new jet pump curves. Note the singularity in the HR/FR curve at $Q_s/Q_e \approx 0.7$. At this flow fraction, the jet pump switches from an annular-drive to a center-drive jet pump.

Discussion of the New Jet Pump Curve

The new jet pump curves solve the major problems with the HR/FR curve. Since two equations (or two curves) characterize jet pump performance, there is enough information for a pumping system model. Since the new jet pump curves specify variables at the bolt-in points of the jet pump, a designer to does not need to estimate head losses inside a jet pump. Moreover, this also eliminates a difficult measurement problem from experimental studies.

The new jet pump curves are consistent with existing fluid mechanics practice. In a generic sense, a wye or a tee in a piping network is a jet pump. This is because a wye or a tee combines a high and low speed fluid flow to produce a mixed fluid flow leaving the device. Thus we should characterize jet pumps, wyes and tees in the same way. The new jet pump curves do this. Piping wyes and tees are modeled using two loss coefficients with equations like (14) and (15) (Blevins, 1984; ASHRAE, 1989).

The new jet pump curves are similar to a HR/FR curve. Dividing Eq. (14) by Eq. (15) gives head ratio as a function of flow fraction. Flow ratio M is easily found from flow fraction using continuity. Thus results presented using the new jet pump curves can quickly be converted to a HR/FR curve. This may be important to researchers familiar with a HR/FR curve, and it also provides continuity with the existing literature. Similar to the HR/FR curve, the new jet pump curves can be developed using either experimental results or analytical results. Also, the effort to produce the information for the new jet pump curve is the same as the effort to produce the information for the HR/FR curve.

Finally, to be consistent with existing practice (wyes and tees), exit velocity V_e was used to nondimensionalize K_s and K_j. This choice may not always be the best, e.g., in a gas ejector, the jet can be sonic, and one may wish to select an inlet velocity for nondimensionalization.

Conclusions

Using a Head-Ratio, Flow-Ratio (HR/FR) curve to model jet pump performance introduces several problems. The first problem is that two equations are needed to characterize jet pump performance. The HR/FR curve gives only one equation, and the result is that we cannot calculate the operating point of a pumping system (a pumping system is jet pump, a centrifugal pump, piping, valves, etc. operating as a system). The second problem is that the locations in a jet pump where variables are given by a HR/FR curve are inappropriate. A pumping-system designer is forced to estimate head losses inside a jet pump. Moreover, experimental data acquisition is very difficult.

To represent jet pump performance, two equations (or curves) are proposed; Eqs. (14) and (15) define the equations, and Fig. 4 shows the equations in graphical form. The new jet pump curves eliminate the problems associated with a HR/FR curve by (i) using two equation (or curves) to characterize jet pump performance, and (ii) by specifying variables at the bolt-in points of the jet pump.

The new jet pump curves are consistent with conventional fluid mechanics practice in two important ways. First, giving the new jet pump curves gives enough information to find a HR/FR curve; this provides continuity with existing HR/FR curves in the literature. Moreover, the new jet pump curves are just as easy to produce as a HR/FR curve. Second, the new jet pump curves characterize a jet pump like a piping wye or tee is characterized. This makes sense because a jet pump is generically identical to a piping wye or tee.

APPENDIX A

Equating Suction and Jet Line Static Pressure

We have noticed that some researchers equate the suction line static pressure to the jet line static pressure, $P_{j3} = P_{s3}$ (Gosline and O'Brien, 1934; Reddy and Kar, 1968; Cunningham, 1957; Mussalli et al., 1978). There are two problems with this assumption.

First, jet flow can be injected into the mixing region of a jet pump at multiple locations. Figure A1 shows two examples of jet pumps from the patent literature which use multiple injection ports. Since there are multiple locations where the jet and suction flows mix, we could say $P_{j3} = P_{s3}$ only if static pressure in a jet pump mixing tube was uniform in the axial direction. However, experimental data by Taylor (1990) and by Razinsky and Brighton (1971) shows that pressure in the mixing tube often varies dramatically in the axial direction.

Second, experimental data show that the jet line and suction line static pressures are not equal. Two different jet pump apparatus were used to acquire this data. One apparatus was an air/air jet pump, and the other apparatus was a water/water jet pump. Both jet pumps had the shape shown in Fig. 5, except the suction line extended about 5 cm into the exit line. This shape was used to promote parallel flow prior to the

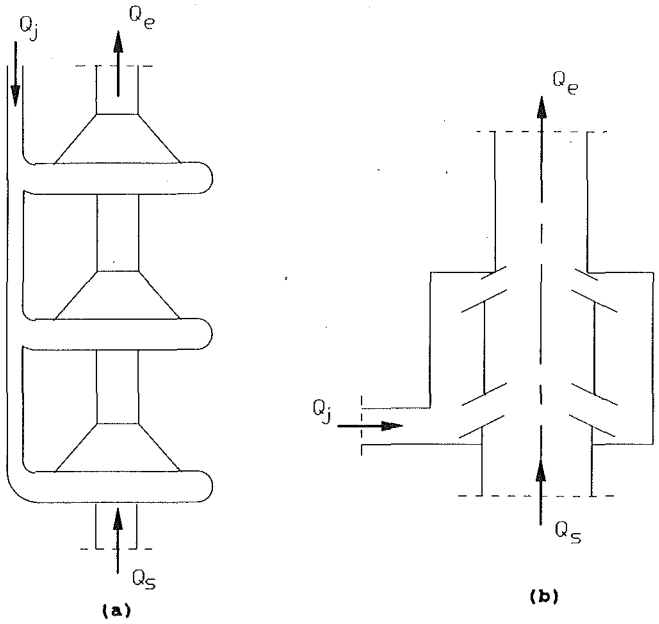

Fig. A1 Simplified sketches of two patented jet-pumps: (*a*) from U.S. Patent 3,857,651 (Bruno, 1974), and (*b*) from U.S. Patent 4,028,009 (Gudzenko et al., 1977)

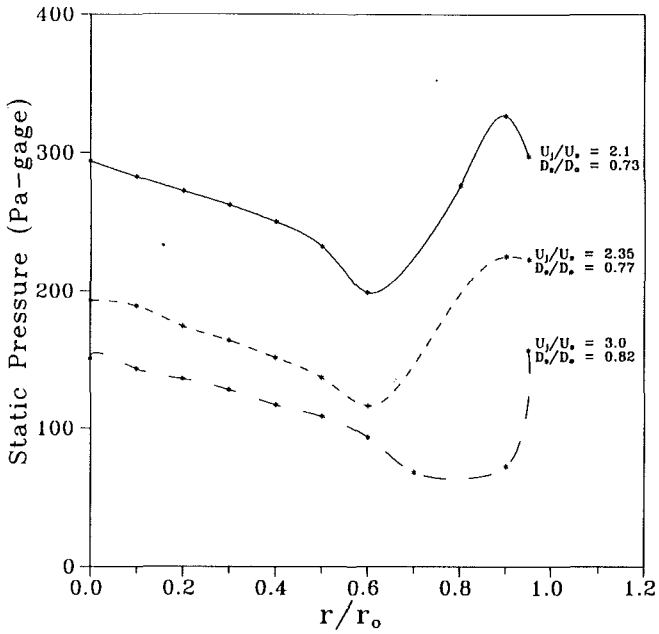

Fig. A2 Static pressure distribution across the entrance to the mixing region of a straight annular jet pump; D_s is the suction line inside diameter, D_0 is the exit line inside diameter; for clarity, lines connect the data points; data from Taylor (1990); estimated uncertainty is 35 Pa

entrance to the mixing region. In both experiments, the suction flow was fully developed and the jet flow was developing ($L/D \approx 10$). Flow straighteners were used in both the suction and jet pipes.

Figure A2 shows radial static pressure distributions measured across plane 3 in the air/air jet pump. The pressure data were measured with a pitch probe, and the velocity data were measured with a flow nozzle. The pitch probe, which looks similar to a pitot tube, has three impact pressure taps on the 0.38 by 0.13 cm tip and no static pressure tap. One pressure tap aligns with the axis of the pitch probe, and the other two taps are aligned at ± 45 deg to the probe axis, respectively. Rajaratnam and Muralidhar (1967) describe how to process the impact pressure data to give velocity magnitude and direction, and static pressure. Taylor (1990) gives the details of the experimental apparatus and measurement techniques. Figure A2 shows that the radial static pressure variation is of the order of 30 to 80 percent of the mean pressure.

Figure A3 compares the wall static pressure in the jet line P_{j3} to the wall static pressure in the suction line P_{s3}, as measured in the water/water jet pump. The pressure data were measured with a solid-state piezo-resistive transducer, and velocity data were measured with an orifice meter. The static pressure in the suction line was measured at plane 2 and then corrected for pressure drop between plane 2 and plane 3. McLam (1990) gives other details of the experimental apparatus and measurement techniques. Figure A3 shows that P_{j3} does not equal P_{s3} in an average sense.

Why have researchers set $P_{j3} = P_{s3}$? We speculate that this follows from the common practice used when a subsonic jet exits into a large reservoir. A jet exiting into a reservoir has no radial pressure gradient, and the pressure across the exit plane equals the reservoir pressure. The reason this is true is that the streamlines in the jet are straight and parallel, and hence cannot have a radial pressure gradient.

Because the flow field in a jet pump is unlike that of a jet exiting into a reservoir, $P_{j3} \neq P_{s3}$. In general, streamlines in a jet pump are curved, and hence the pressure and velocity fields are two or three dimensional. There are at least three causes of streamline curvature:

1. Many jet pumps have a geometry that inherently produces

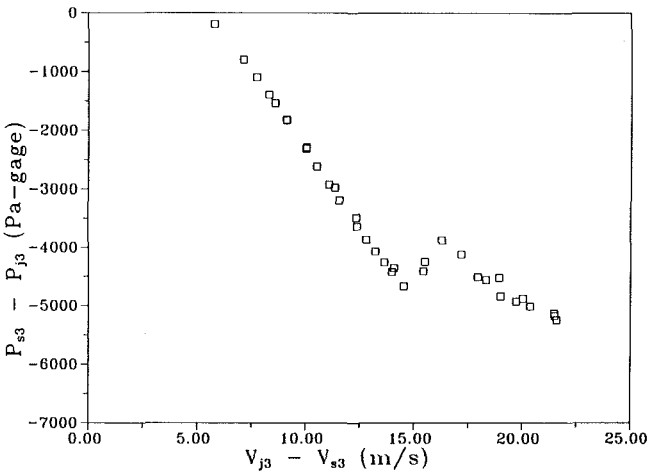

Fig. A3 The difference between the suction line wall static pressure P_{s3} and the jet line wall static pressure P_{j3} as a function of the difference between the jet line average velocity V_{j3} and the suction line average velocity V_{s3}; estimated bias uncertainty is 600 Pa; precision uncertainty is 50 Pa

curved streamlines. For example in a center-drive jet pump, the suction nozzle often forms a converging annular passage, and the jet pipe ends is an abrupt neckdown which is situated in the converging suction nozzle (Blevins, 1984). How could the streamlines be straight and parallel in such a geometry?

2. In a jet pump, the jet flow (and possibly the suction flow) is neither fully developed or uniform. When a velocity field is developing, even in a straight-wall pipe, the streamlines are curved and the velocity and pressure fields are two dimensional.

3. The velocity field in both the suction and jet pipes is influenced by the flow patterns in the jet pump mixing region. This is because the velocity field in any pipe is influenced by the exit boundary conditions.

For example, in a straight annular drive jet pump, there is often a large recirculation bubble in the center of the mixing

region (Taylor, 1990). This recirculation bubble can begin very close to plane 3. Fluid moving down the mixing region must flow around this recirculation zone. This is probably why the Fig. A2 data shows a two-dimensional pressure field across plane 3.

Acknowledgments

The financial support of the J. R. Simplot Company is gratefully acknowledged.

References

ASHRAE Handbook—1989 Fundamentals, American Society of Heating, Refrigerating and Air-Conditioning Engineers, Inc., Atlanta, pp. 32.7–32.9.

Blevins, Robert D., 1984, *Applied Fluid Dynamics Handbook*, Van Nostrand, New York, pp. 89–94, 257–262.

Bonnington, S. T., and King, A. L., 1976, *Jet Pumps and Ejectors, A State of the Art Review and Bibliography, 2nd Edition*, BHRA Fluid Engineering, Cranfield, Bedford, England.

Bruno, A. I., 1974, "Pump Units for Cyclonic Elevator," U.S. Patent 3,857,651.

Cunningham, R. G., 1957, "Jet Pump Theory and Performance with Fluids of High Viscosity," *Trans. ASME*, Vol. 79, pp. 1807–1820.

Gosline, J. E., and O'Brien, M. P., 1934, "The Water Jet Pump," Univ. California Publ. in Engr., Vol. 3, No. 3, pp. 167–190.

Gudzenko, N. V., Zaichenka, M. E., and Larin, L., 1977, "Jet Pump," U.S. Patent 4,028,009.

McLam, E. T., 1990, "The Engineering of an Annular Jet Pump System," M.S. thesis, University of Idaho.

Mussalli, Y., Larsen, J., and Hilke, J. L., 1978, "Performance Characteristics of Peripheral Type Jet Pumps," *Proceedings of the Joint Symposium on Design and Operation of Fluid Machinery*, Vol. II, pp. 123–131.

Rajaratnam, N., and Muralidhar, D., 1967, *Yaw and Pitch Probes*, Technical Report, Dept. of Civil Engr., University of Alberta, Edmonton.

Razinsky, E., and Brighton, J. A., 1971, "Confined Jet Mixing for Nonseparating Conditions," *ASME Journal of Basic Engineering*, Vol. 93, pp. 333–349.

Reddy, Y. R., and Kar, S., 1968, "Theory and Performance of Water Jet Pump," *Journal of the Hydraulics Division ASCE*, pp. 1261–1281.

Shimizu, Y., Nakamura, S., Kazuhara, S., and Kurata, S., 1987, "Studies of the Configuration and Performance of Annular Type Jet Pumps," ASME JOURNAL OF FLUIDS ENGINEERING, Vol. 109, pp. 205–212.

Silvester, R., and Mueller, N. H. G., 1968, "Design Data for the Liquid-Liquid Jet Pump," *J. Hydraulic Research*, Vol. 6, pp. 129–168.

Taylor, S. J., 1990, "Flow Patterns in the Mixing Region of Straight Annular-Drive Jet Pumps," M.S. thesis, University of Idaho.

Mean Flow Field and Reynolds Stress Behavior in Coannular Jet Flow With Swirl Along a Centerbody

M. O. Frey
Research Assistant.

F. B. Gessner
Professor.

Department of Mechanical Engineering,
University of Washington,
Seattle, WA 98195

An experimental study was conducted of an incompressible turbulent flow which exits from two concentric annular nozzles and develops along an unconfined centerbody. The operating Reynolds number based on centerbody diameter and the axial bulk velocity of the inner stream at the nozzle exit was 8×10^4. Swirl was imparted only to the inner stream, and the outer-to-inner stream mass flow rate ratio was fixed at unity. The results show that streamwise oscillations exist in the mean flow which apparently arise when vortices shed at the nozzle lip separating the two streams interact with the centerbody boundary layer. A comparison of Reynolds shear stress profiles with mean strain rates in the flow indicates that departures from local equilibrium exist in the mixing layer downstream of the nozzle exit. Local law-of-the-wall behavior is observed, however, near the centerbody surface. Analysis of the results shows that the use of conventional wall functions for the turbulence kinetic energy may not be appropriate for this flow situation, and that closure at the full Reynolds stress transport equation level is required for prediction purposes.

Introduction

This study is an experimental investigation of an incompressible, coannular jet flow which develops along an unconfined centerbody with swirl present in the inner stream. This particular flow situation simulates the essential features of a swirling turbofan engine flow which mixes with an axially directed bypass flow. The overall flow is characterized by turbulent mixing between the inner and outer streams in the presence of a turbulent boundary layer which develops along the centerbody. The overall flow can thus be expected to exhibit some of the characteristics of unconfined coaxial jet flows and of unconfined annular flows which develop along a stationary cylinder after swirl is introduced into the flow upstream. In the present study, the inclusion of a centerbody obviates the possible formation of a recirculation zone downstream of the nozzle exit, except when the overall flow is confined and the mass flow rate of the outer stream is below a certain level (Mattingly and Oates, 1986). Thus, local flow reversal is not observed in the present flow situation as it is in strongly swirling jet flows (Sislian and Cusworth, 1986; Dellenback, et al. 1988; Farokhi, et al., 1989), or in confined, coaxial swirling jet flows (Vu and Gouldin, 1982; Habib and Whitelaw, 1980; So and Ahmed, 1987).

Previous experimental studies of unconfined, coaxial jet flows without swirl have focused on conditions leading to self-preservation within the mixing layer (Champagne and Wygnanski, 1971; Durão and Whitelaw, 1973; Ko and Kwan, 1976). In more recent work, the influence of swirl in the outer stream on self-similar behavior has been investigated by Ribeiro and Whitelaw (1980). In that study, probability density distributions measured in the mixing layer indicated the presence of coherent structures within the flow. These coherent structures were the result of vortex shedding at the lip of the tube which separated the two streams. For coaxial jet flows which emanate from two concentric, thin-walled nozzles, the results of Ko and his co-workers show that a train of vortices is generated at the lip of each nozzle. These vortical flow structures have been observed when the ratio of outer-to-inner core flow velocity at the nozzle exit ($\lambda \equiv U_0/U_i$) is less than unity (Ko and Kwan, 1976; Ko and Lam, 1989) and also when this ratio is greater than unity (Ko and Au, 1985; Au and Ko, 1987). For $\lambda < 1$ (which simulates the operating conditions of the present study) the results of Ko and Kwan (1976) show that relatively high frequency vortices are generated in the inner mixing region and that lower frequency vortices exist in the outer region. Subsequent results presented by Kwan and Ko (1977) show that these vortices influence the covariance between the axial (u) and radial (v) velocity fluctuations to the extent that the $\overline{uv}$ correlation at points in the mixing layer is dominated by the vortical flow structure, rather than by mean strain rates in the flow. This behavior implies that departures from local equilibrium existed in their flow, and that similar departures can be anticipated in the present flow.

In reference to the region adjacent to the centerbody of the present flow configuration, the experimental results of Higuchi and Rubesin (1979) and Driver and Hebbar (1987) are relevant. In both studies measurements were made within a turbulent

Contributed by the Fluids Engineering Division for publication in the JOURNAL OF FLUIDS ENGINEERING. Manuscript received by the Fluids Engineering Division January 29, 1990.

boundary layer developing along a circular cylinder after it was subjected to a sudden transverse strain by means of a coaxial, rotating cylinder immediately upstream. For these operating conditions, the swirl component of velocity (W) in the outer region of the flow decays with increasing radial distance, so that radial gradients of angular momentum $[(1/r)\partial(rW)/\partial r]$ are negative in this region. This condition can lead to centrifugal instabilities in the flow, but the results of Higuchi and Rubesin (1979) and Driver and Hebbar (1987) show no outward signs of this effect. More recent experiments by Driver and Hebbar (1989) indicate, however, that the presence of swirl can have a destabilizing influence on the flow, as reflected by a change in length-scale behavior within the boundary layer and in higher streamwise velocities near the wall as a result of enhanced mixing and momentum transfer. In view of the above considerations, it can be anticipated that the flow field investigated in the present study will be sensitive to both vortex shedding and centrifugal instability effects.

In this paper, experimental results for coannular turbulent jet flow with swirl along a centerbody are presented which demonstrate mean flow field and Reynolds stress behavior downstream of the nozzle exit. Local skin friction coefficient distributions on the centerbody are also presented. The results are analyzed from the point of view of assessing the applicability of conventional turbulence models and wall functions to the present flow situation. Other results related to swirl angle behavior in the flow, turbulence kinetic energy production, component eddy viscosity behavior, Richardson number behavior, and lead-lag behavior of stress-mean strain rates are reported in a related paper (Frey and Gessner, 1990).

Experimental Apparatus and Procedure

Basic Flow Facility. The basic flow facility is the same as the one utilized by Mattingly and Oates (1986) in their coannular swirling flow experiments, except that their blow-down air supply system was replaced by a continuous flow, high pressure fan. Flow from the fan was split into two streams which entered a dual concentric plenum chamber fitted with honeycombs and screens. Swirl was imparted to the inner stream by means of twenty adjustable, airfoil-shaped (NACA-0024) blades mounted on a swirl generator inside the plenum, as shown in Fig. 1. The inner and outer streams exited from the plenum at atmospheric pressure and at a nominal temperature of 17°C (72°F) through two concentric annular nozzles. The streams were separated by a thin-walled aluminum tube with

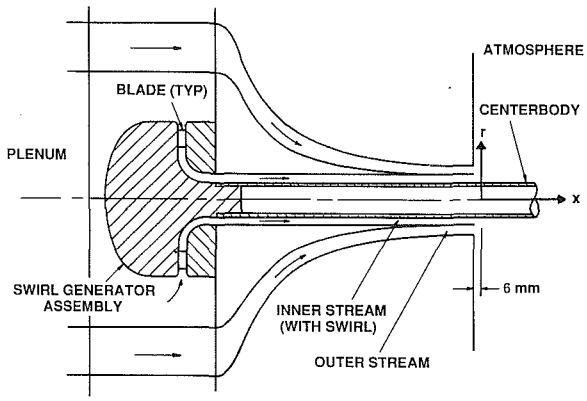

Fig. 1 Physical flow configuration and coordinate system

a lip thickness of 1.2 mm (0.048 in.) at the nozzle exit. The radial widths of the inner and outer streams at the nozzle exit were 25.4 mm (1.000 in.) and 23.3 mm (0.981 in.), respectively. The axial bulk velocity of the inner stream at the first station where data were taken (at $x/D = 0$, which is 6 mm downstream of the nozzle exit, as shown in Fig. 1) was maintained constant at $U_{b,i} = 11.7$ mps (38.4 fps). The outer-to-inner stream mass flow rate ratio at this location was fixed at unity ($\dot{m}_0/\dot{m}_i = 1$). The swirl angle of the inner stream at $x/D = 0$ was nominally uniform across the width of the nozzle (approximately 35 deg), corresponding to a swirl number of 0.52 for the inner stream. The aluminum centerbody had a polished surface, an outside diameter of 101.6 mm (4.000 in.), and extended both upstream and downstream of the nozzle exit, as shown in Fig. 1.

All measurements in the flow were made by means of forward-facing probes mounted on an arm whose pivot point coincided with the sensor location, as shown in Fig. 2. This arm was pivoted relative to a horizontal plate mounted on guide rails parallel to the centerbody. By moving the horizontal plate in the axial direction, data could be taken at various x/D locations. The horizontal plate was located approximately 2.2 centerbody diameters above the centerbody surface, which was well beyond the shear layer thickness at the last station where data were taken ($x/D = 6$). Probes were translated in the vertical direction by means of an electrically-activated position transducer (Lockheed Electronics Model WR8-1132/15B). Positions relative to the centerbody surface could be set to within an estimated accuracy of ±0.05 mm (±0.002 in.).

Nomenclature

C = empirical constant, $C = 5.2$
C_{fx} = streamwise skin friction coefficient, $C_{fx} = \tau_{wx}/(1/2)\rho U_{b,i}^2$
$C_{f\theta}$ = circumferential skin friction coefficient, $C_{f\theta} = \tau_{w\theta}/(1/2)\rho U_{b,i}^2$
C_p = static pressure coefficient, $C_p = (P - P_a)/(1/2)\rho U_{b,i}^2$
C_{pw} = wall pressure coefficient, $C_{pw} = (P_w - P_a)/(1/2)\rho U_{b,i}^2$
C_μ = empirical coefficient, $C_\mu = 0.09$
D = centerbody diameter
k = turbulence kinetic energy
$\dot{m}_i$ = inner mass flow rate
$\dot{m}_0$ = outer mass flow rate
P = static pressure
P_a = atmospheric pressure
P_w = wall static pressure
R = centerbody radius
x, r, θ = cylindrical coordinates, Fig. 1
y = wall coordinate
u, v, w = velocity fluctuations in the x, r, θ directions, respectively
$\overline{u^2}, \overline{v^2}, \overline{w^2}$ = Reynolds normal stress components
$\overline{uv}, \overline{uw}, \overline{vw}$ = Reynolds shear stress components
U, V, W = mean velocity components in the x, r, θ directions, respectively
$U_{b,i}$ = bulk velocity of inner stream
U_i = core flow velocity of inner stream
U_0 = core flow velocity of outer stream
U_β = mean velocity component in yaw plane, $U_\beta = (U^2 + W^2)^{1/2}$
U_τ = friction velocity, $U_\tau = (\tau_w/\rho)^{1/2}$
β = yaw angle, $\beta = \tan^{-1}(W/U)$
ϵ = dissipation rate of turbulence kinetic energy
κ = von Karman's constant, $\kappa = 0.41$
λ = core flow velocity ratio, $\lambda = U_0/U_i$
ν = kinematic viscosity
ν_t = kinematic eddy viscosity
ρ = fluid density
τ_w = wall shear stress

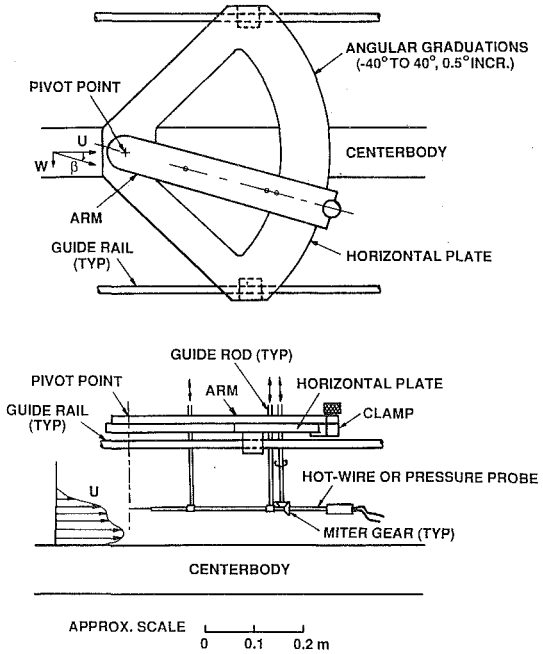

Fig. 2 Traversing mechanism and probe orientation

Pressure Probe Instrumentation. Three custom-made pressure probes, consisting of a pitot-static tube (OD = 1.5 mm or 0.062 in.), a total pressure probe (OD = 0.7 mm or 0.028 in.), and a Conrad (yaw angle) probe (OD = 0.6 mm or 0.024 in. with an apex angle of 75°) were constructed for use in this study. The static pressure on the centerbody surface was sampled by means of 0.5 mm (0.020 in.) diameter wall taps connected to a Type J, 48-port Scanivalve. All static, total, and differential pressures were measured by means of a Datametrics Type 590D-10W-2P8-V1X-4D Barocel pressure transducer operating in conjunction with a Datametrics Type 1400 electronic manometer. Initial data were taken at six streamwise stations (x/D = 0, 0.5, 1.5, 3, 4.5, and 6) with the Conrad probe operated in the nulling mode in order to determine the radial variation of yaw angle $\beta = \tan^{-1}(W/U)$, defined as shown in Fig. 2. Subsequent data were taken with the pitot-static and total-pressure probes aligned sequentially with the local mean flow direction in the yaw plane at each measuring point in order to determine the local static pressure (P), and the magnitude of the mean velocity component in this plane [$U_\beta \equiv (U^2 + W^2)^{1/2}$]. This procedure for determining P, U, and W presumes that the radial mean velocity component (V) is small in comparison to U_β, a condition later verified by the hot-wire measurements.

Local wall shear stress measurements were made by means of three different-diameter Preston tubes (OD = 0.7, 1.6, and 3 mm or 0.028, 0.065, and 0.120 in.) resting on the centerbody surface and aligned with the local mean flow direction at each streamwise location. For these measurements, the local flow angle across the height of the largest-diameter Preston tube varied by less than 2 deg, as determined by comparing yaw angles measured near the centerbody with streamline patterns on the centerbody surface made visible by an oil-fluorescent dye coating. The Preston tube data were reduced by means of tabulated calibration data presented by Head and Vasanta Ram (1971). This method of evaluating wall shear stress presumes that the two-dimensional form of the law-of-the-wall is valid when written in terms of the total mean velocity and a friction velocity based on the total wall shear stress. The present results justify this approach, as will be demonstrated shortly.

Hot-Wire Instrumentation. The hot-wire results reported in this paper are based on the single-wire probe rotation technique developed by Al-Beirutty and Gessner (1989) for moderate intensity flows. This technique is based on the sequential use of normal and slant-wire probes. The prongs of these probes were similar in design to configurations recommended by Comte-Bellot et al. (1971) for minimizing aerodynamic interference effects in the flow. The distance between prong tips (approximately 4 mm or 0.16 in.) was spanned by 4μ (0.00015 in.) diameter platinum-plated tungsten wire having a centered active length of approximately 1 mm or 0.040 in. The probes were energized by means of a TSI Model 1010 constant temperature anemometer operating in conjunction with a DISA Type 55M25 linearizer. The mean output voltage was read on a DISA Type 55D31 digital voltmeter, and the mean square of the fluctuating voltage was read on a second DISA Type 55D31 digital voltmeter connected to a TSI Model 1060 rms voltmeter.

The slant-wire probe was initially calibrated in fully-developed turbulent pipe flow in order to prescribe a value (0.2) for the yaw sensitivity factor (k) in the hot-wire response equations. The pitch sensitivity factor (h) was specified as 0.9 on the basis of calibration data obtained by Arterberry (1982). Both normal and slant-wire probes were calibrated on-site in the core region of the axially-directed outer stream. The calibrations were performed before and after each run and at time intervals of 3 to 4 hours for the longer runs. If the mean voltage at a fixed reference point in the flow differed by more than 1.0 percent over successive calibrations, then the data obtained between calibrations were discarded, a new wire was mounted, and repeat data were taken.

Initial hot-wire data were taken with the slant-wire probe with the probe body aligned with the local mean flow direction in the yaw plane, as determined from the Conrad probe measurements. The probe body was rotated about its axis by means of the miter gear assembly shown in Fig. 2 to eight angular positions 45 deg apart, and both mean and mean-square fluctuating voltage data were recorded. The rotational sequence was 0, 180 deg (in the xr plane) 90, 270 deg (in the $x\theta$ plane) and 45, 135, 225, and 315 deg to minimize wire drift effects on the results. The 0 deg reference position was set with the aid of a K&E surveyor's transit. Subsequent data were taken with the normal wire probe by aligning the probe body with the local mean flow direction in the yaw plane and positioning the wire in the xr plane. The normal and slant-wire data were analyzed by means of the data reduction technique described by Al-Beirutty and Gessner (1989). This method of data reduction is second-order accurate relative to the turbulence fluctuations, a feature which enhances measurement accuracy in moderate intensity flows. The overall technique requires an interative method of solution in order to solve for the three mean velocity components and the six Reynolds stress components. A coordinate axis transformation was applied to convert the results (which are referred to a coordinate system aligned with the yawed probe body) to $xr\theta$ coordinates aligned with the centerbody, as shown in Fig. 1.

Uncertainty Estimates. Static pressure measurements with the pitot-static tube were influenced by relatively high turbulence intensities in the outer region of the flow (a point which will be addressed in more detail shortly). As a result, the estimated uncertainty in the measured static pressure coefficient (C_p) increases from approximately ± 0.05 in the vicinity of the centerbody surface to ± 0.1 in the outer region of the flow. In contrast, C_p values calculated by integration of the radial direction momentum equation are estimated to be accurate to within ± 0.03 over the width of the shear layer where results are reported ($1 \leq r/R \leq 2.5$). C_p values on the centerbody surface based on wall tap readings are accurate to within ± 0.002. The uncertainty in pressure-probe-based, normalized velocity components $U/U_{b,i}$ and $W/U_{b,i}$ is estimated to increase from ± 0.05 in the vicinity of the centerbody to ± 0.1 in the outer region of the flow. Streamwise and circum-

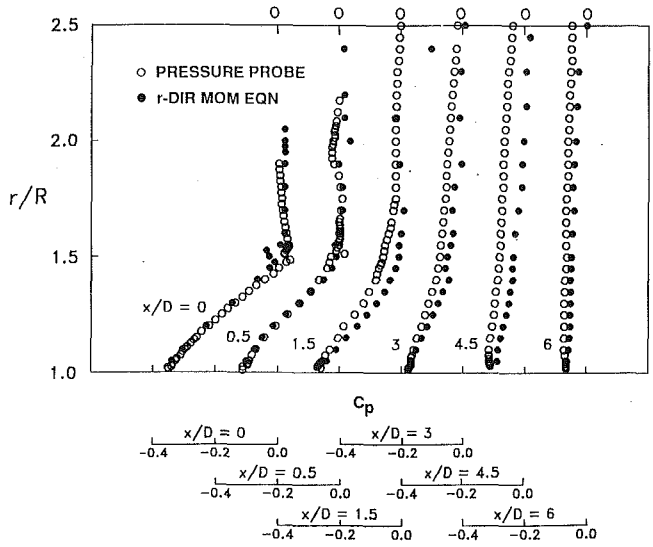

Fig. 3 Static pressure coefficient distributions

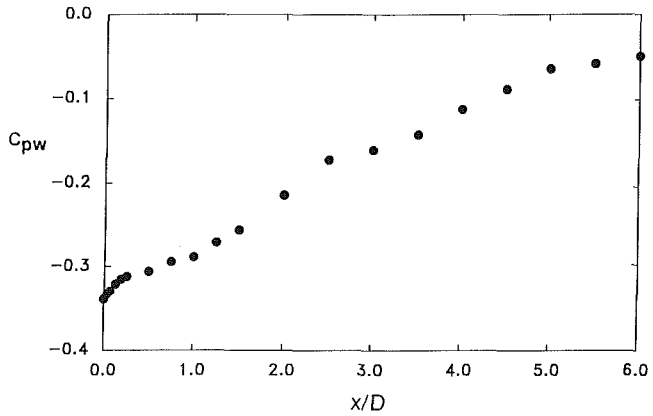

Fig. 4 Wall static pressure coefficient distribution

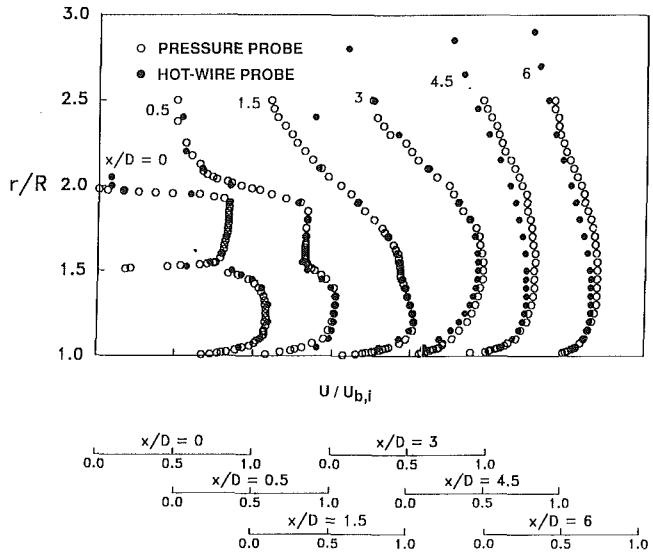

Fig. 5(a) Axial component

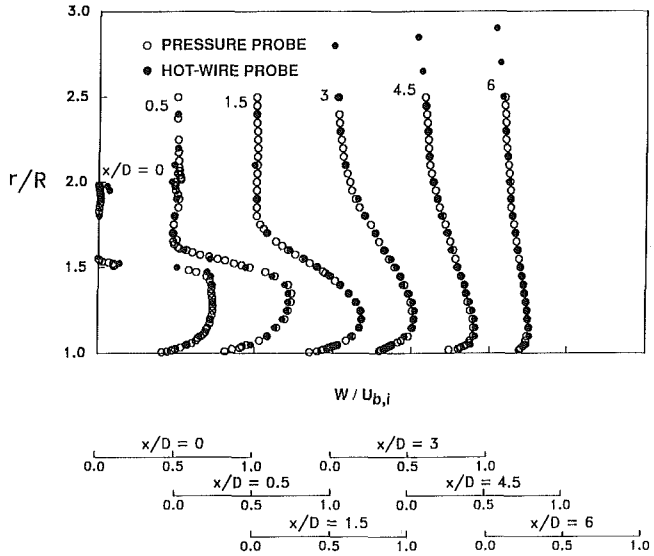

Fig. 5(b) Circumferential component

Fig. 5 Mean velocity component profiles

ferential skin friction coefficient values (C_{fx} and $C_{f\theta}$, respectively) are accurate to within ± 0.0002.

The uncertainties in hot-wire based results were estimated from an error analysis presented by Al-Beirutty (1987). In that analysis the effects of uncertainties in the slant-wire angle α, pitch and yaw sensitivity factors h and k, normal and slant-wire calibration intercept values $E_{0,n}$ and $E_{0,s}$, slant-wire calibration slope B_c, and measured normal and slant-wire voltages $\overline{E_n}$, $\overline{E_s}$, $\overline{e_n^2}$, $\overline{e_s^2}$ are taken into account. In the present study, hot-wire based distributions were truncated at a radial position where the local turbulence intensity began to exceed 60 percent. This was done to eliminate data in regions of the flow where local flow reversal effects induce rectification errors in the results.

If the above considerations are applied to the present results, then the uncertainties in hot-wire based values of $U/U_{b,i}$, $V/U_{b,i}$, and $W/U_{b,i}$ in the inner region of the flow near the centerbody surface, namely ± 0.01, ± 0.02, and ± 0.02, respectively, approximately double at a radial location where the turbulence intensity is 60 percent. There is a corresponding three-fold increase in the uncertainties of the Reynolds normal stress components $\overline{u^2}/U_{b,i}^2$, $\overline{v^2}/U_{b,i}^2$, and $\overline{w^2}/U_{b,i}^2$, whose uncertainty levels near the centerbody surface are ± 0.002, ± 0.004, and ± 0.004, respectively. There is also an approximate doubling of the uncertainties of the Reynolds shear stress components $\overline{uv}/U_{b,i}^2$, $\overline{uw}/U_{b,i}^2$, and $\overline{vw}/U_{b,i}^2$, whose uncertainty levels in the vicinity of the centerbody are ± 0.003, ± 0.003, and ± 0.005, respectively. The above estimates appear to be conservative, inasmuch as repeat hot-wire data taken at several streamwise locations, when compared with original data, were always bounded by the above estimates.

Results and Discussion

Mean Flow Results. Static pressure coefficient distributions measured at six streamwise stations are shown in Fig. 3. The open symbols in this figure denote results based on measurements with the pitot-static tube nominally aligned in the yaw plane at each radial position. The solid symbols denote values based on radial integration of the r-direction momentum equation, starting the calculations at the centerbody surface ($r/R = 1$) with the measured wall static pressure. In the initial mixing region ($x/D = 0$ and 0.5) Fig. 3 shows that there is generally good agreement between corresponding values, noting that the local static pressure in the inner swirling stream is below atmospheric pressure (C_p negative) as a result of streamline curvature effects. These effects diminish in the downstream region, so that the near-wall flow is subjected to an adverse pressure gradient, as indicated by the wall pressure coefficient distribution shown in Fig. 4. In the downstream region (e.g., at $x/D = 4.5$ and 6), Fig. 3 shows that pressure-probe based C_p values are consistently negative in the outer

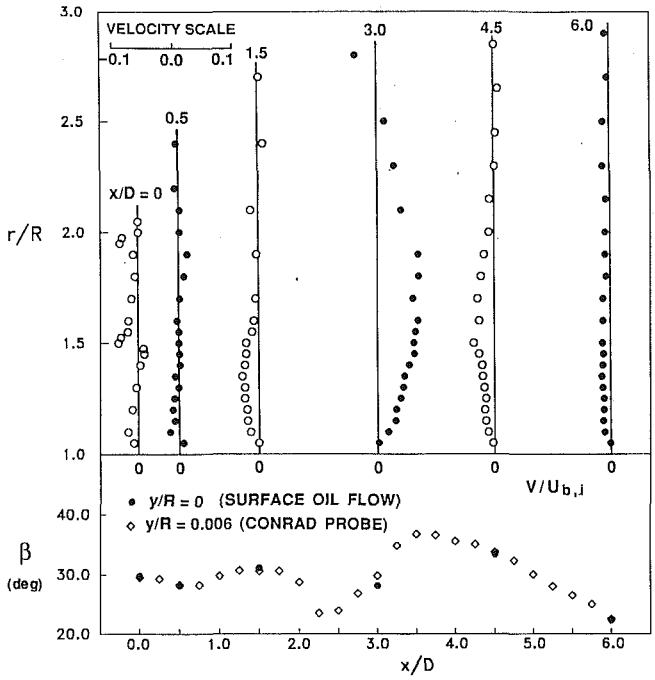

Fig. 6 Radial mean velocity component profiles and surface flow angle distribution

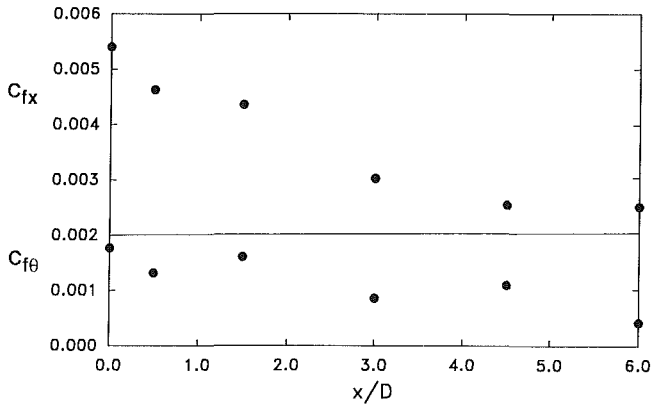

Fig. 7 Skin friction coefficient distributions

region of the flow, whereas values based on integration from the wall approach the correct limiting value of zero. This behavior implies that static pressure values measured with the pitot-static tube are too low in this region, probably because of the relatively high turbulence levels in this region, and that values based on integration from the wall (i.e., the solid symbols) depict more accurate behavior.

If the local static pressure is underestimated when measured by means of a pitot-static tube, one would anticipate the local mean velocity values based on the difference between total pressure probe data (assumed correct) and pitot-static data would be overestimated. This behavior can be seen to some extent in Fig. 5(*a*) specifically at $x/D = 4.5$ and 6, where U component values based on pressure probe measurements slightly exceed their counterparts measured by means of the hot-wire technique. At other streamwise locations (e.g., at $x/D = 0$, 0.5, 1.5, and 3), there is generally good agreement between U component values measured by means of both techniques. This is especially true at all streamwise locations for the W component, where both techniques yield results that agree very well (refer to Fig. 5(*b*)).

Although the results in Figs. 3–5 do not show outward manifestations of coherent structures in the flow, other mean-flow results indicate that they are present. Figure 6 shows radial velocity component profiles measured at the six streamwise

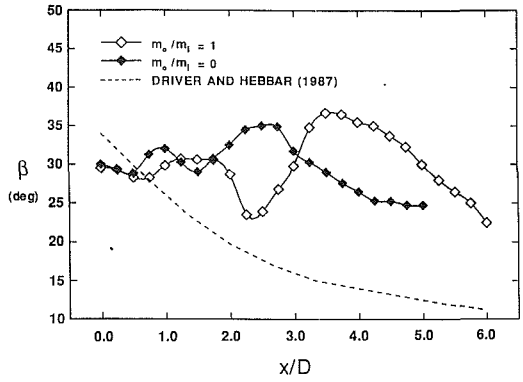

Fig. 8 Surface flow angle distributions with and without an outer stream present

stations (upper portion) and the variation of the mean swirl angle ($\beta \equiv \tan^{-1} W/U$) with streamwise position measured on and near the centerbody surface (lower portion). From the figure it can be seen that the radial velocity component is negative at $x/D = 1.5$, and then becomes positive at $x/D = 3$ before becoming negative again at $x/D = 4.5$. This pattern was confirmed through repeat measurements and is indicative of a mean streamline pattern which undulates around the centerbody as the flow proceeds downstream. Associated with this behavior are undulations in the mean swirl angle on and near the centerbody surface, as shown in the lower portion of Fig. 6, which lead to corresponding undulations in the circumferential skin friction coefficient ($C_{f\theta}$) distribution (refer to Fig. 7).

In order to seek an explanation for this behavior, the outer stream was turned off ($\dot{m}_0/\dot{m}_i = 0$), $U_{b,i}$ was reset to its original value, and flow angle (Conrad probe) data were repeated in the immediate vicinity of the cylinder surface. The results are shown in Fig. 8, and indicate that more rapid (higher frequency) oscillations in surface flow angle occur when $\dot{m}_0/\dot{m}_i = 0$. For this operating condition, more rapid vortex shedding occurs at the nozzle lip separating the inner and outer streams because mean shear rates in the outer region of the inner stream near the nozzle exit are increased when the outer stream is turned off. The interaction of vortices shed at the nozzle lip with the centerbody boundary layer apparently leads to oscillations in the mean swirl angle near the centerbody surface, inasmuch as an increase in oscillation frequency of this time-averaged quantity correlates directly with an increase in vortex shedding frequency when $\dot{m}_0/\dot{m}_i = 0$ (refer to Fig. 8). Normally, in an unconfined flow, the presence of periodically shed vortices would not be detected by time-averaged flow angle measurements. The oscillations seen in Fig. 8 were, in fact, not detected in the outer region of the inner mixing layer ($1.3 \leq r/R \leq 1.5$), where the mean swirl angle measured at a given radial distance from the centerbody surface decayed monotonically in the streamwise direction (cf. Fig. 4 in Frey and Gessner, 1990). In the immediate vicinity of the centerbody, however, where steep mean velocity gradients exist, the presence of embedded vortices in the flow can be inferred from the oscillating results shown in Figs. 6 and 8.

It should be noted here that the oscillations which appear in Figs. 6 and 8 are not related to centrifugal instability effects. This claim can be justified by comparing the surface flow angle distributions shown in Fig. 8 (actually measured at $y/R = 0.006$) with a comparable distribution measured by Driver and Hebbar (1987). Their study was an experimental investigation of local flow behavior in the relaxation zone above a stationary cylinder immediately downstream of an in-line, rotating cylinder (same diameter) preceded by another stationary cylinder over which an axially-directed turbulent boundary layer had developed. Their flow situation thus corresponds to one in which W is a maximum near the cylinder surface in the relax-

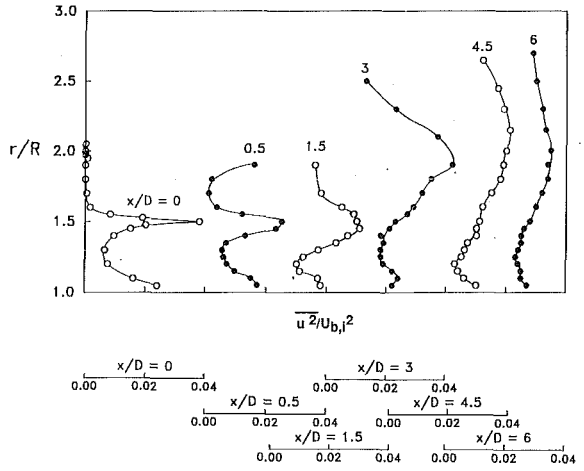

Fig. 9(*a*) Axial component

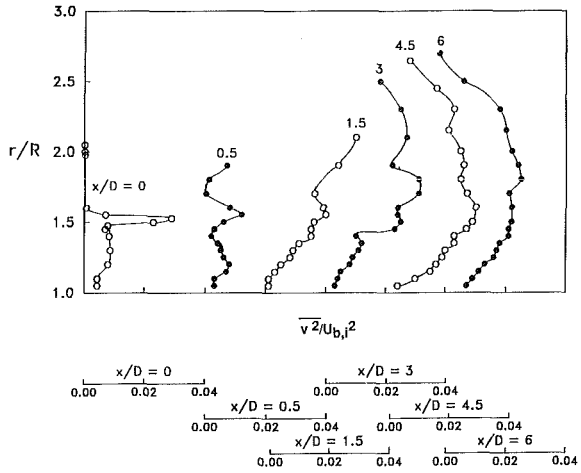

Fig. 9(*b*) Radial component

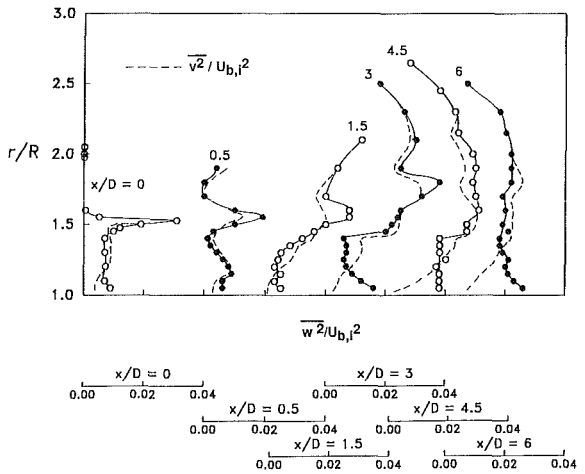

Fig. 9(*c*) Circumferential component

Fig. 9 Reynolds normal stress component profiles

ation zone, and decreases with increasing radial distance from the surface. For their prescribed operating conditions, negative angular momentum gradients exist in the relaxation zone which are comparable to those encountered in the present work. Figure 8 shows, however, that the surface flow angle distribution measured by Driver and Hebbar over the same streamwise interval considered in the present study ($0 \leq x/D \leq 6$, with $x/D = 0$ at the start of the relaxation zone) is free of the oscillations noted in this study. On the basis of this comparison, it can be inferred that the oscillatory behavior seen in Figs. 6 and 8 is not caused by centrifugal instabilities in the flow.

Reynolds Stress Distributions. Reynolds normal stress profiles measured at six streamwise stations are shown in Fig. 9. In accordance with earlier comments, the profiles measured at $x/D = 0.5$, 1.5, 3, 4.5, and 6 are truncated at a radial position where the local turbulence intensity begins to exceed 60 percent to avoid rectification errors caused by local flow reversal. The profiles measured immediately downstream of the nozzle exit (at $x/D = 0$) indicate that the exiting swirling inner stream emanates from a well-developed turbulent boundary layer flow within the inner nozzle, whereas flow emanating from the outer nozzle is at a relatively low turbulence level. Figure 9 also shows that peak intensity levels exist in the shear layer region between the inner and outer streams (near $r/R = 1.5$) immediately downstream of the nozzle exit. This effect diminishes in the downstream direction as turbulent mixing occurs between the two streams. One interesting observation is that near-wall levels of $\overline{w^2}$ increase markedly in the downstream direction while $\overline{v^2}$ levels in this region remain relatively constant. (Compare the solid and dashed-line distributions in Fig. 9(*c*)). Also, $\overline{w^2}$ levels in the near-wall region tend to approach $\overline{u^2}$ levels well downstream of the nozzle exit (compare the distributions at $x/D = 6$ in Figs. 9(*a*) and 9(*c*)). This behavior is indicative of a change in the anisotropy among $\overline{u^2}$, $\overline{v^2}$, and $\overline{w^2}$ as the flow proceeds downstream, which implies that departures from local equilibrium have occurred.

The extent to which the flow is in non-equilibrium at the downstream stations can be seen more clearly by referring to the Reynolds shear stress profiles in Fig. 10. Figure 10(*a*) shows $\overline{uv}$ profiles measured at the six stations. The axial mean velocity component profile measured at $x/D = 3$ is shown superimposed on this figure (dashed-line distribution; arbitrary units). From the figure it can be seen that $\overline{uv} = 0$ at a radial position where $\partial U/\partial r$ is nonzero, and that $\overline{uv}$ undergoes a sign change in a region where $\partial U/\partial r$ remains positive. At this same streamwise location ($x/D = 3$), Fig. 10(*c*) shows that $\overline{vw}$ remains positive throughout the region where $\partial W/\partial r$ changes sign. This behavior also exists at $x/D = 4.5$ and 6 and implies that eddy viscosity or length-scale type modeling will not be adequate for this flow. Inasmuch as the conventional form of the $k - \epsilon$ turbulence model employs an eddy viscosity defined as $\nu_t = C_\mu k^2/\epsilon$, where ν_t is always positive, this model will also be inadequate for predicting the present flow. Thus, closure at the full Reynolds stress transport equation level is required if the mean flow and Reynolds stresses are to be predicted with reasonable accuracy. Models of the type developed by Launder, Reece, and Rodi (1975) should be adequate for this purpose. More advanced models will be required, however, to predict the oscillatory flow behavior which has been observed in this study, as indicated by the results shown in Figs. 6 and 8.

Wall Function Behavior. The use of wall functions for predicting the present flow was also analyzed. Figure 11 shows resultant mean velocity profiles measured in the yaw plane at the six streamwise stations and plotted in terms of law-of-the-wall coordinates. In this figure U_β is the magnitude of the vector sum of U and W, U_τ is the resultant wall shear stress, and yU_τ/ν or y^+ is terminated at a radial position where U is below its maximum value (e.g., at $r/R = 1.3$ for data taken at $x/D = 3$, 4.5, and 6; refer to Fig. 5(*a*). The results in Fig. 11 are based on wall shear stress data obtained with the 1.6 mm (0.065 in.) OD Preston tube. The normalized distance corresponding to the outside diameter of this probe (d_0U_τ/ν) is shown superimposed on the velocity profiles. These profiles all obey the two-dimensional form of the law-of-the-wall very well. This behavior is rather remarkable, inasmuch as the swirling near-wall flow is oscillatory (Fig. 6) and develops in the presence of an adverse pressure gradient (Fig. 4).

On the basis of the results shown in Fig. 11 alone, it appears that the wall function approach can be applied to the present

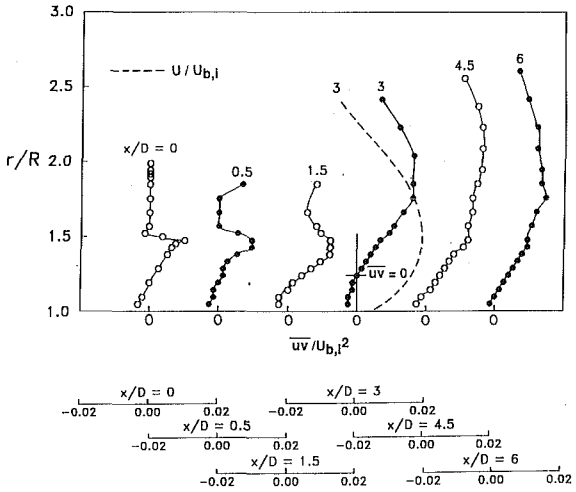

Fig. 10(*a*) *xr* plane component

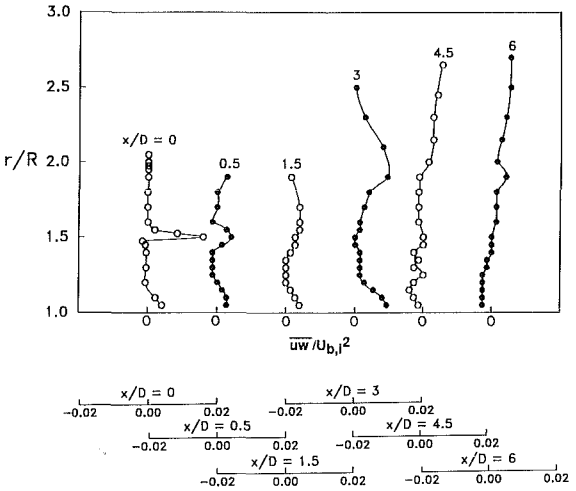

Fig. 10(*b*) *xθ* plane component

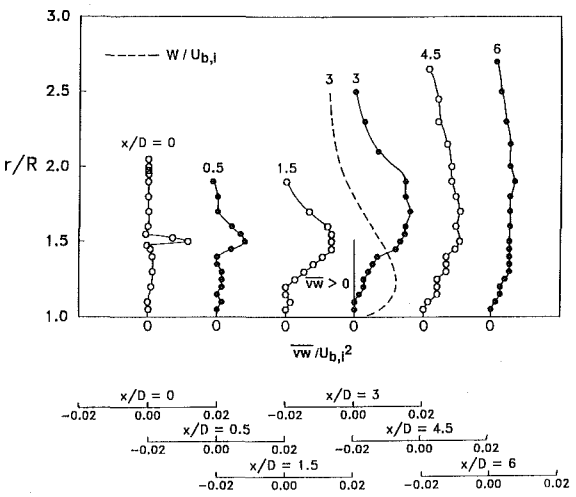

Fig. 10(*c*) *rθ* plane component

Fig. 10 Reynolds shear stress component profiles

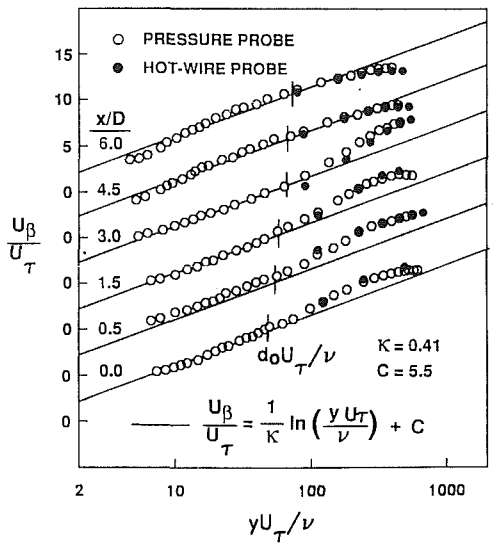

Fig. 11 Law-of-the-wall velocity profiles in the near-wall region

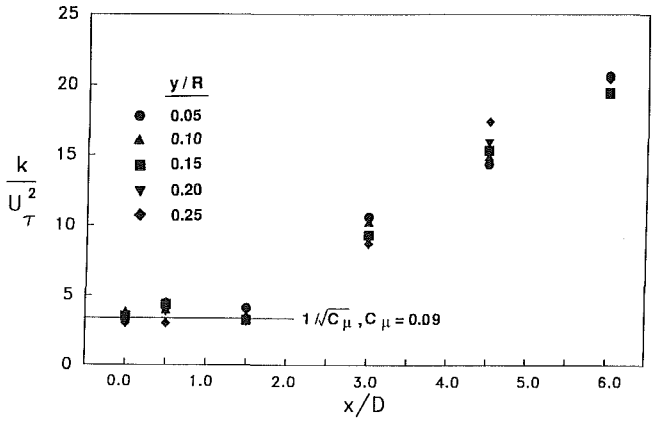

Fig. 12 Turbulence kinetic energy distributions in the near-wall region

flow, provided that the first grid line parallel to the cylinder surface is such that $30 \leq y^+ \leq 80$ on this line. A more stringent requirement applies, however, if one examines near-wall distributions of k/U_τ^2, plotted as shown in Fig. 12, where k is the turbulence kinetic energy. At $x/D = 0$, 0.5, and 1.5, the conventional form of the wall function for k, namely $k/U_\tau^2 = 1/\sqrt{C_\mu}$ is well satisfied on the traverse $y/R = 0.05$, and, indeed, on traverses more distant from the cylinder surface. At the downstream stations, k/U_τ^2 values increase dramatically until $k/U_\tau^2 \cong 20$ at $x/D = 6$. This increase occurs because turbulence kinetic energy levels still equal or exceed their upstream values, while the local wall shear stress (friction velocity) has diminished significantly. On the first traverse adjacent to the cylinder surface ($y/R = 0.05$), $y^+ = 74$ at $x/D = 6$, and the condition $k/U_\tau^2 = 1/\sqrt{C_\mu}$ with $C_\mu = 0.09$ no longer holds. From a computational point of view, therefore, the first mesh line will have to be located significantly closer to the surface than $y/R = 0.05$, so that $y^+ < 74$, and, even then, there is no assurance that the conventional wall function for k will be applicable at, say, $y^+ = 30$, which is the lower limit usually assumed where the law-of-the-wall is still applicable. Caution must be observed, therefore, in specifying the grid configuration used to analyze the present flow. If computations based on the wall function approach do not yield results which simulate the dramatic rise in k/U_τ^2 values seen in Fig. 12, then wall-specified boundary conditions will have to be imposed. These considerations should be kept in mind when predictions are compared with the present results.

Turbulence Model Assessment. The experimental results presented in this paper can serve as a basis for comparison with numerical results generated from turbulence models which purportedly can predict swirling turbulent flows. From a computational point of view, the initial conditions are well-posed, i.e., complete data for the mean flow field (P, U, V, and W) and Reynolds stress field ($\overline{u^2}$, $\overline{v^2}$, $\overline{w^2}$, $\overline{uv}$, $\overline{uw}$, and $\overline{vw}$) are

available in tabulated form (Frey, 1990). This reference also includes data in tabulated form at each of the five downstream stations where measurements were made (x/D = 0.5, 1.5, 3, 4.5, and 6). If a transport equation for the dissipation rate ϵ is included in the overall turbulence model, then the initial distribution of ϵ can be estimated from the relationship $\epsilon = C_\mu(k^2/-\overline{uv})\partial U/\partial r$. This relationship has been applied in recent predictions of strongly swirling jet flows (Leschziner and Rodi, 1984; Truelove and Mahmud, 1986) and should be adequate for the present flow, inasmuch as the flow is in local equilibrium at $x/D = 0$, where initial values of $-\overline{uv}$ and $\partial U/\partial r$ at a given radial location are nominally of the same sign (compare the results at $x/D = 0$ in Figs. 5(*a*) and 10(*a*)), so that ϵ remains positive across the width of the shear layer. Results presented in the previous section have shown that the conventional wall function approach may not be applicable to the present flow situation. If this is true, then the conventional wall functions must either be replaced by alternate forms which model the effect of vortex shedding on departures from local equilibrium and turbulence amplification (as reflected in k/U_τ^2 behavior) or be replaced by wall-specified boundary conditions. The former approach is perhaps an impossible task (given the present state-of-the-art), and the latter approach requires utilization of the fully viscous forms of the Reynolds stress transport equations and the dissipation rate equation. Further refinements in currently available Reynolds stress closure models will be required in order to predict the streamwise oscillations which have been observed in this study and their attendant influence on the overall flow structure.

Concluding Remarks

Coannular turbulent jet flow along a centerbody with swirl present in the inner stream has been investigated experimentally. For an outer-to-inner stream mass flow rate ratio of unity at the nozzle exit, the results show that mean streamlines in the flow undulate around the centerbody as the flow proceeds downstream. This behavior is attributable to vortex shedding at the nozzle exit where the two streams first meet, rather than to centrifugal instabilities induced by negative radial gradients of angular momentum which exist in the flow. This shedding effect gives rise to streamwise oscillations in flow adjacent to the centerbody and in the skin friction coefficient on the centerbody surface. Local flow development downstream of the nozzle exit is characterized by changes in anisotropy among the Reynolds normal stress components and departures from local equilibrium. As a result, conventional length scale, eddy viscosity, and $k - \epsilon$ transport equation models are not adequate for predicting the present flow. In order to gain further insight into the mechanisms responsible for the time-averaged oscillations observed in this study, data should be taken using either conditional sampling or time-domain averaging techniques. Implementation of these measurements would clarify the role of embedded vortices in the flow and their interaction with the centerbody boundary layer as the originating source of the oscillations.

Acknowledgment

The authors would like to express their appreciation to the Air Force Office of Scientific Research who sponsored this work under AFOSR Grant No. 85-0273.

References

Al-Beirutty, M. H., and Gessner, F. B., 1989, "A Hot-wire Measurement Technique for Moderate Intensity, Skewed Turbulent Flows," *Proceedings, 7th Symposium on Turbulent Shear Flows*, Stanford University, Stanford, CA, pp. 19.3.1–19.3.6.

Al-Beirutty, M. H., 1987, "Development of a Hot-Wire Measurement Technique for Moderate Intensity, Three-Dimensional Flows," PhD thesis, Department of Mechanical Engineering, University of Washington, Seattle, WA.

Arterberry, S. H., 1982, "An Improved Method of Flow Field Determination in Three-Dimensional Flows of Low Intensity Moderate Skewness," MS thesis, Department of Mechanical Engineering, University of Washington, Seattle, WA.

Au, H., and Ko, N. W. M., 1987, "Coaxial Jets of Different Mean Velocity Ratios, Part 2," *Journal of Sound and Vibration*, Vol. 116, No. 3, pp. 427–443.

Champagne, F. H., and Wygnanski, I. J., 1971, "An Experimental Investigation of Coaxial Turbulent Jets," *International Journal of Heat and Mass Transfer*, Vol. 14, pp. 1445–1464.

Comte-Bellot, G., Strohl, A., and Alcaraz, E., 1971, "On Aerodynamic Disturbances Caused by Single Hot-Wire Probes," ASME *Journal of Applied Mechanics*, Vol. 38, pp. 767–774.

Dellenback, P. A., Metzger, D. E., and Neitzel, G. P., 1988, "Measurements in Turbulent Swirling Flow Through an Abrupt Axisymmetric Expansion," *AIAA Journal*, Vol. 26, No. 6, pp. 669–681.

Driver, D. M., and Hebbar, S. K., 1987, "Experimental Study of a Three-Dimensional, Shear-Driven, Turbulent Boundary Layer," *AIAA Journal*, Vol. 25, No. 1, pp. 35–42.

Driver, D. M., and Hebbar, S. K., 1989, "Three-Dimensional Shear-Driven Boundary Layer Flow with Streamwise Adverse Pressure Gradient," *AIAA Journal*, Vol. 27, No. 12, pp. 1689–1697.

Durão, D., and Whitelaw, J. H., 1973, "Turbulent Mixing in the Developing Region of Coaxial Jets," ASME JOURNAL OF FLUIDS ENGINEERING, Vol. 95, Pt. 4, pp. 467–473.

Farokhi, S., Taghavi, R., and Rice, E. J., 1989, "Effect of Initial Swirl Distribution on the Evolution of a Turbulent Jet," *AIAA Journal*, Vol. 27, No. 6, pp. 700–706.

Frey, M. O., 1990, "Investigation of an Unconfined Coannular Jet Flow with Swirl Along a Centerbody," MS thesis, Department of Aeronautics and Astronautics, University of Washington, Seattle, WA.

Frey, M. O., and Gessner, F. B., 1990, "Experimental Investigation of Coannular Jet Flow with Swirl Along a Centerbody," AIAA Paper No. 90-1622, presented at the AIAA 21st Fluid Dynamics, Plasma Dynamics and Lasers Conference, Seattle, WA, 18–20 June 1990 (accepted for publication in the *AIAA Journal*).

Habib, M. A., and Whitelaw, J. H., 1980, "Velocity Characteristics of Confined Coaxial Jets With and Without Swirl," ASME JOURNAL OF FLUIDS ENGINEERING, Vol. 102, pp. 47–53.

Head, M. R., and Vasanta Ram, V., 1971, "Simplified Presentation of Preston-Tube Calibration," *The Aeronautical Quarterly*, Vol. 22, Pt. 3, pp. 295–300.

Higuchi, H., and Rubesin, M. W., 1979, "Behavior of a Turbulent Boundary Layer Subjected to Sudden Transverse Strain," *AIAA Journal*, Vol. 17, No. 9, pp. 931–941.

Ko, N. W. M., and Au, H., 1985, "Coaxial Jets of Different Mean Velocity Ratios," *Journal of Sound and Vibration*, Vol. 100, No. 2, pp. 211–232.

Ko, N. W. M., and Kwan, A. S. H., 1976, "The Initial Region of Subsonic Coaxial Jets," *Journal of Fluid Mechanics*, Vol. 73, Pt. 2, pp. 305–332.

Ko, N. W. M., and Lam, K. M., 1989, "Flow Structures of Coaxial Jet of Mean Velocity Ratio 0.5," *AIAA Journal*, Vol. 27, No. 5, pp. 513–514.

Kwan, A. S. H., and Ko, N. W. M., 1977, "The Initial Region of Subsonic Coaxial Jets. Part 2," *Journal of Fluid Mechanics*, Vol. 82, Pt. 2, pp. 273–287.

Launder, B. E., Reece, G. J., and Rodi, W., 1975, "Progress in the Development of a Reynolds Stress Turbulence Closure," *Journal of Fluid Mechanics*, Vol. 68, Pt. 3, pp. 537–566.

Leschziner, M. A., and Rodi, W., 1984, "Computation of Strongly Swirling Axisymmetric Free Jets," *AIAA Journal*, Vol. 22, No. 12, pp. 1742–1747.

Mattingly, J. D., and Oates, G. C., 1986, "An Experimental Investigation of the Mixing of Coannular Swirling Flows," *AIAA Journal*, Vol. 24, No. 5, pp. 785–792.

Ribeiro, M. M., and Whitelaw, J. H., 1980, "Coaxial Jets With and Without Swirl," *Journal of Fluid Mechanics*, Vol. 96, Pt. 4, pp. 769–795.

Sislian, J. P., and Cusworth, R. A., 1986, "Measurements of Mean Velocity and Turbulent Intensities in a Free Isothermal Jet," *AIAA Journal*, Vol. 24, No. 2, pp. 303–309.

So, R. M. C., and Ahmed, S. A., 1987, "Behavior of Carbon Dioxide Jets in Confined Swirling Flow," *International Journal of Heat and Fluid Flow*, Vol. 8, No. 3, pp. 171–176.

Truelove, J. S., and Mahmud, T., 1986, "Calculation of Strongly Swirling Jet Flows," *Proceedings, 9th Australasian Fluid Mechanics Conference*, Auckland, New Zealand, pp. 492–495.

Vu, B. T., and Gouldin, F. C., 1982, "Flow Measurements in a Model Swirl Combustor," *AIAA Journal*, Vol. 20, No. 5, pp. 642–651.

Initial Drop Size and Velocity Distributions for Airblast Coaxial Atomizers

H. Eroglu

N. Chigier

Department of Mechanical Engineering,
Carnegie Mellon University,
Pittsburgh, PA 15213

Initial drop size and velocity distributions, after complete disintegration of coaxial liquid jets, were determined by phase Doppler measurements. The measured radial distributions of Sauter mean diameter (SMD) were compared with the photographs of the disintegrating liquid jet. The SMD distribution was found to be strongly affected by the structure and behavior of the preceding liquid intact jet. The results showed that SMD increases with increasing liquid supply pressure as well as with decreasing air supply pressure. The axial measurement stations were determined from the photographs of the coaxial liquid jet at very short distances (1–2 mm) downstream of the observed break-up locations. The droplets accelerated at these regions under the influence of the air velocity. Smaller droplets were found to reach higher velocities because of their larger drag-to-momentum ratio. In general, minimum droplet mean velocities were found at the center, and the maximum velocities were near the spray boundary. Size velocity correlations show that the velocity of larger drops did not change with drop size. Drop rms velocity distributions have double peaks whose radial positions coincide with the maximum mean velocity gradients.

Introduction

Atomization of liquid jets is of primary importance in many combustion systems including liquid rocket combustion chambers, gas turbines, internal combustion engines and others. Atomization of a liquid is most effectively achieved by generating a high relative velocity between a liquid jet and the surrounding gas. In airblast atomizers, the high relative velocity is created by injecting the liquid jet into a high-velocity gas stream. The rate and efficiency of combustion of a spray is a strong function of the size and velocity distribution of drops.

Liquid jet atomization has been investigated previously by many researchers. Detailed reviews of earlier work are reported by Giffen and Muraszew (1953), Chigier (1981), and Lefebvre (1989). In the past, sprays have been characterized by the spray angle, fuel patternation (mass distribution), and mean drop size. However, new optical methods allow simultaneous drop size and velocity measurement and are capable of providing other spray characteristics such as local drop size, and number density as well as mean and rms velocities. Among these methods, the phase Doppler particle analyzer (PDPA) was developed by Bachalo and Houser (1984) and is proving to be the most effective.

Kraemer and Bachalo (1986) measured drop size, velocity and number density distributions of dense sprays from a gas turbine fuel injector using the PDPA. The results provided useful information for combustor development and modeling of the air-fuel mixing process. Pitcher and Wigley (1989) studied automotive fuel injection processes under realistic engine conditions using laser and phase Doppler anemometry. The probability of detecting diesel fuel droplets was found to be highly dependent on the location of the measurement point relative to the spray and was strongly constrained by both the spatial and temporal development of the spray and the onset of combustion (Pitcher and Wigley, 1989). An interpretation of the droplet velocity-time profiles provided support for the development of a conceptual model for the evolution and break-up of the spray (Pitcher and Wigley, 1989). Brena de la Rosa et al. (1989) reported results of an investigation of the effect of swirl on the dynamic behavior of drops and on the velocity and turbulence fields of an isothermal spray using PDPA. A comparison of the results for the atomizer spraying into quiescent and swirling air flow fields has shown that droplet size, velocity, and number density distributions are quite different. Presser et al. (1990) investigated the effect of fuel properties on the structure of swirling spray flames. Size and velocity measurements were obtained in pressure-atomized spray flames using phase Doppler interferometry. Measurement results revealed that droplet mean velocity and size are influenced primarily by the fuel viscosity. No detectable trend was observed due to the changes in surface tension.

Fundamental aspects of pressure and airblast atomization were examined for both the break-up and drop dispersion regimes by Mao et al. (1991). These investigations involved both experiments using high-magnification photography and

Contributed by the Fluids Engineering Division for publication in the JOURNAL OF FLUIDS ENGINEERING. Manuscript received by the Fluids Engineering Division June 19, 1990.

PDPA, and computational analysis and modeling, for a prefilmed atomizer. The increase in fuel flow rate resulted in shorter break-up lengths for pressure swirl atomizers. Because of the faster rate of decrease of the film thickness, mean drop size became smaller. However, an opposite trend was observed in airblast atomization. The increase in fuel flow rate resulted in longer break-up length and larger mean drop diameter. The initial film thickness was found to be very critical in determining subsequent spray characteristics except for the spray angle which was not so sensitive to the initial film thickness.

Mansour and Chigier (1990) studied the development, stability, and disintegration of liquid sheets emerging from a two dimensional air assisted nozzle using photography and PDPA. The effect of large and small scale cell structures on the particle size and velocity distributions were investigated. It was concluded that the large diameter ligaments bounding the cell structures generated the large droplets in the spray. Smaller droplets were formed from the membranes stretched between the ligaments. The droplets were observed to be redistributed according to their size class by the boundary layer growth and turbulent mixing.

An analysis of sprays issuing from airblast coaxial atomizers, similar to that of Mansour and Chigier (1990), using high speed, high magnification, and high contrast photography, was conducted by Farago and Chigier (1990). The present paper focuses on the initial drop size and velocity distributions after the disintegration of coaxial liquid jets, using the PDPA. The PDPA measurement locations were determined using the intact length results reported by Eroglu et al. (1991). The photographic and PDPA experiments revealed that the initial particle size distribution is directly influenced by the structure and behavior of the preceding intact liquid jet.

Experimental Setup

The experimental setup consists of a pressurized tank for the liquid supply, the coaxial atomizer, its positioner, exhaust system, PDPA, and the camera systems. All components of the experimental setup are mounted on an optical table.

Test Rig. House air is used both to provide atomizing air for the nozzle and to pressurize the liquid in the tank, in order to achieve controllable inlet conditions for both phases. The liquid phase is injected through the central tube, and the atomization is accomplished by discharging high-velocity air from the surrounding annular tube. The inlet pressure of the atomizing air can be varied from zero to 3.625 psig (25 kPa), the latter being associated with an air mass flow rate of 70 kg/h and a velocity of 180 m/s. Water is stored in a 10-liter-capacity tank. The water tank can supply a maximum pressure of 87 psig (600 kPa) if no air is used to assist atomization. However, the maximum achievable water supply pressure is reduced to 72 psig (500 kPa) if the maximum air flow rate is used for airblast atomization. This water supply delivers a pulsation-free and vibration-free water flow with a very high repeatability.

The length of the coaxial atomizer is sufficiently long to provide undisturbed and fully developed liquid flow conditions. A screen acts as a flow straightener and reduces the air turbulence. The convergence of the air tube diameter at the exit produces an almost uniform velocity profile at the outlet.

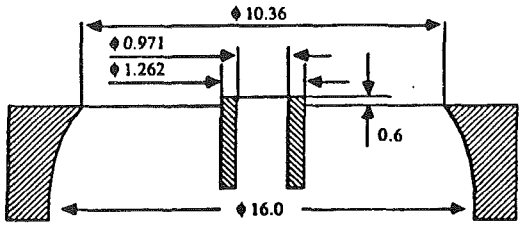

Fig. 1 Nozzle exit geometry (dimensions are in mm)

Figure 1 shows the nozzle exit geometry; all dimensions are in millimeters.

The exhaust system generates an environmental air velocity of 0.5 m/s around the spray when no atomizing air is supplied to the nozzle. This is necessary to protect the spray surroundings from unintentional air movements caused by opening doors or room heating. Both the atomizer and the exhaust system are connected to the same three-directional (z-r-phi) positioner in order to keep the axial distance between the atomizer outlet and the exhaust inlet constant (120 mm). The accuracy of the positioner is 10 μm in the axial and radial (z, r) directions and 0.1 degree in rotation.

Camera System and PDPA. A Canon F1 camera with f = 200 mm macro lens and different extension tubes and bellows were used for photography. Film sensitivity was 400 ASA. An Electro-Optics EG&G 549 microflash system with 0.5 μs flash duration was used to freeze the spray motion.

Droplet size and velocity distributions were measured using an Aerometrics single channel phase Doppler particle analyzer (PDPA). The receiving optics were arranged at the 30 deg off-axis forward scatter mode. A 15 mW, Spectra-Physics Model 124B He-Ne laser provided a light source of wavelength 632.8 nm. The photomultiplier voltage was adjusted at each measurement location in order to obtain maximum sensitivity without saturation. Therefore, optimum measurement conditions could be achieved for both large and small particles within the local particle size range. At each measurement location, 5000 samples were collected. The PDPA only validates data from spherical droplets. The drop size measurements are performed using the three photodetectors of the instrument, one pair at a time. Therefore, two independent size measurements are made of each droplet from two different pairs of photodetectors. The validation criterion for the instrument is that the ratio of the two measured diameters should be within 0.9 and 1.1. The PDPA software counts the total number of data rejections due to 1) deviations from sphericity, 2) multiple droplets in the measurement volume, and 3) noisy signals. The percent data rejection was typically 12 percent at the spray center, 5–8 percent at the intermediate radii, and 19 percent at the spray boundary. Therefore, the number of rejections due to deviations from sphericity in the measurement volume should be lower than the percentage of total rejections. The PDPA system and the principles of the measurement technique are described in detail by Bachalo and Houser (1984).

Uncertainty Analysis. The measurement uncertainties of liquid and air supply pressures are ±0.05 psig (0.345 kPa) and ±0.0036 psig (0.025 kPa) respectively at 95 percent confidence

Nomenclature

d = central tube diameter
$\dot{m}$ = mass flow rate
P = pressure
θ = rotational direction
r = radius, radial direction
Re = Reynolds number
V = velocity
We = Weber number
x = axial distance, axial direction

Subscripts

w = liquid (water)
air = air

Table 1 Axial measurement locations (x/d) at corresponding test conditions

(Uncertainty in x/d = ±0.01)

Water supply pressure "psig (kPa)"	Air supply pressure "psig (kPa)"			
	0.433 (2.986)	0.866 (5.972)	1.732 (11.944)	2.598 (17.916)
0.7 (4.826)	10	8		
1 (6.895)	12	9	10	7
2 (13.790)		11	10	9
5 (34.474)			12	11

Table 2 Ranges of nozzle exit flow parameters

Liquid supply pressure (P_w):	0.7–5 psig ± 0.05 psig (4.83–34.5 ± 0.345 kPa)
Liquid exit velocity (V_w):	1.1–4.5 ± 0.01 m/s
Liquid flow rate (m_w):	2.9–12 ± 0.015 kg/h
Liquid Reynolds number (Re_w):	1097–4370
Air supply pressure (P_{air}):	0.43–2.60 ± 0.0036 psig (2.99–17.92 ± 0.025 kPa)
Air exit velocity (V_{air}):	64.8–158.7 ± 1.95 m/s
Air flow rate (m_{air}):	24–58.8 ± 0.71 kg/h
Air Reynolds number (Re_{air}):	36970–90540
Weber number:	29–200

level. The uncertainty values for the liquid and air flow rates are ±0.015 kg/h and ±0.71 kh/h, and for the corresponding liquid and air velocities at the nozzle exit, are ±0.01 m/s and ±1.95 m/s respectively. The uncertainty of the vertical, transverse and axial traverses of the nozzle positioning system is ±0.01 mm. The maximum uncertainties of the SMD and the drop mean velocity are ±2 percent and ±1 percent (Baird, 1962), respectively, at 95 percent confidence level. These uncertainty values are also given in Tables 1 and 2 and in the figure captions.

Results and Discussion

The PDPA measurements were carried out at 11 test conditions of the coaxial atomizer each of which is specified by a pair of water and air supply pressures. Radial distributions of drop size and velocity were measured at an axial location of about 2 mm downstream of the break-up point for each test condition. The break-up points were obtained from the results of the photographic investigations reported by Farago and Chigier (1990) and Eroglu et al. (1991). The measured drop size and velocity distributions are, therefore, the direct result of liquid jet disintegration without significant influence of droplet evaporation and coalescence. The test conditions and the corresponding axial measurement locations are listed in Table 1. These test conditions provide a Weber number range of 29–200 at the nozzle exit. Table 2 gives the ranges of respective flow parameters.

Drop Size Distributions. Figures 2 through 5 show radial variations of Sauter mean diameter (SMD) at various air and water supply pressures. The SMD is defined as

$$\text{SMD} = \frac{\Sigma N_i D_i^3}{\Sigma N_i D_i^2}$$

where N_i is the number of drops in size range i, and D_i is the middle diameter of size range i. The SMD values decrease with a reduction in water supply pressure and an increase in the air supply pressure. This is expected since the increase in the air supply pressure provides higher relative velocity at the interface of the liquid and gas phases, and it is well established that SMD is inversely proportional to the relative velocity. Lorenzetto and Lefebvre (1977) also reached the same conclusion as a result of their investigation of plain jet airblast atomizers. In general, the variation of water supply pressure also changes the relative velocity with a subsequent influence on SMD which is inversely proportional to the relative velocity. However, the

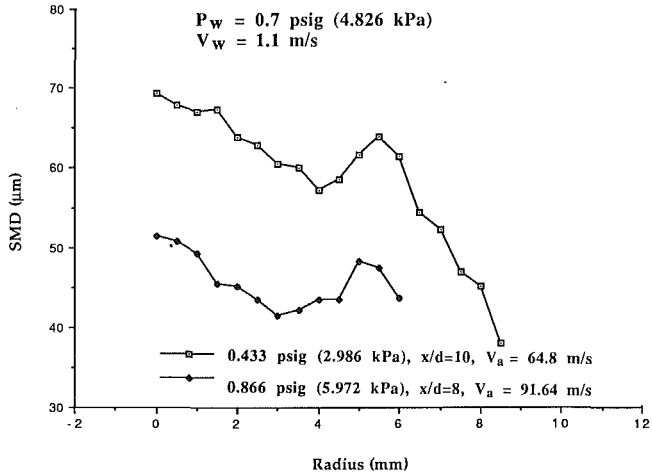

Fig. 2 Radial distribution of SMD for P_w = 0.7 psig (4.826 kPa). (Uncertainty in SMD = ±2 percent, in radius = ±0.01 mm at 20:1 odds.)

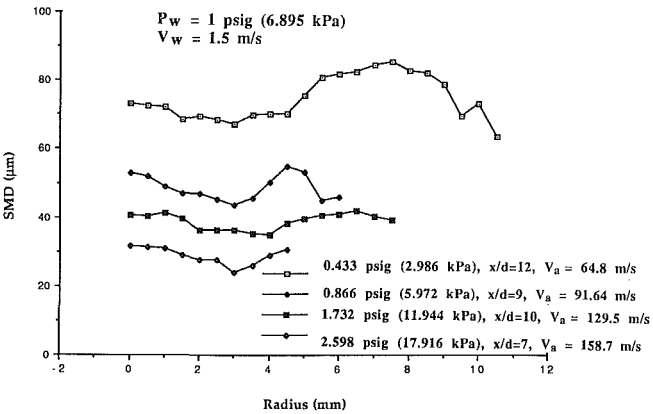

Fig. 3 Radial distribution of SMD for P_w = 1 psig (6.895 kPa). (Uncertainty in SMD = ±2 percent, in radius = ±0.01 mm at 20:1 odds.)

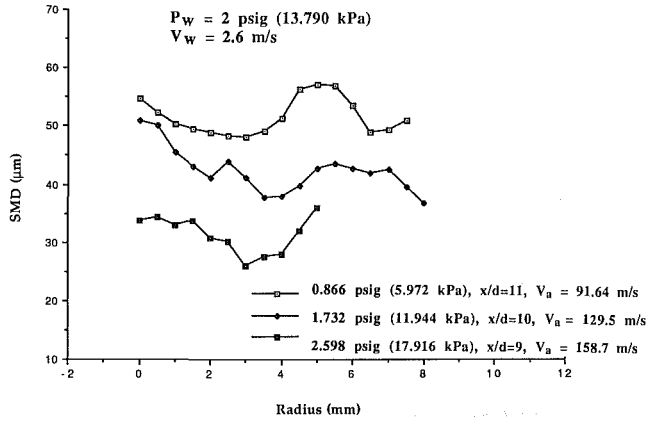

Fig. 4 Radial distribution of SMD for P_w = 2 psig (13.790 kPa). (Uncertainty in SMD = ±2 percent, in radius = ±0.01 mm at 20:1 odds.)

range of water supply pressures in the present experiments provided a liquid jet velocity range of 1.1–4.5 m/s. The influence of liquid velocity in this range is not as significant on the resulting relative velocity variation as that due to the air velocity (64.8–158.7 m/s). Therefore, the influence of the water supply pressure in this study on the SMD can be attributed to the change in water jet momentum rather than the change in the relative velocity at the liquid/gas interface. An increase in water jet momentum results in a larger liquid intact length and, consequently, a higher SMD.

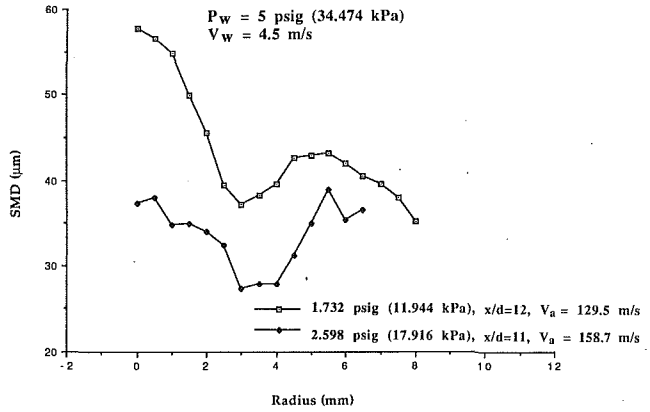

Fig. 5 Radial distribution of SMD for P_w = 5 psig (34.474 kPa). (Uncertainty in SMD = ±2 percent, in radius = ±0.01 mm at 20:1 odds.)

The radial distributions of SMD in figures show generally higher values at the center and toward the spray boundary. A lower SMD region is observed between these regions in each plot, and the lower SMD region is located at about 2–4 mm radii. This distribution is a direct result of the disintegration of the coaxial liquid jet. The coaxial liquid jet disintegration mechanism was investigated by Farago and Chigier (1990) by studying more than 1500 photographs of the atomization process. Figure 6 shows photographs of the coaxial liquid jet disintegration for 1.1 m/s nozzle exit water flow velocity, and 45.8 m/s air velocity. The corresponding water mass flow rate and Reynolds number are 2.9 kg/h and 1097, respectively. For the air flow, these values are 17 kg/h and 26130. Although the photographs of Fig. 6 were taken at the same test condition, the different size and appearance of the structures are random due to the different triggering time of the spark source. These photographs demonstrate cylindrical liquid jets transforming into thin water sheets which curl up forming shallow half-bowls or ladles. The ladle shape is most obvious in Fig. 6(A). Figure 6(B) shows the initial stage of a ladle formation. During this stage, the unstable liquid jet deviates from the main stream direction probably due to the radial motion of large scale turbulent structures in air. The air pressure at the wind-side of the water cylinder results in formation of a hook shape as shown at the center of Fig. 6(B). The air pressure begins to stretch the liquid membrane, and the fully developed ladle can be seen in Fig. 6(A) which subsequently bursts into ligaments and drops. The largest drops are generated at the locations where the handles of the ladles and the rims framing the stretched membranes disintegrate. The bursting membranes are responsible for the small droplets. The effect of ladle formation and the subsequent bursting of these structures on the radial SMD distributions are observed in Figs. 6. Due to the flapping motion of the unstable liquid cylinder, the larger drops that originate from the disintegration of the handles of the "ladle" can accumulate either at larger radii as shown in Figs. 6(A), (B), and (C) or at smaller radii as shown in Figs. 6(C) and 6(D). The flapping motion is also important for the subsequent motion and break-up of ligaments and drops influencing the radial size distributions. The ligaments branching from the handles of the ladles as shown in Fig. 6(B) probably affect the size distribution at the spray boundary causing the SMD to decrease with further increase in radius. At much higher air velocities (129.5 m/s), it was reported by Farago and Chigier (1990) that the ladle formation was not as obvious, but instead, a cloud of ligaments and drops with a shape similar to the cupping of the palm of a hand was observed. This was also attributed to the same mechanism which caused the ladle formation.

The peak of SMD variation close to the spray boundary occurs at slightly different radii for some of the test conditions. This is due to the change in the liquid intact length for the different test conditions and the expansion of the spray in the downstream direction. As the water supply pressure was in-

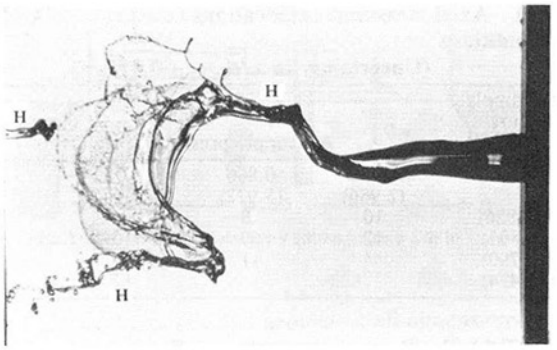

Fig. 6(A)

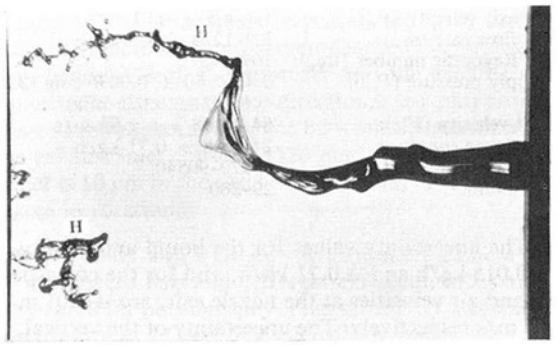

H = Handle

Fig. 6(B)

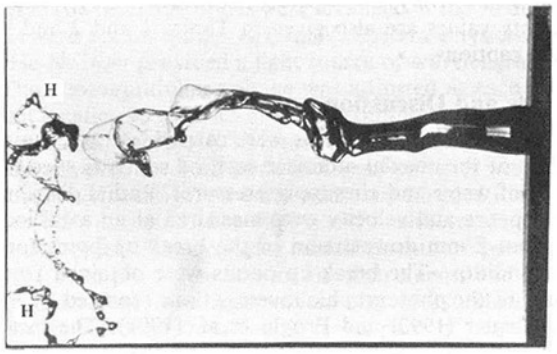

Fig. 6(C)

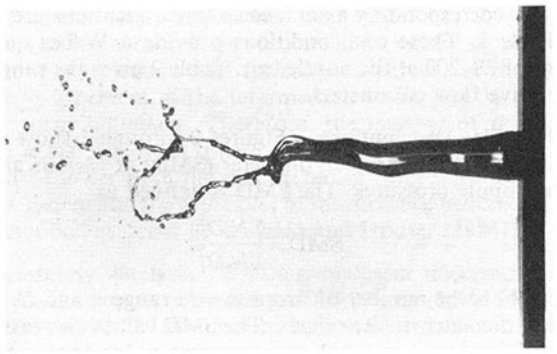

H = Handle

Fig. 6(D)

Fig. 6 Disintegration of coaxial liquid jets (P_w = 0.7 psig "4.826 kPa," V_w = 1.1 m/s; P_{air} = 0.217 psig "1.493 kPa," V_a = 45.8 m/s).

creased [5 psig (34.474 kPa)], the relative velocity required for the disintegration of the higher momentum liquid jet could only be provided by higher air supply pressures [1.732, 2.598 psig (11.944, 17.916 kPa)]. Therefore, SMD distributions for the 5 psig (34.474 kPa) water supply pressure are only presented at these air supply pressures as shown in Fig. 5. At 1.732 and 2.598 psig (11.944 and 17.916 kPa) air supply pressures, the SMD values of the central peak seem to be more sensitive to the variation of the water supply pressure than at 0.433 and 0.866 psig (2.986 and 5.972 kPa) air supply pressures. At the latter air supply pressures, the SMD values are more sensitive to water pressure towards the spray boundary. This behavior may be attributed to two reasons. The first reason is that the amplitude of the flapping motion of the unstable liquid jet is reduced due to the suppressing action of the surrounding air with higher momentum. This causes larger diameter drops to be accumulated at smaller radii. The change of liquid supply pressure affects the momentum of the liquid jet and this has further consequence on its stability which is closely related to the amplitude of the flapping motion. This can cause considerable variation of SMD values as a function of water supply pressure at high air pressures. The second reason is that the ligaments and drops generated after break-up at larger radii experience higher air velocity as will be described in the next section. It seems that secondary atomization may take place at these radii, depending on the local Weber number, with the subsequent effect on the SMD distribution.

Drop Mean Velocity Distribution. Figures 7 and 8 show radial distributions of droplet mean velocity as a function of water supply pressure at two different air supply pressures. Droplet velocities are, in general, minimum at the center and reach a maximum near the spray boundary under the influence of the air velocity profile. Some of the differences of droplet mean velocity profiles at different test conditions are due to the variation of intact length and the subsequent radial extent of the water jet. Changes in velocity profiles are also due to the difference in drop sizes. The measurement locations correspond to the acceleration region of the droplets where the air velocity is significantly higher than the local drop velocities. This imposes a drag force on the droplets in the axial direction away from the atomizer exit. The smaller droplets accelerate faster due to their lower momentum. When the air velocity is higher than the liquid velocity, the smaller droplets at the lower water supply pressure (P_w) = 0.7 psig "4.826 kPa," x/d = 10 reach higher velocities as shown in Fig. 7. Although the axial measurement location for the higher water pressure [1 psig (6.895 kPa)] is further downstream (x/d = 12) providing the droplets with more distance to accelerate, the effect of drop size on acceleration appears to be more dominant at 0.433 psig (2.986 kPa) air supply pressure. At 0.866 psig (5.972 kPa) air pressure, the drop mean velocity is higher for the higher water pressures at radii smaller than 4 mm. The measurement locations for the higher water pressures are farther from the nozzle exit due to longer liquid intact lengths. The larger droplets, corresponding to higher water pressures, require larger distances for acceleration. However, when the radius is over 4 mm, the drag to momentum ratio, due to the local air velocity, seems to cause the smaller droplets to accelerate faster. Therefore, mean droplet velocities for the lower water supply pressures are higher at larger radii than 4 mm. When the axial measurement station is the same (x/d = 10), the smaller droplets corresponding to lower water pressure [1 psig (6.895 kPa)] as shown in Fig 8 where P_{air} = 1.732 psig (11.944 kPa) have higher drop mean velocities than for the 2 psig (13.790 kPa) water pressure spray. A comparison of the mean drop size distributions for 2 and 5 psig (13.790 and 34.474 kPa) water supply pressures reveal that the drop size and measurement location effects counter-balance each other at radii over 2 mm. At smaller radii, the air velocity is too low to accelerate the

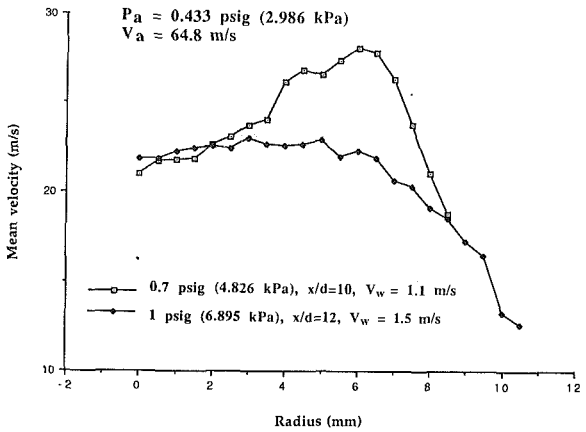

Fig. 7 Radial distribution of drop mean velocity for P_{air} = 0.433 psig (2.986 kPa). (Uncertainty in drop mean velocity = ±1 percent, in radius = ±0.01 mm at 20:1 odds.)

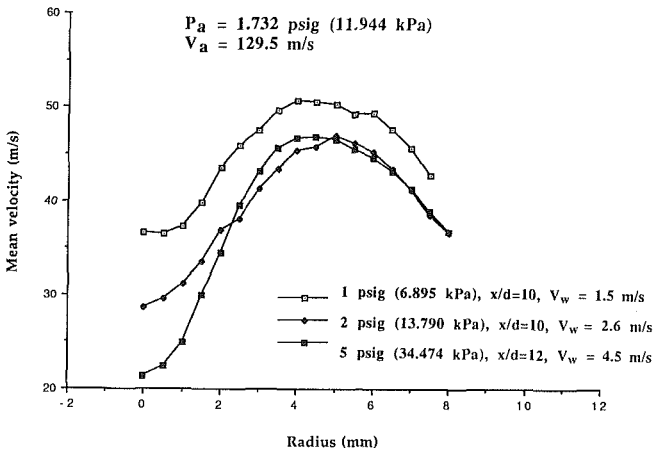

Fig. 8 Radial distribution of drop mean velocity for P_{air} = 1.732 psig (11.944 kPa). (Uncertainty in drop mean velocity = ±1 percent, in radius = ±0.01 mm at 20:1 odds.)

larger drop at 5 psig (34.474 kPa) water pressure, at the measurement location (x/d = 12). These plots show that velocity is not sensitive to the water supply pressure because of the counter-balancing influence of the axial measurement locations. Figures 7 and 8 also show that drop mean velocities increase significantly with the air supply pressure.

Histograms and Size-Velocity Correlations. Figure 9 shows typical histograms of drop size and velocities at P_{air} = 0.866 psig (5.972 kPa) and P_w = 0.7 psig (4.826 kPa) where x/d = 8. The full sections of the size histograms represent the uncorrected size bins. The open sections denote the size bins corrected for the effective size of the corresponding sample volume. The histograms (A, B, C) display the size and velocity distributions at 0.5, 3 and 5 mm radii corresponding to the central peak, minimum and the second peak of SMD.

Size/velocity correlations exist for small size droplets. Above 45 μm diameter, the drop velocity is independent of drop size. The smaller diameter droplets accelerate to higher velocities with increasing radius due to the increase in the air velocity and higher drag-to-momentum ratios. Because the velocities of the air are much higher than the velocities of the liquid, small drops will be accelerated rapidly from the liquid interface into the high velocity air stream. Large drops, because of their lower drag to momentum ratio, will require more time to be accelerated to the higher air velocities. However, this is not observed at radii greater than about 6 mm because of a decrease in the local air velocity due to the outer boundary layer and entrainment effects from the surrounding air. The flapping

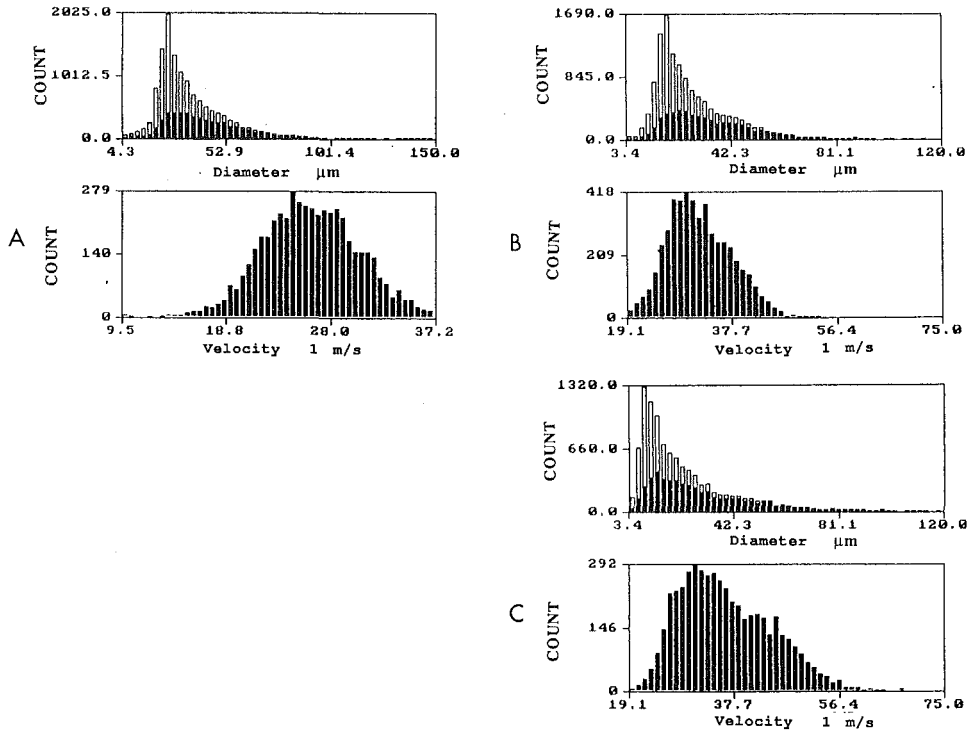

Fig. 9 Drop size and velocity histograms at P_{air} = 0.866 psig "5.972 kPa," and P_w = 0.7 psig "4.826 kPa" (A. r = 0.5 mm, B. r = 3 mm, C. r = 5 mm)

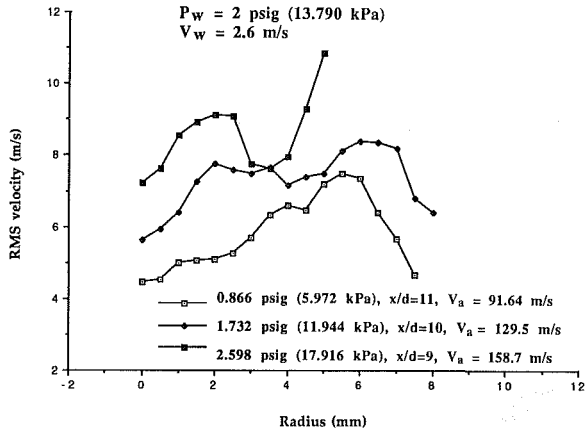

Fig. 10 Radial distribution of drop RMS velocity for P_w = 2 psig (13.790 kPa)

motion of the intact liquid jet prior to breakup (Fig. 6) also contributes to this behavior.

Drop RMS Velocity Distributions. The radial distributions of drop RMS velocities were obtained at all the test conditions by PDPA measurements. The results showed in general two peaks corresponding to the slopes of the drop mean velocity distributions. Figure 10 shows typical rms velocity profiles at P_w = 2 psig (13.790 kPa), and P_{air} = 0.866, 1.732, and 2.598 psig (5.972, 11.944, and 17.916 kPa). In general, rms values are higher for the smaller droplets with the higher air supply pressures where these small droplets follow the air velocity fluctuations more closely. Accordingly, the drop rms velocity peaks are also more pronounced for these small droplets. Such double peaks of velocity fluctuations at the locations with high mean velocity gradient were also reported by Brena de la Rosa et al. (1989).

Conclusions

Initial drop size and velocity distributions after the disintegration of coaxial liquid jets were measured by phase Doppler anemometry. The results showed that the SMD increases with the liquid supply pressure and decreases with the air supply pressure. The increase in the air supply pressure increases the relative velocity at the liquid/air interface which is inversely proportional to the SMD. The increase in liquid supply pressure increases the momentum of the water jet making it more stable. The radial distribution of SMD shows two peak regions, one at the center, the other towards the spray boundary. This distribution is a direct result of the coaxial liquid jet disintegration which first forms ladle shaped structures with a membrane bounded by thicker rims and a handle. This structure bursts into ligaments and droplets with the larger drops generated by the handles and the rims, and the smallest droplets by the membranes. Size distribution is further modified by the flapping motion of the disintegrating liquid jet which disperses the drops over a much wider area.

The drop mean velocity distributions are affected by the axial measurement locations because of the different corresponding air velocity profiles and the drop size distributions. The radial distribution of the drop mean velocity has a minimum at the center and has a peak towards the spray boundary under the influence of the air velocity profile. For a fixed location in the spray, the smaller droplets will have attained higher velocities than larger droplets as a result of higher drag for the case of air velocity higher than liquid velocity.

The drop size range was found to be wider close to the spray boundary as compared to that at the minimum SMD location. Size/velocity correlations exist for droplets smaller than 45 μm, with the smaller droplets reaching higher velocity.

The drop rms velocity distributions show double peak profiles. The peaks occur at the radial locations where the mean velocity gradients are steepest.

Acknowledgments

The authors thank Zoltan Farago for the photographs. This research has been sponsored by NASA Marshall Research Center (grant no. NAG8-126), Huntsville, Alabama.

References

Bachalo, W. D., and Houser, M. J., 1984, "Development of the Phase/Doppler Spray Analyzer for Liquid Drop Size and Velocity Characterizations," AIAA paper No. 84-1199, AIAA/SAE/ASME 20th Joint Propulsion Conference, Cincinnati, Ohio, June.

Bachalo, W. D., and Houser, M. J., 1984, "Phase/Doppler Spray Analyzer for Simultaneous Measurements of Drop Size and Velocity Distributions," *Optical Engineering*, Vol. 23, No. 5, pp. 583–590, Sept.–Oct.

Baird, D. C., *Experimentation*, 1962, Prentice-Hall, Englewood Cliffs, N.J.

Brena de la Rosa, A., Bachalo, W. D., and Rudoff, R. C., 1989, "Spray Characterization and Turbulence Properties in an Isothermal Spray with Swirl," ASME Paper No. 89-GT-273, 34th ASME International Gas Turbine & Aeroengine Congress, Toronto, Canada, June.

Chigier, N., 1981, *Energy, Combustion and Environment*, McGraw-Hill.

Eroglu, H., Chigier, N., and Farago, Z., 1991, "Coaxial Atomizer Liquid Intact Lengths," *Physics of Fluids A*, Vol. 3, No. 2, pp. 303–308.

Farago, Z., and Chigier, N., 1990, "Parametric Experiments on Coaxial Liquid Jet Atomization," ASME Paper No. 30-GT-81, ASME 35th International Gas Turbine Conference, Brussels, Belgium, June.

Giffen, E., and Muraszew, A., 1953, *The Atomization of Liquid Fuels*, Wiley, New York.

Kraemer, G., and Bachalo, W. D., 1986, "Evaluation of a Phase Doppler Particle Analyzer for Measuring Dense Sprays from a Gas Turbine Fuel Injector," AIAA paper No. 86-1532, AIAA/ASME/SAE/ASEE 22nd Joint Propulsion Conference, Huntsville, Alabama, June.

Lefebvre, A. H., 1989, *Atomization and Sprays*, Hemisphere Publishing Company, New York.

Lorenzetto, G. E., and Lefebvre, A. H., 1977, "Measurements of Drop Size on a Plain Jet Airblast Atomizer," *AIAA Journal*, Vol. 15, No. 7, pp. 1006–1010.

Mansour, A., and Chigier, N., 1990, "Disintegration of Liquid Sheets," *Physics of Fluids A*, Vol. 2, No. 5, May, pp. 706–719.

Mao, Chien-Pei, Chuech, S. G., and Przekwas, A. J., 1991, "An Analysis of Pressure Swirl and Pure Airblast Atomization," *Atomization and Sprays*, Vol. 1, No. 2, pp. 215–235.

Pitcher, G., and Wigley, G., 1989, "Laser and Phase Doppler Anemometry Measurement Techniques for Automotive Fuel Sprays," Third International Conference on Laser Anemometry—Advances and Applications, Swansea, Wales, Sept.

Pitcher, G., and Wigley, G., 1989, "Velocity and Dropsize Measurements in Fuel Sprays in a Direct Injection Diesel Engine," International Conference on Mechanics of Two-Phase Flows, Taipei, Taiwan, R.O.C., June.

Presser, C., Gupta, A. K., Avedisian, C. T., and Semerjian, H. G., 1990, "Study of Droplet Transport in Alcohol-Based Spray Flames Using Phase/Doppler Interferometry," ILASS-Americas 4th Annual Conference, Hartford, CN, pp. 243–247, May.

A Theoretical and Experimental Study of the Characterization of Bubbles Using Light Scattering Interferometry

A. Breña de la Rosa

S. V. Sankar

B. J. Weber

G. Wang[1]

W. D. Bachalo

Aerometrics, Inc.,
Sunnyvale, CA 94086

The present work details the theoretical and experimental research undertaken to determine the size and morphology of bubbles, and their dynamic characteristics such as velocity, number density, and volume flux using light scattering interferometry. The approach is based on the measurement of the phase difference of the interference fringe pattern which is produced when a particle passing through the probe volume defined by the intersection of two laser beams scatters light and interferes in the surrounding medium. Detailed analytical/numerical modeling of the phase Doppler approach using Mie scattering theory and the geometrical optics approximation resulted in optimum light scattering collection angles and calibration curves for bubble diagnostics. Using several techniques to generate a steady stream of monosize bubbles in the range from 6 μm to 1800 μm in diameter, the measurements obtained using the phase Doppler method were compared with direct photography yielding an agreement of better than 95 percent. The morphology of spheroidal bubbles was also investigated by placing the transmitting and receiving optical units at specified locations with respect to the scatterers. It is believed that this theoretical and experimental work has given the phase Doppler method general validity as applied to bubble diagnostics and promises to become a powerful research tool in the study of two phase flows.

Introduction

The problem of determining bubble size and velocity distributions, the local phase velocities, and other relevant parameters, in cavitating two phase flows has considerable generality since it does not only pertain to engineering disciplines but also to other fields such as biology and chemistry. For example, in the aeration of water shields in nuclear reactors or in flotation ponds for water purification, the determination of bubble size distribution and growth is required locally.

Until recently, most of the data concerning bubble size, velocity, number density, etc. in two-phase flows has been obtained by analyzing and classifying high speed photographic images, a procedure which is very time consuming. There are areas, however, where online analysis of the flows is required and where high rates of data acquisition are needed to monitor the unsteady nature of some processes. Laser based diagnostic techniques have the potential of providing in-situ data of two-phase flows, however, there is still much work left to be done to further develop these techniques on rigorous theoretical grounds to be successfully applied to the characterization of two phase flows.

Several researchers have developed useful instruments to measure different properties of nuclei. Oldenziel (1982) developed the cavitation susceptibility meter which measures the minimum tensile stress in a liquid at which nuclei start to explode. The instrument measures both microbubbles and particulate nuclei, however, it has the disadvantage that it needs a venturi tube to take the measurements and, therefore, interferes with the flow and it does not give directly other relevant parameters in two phase flow such as bubble size distribution, bubble velocity, number density, and void fraction.

An on-line method was developed by Billet (1986) to discriminate between the light scattered from bubbles and particulates. Based on an analytical investigation, Kohler and Billet (1981) showed that using the asymmetry of the particulate relative to the assumed spherical symmetry of the bubbles, a discrimination can be accomplished by comparing the intensities of scattered light at opposing angles. The disadvantages of this method are the precalibration needed to perform the measurements, in this case with plolysterene latex spheres of 21 μm in diameter, inferring the measurement of the bubble size from the intensity of scattered light, and the fact that no velocity information is obtained from this method. Also, the nonuniform illumination of the probe volume by the Gaussian intensity distribution of the laser beam gives rise to uncertainties in the measurement of the actual size distribution. Other techniques which have been successfully used in the detection of cavitation nuclei are the holographic and coulter

[1]Prof., Jet Propulsion Department, Beijing University of Aeronautics and Astronautics, China.

Contributed by the Fluids Engineering Division for publication in the JOURNAL OF FLUIDS ENGINEERING. Manuscript received by the Fluids Engineer Division January 15, 1990.

counter (O'hern et al., 1988), the light scattering using a white light source (Gowing et al., 1987), the triple-peak (Yu and Varty, 1987), and the acoustic (Billet, 1985).

There have been other investigators who have used the phase Doppler technique to determine bubble size and bubble concentration. Saffman et al. (1984), carried out measurements of air bubbles from 5-500 μm in diameter in a cavitation channel. In this work, calibration curves of phase shift versus diameter of the bubbles are shown up to 10 μm in diameter at a scattering angle of 72 deg and for different collection lenses. In their work they use electrolysis and a 10 μm diameter wire to generate their monodisperse bubbles. The results are inconclusive, however, because the measured "monodisperse" bubbles covered sizes of 8–16 μm in diameter and there was no additional measuring technique to verify that the sizes measured with the phase Doppler technique were correct.

In another work, Tanger and Weitendorf (1989) have presented measurements of spherical polysterene latex (PSL) particles and dirt simultaneously in water. They have also attempted to measure a mixture of 45 μm and 90 μm diameter PSL particles in water containing dirt particles. Their results show that both dirt and PSL particles can be combined into one histogram in spite of the fact that dirt reflects light predominantly and PSL particles refract light predominantly at the specified 72 deg collection angle. The wide distribution of sizes presented by the PSL particles is attributed by Tanger and Weitendorf (1989) to the large variation in their nominal size. However, the standard deviation is typically of the order of 2 percent for these PSL particles. Moreover, the authors have not explained what is the effect of small dirt particles (6 μm) attached to much larger PSL particles (75 μm) on the measurements performed by their instrument. The reader is referred to Sankar et al. (1990) for a detailed theoretical and experimental study of the phase Doppler technique for sizing small PSL particles in water.

The phase Doppler technique has become the most widely used for measuring the size and velocity of liquid sprays in both isothermal and reactive conditions Bachalo (1980), Kraemer and Bachalo (1986), Dodge and Schwalb (1988), McDonell and Samuelsen (1988), and Breña de la Rosa et al. (1990). The focus of the present research has been to lay the theoretical and experimental work for extending the technique to include the characterization of bubbles and to use flow visualization techniques to verify the phase Doppler measurements.

The Light Scattering of Bubbles

The accurate determination of bubble diagnostics poses a different problem than that of liquid particles in air, since the light scattering from dielectric spheres and from liquid drops is quite different, Chylek et al. (1980), Marston et al. (1981). Mie's solution to the problem of scattering efficiency and pattern of a dielectric sphere is given as a function of the index of refraction $m = n_i/n_0$ (the ratio of the index of refraction of the scatterer to that of the surroundings) and is usually expressed in terms of the scattering parameter $x = 2\pi r/\lambda_0$, where r is the sphere radius and λ_0 is the wavelength in the outer dielectric. In the case where the refractive index of the sphere exceeds that of the surroundings, forward scattering, the rainbow, and the glory are the regions in which light scattering is important, van de Hulst (1957). In the case where the refractive index of the sphere is less than that of the surroundings, for example in air bubbles, refraction in the rainbow region is not present, however, a new region, which is known as the critical scattering region appears, Marston (1979), Marston et al. (1981). Scattering is important in this region due to an abrupt change in the amplitude of the reflected wave as the local angle of incident, β, of the ray changes from $\beta<\beta_c$ for small impact parameters to $\beta>\beta_c$ for large ones. Here $\beta_c = \arcsin(m^{-1})$ is the critical angle for a plane surface and $\psi_c = \pi - 2\beta_c = 82.82$ deg is the critical scattering angle for an air bubble in water.

Marston (1979, 1981), has proposed a model for the light scattering of bubbles which adopts the geometrical optics approximation. It consists of a coarse structure in the Mie scattering for $\beta<\beta_c$, and a superposed fine structure near β_c. Marston's results can be summarized as follows. First, the intensity of scattered light at several angular regions exceeds that of geometric scattering from a perfectly reflecting sphere of the same radius. Second, the interference of the reflected wave with certain rays that penetrate the sphere and are refracted to angles in the vicinity of the critical scattering region becomes significant when an air bubble has a diameter of <800 μm. This interference produces oscillations in the intensity with an angular quasi-period of magnitude $\Omega = (\lambda/r)^{1/2}$ radians near β_c.

Three important points can be noted from Marston's analysis. First, since the oscillations in the intensity are significant in the particle size range of interest, it is not the intensity of scattered light which should be measured to size the bubbles, but rather the phase shift as is proposed here. Second, due to diffraction near ψ_c, it is preferable to detect scattering with $\psi \le \psi_c - \Omega$ than to observe it with $\psi \simeq 90$ deg, which is the usual practice for bubbles in water, Keller (1972). Third, Marston's investigation suggests that the reflective component might be the dominant scattering phenomena at some scattering angles for air bubbles. This last point is paramount from the standpoint of bubble sizing using the phase Doppler approach since Bachalo (1980) showed that the scattered light is phase-shifted by an amount directly proportional to the sphere diameter. Moreover, if any one of the scattering components, namely

Nomenclature

b_0 = beam radius
d = sphere diameter
$|E|$ = resulting amplitude of scattered light
G = divergence
I = light intensity
m = refractive index
N_d = bubble number density, number/cm^3
Q_f = volume flux, cm^3/s cm^2
R = receiver distance from probe volume
$|S|$ = amplitude of scattered light
r = sphere radius
t = time
x, x' = spatial coordinates, defined in Fig. 3
x = size parameter, $x = 2\pi r/\lambda$
y = spatial coordinate, defined in Fig. 3
z, z' = spatial coordinates, defined in Fig. 3
α = incidence angle
β = angle of incidence of ray on scatterer
γ = beam intersection angle
δ = phase shift due to optical path length
ϵ = fringe spacing
η = resulting phase shift of scattered light
θ = scattering angle
λ = wavelength of light
σ = phase shift of scattered light
ϕ = phase difference between detectors
ψ_c = critical scattering angle
ω = frequency

Subscripts

D = Doppler difference
i = incident laser beam; 1, 2
inc = incident light
j = detector number
n = polarization; 1-perpendicular; 2-parallel
p = scattering mode
scat = scattered light

reflection or refraction, is dominant then the phase relationship is exact.

In light of the above, the objective of the present investigation is twofold: to determine if the phase shift of the scattered light can be used to measure bubble sizes in the range of 1 to 3000 μm in diameter, and to determine calibration curves and suitable light scattering collection angles for optimum bubble diagnostics. The present work extends the application of the phase Doppler technique to the diagnostics of bubbles and sets it on strong theoretical grounds by carrying out analytical/numerical modeling of light scattering interferometry using the geometrical optics approximation and the more rigorous Mie theory. The analytical work has been complemented with experimental measurements including flow visualization.

The Phase Doppler Method. The concepts which provide the basis for the present investigation stem from the work of Bachalo (1980) who derived a theory for particle sizing utilizing the phase shift of the light transmitted through or reflected from spherical particles and collected at large off-axis angles. The need to measure particles of size larger than approximately 50 μm in diameter with good resolution, suggested the analysis of light scattered by reflection or refraction rather than by diffraction. The measurement of the energy scattered at angles away from the forward direction (greater than 20 deg) can be used to avoid the light scattered by diffraction. Moreover, the angular distribution of the light scattered by reflection and refraction is independent of the particle size except for the higher frequency resonant lobes produced by the interference between the scattering components. The following is a brief explanation of the phase Doppler principle, a detailed analysis can be found in (Bachalo, 1980) and (Bachalo and Houser, 1984a-b).

The optical path length of a light ray passing through a sphere relative to a reference ray deflected at the center of the sphere can be expressed as,

$$\eta = 2\frac{\pi d}{\lambda}(\sin\tau - pm\sin\tau') \tag{1}$$

where p is a parameter that characterizes the emerging rays and relates to the interface from which it emerges. For example $p = 0$ for the first surface reflection, $p = 1$ for the transmitted ray and $p = 2$ for the ray emerging after one internal reflection, m is the index of refraction, τ and τ' are the angles between the surface tangent and the incident and refracted rays, respectively.

The phase shift can be obtained using light scattering interferometry produced with a standard dual beam laser Doppler velocimeter. The rays from each beam are incident upon the sphere at different optical angles and therefore reach the common points on the receiver unit by different optical paths. Neglecting the phase shifts at reflection and focal lines, the relative phase shift due to the difference in optical path lengths is described as,

$$\delta = \frac{2\pi d}{\lambda}\left\{(\sin\tau_1 - \sin\tau_2) - pm(\sin\tau_1' - \sin\tau_2')\right\} \tag{2}$$

where the subscripts represent beams 1 and 2. Since the angles τ are fixed by the receiver geometry, the phase difference only changes as a result of the sphere diameter d. These phase differences produce an interference fringe pattern which can be analyzed to obtain the size and velocity of the spherical scatterer. The temporal frequency of the fringe pattern is the Doppler difference frequency which is a function of the beam intersection angle, laser wavelength, and the velocity of the scatterer. The spatial frequency of the fringe pattern, which is linearly related to the size of the sphere, is dependent on the beam intersection angle, laser wavelegnth, angle of observation, and on the scatterer diameter and index of refraction. Therefore, the mathematical description of the interference fringe pattern which includes the effects of all the optical parameters, is required to infer the size of the scatterer. With the theoretical description of the scattered fringe pattern for the appropriate parameters, there is no longer any need to calibrate the system for each measurement task. The size of the scatterer can subsequently be obtained from the accurate measurement of the spatial frequency of the interference fringe pattern.

A direct means of measuring the interference pattern was developed by Bachalo and Houser (1984a-b). The configuration uses pairs of photodetectors separated by fixed spacings and located at known angles relative to the laser beam. As the scatterer passes through the beam intersection region, it produces a scattered interference fringe pattern which appears to move past the receiver. Doppler burst signals with a relative phase shift, which is linearly related to the size of the scatterer, are produced by each of the detectors. It is possible to distinguish between a liquid drop or a bubble by the direction of movement of the scattered interference pattern. If it is assumed that a sphere, $m > 1$, is moving downward through the region of intersection of the two laser beams, the fringe pattern will also sweep downward. If, on the other hand, a scatterer $m < 1$ is moving downward through the intersection region, the scattered fringe pattern will sweep upward. Because frequency shifting, which acts as a velocity offset, has been incorporated into the hardware and software of the phase Doppler instrument, it is irrelevant whether the scatterer is moving in either direction or if it is stationary, the method still applies.

Theoretical Model. In a recent paper, Bachalo and Sankar (1988) presented a theoretical model of light scattering based on geometrical optics to simulate various experimental aspects of the phase Doppler technique for measuring liquid particles. In the present work the model is extended to simulate the light scattering of bubbles using both the geometrical optics and the Lorenz-Mie theory. The model takes into consideration the non-uniform (Gaussian) illumination of the particles, their trajectory and orientation as they pass through the probe volume, and their index of refraction. The objective of this model is to generate instrument response curves for optimum light scattering collection angles by performing spatial and temporal integration of the scattered intensity distribution over the receiver lens surface. Only a brief analysis of the geometrical optics approach is dealt with here, details of the model can be found in Bachalo and Sankar (1988).

van de Hulst (1957) has shown that for spheres much larger than the wavelength of the incident light (i.e., $\pi d/\lambda \gg 1$) it is possible to approximate the Mie scattering by the interference of diffracted, refracted, and reflected rays—the fundamental basis for the geometrical optics approach. In the present analysis, contributions from scattering components up to and inclusive of the second internal reflection have been accounted for, Fig. 1. Diffraction effects have been neglected and it is reasonable to do so if the analysis is restricted to angles greater than about 20 deg. The model, though valid for any refractive index, will be discussed here from the point of view of sizing air bubbles ($m = 0.75$) alone. Figure 2 shows schematically, for an air bubble, the classification of the scattering angles into different regions depending upon the type and number of scattering components present.

The coordinate system chosen for this analysis is shown in Fig. 3. Two incident laser beams *beam1* and *beam2* lying in the $x-y$ plane intersect at an angle γ to form a probe volume. Spherical air bubbles moving through the probe volume in the x-direction scatter the incident light beams and the scattered light interferes to form spatial fringe patterns. A receiving lens placed in the axisymmetric $y-z$ plane at a distance R from the probe volume and at an angle θ from the $x-y$ plane collects the scattered light and a system of optics image the collected

light from three different areas of the lens on to three separate photodetectors, Fig. 4.

The output of each of the three detectors is a Doppler burst similar to that of a conventional two beam LDV. However, the phase differences ϕ_{12} and ϕ_{13} between the detector outputs provide a measure of the size of the moving scatterer.

In order to generate calibration curves that relate the phase difference $\phi_{12}$and ϕ_{13} to the diameter of the bubble, it is necessary to compute the amplitude and phase of the different scattering components reaching the receiver surface. For each point (x', z') on the receiving aperture it is possible to calculate θ_1 and θ_2, the scattering angles (Fig. 3) for *beam1* and *beam2*, respectively.

Without going into further detail (the interested reader is referred to Bachalo and Sankar (1988) for the full derivation), at each point on the receiver surface, the various scattering components reaching it interfere to yield an amplitude function which can be expressed as

$$\sum_{i=1}^{2}\sum_{p=0}^{3}|S_{ipn}|\cos(\omega_i t+\sigma_{ipn})=\sum_{i=1}^{2}|E_{in}|\cos(\omega_i t+\eta_{in})$$
$$\text{for } n=1, 2 \tag{3}$$

This interference, which involves scattered light of two different frequencies (because of the Doppler effect), results in light intensity variation with the Doppler difference frequency

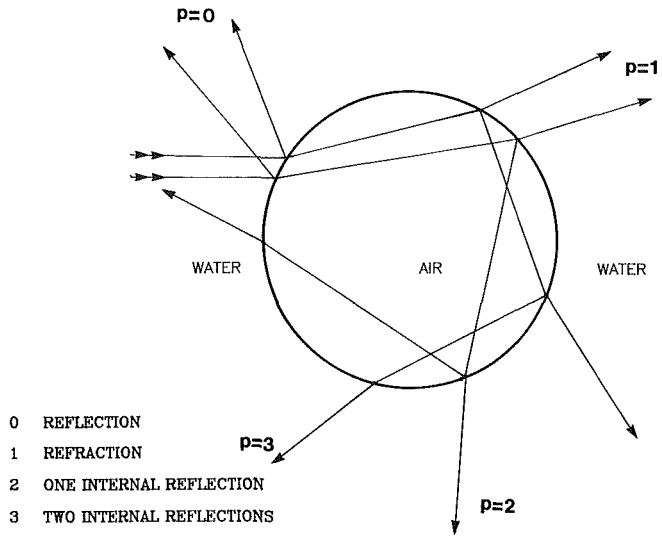

Fig. 1 Ray trace for an air bubble

at each point on the receiver surface. This can be expressed as

$$I_{\text{scat},n}(x', z')=|E_{1n}|^2+|E_{2n}|^2+2|E_{1n}||E_{2n}|\cos(\omega_D t+\eta_{1n}-\eta_{2n}) \tag{4}$$
$$\text{for } n=1, 2$$

In the present analysis the incident light is assumed to be linearly polarized in the axisymmetric $y-z$ plane. Furthermore, since the receiving lens is also placed in the $y-z$ plane it is reasonable to assume that only parallel polarized light (i.e., $n=2$) is present. Hence, any further reference to scattered intensity implies parallel polarization.

Integrating the scattered light intensity over the collection areas of the three photodectectors (Fig. 4) the result, at an instant of time t, can be expressed as

$$\sum_{x'}\sum_{z'} I_{\text{scat},j}(x', z')=A_j+B_j\cos(\omega_D t+\phi_j) \tag{5}$$
$$\text{for } j=1, 2, 3$$

where A_j and B_j correspond to the d-c level and amplitude of the a-c component, respectively, of the output of the j_{th} detector. The two quantities, A_j and B_j are, of course, time dependent. From the above equation the phase difference between the detectors

$$\phi_{12}=\phi_1-\phi_2 \tag{6}$$

and

$$\phi_{13}=\phi_1-\phi_3 \tag{7}$$

can be determined.

One additional factor that needs to be considered in the generation of the calibration curves is the motion of the particle through the probe volume. As the particle moves through the probe volume the phase difference between the detectors can change slightly because the particle is exposed to varying incident light intensities as a result of the Gaussian illumination. Thus, the relative contributions from reflection and refraction vary with time. Since the magnitude and sign of the phase due to reflection are different from those due to refraction, the resulting phase at each point on the receiver also changes with time. This effect can be particularly important for particles moving through the edges of the probe volume. To account for this, the phase differences between the detectors should be computed at different instances of time and subsequently time averaged to simulate the response of the actual instrument.

Using the theoretical model based on geometrical optics, calibration curves were generated for various scattering angles for bubbles of different size. Preliminary results showed that

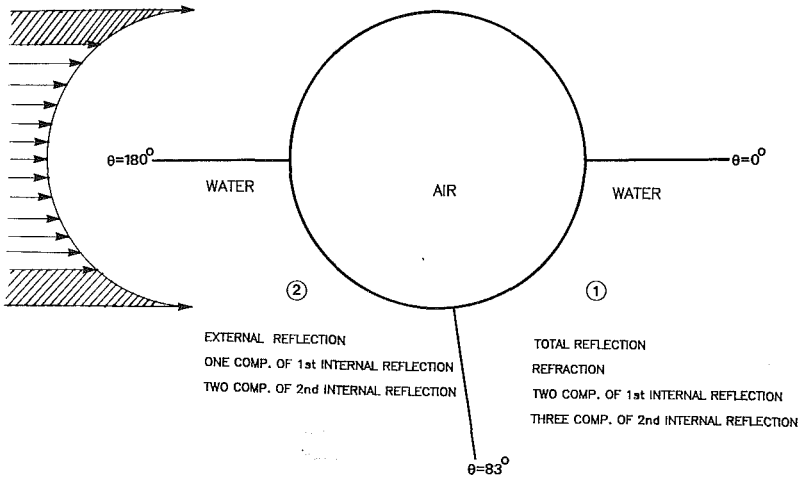

Fig. 2 Division of scattering angles into scattering regions

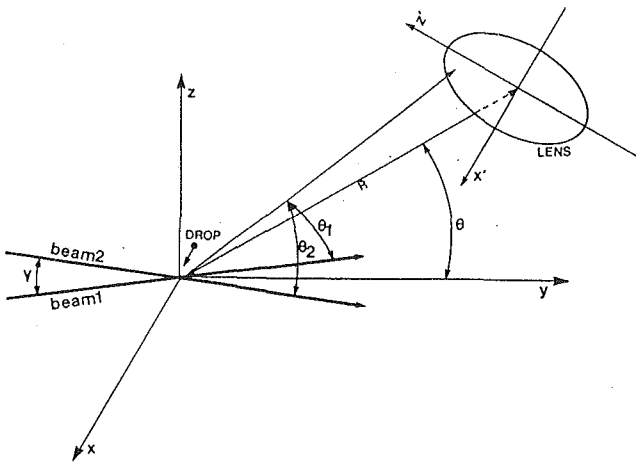

Fig. 3 Coordinate system for the light scattering model

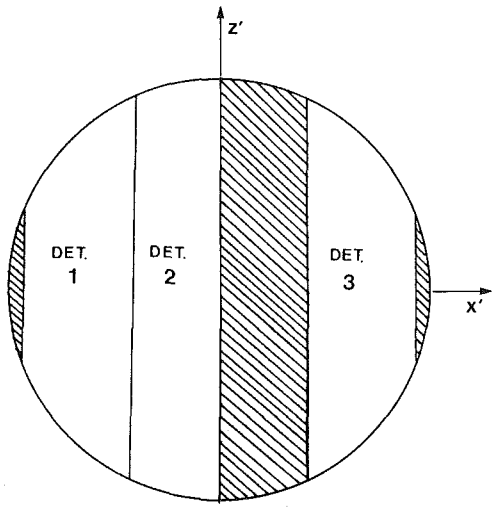

Fig. 4 Schematic of the receiving aperture showing the three areas from which light scattering information is obtained.

bubble sizing could be done in the forward direction at a scattering angle of 60 and 40 deg. The calibration curves of phase difference versus bubble diameter generated for the pairs of photodetectors resulted in a constant slope for a 60 deg scattering angle and for the range 1-3000 μm in diameter, a section of which are shown in Fig. 5. The generation of these calibration curves had to be accomplished in subranges since the Compaq 386/20 computer used in the numerical modeling required over 10 hours of execution time and used virtually all the computer memory of 2 Mbytes of RAM. The upper and lower bounds on the calibration curves indicate a maximum theoretical uncertainty of ± 5 percent which arise from the oscillations predicted by the geometrical optics theory over the diameter range of 1-3000 μm.

Shown in Figs. 6, 7, and 8 are the computer generated spatial fringe patterns that are formed on the receiving lens due to the scattering of light by a 10 μm, 50 μm, and 150 μm air bubbles, respectively, at a scattering angle of 60 deg. The circle in these figures delineates the area of the receiving lens. These fringe patterns contain distinct fringes in the x'-direction and a gradual intensity variation in the z'-direction. The wavelength of the spatial intensity variation in the x'-direction, which is being measured indirectly by determining the phase difference between the outputs of the three detectors, is linearly related to the diameter of the bubble.

Instrument Discrimination Between Refractive and Reflective Scattering. The importance of being able to identify refractive particles from air bubbles present in the water is fundamental to the study of the onset of cavitation. This is because the researcher needs to separate the bubbles and fine particulate which may contain air trapped in them (since the latter can, under certain pressures, give rise to cavitation) from other particulate. At a specified scattering angle, it is possible to know if a spherical scatterer reflects or refracts (in either mode predominantly) the energy incident on it from the relative movement of the spatial interference fringes. In addition, a light scattering analysis of the rays incident on a particle, also gives the regions where the different modes of scattering are predominant, see Fig. 2 and Bachalo and Sankar (1988).

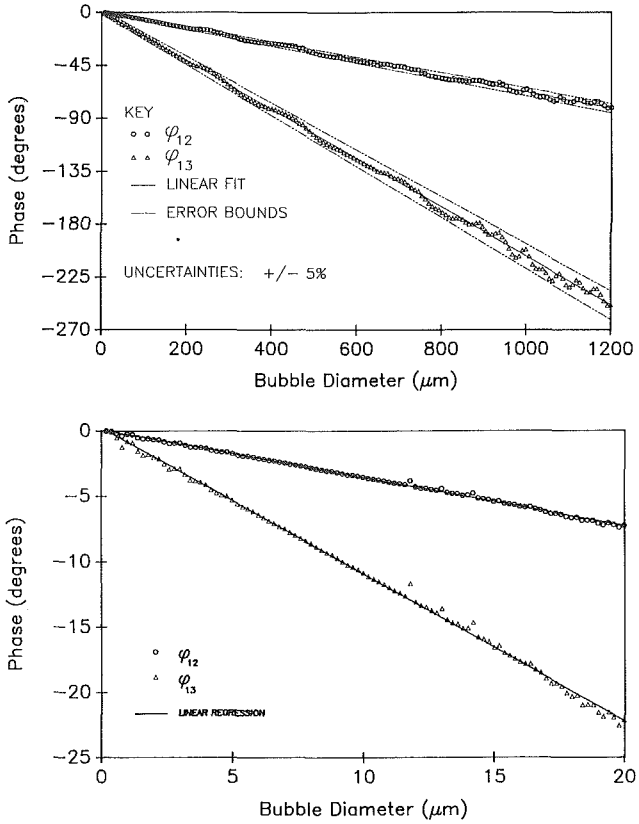

Fig. 5 Calibration curves for bubble sizing at a 60 deg scattering angle. The phase difference ϕ_{12}, ϕ_{13}, is that between photodetectors 1-2, and 1-3, respectively. The same constant slope calibration curves apply to bubbles in the range 1-3000 μm in diameter.

The light scattering of a particle for which the dominant mode of scattering is refraction and that of an air bubble is different because the incident rays of light on these particles travel through media of different refractive indices. For a particle for which $m > 1$, refraction is the dominant scattering mode at some scattering angles, whereas for an air bubble $m < 1$, the dominant scattering mode is reflection at some scattering angles. As a bubble passes through the probe volume the interference fringe pattern sweeps the receiver lens in the direction opposite to its main direction of flow. In the case of a liquid particle, the interference fringe movement is in the direction of the drop. The validation criteria built into the PDPA instrument makes use of the ratio $K = \phi_{13}/\phi_{12}$ of the phase shift between the photodetectors 1-3 and 1-2 and preestablished bounds to accept the Doppler signals. When the instrument is configured to measure, say bubbles, the flow of a refractive scattering particle through the probe volume results in the interference fringe pattern sweeping the photodetectors in reverse order to that which results from the flow of the bubbles, the value of K falls outside of the preset bounds and the particle is rejected. This validation criteria is very powerful and avoids situations such as those depicted by Tanger and

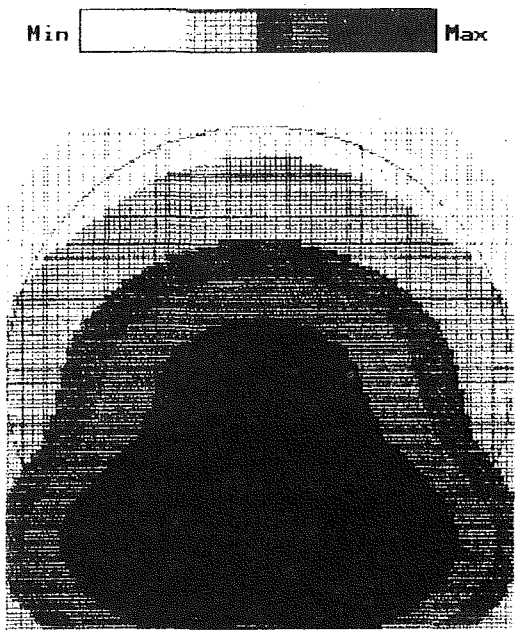

Fig. 6 Computer generated spatial fringe pattern for a 10 μm diameter air bubble using Mie theory. Reflection is the dominant scattering component. Mean scattering angle of 60 deg.

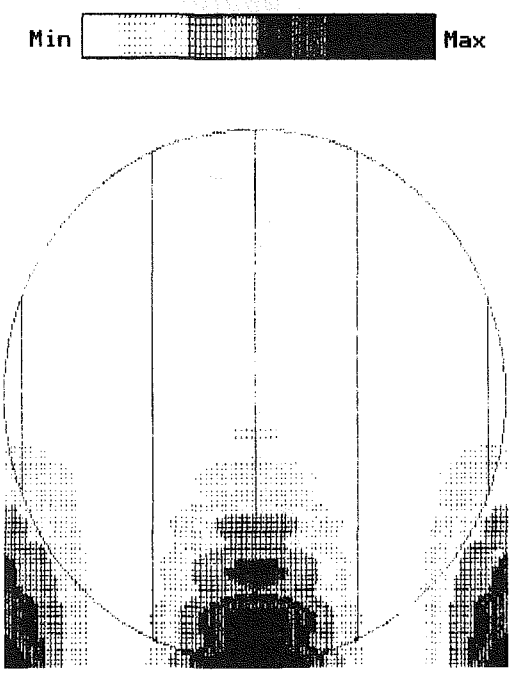

Fig. 7 Computer generated spatial fringe pattern for a 50 μm diameter air bubble using Mie theory. Reflection is the dominant scattering component. Mean scattering angle of 60 deg.

Weitendorf (1989) where both refractive and reflective scattering are counted in the same histogram resulting in erroneous bubble size and concentration measurements.

Determination of Flow Parameters

Volume Flux. Volume flux is determined from the measured volume mean diameter D_{30}, the sampling cross sectional area A, and the number of bubbles N counted in the sampling time interval t. The volume flux, Q_f, is calculated from,

$$Q_f = \frac{\pi}{6} D_{30}^3 \frac{N}{At} \tag{8}$$

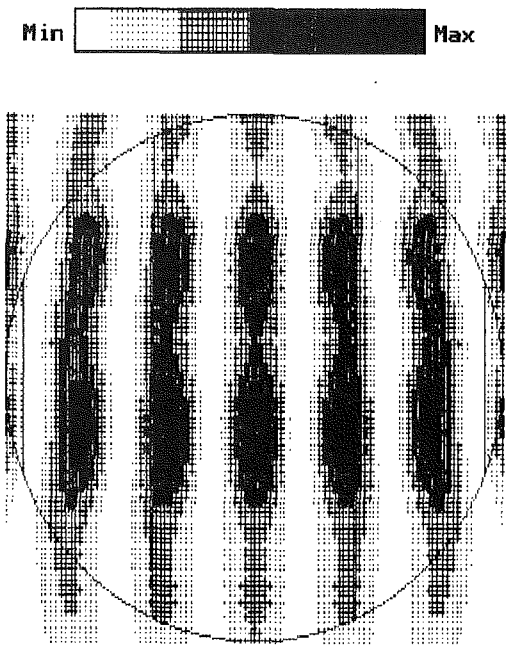

Fig. 8 Computer generated spatial fringe pattern for a 150 μm diameter air bubble using Mie theory. Reflection is the dominant scattering component. Mean scattering angle of 60 deg.

where N, the total number of bubbles, is the summation of the number of bubbles $N(d_i)$ in each size bin in the size histogram, that is,

$$N = \sum_{i=1}^{50} N(d_i) \tag{9}$$

The quantity D_{30} is influenced most by the largest bubbles in the distribution. Because size distributions are highly skewed with a relatively small population in the larger size classes, it is important that a large number of bubbles are measured to obtain a good statistical representation of them. In addition, D_{30} is cubed so the accurate determination of this quantity is most important in realizing good volume flux measurements.

The accurate calculation of the sampling cross section of a single particle counter instrument which uses laser beams with Gaussian beam intensity distribution is a complex task. The sampling cross section changes with the scatterer size as well as with the measurement conditions and instrument setup parameters.

During the development process of the phase Doppler method, Bachalo and Houser (1984a-b) acknowledged that the light scattering interference fringes formed an intrinsic scale with which the diameter of the sampling cross section could be measured as a function of the scatterer diameter. By counting the number of cycles in the Doppler burst signal, the desired information can be obtained. Although the scatterers will pass the beam on random trajectories, the greatest number of them will pass through the trajectory with the maximum number of fringe crossings, $N_{\max}(d_i)$, followed by a lower likelihood for those scatterers crossing $N_{\max}(d_i) - 1$ fringes, and so on. The maximum number of fringe crossings, $N_{\max}(d_i)$, for the scatterers of diameter d_i, provides the desired beam diameter,

$$D(d_i) = N_{\max}(d_i)\epsilon \tag{10}$$

where the fringe spacing, ϵ, is given by

$$\epsilon = \frac{\lambda}{2 \sin(\gamma/2)} \tag{11}$$

where γ is the beam intersection angle. Since there is a minimum number of fringe crossings required for signal processing, the

actual width, $w(d_i)$, of the measurement cross section which forms the sampling area is,

$$w(d_i) = (y(d_i)^2 - (N_{\min}(d_i)\epsilon)^2)^{1/2} \quad (12)$$

where $N_{\min}$ is the minimum number of cycles required for processing the signals.

This method of determining the width, $w(d_i)$, of the measurement cross section is satisfactory since it does not require, a priori, the knowledge of the optical parameters determining the beam waist diameter except for the intersection angle and laser wavelength.

Bubble Number Density. Local bubble number density can also be determined with the phase Doppler method. Bubble number density is calculated from the measured number of scatterers, N_d, passing the sample cross section,

$$N_d = \frac{1}{A}\sum_{i=1}^{50}\left\{\frac{n_i}{|v_i|}\left(\sum_{j=1}^{n_i}\Delta t_{ij}\right)^{-1}\right\} \quad (13)$$

where the summation is taken over the 50 size bins of the size histogram, A is the cross sectional area of the sample volume, n_i and v_i are the number of bubbles and velocity in the ith bin, and Δt_{ij} is the interarrival time between bubbles of size j in the ith velocity bin. A more detailed coverage of the determination of volume flux and number density is given by Bachalo et al. (1988).

Experimental

The PDPA instrument was configured with the receiver unit located at 60 deg from the forward direction. A He-Ne laser of 20 mW of power was used for all the measurements and a 50 and 25 μm slit on the receiver was imaged accross the probe volume to control the length of the sampling cross section.

In order to validate the theoretical predictions for bubble sizing it was required first to generate a stream of monosize bubbles, a task which proved to be more difficult than that of generating monosize drops. A steady stream of bubbles was generated using a micropipette of 200 μm ID and a syringe pump with a flow rate of 50 cm^3/min. The results are shown on Fig. 9, with a mean bubble size of D_{10} = 1365 μm. Direct photographs of this measurement yielded a mean bubble diameter of D_{10} = 1420 μm, a difference of 3.9 percent. Typical particle size histograms are comprised of 50 size ranges or bins. For this experiment the number density and the volume flux were N_d = 390 cm^3/s and Q_f = 11.5 cm^3/s cm^2, respectively. The experiments were performed using a solution of 1/10 by volume of ethylene glycol and water, which resulted in the production of smaller size bubbles.

Direct photography was used as a mean of verifying the results obtained with the light scattering interferometry method. In the case of large bubbles, $1000 < D_{10} < 1500$ μm, the agreement was within 5 percent in most cases, the worst case being a difference of 8 percent when the bubble formation rate was not as stable yielding a somewhat wider distribution of sizes.

The photographs of the large bubbles formed with the micropipette also showed that at the onset of bubble formation the shape of the bubbles was spherical, however, their morphology progressively evolved into spheroids by the time they reached the scattering probe volume which was located 12 mm above the tip of the micropipette. In the experimental setup, the transmitter and receiver units were located on a horizontal table with the incoming laser beams contained in a vertical plane. The bubbles were issuing vertically upward and moving in a direction perpendicular to the direction of the interference fringes. The major axis of the spheroids was horizontally oriented with their minor (vertical) axis being the dimension measured in this particular setup.

The morphology of large spheroidal bubbles in the range

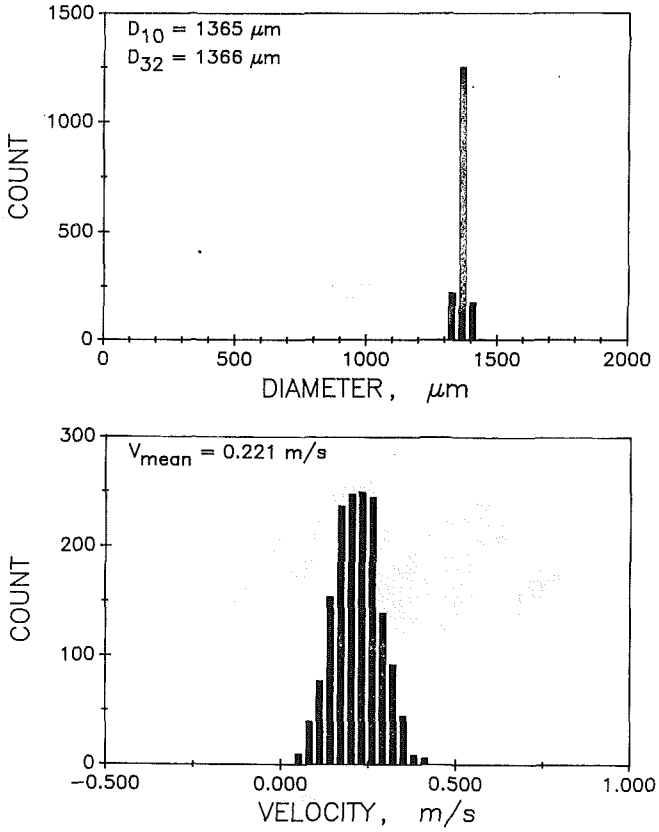

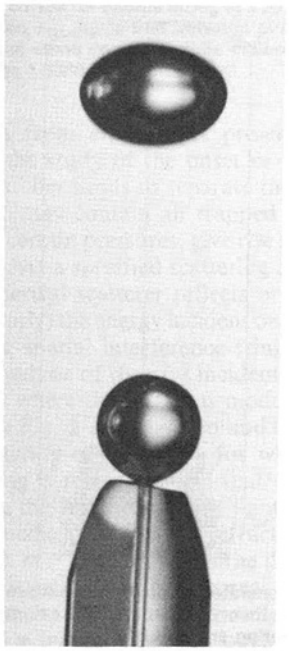

Fig. 9 Comparison of results obtained with the phase Doppler method D_{10} = 1365 μm and direct photography D_{10} = 1420 μm for a stream of monosize bubbles generated with air flowing through a micropipette. The dimension of the spheroid being measured is the minor (vertical) axis.

1400 μm to 1800 μm was also investigated by placing the transmiting and receiving optical units in different planes with respect to the flow direction of the scatterers, such that the major and minor axes of the spheroidal bubbles could be determined. Figure 9 shows a photograph of a spheroidal bubble, the dimension reported D_{10} = 1420 μm corresponds to the minor axis of the scatterer.

A second technique for generating a very steady stream of

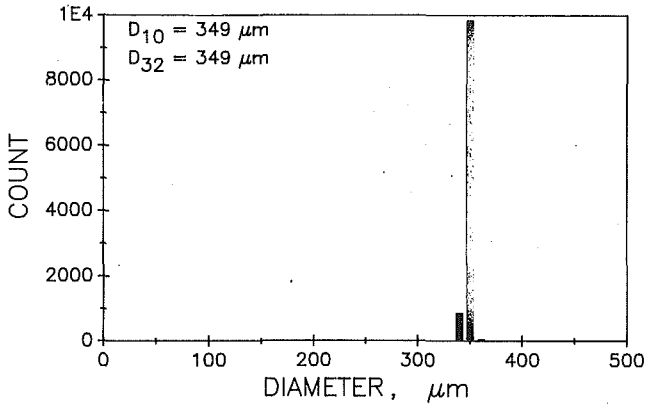

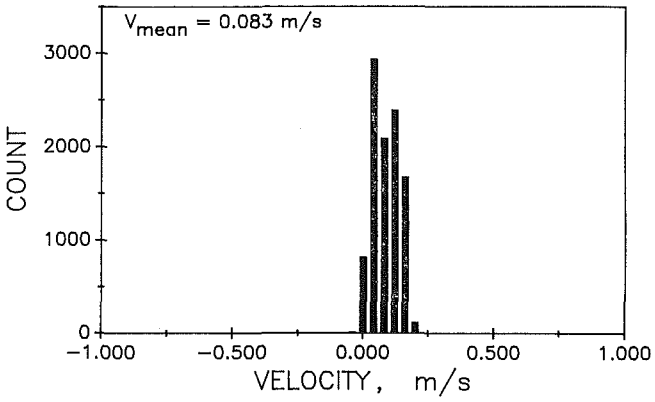

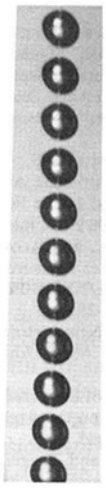

Fig. 10 Comparison of results obtained with the phase Doppler method D_{10} = 349 μm and direct photography D_{10} = 360 μm for a stream of monosize bubbles generated using a thin thermocouple wire inserted in a micropipette and blowing air through it

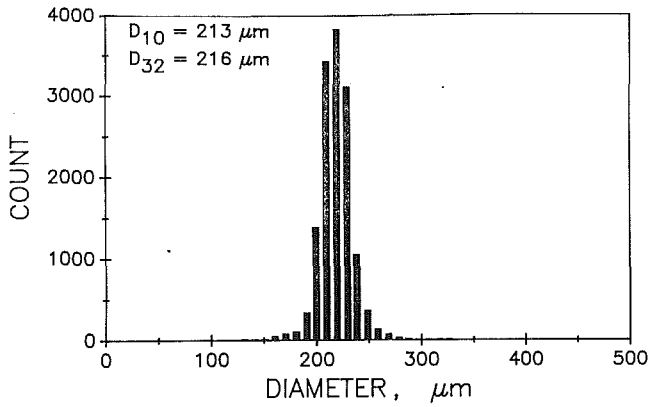

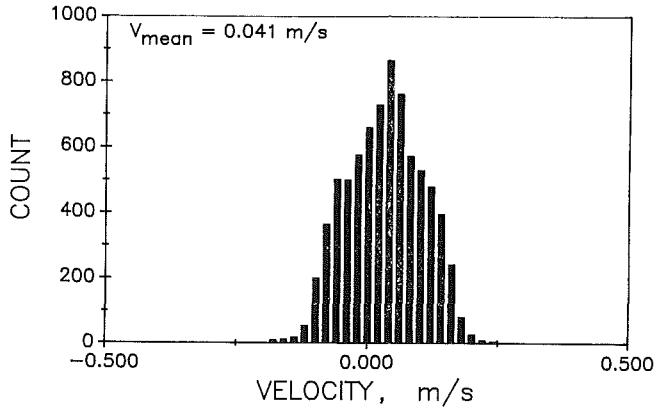

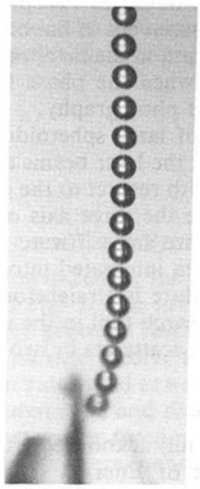

Fig. 11 Comparison of results obtained with the phase Doppler method D_{10} = 213 μm and direct photography D_{10} = 220 μm for a stream of monosize bubbles generated using a thin thermocouple wire inserted in a micropipette and blowing air through it

monosize bubbles consisted of a thin thermocouple wire inserted inside the micropipette (200 μm ID) to reduce the flow area and blowing air through the micropipette. By changing the diameter of the wire different bubble sizes could be obtained in the range of 100 to 400 μm in diameter. Figure 10 shows the results obtained using the phase Doppler method D_{10} = 349 μm, and direct photograph D_{10} = 360 μm for a stream of monosize bubbles. Figure 11 shows a comparison of bubble sizes using this technique of generating bubbles, the mean diameter obtained using photography was D_{10} = 220 μm, the difference with the phase Doppler method is 3.1 percent. In this experiment, the negative velocities in the velocity histogram were caused by an oscillatory movement of the bubbles as they passed through the probe volume. The agreement between the two measuring techniques when using this method of generating bubbles was always better than 95 percent. It is believed that the overall accuracy of the phase Doppler approach for sizing bubbles is better than 97 percent, the measurement innaccuracy of the results presented here in excess of 3 percent can be attributed to the non-uniform generation of monosize bubbles and in using the geometrical optics theory for determining the calibration response curves.

The electrolysis technique was used to generate bubbles in the range from 10 μm to 100 μm in diameter. In the lowest size range a typical histogram of sizes covered bubbles from 6 μm to 30 μm in diameter. Under these conditions the linear mean diameter and the volume mean diameter, measured with the phase Doppler instrument were D_{10} = 17.0 μm and D_{30} = 17.4 μm, respectively. Direct photography yielded $D_{10} \approx 18$ μm. The electrolysis technique for generating small bubbles was

also used as a means of generating a polydispersion of bubble sizes and direct photographs confirmed that the phase Doppler technique was measuring the correct bubble size range with an accuracy of 95 percent.

Conclusions

The results obtained in this investigation show that the phase of the interference fringe pattern can be successfully applied to determine the size and the velocity of the bubbles as well as other relevant parameters such as bubble number density and volume flux. Void fraction can also be determined using this method. It has the advantage over other sizing techniques that very fast data rates can be achieved (150,000 particles/second), velocity information is directly available, and there is no need for calibration of the instrument. Moreover, the method has the capability of discriminating between the light scattering of a bubble and that of a particle from the direction of movement of the scattered interference fringe pattern, therefore, the appropriate validation logic and criteria have been incorporated into the signal processing of the instrument.

A detailed analysis based on the Lorenz-Mie scattering theory and the geometrical optics approximation has given a strong theoretical background and validity to the phase Doppler approach as applied to bubble diagnostics. The inclusion of nonuniform illuminated probe volume, random orientation of the scatterer as it passes through the scattering region, and the spatial and temporal integration of the interference fringe pattern over the collection optics have given the analytical model a unique generality. The investigation resulted in the analytical determination of optimum collection angles and calibration curves, and the experimental measurement of relevant parameters in the study of nuclei in two phase flows. The overall accuracy of the measurement of bubbles covering a size range from 10 μm to 1500 μm in diameter resulted in differences of less than 5 percent when the phase Doppler technique was compared with direct photography.

The morphology of large spheroidal bubbles was also investigated by placing the laser beams and the receiving optics in different planes with respect to the direction of flow of the scatterers to measure the three axis of a spheroidal bubble. Although the hardware and software to fully exploit this capability have not been integrated into the phase Doppler instrument, the procedure is straightforward and promises to offer a powerful research tool in the investigation of the dynamics of spheroidal scatterers in two phase flows.

Acknowledgments

The authors gratefully acknowledge the support of this work by the Department of Energy, Contract No. DE-AC03-88ER80679 with Mrs. Carol Boghosian as Contract Monitor. The authors are also indebted to Mr. Mark Yoneyama and Mr. Martin Holladay for their collaboration in the experimental setup and data reduction phases of this program.

References

Bachalo, W. D., 1980, "Methods for Measuring the Size and Velocity of Spheres by Dual-Beam Light-Scatter Interferometry," *Applied Optics*, Vol. 19, No. 3.

Bachalo, W. D., and Houser, M. J., 1984a, "Analysis and Testing of a New Method for Drop Size Measurement Using Laser Light Scatter Interferometry," Nasa Report No. 174636.

Bachalo, W. D., and Houser, M. J., 1984b, "Development of the Phase Doppler Spray Analyzer for Liquid Drop Size and Velocity Characterization," AIAA Paper No. AIAA-84-1199.

Bachalo, W. D., and Sankar, S. V., 1988, "Analysis of the Light Scattering Interferometry for Spheres Larger than the Light Wavelength," Paper presented at the 4th International Symposium on Applications of Laser Anemometry to Fluid Mechanics, Lisbon, Portugal, July 11–14.

Bachalo, W. D., Rudoff, R. C., and Breña de la Rosa, A., 1988, "Mass Flux Measurements of a High Number Density Spray System Using the Phase Doppler Particle Analyzer," Presented at the AIAA 26th Aerospace Sciences Meeting, Reno, Nev., Jan. 11–14.

Billet, M. L., 1986, "Cavitation Nuclei Measurements with an Optical System," ASME JOURNAL OF FLUIDS ENGINEERING, Vol. 108, Sept. pp. 366–372.

Billet, M. L., 1985, "Cavitation Nuclei Measurements—A Review," Presented at the ASME Cavitation and Multiphase Flow Forum, Albuquerque, NM., June 24–26.

Breña de la Rosa, A., Wang, G., and Bachalo, W. D., 1990, "The Effect of Swirl on the Velocity and Turbulence Fields of a Liquid Spray," Presented at the 35th ASME Gas Turbine and Aeroengine Congress and Exposition, Brussels, Belgium, June 11–14.

Chylek, P., Kiehl, J. T., Ko, M. K., and Ashkin, A., 1980, "Surface Waves in Light Scattering by Spherical and Non-Spherical Particles," *Light Scattering by Irregularly Shaped Particles*, Scheuerman, D., ed., Plenum, New York, p. 153.

Dodge, L. G., and Schwalb, J. A., 1988, "Fuel Spray Evolution: Comparison of Experimental and CFD Simulation of Nonevaporating Spray," Presented at the 33rd ASME Gas Turbine and Aeroengine Congress and Exposition, Amsterdam, The Netherlands, June 5–9.

Gowing, S., McDevitt, T., and Dreyer, J., 1987, "Comparison of Light Scattering and Holographic Techniques for Bubble and Seston Measurements in a Lake," Presented at the ASME Cavitation and Multiphase Flow Forum, Cincinnati, Ohio, June 14–17.

Keller, A., 1972, "The Influence of the Cavitation Nucleus Spectrum on Cavitation Inception," ASME *Journal of Basic Engineering*, Vol. 94, pp. 917–925.

Kohler, R. A., and Billet, M. L., 1981, "Light Scattering by a Nonspherical Particle," Cavitation and Polyphase Flow Forum-1981, ASME, Boulder, Colo.

Kraemer, G., and Bachalo, W. D., 1986, "Evaluation of a Phase Doppler Particle Analyzer for Measuring Dense Sprays from a Gas Turbine Fuel Injector," AIAA/ASME/SAE/ASEE 22nd Joint Propulsion Conference, June 16–18, Huntsville, Ala.

Marston, P. L., Langley, D. S., and Kingsbury, D. L., 1981, "Light Scattering by Bubbles in Liquids or in Glass," Technical Report No. 1, Department of Physics, Washington State University, Sept.

Marston, P. L., 1979, "Critical Angle Scattering by a Bubble: Physical-Optics Approximation and Observations," *Journal of Optical Society of America*, Vol. 69, No. 9, Sept.

McDonell, V. G., and Samuelsen, G. S., 1988, "Evolution of the Two-Phase Flow in the Near Field of an Air-Blast Atomizer Under Reacting and Non-Reacting Conditions," Presented at the Fourth International Symposium on Applications of Laser Anemometry to Fluid Mechanics, Lisbon, Portugal.

O'hern, T. J., d'Agostino, L., and Acosta, A. J., 1988, "Comparison of Holographic and Coulter Counter Measurements of Cavitation Nuclei in the Ocean," Presented at the AIAA/ASME First National Fluid Dynamics Congress, Cincinnati, Ohio, July 24–28.

Oldenziel, D. M., 1982, "A New Instrument in Cavitation Research: The Cavitation Susceptibility Meter," ASME JOURNAL OF FLUIDS ENGINEERING, Vol. 104, June, pp. 136–142.

Saffman, M., 1986, "The Use of Polarized Light for Optical Particle Sizing," Third International Symposium on the Applications of Laser Anemometry to Fluid Mechanics, Lisbon, Portugal, July.

Saffman, M., Buchhave, P., and Tanger, H., 1984, "Simultaneous Measurement of Size, Concentration and Velocity of Spherical Particles by a Laser Doppler Method," Second International Symposium on the Applications of Laser Anemometry to Fluid Mechanics, Lisbon, Portugal, July 2–4.

Sankar, S. V., Weber, B. J., Kamemoto, D. Y., and Bachalo, W. D., 1990, "Sizing Fine Particles with the Phase Doppler Interferometric Technique," *Proceedings of the 2nd International Congress on Optical Particle Sizing*, Tempe, Ariz. Mar. 5–8.

Tanger, H., and Weitendorf, E. A., 1989, "Applicability Tests for the Phase Doppler Anemometer for Cavitation Nuclei Measurements," Presented at the ASME Third International Symposium on Cavitation Inception, San Francisco, Calif., Dec. 10–15.

van de Hulst, H. C., 1957, *Light Scattering by Small Particles*, Wiley, New York.

Yu, P. Y. W., and Varty, R. L., 1987, "Laser-Doppler Measurement of Bubbles Using the Triple-Peak Technique," ASME Third International Symposium on Laser Anemometry, Boston, Mass., Dec. 13–18.

Characterization of Injection Nozzles for Gas-Solid Flow Applications

F. T. Dodge
Institute Engineer.
Fellow ASME

S. T. Green
Senior Research Engineer.
Mem. ASME

J. E. Johnson
Manager.

Department of Fluid Systems,
Southwest Research Institute,
San Antonio, Texas 78228

Laser phase-doppler velocimetry measurements have been used to characterize the particle-gas sprays produced by straight-tube nozzles that simulate idealized fuel injectors for solid fuel combustion systems. Tests were conducted on two nozzle sizes, for two particle sizes, two loading ratios, and two gas velocities. The Reynolds numbers was varied from 9500 to 19000, and the Stokes number from 1.9 to 61.4. It was found that the velocities of the particles in the spray decelerate more slowly, and the velocity profiles are generally more narrow, than for a single-phase free-jet. The turbulence level of the particles in the sprays was found to be less than half the turbulence level of a single-phase free-jet, and the turbulent velocity profiles were not yet fully developed at X = 40D. The hydrodynamic characteristics of the nozzles that are the most important for combustion systems were found to be: (a) the particle spray expands radially at a cone angle of 2° (measured at the radius corresponding to the peak of the particle mass flux distribution); and (b) the nozzle pressure drop and particle mass flow can be related by a correlation that depends on loading ratio, Reynolds number, Stokes number, and the pressure drop coefficient of the nozzle for a single phase flow.

Introduction

Injection nozzles for combustion systems must break up the bulk fuel and deliver it as a spray with sufficient velocity to penetrate and mix with the combustion air, and with sufficient fuel surface area to react with the air in the available residence time. Specifying the characteristics of a nozzle that can accomplish these objectives is not a straightforward task. As a minimum, one should consider (*a*) the fuel mass flow rate as a function of pressure drop, (*b*) the distribution of fuel particle sizes, and (*c*) the spatial distribution of the fuel in the jet. These *hydrodynamic* characteristics are a combined function of the nozzle design and the turbulence properties of a two-phase jet injected into air (Dodge, 1988). In this paper, idealized straight-tube injectors for solid fuel applications are considered. The tests have the dual objective of obtaining (*a*) practical measures of the hydrodynamic performance of the nozzle, for comparison to other nozzle designs, and (*b*) more fundamental data, such as velocity profiles and turbulence levels, for use in validating models of gas-solid sprays. To simplify the data acquisition requirements and any subsequent model verification efforts, the particles used in the tests were monodisperse, micron-size glass beads, which can be well characterized geometrically, rather than, for example, a more random medium such as micronized coal.

Contributed by the Fluids Engineering Division for publication in the JOURNAL OF FLUIDS ENGINEERING. Manuscript received by the Fluids Engineering Division September 17, 1990.

Experimental Facility and Test Procedures

All the tests were conducted in the laminar flow facility shown schematically in Fig. 1. The main components of the facility are the 185-liter pressure vessel which contains the particle reservoir, the particle feeder, the air-particle mixer, and a water droplet generator used as a seeding source for air-only jet velocity measurements, and the 51 cm square by 51 cm long laminar flow test section fitted with optical-grade clear plastic walls. The test nozzles were connected to the air-particle mixer in the pressure vessel by a 1.27 cm dia by 12.7 cm long outlet tube; the diameter of this tube was slightly larger than the diameter of the largest nozzle. To prevent flow recirculation in the test section, a flow of low velocity air ($\approx$ 0.1 m/s) was passed downward through the entire test section, entering and exiting the test section through the upper and lower honeycomb flow straightener panels.

The facility instrumentation included: (*a*) a laser phase-doppler velocimeter (Aerometrics®) to sample the velocity and number density of the particles in the spray; (*b*) a flow meter (located in the air supply line to the pressure vessel) to measure air flow rates into the vessel; (*c*) a rotational speed indicator on the particle feeder motor to measure the mass flow of the particles (by calibration); and (*d*) a pressure transducer located in the pressure vessel to measure the vessel pressure. (The external pressure gage indicated in Fig. 1 was used only for quick estimates.) The velocimeter was mounted on a vertically and horizontally translating table having a minimum position adjustment of 0.0025 cm.

To conduct a test, the air flow into the pressure vessel was

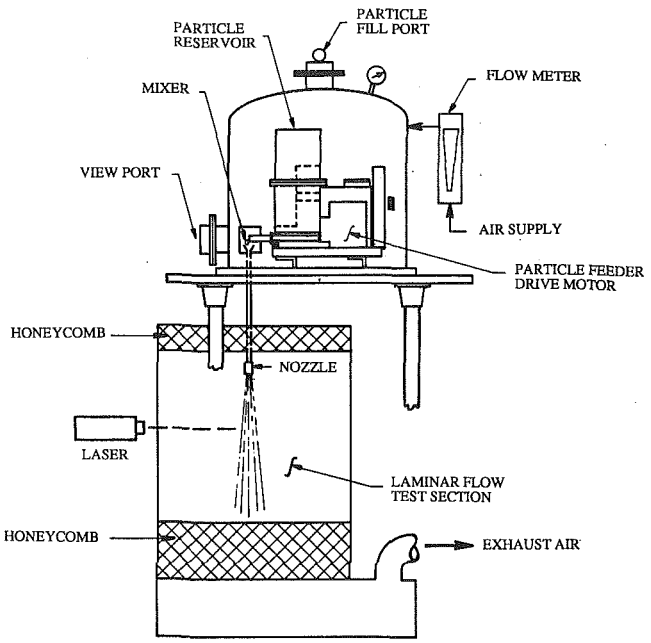

Fig. 1 Apparatus used to test gas-solid nozzles

regulated to the desired value and maintained until the outlet flow through the test nozzle became equal to the inlet flow, as indicated by a steady vessel pressure. The particle feeder was then turned on and regulated. Steady state conditions were assumed when the vessel pressure again stabilized at a higher value. Steady and fluctuating velocities and the number density distribution of the particles were measured at 12 axial locations (1 to 40 nozzle diameters) along the spray centerline and at 8 radial positions across the spray for 4 of the axial locations.

Uncertainty Analysis

By optical measurement, the particle diameters were found to differ from the nominal diameter by less than ±6 percent; over 90 percent of the particles had the nominal diameter. The uncertainties in the measurements of the calibrated pressure tranducer and the air flow meter were less than ±1 percent. The particle feeder motor speed was correlated with particle mass flow rate by direct measurement; the resulting uncertainty in particle mass flow rate injected into the nozzle was also ±1 percent. The position of the velocimeter could be set to ±0.0025 cm, which corresponds to a maximum uncertainty of ±0.5 percent in both the radial and axial directions. The uncertainty in the steady and unsteady velocity measurements is estimated to be ± 5 percent.

The uncertainty in the measurement of particle mass flow in the spray downstream of the test nozzles depends on the sampling techniques inherent in the design and data acquisition system of the laser phase-doppler velocimeter. The velocimeter software rejects particle "counts" for a variety of reasons, such as more than one particle in the sampling volume, the lack of adequate optical purity for a substantial fraction of the glass beads, and the instrument sensitivity to particle size variations. Generallly, the ratio of the number of "accepted counts" to "attempts" for these tests was indicated to be about 0.40. Compounding this counting problem was the need to terminate the measurements in some tests before enough time had elapsed to obtain a completely valid count for regions near the edge of the spray, in order not to deplete the particle reservoir. Altogether, the total mass flow of particles in the spray, as computed from the downstream measurements of particle flux, was found to be only about 50 percent of the particle mass flow injected by the particle feeder into nozzle. Since the measurements thus indicate that the particle mass flow rate was not conserved, the laser phase-doppler velocimeter can be considered to have a *bias* error of about −50 percent. However, the measured mass flow of particles from one downstream location to another for a given test, and between one test and another, never differed by more than 14 percent (i.e., the integrated mass flow was always −50 ±7 percent of the feeder flow rate). This ±14 percent is therefore taken as the *uncertainty* for the measurements of particle mass flow in the spray.

Test Program

Two different straight-tube nozzles were used in the tests. Both nozzles had a length to diameter ratio of ten. For each nozzle, tests were conducted for all combinations of two air velocities, two particle sizes, and two loading ratios. The gas velocities were selected to give the same Reynolds numbers (9500 and 1900) for both nozzles. The particle Stokes number, defined as:

$$\mathrm{St} = \frac{\rho_p d_p^2 U_g}{18 \mu_g L} \tag{1}$$

was also varied systematically from 1.0 to 61.4 to examine the

Nomenclature

A = cross-sectional area of nozzle
C = dimensionless coefficient in Eqs. (3) and (4)
d_p = particle diameter
D = nozzle diameter
K_g = nozzle pressure drop coefficient for gas-only flow
L = nozzle length
$\dot{m}$ = particle flux per unit gas area per unit time
$\dot{m}_p$ = total mass flow rate of particles
R = radial distance from jet centerline
R_{max} = radius at which peak particle flux occurs
$R_{1/2}$ = radius at which $U = 0.5U_c$ for a gas-only jet
Re = Reynolds number based on nozzle diameter
St = Stokes number, Eq. (1)
u = rms value of gas-only jet axial fluctuating velocity
u_p = rms value of particle axial fluctuating velocity
U = velocity of gas-only jet
U_c = centerline velocity of gas-only jet
U_g = cross-sectional average velocity of gas in the nozzle
U_p = particle velocity
$U_{p,c}$ = centerline velocity of particles at axial position X
$U_{p,i}$ = particle velocity at center of nozzle entrance
$U_{p,0}$ = particle velocity at center of nozzle exit
X = axial distance downstream of nozzle exit
Z = loading ratio: mass flow of solids per mass flow of gas
ΔP_g = nozzle pressure drop for gas-only flow
ΔP_{gs} = nozzle pressure drop for gas-solid flow
θ_c = spray cone angle
ρ_g = density of gas phase
μ_g = gas viscosity

Table 1 Parameters used in tests

Reyn. No.	Stokes	Nozzle dia, cm	Particle dia, μm	Gas velocity, m/s	Loading kg solid/kg gas
9500	1.9	0.95	40	15	1, 2
	7.7	0.95	80	15	1, 2
	7.7	0.48	40	30	1, 2
	30.8	0.48	80	30	1, 2
19000	3.8	0.95	40	30	1, 2
	15.4	0.95	80	30	1, 2
	15.4	0.48	40	60	1, 2
	61.4	0.48	80	60	1, 2

influence of aerodynamic forces; the Stokes number range for the two nozzles overlapped. Table 1 summarizes the test program.

Air Jet Characteristics

Steady Velocity Characteristics. Air-only jets, seeded with water particles in order to make laser velocimetry measurements, were used to check the operation and the turbulence level of the facility. The jet centerline velocity was found to agree with the established correlation $U_c/U_\infty = 5.6(D/X)$ to within ± 3 percent for axial locations greater than $8D$, and the velocity profiles at all axial locations $X > 10D$ were found to agree with established correlations to within ± 5 percent [Schlichting, 1979]. The half radius of the jets was found to agree with the established correlation $R_{1/2} = 0.848X$ to within ± 5 percent. This good agreement of the measured steady-flow characteristics with established correlations, the overall small free-stream turbulence level in the test section, and the lack of recirculation cells indicate that the facility operated as desired.

Turbulence Characteristics. The rms value of the fluctuating component of the gas jet axial velocity is shown in Fig. 2. Previous hot wire measurements (Gibson, 1963) for $X = 50D$ are shown for comparison. Although the turbulence distribution for both of the two air velocities employed with each nozzle show a satisfactory correlation, the two sets of distributions do not overlay each other. Furthermore, none of the distributions agree completely with Gibson's hot wire results, but the difference between Gibson's results and the results for the 0.95 cm nozzle is not large. It is concluded that none of the turbulence distributions is fully developed; this conclusion agrees with Schetz (1984) who states that $X/D > 200$ is required for free jets to obtain fully developed, similar profiles.

Particle Velocity Results

Centerline Velocity. The particles entered the test nozzles from the air-particle mixer tube with a relatively low velocity and were accelerated in the nozzle by the higher velocity air flow. None of the nozzles, however, had a sufficiently large enough L/D to accelerate the particles completely to the gas velocity before the particles exited the nozzle. Figure 3, which summarizes all the exit-velocity test results, show that, in fact, the particle exit velocity approximated the gas velocity only for the smallest of the Stokes numbers used in the tests. The exit-velocity data could be correlated reasonably well by an expression derived theoretically for an isolated particle in a uniform flow stream:

$$\ln\left(\frac{1-(U_{c,i}/U_g)}{1-(U_{c,0}/U_g)}\right)+\frac{U_{c,i}}{U_g}-\frac{U_{c,0}}{U_g}=\frac{2}{\mathrm{St}} \qquad (2)$$

as shown in Fig. 3 by the solid line. (Generally, the particle velocity $U_{c,i}$ at the inlet of the test nozzle can be neglected in Eq. (2) in comparison to the exit velocity $U_{c,0}$.) Equation (2) should be satisfactory for design studies of straight-tube nozzles for loading ratios less than about 10.

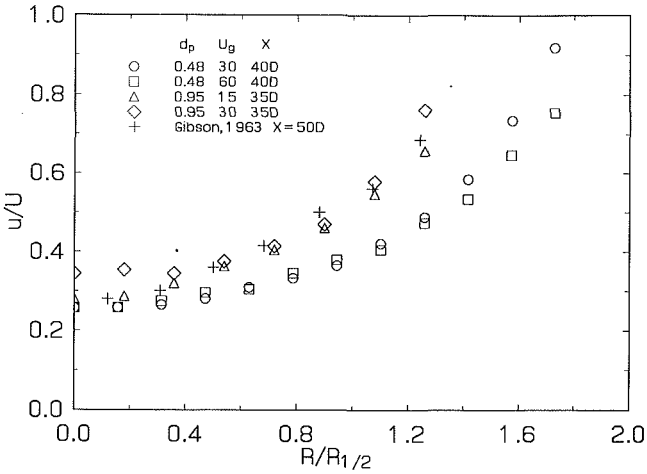

Fig. 2 Turbulent velocity profiles for free jets. (Uncertainty in velocity ratio is ± 3 percent).

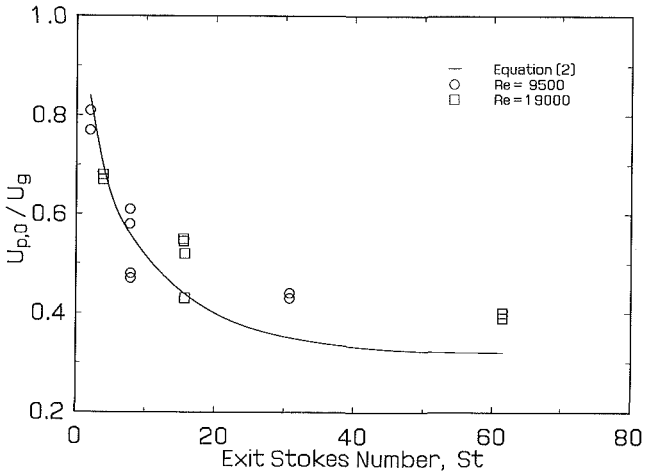

Fig. 3 Nozzle exit velocity of particles for gas-solid jets. (Uncertainty in velocity ratio is ± 3 percent.)

Figure 4 shows the centerline velocity of the particles in the spray, normalized by the particle centerline velocity at the nozzle exit, as a function of downstream distance X divided by nozzle diameter D. Because of the lower exit velocity of the particles relative to the air, aerodynamic drag caused the particles to continue to accelerate for about 10 diameters. Eventually, however, the particles began to decelerate, presumably at the point where their velocity became equal to the corresponding air jet velocity. The deceleration of the 40 μm particles was considerably larger than that of the 80 μm particles because of their smaller ratio of inertia to drag (which is proportional to d_p^2). These centerline velocity profiles are similar to those measured by Shuen et al. (1985), although quantitative comparisons are not possible since Shuen et al., employed smaller particles and gas velocities.

Figure 4 also shows that, for the same particle size, the eventual particle deceleration for the 0.48 cm nozzle is slightly less than the 0.95 cm nozzle. There is no obvious physical reason to explain this behavior. Furthermore, the particle deceleration for the 15 m/s, 40 μm bead tests (0.95 cm nozzle) was about the same as that of a free gas jet, regardless of the particle loading. The particle deceleration for all other cases was, however, less than a free gas jet; in fact, for the 30 and 60 m/s, 80 μm bead tests with the 0.48 cm nozzle, the particle deceleration was almost negligible over the axial distances for

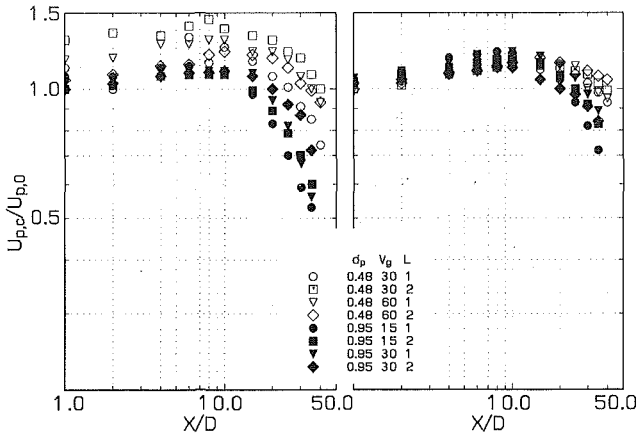

Fig. 4 Particle centerline velocity profiles for gas-solid jets; (*a*) 40 μm particles; (*b*) 80 μm particles. (Uncertainty in velocity ratio is ± 5 percent.)

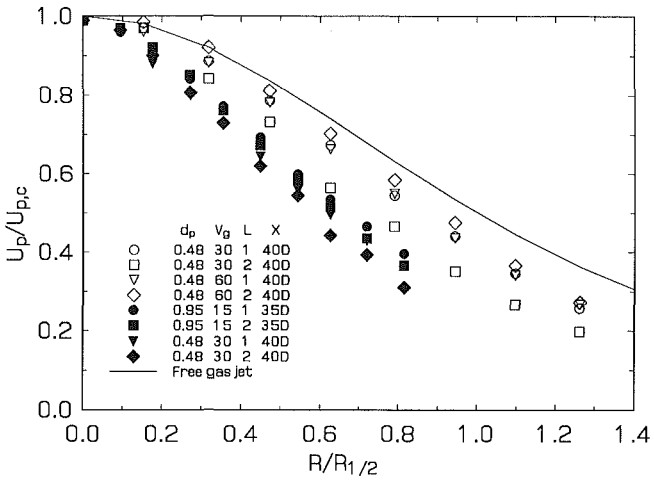

Fig. 5 Particle velocity profiles for gas-solid jets; particle diameter = 40 μm. (Uncertainty in velocity ratio is ± 5 percent.)

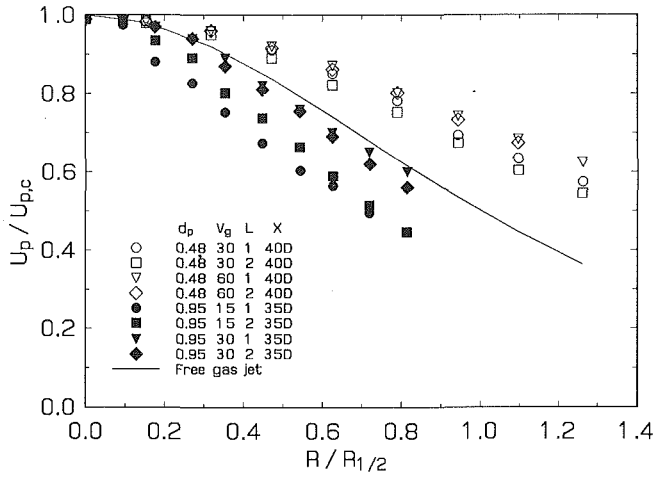

Fig. 6 Particle velocity profiles for gas-solid jets; particle diameter = 80 μm. (Uncertainty in the velocity ratio is ± 5 percent.)

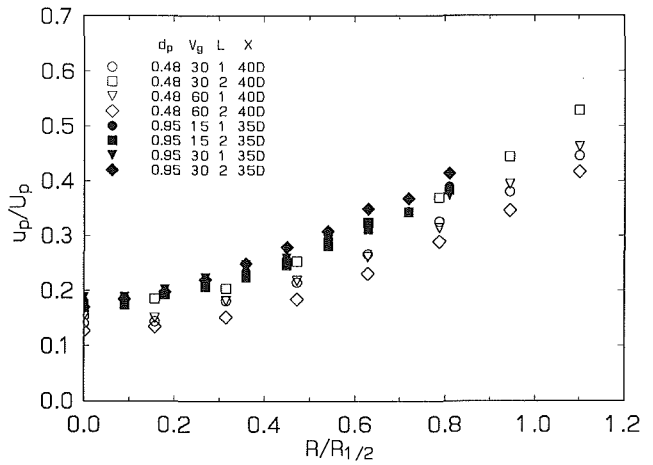

Fig. 7 Particle turbulent velocity profiles for gas-solid jets; particle diameter = 40 μm. (Uncertainty in the velocity ratio is ± 5 percent.)

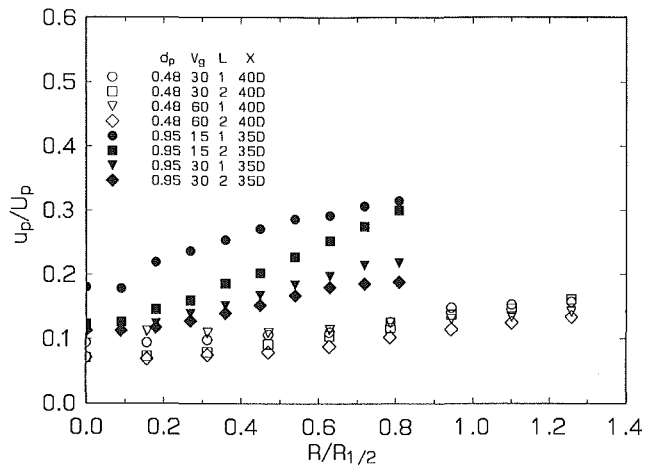

Fig. 8 Particle turbulent velocity profiles for gas-solid jets; particle diameter = 80 μm. (Uncertainty in the velocity ratio is ± 5 percent.)

which measurements were made. Note that the experimental setup did not permit the actual gas velocities in the particle-gas sprays to be measured.

Steady Velocity Characteristics. Figures 5 and 6 show the velocity profiles of the particles across the spray width at a downstream distance of 35D for the 0.95 cm nozzle and 40D for the 0.48 cm nozzle. The radial position is normalized by the half-radius of a free gas jet (i.e., $0.0848X$) in order to make comparisons more evident, and the velocity is normalized by the particle centerline velocity at the axial location. For the 40 μm particles (Fig. 5), it is observed that the profiles for both nozzles are narrower than for a free gas jet, and the individual effects of loading ratio and gas velocity on the profile are comparable. For the 80 μm particles (Fig. 6), the profiles for the 0.48 cm nozzle are considerably wider than for a free jet, whereas they are slightly narrower for the 0.95 cm nozzle. The effect of nozzle diameter on these profiles is pronounced, and for a given velocity and nozzle diameter, there is a somewhat smaller effect of loading ratio. The measurements roughly agree with those of Fleckhaus et al. (1987), Shuen et al. (1985), and Modaress et al. (1984) for tests using similar velocities and particle diameters and with those of Barlow and Morrison (1990) for much smaller velocities.

The data indicate that the steady velocity characteristics of gas-solid jets depend at least on the Stokes number, the Reynolds number, and the loading ratio, and perhaps on the nozzle diameter. Similarity parameters that might help to correlate the data must therefore involve more than just the half-radius and centerline velocity used in single-phase free-jet theory.

Turbulence Characteristics. Figures 7 and 8 show the measured rms values of the fluctuating component of the particle axial velocity for locations $X = 35D$ and $40D$. The overall

turbulence level for all the tests was found to be much less than for the corresponding free gas jet tests. Furthermore, the turbulence level of the 80 μm beads (Fig. 8) was found to be only about one-half that of the 40 μm beads (Fig. 7) for otherwise similar conditions. These profiles are approximately the same shape and the turbulence levels have roughly the same numerical magnitude as those measured by Barlow and Morrison (1990) and Modaress et al. (1984). Just as for the free gas jet, the turbulence profiles were not yet fully developed at $X = 40D$.

Nozzle Pressure Drop. The pressure drop across the nozzle was found to depend on the loading ratio, the Reynolds number, and the Stokes number. Figure 9 summarizes the test results, in terms of the ratio of the gas-solid pressure drop ΔP_{gs} to the gas-only pressure drop ΔP_g for the same air flow rate. Note that the pressure ratio increases with the loading ratio (i.e., with the average density of the flow) when all other conditions are held constant, although the increase is not linear. It also increases with the Reynolds number (i.e., with the momentum change or acceleration of the particles through the nozzle), and decreases slightly with the Stokes number.

The solid lines in Fig. 9 are the predictions of an empirical correlation derived from the data:

$$\frac{\Delta P_{gs}}{\Delta P_g} = 1 + CZ \tag{3}$$

where C is a coefficient that depends on Re and St:

$$C = 1.15 - 0.097\ln(\mathrm{St}) \quad \mathrm{Re} = 19000 \tag{4a}$$

$$C = 0.86 - 0.059\ln(\mathrm{St}) \quad \mathrm{Re} = 9500 \tag{4b}$$

This correlation is based on ideas developed by Crowe and Plank (1984). The correlation coefficient for Eq. (3) is greater than 0.91 for both Reynolds numbers. The tests results do not cover a wide enough range of Re to propose a single correlation.

Particle Flux Distributions. The particle mass flux at a point in the spray is defined as the product of the measured particle velocity, the measured number density, and the particle density; it has dimensions of mass per unit gas area per unit time. Figure 10 shows a typical set of mass flux distributions measured in the tests. In Fig. 10(a), the flux is normalized by the flux at the centerline of the nozzle exit, and the radial location is normalized by the nozzle diameter. This plot clearly illustrates how the actual width of the particle spray varies with downstream distance. In Fig. 10(b), the flux is normalized by the flux at the centerline of the spray at the relevant downstream location, and the radial distance is normalized by downstream distance (analogous to single-phase free-jet theory). These plots, which are similar to those measured by Fleckhaus et al. (1987) and Barlow and Morrison (1990), show that the width of the particle velocity profiles increases less rapidly with X than does the underlying gas jet, whose width increases in proportion to X.

Since the flow area of the spray increases with both radius from the centerline and downstream distance, the profiles shown in Fig. 10 give a distorted spatial picture of the particle mass distribution. A clearer picture can be obtained by adjusting the measurements to compensate for the larger cross-sectional flow area occupied by the particles farther from the nozzle. This adjustment can be accomplished by multiplying the flux at a given radial position by the annular flow area represented by that radius. The adjusted flux at, say, location i is therefore computed as:

$$2\pi \dot{m}_i R_i (R_{i+1/2} - R_{i-1/2})$$

where the $\pm 1/2$ indicate that the annular ΔR_i is centered around the measurement point. The adjusted flux at location R, X is then normalized by the sum of all the adjusted fluxes for that X. (The sum represents the total mass flux of particles measured at that downstream location).

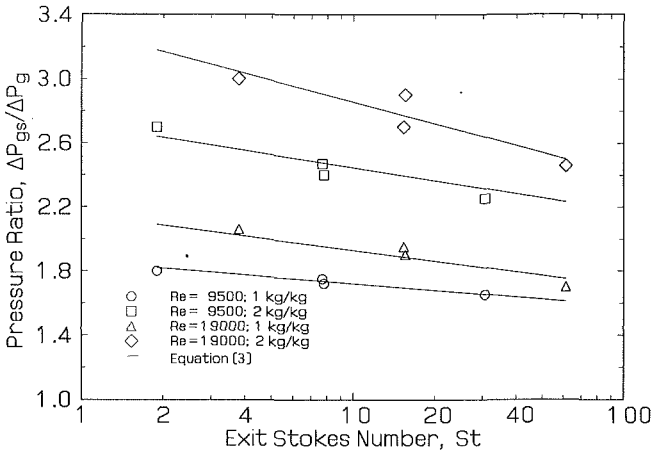

Fig. 9 Nozzle pressure drop for gas-solid flows. (Uncertainty in the pressure ratio is ±0.5 percent.)

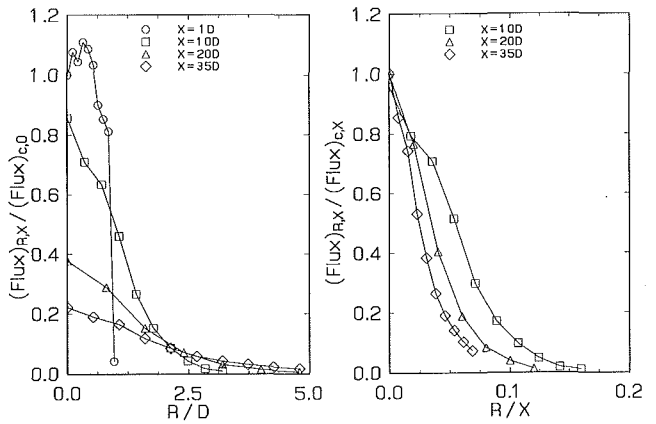

Fig. 10 Particle flux profiles for gas-solid jets; (*a*) 40 μm particle; (*b*) 80 μm particles. (Uncertainty in the flux ratio is ±14 percent)

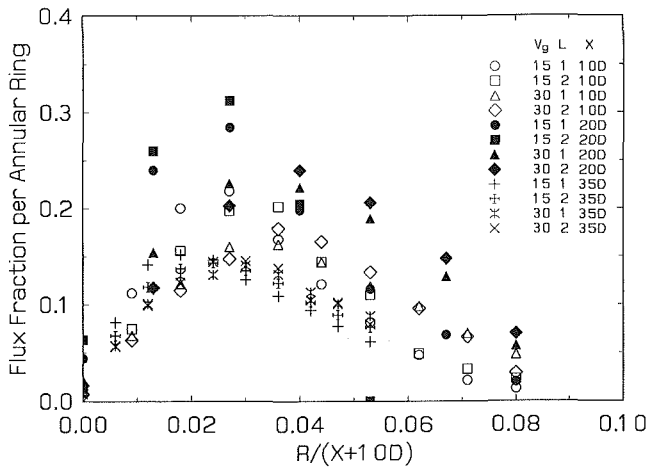

Fig. 11 Particle mass flux fractions for gas-solid jets; nozzle dia = 0.95 cm; particle dia = 40 μm. (Uncertainty in the flux ratio is ±14 percent.)

Plots of these adjusted particle flux distributions suggested that they were "similar" in the sense that the peak of the distribution tended to occur at the same value of R/X for all values of X/D. In fact, further analysis of the data showed that this similarity could be improved significantly by adding an empirically determined development length of about 10D to the downstream distance X. Figures 11 and 12 show some

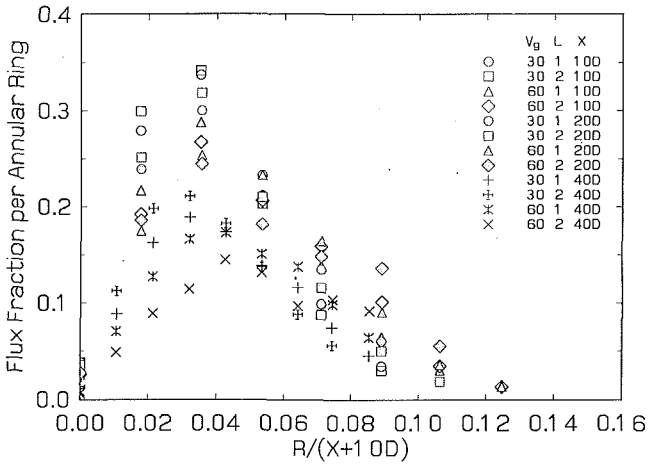

Fig. 12 Particle mass flux fractions for gas-solid jets; nozzle dia = 0.48 cm; particle dia = 80 μm. (Uncertainty in the flux ratio is ± 14 percent.)

typical adjusted distributions plotted against this corrected downstream distance $R/(X+10D)$. Figure 11 represents the "best" correlation of the peak fluxes and Fig. 12 the "worst." For all the data, the radius at which the peak flux occurred was found to be correlated by

$$R_{\max} = 0.0354(X+10D) \tag{5a}$$

with a standard deviation of 0.007. The correlation can be expressed equally well in terms of a spray cone angle θ_c:

$$\theta_c = \tan^{-1}(0.0345) \approx 2° \tag{5b}$$

It should be noted that the values of the mass flux fractions shown in the figures depend on ΔR_i, which varies with axial location. Thus, it is not valid to compare the *magnitudes* of the flux fractions for one X/D to those for another X/D; only the relative shapes of the plotted data have meaning. Similarly, the *sum* of the flux values for the plotted data, and not the *area* under a curve through these values, represents the total particle flux.

Conclusions

The practical conclusions of this study of straight-tube nozzles for gas-solid applications can be summarized as follows. The *particle size* is set by the distribution in the feed stream. (This might not always be the case in applications where agglomeration of the particles can occur.) The virtual *spray cone angle*, which characterizes the position of the maximum particle flux, is constant and equal to 2° for all downstream locations $X > 10D$. The *particle* mass flow is thus the only variable parameter, and it be correlated by a non-dimensional pressure drop, analogous to a valve coefficient, which is a function of Reynolds number, Stokes number, and loading ratio. By manipulating Eq. (3), the mass flow correlation can be expressed in terms of the total mass flow rate of particles $\dot{m}_p$ and the two-phase nozzle pressure drop ΔP_{gs}:

$$\frac{\dot{m}_p Z\sqrt{1+CZ}}{A\sqrt{\rho_g \Delta P_{gs}}} = K_g \tag{6}$$

where K_g is the nozzle pressure drop coefficient for a *single-phase* flow; note that K_g can either be calculated or determined by single-phase flow tests. Typical correlations for C in Eq. (6) are given by Eq. (4). These hydrodynamic characteristics should allow performance comparisons to be made with other nozzle designs.

The particle velocity and turbulence measurements show a complicated dependence on Reynolds number, Stokes number, loading ratio, and (apparently) nozzle diameter. Appropriate similarity parameters that would correlate the results are not evident from these data. Improved theoretical models (e.g., Shuen et al., 1983, 1985) might provide guidance for the choice of similarity parameters. The present data set is more extensive than some others in the literature and is organized so that the same Reynolds number, Stokes number, and loading ratio can be obtained by different combinations of the dimensional parameters; it should therefore be especially useful in evaluating and validating the theoretical models.

Acknowledgment

The work reported here was sponsored by the Morgantown Energy Technology Center of the U.S. Department of Energy as part of the Contract DE-AC21-86MC23005. The advice and help of Mr. Lee G. Dodge at Southwest Research Institute in using the laser phase-doppler anemometer is gratefully acknowledged.

References

Barlow, R. S., and Morrison, C. Q., 1990, "Two-Phase Velocity Measurements in Dense Particle-Laden Jets," *Experiments in Fluids*, Vol. 9, pp. 93–104.

Crowe, C. T., and Plank, D., 1984, "Metering the Flow Rates of Gas-Solid Suspensions Through Venturimeters by Measuring Pressure Drop and Light Attenuation," *Gas-Solid Flows*, ASME Fluid Engineering Division, Vol. 10, pp. 43–46.

Dodge, L. G., 1988, "Representation of Average Drop Sizes in Sprays," *AIAA J. Propulsion and Power*, Vol. 4, pp. 490–496.

Fleckhaus, D., Hishida, K., and Maeda, M., 1987, "Effect of Laden Solid Particles on the Turbulent Flow Structure of a Round Free Jet," *Experiments in Fluids*, Vol. 5, pp. 323–333.

Gibson, M. M., 1963, "Spectra of Turbulence in a Round Jet," *J. Fluid Mechanics*, Vol. 15, pp. 161–173.

Modaress, D., Tan, H., and Elghobashi, S., 1984, "Two-Component LDA Measurement in a Two-Phase Turbulent Jet," *AIAA J.*, Vol. 22, pp. 624–630.

Schetz, J. A., 1984, *Foundations of Boundary Layer Theory*, Chapter 8, Prentice-Hall, Englewood Cliffs.

Schlichting, H., 1979, *Boundary Layer Theory*, 7th edition, Chapter 24, McGraw-Hill, New York.

Shuen, J.-S., Chen, L-D, and Faeth, G. M., 1983, "Evaluation of a Stochastic Model of Particle Dispersion in a Turbulent Round Jet," *AIChE J.*, Vol. 29, pp. 167–170.

Shuen, J-S, Solomon, A. S. P., Zhang, Q-F, and Faeth, G. M., 1985, "Structure of Particle-Laden Jets: Measurements and Predictions," *AIAA J.*, Vol. 23, pp. 396–404.

Experimental and Analytical Study of Flow Diversion Beyond an Underexpanded Nozzle

E. C. Hansen
Assistant Professor,
Mechanical Engineering,
University of Florida,
Gainesville, FL

A steady-state flow apparatus was used to investigate the process of gun gas diversion through a single hole perforated disk diverter. The amount of diverted flow was found to depend on the distance between the nozzle and the diverter disk and the ratio of nozzle pressure to diverter exit pressure. Experimental studies used nitrogen and carbon dioxide as the working fluids to show the effect of specific heat ratio. At ratios of nozzle pressure to ambient pressure ranging from 4 to 60 diversion efficiencies of 50 to 99 percent were produced. A one-dimensional analytic gas flow model was developed. Results of the analytic model paralleled the experimental data for pressure ratios over 10.

Introduction

The flow diversion beyond an underexpanded free jet is of interest in ballistics. After a projectile leaves the muzzle of an aircraft cannon, the gun gas inside the barrel discharges into a region about 20 feet beyond the muzzle. When multiple firings occur in flight, the concentration of gun gas in this region increases and can produce secondary flash as described by Heiney and Powers (1977) and Carfagno (1961). Diversion of the gun gas away from the front of the gun and the aircraft's engines is desirable. Muzzle devices that divert the gun gas or suppress secondary flash are discussed by Schmidt (1988) and Yates et al. (1983). The gun gas is diverted by turning it 90 degrees or more.

There are few quantitative measurements available which indicate the ability of such devices to divert flow. Most analytical models deal with forces on the diverter rather than the fraction of mass flow that can be diverted. Hansen (1988) proposed that the effectiveness of the gun gas diversion depends on the geometry of the diversion device and the pressure at the underexpanded muzzle. The effectiveness of a gun gas diverter is defined as the ratio of the mass flow being diverted to the mass flow leaving the gun barrel. One simple gun gas diverter geometry is a flat disk placed in front of and normal to a gun barrel. The disk has a hole that is in line with the barrel so the projectile can pass through. This geometry is the basis for most gun gas diverters. Designers often use this type of geometry with modifications to meet their special needs.

Experimental data and analytical models of diversion effectiveness are not currently available to the diverter designer. The objective of this work was to provide experimental data and an analytical model of the diversion effectiveness. The geometry of the muzzle device used in this study was a single hole perforated disk.

Contributed by the Fluids Engineering Division for publication in the JOURNAL OF FLUIDS ENGINEERING. Manuscript received by the Fluids Engineering Division June 13, 1990.

Experimental Procedure and Apparatus

Tests were not conducted with an actual gun because of the difficulty of measuring the flow out the diverter hole that is in line with the projectile travel. Gas flow from a gun was modelled using a steady flow of high pressure gas into a single hole perforated disk diverter.

Figure 1 shows a cross section of the geometry of the test fixture. The simulated muzzle was a 1.59 mm (0.0625 in.) diameter sonic nozzle. This hole was placed at the center of a 89 mm (3.5 in.) diameter disk. Downstream of the sonic nozzle

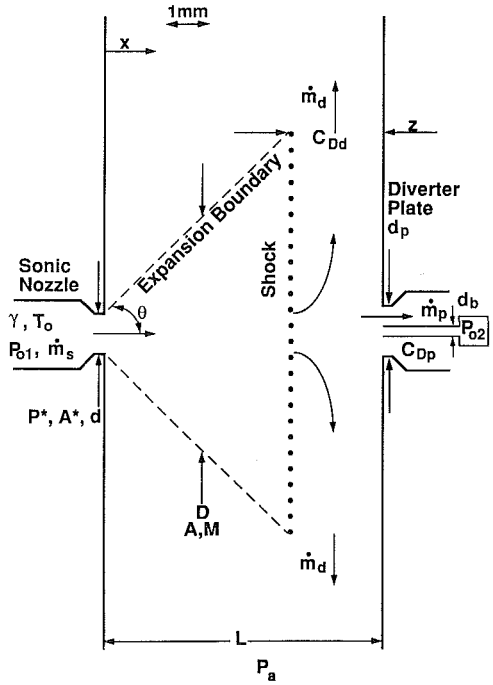

Fig. 1 Steady flow gas diverter apparatus

was a 1.98 mm (0.078 in.) hole in another 89 mm (3.5 in.) diameter disk. The downstream hole is 25 percent larger than the sonic nozzle to allow a yawed projectile to still pass through the hole. Only one set of hole sizes was used. The disks were attached to one another by guide rods that allowed adjustment of the separation distance and also assured that the two holes remained in line. Standard gas cylinders supplied the test gases, nitrogen, and carbon dioxide. To obtain the pressures and flow rates needed in this experiment no pressure regulators were used.

The mass flow rates through the sonic nozzle and through the perforated disk were treated as flows through sonic nozzles. The mass flow rate through such nozzles are functions of the specific heat ratio, the gas constant, the stagnation pressure, the throat area, the discharge coefficient, and the stagnation temperature. For a constant specific heat ratio, the mass flow rate is given by Holman (1989) as,

$$\dot{m} = C_D P_0 A \left(\frac{\gamma}{RT_0}\right)^{0.5} \left(\frac{2}{\gamma+1}\right)^{\frac{\gamma+1}{2(\gamma-1)}} \quad (1)$$

A 5000 psi Gould-Statham PA-4099-5M strain gage type transducer measured the stagnation pressure to the sonic nozzle. The stagnation pressure of the fluid passing through the 1.98 mm (0.078 in.) hole was measured using a 0.71 mm (0.028 in.) diameter stagnation tube connected to a 500 psi Electro Development Corporation strain gage pressure transducer. The stagnation pressure of the diverted flow was measured by a Validyne 10 psid pressure transducer connected to a 0.71 mm (0.028 in.) diameter stagnation tube positioned at 44.5 mm (1.75 in.) from the axis of flow and between the two 89 mm diameter disks.

The stagnation temperature was not measured. It was not needed to calculate a ratio of mass flow rates because the stagnation temperature, T_0, was the same at all measuring locations.

A Rapid Systems digital oscilloscope recorded the three pressure measurements as a function of time. Because of the large flow rate, the gas cylinder was emptied after several minutes of operation. The varying pressure as the cylinder emptied through the sonic nozzle produced a variation of the nozzle to ambient pressure ratio. Nitrogen and carbon dioxide gases provided specific heats ratios of 1.4 and 1.29. Typical gun gas has a specific heat ratio of about 1.24.

Theoretical Model

A shadowgraph of the diversion process shows the rapid expansion and shock downstream of the sonic nozzle, Fig. 2. The expansion process is much like a cone as seen in Schmidt (1988) and Crist et al. (1966). Adamson and Nicholls (1959) describe how the cone shape is modified by expansion waves to produce a bottle type of shape. The area ratio produced by such a shape is less than that of a straight cone. A strong nearly normal shock occurs just upstream of the diverter plate.

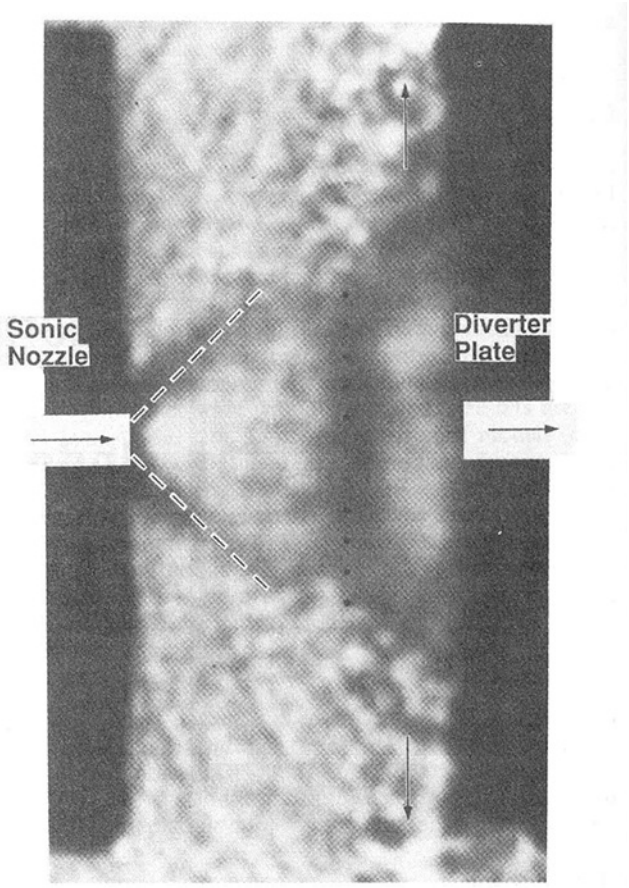

Fig. 2 Shadowgraph of gas diversion process at a pressure ratio of 65.7 and disk distance, L/d = 7

The following is a description of how the actual flow in Fig. 2 is modelled as the idealized flow shown in Fig. 1. The flow expands isentropically from the sonic nozzle to a supersonic velocity. The flow then passes through a normal shock that dissipates much of the stagnation pressure. Most of the flow turns and exits radially through the area between the shock and the diverter plate. The undiverted flow passes through the diverter plate hole.

The jet downstream of the underexpanded sonic nozzle approximately forms a cone of half angle θ.

Nomenclature

A = cross-sectional area of conical jet downstream of sonic nozzle
A^* = area of sonic nozzle
C_D = discharge coefficient
C_{Dd} = discharge coefficient of the diverted flow
C_{Dp} = discharge coefficient of the flow through the diverter disk (plate)
d = diameter of sonic nozzle
d_b = blockage diameter
d_p = diameter of hole in diverter disk (plate)
D = diameter of jet downstream of sonic nozzle
L = distance from the sonic nozzle to the downstream diverter disk
$\dot{m}_s$ = mass flow rate from sonic nozzle
$\dot{m}_p$ = mass flow rate through diverter disk
$\dot{m}_d$ = mass flow rate diverted
M = Mach number downstream of the sonic nozzle just before the normal shock
M_b = Mach number at jet boundary
P^* = static pressure at sonic nozzle
P_a = ambient pressure
P_{o1} = stagnation pressure in sonic nozzle and before normal shock
P_{o2} = stagnation pressure after normal shock
R = gas constant
T_o = stagnation temperature
x = distance downstream of the sonic nozzle
z = distance between the normal shock and the diverter disk
γ = specific heat ratio
η = diversion effectiveness
θ = 1/2 cone angle of the expansion beyond the sonic nozzle

$$\frac{D}{d} = 1 + 2\frac{x}{d}\tan\theta \tag{2}$$

The conic expansion is only an approximation that is good at large P^*/P_a ratios and at low L/d ratios. Because of the actual bottle shape of the expansion, the cone shape over predicts the expansion and so over predicts the diversion effectiveness. The angle, θ, is the angle through which the flow turns to adjust to the ambient pressure condition just outside the nozzle. The Mach number at the boundary, M_b, is supersonic. The angle (Prandtl-Meyer angle) of the flow, θ, depends upon M_b and the specific heat ratio of the gas, γ, (Owczarek, 1968).

$$\theta = \left(\frac{\gamma+1}{\gamma-1}\right)^{0.5} \arctan\left\{\left[\frac{\gamma-1}{\gamma+1}(M_b^2-1)\right]^{0.5}\right\} - \arctan(M_b^2-1)^{0.5} \tag{3}$$

At the jet boundary the pressure changes from P^* to P_a and the Mach number increases from 1 to M_b. The flow is assumed to be isentropic.

$$M_b = \left\{\left[\left(\frac{P^*}{P_a}\right)^{\left(\frac{\gamma+1}{\gamma}\right)} \frac{\gamma+1}{2} - 1\right]\frac{2}{\gamma-1}\right\}^{0.5} \tag{4}$$

The flow expands in an approximate cone to Mach numbers of from 2 to 6. The area ratio is a result of the expansion process.

$$\frac{A}{A^*} = \left(\frac{D}{d}\right)^2 \tag{5}$$

Isentropic flow with area change gives a relationship between the Mach number, M, within the cone and the area ratio. There is a Mach number distribution across the cone diameter, D. The present analysis assumes there is a core flow across D which can be characterized by a single Mach number (Owczarek, 1968).

$$\frac{A}{A^*} = \frac{1}{M}\left(\frac{1+\frac{\gamma-1}{2}M^2}{\frac{\gamma+1}{2}}\right)^{\frac{\gamma+1}{2(\gamma-1)}} \tag{6}$$

The flow continues to expand until it passes through a normal shock. The stagnation pressure drops across the shock based on the upstream Mach number, M, (Owczarek, 1968).

$$\frac{P_{o2}}{P_{o1}} = \frac{\left[\frac{(\gamma+1)\frac{M^2}{2}}{1+(\gamma-1)\frac{M^2}{2}}\right]^{\frac{\gamma}{\gamma-1}}}{\left[\frac{2\gamma M^2}{(\gamma+1)} - \frac{(\gamma-1)}{(\gamma+1)}\right]^{\frac{1}{\gamma-1}}} \tag{7}$$

The shock stands upstream of the second disk by the distance z with enough cross-sectional area to pass the diverted mass flow. This flow through the cylindrical cross-sectional area between the disk and the shock is assumed to be choked. The flows through the sonic nozzle and the second disk hole are also both assumed to be choked. The mass flow through each of these three areas was determined using Eq. (1). The discharge coefficient C_D of the sonic nozzle was assumed to be 1. The discharge coefficient of the nozzle at the diverter disk, C_{Dp}, was assumed to be 0.6 which is typical of a square edged orifice.

The discharge coefficient of the choked flow between the shock and the diverter disk was assumed to have a range between 0.6 and 1.0. This range represents types of flow conditions between an orifice plate (C_D = 0.6) and a smooth nozzle (C_D = 1.0). The choked flow between the shock and the diverter disk has the characteristics of an orifice plate flow when flow crosses the shock and then turns 90 degrees. However, along the diverter plate the flow is parallel to the boundary surface and is similar to nozzle flow. The assumed range of discharge coefficient produces a range of the theoretical answer. The specific heat ratio, the gas constant and the stagnation temperatures were assumed the same at each location. The ratio of mass flow rates is only a function of the stagnation temperature, the discharge coefficient, and the cross sectional area as given in Eq. (1). P_{o2} is assumed to be the stagnation pressure of the diverted flow and of the flow through the diverter disk hole. A mass balance around the diverter produces a relationship for the shock to disk distance, z. Blockage of the probe at the diverter disk hole was accounted for.

$$\frac{z}{d} = \frac{d}{D}\frac{\left(\frac{P_{o1}}{P_{o2}C_{Dd}} - \frac{d_p^2-d_b^2}{d^2}\frac{C_{Dp}}{C_{Dd}}\right)}{4} \tag{8}$$

The shock to disk distance determines the area ratio at which the shock occurs.

$$\frac{A}{A^*} = \left(\frac{d}{D}\right)^2 = \left(1 + 2\frac{L-z}{D}\tan\theta\right)^2 \tag{9}$$

When solved explicitly, Eqs. (3) and (4) determine the cone half angle. The implicit solution of Eqs. (5)–(9) provides the shock to disk distance, z, and the stagnation pressure ratio across the shock. The stagnation pressure change across the shock is the physical phenomenon which determines the diversion effectiveness. If the shock is weak, the stagnation pressure decreases slightly and much of the flow is undiverted and passes through the diverter disk hole. If the shock is very strong, the stagnation pressure is greatly reduced and much of the flow is diverted.

Results

The mass fraction diverted or diversion effectiveness is the performance measure of a diverter and is calculated as $1 - \dot{m}_p/\dot{m}_s$.

$$\eta = 1 - \left(\frac{d_p^2-d_b^2}{d^2}\right) C_{Dp}\frac{P_{o2}}{P_{o1}} \tag{10}$$

Two parameters, the pressure ratio, P^*/P_a, and the disk to disk length ratio, L/d, govern the diversion effectiveness. The pressure ratio is the ratio of the static pressure at the sonic nozzle exit to the stagnation pressure at the exit of the diverter. The length ratio is the ratio of the distance between disks to the diameter of the sonic nozzle.

The following figures show experimental and theoretical diversion effectiveness as a function of pressure ratio and length ratio. The bounds about the experimental data come from the uncertainty of the pressure measurements and indicate the experimental uncertainty of the measurements at 99 percent confidence limits. The range of the analytical model depends upon C_{Dd}, which was estimated to be between 0.6 and 1.0, as discussed earlier.

Figure 3 contains the results of the nitrogen tests. The smallest diverter had a length ratio equal to one and the lowest diversion effectiveness. The trends between theory and experiment were similar. The diversion effectiveness rose quickly as the pressure ratio increased and soon reached a plateau. The agreement between theory and experiment increased with pressure ratio. This probably indicates that at higher pressure ratios a cone better represents the flow expansion.

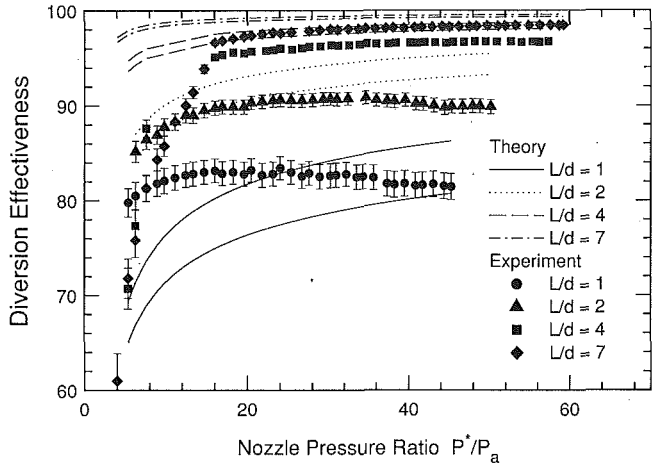

Fig. 3 Experimental diversion effectiveness compared with the range predicted by the analytical model for disk to disk distances of *L/d* = 1, 2, 4, and 7 using nitrogen, γ = 1.4

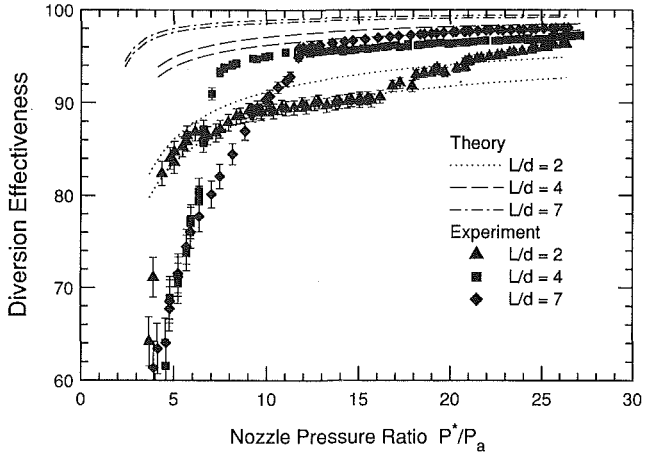

Fig. 4 Experimental diversion effectiveness compared with the range predicted by the analytical model for a disk to disk distance of *L/d* = 2, 4, and 7 using carbon dioxide, γ = 1.29

Theory and experiment agree quite well for the length ratio of 2. The diversion effectiveness rises quickly to a plateau. The effectiveness at the plateau is 7 to 8 percent higher than that at a length ratio of 1. Higher diversion was a result of more flow expansion in the longer diverter. The expansion produced a higher Mach number before the shock and a lower stagnation pressure after the shock. Because the stagnation pressure was lower at the hole in the second disk, the undiverted flow rate was smaller.

At the higher length ratio of 4 the diversion effectiveness again increased. When the pressure ratio was greater than 10, the theory nearly paralleled the experiment. The length ratio of 7 produced almost complete diversion, 98 percent. The agreement was good when the pressure ratio was greater than 15. At higher pressure ratios the flow expands in a more conical fashion. The expansion of the flow at low pressure ratios resembles a bottle more than a cone and reduces the diversion effectiveness. This means that in general the theory tends to overpredict the diversion effectiveness.

The second series of tests, Fig. 4, used carbon dioxide, γ = 1.29, to determine the effect of specific heat ratio. The highest pressure ratios were lower than those in the nitrogen test, because the maximum supply pressure was lower in the carbon dioxide cylinder. The results of theory and experiment, as shown in Fig. 4, parallel each other. Below a certain pressure ratio theory and experiment seem to diverge. At length ratios of 4 and 7 those pressure ratios were 7 and 12, respectively. The results shown in Fig. 3 are very similar to Fig. 4. This indicates that the specific heat ratio has little affect on the diversion effectiveness. A decrease of specific heat ratio from 1.4 to 1.29 may only increase the diversion effectiveness by 1 or 2 percent.

Conclusions

1. Diversion efficiencies of greater than 90 percent are achievable using a single hole perforated disk diverter with L/d = 2 to 7 and muzzle pressure ratio greater than 12.
2. Pressure ratios above 15 have little affect on the diversion effectiveness. Pressure ratios below 15 begin to significantly decrease the diversion effectiveness.
3. Decreasing the specific heat ratio from 1.4 to 1.29 may increase the diversion effectiveness by only 1 to 2 percent.

Acknowledgments

This work was sponsored by the Air Force Office of Scientific Research, Bolling AFB, DC. Their support was greatly appreciated. Gratitude is also expressed to God for His grace and wisdom during this work.

References

Adamson, T. C., and J. A. Nicholls, 1959, "On the Structure Of Jets From Highly Underexpanded Nozzles Into Still Air," *Journal of the Aerospace Sciences*, Vol. 26, pp. 16-24.

Carfagno, S. P., 1961, *Handbook on Gun Flash*, Franklin Institute.

Crist, S., Sherman, P. M., and D. R.Glass, 1966, "Study of the Highly Underexpanded Sonic Jet," *AIAA Journal*, Vol. 4, No. 1, pp. 68-71.

Hansen, E. C., 1988, "Final Report—Advanced Gun Gas Diversion," Universal Energy Systems and Air Force Office of Scientific Research.

Heiney, O. K., and R. J. Powers, 1977, "Secondary Muzzle Gas Combustion Considerations in Aircraft Cannon," 14th JANNAF Combustion Meeting.

Holman J. P., 1989, *Experimental Methods for Engineers*, Fifth Edition, McGraw-Hill, pp. 244-245.

Owczarek, J. A., 1968, *Fundamentals of Gas Dynamics*, International Textbook Company, Scranton, PA, pp. 472-481.

Schmidt, E. M., 1988, "Muzzle Flow Gas Dynamics," *Gun Propulsion Technology*, ed. L. Stiefel, *Progress in Astronautics and Aeronautics*, Vol. 109, p. 161.

Yates, J., Robinson, R. E., and J. C. Kennedy, 1983, Test Report for XPD Gun-Gas Diverter, A-10 SPO 19.

Computational Analysis of the Transonic Flow Field of Two-Dimensional Minimum Length Nozzles

B. M. Argrow
Assistant Professor.

G. Emanuel
Professor.

School of Aerospace and Mechanical Engineering, The University of Oklahoma, Norman, OK 73019

The method of characteristics is used to generate supersonic wall contours for two-dimensional, straight sonic line (SSL) and curved sonic line (CSL) minimum length nozzles for exit Mach numbers of two, four and six. These contours are combined with subsonic inlets to determine the influence of the inlet geometry on the sonic-line shape, its location, and on the supersonic flow field. A modified version of the VNAP2 code is used to compute the inviscid and laminar flow fields for Reynolds numbers of 1,170, 11,700, and 23,400. Supersonic flow field phenomena, including boundary-layer separation and oblique shock waves, are observed to be a result of the inlet geometry. The sonic-line assumptions made for the SSL prove to be superior to those of the CSL.

1 Introduction

A minimum length nozzle (MLN) is a supersonic nozzle designed to produce an inviscid uniform flow with a minimum ratio of nozzle length to throat height (Argrow and Emanuel, 1988; Emanuel, 1986). In contrast to the smoothly contoured throat of more conventional nozzles, the MLN is characterized by a sharp throat. As a result, it is often referred to as a sharp-corner nozzle (Shapiro, 1953), a nozzle with a sharp-edged throat (Vanco and Goldman, 1968), a nozzle with a corner point (Pirumov and Roslyakov, 1978) or a rapid expansion nozzle (Greenberg et al., 1972).

Engineering applications of the MLN have been primarily limited to the gasdynamic laser (GDL) (Anderson, 1976; Emanuel, 1986; Greenberg et al., 1972; Wada et al. 1987; Wagner, 1971). Although the MLN was originally conceived for supersonic wind tunnels, it has never been widely used in this application. Evidently, the presence of a sharp corner at the throat was expected to result in flow separation (Dumitrescu, 1975; Wagner, 1971) and high heat transfer rates. However, GDL applications (Anderson, 1976; Greenberg et al., 1972; Wagner, 1971) and one wind tunnel application (Dumitrescu, 1975) have shown that the MLN can produce a uniform flow without separation. Recently, conceptual designs of the national aerospace plane have included the MLN as an integral component of the propulsion unit (Bae and Emanuel, 1991).

The MLN exists for both two-dimensional and axisymmetric geometries. Classical MLN theory uses two sonic-line models to start the calculation that determines the supersonic wall contour. The first assumes a straight sonic line and is referred to as the straight sonic line (SSL) MLN (Anderson, 1976, 1982; Argrow, 1986, 1988; Argrow and Emanuel, 1988; Emanuel, 1986; Greenberg et al., 1972; Nachshon, 1983; Pirumov and Roslyakov, 1978; Sadaat, 1982; Shapiro, 1953; Vanco and Goldman, 1968; Wada et al., 1987; Wagner, 1971). The second assumes a curved (circular arc) sonic line and is referred to as the curved sonic line (CSL) MLN (Argrow 1989; Argrow and Emanuel, 1988; Bae and Emanuel, 1991; Dumistrescu, 1975; Emanuel, 1986; Foelsch, 1949). Once the sonic-line shape is chosen, the remainder of the inviscid, supersonic flow field, including the wall contour, is generally computed analytically or with the method of characteristics (MOC).

The transonic flow field of supersonic nozzles with smooth throat contours has been extensively studied. Brown and Hamilton (1976) present a survey of the methods of nozzle flow analysis. This survey includes both analytical (series expansion) and computational (finite element, time dependent, relaxation, etc.) methods. Of these, the series-expansion and time-dependent methods have proven to be the most successful.

A large number of series-expansion methods have been used to predict transonic nozzle flow (Ahlberg et al., 1961; Brown and Hamilton, 1976; Dutton and Addy, 1981; Hall, 1962; Hopkins and Hill, 1966; Kliegel and Levine, 1969; Oswatitisch and Rothstein, 1949; Pirumov and Roslyakov, 1978; Sauer, 1947). In most instances, the solutions from these methods rapidly deteriorate as the throat radius of curvature r_{th} (all linear dimensions are normalized by the throat half-height h) becomes small ($r_{th} < 2$). However, some of these methods have proven to be accurate even for $r_{th} < 1$.

Pirumov and Roslyakov (1978) analyze the transonic flow field of a nozzle with a corner point. The inviscid, transonic flow field is first computed analytically for a nozzle without a corner point. This solution is used to provide "starting characteristics" for a MOC calculation that begins upstream of a

Contributed by the Fluids Engineering Division for publication in the JOURNAL OF FLUIDS ENGINEERING. Manuscript received by the Fluids Engineering Division July 31, 1990.

contour with a corner point. Thus, they assume that the sonic line begins upstream of the corner point.

Brown and Hamilton (1976) discuss several time-dependent methods. Included in their discussion are the methods of Laval (1971), which computes the inviscid flow field for nozzles with r_{th} as small as 0.1, and Cline (1974), which employs the MacCormack finite-difference scheme. Cline (1976, 1981) later expanded his method to include viscous nozzle calculations.

Other recent computational studies of transonic nozzle flows include the relaxation methods presented by Brown et al. (1977) and Baker (1981). Also, Park and Caughey (1986) present a finite-volume method.

Wada et al. (1987) perform a computational analysis of several GDL nozzle geometries including a MLN. The authors reference Shapiro (1953), which implies a two-dimensional SSL, MLN, and they refer to their result as a shock-free MLN. For their analysis they compute inviscid, quasi-one-dimensional and two-dimensional solutions to examine the effects of the various nozzle geometries on GDL performance. From this analysis, they determine that the MLN geometry is superior to the other configurations.

Very little experimental data exist for the MLN. In a series of experiments, Back et al. (1965, 1967, 1969, 1972), Back and Cuffel (1966, 1971), Back and Massier (1972) and Cuffel et al. (1969) present results for the transonic flow of conical nozzles with r_{th} as small as 0.625 and an inlet convergence angle α as large as 75 deg. Although these nozzles are not MLNs, they do provide valuable insight into the effects of α and a relatively small r_{th} on the transonic flow field.

Ahlberg et al. (1961) apparently present a plot of the experimental pressure distribution for a portion of a MLN used in a cold-flow experiment. Unfortunately, there is no indication of the MLN type or the exit Mach number for which it was designed.

Wagner (1971) provides extensive experimental data for a two-dimensional MLN array that models an array used in a GDL. However, the focus of the experiment is on the exit flow and the interaction of the multiple jets. Greenberg et al. (1972) also present experimental data for a GDL nozzle. Their study focuses primarily on the effect of the subsonic inlet angle and the radius of curvature upstream of the throat on the amount of vibrational energy frozen in the gas.

In conventional nozzle design, the contour near the throat is smooth and often symmetric about the throat plane. This enables the methods discussed, in particular the series-expansion methods, to be used to generate initial data for the MOC. Because the throat of a MLN is sharp and there is usually no throat-plane symmetry, analytical methods cannot be used to predict the transonic flow field. As a result, the MLN is traditionally designed by assuming a sonic line shape as previously stated.

Assuming a sonic-line shape implies that a subsonic contour can be designed to produce that shape. However, Pirumov and Roslyakov (1978) state that it is not possible to specify a priori the inlet contour of a nozzle that insures straightness of the sonic line. Although they are referring to the specific case of a straight sonic line, it is reasonable to assume this applies in general. They also state that profiling the supersonic part of a nozzle does not depend on that of the subsonic part. This statement is true in that the supersonic portion of a nozzle depends only on conditions at the sonic line. However, this ignores the fact that conditions at the sonic line depend on several subsonic parameters. Hopkins and Hill (1966) show that the shape and location of the sonic line depends on r_{th} and to a lesser degree α. Also Back et al. (1965, 1967, 1969, 1972), Back and Cuffel (1966, 1971), Back and Massier (1972) and Cuffel et al. (1969) provide experimental results for conical nozzles that show that the transonic flow is influenced not only by r_{th} and α but also by the inlet boundary-layer thickness and Reynolds number. For conventional nozzle design, these parameters can be ignored since contraction angles are usually shallow, the transonic boundary layer is generally very thin, especially at the throat, and r_{th} is typically large. Consequently, flow gradients in these nozzles are so mild that moderate changes in subsonic conditions do not significantly affect sonic conditions. However, this is not the case for a MLN since the throat is sharp and α may be as large as 90 deg. Also, it has not previously been determined how the boundary layer behaves in the vicinity of a sharp throat.

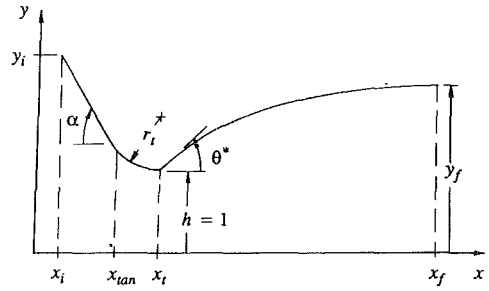

Fig. 1 Minimum length nozzle geometry

The surveyed literature indicates that the transonic flow field of conventional nozzles has been studied extensively. In contrast, very little has been done to analyze the transonic flow of the MLN family of nozzles. This may be attributed to the fact that analytical techniques break down as r_{th} becomes small. Also, phenomena associated with the intense flow gradients and boundary layer in the vicinity of the sharp throat can be difficult to model numerically.

The purpose of this research is to provide the first comprehensive analysis of the transonic flow field of two-dimensional MLNs. By plotting the computed sonic line and the flow angle distribution along it, we show the effect of the subsonic geometry on the sonic-line shape, its location and the flow angle. This allows a direct comparison of the actual sonic-line parameters to those assumed when generating the supersonic contour. While references such as Dumitrescu (1975) emphasize the shape of the sonic line, it is shown that the flow angle distribution has a greater influence on the supersonic flow field.

While it has been discussed that the sharp throat of a MLN may produce boundary-layer separation and shock waves (Wagner, 1971; Dumitrescu, 1975), we show that these phenomena do occur in some cases and describe the mechanisms that generate them. From this investigation, we determine that one of the MLN types is superior to the other in generating unseparated, shock-free flows and is more closely modeled by the inviscid MOC calculations.

2 Numerical Method

2a MLN Geometry and Contour Generation. A schematic of a two-dimensional MLN half-plane is shown in Fig. 1. The converging planar wall begins at x_i with an inclination angle of α. At $x_{\tan}$, the planar section is tangent to a circular arc of radius r_t. The slope of this section decreases to zero at the throat located at x_t. Thus α and r_t determine the inlet geometry. At the throat, the wall inclination discontinuously changes to the initial wall angle θ^* of the supersonic contour, which is a function of the ratio of specific heats γ and the exit Mach number M_f. For the SSL MLN

$$\theta^* = \frac{1}{2}\nu(M_f)$$

where ν is the Prandtl-Meyer function. For the CSL MLN, at low M_f values

$$\theta^* = \nu(M_f)$$

Emanuel (1986) discusses the bifurcation that occurs in the $\theta^*(M_f)$ relation for the CSL MLN. For M_f values beyond this

point, the MLN solution requires a finite straight wall section that begins at the throat before the curved portion of the supersonic contour. Once this point is reached, θ^* is determined by a more complicated expression and its magnitude can actually decrease as M_f increases. The M_f value at which this bifurcation occurs is a function of γ. For $\gamma = 1.4$, it occurs at $M_f \approx 2.8$.

A modified version of the code MOC2 (Argrow, 1986) called MOC2D is used to generate the two-dimensional SSL MLN contour. The supersonic contour of the two-dimensional CSL MLN is generated using the code MOC2DC that is based on the analysis of Emanuel (1986). Details of both methods of contour generation can be found in Argrow (1989).

In order to examine the performance of the supersonic contours, they are joined to the subsonic inlet at the throat as described earlier. Often in nozzle design, the inviscid contour represents the edge of the inviscid core of a viscous flow and is used to determine a displaced contour that accounts for boundary-layer growth. This is not done in the present analysis since we are interested in how well the inviscid contour performs without an additional boundary-layer correction.

2b Flow Field Computation. VNAP2 was developed by M. Cline (1981) at the Los Alamos National Laboratory. It employs the unsplit MacCormack scheme to solve the two-dimensional (planar and axisymmetric), time-dependent, Navier-Stokes equations. Options are available for the computation of inviscid and laminar or turbulent viscous flows. Several investigators have used or discussed VNAP2, or its earlier versions, in their publications (Brown and Hamilton, 1976; Cline, 1974, 1976; Cline and Wilmoth, 1983, 1984; Emanuel and Cline, 1981; Zucrow and Hoffman, 1977). Cline (1974, 1976) compares both inviscid and viscous nozzle flow solutions to experimental data to validate the accuracy of the code. In addition, Cline (1981) shows other flow geometries, including external flows, in which the code computes solutions that show close agreement with experimental data. Thus, the code has been well validated for the computation of nozzle flows. As a result of this fact and its ability to compute flows involving boundary-layer separation and shock waves (Cline and Wilmoth 1983, 1984; Emanuel and Cline, 1981), it was chosen for the current study, with some modifications (Argrow, 1989).

The gas is air ($\gamma = 1.4$) with all transport coefficients proportional to $T^{0.7}$. The Reynolds number is defined in terms of the throat half-height h, stagnation density ρ_0, stagnation viscosity μ_0 and the maximum speed $u_{\max}$ as

$$\mathrm{Re} = \frac{h\rho_0 u_{\max}}{\mu_0}$$

The maximum speed $u_{\max}$ can be written in terms of the stagnation enthalpy h_0 or the stagnation pressure and temperature p_0 and T_0 as

$$u_{\max} = (2h_0)^{1/2} = \left(\frac{2\gamma R T_0}{\gamma - 1}\right)^{1/2}$$

where R is the specific gas constant. Using this definition, Re is written in terms of p_0 and T_0 as

$$\mathrm{Re} = \left[\frac{2\gamma}{R(\gamma-1)}\right]^{1/2} \frac{hp_0}{C_\mu T_0^{\omega+1/2}}$$

where C_μ is the viscosity proportionality coefficient and $\omega = 0.7$.

A variable physical-space grid is used that allows compression of the mesh near the wall and the throat plane. Cases were run using 30 × 30, 40 × 30, 40 × 40, 50 × 50, 60 × 40, and 60 × 50 grids to determine a balance between solution stability, resolution and CPU time. For inviscid cases, solutions show very little variation for the different grid sizes. This is particularly true when compression is used to increase the grid density in the vicinity of the throat. The most important factor in determining an appropriate grid is the stability of the solution in the vicinity of the sharp throat. For more coarse grids, compression near the throat is required even for the inviscid cases because of the large gradients. This is most critical if a shock is generated just downstream of the throat. For the viscous cases the most important factor for determining the grid density is resolution of the boundary layer, particularly when separation occurs. Most of the tabulated cases, both viscous and inviscid, use a 60 × 40 grid with compression towards the wall and throat plane. For some of the more extreme inlet geometries, a 60 × 50 grid is used. For the viscous cases, if there is any indication of reverse flow in the boundary layer the case is run again with a more dense grid in the boundary layer to determine if separation actually occurs.

In all cases, p_0, T_0, and the angle of the velocity θ are specified at the inflow boundary. The inflow-boundary location x_i is in the range $-1.0 \le x_i \le -0.5$ and is set far enough upstream to insure that the flow passes through a converging section with a planar wall before encountering the circular-arc section. From preliminary computations, it was found that lengthening the subsonic inlet does not significantly alter the transonic flow. Therefore, the subsonic inlet is kept relatively short to decrease computation time.

The outflow boundary can be either an outflow or a mixed inflow-outflow boundary. For computations with $M_f = 2$ that involve the entire supersonic contour, the exit pressure p_f is specified such that $p_f/p_0 = 0.1$. The specified p_f is used as a boundary condition for the subsonic portion of the outflow boundary; extrapolation is used for the supersonic portion. For the $M_f = 4$ and 6 cases, the nozzle lengths are too long for a detailed analysis of the entire supersonic flow field. Therefore, the supersonic contours are truncated at approximately $x = 5$. This is far enough downstream to examine the development of a portion of the kernel region and to detect boundary-layer separation and shock waves in the vicinity of the throat.

Because of the relatively short nozzle length of the $M_f = 2$ MLNs, the entire supersonic flow field is computed. Consequently, some of these flows are considered to be nominal cases and are used as a basis for most comparisons. At the nominal Reynolds number, Re = 11,700, the corresponding stagnation pressure and temperature are $p_0 = 1$ atm and $T_0 = 1000$ K. These values are also used for all the inviscid cases. The Reynolds number scales linearly with p_0 and p_0 is used to vary Re. The Re = 23,400 cases are only for the $M_f = 2$ MLN.

Some cases require the use of an explicit artificial viscosity. In these cases, the minimum amount is used to stabilize the computations. Generally, it is only required for cases involving separated flow accompanied by a shock wave or in the lowest Reynolds number cases that require a relatively coarse grid.

A time-of-flight check for convergence to steady state consists of computing the number of traverses through the computational grid made by a fluid particle on the nozzle centerline. This proves to be a reliable method of determining convergence. After a series of test cases that were advanced through several particle traverses, it was determined that when using a one-dimensional flow initial surface, no significant flow field variations occur with time after approximately 3.5–4 traverses for both the inviscid and viscous flows. If the final solution surface of a similar case is used as an initial surface, the number of required traverses reduces to three or less. Despite this, most cases were run to at least four or five particle traverses.

Another method used to monitor steady-state convergence is the location of the x-coordinate of the intersection of the sonic line and the centerline x_s and the y-coordinate of the intersection of the sonic line and the throat plane y_s. The values of x_s and y_s converge to fixed values as steady-state is approached. It is assumed that the solution is converged once

Table 1 Straight sonic line, minimum length nozzle flow parameters, $M_f = 2$

Re	r_t	α (deg)	x_s	y_s	Bound.-Layer Sep.	Comp. or Shock	Inviscid Core A_f (%)	Inviscid Core $(M_f)_{ave}$	Inviscid Core ΔM_f (%)	Inviscid Core $\Delta\rho_f/\rho_0$ (%)
1170	0.0	0	0.099	0.555	no	no	64.6	1.874	4.60	7.29
1170	0.0	15	0.305	*	no	no	64.1	1.809	3.29	9.62
1170	0.0	30	0.366	*	no	comp	64.6	1.884	4.55	8.93
1170	0.0	60	0.431	*	no	comp	61.9	1.884	3.63	12.45
1170	0.5	15	0.260	0.737	no	comp	64.6	1.814	3.71	9.87
1170	0.5	30	0.284	0.689	no	no	64.6	1.825	4.07	10.54
1170	0.5	60	0.193	0.567	no	no	64.6	1.827	4.48	12.10
1170	1.0	15	0.216	0.677	no	no	67.2	1.899	6.41	6.14
1170	1.0	30	0.222	0.632	no	no	64.6	1.866	4.73	9.54
1170	1.0	60	0.193	0.567	no	no	64.6	1.841	4.87	10.83
11700	0.0	0	0.007	0.160	no	no	87.0	1.984	4.91	7.32
11700	0.0	15	0.308	0.953	no	no	86.3	1.951	1.87	8.04
11700	0.0	30	0.372	0.962	no	comp	86.3	1.975	2.65	11.63
11700	0.0	60	0.423	0.806	yes	shock	85.4	2.052	6.93	14.53
11700	0.5	15	0.258	0.737	no	no	85.0	1.973	1.56	5.68
11700	0.5	30	0.279	0.687	no	no	85.0	1.966	1.14	6.43
11700	0.5	60	0.275	0.641	no	no	85.4	1.982	1.70	7.33
11700	1.0	15	0.219	0.671	no	no	85.0	1.959	2.09	5.23
11700	1.0	30	0.222	0.629	no	no	85.0	1.968	2.01	5.24
11700	1.0	60	0.201	0.558	no	no	85.4	1.979	4.08	5.29
23400	0.0	0	-0.009	0.000	no	no	90.7	1.982	5.17	6.75
23400	0.0	15	0.308	0.931	no	no	88.9	1.988	1.31	7.03
23400	0.0	30	0.371	0.926	no	comp	88.9	2.019	2.82	9.54
23400	0.0	60	0.434	0.795	yes	shock	89.1	2.080	10.45	20.99
23400	0.5	15	0.256	0.748	no	no	88.9	1.990	2.16	4.93
23400	0.5	30	0.281	0.686	no	comp	88.9	1.987	1.68	7.70
23400	0.5	60	0.276	0.642	no	comp	85.0	1.986	1.34	6.96
23400	1.0	15	0.216	0.673	no	no	90.7	1.985	5.09	7.11
23400	1.0	30	0.223	0.621	no	no	88.9	1.976	1.32	5.95
23400	1.0	60	0.211	0.616	no	no	88.9	1.989	1.59	5.99
inv	0.0	0	0.134	0.957	-	no	100.0	2.001	3.61	7.50
inv	0.0	15	0.326	0.961	-	shock	100.0	2.023	6.57	16.71
inv	0.0	30	0.385	0.972	-	shock	100.0	2.051	9.00	19.12
inv	0.5	15	0.261	0.737	-	comp	100.0	2.015	3.82	7.71
inv	0.5	30	0.275	0.670	-	shock	100.0	2.025	6.32	12.59
inv	1.0	15	0.225	0.620	-	comp	100.0	2.007	2.26	4.20
inv	1.0	30	0.222	0.603	-	comp	100.0	2.016	2.87	5.55

Table 2 Straight sonic line, minimum length nozzle flow parameters, $M_f = 4$

Re	r_t	α (deg)	x_s	y_s	Bound.-Layer Sep.	Comp. or Shock
1170	0.0	0	0.081	0.481	no	no
1170	0.0	15	0.282	0.810	no	no
1170	0.0	30	0.351	*	no	no
1170	0.0	60	0.413	0.797	no	no
1170	0.5	15	0.241	0.707	no	no
1170	0.5	30	0.268	0.669	no	no
1170	0.5	60	0.265	0.633	no	no
1170	1.0	15	0.214	0.656	no	no
1170	1.0	30	0.212	0.610	no	no
1170	1.0	60	0.181	0.538	no	no
11700	0.0	0	-0.003	0.000	no	no
11700	0.0	15	0.300	0.869	no	no
11700	0.0	30	0.367	0.958	no	no
11700	0.0	60	0.418	0.792	yes	shock
11700	0.5	15	0.258	0.731	no	no
11700	0.5	30	0.280	0.695	no	no
11700	0.5	60	0.274	0.663	no	no
11700	1.0	15	0.213	0.680	no	no
11700	1.0	30	0.213	0.642	no	no
11700	1.0	60	0.183	0.586	no	no
inv	0.0	0	0.021	0.987	-	no
inv	0.0	15	0.316	0.972	-	comp
inv	0.0	30	0.374	0.953	-	shock
inv	0.5	15	0.260	0.734	-	comp
inv	0.5	30	0.273	0.679	-	comp
inv	1.0	15	0.224	0.669	-	comp
inv	1.0	30	0.374	0.955	-	comp

these values show no change in the fourth or fifth decimal digit.

3 Results

Computational results are concisely summarized in Tables 1–6, where the cases are for an adiabatic wall. Tables 1–3 show results for the SSL MLN for $M_f = 2$, 4, and 6, while Tables 4–6 are for the CSL MLN. The inlet geometry is controlled by the parameters r_t and α, where r_t has values of 0.0, 0.5 and 1.0 and α is set at 0, 15, 30, and 60 deg.

The location of the sonic line is indicated by x_s and y_s. An asterisk in the y_s column indicates that the sonic line is everywhere downstream of the throat plane. The presence of boundary-layer separation and compression or shock waves is indicated in the next two columns. Because shock waves are smeared over several grid points, it is often a matter of judgment to distinguish between a simple compression wave and a shock wave. For the $M_f = 2$ cases, this distinction is made by examining both the Mach number and p/p_0 plots. The wave is considered to be a compression if there is a noticeable decrease in the Mach number in any portion of the inviscid core but with no discernible increase in p/p_0 along the nozzle centerline. If there is a decrease in M and an accompanying increase in p/p_0 on the centerline, this indicates the presence of an oblique shock that reflects from the centerline.

Since only a portion of the supersonic flow field is computed for the $M_f = 4$ and 6 cases, any shock or compression waves present are not observed to reflect from the centerline. In these cases, the closeness of the M-contours coupled with a notice-

Table 3 Straight sonic line, minimum length nozzle parameters, $M_f = 6$

Re	r_t	α (deg)	x_s	y_s	Bound.-Layer Sep.	Comp. or Shock
1170	0.0	0	0.081	0.477	no	no
1170	0.0	15	0.285	0.744	no	no
1170	0.0	30	0.349	*	no	no
1170	0.0	60	0.408	0.793	no	no
1170	0.5	15	0.249	0.706	no	no
1170	0.5	30	0.275	0.671	no	no
1170	0.5	60	0.266	0.629	no	no
1170	1.0	15	0.223	0.658	no	no
1170	1.0	30	0.214	0.607	no	no
1170	1.0	60	0.183	0.537	no	no
11700	0.0	0	0.000	0.039	no	no
11700	0.0	15	0.299	0.868	no	no
11700	0.0	30	0.362	0.870	no	no
11700	0.0	60	0.415	0.787	yes	comp
11700	0.5	15	0.260	0.756	no	no
11700	0.5	30	0.279	0.681	no	no
11700	0.5	60	0.281	0.662	no	no
11700	1.0	15	0.227	0.679	no	no
11700	1.0	30	0.229	0.611	no	no
11700	1.0	60	0.217	0.568	no	no

Table 4 Curved sonic line, minimum length nozzle flow parameters, $M_f = 2$

Re	r_t	α (deg)	x_s	y_s	Bound.-Layer Sep.	Comp. or Shock	Inviscid Core A_f (%)	Inviscid Core $(M_f)_{ave}$	Inviscid Core ΔM_f (%)	Inviscid Core $\Delta\rho_f/\rho_0$ (%)
1170	0.0	0	0.068	0.462	no	comp	64.6	1.902	3.25	12.76
1170	0.0	15	0.287	0.819	no	comp	64.6	1.809	3.29	19.73
1170	0.0	30	0.356	*	no	comp	64.6	1.825	4.27	22.37
1170	0.0	60	0.416	0.849	no	shock	61.9	1.934	6.88	23.11
1170	0.5	15	0.248	0.715	no	comp	64.6	1.812	3.08	19.55
1170	0.5	30	0.274	0.676	no	comp	64.6	1.823	3.46	21.14
1170	0.5	60	0.265	0.636	no	comp	64.6	1.830	3.74	22.50
1170	1.0	15	0.221	0.664	no	comp	64.6	1.816	3.14	19.22
1170	1.0	30	0.211	0.612	no	comp	64.6	1.848	3.56	20.43
1170	1.0	60	0.182	0.545	no	comp	64.6	1.838	4.11	20.63
11700	0.0	0	-0.003	0.000	no	shock	87.0	2.021	9.14	19.21
11700	0.0	15	0.303	0.952	no	shock	87.0	2.021	12.26	25.04
11700	0.0	30	0.365	0.916	yes	shock	85.0	2.141	10.96	22.60
11700	0.0	60	0.412	0.794	yes	shock	87.0	2.107	13.37	24.60
11700	0.5	15	0.252	0.744	no	shock	87.0	2.026	9.94	20.99
11700	0.5	30	0.277	0.699	no	shock	85.0	2.009	10.84	22.19
11700	0.5	60	0.277	0.632	yes	shock	85.0	2.022	9.96	20.38
11700	1.0	15	0.219	0.672	no	shock	87.0	2.028	9.08	18.56
11700	1.0	30	0.225	0.622	no	shock	85.0	2.003	10.55	21.61
11700	1.0	60	0.209	0.578	no	shock	85.0	2.013	10.03	20.64
23400	0.0	0	-0.019	0.000	no	shock	90.7	2.032	11.32	23.97
23400	0.0	15	0.305	0.902	no	shock	88.9	2.016	12.29	24.74
23400	0.0	30	0.366	0.920	yes	shock	88.9	2.038	12.03	23.88
23400	0.0	60	0.419	0.822	yes	shock	88.9	2.081	9.74	21.45
23400	0.5	15	0.261	0.756	no	shock	88.9	2.015	12.34	24.70
23400	0.5	30	0.281	0.684	yes	shock	88.9	2.057	12.62	25.64
23400	0.5	60	0.278	0.629	yes	shock	88.9	2.056	11.26	23.05
23400	1.0	15	0.225	0.665	no	shock	88.9	2.023	11.81	23.91
23400	1.0	30	0.223	0.616	no	shock	88.9	2.048	10.79	22.56
23400	1.0	60	0.214	0.589	no	shock	89.4	2.041	11.75	24.35
inv	0.0	0	0.146	0.978	-	shock	100.0	2.046	14.62	28.52
inv	0.0	15	0.373	0.971	-	shock	100.0	2.040	16.85	33.44
inv	0.0	30	0.374	0.953	-	shock	100.0	2.031	16.54	30.14
inv	0.5	15	0.267	0.704	-	shock	100.0	2.033	16.22	30.25
inv	0.5	30	0.279	0.698	-	shock	100.0	2.044	16.56	30.59
inv	1.0	15	0.233	0.640	-	shock	100.0	2.026	16.05	29.80
inv	1.0	30	0.229	0.649	-	shock	100.0	2.033	15.92	29.45

Table 5 Curved sonic line, minimum length nozzle flow parameters, $M_f = 4$

Re	r_t	α (deg)	x_s	y_s	Bound.-Layer Sep.	Comp. or Shock
1170	0.0	0	0.090	0.500	no	no
1170	0.0	15	0.284	0.806	no	no
1170	0.0	30	0.349	*	no	no
1170	0.0	60	0.408	0.790	no	no
1170	0.5	15	0.250	0.705	no	no
1170	0.5	30	0.275	0.668	no	no
1170	0.5	60	0.266	0.629	no	no
1170	1.0	15	0.225	0.659	no	no
1170	1.0	30	0.217	0.609	no	no
1170	1.0	60	0.185	0.538	no	no
11700	0.0	0	-0.002	0.000	no	shock
11700	0.0	15	0.298	0.854	no	shock
11700	0.0	30	0.359	0.866	no	shock
11700	0.0	60	0.414	0.786	yes	shock
11700	0.5	15	0.263	0.754	no	shock
11700	0.5	30	0.284	0.688	no	shock
11700	0.5	60	0.284	0.664	no	shock
11700	1.0	15	0.230	0.665	no	shock
11700	1.0	30	0.231	0.609	no	shock
11700	1.0	60	0.218	0.564	no	shock
inv	0.0	0	0.149	0.978	-	shock
inv	0.0	15	0.312	0.967	-	shock
inv	0.5	15	0.260	0.748	-	shock
inv	1.0	15	0.230	0.697	-	shock

Table 6 Curved sonic line, minimum length nozzle parameters, $M_f = 6$

Re	r_t	α (deg)	x_s	y_s	Bound.-Layer Sep.	Comp. or Shock
1170	0.0	0	0.084	0.491	no	no
1170	0.0	15	0.284	0.794	no	no
1170	0.0	30	0.349	*	no	no
1170	0.0	60	0.408	0.797	no	no
1170	0.5	15	0.249	0.707	no	no
1170	0.5	30	0.273	0.670	no	no
1170	0.5	60	0.265	0.629	no	no
1170	1.0	15	0.223	0.659	no	no
1170	1.0	30	0.214	0.609	no	no
1170	1.0	60	0.183	0.537	no	no
11700	0.0	0	-0.001	0.000	no	no
11700	0.0	15	0.299	0.860	no	no
11700	0.0	30	0.361	0.876	no	no
11700	0.0	60	0.415	0.788	yes	comp
11700	0.5	15	0.262	0.751	no	no
11700	0.5	30	0.283	0.682	no	no
11700	0.5	60	0.280	0.662	no	no
11700	1.0	15	0.229	0.666	no	no
11700	1.0	30	0.229	0.636	no	no
11700	1.0	60	0.216	0.572	no	no

able decrease in magnitude and a deflection of the velocity vectors is used to distinguish between compression and shock waves.

Exit plane parameters for the inviscid core flow are tabulated for the $M_f = 2$ cases. These parameters indicate the percent of the exit plane area occupied by the inviscid core, the average M_f value across the exit plane, $(M_f)_{ave}$, and the relative percent difference between the maximum and minimum values of M_f and the density ratio ρ_f/ρ_0, ΔM_f and $\Delta\rho_f/\rho_0$, respectively.

3a Sonic-Line Shape and Location. Figures 2 and 3 illustrate the influence of r_i and α on the sonic-line shape and its location for the nominal cases. The local wall contour is plotted with a vertical line representing the throat plane. The sonic line and the velocity vector distribution along it are also shown. The sonic-line shape is obtained from a linear interpolation of the code output. It begins at the nozzle centerline and advances toward the wall. It terminates once the sonic line turns downstream in or near the boundary layer, which explains the gap that appears between the sonic line and the wall.

A comparison of Figs. 2 and 3 shows that for a given r_t and α, the sonic-line shapes and locations are almost identical for the two MLN types. This is also apparent from the x_s and y_s

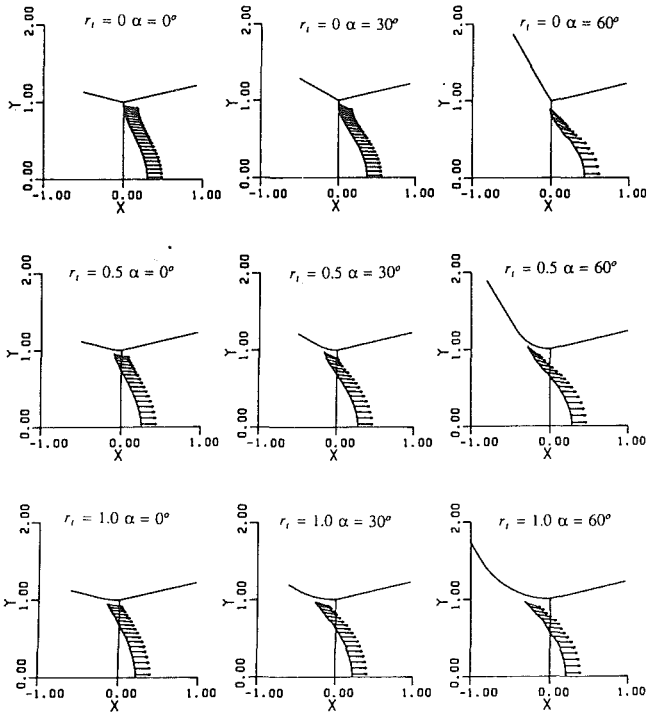

Fig. 2 Sonic lines for the nominal straight sonic line, minimum length nozzle cases

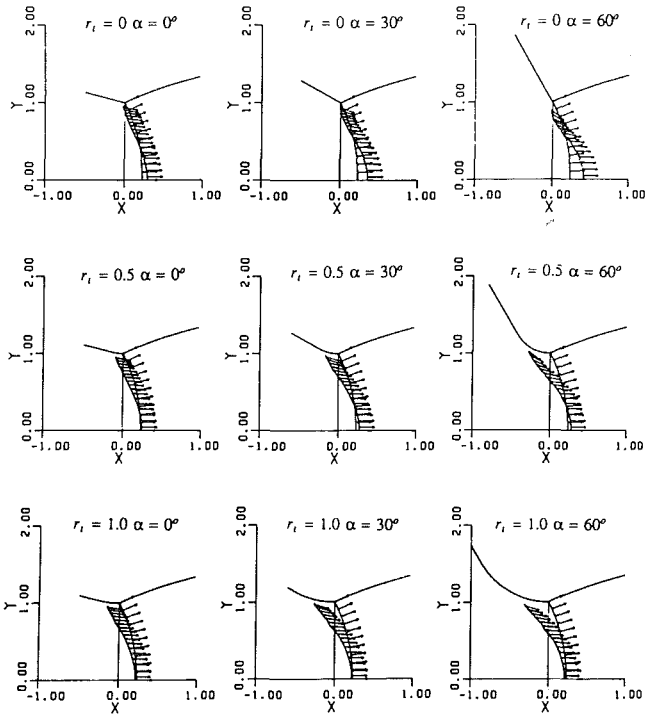

Fig. 3 Sonic lines for the nominal curved sonic line, minimum length nozzle cases

values tabulated for the same cases in Tables 1 and 4. By examining these and the other tables, we see that x_s and y_s also show little dependence on M_f or Re (including the inviscid cases). This is to be expected since the supersonic flow field has no upstream influence except through the subsonic portion of the boundary layer. Another item that is evident from the tables is that the M_f and Re influence, although small, increases as r_t decreases. From each of the columns, increasing r_t causes the sonic line near the wall to move upstream from the throat plane. In fact, the entire sonic line is shifted slightly upstream with the effect being most apparent in the portion nearest the

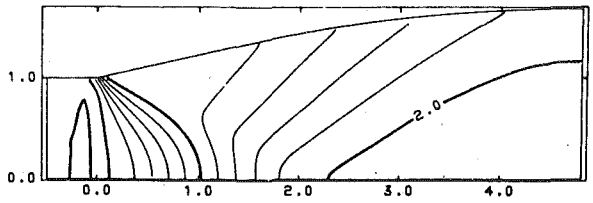

Fig. 4(a)

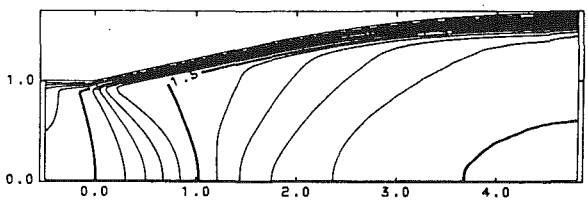

Fig. 4(b)

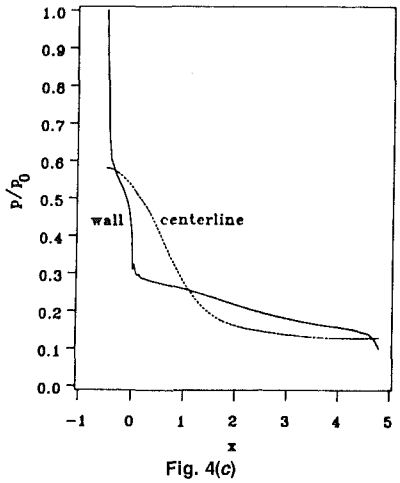

Fig. 4(c)

Fig. 4 Nominal straight sonic line, minimum length nozzle with $r_t = 0$ and $\alpha = 0°$; (a) inviscid Mach number contours, (b) Mach number contours and (c) pressure distribution for the viscous case

wall. The primary influence of α is on the θ distribution, with the distribution becoming less parallel, especially near the wall, as α increases. This effect is lessened as r_t increases.

In the $r_t = 0$ row of Figs. 2 and 3, as α increases, y_s is almost stationary, while x_s increases. The primary change is the steepening of the flow angle near the wall, as would be expected, as the wall inclination increases. However, the effect is noticeably limited to a region near the wall even in the $\alpha = 60$ deg case. For $r_t = 0.5$, x_s also increases as α increases but the upstream location of the sonic line near the wall moves upstream from the throat plane. Next, for $r_t = 1.0$, the entire sonic line moves slightly upstream. In addition, the sonic lines for $r_t \leq 0.5$ show an inflection point that becomes more obvious as r_t decreases.

In all cases, the sonic line appears more curved than straight. The velocity vectors indicate the flow is mostly parallel except for the larger values of α where flow convergence near the wall is more obvious. Therefore, the sonic-line shape appears to be closer to the CSL assumption, yet the velocity distribution is closer to the parallel flow of the SSL assumption.

3b Inlet-Geometry Influence on the Supersonic Flow Field. Figures 4-9 display M-contours, velocity vector fields and wall and centerline pressure distributions for the nominal SSL and CSL MLN cases. Because of the large number of plots generated (Argrow, 1989), only a portion are included here for discussion. The M-contours are plotted in 0.1 increments with a bold contour plotted every 0.5 increments. The velocity vectors are plotted at the physical-space grid points. The pressure distributions are plotted in terms of the ratio p/p_0.

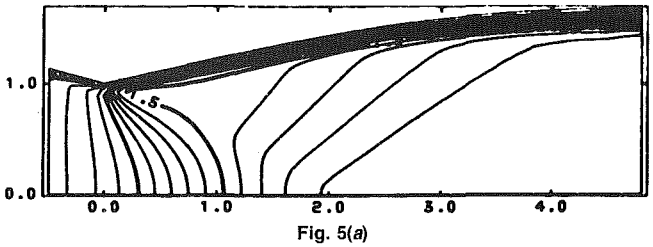

Fig. 5(a)

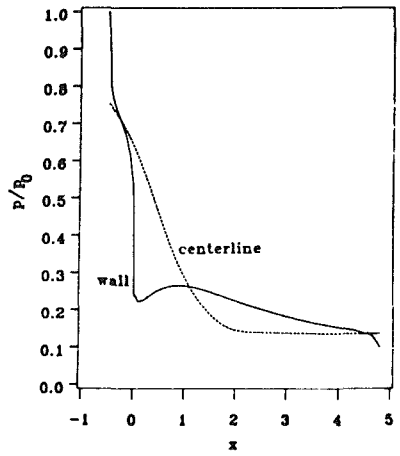

Fig. 5(b)

Fig. 5 Nominal straight sonic line, minimum length nozzle with $r_t = 0$ and $\alpha = 15°$; (a) Mach number contours, (b) pressure distribution

Figure 4(a) shows the inviscid solution for a $M_f = 2$ and $\alpha = 0$ deg SSL MLN. The inlet flow is slightly subsonic to sonic as indicated by the M-contour in the planar inlet. The sonic line that shows the initiation of the throat expansion begins slightly downstream of x_t at the centerline. The converging M-contours at the throat plane indicate the Prandtl-Meyer expansion fan emanating from the shoulder. A clearly defined kernel boundary that extends from the shoulder is evident where the curved contours of the nonsimple-wave kernel region become straight along the C_+ (left running) family of characteristics of the simple-wave transition region. The kernel terminates on the centerline where $M_f = 2$ at $x \approx 2.3$. This is downstream of $x = 1.908$ from the MOC computation. Yet, as a whole, the flow field is very similar to that predicted by the inviscid MOC result with a very uniform exit flow at $x_f = 4.81$.

Figure 4(b) shows the same nozzle at the nominal Re = 11,700 value. The M-contours show that the presence of the boundary layer forces the upper portion of the sonic line upstream as if the straight horizontal section has a nonzero α. The throat expansion is not centered, but spread over a substantial portion of the transonic contour. The p/p_0 plot of Fig. 4(c) shows a large pressure drop along the wall as the flow is accelerated in the region upstream of the throat. A favorable pressure gradient continues along the supersonic wall. The small abrupt drop at the exit is a result of the subsonic boundary layer matching the exit pressure p_f. The centerline distribution shows a smooth decrease from the entrance to the exit.

For Fig. 5, α is increased to 15 deg. This results in a more centered throat expansion. A well defined kernel terminates at $x \approx 2.0$, slightly greater than $x = 1.908$ from the MOC calculation. The M_f value is also slightly less than the MOC value of 2.0. This decrease in M_f is primarily due to the boundary-layer growth along the supersonic wall. The boundary-layer displacement decreases the ratio of the inviscid exit-plane area to the cross sectional area of the sonic condition A_f/A^*, thus reducing M_f. Again, the straight M-contours in the transition region emphasize the straight C_+ characteristics of this simple-wave region. The centerline pressure ratio smoothly

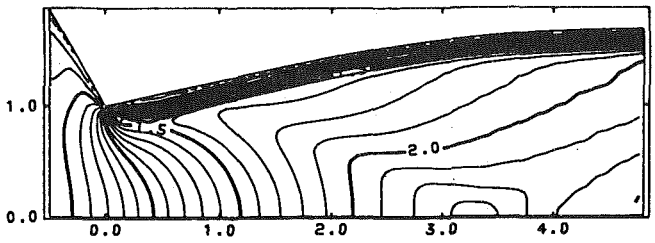

Fig. 6(a)

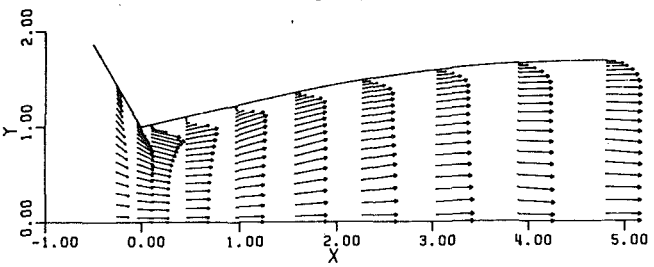

Fig. 6(b)

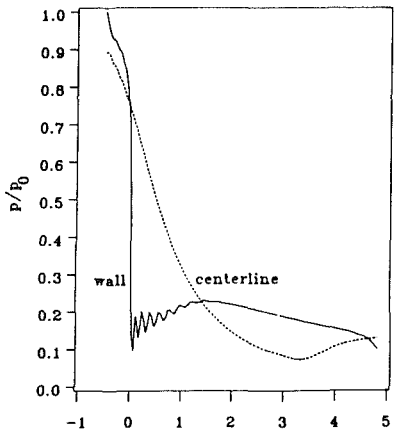

Fig. 6(c)

Fig. 6 Nominal straight sonic line, minimum length nozzle with $r_t = 0$ and $\alpha = 60°$; (a) Mach number contours, (b) velocity field, (c) pressure distribution

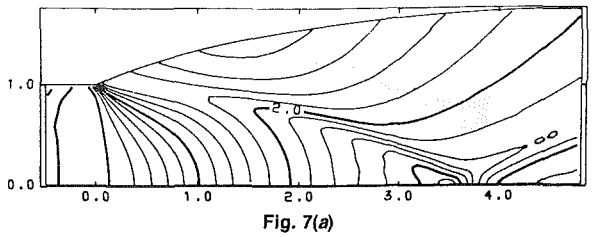

Fig. 7(a)

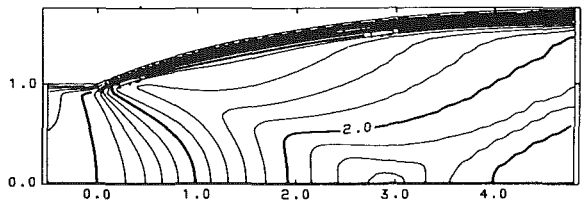

Fig. 7(b)

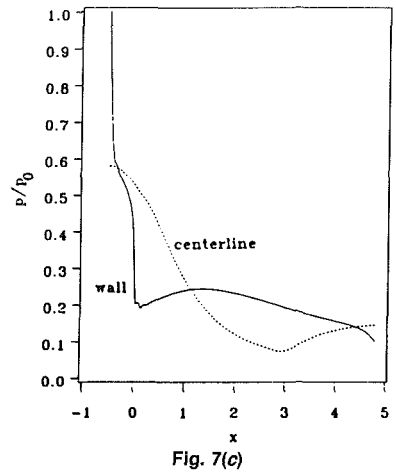

Fig. 7(c)

Fig. 7 Nominal curved sonic line, minimum length nozzle with $r_t = 0$ and $\alpha = 0°$; (a) inviscid Mach number contours, (b) Mach number contours and (c) pressure distribution for the viscous case

decreases through the subsonic inlet and the kernel then abruptly reaches a constant value beginning at $x \approx 2.0$. The slope change indicates the end of the kernel and the beginning of the uniform flow region as in the MOC calculations. The wall pressure ratio shows a steep decrease through the transonic region, indicating that the fluid particles near the wall experience a much greater acceleration than those near the centerline. This decrease continues through the throat plane. Slightly downstream of x_t there is a pressure rise between $x \approx 0.1$ and $x \approx 1.0$, followed by an almost linear decrease to the exit plane.

The MOC solutions of the SSL or CSL MLNs do not show an adverse pressure gradient along any portion of the wall. In the case of the SSL MLN, this is because the Prandtl-Meyer expansion centered at the throat discontinuously expands the flow at a single point. However, in the cases examined here, there are two other factors that influence the flow in the vicinity of the throat. First, the presence of a boundary layer prevents the expansion fan from being centered. Instead, the sharp turn at the wall appears slightly rounded to the inviscid core flow and the expansion fan is spread over a finite length of the wall. This, in part, explains the continued pressure drop immediately downstream of x_t.

The second factor that must be considered is the total throat turn angle $\delta = \alpha + \theta^*$. Again, because the SSL MLN assumes a flow parallel to the centerline at the throat plane, it does not account for the converging flow associated with a subsonic inlet. For the $M_f = 2$ SSL MLN, θ^* (M_f) is fixed at 13.19°, thus for the present case, $\delta = 28.19$ deg. This is more than twice the θ^* of the SSL nozzle. Because the convergence angle at the inlet is proportionately distributed with respect to distance from the centerline, flow near the wall is at a higher convergence angle than that near the centerline. As a consequence, the fluid particles of the inviscid core that pass near the wall experience an overexpansion due to the total turn angle δ. As discussed by Back et al. (1965, 1966, 1972); the overexpansion is a result of the angular momentum of the fluid particles that make the turn at the throat. The excess angular momentum of the inviscid core effectively forces the flow near the wall into an overexpansion followed by a compression as the particles are forced to realign with the downstream wall. Thus, the overexpansion is associated with the inviscid portion of the flow and can be observed in both the viscous and inviscid cases when $\delta > \theta^*$. As will be seen, the compression along the wall increases in strength as δ increases. This results in a wave that focuses as it approaches the centerline until ultimately, an oblique shock is generated and, in some instances, boundary-layer separation also occurs. It will be shown, that the overexpansion and the subsequent compression is relieved as r_t is increased.

Figure 6 shows that an increase of α to 60 deg results in boundary-layer separation with an accompanying oblique shock. The reverse flow adjacent to the wall in the separated region is not apparent in Fig. 6(*b*) because of the small magnitude of the velocity in this region. The separated region is confined to a "bubble" between $x = 0.1$ and $x = 1.0$, where

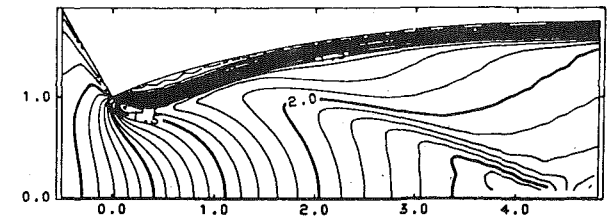

Fig. 8(a)

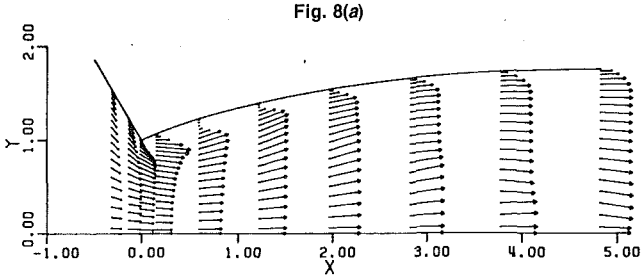

Fig. 8(b)

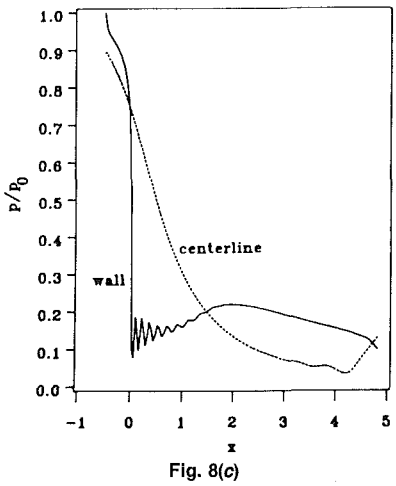

Fig. 8(c)

Fig. 8 Nominal curved sonic line, minimum length nozzle with $r_t = 0$ and $\alpha = 60°$; (a) Mach number contours, (b) velocity field, (c) pressure distribution

reattachment occurs. The oscillations in Fig. 6(*c*) make it difficult to make quantitative observations about the adverse pressure gradient along the wall. These numerical oscillations occur in only a small region near the wall even with the presence of artificial viscosity. The rest of the flow field is not disturbed by these oscillations. It is apparent that the minimum value of p/p_0 downstream of x_t has continued to decrease from the previous cases and achieves a minimum for the cases investigated. This results in a steeper adverse gradient downstream of x_t. The oblique shock can be traced in Fig. 6(*a*) from just outside the separated boundary layer and along the edge of the distorted kernel. It then reflects from the centerline at $x \approx 3.4$, which is evident from the centerline pressure rise. A slight shift in θ and velocity magnitude as the flow crosses the oblique shock is also noticeable in Fig. 6(*b*).

In all the cases that involve an oblique shock wave, the pressure rise associated with the shock begins at the wall in the form of an adverse pressure gradient spread along several grid points (usually about 15 depending on the grid spacing). As the shock moves away from the wall, it becomes more focused so that when it strikes the centerline, the pressure jump through the incident shock and its reflection is generally spread over four or five grid points for the inviscid cases and slightly more for the viscous cases. With α fixed at 60 deg, the sonic line moves farther upstream as r_t increases, as discussed in the previous section. This spreads the throat expansion over a larger portion of the wall and effectively reduces the influence of α. As a result, the magnitude of the wall pressure gradient decreases. Thus, the tendency for shock waves and boundary-layer separation also decreases and the expansion is spread over a larger portion of the centerline. This causes a slight increase in M_f near the centerline which is evident in later plots of the exit plane M_f profile.

Figure 7 begins the CLS MLN discussion with $M_f = 2$, $r_t = 0$ and $\alpha = 0$ deg. In Fig. 7(*a*) the supersonic flow field is dominated by an oblique shock that reflects from the centerline at $x \approx 3.8$. A centered expansion, similar to the corresponding SSL case (Fig. 4(*a*)), emanates from the shoulder at the throat. It is apparent by the increased number of M-contours in the expansion fan, that because of the larger θ^* of the CLS MLN, the flow is overexpanded at the throat. This results in the formation of the oblique shock. A continuation of this inviscid flow pattern is seen in the other CSL cases.

In Fig. 7(*b*,*c*), we observe a supersonic flow field that is more disturbed than the corresponding SSL MLN case and that involves a small separation bubble combined with a weak oblique shock, which reflects from the centerline near $x = 3.0$. This is verified by the rise in the centerline pressure ratio starting at $x \approx 3.0$ and the adverse pressure gradient along the wall.

The presence of an adverse pressure gradient and an oblique shock is a result of the angle δ, which in this case is equal to θ^*. Recall that for M_f values below 2.8, θ^* for the CSL MLN is exactly twice that of the corresponding SSL MLN. Beyond this M_f value, θ^* for the CSL MLN remains larger than for the SSL MLN but decreases until the two values are equal at $M_f \approx 5.9$. For $M_f > 5.9$, the θ^* for the CSL MLN is increasingly smaller than for the SSL MLN (Argrow and Emanuel, 1988; Emanuel, 1986).

Increasing α to 60 deg, Fig. 8, shows a clearly defined oblique shock and separation bubble. Again, the wall pressure oscillates in the separated region, but the drop in pressure just downstream of the throat followed by an adverse gradient is evident. The centerline pressure distribution indicates a reflecting oblique shock at $x \approx 4.2$.

3c Exit-Plane Uniformity. A primary purpose of a MLN is to produce a uniform inviscid flow in the shortest possible distance. To evaluate the degree of uniformity of M_f at the exit plane, Fig. 9 displays M_f profiles across the inviscid core of the exit plane for several cases. Additional exit-plane information for the viscous $M_f = 2$ cases are provided in Tables 1 and 4.

The generation of Fig. 9 and Tables 1 and 4 requires the definition of a viscous boundary-layer edge. Because the $M_f = 2$ nozzle is slightly underexpanded, there is a slight expansion near the wall in the exit plane. This is most noticeable in the subsonic portion of the thick boundary layer for the Re = 1,170 cases, but it can also be seen as a slight overshoot of the M_f profiles near the boundary-layer edge in Fig. 9(*a*,*b*). As a result, the axial velocity component u, which is parallel to the wall at the exit plane, is scanned at each grid point starting at the centerline. The boundary-layer edge is defined here to be the first point where the u-component varies from that of the next grid point by more than 0.99 percent. Interpolation is not required since the points are very closely spaced near the wall.

Figure 9(*a*) shows the M_f profile for the $r_t = 0$, SSL cases. We can see that for $\alpha \leq 30$ deg, the exit profile is fairly uniform from the centerline to $y/y_f \approx 0.8$. As α is increased from 0 deg, the profiles move closer to the design M_f value of two. We see that an increase in α does not greatly increase nonuniformity until $\alpha = 60$ deg. In this case, the overexpanded flow at the throat results in boundary-layer separation and an oblique shock that crosses the exit plane at $y/y_f \approx 0.4$. The shock is smeared over several grid points, therefore the M_f profile does not show an abrupt change. Figure 9(*b*) shows

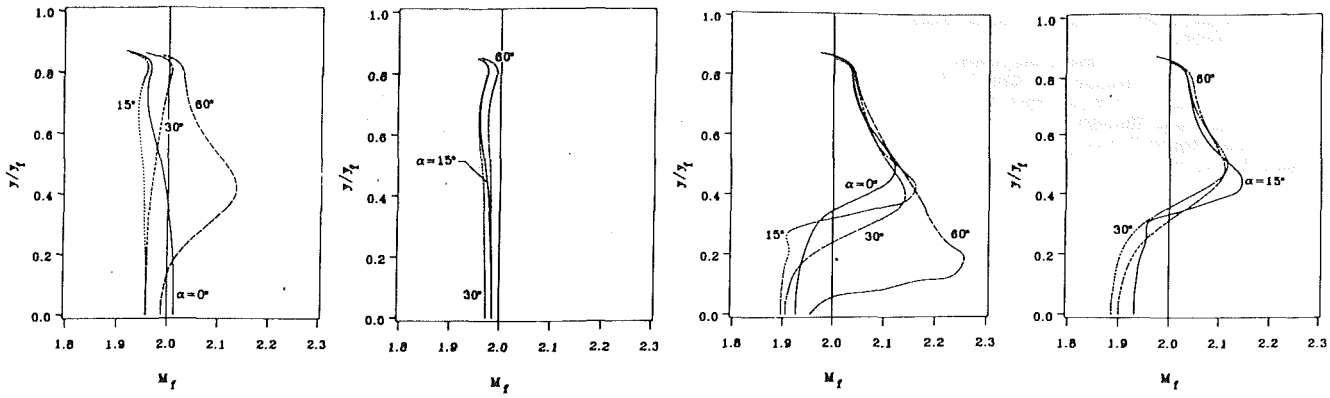

Fig. 9(a) Fig. 9(b) Fig. 9(c) Fig. 9(d)

Fig. 9 Nominal straight sonic line MLN exit Mach number profile; (a) $r_t = 0$, (b) $r_t = 0.5$. Nominal curved sonic line MLN exit Mach number profile; (c) $r_t = 0$, (d) $r_t = 0.5$.

that the increase of r_t to 0.5, greatly reduces the effect of α on the M_f profile. Also from Table 1, we can see that ΔM_f is decreased below the values of the previous cases and remains almost constant. The same is true for $\Delta\rho_f/\rho_0$.

Figure 9(*c*,*d*) and Table 4 show that for the CSL MLN, the exit-plane flow is much less uniform than that of the corresponding SSL cases. While the (*c*) and (*d*) figures show the same decrease of α influence as r_t increases, they also show that the strength of the shock that crosses the exit plane also decreases. From Table 4, we can see that in all the CSL, MLN nominal cases, $(M_f)_{ave}$ is above the design M_f of two, while the degree of nonuniformity ΔM_f ranges from 9.1 to 13.4 percent. The density nonuniformity $\Delta\rho_f/\rho_0$ is consistently greater than the corresponding SSL cases, ranging from about 18.5 to 25.8 percent.

For the viscous cases of Tables 1 and 4, the inviscid core area is decreased from approximately 86 to about 65 percent for an order-of-magnitude decrease in Re to 1,170. As expected, the increased boundary-layer thickness further reduces the effective A_f/A^*, reducing $(M_f)_{ave}$ for both MLN types. The thickened boundary layer reduces the distinction between the two supersonic geometries as is obvious from the comparable values of ΔM_f for each MLN type. Because of the small range of ΔM_f, it indicates a decreased influence from the inlet geometry parameters r_t and α.

The tables show the result of increasing Re to 23,400. Because this increase results in a thinner boundary layer, the inviscid core indicated in Table 1 is closer to that assumed in the SSL MOC design. However, because of the flow convergence near the throat plane caused by the inlet, the thinner boundary layer enhances the defects of the CSL assumptions near the throat. It should be emphasized that this is a result of the assumption of a source flow along the sonic line. As a consequence, Table 1 shows that for the SSL MLN, ΔM_f remains approximately the same as that for the Re = 11,700 cases, with some improvement in several instances. The same is true for $\Delta\rho_f/\rho_0$. For the CSL MLN cases in Table 4, ΔM_f and $\Delta\rho_f/\rho_0$ increase slightly in almost every instance when compared to the lower Re cases.

4 Summary and Conclusions

VNAP2 (Cline, 1981), a well documented and validated code for the computation of inviscid and viscous nozzle flow, is used to compute the transonic flow fields of two families of two-dimensional MLNs. Supersonic wall contours for the SSL MLN are generated using the MOC (Argrow, 1986); CSL MLN supersonic contours are generated using an analytical technique based on a source-flow assumption (Emanuel, 1986). The subsonic inlet is a combination of a straight wall section with a circular arc that represents a generic geometry that includes the salient features of any reasonable inlet.

It is shown that the sonic line is primarily dependent on the inlet parameters r_t and α, with a relatively minor dependence on M_f, Re or MLN type. The radius r_t primarily determines the sonic-line location and overall shape. The θ distribution along the sonic line has a greater influence than its actual shape. In all cases the flow is mostly parallel along the sonic line. The highly convergent flow along the sonic line is primarily near the wall with θ rapidly increasing toward zero away from the wall. In none of the cases did the flow along the sonic line appear to have $\theta > 0$ deg. This implies that for the cases investigated, the source flow assumption of the CSL, which requires $\theta \geq 0$ deg, is inaccurate.

The supersonic flow field of the SSL MLN behaves much as predicted by the MOC over the entire range of Re and M_f, except for the case of $r_t = 0$ and $\alpha = 60$ deg, which shows boundary-layer separation and an oblique shock at Re $\geq$ 11,700 and in some of the inviscid cases. The corresponding CSL MLN cases show an oblique shock that increases in intensity as Re increases for all cases with Re $\geq$ 11,700. In addition, boundary-layer separation occurs at lower α and larger r_t values than for the SSL cases.

The oblique shock waves in the CSL MLN are a result of an overexpansion at the throat followed by a rapid compression as the flow is forced to align with the supersonic wall contour. The same type of overexpansion occurs for the SSL MLN but is less severe since δ is smaller for the corresponding SSL MLN when $M_f \leq 5.9$. This phenomena is most evident in the inviscid cases and persists in all but the lowest Re cases, where defects in the design assumptions are less important because of the relatively thick boundary layer. The downstream compression is relieved by either decreasing α or increasing r_t.

The trends continue when M_f is increased to four. When M_f is increased to six, however, the supersonic wall contours of the two MLN types are very similar. As a result, the flow fields produced show the trends of the earlier SSL MLN cases and are virtually indistinguishable.

References

Ahlberg, J. H., Hamilton, S., Migdal, D., and Nilson, E. N., 1961, "Truncated Perfect Nozzles in Optimum Nozzle Design," *Journal of the American Rocket Society*, Vol. 31, No. 5, pp. 614–620.

Anderson, J. D., Jr., 1976, *Gasdynamic Lasers: An Introduction*, Academic Press, New York, p. 139.

Anderson, J. D., Jr., 1990, *Modern Compressible Flow*, 2nd Ed., McGraw-Hill, New York, pp. 325–331.

Argrow, B. M., and Emanuel, G., 1988, "Comparison of Minimum Length Nozzles," ASME Journal of Fluids Engineering, Vol. 110, No. 3, pp. 283–288.

Argrow, B. M., 1989, "A Computational Analysis of the Transonic Flow

Field of Two-Dimensional Minimum Length Nozzles," Ph.D. dissertation, University of Oklahoma.

Argrow, B. M., 1986, "Design and Analysis of an Axisymmetric Minimum Length Nozzle with a Straight Sonic Line," Thesis, University of Oklahoma.

Back, L. H., Massier, P. F., and Gier, H. L., 1965, "Comparison of Measured and Predicted Flows Through Conical Supersonic Nozzles, with Emphasis on the Transonic Region," *AIAA Journal*, Vol. 3, No. 9, pp. 1606–1614.

Back, L. H., and Cuffel, R. F., 1966, "Detection of Oblique Shocks in a Conical Nozzle with a Circular-Arc Throat," *AIAA Journal*, Vol. 4, No. 12, pp. 2219–2221.

Back, L. H., Massier, P. F., and Cuffel, R. F., 1967, "Flow Phenomena and Convective Heat Transfer in a Conical Supersonic Nozzle," *AIAA Journal of Spacecraft and Rockets*, Vol. 4, No. 8, pp. 1040–1047.

Back, L. H., Cuffel, R. F., and Massier, P. F., 1969, "Laminarization of a Turbulent Boundary Layer in Nozzle Flow," *AIAA Journal*, Vol. 7, No. 4, pp. 730–733.

Back, L. H., and Cuffel, R. F., 1971, "Flow Coefficients for Supersonic Nozzles with Comparatively Small Radius of Curvature Throats," *AIAA Journal of Spacecraft and Rockets*, Vol. 8, No. 2, pp. 196–198.

Back, L. H., Cuffel, R. F., and Massier, P. F., 1972, "Influence of Contraction Section Shape and Inlet Flow Direction on Supersonic Nozzle Flow and Performance," *AIAA Journal of Spacecraft and Rockets*, Vol. 9, No. 6, pp. 420–427.

Back, L. H., and Massier, P. F., 1972, "Viscous Non-Adiabatic Laminar Flow through a Supersonic Nozzle: Experimental Results and Numerical Calculations," ASME *Journal of Heat Transfer*, Vol. 94, No. 11, pp. 437–445.

Bae, Y. Y., and Emanuel, G., 1991, "Performance of an Aero-Space Plane Propulsion Nozzle," *AIAA Journal of Aircraft*, Vol. 28, No. 2, pp. 113–122.

Baker, T. J., 1981, "Numerical Computation of Transonic Potential Flow Through Nozzles," *Aeronautical Quarterly*, Vol. 32, Feb., pp. 31–42.

Brown, E. F., and Hamilton, G. L., 1976, "Survey of Methods for Exhaust-Nozzle Flow Analysis," *AIAA Journal of Aircraft*, Vol. 13, No. 1, pp. 4–11.

Brown, E. F., Brecht, T. J., and Walsh, K. E., 1977, "A Relaxation Solution of Transonic Nozzle Flows Including Rotational Effects," *AIAA Journal*, Vol. 14, No. 10, pp. 944–951.

Cline, M. C., 1974, "Computation of Steady Nozzle Flow by a Time-Dependent Method," *AIAA Journal*, Vol. 12, No. 4, pp. 419–420.

Cline, M. C., 1976, "Computation of Two-Dimensional, Viscous Nozzle Flow," *AIAA Journal*, Vol. 14, No. 3, pp. 295–296.

Cline, M. C., 1981, "VNAP2: A Computer Program for Computation of Two-Dimensional, Time-Dependent, Compressible, Turbulent Flow," Los Alamos National Laboratory Report LA-8872.

Cline, M. C., and Wilmoth, R. G., 1983, "Computation of High Reynolds Number Internal/External Flows," *AIAA Journal*, Vol. 21, No. 2, pp. 172–173.

Cline, M. C., and Wilmoth, R. G., 1984, "Computation of the Space Shuttle Solid Rocket Booster Nozzle Start-Up Transient Flow," AIAA Paper 84-0462.

Cuffel, R. F., Back, L. H., and Massier, P. F., 1969, "Transonic Flowfield in a Supersonic Nozzle with Small Throat Radius of Curvature," *AIAA Journal*, Vol. 7, No. 7, pp. 1364–1366.

Dumitrescu, L. Z., 1975, "Minimum Length Axisymmetric Laval Nozzles," *AIAA Journal*, Vol. 13, No. 4, pp. 520–521.

Dutton, J. C., and Addy, A. L., 1981, "Transonic Flow in the Throat Region of Axisymmetric Nozzles," *AIAA Journal*, Vol. 19, No. 6, pp. 801–804.

Emanuel, G., 1986, *Gasdynamics: Theory and Applications*, AIAA Educational Series, New York, pp. 307–328.

Emanuel, G., and Cline, M. C., 1981, "Laser-Induced Disturbance with Application to a Low Reynolds Number Flow," *AIAA Journal*, Vol. 19, No. 2, pp. 226–231.

Foelsch, K., 1949, "Analytical Design of an Axially Symmetric Laval Nozzle for a Parallel and Uniform Jet," *Journal of the Aeronautical Sciences*, Vol. 16, Mar., pp. 161–166, 188.

Greenberg, R. A., Schneiderman, A. M., Ahouse, D. R., and Parmentier, E. M., 1972, "Rapid Expansion Nozzles for Gas Dynamic Lasers," *AIAA Journal*, Vol. 10, No. 11, pp. 1494–1498.

Hall, I. M., 1962, "Transonic Flow in Two-Dimensional and Axially Symmetrical Nozzles," *Quarterly Journal of Mechanics and Applied Math*, Vol. XV, Pt. 4, pp. 487–508.

Hopkins, D. F., and Hill, D. E., 1966, "Effect of Small Radius of Curvature on Transonic Flow in Axisymmetric Nozzles," *AIAA Journal*, Vol. 4, No. 8, pp. 1337–1343.

Kliegel, J. R., and Levine, J. N., 1969, "Transonic Flow in Small Throat Radius of Curvature Nozzles," *AIAA Journal*, Vol. 7, No. 7, pp. 1375–1378.

Laval, P., 1971, "Time-Dependent Calculation Method for Transonic Nozzle Flows," NASA TT-F14, 033.

Nachshon, Y., 1983, "Simple and Accurate Calculation of Supersonic Nozzle Contour," *AIAA Journal*, Vol. 21, No. 5, pp. 783–784.

Oswatitsch, K., and Rothstein, W., 1949, "Flow Pattern in a Converging-Diverging Nozzle," NACA TM 1215.

Park, M. and Caughy, D. A., 1986, "Transonic Potential Flow in Hyperbolic Nozzles," *AIAA Journal*, Vol. 24, No. 6, pp. 1037–1039.

Pirumov, U. G., and Roslyakov, G. S., 1978, *Gas Flow in Nozzles*, Springer Series in Chemical Physics, Vol. 29, Springer-Verlag, New York, pp. 145–158.

Sadaat, A., 1982, "Analysis of Minimum Length Two-Dimensional Nozzles," Thesis, University of Oklahoma.

Sauer, R., 1947, "General Characteristics of the Flow through Nozzles at near Critical Speeds," NACA TM 1147.

Shapiro, A., 1953, *Compressible Fluid Flow*, Vol I, The Ronald Press Co., New York, pp. 512–516.

Vanco, M. R., and Goldman, L. J., 1968, "Computer Program for Design of Two-Dimensional Supersonic Nozzle with Sharp-Edged Throat," NASA TM X-1502.

Wada, Y., Yamaguchi, M., and Kubota, H., 1987, "Numerical Investigation of Nozzle Shape Effects on CO_2 Gas Dynamic Laser Performance," AIAA Paper 87-1452.

Wagner, J. L., 1971, "A Cold Flow Field Experimental Study Associated with a Two-Dimensional Multiple Nozzle," Naval Ordnance Laboratory, NOLTR 71-78.

Zucrow, M. J., and Hoffman, J. D., 1977, *Gas Dynamics*, Vol. 2, Wiley, New York, pp. 104–111.

ERRATA

Errata on "Viscosity Flow Correction for Small Control Valve Trim," by H. D. Baumann, published in the March 1991 issue of the **Journal of Fluids Engineering**, Vol. 113, pp. 86-89.

Equation (8) has a typographical error; the numerator under the radical should have been 10,000.

The Oscillation of Horseshoe Vortex Systems

C. J. Baker
Department of Civil Engineering,
Nottingham University,
University Park,
Nottingham NG7 2RD, United Kingdom

The oscillation of horseshoe vortex systems around the base of wall mounted obstacles in the transition range is considered. Existing experimental data from a variety of sources is reanalyzed in the light of two hypotheses—that vortex oscillations are caused by (a) oscillations of the entire vortex system, and (b) by vortex core instabilities. It is shown that both types of oscillation exist, and the regions in parameter space in which each exist are determined. The interaction between the different types of oscillation is also described.

1 Introduction

The phenomenon of the horseshoe vortex is a well known and well documented one, and has been investigated by many investigators in the past, including the author (Baker, 1978, 1979, 1980, 1985). Essentially horseshoe vortices are caused by the rolling up of separated shears upstream of wall mounted obstacles. If the upstream boundary layer on the wall is laminar then the flow patterns that are produced can be beautifully intricate. Figure 1 is a reproduction of a well known photograph by E. P. Sutton (Thwaites, 1960) that illustrates this point well. This figure shows 3 clockwise and 3 anticlockwise rotating vortices on the plane of symmetry upstream of the cylinder.

This paper will, in the main, concentrate on one particular aspect of this phenomenon—that is the oscillatory behavior of such vortices in the transitional regime, between the steady laminar horseshoe vortices which occur at low Reynolds number and the fully turbulent horseshoe vortices that occur at higher Reynolds numbers. Earlier experiments by both Schwind (1962) and the author (Baker, 1978) suggest that two sorts of oscillations can exist at any one set of flow conditions, with the flow intermittently switching from one type of oscillation to another. The author termed these primary and secondary oscillations, with the primary oscillations tending to be rather more severe than the secondary, and persisting to substantially higher Reynolds numbers. This switching behavior was very apparent, both from visual observations and from oscilloscope observations of hot wire probe signals, where the traces produced by the different types of oscillation could be clearly seen.

Now the author in his earlier work attempted to quantify these oscillations, and to determine the relevant scaling parameters, as had several other authors (Schwind, 1962; Roper, 1967; Norman, 1972). He met, however, with only limited success and it has to be said that the way in which these oscillations scale on the flow parameters was not fully determined. However, since this work was carried out a further major series of tests has been carried out in India by Sharma, 1988, and a substantial amount of data was obtained for vortex oscillation around a variety of body shapes. These data will be used, alongside all the earlier data, in what follows.

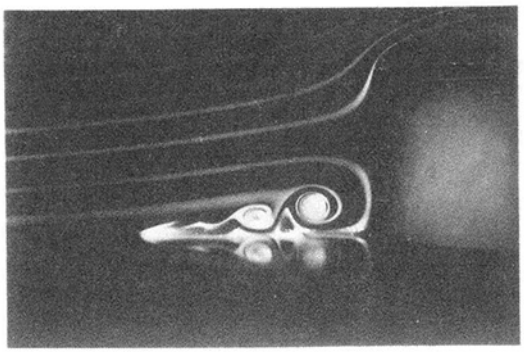

Fig. 1 The experiments of Sutton

First, however, it is necessary to set up a framework for the investigation through the use of dimensional analysis. In what follows it will be assumed that the following functional relationship is valid.

$$\frac{fD}{U} = fn\left(\text{obstacle geometry}, \frac{UD}{\nu}, \frac{D}{\delta^*}, \frac{l}{\delta^*}, H\right) \tag{1}$$

where f is the vortex oscillation frequency, D is the effective diameter of the wall mounted body (which will be defined more precisely in what follows) and l is its length, U is the free-stream velocity; δ^* is the undisturbed boundary layer displacement thickness, H is the boundary layer form parameter, and ν is the kinematic viscosity of the fluid. In most of what follows it will be assumed that $H = 2.59$, the laminar boundary layer zero pressure gradient value, and that l/δ^* is large i.e., the obstacle extends well out of the boundary layer. Thus in such a case, for a fixed obstacle geometry

$$\frac{fD}{U} = fn\left(\frac{UD}{\nu}, \frac{D}{\delta^*}\right) \tag{2}$$

The data that will be used are shown in Table 1, together with the values of the relevant dimensionless groups.

Even if $H = 2.59$, the value of l/δ^* is large and the geometry

Contributed by the Fluids Engineering Division for publication in the JOURNAL OF FLUIDS ENGINEERING. Manuscript received by the Fluids Engineering Division November 20, 1990.

Table 1 Horseshoe vortex oscillation data

Author	Geometry	$\frac{UD}{\nu}$	$\frac{D}{\delta^*}$	$\frac{l}{\delta^*}$	H
Roper, 1967	Cylinder	2911	1.42	6.9	2.59*
Norman, 1972	Prisms	3000	16.7	16.7	2.59*
Baker, 1978 A	Long cylinder	4000–15000	18–55	86–264	2.55–2.75
Baker, 1978 B	Short cylinder	5181	23	11.5	2.59*
Sharma, 1988 A	Cylinder	2440–4610	5.8–9.5	35–57	2.59*
Sharma, 1988 B	Cylindrical pier	2400–4750	5.9–9.5	35–57	2.59*
Sharma, 1988 C	Rectangular pier	1400–3300	4.0–7.5	24–45	2.59*
Sharma, 1988 D	Wedge pier	3100–4500	7.0–9.5	42–57	2.59*
Sharma, 1988 E	Lenticular pier	3100–4500	7.0–9.5	42–57	2.59*

*Assumed value.

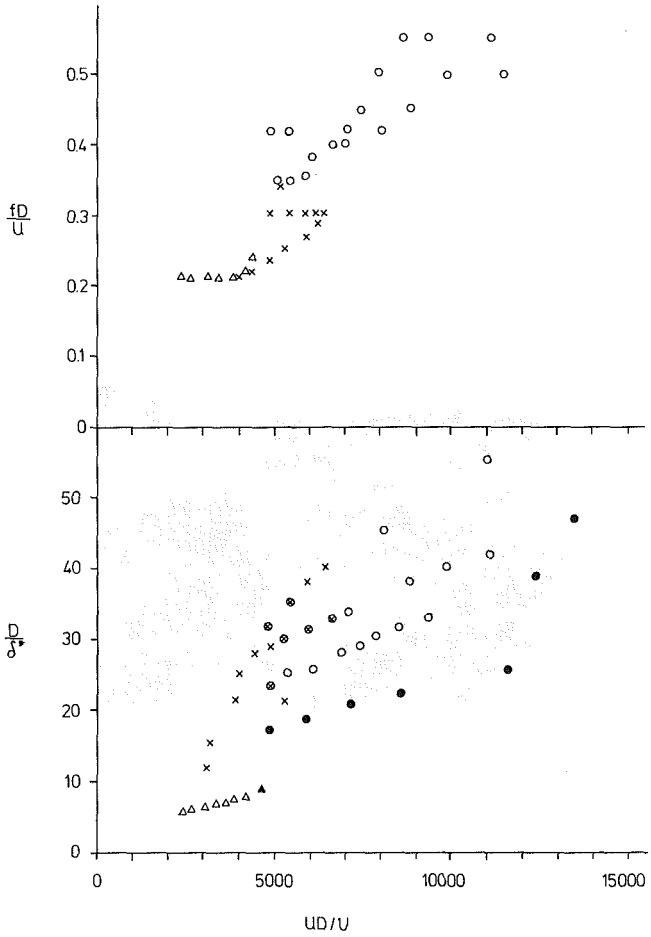

Fig. 2 Vortex oscillation data for cylinders.
(○ Baker, 1978 A Primary oscillations; × Baker 1978 A Secondary oscillations;
• Baker 1978 A Fully turbulent flow; △ Sharma 1988 A Oscillations; ▲ Sharma 1988 A
Fully turbulent flow)

is fixed, the data are still complex. Figure 2 shows the data points for cylinders in the UD/ν versus D/δ^* plane and fD/U plotted against UD/ν. It can be seen that these graphs are somewhat confused. The results of Baker A show the two types of oscillation already mentioned, but the other results do not. In general fD/U increases as UD/ν increases.

This paper thus sets out to investigate this problem of scaling and effectively attempts to answer two questions.

(a) Over what parameter range will horseshoe vortex oscillations occur?

(b) How does the frequency of oscillation vary, and with what parameters?

In the first instance only the data for tall cylinders will be considered, as in Fig. 2, but with the additional constraint that $D/\delta^* > 5$ i.e., that the cylinder diameter is comparable to or greater than the boundary layer thickness $\delta(\approx 3\delta^*$ for laminar boundary layers). Two hypotheses concerning the nature of horseshoe vortex oscillations will be tested, viz.

(a) that the horseshoe vortex oscillations are due to an oscillation of the entire separated flow system upstream of the cylinder (and thus scale on the size of this system), and

(b) that the horseshoe vortex oscillations are due to an oscillation of the vortex core of the primary vortex (the major clockwise rotating vortex in Fig. 1).

These two hypotheses are considered further in Sections 2 and 3, respectively. Section 2 is mainly a reanalysis of experimental data, and Section 3 presents the results of a linear stability analysis of the vortex core. It will be seen that the experimental results are consistent with the above hypotheses, and Baker's primary oscillations can be identified with oscillations caused by hypothesis (a) and Baker's secondary oscillations with those caused by hypothesis (b). Section 4 considers the interaction between these two types of oscillations, and their regions of existence in parameter space. Section 5 then goes on to consider the effect of the restrictions imposed above and considers the experimental data for $D/\delta^* < 5$ and for small l/δ^*, and considers obstacle shapes other than circular cylinders. Section 6 then goes on to discuss a number of other points that arise out of the earlier considerations, that whilst not of direct relevance to the discussion of oscillating vortex systems are nonetheless of some interest and some concluding remarks are made.

At this point mention must be made of the errors that are involved. This is in many ways difficult to quantify since many of the results that will be used were obtained by investigators other than the author. However normal wind tunnel practice should result in values of UD/ν, D/δ^*, l/δ^* that are accurate to around 3 percent and values of H accurate to around 5 percent. However from the author's experience values of fD/U are only repeatable within wide scatter bands (say 10 to 25 percent). These values were obtained from visual inspection of oscilloscope traces of hot wire and pressure transducer outputs, and the variability seems to be a feature of the problem. It should be noted that the results obtained by the author in Baker (1978) have been smoothed and averaged for the purposes of the work reported here, to minimize possible confusion due to this scatter. This was achieved by fitting a curve through the data obtained from any one set of wind tunnel runs with a fixed geometrical configuration, and taking values from this curve. Physically this procedure simulates the collection of data over a much longer period of time than was actually the case.

2 Oscillations of the Separated Flow Region

If the observed oscillations of the horseshoe vortex system are due to oscillations of the separated flow region upstream of the wall mounted obstacle then one would expect that the

frequency of oscillation would be given by an expression of the form

$$\frac{fL}{U} = fn\left(\frac{UL}{\nu}\right) \tag{3}$$

where the conditions stated in Section 1 apply, and L is a typical length scale of the separated flow region. In addition, one might perhaps expect that there would be a reasonably well-defined value of UL/ν for which vortex oscillations begin, and perhaps another well-defined value for which these oscillations break down into random turbulence. One might expect this length scale L to be a function of the obstacle diameter D and the boundary layer thickness δ (or δ^*). Assume that L can be taken as $(D)^x(\delta^*)^{1-x}$. An extensive investigation of the experimental data shows that for tall cylinders a value of $x = 0.5$ collapses the data for the results of Baker A (primary oscillations), Baker B and Sharma A remarkably well (Fig. 3). Vortex oscillations begin a $U(D\delta^*)^{0.5}/\nu \approx 1000$, and break down into full turbulence at $U(D\delta^*)^{0.5}/\nu \approx 1600$. $f(D\delta^*)^{0.5}/U$ increases from approximately 0.07 to 0.09 over this range. The other cylinder data for the conditions considered (Baker A (secondary oscillation)) does not collapse in the same way. To the author the collapse of data shown in Fig. 3 indicates fairly strongly that the oscillations shown (primary oscillations) are due to oscillations of the separated flow region upstream of the body. The value of the exponent x of 0.5 seems very reasonable, and makes the length scale L a form of "hydraulic radius" of the separated flow region.

3 Oscillations of the Vortex Core

The Appendix sets out a linear stability analysis of the horseshoe vortex core. This is based on the mean flow analysis carried out by the author in his doctoral study (Baker, 1978), in which the main assumption was made that, on the plane of symmetry upstream of the obstacle, the radial velocity in the vortex core is proportional to the distance from the center of the vortex core, which was shown experimentally to be a reasonable assumption. The results of this analysis, shown in Fig. 4, show the boundary between the stable and the unstable regions in the $\alpha - \Phi_3$ plane. α is the dimensionless instability wave number given by $2\pi r_*/\lambda$, where r_* is the radius of the vortex core and λ is the instability wavelength. Φ_3 is a Reynolds number $u_* r_*/\nu$ where u_* is the radial velocity at the edges of the vortex core. It can be seen that there is a critical value of Φ_3 for stability of 2.51. The maximum growth rate of instabilities is shown in the Appendix to be for $\alpha = 0$. This is of course unrealistic, since as α approaches zero, λ becomes much larger than the vortex core. One would thus expect the analysis to break down for low values of α, and for the maximum growth rate of instabilities to occur for a small, finite α.

Now it is possible to relate Φ_3 and α to more physically measurable parameters (although Baker (1978) did attempt to obtain some experimental values of Φ_3—see below). If one says that the flow into the vortex core is proportional to the flow in the upstream boundary layer then one can write

$$U(\delta - \delta^*) \propto u_* r_*$$

Now as $\delta \approx 3\delta^*$ for laminar boundary layers this implies

$$\Phi_3 = \frac{u_* r_*}{\nu} \propto \frac{U\delta^*}{\nu} \tag{4}$$

Also the frequency of oscillation f can be related to the disturbance wavelength λ by

$$f = v_*/\lambda$$

where v_* is the circumferential velocity at the edge of the vortex core

$$\therefore f = \frac{v_* \alpha}{2\pi r_*}$$

$$\frac{f r_*}{v_*} = \frac{\alpha}{2\pi}$$

Since one would expect $r_* \approx \delta^*$ and $v_* \approx U$

$$\alpha \approx 2\pi \frac{f\delta^*}{U} \tag{5}$$

Thus this analysis would lead one to expect that a plot of $f\sigma^*/U$ against $U\delta^*/\nu$ would show a critical value of $U\delta^*/\nu$ for instability, with the values of $f\delta^*/U$ collapsing onto a single curve. Such a plot is presented in Fig. 5 for the data that did

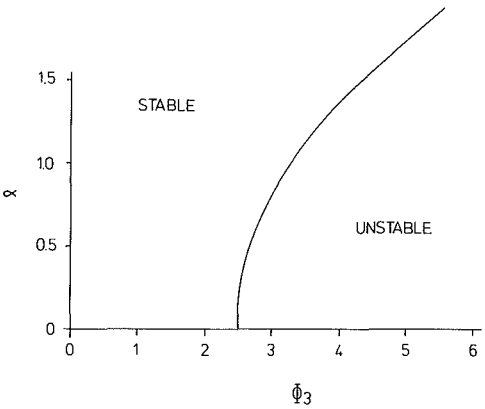

Fig. 4 Results of vortex stability analysis

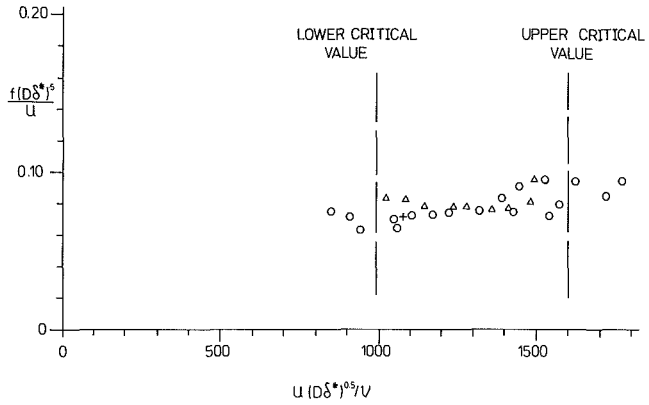

Fig. 3 Test of hypothesis 1—vortex oscillations scale on size of vortex system.
(○ Baker, 1978 A Primary oscillations; + Baker 1978 B; ▲ Sharma 1988 A Oscillations;)

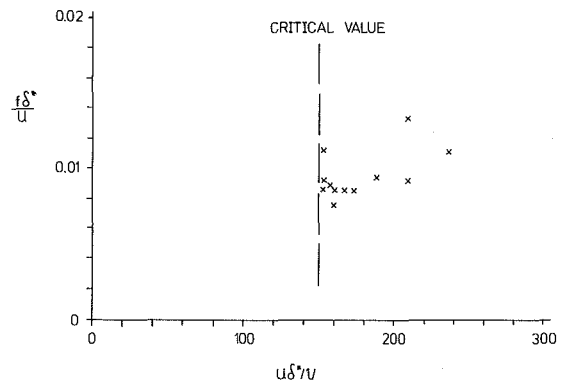

Fig. 5 Test of hypothesis 2—vortex oscillations due to instability of vortex core.
(× Baker 1978 A Secondary oscillations;)

not conform to the plot of Fig. 3 i.e., the Baker A (secondary oscillation) results. The results are perhaps not quite so conclusive as one could wish, but a definite minimum value of $U\delta^*/\nu = 150$ is observable, and the values of $f\delta^*/U$ are approximately 0.01. Experimental measurements reported in Baker, 1978, suggest that for a vortex system very close to oscillation a value of $\Phi_3 \approx 2.0$ is appropriate, within a considerable margin of error. This is not inconsistent with the above analysis. Also a value of $f\delta^*/U$ of 0.01 corresponds to $\alpha \approx 0(0.1)$ from the above analysis, which seems to be a reasonable value from Fig. 4. Thus these results indicate, perhaps somewhat tentatively, that the secondary oscillations described by Baker (1978), (1979) can be attributed to unstable oscillations of the vortex core.

4 Interaction Between the Different Types of Oscillation

The results of Baker A show that the two types of oscillation (primary and secondary) can both exist at one particular set of flow parameters, with the primary oscillations tending to occur at higher Reynolds numbers. The question that thus arises is why the results of Sharma (1988) do not similarly show two distinct oscillation frequencies. The answer to this question will become apparent in what follows.

Consider first the oscillations described in Section 2 (primary oscillations). These oscillations occur between fairly well defined values of $U(D\delta^*)^{0.5}/\nu$ (1000 to 1600). In the parameter plane of D/δ^* against UD/ν, this implies that these critical conditions exist along lines for which

$$(1000)^2 D/\delta^* = (UD/\nu)^2 \text{ for the lower critical value} \quad (6)$$

$$\text{and } (1600)^2 D/\delta^* = (UD/\nu)^2 \text{ for the upper critical curve} \quad (7)$$

Similarly the secondary oscillations of Section 3 begin at a well defined value of $U\delta^*/\nu$ (= 150). In the above parameter plane this implies

$$150\, D/\delta^* = UD/\nu \quad (8)$$

Figure 6 is a modified version of Fig. 2(*b*), with the above critical condition curves also shown. Also shown is the line corresponding to $U\delta^*/\nu = 645$, i.e.,

$$645 \frac{D}{\delta^*} = \frac{UD}{\nu} \quad (9)$$

which is the value for natural boundary layer transition (Schlichting, 1968). (The various sets of experimental data in this plane tend to be along lines for which

$$D/\delta^* \propto (UD/\nu)^{1/2} \quad (10)$$

which is to be expected for essentially flat plate boundary layers—see Baker, 1978.) It must, however, be borne in mind when considering the plot of Fig. 7 that the boundaries indicated between the different flow regimes can only be regarded as approximate. There are no absolutely fixed values of flow parameters that mark the transition from steady to oscillatory flows, or from oscillatory flows to fully turbulent flows. Thus there is some overlap of the data over the indicated boundaries of the different flow regions. This is particularly the case for the values of the Baker A dataset at the bottom end of the D/δ^* range investigated, where no regular oscillations were seen. This may well be due to the combination of the lack of precision noted above, and the narrowing of the primary oscillation range as D/δ^* decreases. However, this imprecision does not invalidate the main conclusion, that the different types of oscillation exist in different areas of parameter space, and that there are some regions where both types can exist with the flow switching intermittently from one type to another.

Now if one considers the frequencies of oscillation of primary and secondary oscillations these can be seen to be identical if, from Figs. 3 and 5,

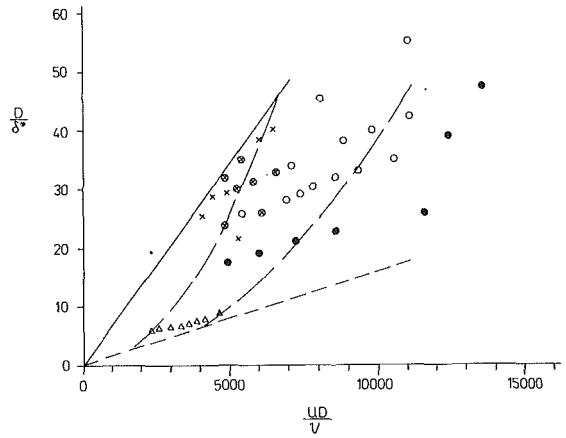

Fig. 6 Vortex oscillation data for cylinders, showing regions of existence of primary and secondary oscillations and fully turbulent flows. (○ Baker (1978) A Primary oscillations; × Baker (1978) A Secondary oscillations: • Baker (1978) A Fully turbulent flow; △ Sharma (1988) A Oscillations; ▲ Sharma (1988) A Fully turbulent flow) (— Eqs. (6) and (7) for lower and upper critical values for primary oscillations;—Eq. (8) for lower critical value for secondary oscillations; – Eq. (9) for boundary layer transition on a flat plate.)

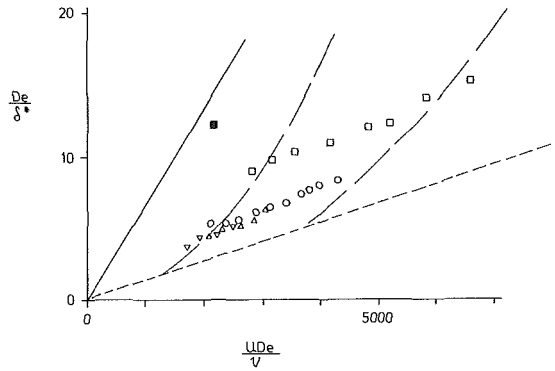

Fig. 7 Effect of obstacle shape on vortex oscillations (for key to lines see Fig. 6; ○ Sharma (1988) B—Cylindrical pier; □ Sharma (1988) C—Rectangular pier; △ Sharma (1988) D—Wedge pier; ▽ Sharma (1988) E—Lenticular pier; ■ Norman (1972), Square prism.)

$$0.01 \frac{U}{\delta^*} = 0.08 \frac{U}{D} \quad (11)$$

i.e., for $D/\delta^* = 8.0$. Thus at low values of D/δ^*, close to the values observed by Sharma, it seems likely that only one type of oscillation would be observed because of the similarity in oscillation frequency of the primary and secondary modes.

Figure 6 also illustrates the substantial lowering of the non-disturbed flat plate boundary-layer Reynolds number by a wall mounted obstacle, for a fixed value of D^*. For $UD/\nu > 3970$, where the line of Eq. (9) crosses the parabola of Eq. (7), transition to a fully turbulent flows occurs at values of $U\delta^*/\nu$ less than the flat plate values.

This figure thus indicates the region of existence of primary and secondary horseshoe vortices in the parameter plane D/δ^* versus UD/ν, for tall circular cylinders in zero pressure gradient boundary layers ($1/\delta^*$ large, $H = 2.59$), for $D/\delta^* > 5$. The next section goes on to examine what happens when $D\delta^* < 5$, and for small values of $1/\delta^*$, and also looks at the effect of different obstacle shapes.

5 Vortex Oscillations for Other Flow Conditions

The question now arises as to what is the effect on vortex oscillations of moving away from the standard flow conditions

Table 2 Effective diameters for various shapes of piers

Data	S/D	S/D (equivalent cylinder)	D_e/D
Sharma B (Cylindrical pier)	1.55	1.75	0.89
Sharma C (Rectangular pier)	3.5	1.75	2.0
Sharma D (Wedge pier)	1.17	1.75	0.67
Sharma E (Lenticular pier)	0.96	1.75	0.55
Norman (Square plate)	0.72	0.98	0.73

described in previous sections. Let us first consider what would be the effect of small D/δ^* (<5, say) or small l/δ^*. Essentially in these conditions the pressure gradient upstream of the obstacle will be reduced, and thus one would expect the horseshoe vortex system to be less vigorous, and the region of upstream separated flow less extensive. One would expect that this would be equivalent to a decrease in the effective obstacle diameter. Thus higher values of UD/ν and D/δ^*, with D the actual obstacle diameter, would be needed for any particular critical condition to occur. So if the boundaries between flow regions are plotted as in Fig. 6 one would expect the various boundaries to be skewed to the right at low values of D/δ^* for large l/δ^*, or moved to the right generally for low values of l/δ^*. There is only limited data available to check this assertion. Firstly, let us consider the results of Roper (1967). From his results one can calculate the following set of parameters for vortex oscillations.

$$\frac{UD}{\nu}=2911, \quad \frac{D}{\delta^*}=1.42, \quad \frac{fD}{U}=.124$$

Clearly these results lie well to the right of the fully turbulent line in Fig. 6 as would be expected from above. If an effective diameter D_e of $0.5D$ is assumed then Roper's data are brought into the region of vortex oscillations as would be expected. Also if this is done then

$$U(D_e\delta^*)^{0.5}/\nu=1700 \quad f(D_e\delta^*)^{0.5}/U=0.072$$

which is just about consistent with the results of Fig. 3, although the value of the Reynolds number is rather high. (It should, however, be noted that Roper's data is rather odd in that $U\delta^*/\nu = 1995$—well above the value one would normally expect in a laminar boundary layer.)

The second set of results that can be used to check the above hypothesis are some further, so far unconsidered, results for the Baker B dataset. The following set of parameters can be derived from the data for the onset of vortex oscillations.

$$UD/\nu=6710, \quad D\,\delta^*=7.2$$

which again lies well to the right of the fully turbulent curve.

The concept of equivalent diameter is also useful when considering the effect of obstacle geometry. Let us define an effective diameter as D_e where the ratio of D_e to D is given by the ratio of the distance of the primary separation point from the obstacle leading edge to the similar distance for a circular cylinder of similar diameter. Using such a definition the results of Sharma B, Sharma C, Sharma D, Sharma E, and Norman were plotted (in the form of Fig. 6) in Fig. 7 for cylindrical nosed piers, rectangular nose piers, wedge nose piers, lenticular nose piers and square plates respectively. The ratio of D_e/D for each of the Sharma datasets were obtained from experimental measurements of separation positions. For the Norman dataset, the values of the square plate separation distances were found experimentally while the equivalent cylinder value was calculated from the work of Baker (1985). Values of D_e/D are shown in Table 2.

Note that in plotting Fig. 7 the oscillations recorded by Sharma for the wedge and lenticular piers are taken to be aperiodic and turbulent rather than as having a fixed frequency as Sharma assumed. This is supported by an examination of his original data, and also by the fact that the dominant frequencies picked out by Sharma and presented by him show very considerable scatter.

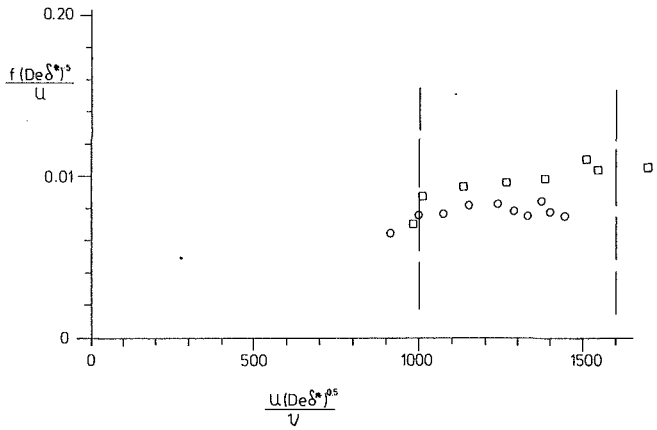

Fig. 8 Vortex oscillation frequencies for rectangular and cylindrical piers

(for key to points see Fig. 7)

It can be seen that the Sharma B and C data fit into the primary oscillation zones well in this form. The irregular oscillations of the Sharma D and E data are close to the fully turbulent boundary layer line. It is thus perhaps not surprising that oscillations were not observed for these tests. The data point of Norman (which is for the onset of oscillations) lies in the secondary oscillation region of parameter space. The Sharma B and C data are plotted in the form of Fig. 3 in Fig. 8, with the diameter given by D_e. Again this data can be seen to agree with that of Fig. 3 quite well, thus again suggesting that they can be classified as primary oscillations.

6 Discussion and Concluding Remarks

The results presented in previous sections suggest that, at moderate to high values of D_e/δ^*, as the Reynolds number UD/ν increases then secondary oscillations are first observed, caused by instability in the vortex core. These oscillations occur above a critical value of $U\delta^*/\nu$ ($\approx$ 150) and the frequency of oscillations is given by $f\delta^*/U \approx 0.01$. These oscillations appear to initiate the stronger primary oscillations for values of $U(\delta^*D_e)^{0.5}/\nu$ greater than about 1000. These oscillations persist up to values of $U(\delta^*D_e)^{0.5}/\nu$ of about 1600, where the vortex flow becomes fully turbulent, with an oscillation frequency of $f(\delta^*D_e)^{0.5}/U$ of about 0.08. At low values of D_e/δ^* it seems that oscillations only occur at a single frequency, since the frequencies of primary and secondary oscillations are close to each other. From this information one can thus determine regions in the UD_e/ν versus D_e/δ_* parameter space where the various sorts of oscillations occur.

The considerations set out earlier also allow one to speculate about another interesting and related phenomenon i.e., why, for steady laminar horseshoe vortices, does the number of vortices increase as the Reynolds number increases (Baker, 1978). It seems to the author that a possible explanation might be as follows. As the Reynolds number increases the local vortex core Reynolds number (Φ_3) within the primary vortex will increase, up to a point where the critically stable value is passed. Above this Reynolds number the primary vortex will begin to oscillate. The immediate effect of such an oscillation will be to sever the shear layer feeding that vortex, thus reducing the local Reynolds number. This shear layer will then roll up to form a vortex pair upstream of the primary vortex, whilst the primary vortex returns to its stable state. As the Reynolds number increases further the local Reynolds number of both the primary vortex and the newly created vortex will increase until one of them again becomes momentarily unstable, which results in a third vortex pair being formed (such as in Fig. 1).

When the separated flow regions upstream of the obstacle is occupied by, say, 3 vortices and their counterrotating partners, it seems reasonable to assume there is simply no room for further vortices, so when instabilities are initiated, these will continue i.e., secondary oscillations will occur. Such an explanation of the variation of vortex number is perhaps somewhat at variance with the more orthodox explanation that the number of vortices increases due to flow separation on the wall beneath the vortex system. It does, however, have the advantage of making it unnecessary to postulate flow separation in regions of an effective favorable pressure gradient (see Baker, 1979).

Such considerations lead one to further speculations. There is evidence that the number of vortices in turbulent horseshoe vortex systems is also Reynolds number dependent, for both low speed and supersonic flows, (Pierce and Tree, 1990; Sedney and Kitchens, 1975). The variation is by no means straightforward with vortex number sometimes increasing and sometimes decreasing with Reynolds number. It would seem possible to the author that such variations may well be caused by a complex interaction between vortex instabilities and a variable position for the upstream separation line, which could result in a variation of vortex number depending upon the stability of the vortices, and the space available within the separated flow region for these vortices to multiply in number. Since these instabilities depend upon $U\delta^*/\nu$ and the separation line position depends upon the same parameter, it is likely that this parameter will control the number of vortices in a turbulent flow.

Also in a recent intriging paper low frequency turbulent horseshoe vortex oscillations have been noted (Devenport and Simpson, 1990) with $f\delta/U = 0.05$ where δ is the undisturbed boundary-layer thickness. How such oscillations are related to those described in this paper is by no means clear, but it could well be that such oscillations are oscillations of the complete vortex system. (This assumes a value of L of around 1.6δ which seems reasonable.) Also such oscillations can be inferred from the supersonic experiments of Sedney and Kitchens (1975), who present surface oil flow visualization with streamlines on the plane of symmetry upstream of the cylinder which cross apparent separation lines. Such a flow is of course impossible for a steady flow, and it is likely that these flow visualization results were obtained in unsteady, oscillatory flows and show merely a time average of different flow patterns. Perhaps with more data it will be possible to draw a generalized picture similar to Fig. 6, that shows regions of different types of flow for all types of horseshoe vortex systems—subsonic and supersonic, laminar and turbulent, steady or oscillatory.

Finally some comments are relevant here about the transition process as a whole within horseshoe vortices. It would seem quite possible to discuss these processes using the language of nonlinear dynamics i.e., chaos theory. As the Reynolds number increases the number of horseshoe vortices increases from 2 to 4 to 6, 2 distinct sorts of oscillation then occur (examples of period doublings), before a final breakdown to turbulence (or chaos). If the above speculations are correct then it is also possible that a similar process occurs in turbulent vortex systems at even higher Reynolds numbers. Such a description is an attractive one, but in essence is no more than an analogy. If the "route to chaos" offered by horseshoe vortex systems is to be fully described, a great deal more experimental work is required to describe the process fully. If this is done, however, it perhaps offers a way in which an "engineering scale" transition problem can be analyzed by using the powerful techniques of nonlinear dynamics.

References

Baker, C. J., *1978*, "Vortex Flows Around the Bases of Obstacles," PhD thesis, Cambridge University.

Baker, C. J., 1979, "The Laminar Horseshoe Vortex," *Journal of Fluid Mechanics*, Vol. 95, pp. 347-367.

Baker, C. J., 1980, "The Turbulent Horseshoe Vortex," *Journal of Wind Engineering and Industrial Aerodynamics*, Vol. 6, pp. 9-23.

Baker, C. J., 1985, "The Position of Points of Maximum and Minimum Shear Stress Upstream of Cylinders Mounted Normal to Flat Plates," *Journal of Wind Engineering and Industrial Aerodynamics*, Vol. 18, pp. 263-274.

Devenport, W. J., and Simpson, R. L., 1990, "Time Dependent and Time Averaged Turbulence Structure Near the Nose of a Wing Body Junction," *Journal of Fluid Mechanics*, Vol. 210, pp. 23-55.

Hall, M., 1966, "The Structure of Concentrated Vortex Cores," *Progress in Aero Sci.*, Vol. 7, Pergamon.

Norman, R. S., 1972, "On Obstacle Generated Secondary Flows in Laminar Boundary Layers and Transition to Turbulence," PhD dissertation, Illinois Institute of Technology.

Pierce, F. J., and Tree, I. K., 1990, "The Mean Flow Structure in the Symmetry Plane of a Turbulent Horseshoe Vortex," ASME JOURNAL OF FLUIDS ENGINEERING, Vol. 112, pp. 16-22.

Roper, A., 1967, "A Cylinder in a Turbulent Shear Layer," PhD thesis, Colorado State University.

Rott, N., 1958, "On the Viscous Course of Line Vortices," *ZAMP*, Vol. 9, pp. 543-553.

Schlicting, H., 1968, *Boundary Layer Theory—6th Ed.*, McGraw-Hill.

Schwind, R., 1962, "The Three Dimensional Boundary Layer Near a Strut," MIT Gas Turbine Lab Report.

Sedney, R., and Kitchens, C., 1975, "The Structure of Three Dimensional Separated Flows in Obstacle/Boundary Layer Interactions," AGARD Conf. Proc. No. 168.

Sharma, S. C., 1988, "Experimental Investigation of Vortex Flow and Its Modification Around Wall/Cylinder Junctions," PhD thesis IIT, Kanpur, India.

Thwaites, B., 1960, "Incompressible Aerodynamics," O.U.P.

APPENDIX

Stability analysis for a laminar horseshoe vortex

A.1 Equations of Motion. In what follows the core of a horseshoe vortex on the plane of symmetry upstream of an obstacle will be considered. Cylindrical coordinates will be used with r the radial coordinate, measured from the center of the vortex core, ϕ the circumferential coordinate and z the longitudinal coordinate measured from the plane of symmetry. The velocities in the r, ϕ, and z directions are u, v and w, respectively. It will be assumed, following Hall (1966), that

(*a*) $\dfrac{\partial}{\partial\phi}=0$ i.e., no circumferential changes

(*b*) $\dfrac{\partial}{\partial z} \ll \dfrac{\partial}{\partial r}$ i.e., changes occur much more rapidly in the radial than in the longitudinal direction.

(*c*) $\dfrac{\partial\rho}{\partial t}=0$ i.e., incompressible flow.

(*d*) for $z = 0$, $w = 0$ i.e., the cross flow is zero on the plane of symmetry where $z = 0$.

The continuity equation can thus be written as

$$\frac{1}{r}\frac{\partial}{\partial r}(ur)+\frac{\partial w}{\partial z}=0 \tag{A.1}$$

and the radial momentum equation can be written as

$$\frac{\partial v}{\partial t}+u\frac{\partial v}{\partial r}+\frac{uv}{r}=\frac{1}{r^2}\frac{\partial}{\partial r}\left(\nu r^2\frac{\partial v}{\partial r}-\frac{v}{r}\right) \tag{A.2}$$

Nondimensionalizing with reference values of r, z and v, r_*, z_*, v_*, and letting $R = r/r_*$, $Z = z/z_*$, $U = u/v_*$, $V = v/v_*$, $W = w/v_*$, $T = tv_*/r_*$, one obtains

$$\frac{1}{R}\frac{\partial}{\partial R}(RU)+\Phi_1\frac{\partial W}{\partial Z}=0 \tag{A.3}$$

$$\frac{\partial V}{\partial T}+U\frac{\partial V}{\partial R}+\Phi_1 W\frac{\partial V}{\partial Z}+\frac{UV}{R} =\frac{1}{\Phi_2}\frac{1}{R}\frac{\partial}{\partial R}\left(R^2\left(\frac{\partial V}{\partial R}-\frac{V}{R}\right)\right) \tag{A.4}$$

where $\Phi_1 = r_*/z_*$ and $\Phi_2 = v_*r_*/\nu$. r_* and u_* can be interpreted physically as the values of r and u at the edge of the vortex core.

Now we make the major assumption that, on the plane of symmetry, the radial velocity is proportional to the distance from the vortex center, i.e., $U = -cR$ (which is the assumption made by Rott (1958) in his analysis). At $R = 1$, if $u = u_*$, then $c_* = u_*/v_*$. From this assumption, and Eq. (A.3) one obtains

$$W = 2cZ/\Phi_1 \tag{A.5}$$

Thus from Eq. (A.4) one obtains

$$R^2 \frac{\partial^2 V}{\partial R^2} + (R + \Phi_3 R^3) \frac{\partial V}{\partial R} - (1 - \Phi_3 R^2) V = \Phi_1 R^2 \frac{\partial V}{\partial T} \tag{A.6}$$

where $\Phi_3 = u_* r_*/\nu$

A.2 Steady-State Solution. Equation (A.6) may be solved for the steady state solution by letting $\partial/\partial t = 0$ and $\Gamma = 2\pi R V$, which results in a considerable simplification. Applying the boundary conditions $V = 0$ at $R = 0$ and $V = 1$ at $R = 1$ the solution is found to be

$$V = \frac{1}{R}\left(\frac{1 - e^{-\Phi_3 R^2/2}}{1 - e^{-\Phi_3/2}}\right) \tag{A.7}$$

The form of this solution is shown in Fig. (A1) for $0 < \Phi_3 < 5$. The velocity is a maximum for

$$R_m = (2.51/\Phi_3)^{1/2} \tag{A.8}$$

and is given by

$$V_m = \left(\frac{\Phi_3}{2.51}\right)^{1/2} \left(\frac{1 - e^{-1.25}}{1 - e^{-\Phi_3/2}}\right) \tag{A.9}$$

A.3 Linearization of Equations of Motion and Stability Analysis. In the conventional way assume that

$$V = \bar{V} + V^1 \tag{A.10}$$

where $\bar{V}$ is the mean component of V and V^1 is the fluctuating component, assumed to be a function of R and T only. Equation (A.6) becomes

$$R^2 \frac{\partial^2 V^1}{\partial R^2} + (R + \Phi_3 R^3) \frac{\partial V^1}{\partial R} - (1 - \Phi_3 R^3) V^1 = \Phi_1 R^2 \frac{\partial V^1}{\partial t} \tag{A.11}$$

Let

$$V^1 = \phi e^{-\alpha i (R - \beta T)} \tag{A.12}$$

where

$$\beta = \beta_r + i\beta_i \tag{A.13}$$

and ϕ is a function of R only. Substituting (A.12) and (A.13) into (A.11) and taking the real part of the equation

$$R^2 \frac{\partial^2 \phi}{\partial R^2} + (R + \Phi_3 R^3) \frac{\partial \phi}{\partial R} + (R^2(\Phi_3 + \Phi_1 \alpha \beta_i - \alpha^2) - 1)\phi = 0 \tag{A.14}$$

This equation can be simplified by letting $\Psi = \phi R$, $R = \Phi_3^{-1/2}\theta$ and $\Phi_4 = (\Phi_1 \alpha \beta_i - \alpha^2)/\Phi_3$, to give

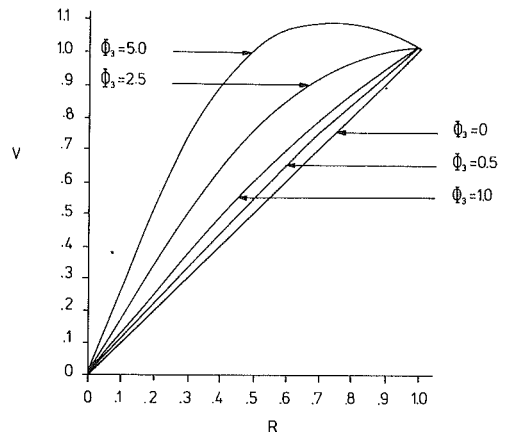

Fig. A1 Mean velocity profile variation in vortex core

$$\theta \frac{\partial^2 \Psi}{\partial \theta^2} + (\theta^2 - 1) \frac{\partial \Psi}{\partial \theta} + \Phi_4 \theta \Psi = 0 \tag{A.15}$$

This can be solved by a series method, with the boundary conditions that $\Psi = 0$ at $\theta = 0$ (i.e., no disturbance at the vortex center) and $\partial\Psi/\partial R = 0$ at $\theta = \Phi_3^{1/2}$ (i.e., the disturbance is a maximum at the edge of the vortex core). One obtains, using the first boundary condition

$$\Psi = \sum_{n=0\ 2\ 4\ \ldots\ldots} a_n \theta^{n+2} \tag{A.16}$$

and

$$a_n = [-(\Phi_4 + n)/(n+2)n] a_{n-2}$$

For neutral stability $\beta_i = 0$ and $\Phi_4 = -\alpha^2/\Phi_3$. Use of the second boundary condition then gives a relationship between α and Φ_3 which is the stability boundary condition in the $\alpha - \Phi_3$ plane. This is plotted in Fig. 4 of the main text. It can be seen that the critical value of Φ_3 is 2.51, which is the value of Φ_3 for which $R_m = 1$ (Section A.2).

Now let us consider the conditions at which disturbances will grow fastest.

For such disturbances the magnification ratio $M (= -\alpha\beta_i)$ will be a maximum. At a fixed value of Φ_3 the second boundary condition for Eq. (A.16) is satisfied if

$$-\alpha_0^2/\Phi_3 = (\Phi_1 \alpha \beta_i - \alpha^2)/\Phi_3 \tag{A.17}$$

where α_0 is the critical stability value shown in Fig. 4. Thus M is given by

$$\Phi_1 M = \alpha_0^2 - \alpha^2 \tag{A.18}$$

Within the stable region of the $\Phi_3 - \alpha$ plane, M is thus a maximum at $\alpha = 0$ i.e., the longest wave lengths are the least stable. This is in a sense unrealistic since such long wavelengths violate some of the earlier assumptions. The consequence of this is discussed in the main text.

The Structure of a Three-Dimensional Tip Vortex at High Reynolds Numbers

D. R. Stinebring

K. J. Farrell

M. L. Billet

Applied Research Laboratory,
The Pennsylvania State University,
State College, PA 16801

The tip vortex structure of a three-dimensional hydrofoil at high Reynolds number was measured experimentally in both the 48 in. (1.22 m) diameter water tunnel and the 48 in. (1.22 m) wind tunnel at the Applied Research Laboratory, Penn State. The flow on and near the hydrofoil was measured in both facilities using a number of flow visualization techniques and laser velocimetry. The downstream tip vortex was measured with a three-component laser velocimeter at a number of streamwise positions. A detailed planar mapping of the flow in the water tunnel was completed near the region of cavitation inception. The effect of roughness on the downstream tip vortex was investigated. In this paper, these measurements are presented with discussion relative to the occurrence of cavitation.

Introduction

The computation of the tip vortex and the prediction of cavitation inception remain design problems for marine lifting surfaces. A three-dimensional, viscous flow field is formed at the tip region of finite-span lifting surfaces. This complex flow field is a direct result of unequal pressure distributions on the pressure and suction sides of the lifting surface. This pressure field convects low momentum fluid from the pressure side around the tip to the suction side, where the fluid rolls up and forms a tip vortex. It becomes apparent that the local tip geometry and fluid viscous forces can have a significant effect on this roll-up process.

Extensive literature is available on the structure of the vortex, and most is directly related to aircraft applications. For the most part, experimental data are confined to regions downstream of the lifting surface and, until the advent of very recent methods, analytical efforts have been confined to inviscid analyses.

For example, early analytical treatments of the roll-up process of the trailing vortex sheet are generally based on papers by Kaden (1931), Betz (1932), and Spreiter and Sacks (1951). The methods of Kaden and Betz do not account for the viscous core. More realistic descriptions (Batchelor, 1964 and Moore and Saffman, 1973) became available based on the models of Rankine and Lamb (1945). In the Rankine model the vorticity is concentrated inside the vortex core with a homogeneous distribution. Lamb's model has a Gaussian vorticity distribution, and Moore and Saffman (1973) define a vorticity spiral that can be approximated by a circulation distribution of vorticity with an outer radius much larger than the vortex core. Although Moore and Saffman (1973) and Moore (1974) use inviscid analyses and fail to predict the core radius, these studies have some significant conclusions. The velocity distribution in the trailing vortex is related to the loading distribution along the span of the wing. Calculations made from an elliptically loaded wing show that 46 percent of the total circulation is present in the tip vortex after a dimensionless time, $t^* = Ut/a$ of 0.1, where U is the downwash velocity, t is the time, and a is the semi-span. After a dimensionless time of 1.0, 80 percent of the circulation was concentrated in the tip vortex. These results of Moore (1974) agreed closely with the similarity power law of Kaden (1931) through adjustment of Kaden's constant.

Two important sets of experiments were conducted that identified important characteristics of the structure of the tip vortex. Tests by McCormick (1962) have identified a relationship between the viscous core – tip boundary layer and the Reynolds number effect. Scheiman et al. (1972) have shown the vortex core size to be dependent upon Reynolds number.

The stability of the tip vortex has been investigated by, among others, Leibovich (1984), Singh and Uberoi (1976), and Garg and Leibovich (1979). Their studies were concerned with the onset of vortex breakdown which has ramifications to aircraft stability and control. Vortex breakdown, it is believed, occurs as a result of rapid deceleration of axial velocity in the core (Garg and Leibovich, 1979) and subsequent loss of axial symmetry (Leibovich, 1984). Experimental evidence with a laminar flow wing has shown a relationship between vortex instabilities and axial velocity changes in the core (Singh and Uberoi, 1976). Vortex wandering, random movement of the vortex, studied by Baker et al. (1974) and Reed (1973), was believed to be primarily due to free-stream turbulence. Recent work by Green (1988), using double pulsed holography, is providing a new understanding of the unsteadiness associated with the vortex.

Historically, significant improvements in the theory have followed experimental data. In particular, Chigier and Consiglia (1971) conducted tip region velocity measurements both upstream and downstream of the trailing edge of a rotating airfoil. Results show the three-dimensionality of the roll-up region and the two-dimensionality of the far-field vortex. The flow field near the tip is three-dimensional, viscous, and has

Contributed by the Fluids Engineering Division for publication in the JOURNAL OF FLUIDS ENGINEERING. Manuscript received at the Fluids Engineering Division February 13, 1990.

large secondary velocities. A solution of the full Navier-Stokes equations would be required for a theoretical prediction of the tip vortex flow field; however, this would require computational resources that are not available. Some promising analytical work is being done by Govindam, Levy, and Shamroth (1984) and Shamroth and Bailey (1979) that utilize parabolized Navier-Stokes equations and a forward marching procedure to compute the tip vortex generation process.

Contemporary three-dimensional models generally cannot predict the development of the vortex sheet as it leaves the surface. Most of the existing models do predict the time deformation of the free shear layer but assume inviscid flow and two-dimensionality. Recently, some of the three-dimensional analyses require a primary flow direction but can account for large secondary velocities.

Cavitation numbers typical of tip vortex cavitation are often higher than any other type of cavitation. Cavitation usually occurs close to the lifting surface on the suction side and resembles a rope. The question of tip vortex cavitation has been addressed by several investigators such as McCormick (1962), Coon (1963), Chandvashebhara (1976), Billet and Holl (1979), Kuiper (1981), and Souders and Platzer (1981). A very good review of tip vortex cavitation and delay is given by Platzer and Souders (1979).

The early work of McCormick (1962) was an experimental and analytical study of the cavitation produced by the vortex system trailing from elliptic, rectangular, and delta wings. It was found that the inception of this cavitation depends upon the boundary layer thickness on the pressure surface of the wing tip. The thickness of the vortex core is apparently not determined by the induced drag. For a given wing shape, the critical cavitation index was found to increase with increasing Reynolds number, increase nearly linearly with angle of attack, remain essentially unchanged by the aspect ratio and depend significantly on the undissolved air content. (In most experiments, this is directly related to the microbubble populations.)

In the present investigation a large three-dimensional hydrofoil was tested in the 48 in. (1.22 m) diameter water tunnel and 48 in. (1.22 m) diameter wind tunnel at the Applied Research Laboratory, The Pennsylvania State University (ARL Penn State). To better understand the factors that influence the structure of the tip vortex, the flow field on and near the hydrofoil was studied. The surface shear direction was observed with oil paint flow visualization, and mini-tufts were used to observe the unsteadiness in the surface flow. The flow leaving the hydrofoil surface was monitored using ejected bubble tracing. The boundary layers on the tip of the hydrofoil were measured with laser velocimetry (LV).

Furthermore, the tip vortex flow was measured at a number of downstream positions using a three-component LV. A detailed mapping of the flow field was made in the plane of cavitation inception. Three-component Reynolds stresses were measured through the vortex during the wind tunnel tests. The effect of tip surface roughness on the vortex structure was also investigated. Lastly, the measured structure of the tip vortex was compared with cavitation inception results. The core pressure was calculated by integrating the radial equilibrium equation from outboard of the hydrofoil.

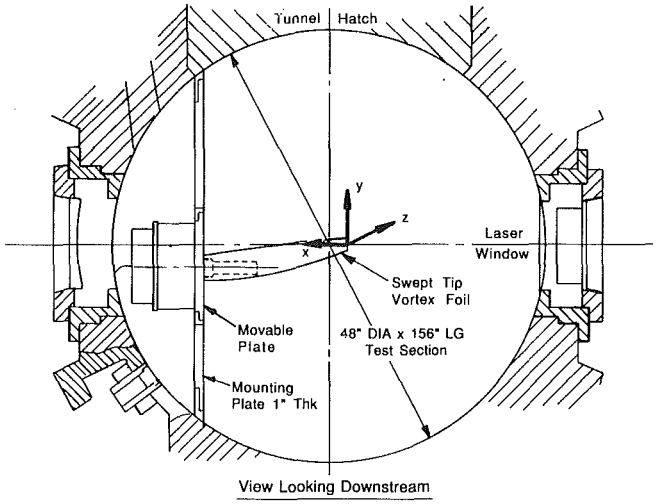

Fig. 1 Schematic of hydrofoil mounted in the test section of the ARL Penn State 48-in. (1.22 m) water tunnel. View is downstream with pressure surface on top.

Experimental Apparatus and Procedures

The experimental measurements were performed in the 48 in. (1.22 m) water tunnel and the 48 in. (1.22 m) wind tunnel at ARL Penn State. The water tunnel is a closed-circuit, closed-jet facility with a 14 ft (4.27 m) long, 4 ft (1.22 m) diameter cylindrical test section. The water velocity is continuously variable to over 55 ft/s (16.8 m/s), and the pressure can be regulated from 3 to 60 psia (21 to 414 kPa). A bypass system exists for varying the air content level to below 2 ppm on a molar basis. The wind tunnel is a closed circuit tunnel with a 16 ft (4.88 m) long, 48 in. (1.22 m) diameter octagon test section with a test section velocity continuously variable to 130 ft/s (39.6 m/s). More complete descriptions of these facilities are given by Lehman (1959) and Lauchle et al. (1989).

A downstream view of the hydrofoil mounted in the water tunnel is presented in Fig. 1, and a top view schematic is shown in Fig. 2. The wind tunnel and water tunnel mountings were similar. In both views the pressure side is on the top surface. The hydrofoil has a 15 in. (38 cm) tip chord, a 32 in. (81.3 cm) root chord, and a 16.2 in. (41.1 cm) span. The projected planform area is 2.86 ft^2 (0.266 m^2) yielding an aspect ratio of 1.28.

The hydrofoil was mounted to a flat plate attached to the side of the tunnel. The tests in water were all conducted at a freestream velocity of 40 ft/s (12.2 m/s) corresponding to a Reynolds number based on tip chord equal to $Re_t = 4.75 \times 10^6$. In the wind tunnel the nominal velocity was 120 ft/s (36.6 m/s) and $Re_t = 8.5 \times 10^5$.

During some test, 300 μm sand grain roughness was applied

Nomenclature

a = hydrofoil semi-span
AR = aspect ratio
c_{ave} = mean chord length
c_t = tip chord length
C_p = pressure coefficient, $(P - P_\infty)/(0.5\,\rho V_\infty^2)$
e = distance to vortex roll-up
p = pressure
P_s = static pressure
P_v = vapor pressure
P_∞ = free-stream pressure
r = radial distance
r_c = vortex core radius
Re_t = Reynolds number based on tip chord length
t = time
t^* = dimensionless time
U = downwash velocity
V_T = vortex tangential velocity
V_∞ = free-stream velocity
x, y, z = cartesian coordinates
u, v, w = velocity components in cartesian coordinates
Γ = circulation
ρ = mass density of water
σ_i = incipient cavitation index, $(P_{s,i} - P_v)/(0.5\,\rho V_\infty^2)$
σ_d = desinent cavitation index, $(P_{s,d} - P_v)/(0.5\,\rho V_\infty^2)$
$'$ = fluctuating quantity

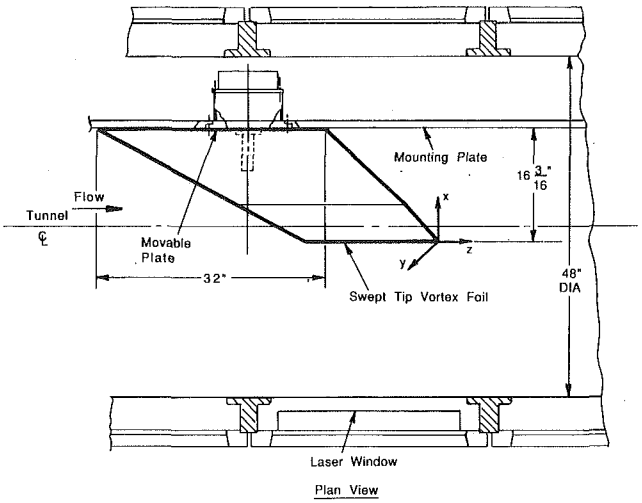

Fig. 2 Schematic of hydrofoil mounted in the test section of the ARL Penn State 48-in. (1.22 m) water tunnel. Top view is shown.

to the hydrofoil tip. In order to minimize the drag penalty, roughness was applied to the regions where the streamlines contributed to the vortex roll-up, as observed with flow visualization. This area amounted to 7 percent of the blade span at the tip.

Flow Visualization. Oil/paint surface flow, tufts, air ejection and cavitation were used to visualize the flow over and near the surface of the hydrofoil in the water tunnel. The surface flow was visualized with the oil/paint mixture and tufts. The oil/paint was applied in droplets located on the pressure and suction sides of the hydrofoil. The number and location of the droplets and also the oil/paint ratio were determined on a trial and error basis to provide a good surface flow pattern. The mixture was first applied to the hydrofoil, the tunnel filled with water, and the tunnel rapidly brought to the test velocity, 40 ft/s (12.2 m/s). The movement of the oil/paint was monitored via videotape while the tunnel speed was increased. There was no discernible change in the flow direction as the flow velocity was increasing. The tunnel velocity was maintained at 40 ft/s (12.2 m/s) until movement of the paint stopped. The tunnel velocity was then decreased to zero, and the outer 33 percent of span was removed and photographed.

The 1.0 in. (2.54 cm) tufts were applied on a grid with 1.0 in (2.54 cm) spacing on the outer 33 percent of the span. The tufts were short lengths of household thread applied with cyanoacrylate cement. The tuft patterns were videotaped and photographed while maintaining 40 ft/s (12.2 m/s) in the water tunnel.

Air was ejected out of several of the 41 pressure taps to visualize the flow from a point on the surface of the hydrofoil. Pressure taps were located at 86.7 percent and 93.3 percent span on the tip. The air ejection tests were performed while maintaining 30 ft/s (9.14 m/s) in the water tunnel. The air bubble trajectories were videotaped with a strobe light synchronized with the video scanning and also photographed using stroboscopic lighting.

Cavitation was used to visualize the location and shape of the tip vortex. The cavitation located the vortex for the LV surveys. Images of the cavitating vortex were retained on videotape and on photographs in a manner similar to the bubble ejection test.

Laser Surveys. The LV systems used for all measurements were TSI two and three-component backscatter systems using a 4-watt argon-ion laser. All channels were frequency shifted using Bragg cells and the photomultiplier signals fed into TSI 1990 counter processors. The data were stored and analyzed with a VAX 11/780 computer. The laser/optics package was

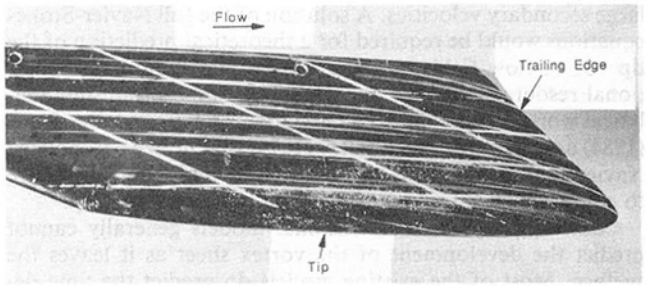

Fig. 3 Oil/paint flow visualization of pressure surface, outer 33 percent span. Flow is from left to right.

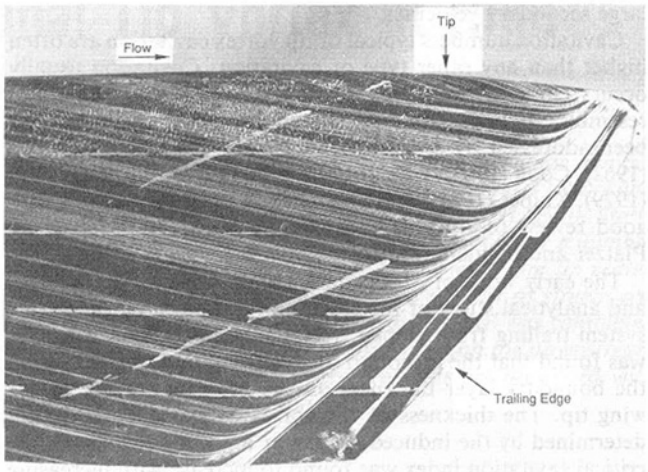

Fig. 4 Oil/paint flow visualization of suction surface, outer 33 percent span. Flow is from left to right.

positioned using a three-axis traversing mechanism. For all tests the theoretical control volume dimensions were 0.013 in. (0.334 mm) by 0.14 in. (3.59 mm). Due to the LV measurement methods employed, the effective probe volume was estimated to be smaller than calculated from the beam crossover. To decrease the effective probe volume the LV optics are first aligned and the photomultiplier signal "optimized" (maximum data rate with minimum noise in the freestream flow). The seeding particles, 1.4 μm silicon carbide or 4 μm metallic coated spheres, were then added to the fluid. The data rate usually increases by a factor of 10 or more due to the addition of the seeding. This indicates that the majority of the data are being generated due to the uniform sized particles. The processor amplifier gain is then decreased by up to 90 percent to reduce the data rate. Now the data are not only primarily due to the seeding, but only the highest signal levels, near the center of the control volume, are being recorded. This is the procedure for all LV measurements by the authors. Spatial resolution was far more important than high data acquisition rates.

Frequency shifting was used since there were reversals in the flow direction for the u- and v-components of velocity. In order to minimize fringe bias, the Bragg cell shift frequency was 0.5 MHz for the u-component, 5 MHz for v-component, and 2 MHz for the w-component of velocity. If the "fringe analogy" is used to describe the crossover, then the fringe velocity was always greater than twice the maximum velocity in the direction of fringe movement. No special sampling techniques were used to reduce velocity bias. Based on local velocity and turbulence intensity measurements through the vortex, the nondimensional velocity bias, referenced to the freestream velocity, was estimated to be under 2 percent.

The uncertainty for the experimental data is as follows: LV measurements: u-component ± 5 percent, v-component ± 2 percent, w-component ± 2 percent; position ± 0.001 in (0.25 mm); test section velocity ± 1 percent; and cavitation indices

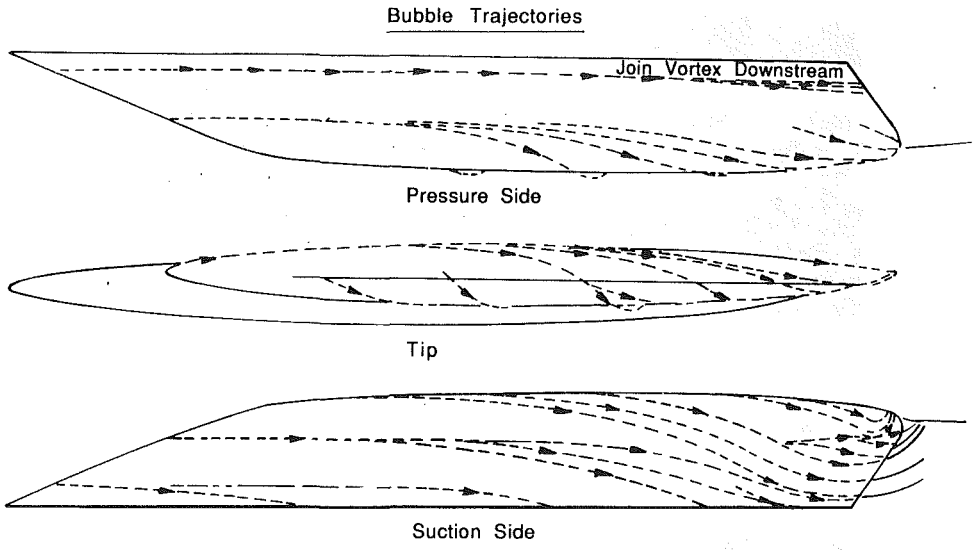

Fig. 5 Trajectories of bubbles ejected through pressure taps

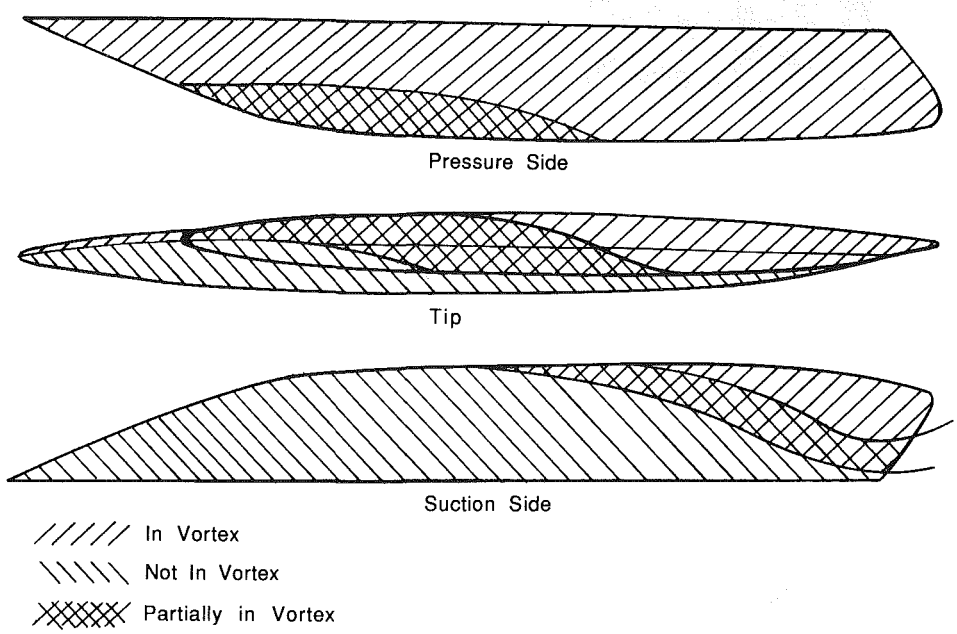

Fig. 6 Location on foil with flow into tip vortex, from bubble trajectory data

±5 percent, due to the inherent subjectivity associated with visual calls of cavitation.

Test Results

Flow Visualization Results. The results of the oil/paint flow visualization are shown in Figs. 3 (pressure side) and 4 (suction side). For the paint photographs, only the outer 5.4 in (13.7 cm, 33 percent span) are shown. Reference lines were drawn chordwise at 1.08 in. (2.74 cm) intervals and spanwise as shown in the figures.

The pressure side flow, Fig. 3, is essentially streamwise up to approximately 75 percent chord and 93 percent span (the lowermost chordwise reference line). Outside of this region there is a spanwise flow toward the tip. The suction side flow is more complex as seen in Fig. 4. There is a separation zone near the trailing edge that converges along the span toward the tip. The paint also shows a spanwise flow toward the tip within this separation zone. From videotapes of the oil/paint test, this spanwise velocity was estimated to be greater than 8 ft/s (2.4 m/s). This was the minimum velocity required to cause movement of the paint droplets. The location of the separated zone corresponds to the trailing edge taper.

As stated previously, the mini-tufts were used to observe the unsteadiness of the surface flow. Most records of the tufts were on videotape with stroboscopic synchronized lighting. The flow appears steady and the tuft directions match the oil/paint flow except in one region—the separation zone near the tip. The oil/paint shows the spanwise flow in the separated region,but the tufts alternately point in a spanwise direction and then a streamwise direction. The view of the hydrofoil from the side shows the sequence of events. The authors suggest that the tuft follows the spanwise direction in the unsteady, separated flow region, is perturbed downward by this unsteady flow, and then deflected into the direction of the freestream velocity.

The results of the air injection tests are summarized in Figs. 5 and 6. Both photographs and videotaped records of the tests were used to prepare the figures. Video viewing allowed one to trace the paths of the bubbles from their ejection point, along the hydrofoil surface, and into the vortex. The air flow rate was adjusted to provide small individual bubbles that would closely follow the flow. Buoyancy effects were minimized by the high velocity of the flow and the small bubble size. The vertical, buoyant migration of the small bubbles

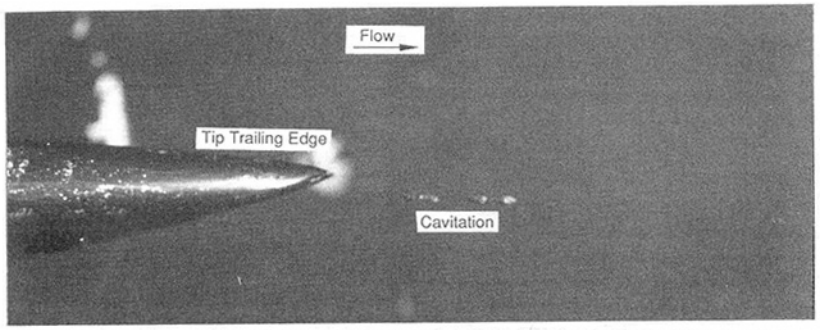

Fig. 7 Location of tip vortex cavitation inception, V_∞ = 40 ft/s (12.2 m/s), σ = 0.61

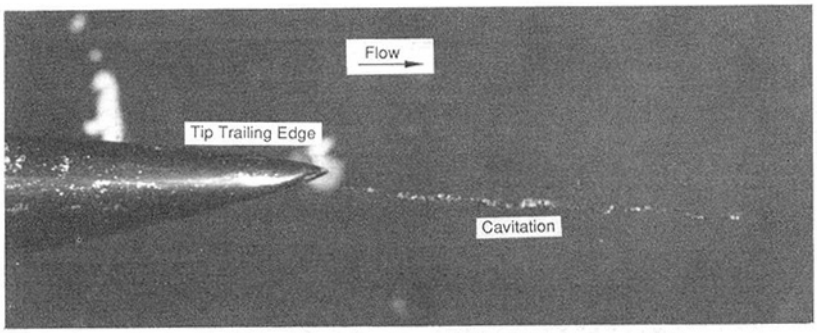

Fig. 8 Cavitating tip vortex, V_∞ = 40 ft/s (12.2 m/s), σ = 0.43

during the transit time through the flow field of interest was calculated to be negligible. The air injection was meant to supplement the surface flow visualization with the bubbles following the flow just off of the surface. A comparison of Fig. 5 and the oil/paint photographs yields many similarities and one obvious difference. The pressure side flow visualization for surface flow and air injection are very similar. However, at the suction surface trailing edge, the air flow travels away from the trailing edge of the hydrofoil while the surface flow moves spanwise through the separation zone. Analysis of the videotape shows that near the tip, some bubbles close to the surface are swept along the hydrofoil and into the vortex. There is also a deflection of the entire bubble flow due to the flow in the separation zone. From observations of the bubbles and minitufts, the separation zone was estimated to be less than 0.25 in. (6.35 mm) thick in the vicinity of the tip.

Figure 6 illustrates the flow which eventually ends up in the vortex. A region where the flow partially merges into the vortex is also shown. Nearly all of the pressure surface flow ends up in the vortex except for a small region near the tip leading edge. On the suction surface, only the flow near the tip trailing edge, from the pressure side, merges with the vortex. These results were obtained by measuring the trajectories of the air bubbles ejected through the pressure taps.

A photograph of tip vortex cavitation inception is shown in Fig. 7, and more developed tip vortex cavitation in Fig. 8. Inception occurs approximately 0.07 c_t downstream of the trailing edge. Two observations are of particular interest in Fig. 8. First, the vortex is displaced below the trailing edge, and second, the vortex is kinked or perturbed. The cavitation bubbles, which convect through the region of minimum pressure in the vortex, provide an approximate location of the vortex axis, but not the structure of the vortex. A straight line fit of the streamwise positions of the vortex center from the LV data, intersects the hydrofoil approximately 0.2 in. (5 mm) below the trailing edge. This displacement corresponds to the thickness of the separated region at the trailing edge of the suction side and suggests that both fluid from the pressure surface and the suction surface separated flow feed into the vortex. Furthermore, this separated flow entering the vortex may be responsible for the observed instabilities.

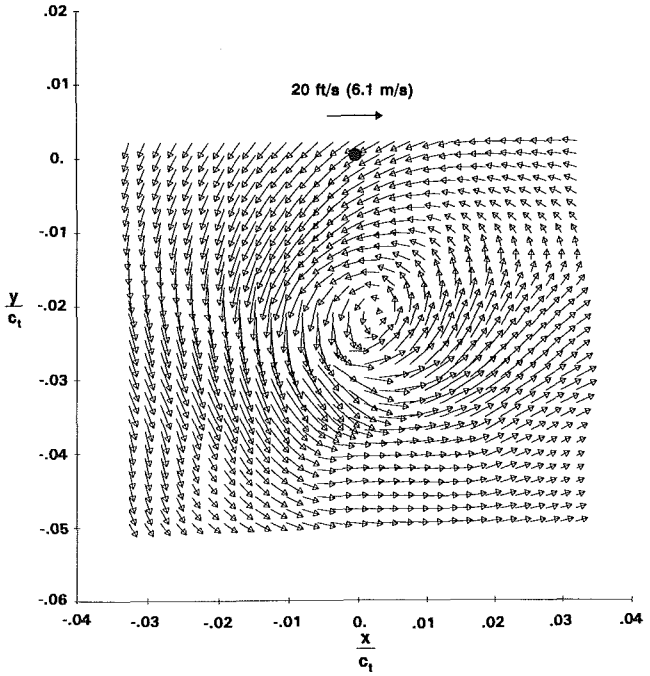

Fig. 9 Vector plot of vortex flow 0.067 c_t downstream.

Structure of the Vortex Core—LV Results. A vector plot of the u- and v-components of velocity near the plane of cavitation inception, 0.067 c_t downstream, is presented in Fig. 9. The plot was generated from a two-dimensional spline fit of 145 data points. Using the analysis of de Boor (1978), the velocity error from the cubic spline interpolation does not exceed ±1.8 percent. The position of the aft-most point on the hydrofoil is also shown. It can be seen that the flow outboard of the hydrofoil follows nearly a circumferential path about the vortex center; however, inboard, there is a strong radial flow away from the vortex center.

A contour plot of the axial, w-component of velocity in the plane of cavitation inception is presented in Fig. 10. The po-

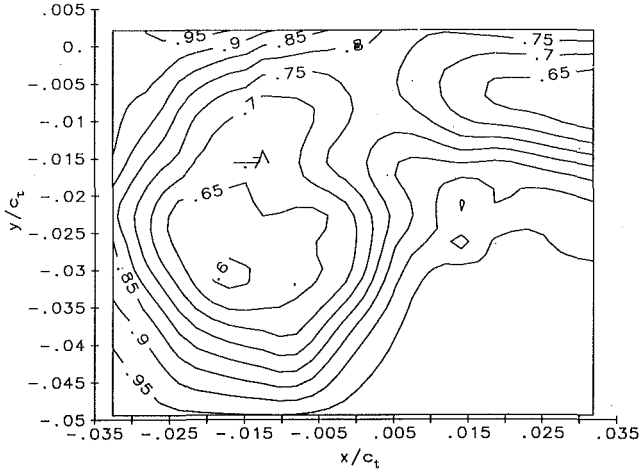

Fig. 10 Axial velocity (w/V_∞) contours in vicinity of vortex, 0.067 c_t downstream of tip, vortex center (based on u and v) at $x/c_t = 0.002$ $y/c_t = -0.023$. Hydrofoil trailing edge indicated by solid circle, $x/c_t = 0.000$ $y/c_t = -0.000$.

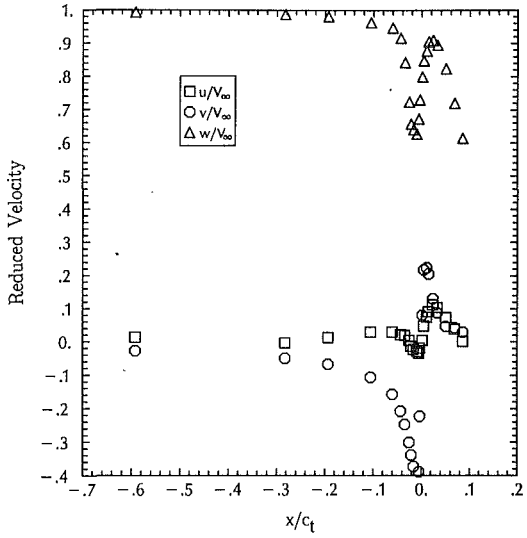

Fig. 12 Velocity survey through the vortex center, smooth tip, 0.667 c_t downstream

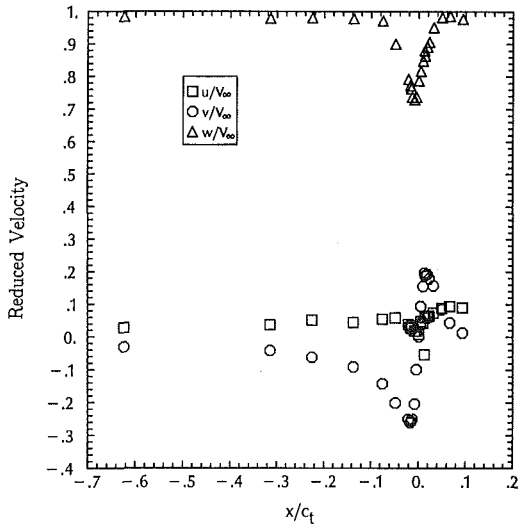

Fig. 11 Velocity survey through the vortex center, smooth tip, 0.073 c_t downstream.

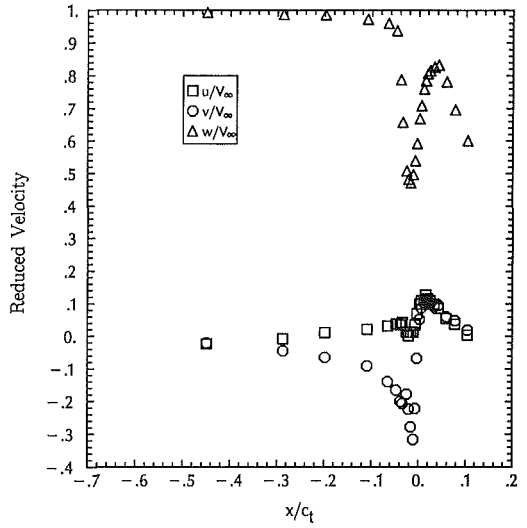

Fig. 13 Velocity survey through the vortex center, roughened tip, 0.067 c_t downstream

sition of the hydrofoil trailing edge and center of the vortex are indicated. It is very important to note that the region of minimum axial velocity is not centered on the region of minimum vortex-induced velocity in the x-y plane. In this roll-up region, this characteristic leads to a highly unstable flow. An axial velocity reduction due to the hydrofoil wake is also seen inboard of the vortex. The plots of all three components, Figs. 11, 12, and 13, show a highly three-dimensional flow field in this region.

Velocity surveys through the center of the vortex are presented at streamwise locations with the distance downstream in tip chord lengths: 0.073 c_t (1.1 in. or 2.8 cm) in Fig. 11, 0.667 c_t (10 in. or 25.4 cm) in Fig. 12, and 0.067 c_t (1 in. or 2.5 cm), but with roughness applied to the tip, in Fig. 13. A comparison of Figs. 11 and 12 shows the streamwise development of the vortex, and a comparison of Figs. 11 and 13 shows the effect of boundary layer thickness on the vortex, at the cavitation inception region. Near the trailing edge of the hydrofoil, the tangential velocity is highly asymmetric. Moreover, there is a large axial velocity deficit and strong radial flow associated with the vortex. Further downstream the tangential velocity is attaining symmetry, and the axial velocity deficit and radial flow are reduced. Roughness on the tip increases the thickness of the vortex core and reduces the maximum tangential velocity.

Cavitation Inception Results. The incipient and desinent cavitation numbers were measured at an air content level of 2 ppm on a molar basis. The cavitation number is defined as

$$\sigma_{i,d} = \frac{P_{s,i,d} - P_v}{\frac{1}{2}\rho V_\infty^2} \quad (1)$$

where P_s is the freestream static pressure, P_v is the vapor pressure, ρ is the mass density of water and V_∞ is the freestream velocity. The subscripts i and d refer to cavitation inception and desinence. For the smooth tip, $\sigma_i = 0.60$ [$P_s = 6.6$ psia (45.5 kPa) $V_\infty = 40$ ft/s (12.2 m/s)] and $\sigma_d = 0.80$ [$P_s = 8.9$ psia (61.4 kPa) $V_\infty = 40$ ft/s (12.2 m/s)]. Measures were taken to maintain a low free air content level in order to minimize free air effects. Cavitation could not be measured for the roughened tip due to the minimum pressure limitations of the hydrofoil mounting plate and pitch change mechanism.

If the cavitation index is used as a measure of the onset of vaporous cavitation in the core, the core mean pressure can be estimated using the measured circumferential velocity from

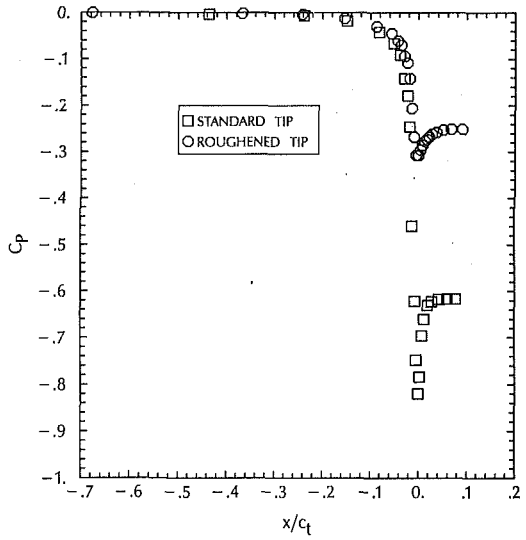

Fig. 14 Calculated pressure coefficient through the vortex centers smooth tip, 0.073 c_t downstream; roughened tip, 0.067 c_t downstream

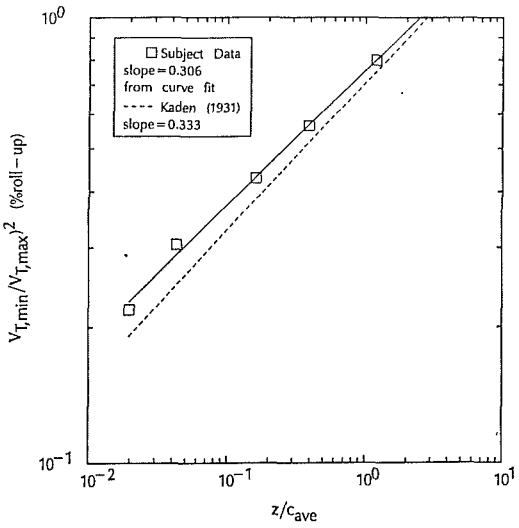

Fig. 15 Calculation of vortex roll-up using differential circulation parameter compared with theoretical results of Kaden (1931). (Uncertainty in z/c_{ave} ±0.002.)

the LV surveys. Since it has been shown that the flow field is highly three-dimensional, an accurate calculation of the core pressure would require an integration of the Navier-Stokes equations. However, one can obtain a reasonable estimate of the mean core pressure using the radial equilibrium equation

$$\frac{dp}{dr}=\frac{\rho V_T^2}{r} \tag{2}$$

Calculations of the pressure coefficient near the location of cavitation inception are shown in Fig. 14 for the smooth tip and the roughened tip. It is apparent that roughness decreases the magnitude of the pressure coefficient in the core. Comparing the incipient and desinent cavitation index for the smooth tip with the calculated pressure distribution, it appears that the mean pressure in the core is sufficient for cavitation inception. If the desinent index is used then the vapor pressure is reached only on the very center of the core. However, the incipient index implies that a larger region of the core is below vapor pressure and that inception may occur off the centerline. The nuclei population feeding into, and distributed through the core, could thus influence vaporization. Surface tension effects on these nuclei will act to reduce the critical pressure for bubble growth. It is also interesting to note that only approximately 25 percent of the pressure reduction for the smooth tip occurs in the core. For comparison, in a classical Rankine vortex, half the pressure reduction occurs in the core, and half in the irrotational region outside the core.

Although the mean pressure in the core, as calculated from the momentum equation, may be low enough for inception, the unsteady velocity creates a fluctuating pressure. A dimensionless fluctuating pressure can be defined as

$$\frac{2\sqrt{p'^2}}{\rho V_\infty^2}=k\,\frac{u'^2+v'^2+w'^2}{V_\infty^2} \tag{3}$$

where primed quantities denote fluctuating components and k is a constant.

The three-component Reynolds stresses were measured through the vortex in the wind tunnel at 0.5 in. (1.3 cm) downstream of the trailing edge. In the core center,

$$\left(\frac{u'}{V_\infty}\right)^2=0.029;\quad \left(\frac{v'}{V_\infty}\right)^2=0.054;\quad \left(\frac{w'}{V_\infty}\right)^2=0.021 \tag{4}$$

thus

$$\frac{2\sqrt{p'^2}}{\rho V_\infty^2}=k(0.104) \tag{5}$$

The calculated rms pressure fluctuations are dependent upon the choice of the constant k. For isotropic turbulence, theoretical values of k range from $k = 0.39$ (Batchelor, 1951), to $1 < k < 2$ (Taylor, 1936). Experiments by Daily et al. (1961) in a boundary layer shear flow suggest $k \gg 1$, and experiments by Sami et al. (1967) in air using a hot-wire and specially designed unsteady pressure probe, measured $k = 3.6$.

Even using a conservative value for the constant, it appears that the fluctuating pressure in the core will have a significant effect upon inception. Both surface tension and pressure fluctuations may account for the difference between incipient and desinent cavitation numbers.

Vortex Roll-up. The vortex structure close to the hydrofoil and its effect upon cavitation inception were the primary areas of interest for this study. However, the vortex roll-up and structure downstream were also investigated to better understand the fluid mechanics of a vortex flow with linear blade loading.

One of the most referenced works pertaining to vortex roll-up is Spreiter and Sacks (1951). Using similarity conditions, the distance to roll-up, non-dimensionalized by the mean chord length, was given as

$$e/c_{ave}=K(AR/C_L)2a/c_{ave} \tag{6}$$

where K is a constant equal to 0.28 from Kaden (1931) for elliptically loaded wings, AR is the aspect ratio, C_L is the lift coefficient, and c_{ave} is the mean chord length. If this hydrofoil had an elliptic lift distribution then roll-up should be complete less than 2.9 c_{ave} downstream.

The authors propose that the tangential velocity asymmetry can be used to examine the roll-up process. A roll-up circulation parameter is defined relating the differential circulation along the circular arc segment $rd\theta$

$$\frac{d\Gamma_a}{d\Gamma_b}=\frac{V_a r_a d\theta}{V_b r_b d\theta}, \tag{7}$$

where a and b are defined at the peaks in the tangential velocity distribution curve on opposite sides of the vortex. The experimental tangential velocity distributions, as shown in Figs. 11, 12, and 13, resemble a Rankine vortex; the inner rotational core is nearly linear across the diameter, and the outer portion decreases approximately as 1/r. With this simplification, the roll-up parameter becomes

$$\frac{d\Gamma_a}{d\Gamma_b}=\frac{V_a^2}{V_b^2}. \tag{8}$$

The parameter $(V_{T,\min}/V_{T,\max})^2$ is plotted as a function of distance from the hydrofoil trailing edge in Fig. 15. The accuracy of the parameter is limited by the spatial resolution of the LV survey and spatial averaging occurring as a result of the vortex wandering.

At complete vortex roll-up, there should be symmetry of the tangential velocity distribution, i.e., $V_{T,\min} = V_{T,\max}$. The data seem to indicate a power law relationship for the vortex roll-up. A straight line fit through the points infers vortex symmetry at 2.50 c_{ave} downstream. This is close to the predictions by Spreiter and Sacks (1951) for an elliptic distribution. Although the data appear to infer a constant power law, it is not known if the shape of the curve would change closer to the roll-up point.

Also shown in Fig. 15 is Kaden's (1931) result for the fraction of vorticity in the vortex for elliptic loading as a function of streamwise distance. The intercept indicating roll-up was chosen to match Spreiter's and Sacks' (1951) calculations. It is interesting to note the similarity between the slope of the curve calculating the fraction of vorticity in the vortex to the curve of the defined circulation parameter using the measured tangential velocities. The lower slope for this present data could be due to the linear lift distribution at the hydrofoil tip. It would be interesting to apply this circulation parameter to hydrofoils with elliptic loading and compare the slope to Kaden's (1931) one-third power law. If the comparison is favorable, then it could be possible to predict vortex roll-up from a single measurement of tangential velocity asymmetry, at a known distance from the hydrofoil, and then applying a power law roll-up relationship.

Conclusions

A series of experiments were conducted on a large three-dimensional hydrofoil to investigate the tip vortex structure and its relationship to cavitation inception. The following summarizes some of the results:

1. The vortex flow field is highly three-dimensional near the hydrofoil in the region of cavitation inception. Further downstream the flow approaches symmetry about the vortex axis.
2. Flow visualization shows clearly the three-dimensionality of the flow on the hydrofoil surface and the position where the surface flow leaves to form the vortex structure.
3. The mean pressure in the vortex core, estimated from integration of the radial equilibrium equation, is sufficient for cavitation inception. However large calculated unsteady pressures in the core can also have a significant offset on inception. In the roll-up region the shed vorticity is not concentrated in the core, and the majority of the pressure reduction in the vortex occurs outside the core region.
4. Roughness applied to the tip of the hydrofoil increases the core pressure by modifying the local boundary layer at the point of separation while having only a minor affect on the overall lift.
5. A vortex symmetry parameter is suggested for calculating the position of the vortex roll-up.

References

Baker, G. R., Barker, S. J., Bofah, K. K., and Saffman, P. G., 1974, "Laser Anemometer Measurements of Trailing Vortices in Water," *J. of Fluid Mechancis*, Vol. 65, Part 2, pp. 325–336.

Batchelor, G K., 1964, "Axial Flow in Trailing Vortices," *J. of Fluid Mechanics*, Vol. 20, Part 4, pp. 645–658.

Batchelor, G. K., 1951, "Pressure Fluctuations in Isotropic Turbulence," *Proceedings of the Cambridge Philosophical Society*, Vol. 47, Part 2, pp. 359–374.

Betz, A., 1932, "Verholten von Wirbelsystem," *ZAMM Bd., XII*, Nr. 3, S. 164–174.

Billet, M. L., and Holl, J. W., 1979, "Scale Effects on Various Types of Limited Cavitation," *ASME International Symposium on Cavitation Inception*, New York, Dec. 1979.

Chandvashebhava, N., 1976, "Analysis of Tip Vortex Cavitation Inception of Hydrofoils and Propellers," Hamburgische Schiffban-Versuchsanstalt, Report 112, May.

Chigier, N. A., and Consiglia, V. R., 1971, "Tip Vortices—Velocity Distributions," 27th National V/STOL Forum of the American Helicopter Society, Washington, D.C., May.

Coon, J. M., 1963, "Propeller Vortex Cavitation Inception Studies," David Taylor Model Basin, Report 1724, Mar.

Daily, J. W., Lin, J. D., and Broughton, R. S., 1961, "Turbulence and Static Pressure in Relation to Inception of Cavitation," *Proceedings of Ninth Convention*, IAHR, Dubrovnile, Yugoslavia, pp. 110–122.

de Boor, C., 1978, *A Practical Guide to Splines*, Springer-Verlag, New York.

Garg, A. K., and Leibovich, S., 1979, "Spectral Characteristics of Vortex Breakdown Flowfields," *Physics of Fluids*, Vol. 22, No. 11, Nov., pp. 2053–2064.

Green, S. I., 1988, "Trailing Vortex Core Unsteadiness—An Exploratory Study of Reynolds Number Effects," First National Fluid Dynamics Congress, AIAA, July.

Govindam, T. R., Levy, R., and Shamroth, S. J., 1984, "Computation of the Tip Vortex Generation Process for Ship Propeller Blades," Scientific Research Associates, Inc., Report 83-920021-F, Office of Naval Research, Apr.

Kaden, H., 1931, "Aufwicklung emer unstabilen Unstetigkeitsflache," *Ingenicur-Archiv*, S. 140–168.

Kuiper, G., 1981, "Cavitation Inception on Ship Propeller Models," NSMB, Wageningen, The Netherlands.

Lamb, H., 1945, *Hydrodynamics, 6th Edition*, Dover, New York, pp. 21–32.

Lauchle, G. C., Billet, M. L., and Deutsch, S., 1989, "High Reynolds Number Liquid Flow Measurements," Lecture Notes in Engineering 46, M. Gad-el-Hak, ed., Frontiers in Experimental Fluid Mechanics, Springer-Verlag Berlin Heidelberg.

Lehman, A. F., 1959,"The Garfield Thomas Water Tunnel," Ordnance Research Laboratory, Report No. NOrd-16597-56, Sept. 30.

Leibovich, S., 1984, "Vortex Stability and Breakdown: Survey and Extension," *AIAA Journal*, Vol. 22, No. 9, Sept., pp. 1192–1206.

McCormick, B. W., 1962, "On Cavitation Produced by a Vortex Trailing from a Lifting Surface," ASME *J. Basic Engineering*, 1962, pp. 369–379.

Moore, D. W., 1974, "A Numerical Study of the Roll-up of a Finite Vortex Sheet," *J. Fluid Mechanics*, Vol. 63, Part 2, pp. 225–235.

Moore, D. W., and Saffman, P. G., 1973, "Axial Flow in Laminar Trailing Vortices," Proc. Royal Soc. London A., 333, pp. 491–508.

Platzer, G. P., and Souders, W. G., 1979, "Tip Vortex Cavitation Delay with Application to Marine Lifting Surfaces—A Literature Survey," DTNSRDC Report 79/051, Aug.

Reed, R. E., 1973, "Properties of Lateral Random Oscillations of Trailing Vortices Observed in Wind-tunnel Tests," NEAR TR 47, Neilsen Engineering and Research, Jan.

Sami, S., Carmody, T., and Rouse, H., 1967, "Jet Diffusion in the Region of Flow Establishment," *Journal of Fluid Mechanics*, Part 2, pp. 231–252.

Scheiman, J., Megrail, J. L., and Shiveis, J. P., 1972, "Exploratory Investigation of Factors Affecting the Wing Tip Vortex," NASA TMX-2516.

Shamroth, S. J., and Bailey, W. R., 1979, "A Viscous Flow Analysis for the Tip Vortex Cogeneration Process," NASA Contractor Report 3184.

Singh, P. I., and Uberoi, M. S., 1976, "Experiments on Vortex Stability," *Physics of Fluids*, Vol. 19, No. 12, Dec., pp. 1858–1863.

Souders, W. G., and Platzer, G. P., 1981, "Tip Vortex Cavitation Characteristics and Delay of Inception on a Three-Dimensional Hydrofoil," DTNSRDC Report No. 81/007, Apr.

Spreiter, J. R., and Sacks, A. H., 1951, "The Rolling Up of the Trailing Vortex Sheet and Its Effect on the Downwash Behind Wings," *J. Aeronautical Sciences*, Vol. 18, No. 1, Jan., pp. 21–32.

Taylor, G. I., 1936, "The Mean Value of the Fluctuations in Pressure and Pressure Gradient in a Turbulent Fluid," *Proceedings of the Cambridge Philosophical Society*, 32, pp. 380–384.

Studies of Scaling of Tip Vortex Cavitation Inception on Marine Lifting Surfaces

C. C. Hsu
David Taylor Research Center,
Bethesda, MD 20084

The roll up of vortex sheet on a lifting surface in early stages is studied. The structures of tip vortex flow, both in the outer inviscid and inner viscous regions, are examined. The velocity in the viscous core is determined and used as basis for the prediction of tip vortex cavitation. Some comparisons between the calculated and measured tip vortex cavitation inception numbers are made, and the results are generally in good agreement.

Introduction

Vortex sheet emanating from a lifting surface rolls up under the action of its self-induced field. The roll up starts generally near the tip of the wing. Such vortex system can have considerable influence on the performance of the lifting surface. On marine lifting surfaces, such vortex system can also have effect on the cavitation performance. Tip vortex cavitation, for instance, is often the first to appear on marine propellers. The tip vortex flow problem, largely stimulated by the concern over the hazard presented by the wake of large aircraft, has received much attention. Extensive reviews may be found in expositions by Widnall (1975), Saffman and Baker (1979), Platzer and Souders (1979), and Leibovich (1983). The vortex system is generally sensitive to ambient flow variations and may, sometimes, become unstable. The flow structures of tip vortex can be quite complicated.

This report is mainly concerned with the cavitation inception of tip vortex. Tip vortex cavitation inception is generally found, both from model experiments and ship trials, to be located very near the propeller blade tip. So the present work is confined to the study of vortex flow field formed in the early stages of the roll up processes. The flow field in such case may be largely determined by inviscid roll up considerations.

In the next section, the structure of vortex flow due to roll up of vortex sheet, based on Betz's model (1933), is examined. The derivation essentially follows the work of Moore and Saffman (1973). In the third section, the expression for tip vortex cavitation inception number on marine lifting surface is derived. Some numerical results, based on a modified lifting line theory, are also given. In the fourth section, a method for predicting tip vortex cavitation inception is proposed. Some calculated tip vortex cavitation inception numbers, based on the proposed method, are compared with the experimental data; the results are generally in good agreement. In the last section, some discussions on further developments are given.

Contributed by the Fluids Engineering Division for publication in the JOURNAL OF FLUIDS ENGINEERING. Manuscript received by the Fluids Engineering Division January 11, 1990.

The Inviscid Roll Up and Effect of Viscosity

In Betz's model, each half of the vortex sheet on the lifting surface rolls up into a vortex with circular core, as depicted in Fig. 1, conserving circulation, impulse, and moment of impulse. Moore and Saffman (1973) applied the Betz model to complete the solution for the class of vortex sheets with circulation distribution

$$\Gamma(y_1) = \bar{\Gamma}(y_1)^{1-n} \tag{1}$$

where y_1 is the distance from the tip. These power-law circulation distributions roll up into vortices having the circulation distribution

$$\Gamma(r) = \bar{\Gamma}(\kappa r)^{1-n} \tag{2}$$

with

$$\kappa = 2 - n = \text{compression factor} \tag{3}$$

as determined by the Betz approximation. The tangential velocity distribution is simply given by

$$v(r) = \frac{\Gamma(r)}{2\pi r} = \frac{\bar{\Gamma}}{2\pi}\kappa^{1-n} r^{-n} \tag{4}$$

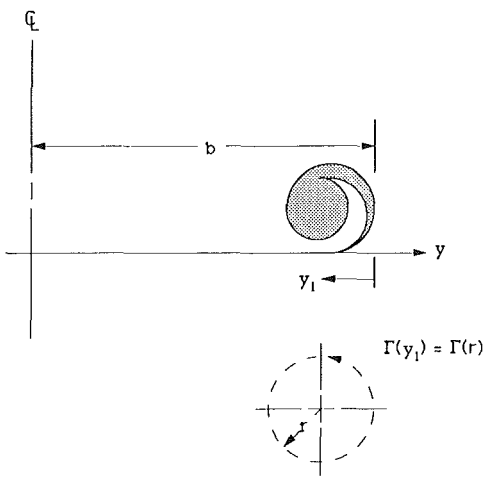

Fig. 1 Illustration of the Betz Roll-up model

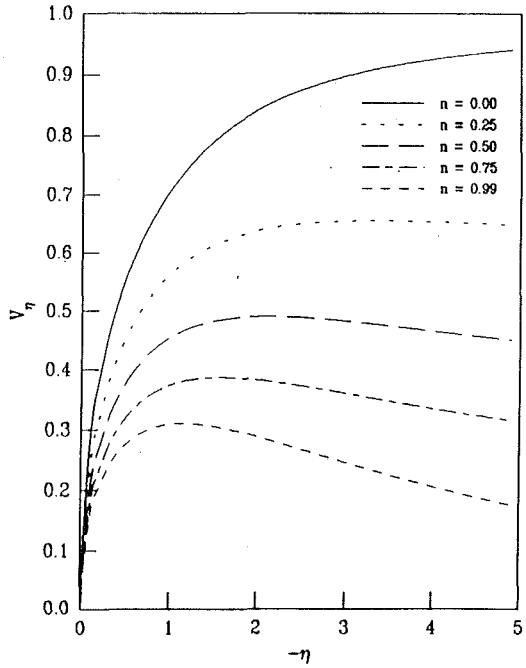

Fig. 2 Values of V_η as function of n

In the region near the tip, the axial gradients can be assumed to be small compared to radial gradients, the momentum equation governing the vortex motion may then be approximated as

$$\frac{1}{\rho}\frac{\partial p}{\partial r}=\frac{v^2}{r} \tag{5}$$

where p and ρ are the pressure and the fluid density respectively. Equation (5) can be integrated to give

$$\frac{\Delta p}{\rho}=\int\frac{v^2}{r}\,dr=-\frac{1}{2n}\left(\frac{\overline{\Gamma}}{2\pi}\right)^2\kappa^{2(1-n)}r^{-2n} \tag{6}$$

Some initial tangential velocity profiles of aircraft vortex wakes, based on the Betz roll theory, have been computed by Donaldson et al. (1974). Except in a small core region, the calculations are shown to be in close agreement with flight data. The tangential velocity, as seen from Eq. (4), is in general singular at the center of the core. The singularity is, in reality, removed by the diffusive action of viscosity. The viscous core can be examined with the aid of unsteady Navier Stokes momentum equation

$$\frac{\partial v}{\partial t}=\nu\left(\frac{\partial^2 v}{\partial r^2}+\frac{1}{r}\frac{\partial v}{\partial r}-\frac{v}{r^2}\right) \tag{7}$$

where t is the time, and ν is the kinematic viscosity of the fluid. Similarity solutions of Eq. (7) have been given by Kirde (1962)

$$v(\eta)=\frac{\overline{\Gamma}}{2\pi}\kappa^{1-n}(\nu t)^{-n/2}V_\eta=\frac{\overline{\Gamma}}{2\pi}\kappa^{1-n}(-4\eta)^{n/2}V_\eta r^{-n} \tag{8}$$

with

V_η = $2^{-n}\Upsilon(3/2-n/2)M(1/2+n/2,\ 2,\ \eta)(-\eta)^{1/2}$
M = hypergeometric function of the first kind
Υ = gamma function
η = $-\dfrac{r^2}{4\nu t}$ = similarity variable

The value of v vanishes at $\eta = 0$ and matches the inviscid solution as $\eta \to -\infty$. The velocity profile V_η for various values of n are shown in Fig. 2. V_η generally rises rapidly to a maximum and then falls slowly to an asymptote. The radius r_0 (with corresponding η_0), at which V_η takes its maximum value, may be regarded as the viscous core radius.

In the present report, the major interest concerns tip vortex cavitation inception which usually occurs very near the lifting surface, the variation in axial flow have therefore been assumed to be negligible. For light or moderately loaded lifting surfaces the solutions given in Eqs. (2), (4), (6), and (8) may provide an adequate description on the flow field of tip vortex near the lifting surface.

Tip Vortex Cavitation Inception

When the local pressure in the tip vortex core reduces to the vapor pressure of the liquid, cavitation generally occurs. The tip vortex cavitation inception number, based on the inviscid approximation (Eq. (6)), may be expressed as

$$\sigma_i=\frac{p_\infty-p^*}{(1/2)\rho U^2}=\frac{p_\infty-p_v}{(1/2)\rho U^2}=-\text{minimum pressure coefficient}$$
$$=\frac{2}{U^2}\int_{r_0}^{\infty}\frac{v^2}{r}\,dr\simeq\frac{1}{n}\left(\frac{\overline{\Gamma}\kappa^{(1-n)}}{2\pi U}\right)^2(r_*)^{-2n}$$
$$=\frac{1}{n}\left(\frac{\overline{\Gamma}\kappa^{1-n}}{2\pi Uc^n}\right)^2(-4\eta_0)^{-n}\mathrm{Rn}^n \tag{9}$$

where p_∞ is the ambient pressure, p_v the vapor pressure, p_* the pressure at $r = r_*$, U is the free-stream speed. In deriving Eq. (9), the maximum tangential velocity used in determining the minimum pressure p^*

$$v(r_*)=\frac{\overline{\Gamma}}{2\pi}\kappa^{1-n}(r_*)^{-n}$$

is assumed to have the value

$$v(\eta_0)=\frac{\overline{\Gamma}}{2\pi}\kappa^{1-n}(-4\eta_0)^{n/2}V_\eta(r_0)^{-n}$$

in which

$$r_0=(-4\eta_0)^{1/2}(\nu t)^{1/2} \tag{10}$$

is the radius of viscous core. For a first approximation, $t = x/U$ (x = distance in the axial direction with origin near the tip), r_0 can then be approximated by:

$$r_0=(-4\eta_0)^{1/2}(\nu x/U)^{1/2}=(-4\eta_0)^{1/2}(x/c)^{1/2}(\nu/Uc)^{1/2}c$$
$$=(-4\eta_0)^{1/2}(x/c)^{1/2}Rn^{-1/2}c \tag{11}$$

with

c = a length parameter, say the chord length
Rn = Reynolds number based on the chosen length parameter = Uc/ν

The value of r_* is then

$$r_*=(-4\eta_0)^{1/2}\mathrm{Rn}^{-1/2}c \tag{12}$$

by requiring $(x/c)^{n/2}$ to be equal to $V_{\eta_0}(-4\eta_0)^{n/2}$.

The span loading for simple lifting surfaces may be expressed as

$$\Gamma=\Gamma_0[(1-y/b)(1+y/b)]^{1-n} \tag{13}$$

where y is the spanwise coordinate, b the semi-span length, and Γ_0 the root (maximum) circulation. The corresponding tip loading is approximately given by

$$\Gamma\simeq\Gamma_0(2y_1/b)^{1-n}=\overline{\Gamma}(y_1)^{1-n} \tag{14}$$

with

$$y_1=b-y\ll b$$

$$\overline{\Gamma}=\Gamma_0(2/b)^{1-n}$$

$$\Gamma_0=(1/2)UcC_L$$

$$C_L=\frac{\text{Lift}}{(1/2)\rho U^2 S}=\text{lift coefficient}$$

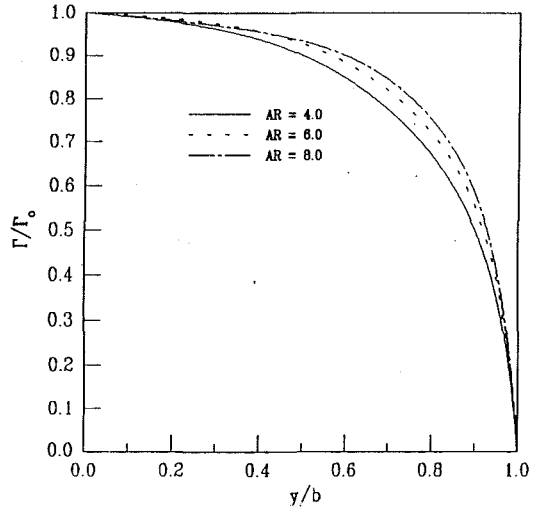

Fig. 3 Circulation distribution for rectangular wing

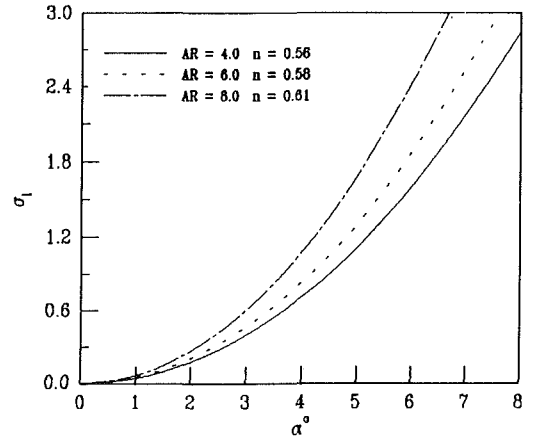

Fig. 4 Cavitation inception number versus angle of attack for rectangular wing, Rn = 10^6

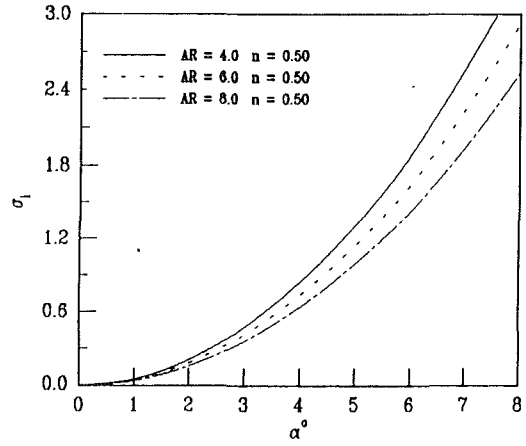

Fig. 5 Cavitation inception number versus angle of attack for elliptic wing, RN = 10^6

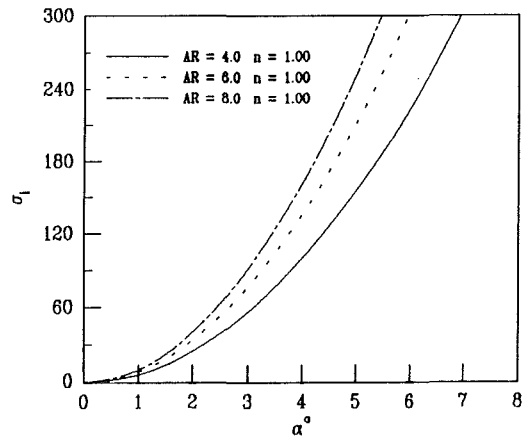

Fig. 6 Cavitation inception number versus angle of attack for rectangular wing, RN = 10^6

c = root chord length

S = wing area

The tip vortex cavitation inception number in this case is then

$$\sigma_i = \frac{1}{n}\left[\frac{C_L}{4\pi}\left(\frac{2\kappa c}{b}\right)^{1-n}\right]^2 (-4\eta_0)^{-n}\mathrm{Rn}^n \qquad (15)$$

The case $n = 0.50$ is for elliptic loading. The value of n generally depends on the planform and aspect ratio of the wing and can be inferred from the circulation distribution. For instances, the values of n for rectangular wings of aspect ratio of 8, 6, and 4 may be deduced from the circulation distributions, shown in Fig. 3, to be 0.61, 0.58 and 0.56, respectively. In Fig. 3, theoretical circulation distributions calculated by De Young and Harper (1948) have been used. Some numerical results for rectangular and elliptic wings of various aspect ratios, and Rn = 1×10^6 are shown in Figures 4 and 5. In these calculations, C_L is assumed to be (based on R. T. Jones' modified lifting line theory, 1941)

$$C_L = \frac{AR}{EAR + 2} C_{L\alpha(2D)}\alpha \qquad (16)$$

where

E = semiperimeter-span ratio
AR = aspect ratio
$C_{L\alpha(2D)}$ = two-dimensional lift-curve slope $\simeq 2\pi$
α = angle of attack

It can be seen that the values of σ_i depend both on aspect ratio and planform. Most authors dealing with the vortex wake problem have taken a Rankine vortex ($n = 1$ or uniform loading) as a starting point. The calculated values of σ_i for $n = 1$ and Rn = 10^6, shown in Fig. 6, are generally two orders of magnitude larger than commonly observed. The Rankine vortex does not provide a realistic model for tip vortex flow.

The tip vortex cavitation inception depends strongly on Reynolds number. In early studies, for instance by McCormick (1962), such dependence is attributed to be the boundary layer effect. The Reynolds number effect on σ_i, in the present treatment, arises largely from fluid diffusion effects.

Method for Tip Vortex Cavitation Inception Predictions

As discussed in the previous section, σ_i may be calculated, if the tip loading distribution characteristics of Γ_0 and n are known. The values of n depend on planforms of lifting surfaces and inflow conditions and can be quite difficult to predict theoretically; it may be more expedient to estimate the values of Γ_0 and n by model experiments.

For lifting wings, Γ_0 is directly related to C_L. By utilizing Eqs. (15) and (16), the value of n, by try and error, can be estimated in conjunction with measured values of C_L and σ_i. To demonstrate, the data of Platzer and Souders (1980) for a cambered wing of elliptic planform with NACA 66-010 sections are compared in Fig. 7 with predictions. In these calculations, corrections due to camber and tunnel wall effects are included and measured lift curve slope is used. The value of n is estimated to be equal to 0.45 and the predicted results are shown to be in good agreement with the experiments.

For propellers, the value of $\Gamma_{o(des)}$ may be assumed to have the form

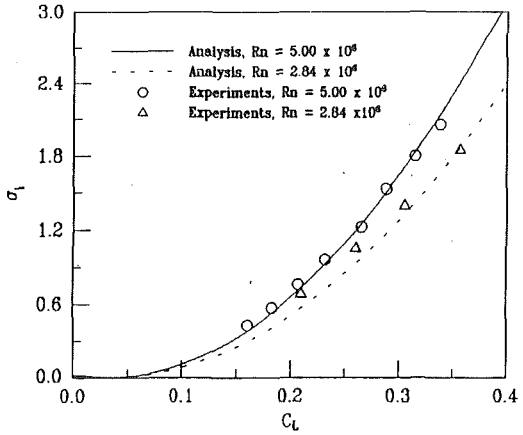

Fig. 7 Comparison with experimental data of Platzer and Souders for a elliptic wing, $AR = 2.55$

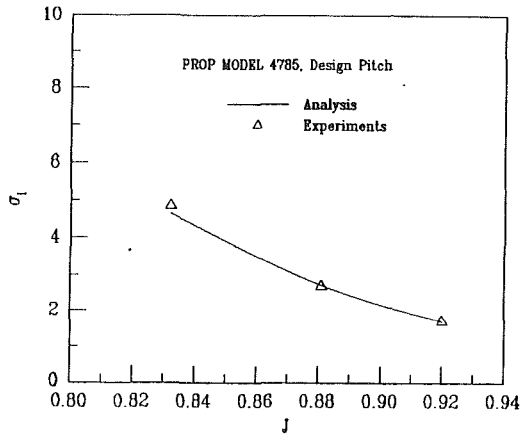

Fig. 8 Comparison with experimental data for propeller model 4785

$$\Gamma_{o(des)} \simeq \frac{VRC_{th}}{Zf_{des}} \tag{17}$$

in which:

C_{th} = $\dfrac{\text{Thrust}}{(1/2)\rho U^2 \pi R^2} = \dfrac{8}{\pi}\dfrac{K_T}{J^2}$ = thrust loading coefficient
f_{des} = a function depending on design loading distribution
J = V/ND = advance coefficient
J_{des} = advance coefficient at design loading distribution
K_T = $\dfrac{\text{Thrust}}{\rho N^2 D^4}$ = thrust coefficient
D = propeller diameter
N = revolutions/second
R = propeller tip radius
V = speed of advance = $U(1 - w_t)$
w_t = wake fraction
Z = number of blades

For a first approximation, the value of Γ_0 may be given by

$$\Gamma_0 \simeq (J_{des}/J)\Gamma_{o(des)} \quad \text{for } J \leq J_{des} \tag{18}$$

Substituting the value of Γ_0 from Eqs. (17) and (18) into Eq. (12) and taking $b = R/2$, the propeller tip vortex cavitation inception number can be approximated as

$$\sigma_i = \frac{1}{n}\left[\frac{4(1-w_t)}{\pi^2 Z}\frac{J_{des}}{J}\frac{K_T}{J^2}\frac{R}{c}\left(\frac{\kappa c}{R}\right)^{1-n} F\right]^2 (-4\eta_0)^{-n}\mathrm{Rn}^n \tag{19}$$

in which $F = 2/f_{des}$

Experimental data for various propellers, measured in the David Taylor Research Center (DTRC) 36-in. Variable Pressure Water Tunnel, have been extensively analyzed. By utilizing Eq. (19) and measured K_T and σ_i, n can be empirically determined. In these analyses, the maximum circulation of the propeller is assumed to occur near 0.7 radius and therefore the values of c and Rn are taken to be

$$c = c_{0.7} = \text{chord length at 0.7 radius}$$
$$\mathrm{Rn} = (Uc_{0.7}/\nu)[1 + (0.7\pi/J)^2]^{1/2}$$

The value of f_{des}, based on the loading distribution of optimum efficiency propellers, is assumed to be

$$f_{des} = (\pi^2/J_{des}) \int_{X_h}^{1} X[(X - X_h)(1 - X^2)]^{1/2} dX$$

with

X = radial coordinate nondimensionalized by propeller tip radius
X_h = hub-tip radius ratio

For an example, the value of n is estimated to be equal to 0.64 for propeller Model 4785. Computed and measured σ_i for propeller Model 4785 at design pitch are given in Fig. 8. The computed results are shown to be in very good agreement with model experiments. It is to be noted that the approximations adopted in these analyses are based on typical propeller series currently in use. It is possible that, for propellers with different design criteria, different approximations may be required.

Independent measurement quantities involved in these experiments and an estiamte of the uncertainty levels of each are listed here. Propeller shaft rotational speed is measured to within about ± 0.1 percent for the values tested. Propeller thrust and torque are determined to within about ± 0.1 percent of the nominal levels. Tunnel pressure can be maintained within 0.025 lb per sq. in. atmospheric at any tunnel conditions. The flow velocity measurements has an uncertainty of about ± 1.2 percent. Gas content, determined as percent of saturation at atmospheric conditions, can be measured to within about ± 3.0 percent. The determination of cavitation inception speeds is dependent on the variance of the tunnel parameters mentioned above and the ability of the individual viewing the propeller to locate each type of cavitation. Results from numerous cavitation experiments with various propellers and test personnel have shown that cavitation inception points can be repeated with a confidence level of 95 percent within an advanced coefficient band of 0.025.

The σ_i measured in model experiments, in conjunction with the estimated values of n, can be used for full scale predictions since the model and ship σ_i are related by

$$\frac{\sigma_{i)s}}{\sigma_{i)m}} = \frac{(\mathrm{Rn}_s)^n}{(\mathrm{Rn}_m)^n} \tag{20}$$

if the scale effect on K_T is assumed to be negligible. Subscripts m and s denote quantities corresponding to model experiment and ship trial respectively. The ship speed for tip vortex cavitation inception in full scale U_s can, in this case, be expressed as

$$U_s = \left(\frac{\rho_m(p_\infty - p_v)_s}{\rho_s(p_\infty - p_v)_m}\right)^{1/(2+n)} \left(\frac{\nu_s}{\nu_m \lambda}\right)^{n/(2+n)} x\, \frac{(1-w_t)_m}{(1-w_t)_s} U_m \tag{21}$$

where λ is the linear ratio. Numerical calculations for U_s/U_m with $n = 0.40$, 0.50, 0.60, and 0.64 have been performed. In these calculations, fluid properties pertinent to model test and full scale trials are

$$\frac{\rho_m}{\rho_s} = 0.973, \quad \frac{\nu_s}{\nu_m} = 1.264,$$
$$\frac{(p_\infty - p_v)_s}{(p_\infty - p_v)_m} = 1.000, \quad \frac{(1-w_t)_m}{(1-w_t)_s} = 1.000$$

The calculations are given in Fig. 9. Also shown in Fig. 9 is the value of U_s/U_m for propeller Model 4785 by full scale ship trials. Good agreement is found between predicted value base

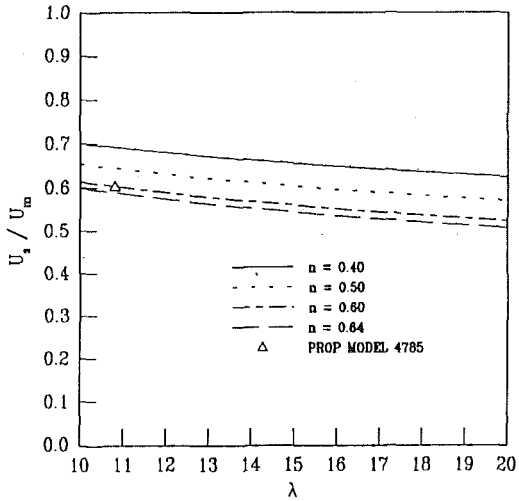

Fig. 9 Scale effect on ship inception speed

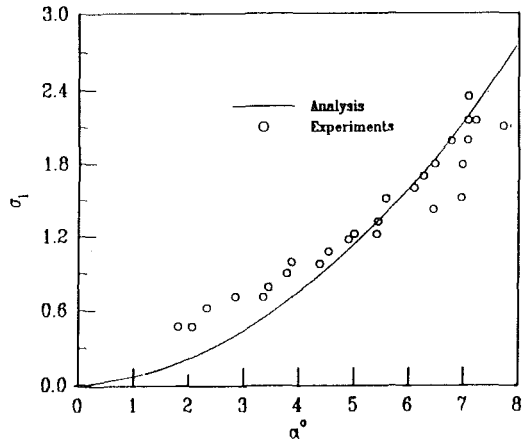

Fig. 10 Comparison with experimental data of McCormick for elliptic wing, $AR = 4.0$

on Model experiments ($n = 0.64$) and trial data, and lends credence to the present approach.

Concluding Remarks

This report presents a method for predicting tip vortex cavitation inceptions on marine lifting surfaces. The tip vortex cavitation inception number varies essentially with the tip loading distribution and therefore depends on geometrical design of the lifting surface and its inflow conditions. Good agreements are generally found between present predictions and experiments.

Predictions, so far, have been made only for high Reynolds numbers flows ($Rn > 2.50 \times 10^6$). At lower Reynolds numbers ($Rn < 10^6$), the value of Γ_0 may be modified considerably by the viscous flow effect. Some data of McCormick for elliptic and rectangular wings with NACA 0015 sections have been analyzed. Theoretical predictions, by using

$C_{L\alpha(2D)} = 2\pi$
$n = 0.50$ for elliptic wing
$n = 0.56$ for rectangular wing

have been performed. The results are given in Figs. 10 and 11. The computed σ_i, in general, are shown to be in qualitatively agreement with data. These data, taken at $Rn = 0.7 \times 10^6$ (transitional flow regime), are, however, quite scattered. Thick NACA 00XX sections are known, especially at low Reynolds numbers, to be susceptible to trailing edge separation. The scattering of these data can therefore be attributed to the effects of transitional flow and flow separation. In full scale operation, the flow on the marine lifting surfaces is generally fully

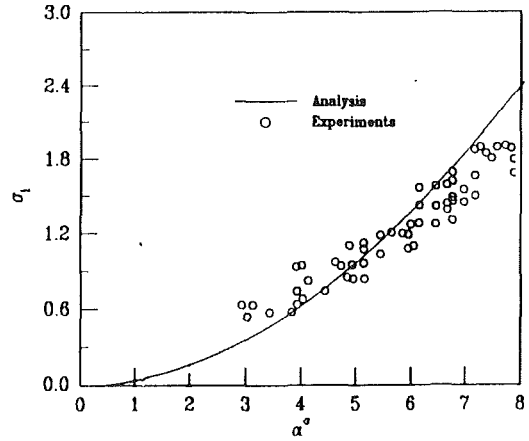

Fig. 11 Comparison with experimental data of McCormick for rectangular wing, $AR = 4.0$

turbulent and may have very small or no flow separation region; therefore, too low Reynolds number model data may not be at all useful for full scale predictions.

With proper lifting surface design, the tip vortex cavitation inception number for a given loading coefficient may be reduced. It is obvious that, in order to delay propeller tip vortex cavitation inception, the values of n and Γ_0 should be minimized. σ_i may also be reduced if the diffusive action of the fluid is increased by artificial means. The optimization depends strongly on the overall performance of the propeller and can be quite complicated. In addition, it is doubtful that the tip loading distribution in non-uniform inflow condition can be accurately determined by existing lifting surface theory. It is clear that, in order to achieve an overall optimal propeller design, extensive systematic theoretical and experimental studies are needed.

Acknowledgments

The work described in this paper was supported by Office of Naval Research under the Applied Hydromechanics Research Program, administered by Code 1504 of David Taylor Research Center. The author would like to acknowledge the benefit of technical discussions with Dr. Michael B. Wilson.

References

Betz, A., 1933, "Behavior of Vortex Systems," National Advisory Committee for Aeronautics Technical Memorandums No. 713.

De Young, J., and Harper, C. W., 1948, "Theoretical Symmetric Span Loading at Subsonic Speeds for Wings Having Arbitrary Planform," NACA TR No. 921.

Donaldson, C. duP., Snedeker, R. S., and Sullivan, R. D., 1974, "Calculation of Aircraft Wake Velocity Profiles and Comparisons with Experimental Measurements," *Journal of Aircraft*, Vol. 11, pp. 547–555.

Jones, R. T., 1941, "Correction of the Lifting-line Theory for the Effect of Chord," NACA TN No. 617.

Kirde, K., 1962, "Untersuchungen uber die zeitliche Weiterntwicklung cines Wirbels mit vorgegebener Anfangsverteillung," *Ingenieur-Archiv*, Vol. 31, pp. 385–404.

Leibovich, S., 1983, "Vortex Stability and Breakdown: Survey and Extension," *American Institute of Aeronautics and Astronautics Journal*, Vol. 22, pp. 1192–1206.

McCormick, B. W. Jr., 1962, "On Cavitation Produced by a Vortex Trailing from a Lifting Surface," ASME *Journal of Basic Engineering*, Vol. 84, pp. 369–379.

Moore, D. W., and Saffman, P. G., 1973, "Axial Flow in Laminar Trailing Vortices," *Proceedings of the Royal Society of London*, Series A 333, pp. 491–508.

Platzer, P. G., and Souders, W. G., 1979, "Tip Vortex Cavitation Delay with Application to Marine Lifting Surfaces," David Taylor NSRDC Report 79/051.

Platzer, P. G., and Souders, W. D., 1980, "Tip Vortex Cavitation Characteristics and Delay on a Three-Dimensional Hydrofoil," *Proceedings of Nineteenth American Tank Conference*, Vol. 2, pp. 989–1022.

Saffman, P. G., and Baker, G. R., 1979, "Vortex Interaction," *Annual Review of Fluid Mechanics*, Vol. 11, pp. 95–122.

Widnall, S. E., 1975, "The Structure and Dynamics of Vortex Filaments," *Annual Review of Fluid Mechanics*, Vol. 7, pp. 141–165.

Journal of Fluids Engineering

Technical Briefs

Oscillatory Fluid Flow Through a Porous Medium Channel Bounded by Two Impermeable Parallel Plates

J. M. Khodadadi[1]

In the absence of the inertia effects, the analytic solution to the fully developed oscillatory fluid flow through a porous medium channel bounded by two impermeable parallel plates is presented. For the limiting case when a highly viscous fluid undergoes slow pulsation in a high porosity medium, the phase lag vanishes and similar velocity profiles are observed. At the other extreme limiting situation, fluid flow near the symmetry plane has a phase lag of 90 deg from the pressure gradient wave. Moreover, the velocity profiles exhibit maxima next to the wall which is similar to the "channeling" phenomenon observed in variable-porosity studies. It is shown that the temporal average of the frictional drag over a period vanishes, indicating no net energy losses due to oscillations.

Nomenclature

a = coefficients of the pressure gradient wave
f = boundary frictional drag coefficient, $4\nu_f \left.\frac{\partial u}{\partial y}\right|_{y=0} / u_{ave}^2$
K = permeability of the porous medium
p = pressure
Re = Reynolds number, $2u_{ave}W/\nu_f$
t = time
u = velocity component in the x-direction
u_{ave} = average velocity
W = channel width
x, y = Cartesian coordinates
α = Stokes number, $(W^2\omega/\nu_f)^{1/2}$
γ = porous medium shape parameter, $(W^2\epsilon/K)^{1/2}$
ϵ = porosity of the porous medium
ν_f = kinematic viscosity of the fluid
ρ_f = density of the fluid
σ_τ = oscillatory amplitude of the frictional drag coefficient
ψ_τ = phase lag of the frictional drag coefficient
ω = angular frequency

Subscripts

osc = oscillatory component
st = steady component

[1]Assistant Professor, Department of Mechanical Engineering, Auburn University, Auburn, AL 36849-5341. Mem. ASME.

Contributed by the Fluids Engineering Division of The American Society of Mechanical Engineers. Manuscript received by the Fluids Engineering Division July 17, 1990.

Introduction

An in-depth knowledge of transport processes through porous media is of great interest in diverse fields ranging from ground-water hydrology, petroleum reservoir modeling to packed-bed chemical catalytic reactors and transpiration cooling. The influence of the inertial forces and solid walls (which are ignored in Darcy's law) on transport processes are known to be marked in the vicinity of the boundary and in high-porosity media, as discussed by Vafai and Tien (1981). Vafai (1984) investigated the effects of variable porosity, presence of a solid boundary and inertial forces in porous media, showing that channeling (velocity showing a maximum near the wall) is observed under these conditions, which leads to enhancement of heat transfer in some cases. Laminar steady fluid flow and heat transfer in a porous medium channel bounded by two parallel plates (Fig. 1) maintained at a constant and uniform temperature was recently studied by Kaviany (1985). Under the assumption of negligible inertia effects, it was observed that heat transfer is enhanced for porous media with large shape parameters. The oscillatory fully developed flow through a porous medium channel has not been studied to date and is presented in this technical brief.

Mathematical Analysis

The fully developed volume-averaged momentum equation for an incompressible fluid flowing through a porous medium with uniform porosity is

$$\underbrace{\frac{\partial u}{\partial t}}_{\text{Local Fluid Acceleration}} = \underbrace{-\frac{1}{\rho_f}\frac{\partial p}{\partial x}}_{\text{Pressure Term}} + \underbrace{\nu_f \frac{\partial^2 u}{\partial y^2}}_{\text{Viscous Term}} \underbrace{-\frac{\epsilon}{K}\nu_f u}_{\text{Darcy Term}} + \underbrace{\frac{F\epsilon^2}{K^{1/2}}u^2}_{\text{Inertia Term}} \quad (1)$$

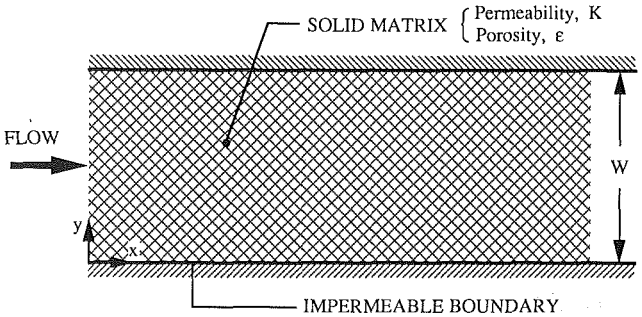

Fig. 1 Schematic of the porous medium channel bounded by two impermeable parallel plates

An analytic solution can be obtained, once the inertia term is ignored in light of the fact that low-speed conditions coupled with high permeabilities are of interest. Moreover, the empirical coefficient, F, is usually very small. For instance, F is about 0.057 for Foametal, which is used in filters, heat exchangers and chemical catalytic reactors. Upon expressing the oscillatory pressure gradient wave in terms of a Fourier series

$$-\frac{1}{\rho_f}\frac{\partial p}{\partial x}=\sum_{n=-\infty}^{\infty} a_n e^{in\omega t} \tag{2}$$

where i is the imaginary unit and applying the boundary conditions at $y = 0$ and $W/2$, the instantaneous velocity is obtained to be of the form

$$\frac{u(y,t)}{u_{\text{ave}}}=-\frac{\sum_{n=-\infty}^{\infty}\left(\frac{a_n}{a_0}\right)\frac{\gamma^3(1+e^{-\gamma})(\gamma^2-in\alpha^2)}{(\gamma^4+n^2\alpha^4)}\left[1-\frac{\cos(2y-1)(-h+ig)}{\cos(-h+ig)}\right]e^{in\omega t}}{[(2-\gamma)-e^{-\gamma}(2+\gamma)]} \tag{3}$$

where g and h are both functions of n, γ, and α. The derivation is similar to the one discussed by Uchida (1956). The instantaneous velocity is composed of two parts, $u(y, t) = u_{st}(y) + u_{osc}(y, t)$. The steady solution corresponds to $n = 0$ and is given by Kaviany (1985). The shape parameter, γ, can be viewed as the ratio of the length scales in this problem, i.e., the channel width (W) and the pore size $(K/\epsilon)^{1/2}$. The oscillatory velocity component is characterized by a nondimensional parameter, α, the Stokes number, which is a measure of the intensity of flow oscillations. At a given location, the phase lag between the nth harmonic of the oscillatory velocity component and the pressure gradient wave is given by $\theta_n = \tan^{-1}(n\alpha^2/\gamma^2)$. Asymptotic expressions for the oscillatory velocity distribution under extreme cases can be obtained.

Case I. When $\gamma^2/n\alpha^2$ is very large (i.e., a highly viscous fluid undergoing slow pulsation in a porous medium with high porosity), the phase lag tends to zero. The oscillatory velocity profile under this condition is similar to that obtained for the steady case, while the magnitude of velocity changes periodically in the same phase with that of the pressure gradient wave.

Case II. For small values of $\gamma^2/n\alpha^2$, it is observed that flow near the symmetry plane has a phase lag of 90 deg from the pressure gradient wave and its amplitude diminishes with increasing harmonics. At the same time, the maxima of the velocity shifts toward the vicinity of the wall.

Finally, the temporal average of the nondimensional boundary frictional drag due to oscillatory flow (f_{osc}) over a period is zero, suggesting that flow oscillations do not have a net effect on friction. More details of the mathematical analysis can be found in Khodadadi (1990) and only the highlights of those findings are presented in this technical brief.

Illustrative Example

In order to demonstrate the general characteristics of the oscillatory flow in porous media, an illustrative example for a sinusoidally varying pressure gradient wave of the form $-1/\rho_f\, \partial p/\partial x = a_0 + a_1 \cos \omega t$ is discussed. The flow field for the limiting cases of $\gamma/\alpha \to 0$ and ∞ were discussed above. Thus, only the oscillatory velocity profiles for the intermediate combinations of γ and α are discussed now. In Fig. 2, the oscillatory velocity profiles for $\gamma = 10$ and $\alpha = 25$ are presented. The maxima of the velocity profiles take place near the solid wall, suggesting that for flow in porous media with fast pulsation, a channeling phenomenon—similar to the one discussed by Vafai (1984) for variable porosity media—can be maintained. The phase lag near the mid-plane for this case is nearly 90 deg. The oscillatory velocity profiles for $\gamma = 10$ and $\alpha = 5$ are shown in Fig. 3. It appears that "channeling" is not present any longer and the phase lag has decreased to about 15 deg everywhere across the flow passage.

The total boundary frictional drag coefficient for the given pressure gradient wave is

$$f=f_{st}\left[1+\left(\frac{a_1}{a_0}\right)\sigma_\tau \cos(\omega t-\psi_\tau)\right] \tag{4}$$

with the steady component being that given by Kaviany (1985), i.e.,

$$f_{st}=\frac{8}{\text{Re}}\frac{\gamma^2[e^{-\gamma}-1]}{[(2-\gamma)-e^{-\gamma}(2+\gamma)]} \tag{5}$$

The variations of the amplitude coefficient (σ_τ) and the phase lag (ψ_τ) for the frictional drag are shown in Figs. 4 and 5, respectively. It is observed that for a given porous medium, the amplitude coefficient decreases and the phase lag increases as the Stokes number is increased. For large values of γ ($\gamma > 30$), σ_τ is equal to unity and the phase lag vanishes. The phase lag of the frictional drag for fast pulsations in porous media with low shape parameters is delayed nearly 45 deg from the pressure gradient wave.

Conclusions

1 The oscillatory fully-developed flow in porous media is shown to be dependent on the porous medium shape parameter, γ and the Stokes number, α.

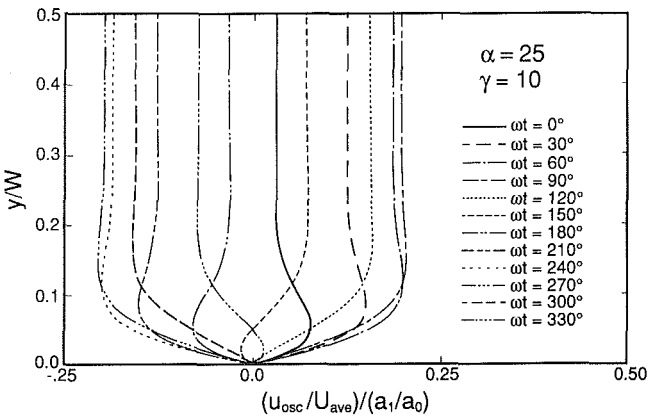

Fig. 2 Velocity profiles at 30 deg phase angle intervals (γ = 10 and α = 25)

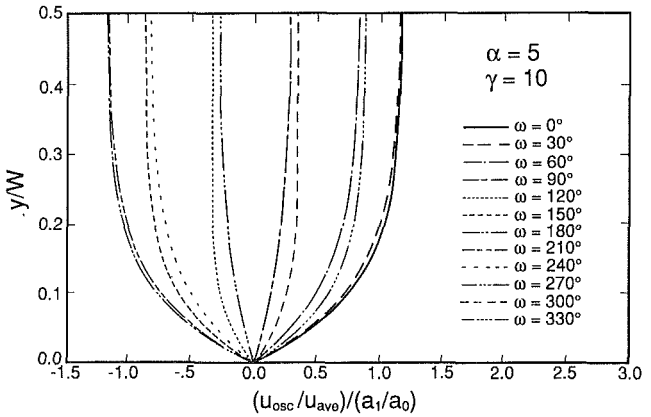

Fig. 3 Velocity profiles at 30 deg phase angle intervals (γ = 10 and α = 5)

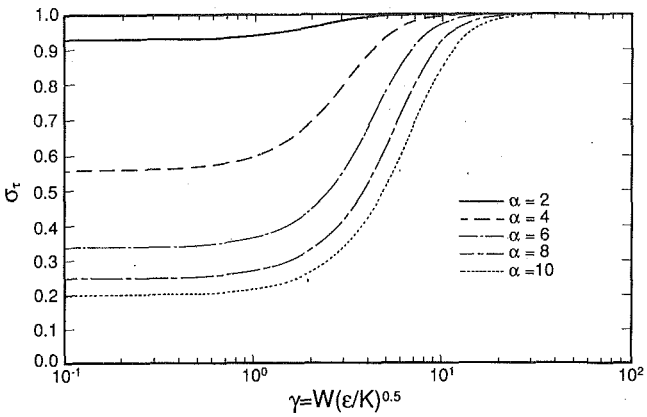

Fig. 4 Amplitude coefficient of the instantaneous frictional drag

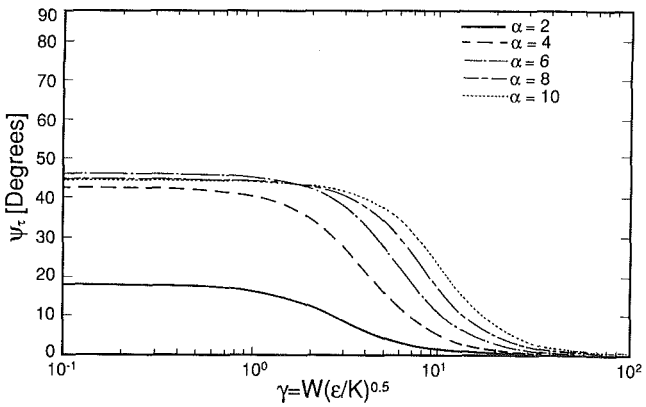

Fig. 5 Phase lag of the instantaneous frictional drag

2 When a highly viscous fluid undergoes slow pulsation in a porous medium with high porosity, the phase lag vanishes and similar velocity profiles in the same phase with that of the pressure gradient wave are observed. At the other extreme limiting situation, fluid flow near the symmetry plane has a phase lag of 90 deg from the pressure gradient wave. In addition, the velocity profiles exhibit maxima in the vicinity of the solid wall, which is similar to the "channeling" phenomenon. The channeling can be maintained for intermediate combinations of γ and α, provided that fast fluid pulsation is present.

3 Over a period, the temporal average of the oscillatory frictional drag vanishes, indicating that flow oscillations do not have a net effect on energy losses in the system, thus making it an excellent candidate for heat and mass transfer augmentation applications.

References

Kaviany, M., 1985, "Laminar Flow Through a Porous Channel Bounded by Isothermal Parallel Plates," *Int'l J. Heat Mass Transfer*, Vol. 28, pp. 851-858.

Khodadadi, J. M., 1990, "Oscillatory Fluid Flow Through a Porous Medium Channel Bounded by Two Impermeable Parallel Plates," *International Symposium on Nonsteady Fluid Dynamics*, FED-Vol. 92, presented at the 1990 ASME Fluids Engineering Spring Conference, Toronto, Ontario, Canada, pp. 243-251.

Uchida, S., 1956, "The Pulsating Viscous Flow Superposed on the Steady Laminar Motion of Incompressible Fluid in a Circular Pipe," *Z. Angew. Math. Phys.*, Vol. VII, pp. 403-422.

Vafai, K., 1984, "Convective Flow and Heat Transfer in Variable-Porosity Media," *J. Fluid Mechanics*, Vol. 147, pp. 233-259.

Vafai, K., and Tien, C. L., 1981, "Boundary and Inertia Effects on Flow and Heat Transfer in Porous Media," *Int'l. J. Heat Mass Transfer*, Vol. 24, pp. 195-203.

Visualization of the Wing-Tip Vortex in Temporal and Spatial Pressure Gradients

X. Liang[1] and B. R. Ramaprian[2]

The evolution of the longitudinal vortex in the near field of a rectangular wing has been visualized using smoke and laser light sheet. The smoke photographs have been used to obtain qualitative and some quantitative information on the effect of small temporal and spatial pressure gradients on the evolution of the vortex in this region. The experiments indicate that even small temporal retardation of the flow can produce a significant increase in the vortex size. This effect becomes larger with increase in retardation, angle of incidence and distance downstream from the trailing edge. Also, vortex "breakdown" was found to occur in many temporal-deceleration experiments. The vortex evolution was, however, found to be relatively insensitive to the presence of small spatial adverse pressure gradients along the flow direction. The study is preliminary in nature and needs to be supported by more extensive quantitative measurements.

Introduction

The study of the evolution of the longitudinal vortex behind a wing and its dynamics in the near field (say within a few chords downstream of the trailing edge) is of considerable interest in fixed and rotary-wing aerodynamics. It has also other possible applications, e.g., in the use of vortex generators for promoting mixing, delaying stall in appliances such as diffusers (Goenka et al., 1989). Some of the recent experimental studies of flow over the wing surface and in the near wake consist of flow visualization. These include the experiments of Francis and Katz (1988) on a hydrofoil in steady flow, and the various studies by Adler and Luttges (1985), Gad-el-Hak and Ho (1986), Freymuth et al. (1985, 1986) and Freymuth (1987, 1989) on wings of rectangular and triangular geometry in unsteady flow. Some quantitative measurements in steady flow in the near-wake region and over the wing surface have been reported by Francis and Kennedy (1974) and more recently by Higuchi et al. (1987).

The present paper is a brief report on some flow visualization studies performed on the trailing tip-vortex from a rectangular wing. Flow visualization was achieved by the use of a combination of smoke and laser light sheet. The smoke photographs were analyzed to obtain some preliminary, but useful quantitative information on the size and growth of the trailing vortex. For the most part, attention has been focussed on the effects of "mild" temporal and/or spatial deceleration of the flow on the evolution of the trailing tip vortex, in the near field downstream of the wing. The work reported can, therefore, be considered as an extension (albeit a modest effort) of some of the previous studies referred to above. It also forms the precursor to some detailed quantitative measurements, proposed to be made in the future, using three-component laser Doppler anemometry (LDA). The flow situations studied are relevant to applications in helicopter rotor blade aerodynamics, cavitation and use of vortex generators as flow controllers in boundary layers and diffusers.

[1]Thermal Engineering Department, Tsinghua University, Beijing, People's Republic of China.

[2]Department of Mechanical and Materials Engineering, Washington State University, Pullman, WA 99164-2920.

Contributed by the Fluids Engineering Division of The American Society of Mechanical Engineers. Manuscript received by the Fluids Engineering Division January 25, 1990.

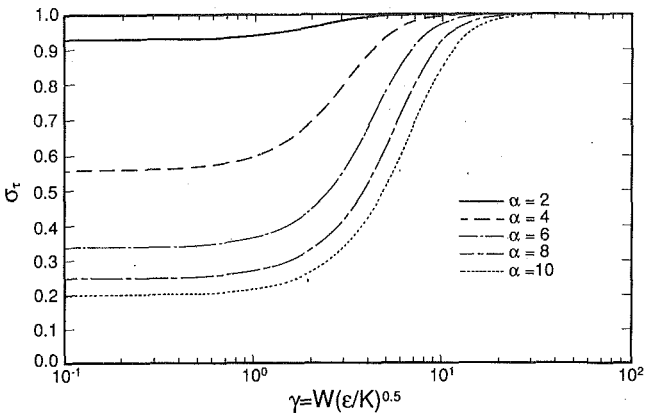

Fig. 4 Amplitude coefficient of the instantaneous frictional drag

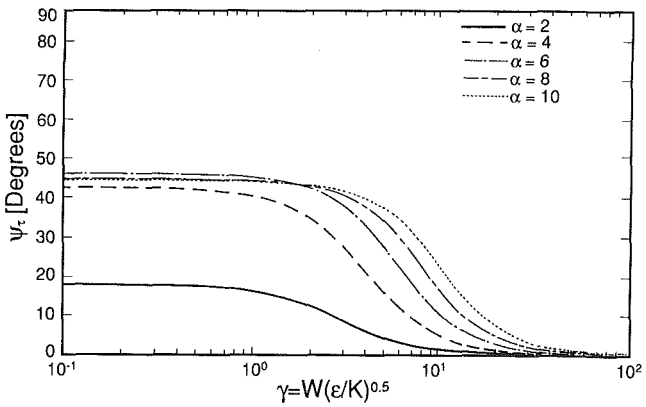

Fig. 5 Phase lag of the instantaneous frictional drag

2 When a highly viscous fluid undergoes slow pulsation in a porous medium with high porosity, the phase lag vanishes and similar velocity profiles in the same phase with that of the pressure gradient wave are observed. At the other extreme limiting situation, fluid flow near the symmetry plane has a phase lag of 90 deg from the pressure gradient wave. In addition, the velocity profiles exhibit maxima in the vicinity of the solid wall, which is similar to the "channeling" phenomenon. The channeling can be maintained for intermediate combinations of γ and α, provided that fast fluid pulsation is present.

3 Over a period, the temporal average of the oscillatory frictional drag vanishes, indicating that flow oscillations do not have a net effect on energy losses in the system, thus making it an excellent candidate for heat and mass transfer augmentation applications.

References

Kaviany, M., 1985, "Laminar Flow Through a Porous Channel Bounded by Isothermal Parallel Plates," *Int'l J. Heat Mass Transfer*, Vol. 28, pp. 851-858.

Khodadadi, J. M., 1990, "Oscillatory Fluid Flow Through a Porous Medium Channel Bounded by Two Impermeable Parallel Plates," *International Symposium on Nonsteady Fluid Dynamics*, FED-Vol. 92, presented at the 1990 ASME Fluids Engineering Spring Conference, Toronto, Ontario, Canada, pp. 243-251.

Uchida, S., 1956, "The Pulsating Viscous Flow Superposed on the Steady Laminar Motion of Incompressible Fluid in a Circular Pipe," *Z. Angew. Math. Phys.*, Vol. VII, pp. 403-422.

Vafai, K., 1984, "Convective Flow and Heat Transfer in Variable-Porosity Media," *J. Fluid Mechanics*, Vol. 147, pp. 233-259.

Vafai, K., and Tien, C. L., 1981, "Boundary and Inertia Effects on Flow and Heat Transfer in Porous Media," *Int'l. J. Heat Mass Transfer*, Vol. 24, pp. 195-203.

Visualization of the Wing-Tip Vortex in Temporal and Spatial Pressure Gradients

X. Liang[1] and B. R. Ramaprian[2]

The evolution of the longitudinal vortex in the near field of a rectangular wing has been visualized using smoke and laser light sheet. The smoke photographs have been used to obtain qualitative and some quantitative information on the effect of small temporal and spatial pressure gradients on the evolution of the vortex in this region. The experiments indicate that even small temporal retardation of the flow can produce a significant increase in the vortex size. This effect becomes larger with increase in retardation, angle of incidence and distance downstream from the trailing edge. Also, vortex "breakdown" was found to occur in many temporal-deceleration experiments. The vortex evolution was, however, found to be relatively insensitive to the presence of small spatial adverse pressure gradients along the flow direction. The study is preliminary in nature and needs to be supported by more extensive quantitative measurements.

Introduction

The study of the evolution of the longitudinal vortex behind a wing and its dynamics in the near field (say within a few chords downstream of the trailing edge) is of considerable interest in fixed and rotary-wing aerodynamics. It has also other possible applications, e.g., in the use of vortex generators for promoting mixing, delaying stall in appliances such as diffusers (Goenka et al., 1989). Some of the recent experimental studies of flow over the wing surface and in the near wake consist of flow visualization. These include the experiments of Francis and Katz (1988) on a hydrofoil in steady flow, and the various studies by Adler and Luttges (1985), Gad-el-Hak and Ho (1986), Freymuth et al. (1985, 1986) and Freymuth (1987, 1989) on wings of rectangular and triangular geometry in unsteady flow. Some quantitative measurements in steady flow in the near-wake region and over the wing surface have been reported by Francis and Kennedy (1974) and more recently by Higuchi et al. (1987).

The present paper is a brief report on some flow visualization studies performed on the trailing tip-vortex from a rectangular wing. Flow visualization was achieved by the use of a combination of smoke and laser light sheet. The smoke photographs were analyzed to obtain some preliminary, but useful quantitative information on the size and growth of the trailing vortex. For the most part, attention has been focussed on the effects of "mild" temporal and/or spatial deceleration of the flow on the evolution of the trailing tip vortex, in the near field downstream of the wing. The work reported can, therefore, be considered as an extension (albeit a modest effort) of some of the previous studies referred to above. It also forms the precursor to some detailed quantitative measurements, proposed to be made in the future, using three-component laser Doppler anemometry (LDA). The flow situations studied are relevant to applications in helicopter rotor blade aerodynamics, cavitation and use of vortex generators as flow controllers in boundary layers and diffusers.

[1]Thermal Engineering Department, Tsinghua University, Beijing, People's Republic of China.

[2]Department of Mechanical and Materials Engineering, Washington State University, Pullman, WA 99164-2920.

Contributed by the Fluids Engineering Division of The American Society of Mechanical Engineers. Manuscript received by the Fluids Engineering Division January 25, 1990.

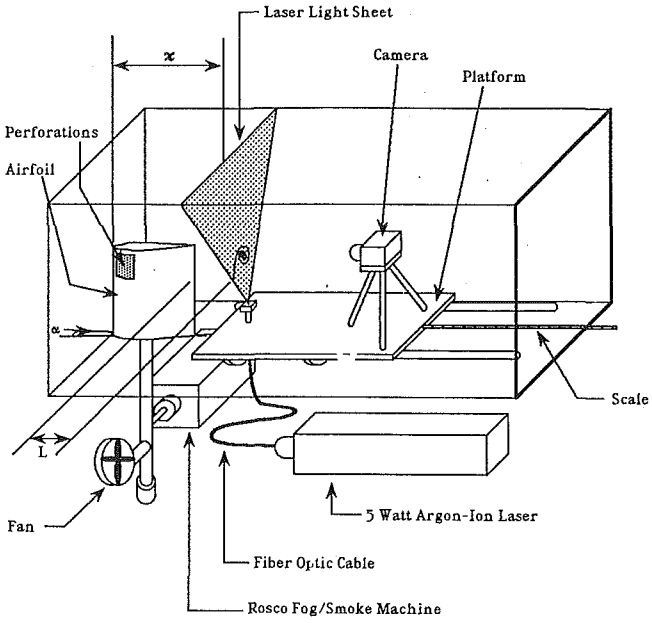

Fig. 1 Experimental arrangement

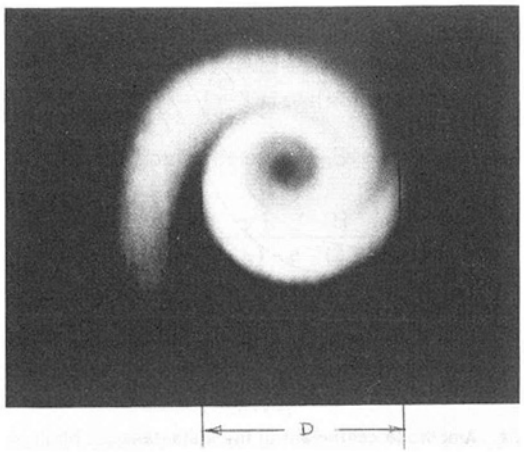

Fig. 2 Photograph of a typical trailing vortex during roll-up

Experimental Conditions

The experiments were conducted in a 1 m × 1 m low-speed wind tunnel. The experimental set-up is shown schematically in Fig. 1. The wing tested was rectangular in planform with a chord (c) of 0.305 m and a semispan of 0.6 m and had a NACA 0015 profile. It was constructed to be hollow. The wing was mounted with its span vertical. The mounting fixture allowed the wing to be set at any angle of incidence (α) in the range ±30 degrees. Smoke produced in a ROSCO Model 1500 Smoke/Fog generator was introduced into the flow through a set of 5 mm diameter holes located near the leading edge on the pressure side of the wing. Smoke particles were illuminated by a laser light sheet of about 1 mm thickness, obtained from a 5-watt argon ion laser. The light sheet was set in a plane perpendicular to the tunnel axis at different distances (L) downstream from the trailing edge of the wing. Photographs were taken with the camera looking upstream towards the wing.

The experiments were conducted at freestream velocities (U) ranging from 4 m/s to 10 m/s. At velocities higher than 10 m/s, the flow could not be visualized very well. The following experiments were performed:

1. Steady flow with zero pressure gradient (ZPG) along the tunnel downstream of the trailing edge
2. Unsteady flow decelerating from a velocity of about 8 m/s to zero, with zero longitudinal pressure gradient downstream of the trailing edge
3. Steady flow with an adverse pressure gradient (APG) along the tunnel (x direction) downstream of the trailing edge
4. Unsteady decelerating flow with the pressure gradient as in 3.

In the second and fourth experiments, the flow was decelerated from a steady velocity of about 8 m/s at approximately constant deceleration, by gradually constricting the inlet of the tunnel fan. The instantaneous tunnel velocity during the deceleration was monitored as a function of time by a hot-wire sensor. Photographs were taken at regular intervals during the deceleration period. This deceleration experiment was repeated several times to obtain the photographs at each of the different longitudinal locations. Two different series of deceleration experiments were performed. In one series (designated as US1), the average deceleration 'a' was about 0.8 m/s^2. In the other series (designated as US2), it was about 1.3 m/s^2. The average decelerations in the two series correspond to "deceleration Reynolds numbers" defined by $R_d \equiv a^{1/2}c^{3/2}\nu^{-1}$ (where ν is the kinematic viscosity) of about 3200 and 4300, respectively. These may be compared with a deceleration Reynolds number of 5200 studied by Freymuth et al. (1986) in their starting-flow tests. Another relevant pressure gradient parameter characterizing the vortex evolution in the near field is β_t defined by ac/U^2. The values of β_t in the two experiments US1 and US2 were about 0.004 and 0.006, respectively.

In the third and fourth cases, the spatial adverse pressure gradient was set up by diverging the top wall of the tunnel at an angle of about 5.5 degrees. The corresponding nondimensional pressure gradient parameter β_x, defined by $(c/U)dU/dx$, was of the order of 0.03. No boundary-layer control was used along the top wall, but there was no indication of any large-scale separation of flow along this wall. Note that even though β_x is quite small, it is still many times larger than β_t. Also, it is reasonable to assume that, under the present experimental conditions in the retardation experiments, the spatial pressure gradient in the tunnel flow remained quasi-steady.

In all the cases, experiments were conducted at several angles of incidence in the range 0–15 degrees. Photographs were obtained at several downstream distances from the trailing edge, generally ranging from 0 to 200 cm. Typical smoke photographs and the quantitative information derived from them are presented and discussed in the following section.

Results and Discussion

Steady Flow in Zero Pressure Gradient. Figure 2 shows a typical smoke photograph obtained in steady flow. The trailing vortex is very clearly seen in these figures. The photograph reveals the presence of two domains; an outer domain in which the vorticity is present in the form of a discrete spiral sheet formed by the rolling up of the plane vortex sheet behind the wing, and an inner domain in which the successive spirals have either merged, or are in the process of merging to form a core.

The manner in which the vortex sheet at the trailing edge rolls up into the longitudinal vortex and attains a fully developed structure is seen typically from the sequential photographs shown in Fig. 3. These pictures correspond to an angle of incidence of 5 degrees and cover the region extending from the trailing edge to about six chord lengths downstream of the trailing edge.

The vortex in the near wake is not axisymmetric. However, a typical length scale for the vortex that can be measured from the smoke photographs with some degree of confidence, is the size D defined arbitrarily as shown in Fig. 2. There was generally no difficulty in determining the outer "edge" of the

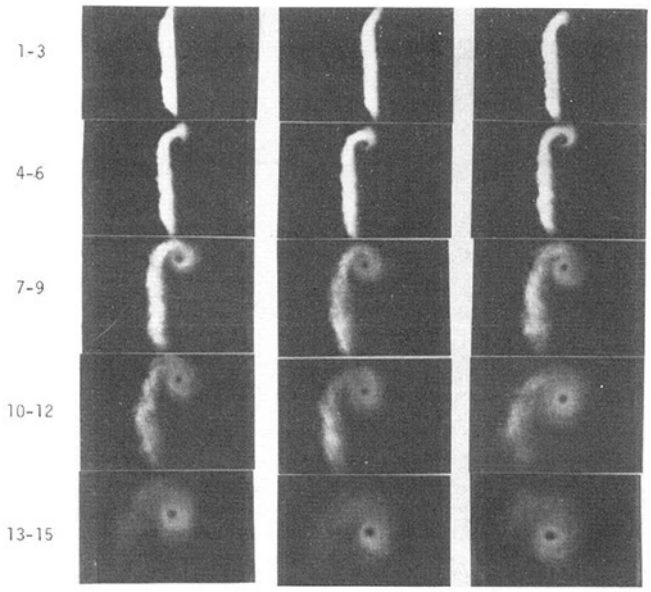

Fig. 3 Sequence of photographs showing vortex development during roll-up α = 5 deg, Re = 144,000. Photographs 1-15 correspond to L = 0, 4, 8, 12, 16, 20, 30, 40, 50, 60, 70, 100, 130, 160, and 200 cm, respectively

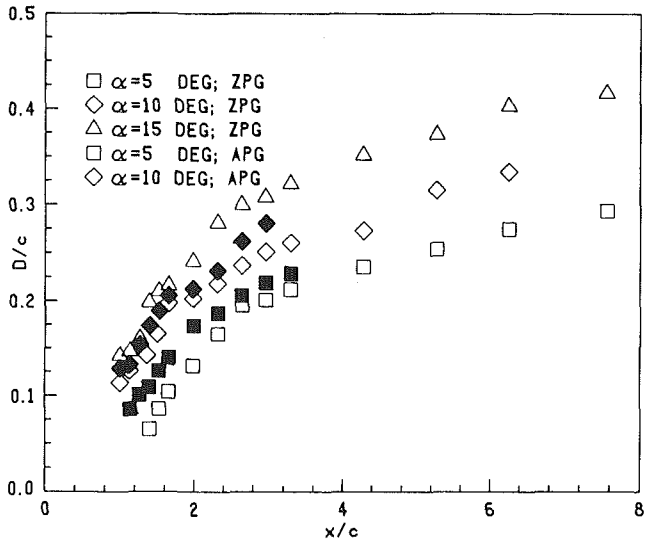

Fig. 4 Growth of vortex size D in steady flow. Reynolds number = 194,000. Results are shown for both ZPG and APG. Uncertainties—x/c: ±0.01, D/c: ±5 percent.

vortex for this purpose (even though the process is somewhat subjective). The uncertainty (scatter) in the estimation of D by this method was found to be typically ±5 percent.

The effect of the angle of incidence on the evolution of the vortex is shown in Fig. 4. These results are for a Reynolds number (Re = Uc/ν) of 194,000, which was the highest Reynolds number studied, but are typical of the results obtained over the (narrow) range of Reynolds numbers studied (80,000–194,000). It is seen that the vortex size increases with angle of incidence. Note that the vortices in all the cases are quite large, with $D \sim 0.1c$ at the trailing edge and increasing ultimately to about $0.3c - 0.4c$, depending on the angle of incidence. The nondimensional size of the vortex at the trailing edge, measured in the present experiments is about the same as that obtained in a towing tank (using fluorescent particles and laser light sheet) by Francis and Katz (1988) on a NACA-66 hydrofoil of aspect ratio 1.5 at similar angles of incidence.

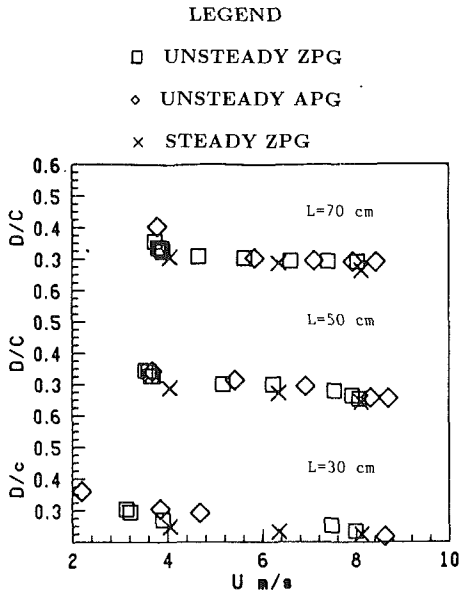

(a) US1 at α = 10 degrees

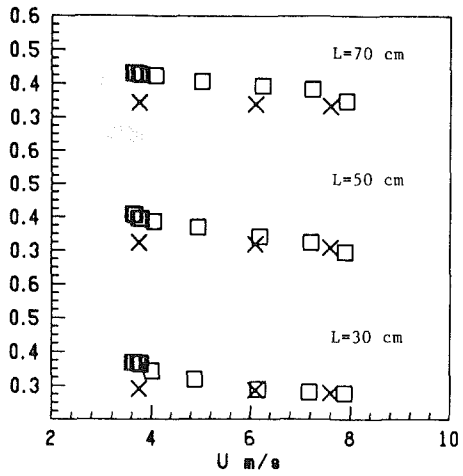

(b) US1 at α = 15 degrees.

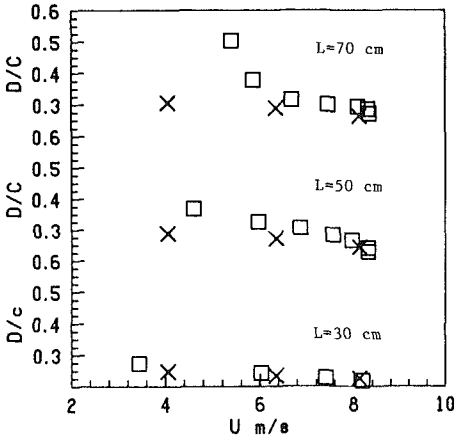

(c) US2 at α = 10 degrees.

Fig. 5 Vortex growth in decelerating-flow experiments. (*a*) US1 at α = 10 degrees, (*b*) US1 at α = 15 degrees, (*c*) US2 at α = 10 degrees. Uncertainties—same as in Fig. 4.

Decelerating Flow. The measured values of the size D as a function of the instantaneous tunnel velocity are shown in Figs. 5(*a*)–5(*c*) for several experiments. The results are shown

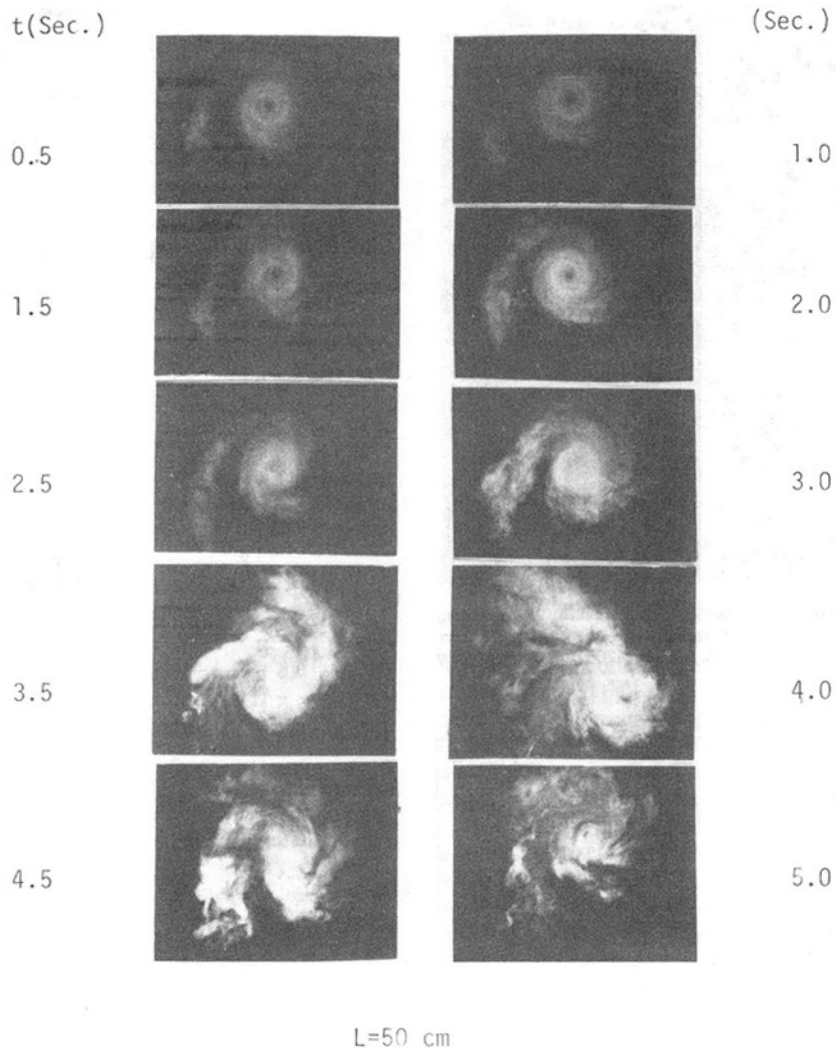

Fig. 6 Sequential photographs from decelerating-flow experiment US2 at α = 10 degrees, showing vortex breakdown

for three downstream locations, L = 30, 50 and 70 cm in the near field ($x/c < 3.3$). The unsteady-flow results are compared, in each case, with those obtained in steady ZPG flow. The latter results can be regarded as corresponding to unsteady flow at *infinitely small* deceleration.

First, it is seen that at the lower value of $\beta_t \approx .004$ and the smaller angle of incidence, namely α = 10 degrees (US1 experiments), retardation of the tunnel flow has practically no effect on the generation and evolution of the vortex. In other words, the vortex dynamics is "quasi-steady." Since the formation of the tip vortex is directly related to the spanwise wing loading, one can conclude that under these conditions, wing loading remains essentially quasi-steady during retardation.

However, the evolution of the vortex departs from quasi-steady behavior at higher angles of incidence and/or higher values of β_t. This is especially noticeable from the results of US2 experiments at L = 70 cm in Fig. 5(b) (for α = 15 degrees and $\beta_t \approx 0.004$), and Fig. 5(c) (for α = 10 degrees, $\beta_t \approx$ 0.006). These figures show that the vortex in the unsteady flow is significantly larger than in the corresponding steady flow. This effect of unsteadiness can be attributed to the possible occurrence of flow separation on the suction side near the trailing edge of the wing. The smoke photographs obtained under these conditions showed a large hole in the center of the vortex, suggesting that flow detachment had probably occurred near the trailing edge. It is known from recent studies (e.g., Simpson et al. 1982) that separated flows and flows close to separation respond strongly to any imposed unsteadiness. Changes in the separation characteristics lead to nonquasi-steady changes in spanwise wing loading, which have a direct effect on the tip vortex size and strength.

In addition to the nonquasi-steady evolution of the vortex, an other interesting phenomenon was observed in the experiments corresponding to Fig. 5(c). In these experiments, the vortex was found to "break down" toward the end of the deceleration period (when the instantaneous tunnel velocity was about 4–5 m/s). No data points are, therefore, shown in Fig. 5(c) for small velocities in such cases. The vortex breakdown phenomenon can be seen from the sequence of photographs shown in Fig. 6. These photographs were taken during one of these tests. These photographs correspond to the downstream location L = 50 cm and were obtained at intervals of approximately 0.5 second starting from the commencement of deceleration. These photographs are typical of those taken at other stations. It is seen that at 3 seconds after the beginning of deceleration, the vortex shows distortions in its spiral geometry and at 3.5 seconds, breaks down completely. Such breakdowns were frequently, but not always, observed at all stations in the experiments at the higher β_t-experiments. The authors feel that these breakdowns indicate the existence of some form of instability associated with the unsteady flow. However, it is possible that these results may, instead, be

arising out of some (unknown) instabilities associated with the smoke-introduction process in unsteady flow. Quantitative information, preferably from LDA measurements, is needed to confirm the present results.

Experiments in Adverse Pressure Gradient. The steady and unsteady-flow experiments described above were repeated after setting up an adverse pressure gradient along the tunnel as described earlier. The smoke photographs did not show any drastic effects of the pressure gradient. Typical results for the vortex diameter in steady flow are included in Fig. 4 and compared with the zero-pressure gradient data. While some consistent increase in the vortex size can be observed at both angles of incidences, the effect of the adverse pressure gradient on the evolution of the vortex is not very significant. Figure 5(*a*) shows some typical comparisons of the results for ZPG and APG experiments in the case of unsteady flows. The tunnel velocity-time history (measured upstream of the wing) was the same in both these experiments. It is seen that even in unsteady flow, the effect of mild spatial adverse pressure gradient is not significant. Similar results were obtained in the experiments at higher deceleration (US2 series) also. In fact, the vortex was found to break down at about the same instant in both the ZPG and APG experiments at the higher deceleration.

Before concluding this paper, it is important to make a few general comments. Some of the present results for the vortex size and growth over the wing tip were found to be in qualitative agreement with those from the earlier studies of Francis and Katz (1988) on a hydrofoil. It should be noted that the quantitative details especially over the wing and in the near wake depend on the wing geometry, wing loading and Reynolds number, as well as the pressure gradient parameters β_t and β_x. Also, flow-visualization results in this region are sensitive to the location and manner of tracer injection. Finally, the present visualizations correspond to a two-dimensional slice across a three-dimensional flow-field and therefore, contain only a part of the complete information. One should therefore exercise some caution while interpreting these results quantitatively.

Conclusions

The present flow-visualization studies have provided useful qualitative and some preliminary quantitative information on the evolution of the wing-tip vortex in steady and unsteady flows. The most important observations, however, are the nonquasi-steady nature of the vortex evolution even at relatively low retardation rates in unsteady flow, and the onset of vortex breakdown under some conditions in unsteady flows. The study has also indicated the relative insensitivity of the vortex evolution process to weak adverse spatial pressure gradients downstream of the wing, in both steady and unsteady flows. These conclusions require final confirmation from velocity/vorticity measurements using preferably nonintrusive instrumentation such as LDA.

Acknowledgment

This work was partially supported by the U.S. Army Research Grant No. DAAL03-87-G-0011. This support is gratefully acknowledged.

References

Adler, J. N., and Luttges, M. W., 1985, "Three-Dimensionality in Unsteady Flow about a Wing," AIAA Paper No. 85-0132.

Francis, T. B., and Katz, J., 1988, "Observations on the Development of a Tip Vortex on a Rectangular Hydrofoil," ASME JOURNAL OF FLUIDS ENGINEERING, Vol. 110, No. 2, pp. 208–215.

Francis, M. S., and Kennedy, D. A., 1974, "Formation of a Trailing Vortex," *Journal of Aircraft*, Vol. 16, pp. 148–154.

Freymuth, P., 1987, "Further Visualization of Combined Wing Tip and Starting Vortex," *AIAA Journal*, Vol. 25, pp. 1153–1159.

Freymuth, P., 1989, "Visualizing the Connectivity of Vortex Systems for Pitching Wings," ASME JOURNAL OF FLUIDS ENGINEERING, Vol. 111, pp. 217–220.

Freymuth, P., Finaish, F., and Bank, W., 1985, "Visualization of Wing Tip Vortices in Accelerating and Steady Flow," *Journal of Aircraft*, Vol. 23, No. 9, pp. 730–733.

Freymuth, P., Finaish, F., and Bank, W., 1986, "The Wing Tip Vortex System in a Starting Flow," *ZFW*, Vol. 10, No. 2, pp. 116–118.

Gad-el-Hak, M., and Ho, C. M., 1986, "Unsteady Vortical Flow Around Three-Dimensional Lifting Surfaces," *AIAA Journal*, Vol. 24, pp. 713–721.

Goenka, L., Panton, R. L., and Bogard, D. G., 1989, "Studies of Flow Patterns in a Diffuser Designed to Generate Longitudinal Vortices," ASME JOURNAL OF FLUIDS ENGINEERING, Vol. 111, No. 2, pp. 111–117.

Higuchi, H., Quadrell, J. C., and Farell, C., 1987, "Vortex Roll-Up for an Elliptical-Loaded Wing at Moderately Low Reynolds Numbers," *AIAA Journal*, Vol. 25, pp. 219–262.

Simpson, R. L., Shivaprasad, B. G., and Chew, Y. T., 1982, "The Structure of a Separating Turbulent Boundary Layer. Part 4. Effects of Periodic Unsteadiness," *Journal of Fluid Mechanics*, Vol. 127, pp. 219–262.